School of Natural Sciences

SπRALS – SOUTHERN HEMISPHERE PARALLAX INTERFEROMETIC RADIO ASTROMETRY LEGACY SURVEY

by

Lucas Jordan Hyland, B.Sc. (Hons)

October 2021

Supervisors:
Prof Simon P. Ellingsen
Dr James A. Green

Submitted in fulfilment of the requirements
for the Degree of Doctor of Philosophy

I declare that this thesis contains no material which has been accepted for a degree or diploma by the University or any other institution, except by way of background information and duly acknowledged in the thesis, and that, to the best of my knowledge and belief, this thesis contains no material previously published or written by another person, except where due acknowledgement is made in the text of the thesis.

Signed: ______________________

Lucas Jordan Hyland

Date: 15/09/21

Signed: ____________________
Lucas Jordan Hyland

Date: 15 / 09 / 21

ABSTRACT

The exact structure of the spiral arms of our home Galaxy, the Milky Way, is an unknown that can be resolved by a higher sampling of parallaxes to high mass star-forming regions from both the Northern and Southern Hemispheres. The Northern Hemisphere has been very well sampled by surveys like BeSSeL and the VERA key project, yet they are unable to observe sources in the southern sky and complete the picture of the Milky Way.

A large maser astrometry project– the Southern Hemisphere Parallax Interferometric Radio Astrometry Legacy Survey or SπRALS , commenced mid–2020 and aims to determine the distances to Southern Hemisphere high mass star formation regions. Using three 12 m and one 30 m radio telescopes spread over Australia, SπRALS will measure parallaxes for dozens of methanol masers in the 3rd and 4th Galactic Quadrant and thereby determine spiral arm properties and Galactic kinematics inaccessible to Northern Hemisphere instruments. However, SπRALS hardware is different and less suited to the task than from the previous large astrometry surveys and effort is required to develop new observing methods and calibration techniques to account for the differences.

The aims of this thesis are as follows:

Firstly, to analyse BeSSeL VLBA data and measure parallaxes for three 22 GHz water masers and one 6.7 GHz methanol maser located in the First Galactic Quadrant. This increases the understanding of Galactic structure and establishes a benchmark for VLBI astrometry for SπRALS to aspire to. I have been able to successfully measure the parallax and proper motion of the methanol maser and 2 of the water masers, and measure proper motions for the last water maser. I then use these results to determine the locations of these all masers in the Galaxy and find all four masers are likely to be in the Perseus spiral arm.

Secondly, to determine a target list for SπRALS by conducting a targeted survey of known Southern Hemisphere 6.7 GHz methanol masers. Significant effort is required to measure parallax and therefore identification of the best targets for each Galactic region is important for time and data quality. I find that there are 53 suitable first targets for SπRALS and a further 29 likely appropriate for future VLBI astrometry. I can determine the compactness of 103 methanol masers, equivalent to a 55% of the surveyed maser where the remaining 45% are too weak or diffuse.

Thirdly, to develop and test inverse MultiView, a phase calibration technique initially conceived for ionospheric calibration. I find that inverse MultiView can be used to model and subtract residual delay errors due to additional effects like residual troposphere and interferometer baseline offsets. I also find that inverse MultiView can outperform traditional techniques and enable target–calibrator separations of at least 8° at 8.4 GHz. With inverse MultiView I can achieve microsecond astrometry on a relatively new interferometric array which will be used for SπRALS , thereby paving the way for future high accuracy Southern Hemisphere maser parallaxes.

ACKNOWLEDGEMENTS

Firstly, I would like to thank Simon. You have always supported me as a supervisor, teacher and colleague, helped me out and been patient. I definitely could have asked for a better person to fulfil the role you did.

I would like to also thank Mark Reid for being a great mentor and teacher. Almost everything I know about this topic comes from you either directly in–person or indirectly through your work.

My parents, Melissa and Glenn, have always been extremely kind and supportive. Thank you so much.

Thank you June, for being my incredible partner and a source of motivation. I could not have finished it all up without you.

Thanks to my colleagues and friends, Patrick, Gabor, Josh, Tiege, Andrew, Andy, Katie, Jayender, Ben, Seb, Magai, Chris, Jamie, Jamie, Cormac, Bev and especially my good friend Jonny.

I would like to acknowledge and thank my examiners, Associate Professor Adam Deller and Dr Mareki Honma, for their comments and suggestions to improve this work.

TABLE OF CONTENTS

TABLE OF CONTENTS

TABLE OF CONTENTS

LIST OF TABLES

LIST OF FIGURES

1 Introduction

The exact structure, number of spiral arms, and size of our home galaxy, the Milky Way, is still largely shrouded in mystery. While numerous optical and radio surveys have determined distances to stars, molecular clouds, or even whole regions, the day is not yet here where we may see the Milky Way in its entirety.

This thesis stands to introduce and discuss a new contender in the pursuit of mapping the Milky Way– the Southern Hemisphere Parallax Interferometric Radio Astrometry Legacy Survey or SπRALS . SπRALS intends to use Very Long Baseline Interferometry to measure trigonometric parallaxes of High Mass Star Forming Regions traced by class II methanol masers. The distances will then be used to infer the otherwise ambiguous spiral structure in the Southern Hemisphere and combine the results from Bar and Spiral Structure Legacy and VLBI Explorer Radio Astronomy projects, which use the same technique from the Northern Hemisphere. Together, the results can produce the most accurate representation of the structure, size, and kinematics of the Galaxy.

In the next few sections, I will discuss the origins of the mystery of Galactic structure and the ongoing resolutions to it, specifically those relevant to the field of astrometry, radio astronomy, and Very Long Baseline Interferometry.

1.1 Structure of the Milky Way

Galaxies are broadly divided into three categories: elliptical, spiral, and irregular. Elliptical galaxies are considered to be 'old', characterised by a low surface brightness, a featureless circular/oblong shape, almost no ongoing star formation and metal–poor stars in a hot dynamic environment (dominated by random radial motion; Hubble, 1936). Spiral galaxies are characterised by an overall flat disk-like structure containing many newly formed stars and a rigid density pattern etched into the face. Spirals also generally contain a central bulge that possesses very similar properties to an elliptical galaxy (Merritt, 1999). Lastly, irregulars are the remaining 2–3% of galaxies which 'lack both rotational symmetry and, in general, dominating nuclei' (Hubble, 1936). Figure 1.1a below is a Hubble telescope image of M51a, the 'Whirlpool Galaxy' and it's near companion NGC5194b. This image shows an example of what a spiral galaxy looks like 'face-on' as seen in visible light. This identification comes from the ability to directly observe the

(a) Pictured here is the typical spiral galaxy: M51 aka the Whirlpool Galaxy and its interacting companion NGC5194b. M51 is approximately 9.5 million parsecs away and is only brought into such clarity by high-resolution Hubble Space Telescope images, which clearly show the fine-detail spiral structure and more importantly, the red hydrogen-α emission in the arms tracing the High Mass Star Formation Regions.

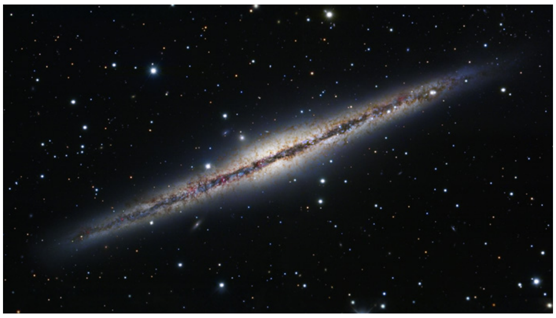

(b) Pictured here is the almost directly edge-on galaxy NGC891 as by the Hubble space telescope. Although NGC891 is very obviously a spiral galaxy due to its flat shape, dust lanes and blue colour, any spiral pattern that it may posses is indiscernible. *Image Credit: Robert Gendler, NAOJ, HST/NASA, BYU, http://www.robgendlerastropics.com/NGC891-Subaru-HST.html.*

density pattern and the relative intragalactic distances. All face-on or partially face-on resolved galaxies in the near universe can be easily classified as such. However, due to our location inside the disc of the Milky Way, our view of the Galaxy is much more similar to that of an edge-on galaxy (much like Figure 1.1b).

1.2 Astrophysical Distances

Distance to celestial objects remains to be one of the most elusive properties for astrophysicists and astronomers to measure, as it the always along the line–of–sight and cannot be measured directly. Distance determination methods can be largely split into model dependant (e.g. standard candles, dispersion, kinematic distances) and model-independent (e.g. trigonometric parallax).

1.2.1 Standard Candles

Most distance measurements rely on indirect or model techniques, such as standard candles – where an object with an approximately known luminosity is measured at a certainly reduced luminosity at Earth, thus giving the distance by the $1/d^2$ dependence (Fernie, 1969). The models are used to approximate the luminosity of the object given other real observables.

For main sequence stars, examples of this are photometric or spectroscopic distances, where the observed intensity of stellar radiation in particular bands or the absorption/emission lines observed in the spectrum infer stellar classification and therefore absolute luminosity. The accuracy of these techniques suffers primarily from dust extinction effects in the line–of–sight reddening of photometric data or insufficient photon counts for spectroscopic data (Carroll & Ostlie, 2017).

Other examples include pulsating stars: Cepheid Variables and RR Lyrae stars. Both stellar classifications have instabilities in their radius and temperature which cause the luminosity to vary periodically, where the period of a variation is proportional to the density. Observations of the stellar period can be therefore used to infer the absolute luminosity and then determine distance (Carroll & Ostlie, 2017).

1.2.2 Dispersion Measure

Another technique worthy of mention is using dispersion measure to determine distance. Dispersion measure is an observable equal to the column density of electrons along the line–of–sight:

$$\mathrm{DM} = \int_0^\infty N dl \qquad \mathrm{pc\ cm^{-3}} \tag{1.1}$$

where l is the line–of–sight distance in pc and N is density of electrons in $\mathrm{cm^{-3}}$. Dispersion measure itself can be measured by using group–velocity arrival times of pulsar pulses at different frequencies. Combining this with a modelled or known electron density N causing the dispersion implies a likely distance (e.g. Cordes, 2004; Yao et al., 2017). Again, modelled techniques suffer from model inaccuracies and ionised regions can additionally corrupt the electron content assumptions (e.g. Sagittarius A*; Reid et al., 1988).

1.2.3 Kinematic Distance

In radio astronomy, kinematic distance estimates are a widely-used and easy method for estimating astrophysical distance, although still plagued by potential systematic uncertainty (Gómez, 2006).

The methodology for kinematic distances is fairly simple: assuming that all matter in the Galaxy rotates in strictly circular paths of the same direction and assuming that the rotational speed is only dependant on the Galactic radius, observed Dopper velocities can be used to infer the Galactic radius. By accounting for projection effects, assuming an *a priori* radius R_0 and rotational velocity Θ_0 of the solar system, distance to objects can be calculated.

Figure 1.2 shows a diagram of kinematic distance estimation: objects rotate clockwise around the Galactic centre with velocity Θ ($\mathrm{km\,s^{-1}}$) given by the rotation curve Ω (in $\mathrm{km\,s^{-1}\ pc^{-1}}$). The

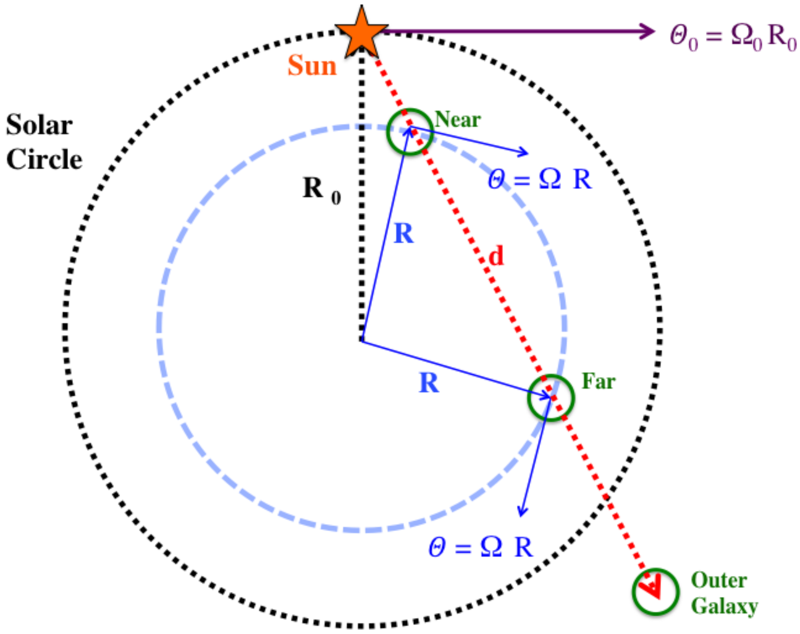

Figure 1.2: Top-down schematic of Galactic rotation.

observed velocity v (in $\mathrm{km\,s^{-1}}$) of an object will be the relative velocity along the line–of–sight:

$$v = \big(\Omega(R)\,R - \Theta(R_0)\big)\,\sin l\,\cos b \tag{1.2}$$

where l, b are the target source's Galactic coordinates and R_0 is the Sun's Galactic radius.

While simple, kinematic distances suffer from a few downsides. Firstly inside the solar circle, two distances (labelled 'near' and 'far'; Figure 1.2) will give the same projected line–of–sight velocity and make the distance ambiguous without further information. In addition, the rotation curve of the Galaxy ($\Omega(R)$) needs to be modelled from distance–velocity data to accurately reflect the Galaxy and therefore needs to be based on another distance estimate.

Finally, any non–circular motion of a gas clump, star, etc. around the Galaxy or internal motions (like water masers with a large velocity spread; Titmarsh et al., 2013) will skew the only measurable quantity. As with any methodology, modelling requires confirmation based on real and direct measurable quantities, which is where the next technique comes in.

1.2.4 Trigonometric Parallax

Trigonometric parallax is known as the 'gold standard' of astronomical distances determinations as it serves as the method by which other distance techniques and standard candles can be calibrated. The technique is geometric, direct and requires no assumptions about luminosities, temperatures or intermediate environments (like dust extinction, electron content).

As the Earth orbits around the Sun, it sweeps out a well-defined ellipse. Parallax is the change in relative angular displacement of any object due to this motion measured with respect to a

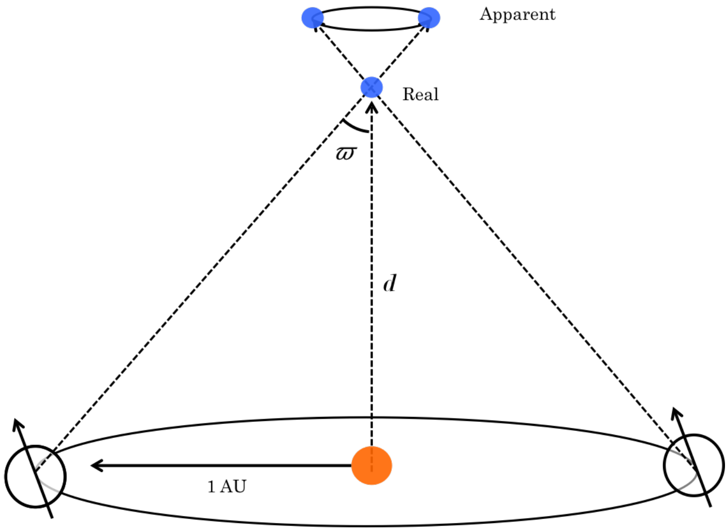

Figure 1.3: Simplified schematic of trigonometric parallax for a target source very close to the North Ecliptic Pole. The parallax ϖ is half the total angle subtended by the Earth (black circle with arrow showing North Pole) and the source (blue dot) as it orbits the Sun (orange circle) when $d \gg 1\,\mathrm{AU}$ relative to some stationary background.

fixed reference point (Figure 1.3). The reason trigonometric parallax (henceforth just 'parallax') is a considered model-independent technique is that the Earth's orbit around the Sun is known extremely precisely.

If the object is d parsecs (pc) away from the Sun, then the parallax ϖ it exhibits will be:

$$\varpi = \frac{1}{d} \tag{1.3}$$

in units of arcsecond (as). The definition is actually the reverse– an object that exhibits a PARallax of 1 arcSECond is 1 PARSEC away.

Friedrich Wilhelm Bessel measured the first parallax to the star 61 Cygni in 1838 of $\varpi = 313.6 \pm 20.2$ mas, which implies a distance of $3.19^{+0.47}_{-0.36}$ pc and within error of the more recent values from *Gaia* of $\varpi = 286.1457 \pm 0.059$ mas (Gaia Collaboration et al., 2018). Not only does this illustrate the accuracy of the parallax technique, but also the large increase in precision that has been achieved over the previous 1.5 centuries (~ 2.5 orders of magnitude). For reasons that I will explain soon, trigonometric parallax techniques have an upper limit on the error that allows meaningful distance determination, so this increase in precision is very important for distant targets. The parallax precision is very much linked to how accurately the position of an object can be determined at each epoch and for an unresolved object, this is proportional to the observing instrumentation resolution. The highest angular resolution and therefore positional accuracy that can be regularly achieved is with Very Long Baseline Interferometry (VLBI), however, for reasons I will discuss in Chapter §2 this can typically only be realised when the target is unresolved. For this reason and others, many of the best targets for VLBI astrometry are masers.

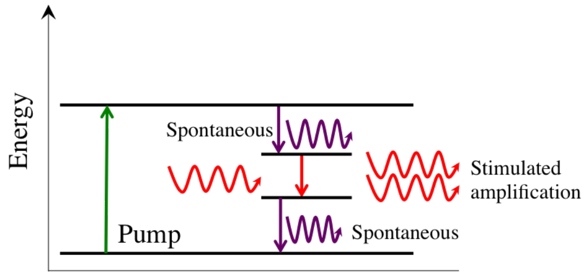

Figure 1.4: Simplified schematic of maser action. The molecule is excited by some pumping mechanism (green) to a higher energy state. Spontaneous de-excitation can occur at some transitions (purple), but at some energy levels spontaneous emission is unfavourable and the molecule remains in a metastable state. Background radiation can stimulate de-excitation, resulting in amplification (red).

1.3 Masers

Astronomical masers (originally MASER: Microwave Amplification by Stimulated Emission of Radiation; colloquially *noun:* maser(s), *verb*: masing, to mase, *adjective*: masable) are physical phenomena that occur in specific conditions in the interstellar medium. While masers predate lasers in laboratory conditions (Gordon et al., 1955, vs. 1960 by T. H., Maiman), they both predate observations of astrophysical masers. The first astrophysical maser discovery did not occur until the '60s, with the OH species around 1.6 GHz. This discovery can be best attributed to Weaver et al. (1965) who was the first to spectrally resolve the emission and noted the clear departure from local thermodynamic equilibrium (LTE) and now characteristically small line–widths.

In modern astrophysics and astronomy, masers predominantly fall into two areas; analysing maser spectra and multiple transitions infer environmental conditions like magnetic fields, local thermodynamics, stellar environments or star-forming regions; and using masers to determine kinematics including outflows, proper motions, Galactic rotation and trigonometric parallax.

1.3.1 Theory

Whereas much emission at radio–frequencies for many molecules occurs via spontaneous transitions and can be related to the statistical thermal temperature of the environment, maser emission is due to unmitigated stimulated emission along the line of sight and are therefore very luminous and highly beamed compared to the latter. The initial trigger for masing is some mechanism that excites a molecular species, called the 'pump'. The nature of the pumping can be anything that can provide adequate energy to excite the molecule into a transitional path containing a maser step. Due to a departure from LTE in the environment, the molecular species is unlikely to undergo damping collisions that might otherwise partition the energy. In addition, the masable step normally has some selection rules that make spontaneous emission from the upper level 'forbidden'. This leads to the molecule having an over–representative population in this higher energy level that is inherently unfavourable – called a population inversion. When a suitable background source is introduced, stimulated emission occurs and all the molecules along the line of sight emit largely coherently – the maser. As long as the rate of pumping is greater than the rate of stimulated emission and much greater than the rate of spontaneous emission, population inversion is maintained and the maser can and will persist.

While the background source can be many different phenomena– spontaneous emission from the molecules themselves, Cosmic Microwave Background radiation or some other source of continuum emission, the primary categorical variable that distinguishes masers from one another

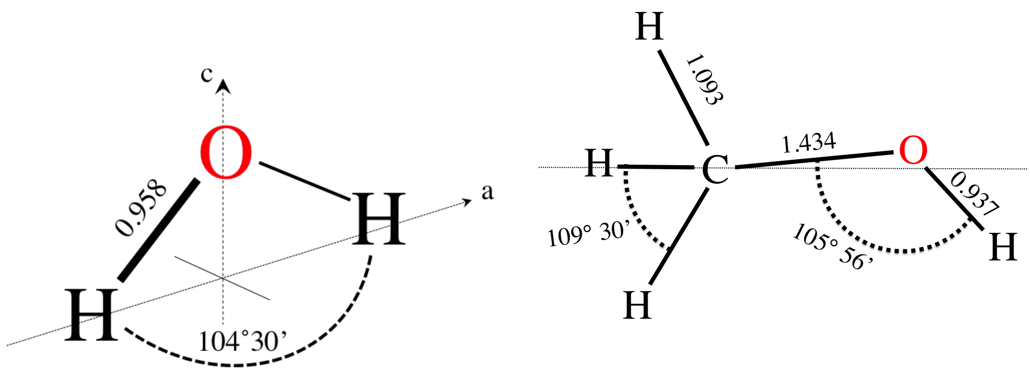

(a) Water H_2O **(b)** Methanol CH_3OH

Figure 1.5: Molecular structure as obtained from microwave spectroscopy. Bond lengths are in angstroms (Å).

is the pumping mechanism. The two types of maser that are typically discussed are collisionally or radiatively pumped – one originating from excitation by molecules in a dense or shocked gas environment, the other from suitably energetic constant sources of radiation.

The masers that will be discussed here originate from rotational transitions, the energy of which are determined by the moment of inertia of the molecule and the various possible modes. While this will be briefly discussed below, both Townes & Schawlow (1955) and Gray (2012) are excellent sources for more theoretical, technical and in-depth further reading.

1.3.2 Water

Water is an asymmetric top and has three axes of rotation. It also has three independent vibrational modes of the hydrogen atoms– two stretches and one bend, where only the bend contributes to the energy structure in space and especially at radio frequencies. Therefore rotational energy levels of water are given as $J_{K_a\,K_c}$ where J is the total angular momentum and K is the angular momentum component in the a and c directions (Figure 1.5a). Lastly, water can come in two sub-species – ortho: where the nuclear spins of the two hydrogens are parallel or para: where the spins are anti-parallel. Only even–even levels exist in para–H_2O and even–odd for ortho–H_2O (Figure 1.6).

The strongest and most prominent maser transition known is the $J_{K_a K_c} = 6_{1\,6} \rightarrow 5_{2\,3}$ 22.2 GHz transition of ortho–H_2O, first detected by Cheung et al. (1969). This transition is associated with early-stage star formation, where the equatorial accretion onto a Young Stellar Object (YSO) leads to molecular outflows from the poles. These molecular outflows impact the ambient interstellar medium, causing shocks that collisionally pump the water masers (Gray, 2012).

I discuss and measure proper motions and trigonometric parallaxes to 22.2 GHz water masers in Chapter §3.

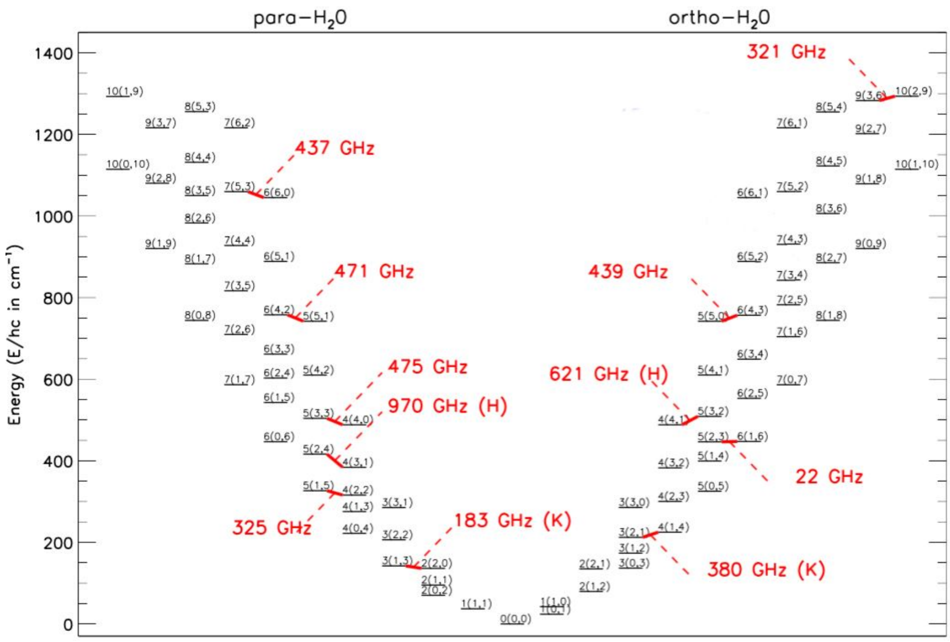

Figure 1.6: Lowest rotational energy levels $J_{K_a K_c}$ for the ground vibrational state of water. **Red:** Common masing transitions and those observed by Kuiper Airborne Observatory (K) and *Herschel* (H) – The most relevant to analysis and discussion in this thesis being the $J_{K_a K_c} = 6_{1\,6} \rightarrow 5_{2\,3}$ 22.2 GHz transition. Adopted from Figure 1. Neufeld et al. (2017).

1.3.3 Methanol

The physics of methanol masers is rather complex due to methanol being a 6–atom molecule and it being an asymmetric top with hindered internal rotation. However, due to the energy levels that can be accessed in an interstellar medium only the lowest–energy vibrational–torsional quantum state is typically considered. Within this, the slightly asymmetric nature of methanol leads to the torsion of the −OH tail group about the CH_3 bond to be split into 2 levels, a non-degenerate A (+ or − due to parity) and degenerate E. These two types of methanol have slightly different orientations of the −OH group relative to the CH_3 group and therefore a different moment of inertia. As such the $^{\pm}A$ and E have different rotational energy levels and transitions (Figure 1.7).

The strongest transition for methanol and the second strongest maser transition known is the $J_K = 5_1 \rightarrow 6_0\, A^+$ transition at 6.66851928 GHz (Menten, 1991b). Methanol masers are divided into two classes based on the source of pumping – collisional class I and radiative class II (Batrla et al., 1987), where the 6.7 GHz transition is class II and (to date) unambiguously associated with sites of HMSF (Ellingsen, 2006; Breen et al., 2013).

Class II maser association with HMSFR is explained via interaction between the ionised region (the HII region) around a high–mass star and surrounding or interior the gas/dust. The current mechanism is that dust down-converts the ionising UV radiation to IR frequencies, which then pump the masing transitions (Gray, 2012).

I discuss and measure a trigonometric parallax to a 6.7 GHz methanol maser in Chapter §3 and

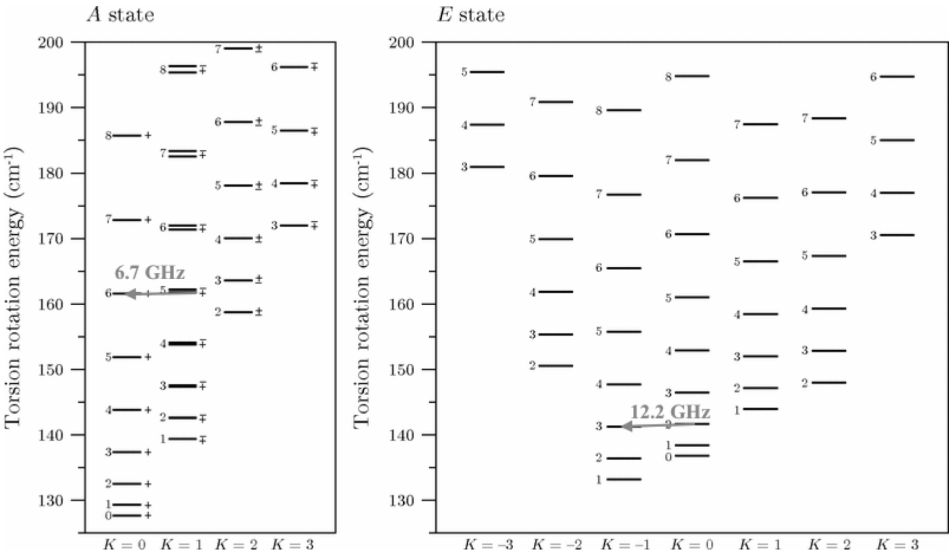

Figure 1.7: Lowest rotational energy levels J_K for the ground vibrational–torsional state ($v = 0$) of E and A–type methanol Jansen et al. (2011). Labelled are the $J_K = 5_1 \rightarrow 6_0\,A^+$ 6.7 GHz and $J_K = 2_0 \rightarrow 3_{-1}\,E$ 12.2 GHz transitions relevant to analysis and discussion in this thesis.

model their spatial structure and compactness in Chapter §4.

Other masers, 12.2 GHz class II methanol, OH and SiO masers are mentioned in passing throughout this thesis but are otherwise not relevant for discussion here.

1.4 SπRALS

1.4.1 Mapping the Milky Way

When considering the structure of the Milky Way, one must first consider the primary issue: that we have a limited perspective of its structure from our position inside it. Figure 1.8 is that perspective, the Galaxy as a projection on a sphere, with no immediate way to determine the 3D structure.

Although objects can be theoretically resolved into their 2D angular separations and angular sizes with higher resolution telescopes, the absolute sizes or distances of objects along the same line of sight remain impossible to directly observe. In addition, the derived angular sizes and separations are meaningless without a reference scale (standard ruler).

While kinematic distances or dispersion measure techniques add a 'depth' axis which can be converted into distance, trigonometric parallax realises the 3D motion and structure of the Galaxy and use that to measure the distance. Therefore trigonometric parallax is the ideal candidate for distance estimates inside the Milky Way, however, it was not until the last few decades that optical or VLBI astrometry could achieve the precision necessary to make it an independent mapping tool on the Galactic scale.

Perhaps the earliest quantitative maps of the Milky Way were produced in the mid-'50s, with

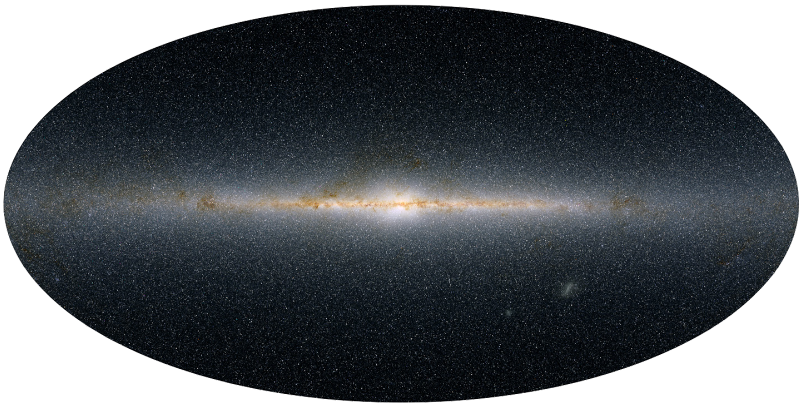

Figure 1.8: Mollweide projection of the entire sky as seen by the Two Micron All-Sky Survey (2MASS). The projection is centered on the Galactic Center, taken to be Sagittarius A*. This point of view represents how the sky appears from the Earth in the Galactic Coordinate system with the centre of the image being $(l, b) = (0°, 0°)$. *Atlas image mosaic courtesy of 2MASS/UMass/IPAC-Caltech/NASA/NSF.*

the first complete map by Oort et al. (1958). This work used the emission at 21 cm (due to the spin inversion of neutral hydrogen) to trace out the density distribution of neutral hydrogen throughout the Galactic system. The immediate observation was that the bulk of the neutral medium was confined to a flat disk approximately 220 pc thick. Distances were approximated using kinematic distance techniques and projection of the 21 cm emission/absorption revealed rudimentary spiral structure (see Figure 1.9).

Oort details the nomenclature of some arms: Orion (containing the Sun), Perseus (outside the solar circle), and Sagittarius (inside the solar circle) and to some extent the 3 kpc arm. Although the names of these arms slightly changed over time, the general locations and associations remained the same. This work stands out as the grounding influence on determinations of Galactic structure, however, numerous problems (many outlined by Oort himself) meant that the spiral arms could not be determined with any accuracy using this method.

Following this, perhaps the next notable chapter begins with Georgelin & Georgelin (1976) (G&G1976). One of the initial works that outlined a model for the spiral structure of the Milky Way, G&G1976 served as a template for many further works. At the time, radio recombination lines from ionised hydrogen and radio molecular lines had only recently been discovered and extensively observed, in addition to optical data of HII and OB stars in the Southern Hemisphere.

In G&G1976, a model of Galactic rotation was initially established by measuring the radial velocities of 151 optical HII regions and spectrophotometric distances to their respective exciting stars. Stellar distances (via spectroscopic parallax) were used wherever they were available, however, when they were unavailable, kinematic distances were calculated using the rotation models derived. Kinematic distance ambiguities were individually removed with reasonable assumptions pertaining to whether the HII region was optically observed (likely near) or not (likely far) in addition to the absorption of lines at a higher velocity (far) and vice versa. Combining the optical results with the radio results, a picture of the Galaxy was formed (Figure 1.10). Assuming that the high-excitation HII regions were of higher importance ('brilliant and extended') and hence more readily trace spiral structure (like seen in external galaxies), 80% of the thus-defined HII regions fell along two symmetric pairs of arms with a pitch angle of 12°.

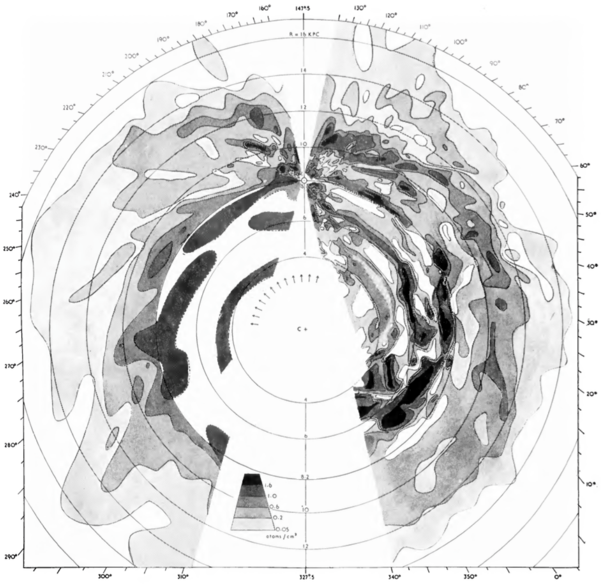

Figure 1.9: Figure 4 from Oort et al. (1958). Original caption: *Distribution of neutral hydrogen in the Galactic System. The maximum densities in the z-direction are projected on the galactic plane, and contours are drawn through the points.*

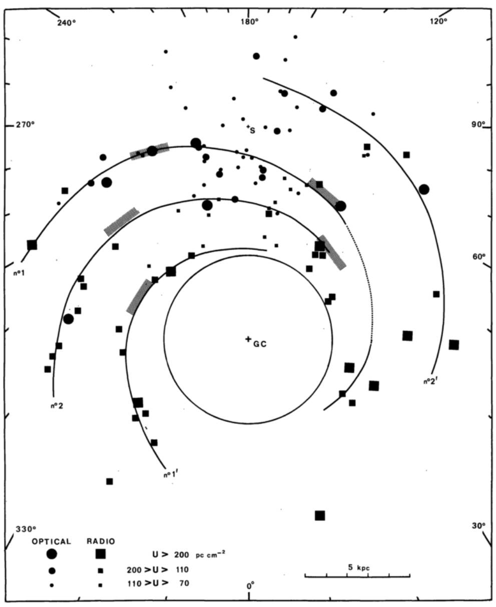

Figure 1.10: Figure 11 from Georgelin & Georgelin (1976). Original caption:
Spiral model of our Galaxy obtained from high-excitation-parameter H II regions (U > 70 pc cm^{-2}); the resulting spiral pattern has two symmetric pairs of arms (i.e for altogether). No. 1 Major arm: Sagittarius-Carina arm*; No. 2 Intermediate arm;* Scutum-Crux arm*; No. 1'. Internal arm:* Norma arm*; No 2'. External arm:* Perseus arm. *Hatched areas correspond to intensity maxima in the radio continuum and in neutral hydrogen.*

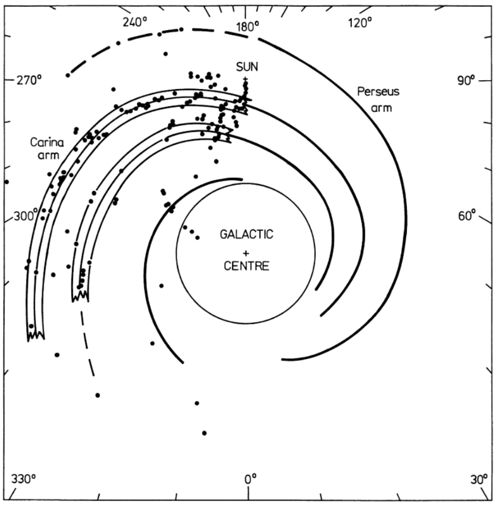

Figure 1.11: Figure 5 Caswell & Haynes (1987). Original caption: *Spiral pattern delineated by* HII *regions in the Galaxy. Individual* HII *regions from the present work are shown only if there is no distance ambiguity. Two segments of spiral arms derived from the present work are shown with a thickness 1 kpc. . . . .*

In a similar vein, Caswell & Haynes (1987) used observations of HII regions traced by radio recombination lines to map the Southern Hemisphere, calculating kinematic distances and resolving ambiguities with techniques including HI absorption. While the authors had collected independent data, they found good agreement with Georgelin & Georgelin (1976) and provided a more refined map of the Southern Hemisphere arms (Figure 1.11).

While it is very difficult to determine spiral structure from optical data due to extinction in the plane, Galactic structure and kinematics can still be determined. In addition, parallax distances to stars can refine models for photometric and spectroscopic distances. To this end, there are two important surveys in the optical regime.

Hipparcos (HIgh Precision PARallax COllecting Satellite) was an astrometry satellite launched by the European Space Agency (ESA) in 1989 and continued operations until 1993. *Hipparcos* had a median astrometric accuracy of $\Delta\theta = 0.8\,\text{mas}$, allowing distances of objects (primarily stars) to be determined up to $\sim 125\,\text{pc}$ from the Sun (to 10% uncertainty; Perryman et al., 1997). In total, *Hipparcos* reported astrometry for $\gtrsim 115000$ stars in the local Galaxy.

Gaia is ESA's space astrometry mission – an optical astrometry satellite capable of measuring absolute positions of stars to an accuracy of between $\gtrsim 4 - 20\,\mu\text{as}$ (depending on magnitude and band; Perryman, 2002). Launched in 2013, *Gaia* is the direct successor to *Hipparcos* and will end its mission sometime after 2022, after which time it is expected to have measured astrometry for over $\sim 1 \times 10^9$ stars.

1.4.2 BeSSeL and VERA

Finally, I would like to discuss the topic most relevant to this thesis: VLBI measurements of water/methanol trigonometric parallax. Class II methanol masers and 22.2 GHz water masers reliably trace HMSFR, which are only found in spiral arms. Accurate and precise distances to these masers via trigonometric parallax, therefore, trace the host HMSFR, which in turn signposts the distance to the over-densities giving rise to them: the spiral arms.

Bar and Spiral Structure Legacy (BeSSeL) survey was a US National Radio Astronomy Organisation (NRAO) Very Long Baseline Array (VLBA) large project. The core aim of BeSSeL was to

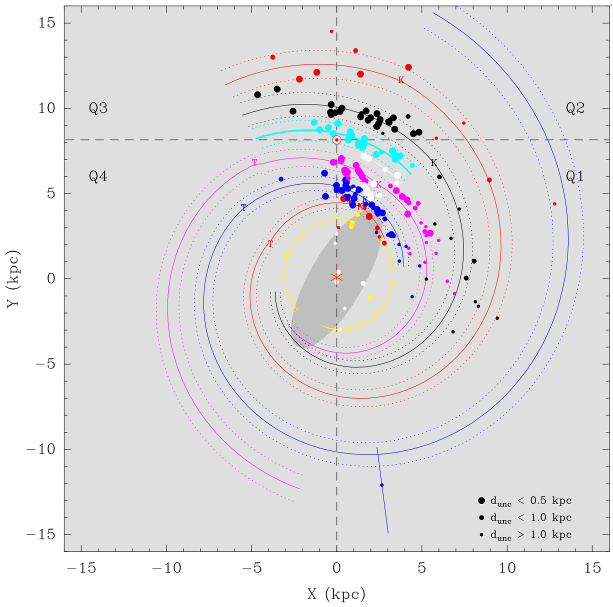

Figure 1.12: Figure 1 from Reid et al. (2019) including BeSSeL and published–VERA parallaxes. Plane–view of the Milky Way where Galactic rotation is clockwise. Spiral arms are fit to inverted parallaxes (dots: size inversly proporitonal to distance uncertainty)– **Cyan:** Local arm; **blue:** Scutum–Centaurus-OSC arm; **black:** Perseus arm; **purple:** Sagittarius-Carina arm; **yellow:** 3 kpc arm(s); **red** Norma–Outer arm; **white:** unclear/spur.

map the Northern Hemisphere spiral structure of the Milky Way via trigonometric parallaxes of 22.2 GHz water and 6.7 GHz/12.2 GHz class II methanol masers (Brunthaler et al., 2011; Reid et al., 2009a, 2014, 2019). The VLBA consists of 10 × 25 m radio telescopes with a maximum baseline of ~ 8600 km. The long baselines combined with well-calibrated, optimal sampled data allowed an expected astrometric accuracy $\Delta\theta \sim 10$ μas, bringing the distant Galaxy ($d \gtrsim 10$ kpc) into sharper focus.

VLBI Exploration of Radio Astrometry (VERA) was a Northern Hemisphere VLBI array/project dedicated to maser astrometry by the National Astronomical Observatory of Japan (NAOJ). VERA (interferometer) is comprised of 4 × 22 m radio telescopes spread over Japan with a maximum baseline of 2300 km. Despite this, it is also the only VLBI array dedicated to phase–reference astrometry. To this effect, they utilise a unique 'dual–beam' receiver system where simultaneous observations of target masers and reference quasars can be conducted, which greatly minimises the ambiguity of calibrating tropospheric line–of–sight effects (Honma et al., 2003).

VERA targets water masers tracing star-forming regions, but also SiO masers tracing evolved stars. The former boasts results with astrometric accuracy comparable to BeSSeL (Reid et al., 2019; VERA Collaboration et al., 2020).

Combined, the two Northern Hemisphere maser–astrometry surveys have measured over 200 maser parallaxes and mapped the 1st, 2nd and 3rd Galactic quadrants Figure 1.12. It is clear from Figure 1.12 that the 4th Galactic quadrant is heavily under-represented.

1.4.3 Southern Hemisphere – SπRALS

The Southern Parallax Interferometric Radio Astrometry Legacy Survey (SπRALS – pronounced 'spirals') in an emerging Australian–led maser astrometry project. While first announced in September 2018 (at the Cagliari Maser IAUS; Hyland et al., 2018), the first iteration of SπRALS dates back to pre–2010 – with the first epoch on the then 'V255' project observed

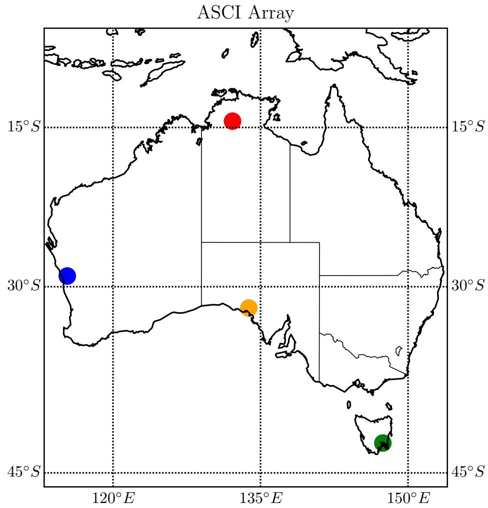

Figure 1.13: The AuScope–Ceduna Interferometer formed with telescopes at Ceduna (yellow), Hobart (green), Katherine (red) and Yarragadee (blue). All radio telescopes are owned and operated by the University of Tasmania.

March 30$^{\text{th}}$ 2008 on the Australian Long Baseline Array (LBA). This project is responsible for the first Southern Hemisphere parallax (Krishnan et al., 2015) and consequent works including Krishnan et al. (2017) and Sanna et al. (2015).

Despite the overall success of Krishnan et al. (2015, 2017), authors report parallax uncertainties ranging $\sigma_{\varpi} = 80 - 150\mu$as, equivalent to measuring a distance of $d < 1.3 - 2.5$ kpc with at least fractional uncertainty $\sigma_{\varpi}/\varpi < 0.2$. As the aims of SπRALS are to measure parallaxes equivalent to distances of $d < 5 - 10$ kpc, I must address shortcomings of the V255 observations which likely lead to parallax uncertainties an order of magnitude too large:

1. At the time of the Krishnan et al. (2015, 2017) V255 observations, LBA telescopes did not have much mutual 6.7 GHz bandwidth (only 32 GHz in dual–polaristion). Authors report this lead to poorly constrained tropospheric delay and clock delay solutions (see Section §2.3.9.2 for specifics on geoblock/tropospheric calibration) and ultimately contributed to worse astrometry.

2. In addition to the low–bandwidth, tropospheric delay determination was proposed to be systematically offset due to erroneous ionosphere corrections resulting from low-resolution total electron content maps and inability to distinguish between dispersive ionospheric delay and non-dispersive troposphere. In addition, static phase errors (which systematically *shift* astrometric positions) resulting from the residual ionosphere were estimated to be as high as 21°.

3. The final issue was poor parallax sampling. Although I will introduce the relevant equations and theory in Chapter §2 at this point I can say that due to non–preferential scheduling availability on the LBA, astrometric epochs did not necessarily align with peak parallax peaks or sample the parallax curve optimally. This leads to a parallax sensitivity reduction of approximately a factor of 2.

Therefore to measure trigonometric parallaxes to distant masers in the southern sky it was decided that a Southern Hemisphere astrometry array was necessary; with appropriate frequency coverage, telescope availability, atmospheric calibration techniques and target pre-selection.

The AuScope array (Lovell et al., 2013) is an existing S/X geodetic array comprised of Hobart 12m, Katherine 12m and Yarragadee 12m. It operates as part of the International VLBI Service (IVS) with a downtime of approximately ~ 100 days/year that is available for parallax observations. Ceduna 30m (McCulloch et al., 2005) operates as part of the LBA with an uptime of only a few weeks/year and therefore the array will be the AuScope–Ceduna Interferometer (ASCI; Figure 1.13) with a maximum baseline of $B \approx 3500$ km. A possible extension to the array is the Warkworth 30m telescope, owned and operated by the Institute for Radio Astronomy and Space Research (IRASR), which would extend the maximum baseline up to $B \approx 5500$ km or $B_\lambda = 120\,\mathrm{M}\lambda$ at 6.7 GHz.

With Hobart 12m and Katherine upgraded to wide–C band capable receivers (completed in 2017 and 2019 respectively), Yarragadee scheduled for upgrade and Ceduna/Warkworth with pre-existing C–band capabilities but planned wideband upgrades, SπRALS aims to measure dozens of trigonometric parallaxes towards High Mass Star Formation regions traced by 6.7 GHz class II methanol masers over the next 3 years.

This thesis aims to answer the questions of target selection, ionospheric calibration and methodology relevant to accomplishing this goal: Chapter 2 goes over appropriate theory and methodology of VLBI astrometric calibration; Chapter 3 demonstrates said calibration via the reduction and analysis of recent BeSSeL VLBA data and determination of new distances towards the Perseus spiral arm; in Chapter 4 I reduce and analyse LBA data to determine target selection for the SπRALS project and to determine Southern Hemisphere methanol maser compactness properties; Chapter 5 discusses atmospheric calibration techniques and introduces MultiView and in Chapter 6 I observe, calibrate and test inverse MultiView calibration and contrast it against traditional phase referencing.

2

VLBI Astrometry and Calibration

Astrometry is the science of accurately positioning objects in the sky and Very Long Baseline Interferometry (VLBI) currently boasts the highest regularly achievable astrometric precision. In this chapter, I will review the calibration techniques necessary to convert this high precision into high accuracy, including relevant theory and discuss why this high accuracy is required for trigonometric parallax. I will also introduce and justify additional modified calibration techniques used throughout the data analysis presented in Chapter 3 and 4, and finish with a summary of steps needed to calibrate VLBI data for astrometry.

2.1 Introduction

This chapter presents specific details about the multiple aspects of VLBI calibration required to obtain high accuracy astrometry necessary for determining Galactic–scale distances. The following topics are discussed:

- Section §2.2 establishes how and why distance determination in the Galaxy via trigonometric parallax is dependent on astrometric uncertainty and delay calibration;
- Section §2.3 Contains a simplified explanation of radio telescopes and Very Long Baseline Interferometry, culminating in the relationship between sky brightness and measured visibility;
- Section §2.3.3 begins discussion of the delay calibration process from the correlation stage and as it continues into the data reduction process;
- Section §2.3.9 discusses atmospheric delays, their cause and calibration techniques to mitigate them;
- Section §2.3.10 introduces phase referencing and discusses how it can be used to combat residual or other uncalibrated delays;
- Section §2.3.4 defines amplitude calibration techniques that are used in this thesis;
- Section §2.4 discusses parallax determination from astrometry, parallax sampling and proper motions;
- Section §2.5 contains a practical summary of astrometric VLBI calibration that is applied in Chapter 3 and Chapter 6.

2.2 Distance and Astrometric Uncertainty

2.2.1 Determination of distance

A given parallax ϖ with uncertainty σ_ϖ yields a distance d with some upper and a lower bound. Since there are more objects (for a uniform distance distribution) outside than inside the distance range (because of the different sampled volumes) a higher number of objects from outside the distance range will scatter in than the number from inside scattering out. A source can have a measured parallax $\varpi \pm \sigma_\varpi$ when it has a true parallax ϖ_T such that the probability distribution of detecting the true parallax is:

$$P(\varpi) \propto \frac{1}{\sqrt{2\pi}\sigma_\varpi} \exp\left(-\left(\frac{\varpi - \varpi_T}{2\sigma_\varpi}\right)^2\right) \tag{2.1}$$

This Gaussian distribution is symmetric in ϖ, with the $[0, \varpi_T + \sigma_\varpi]$ and $[\varpi_T - \sigma_\varpi, 0]$ ranges having equal area and is strongly peaked about the mean/mode $P(\varpi_T)$. However, using traditional

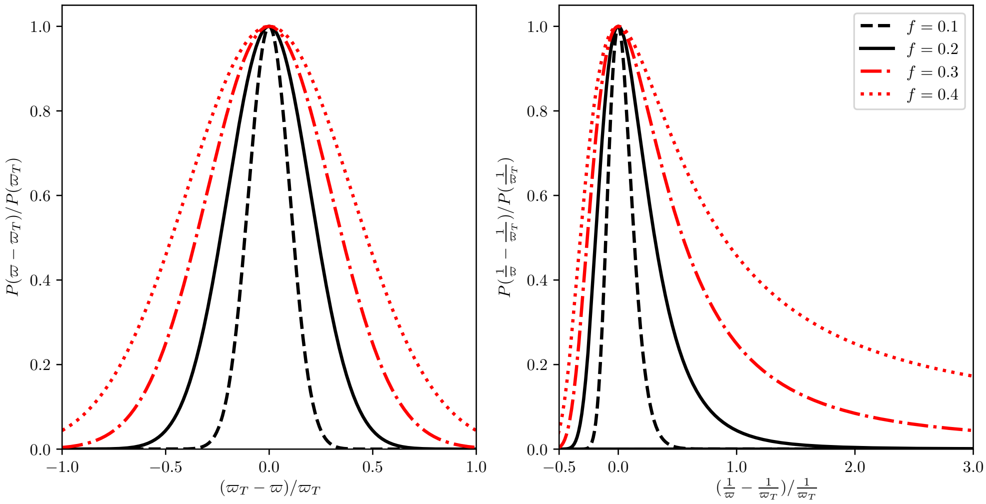

Figure 2.1: Parallax to distance asymmetry as a function of fractional uncertainty f. **Left:** Parallax probability distribution P against parallax ϖ as a function of fractional parallax uncertainty f. X–axis is centred on and normalised by true parallax ϖ_T, y–axis is similarly centred and scaled by $P(\varpi_T)$. **Right:** Distance probability distribution against centred, scaled distance as a function of f. This effectively demonstrates (unnormalised) probability of fractional distance error given f.

Taylor expansion methods to estimate the error in d (σ_d) would yield:

$$d = \frac{1}{\varpi} \tag{2.2}$$

$$\implies \sigma_d = \left| \frac{d(1/\varpi)}{d\varpi} \sigma_\varpi \right| = \frac{\sigma_\varpi}{\varpi^2} \tag{2.3}$$

and systematic underestimation in the error for d. Figure 2.1 shows the effect of increasing the fractional parallax error, $f = \frac{\sigma_\varpi}{\varpi}$ on the (relative) probability of determining to incorrect distance: $P\left(\frac{1}{\varpi} - \frac{1}{\varpi_T}\right) \,/\, \frac{1}{\varpi_T})$. At $f \geq 0.2$ it would not be uncommon to determine a distance that was off by a factor of 2.

It is reported that this effect causes a systematic bias where measured parallaxes will on average yield too small distances (Lutz & Kelker, 1973) and this effect is only a function of f, not total parallax. However, Lutz & Kelker (1973) specifically concerns inverting stellar parallaxes in a magnitude limited sample.

In a more practical vein, authors such as Verbiest et al. (2012); Reid et al. (2014); Bailer-Jones (2015) treat distance determination a Bayesian (or perhaps frequentist Igoshev et al., 2016) problem, not only considering the non–linearity of the parallax–to–distance conversion but also including priors for Galactic size, Galactic kinematics, spirals arms (for masers), magnitude/luminosity (for pulsars and stars).

Considered in isolation, a parallax with $f \geq 0.2$ becomes non–trivial to invert into a distance (Bailer-Jones, 2015). While a parallax that is less precise than $f = 0.2$ does not imply that is it not of use, I will consider this to be the upper–bound benchmark to aim for.

In the Galaxy, masers are expected to be anywhere from 0.4 (e.g. Orion nebula) to 20 kpc away (Sanna et al., 2017) with a reasonable upper–median estimate of 10 kpc. Such a maser will have a trigonometric parallax of 0.1 mas and for the reasonable fractional uncertainty of $\frac{\sigma_{\varpi}}{\varpi} \leq 20\%$ it is required that $\sigma_{\varpi} \leq 20\,\mu$as. The positional uncertainty required to detect this parallax in multiple epochs is $\sigma_\theta \lesssim 40\mu$as and the only way to regularly achieve this positional accuracy at radio/microwave frequencies is with VLBI astrometry.

As I will introduce soon, the path delay between two elements in an interferometer due to a positional offset $\Delta\theta$ goes as $\tau_\theta \approx \Delta\theta\frac{|B|}{c}$ where $|B|$ is the baseline. Therefore to detect the delay due to a very small position offset aka a trigonometric parallax, the interferometric delay needs to be calibrated very accurately.

2.3 Visibility Data Calibration

2.3.1 Response of a Single Antenna

Consider a single radio telescope tracking a celestial source (the target) with intensity distribution $I(\nu, l, m)$ in W m^{-2} Hz^{-1} str^{-1} (with l, m being arbitrary orthogonal angular offsets from the centre) with physical collecting area A and projection of that area onto the source $A(l, m)$ (the beam pattern) in m^2. If the telescope can only 'see' frequencies very close to ν in Hz, then ignoring polarisation, it will receive power at frequency ν, dP_ν:

$$dP_\nu = \frac{1}{2}A(l, m)\; I_\nu(l, m)\; dl\; dm \tag{2.4}$$

in W Hz^{-1} (Perley et al., 1989). In practice, the power measured will be less as, the telescope is affected by various losses in the surface, system, etc. If this loss factor $\eta(\nu)$ (called the antenna efficiency) is known, the measured power values can be calibrated and the intensity distribution of the target can be inferred.

The exact details of how a radio telescope converts the incident electric field at the observing frequency to recorded data are complex and beyond the scope of this thesis, however, I will briefly explain the basic concepts before I introduce interferometry. Concerning radio telescope operations, Tools for Radio Astronomy 2009 (Wilson et al., 2009) and/or Interferometry and Synthesis in Radio Astronomy (Thompson et al., 2017) are excellent sources for further reading.

Suffice to say, the radio telescope outputs a normalised response voltage $V(t)$, which is proportional to the square root of the power received summed up over the whole surface, proportional to the instantaneous electric field strength ϵ:

$$V(t) = \int_{-\infty}^{\infty}\int_{-\infty}^{\infty} \epsilon(t, l, m)\sqrt{A(l, m)}\; dl\; dm \tag{2.5}$$

The Fourier Transform of the instantaneous electric field strength is:

$$\epsilon(t, l, m) = \int_{-\infty}^{\infty} E(\nu, l, m)\; e^{-2\pi i\nu t}\; d\nu \tag{2.6}$$

where $E(\nu)$ is now the electric field strength as a function of frequency. Substitution of Equation 2.6 into Equation 2.5 gives:

$$V(t) = \int_{-\infty}^{\infty} \int_{-\infty}^{\infty} \int_{-\infty}^{\infty} E(\nu, l, m) \sqrt{A(l, m)}\; e^{-2\pi i \nu t}\; dl\; dm\; d\nu \tag{2.7}$$

thereby relating the instantaneous voltage response of a telescope to the frequency dependence of the incident electric field strength.

2.3.2 Radio Interferometry and VLBI

The fundamental aim of interferometry is to measuring the coherence properties of the electromagnetic field. To this end, signals from different radio telescopes can be compared.

Following Thompson et al. (2017), cross–correlating the voltage data $V_j(t)$ from two telescopes serves to form the 'correlation output' or lag function:

$$r(\tau) = \lim_{T \to \infty} \frac{1}{2T} \int_{-T}^{T} V_1(t)\; V_2^*(t - \tau) dt \tag{2.8}$$

where τ is the time delay of V_1 with respect to V_2 and * indicates a complex conjugation. All things being equal, the lag function will spike sharply at the value of τ that matches the true delay difference between V_1 and V_2.

Substitution of Equation 2.7 into Equation 2.8 and simplification by recognising

$$I_\nu(l, m) \propto E(\nu, l, m)\; E^*(\nu, l, m) \tag{2.9}$$

gives:

$$r(\tau) = \int_{-\infty}^{\infty} \int_{-\infty}^{\infty} \int_{-\infty}^{\infty} I_\nu(l, m) \sqrt{A_1(l, m) A_2(l, m)}\; e^{-2\pi i \nu \tau}\; dl\; dm\; d\nu \tag{2.10}$$

To simplify further, the geometric mean of the beam patterns $\overline{A} = \sqrt{A_1(l, m) A_2(l, m)}$ can be substituted and if the tracking centre of the field–of–view is chosen such that $\tau = 0$, then $\nu\tau = ul + vm$.

The two new parameters u and v are very important as they describe the displacement of the two telescopes from one another in the Earth Coordinate frame: u describes the projection in the East-West direction and v in the North-South. The final component w, projection in the direction to target source has been omitted in this derivation for simplicity.

In real systems, the frequency coverage is also not infinite, but in a range about the central frequency $\nu = \nu_{\mathrm{ref}} \pm \frac{1}{2}\Delta\nu$, where $\Delta\nu$ is the bandwidth in Hz with practical condition $\Delta\nu \ll \nu_{\mathrm{ref}}$.

Therefore we have:

$$r = \Delta\nu \int_{-\infty}^{\infty} \int_{-\infty}^{\infty} I_\nu(l, m)\; \overline{A}(l, m)\; e^{-2\pi i (ul + vm)}\; dl\; dm \tag{2.11}$$

Complex visibility can be described as the 2D Fourier Transform of the intensity distribution of the target source (sometimes called the sky brightness or image domain) multiplied by the geometric sensitivity pattern of the two telescopes:

$$\mathcal{V}(u,v) = |\mathcal{V}(u,v)|e^{i\phi} = \int_{-\infty}^{\infty}\int_{-\infty}^{\infty} I_\nu(l,m)\ \overline{A}(l,m)\ e^{-2\pi i(ul+vm)}\ dl\ dm \tag{2.12}$$

in $\mathrm{W\,Hz^{-1}}$ and conversely:

$$I_\nu(l,m)\ \overline{A}(l,m) = \int_{-\infty}^{\infty}\int_{-\infty}^{\infty} \mathcal{V}(u,v)\ e^{2\pi i(ul+vm)}\ dl\ dm \tag{2.13}$$

Such that the correlation output is proportional to the complex visibility:

$$r = \Delta\nu\ \mathcal{V}(u,v) \tag{2.14}$$

with units W. A 'correlator' is a device that can form the $r(\tau)$ function, thereby converting the telescope voltages into complex visibilities.

Real radio interferometers are ensemble pairs of telescopes, henceforth referred to as a baseline. An interferometer with N elements/antennas/telescopes will have $\frac{1}{2}N(N-1)$ baselines and visibility product is required for each one. Connected–element interferometers (like Australia Telescope Compact Array; ATCA or Very Large Array; VLA) can form visibility products in real-time by utilising on-site hardware correlators (Dougherty & Perley, 2011; Wilson et al., 2011).

As the name implies, Very Long Baseline Interferometry (VLBI) is interferometry where the elements are separated by hundreds or thousands of kilometres. Real-time correlation of such data is currently impractical and/or extremely expensive and as a consequence, analogue voltages are digitised on-site, recorded to physical media then shipped/transferred to be correlated at a central location at a later date. I will refer to this form of data as 'baseband' data.

Unlike connected–element interferometers, each VLBI element has independent frequency standards (which I will refer to as the clocks) that have timing offsets and drift compared to one another. Additionally, the atmosphere above each telescope is generally uncorrelated.

Calibration for the VLBI data set involves taking the measured complex visibility $\mathcal{V}$ as output from the correlator and modifying it (represented by a multiplication by complex number $\mathcal{C}$) such that the final Fourier Inversion gives the truest representation of the source brightness distribution:

$$\mathcal{F}\{\mathcal{C}\ \mathcal{V}(u,v)\} = I_\nu(l,m)\overline{A}(l,m) \tag{2.15}$$

where $\overline{A}$ can be independently determined. The process of inverting the complex visibilities and removing the antenna response patterns $\overline{A}$ is called 'imaging' and I will discuss it further in Section 2.3.12.

2.3.3 VLBI Correlation

Baseband data is taken from an array telescopes and correlated to form complex visibilities:

$$\mathcal{V}_{jk}(t,\nu) = |\mathcal{V}_{jk}(t,\nu)|e^{i\phi_{jk}(t,\nu)} \tag{2.16}$$

where $|\mathcal{V}_{jk}(t,\nu)|$ is the *measured* normalised visibility amplitude and $\phi_{jk}(t,\nu)$ is the phase between antenna j and k. Visibility amplitude and phase *or* the real and imaginary components of

$\mathcal{V}_{jk}(t,\nu)$ over discrete time and frequency bins are the principle data for VLBI reduction and analysis. In most cases I will be using $|\mathcal{V}_{jk}(t,\nu)|$ and $\phi_{jk}(t,\nu)$.

So a visibility product is formed for each baselines B_{jk} for $j,k=1\ldots N, j\neq k$ (where N is again the number of telescopes in the array) and 'autocorrelated' baselines B_{jj} (hereafter referred to as the autocorrelations) and each frequency

$$\nu = \nu_{\mathrm{ref}} + n\delta\nu \tag{2.17}$$

where ν_{ref} is the reference/observing frequency, $\delta\nu$ is the spectral resolution and n is the channel number. Therefore $\delta\nu$ is equivalent bandwidth of each complex visibility.

As seen in Equation 2.8, the correlation needs to be performed over an infinite interval $T\to\infty$, however, in practice the infinite condition can be met if $T \gg \frac{1}{\delta\nu} \gg \frac{1}{\nu_{\mathrm{ref}}}$ (therefore $T\sim 2$ s is a suitable example for many applications). So the above visibilities are produced for each integration time T from the start of a scan t_0: $t=t_0+m\,T$ and m are the time bins.

Relating this back to Equation 2.8, and the idea of a real time difference between the signal arrival times, the fundamental relationship between delay τ and phase ϕ is:

$$\phi_{jk} = 2\pi\nu\tau_{jk} \tag{2.18}$$

such that the output phase from the correlator tracking changes over time t and frequency ν will be:

$$\begin{aligned} \phi_{jk}(t,\nu) &= \frac{\partial\phi}{\partial t}(t-t_0) + \frac{\partial\phi}{\partial\nu}(\nu-\nu_{\mathrm{ref}}) \\ \therefore\ \phi_{jk}(m,n) &= 2\pi\nu_{\mathrm{ref}}T\ m\dot{\tau}_{jk} + 2\pi\delta\nu\ n\tau_{jk} \end{aligned} \tag{2.19}$$

where τ_{jk} is the delay in seconds and $\dot{\tau}_{jk}$ is the delay–rate (or just 'rate') in seconds per second between antennas j and k. Delay and rate are conceptually easier to relate to physical effects than phase, and therefore I will use them in further discussions of calibration until I introduce phase referencing (Section §2.3.10).

Equation 2.19 indicate that τ and $\dot{\tau}$ are proportional to the slopes in $\phi_{jk}(t,\nu)$ data against ν and t respectively (by proxy of the channels n and time–bins m). The maximum detectable delay therefore depends on the chosen spectral resolution:

$$\tau_{\mathrm{max}} = \delta\nu^{-1} \tag{2.20}$$

and the maximum rate depends on integration time and observing frequency:

$$\nu_{\mathrm{ref}}\dot{\tau}_{\mathrm{max}} = T^{-1} \tag{2.21}$$

The measured delay (τ) from the slope of the measured phase is comprised of many different effects added in series:

$$\tau(t,\nu) = \tau_{\mathrm{geo}}(t) + \tau_{\mathrm{tropo}}(t) + \tau_{\mathrm{iono}}(t,\nu) + \tau_{\mathrm{cl}}(t) + \tau_{\mathrm{e}} + \tau_{\mathrm{str}} + \tau_{\mathrm{th}} \tag{2.22}$$

where I have (in order) the delay due to: geometry, troposphere, ionosphere, clock offset, electronics, target structure and thermal uncertainty. I will go into each quantity in this expression in more detail in the following sections.

Now returning to the important point, VLBI astrometric calibration aims to take the measured complex visibilities and delays and account for all the sources of delay that are not due to source position offset τ_θ, which is a component of the geometric delay (see Section §2.3.5). Then, when the complex visibilities are inverted the resultant images formed have an accurate and precise representation of the source brightness distribution $I_\nu(l, m)$ (Equation 2.15).

In practice, the correlation stage provides an opportunity to pre-calibrate the VLBI dataset. Many of the delay components can be predicted to a very high accuracy *a priori* and can be as part of a delay model in the correlator (e.g. Deller et al., 2007). This will leave 'small' residual delays that have to be solved for in the data reduction and calibration stage.

In general, the delays corresponding to baseline geometry, troposphere and clock offset have their bulk effects removed in the correlation stage such that the sum of the remaining residual delays have magnitude $|\Sigma_i \tau_i| \lesssim 10$ ns.

2.3.4 Amplitude Calibration

The visibilities output from the correlator will have visibility amplitudes normalised (and will be dimensionless), such that real power (in Jy) received by a baseline jk at time t and in a frequency window around ν will be:

$$\mathcal{V}_{jk}(t, \nu) = \mathcal{G}_{jk}(t)\mathcal{B}_{jk}(\nu)\mathcal{V}_{jk}(t, \nu)_{\text{norm}} \tag{2.23}$$

where $\mathcal{G}_{jk}$ is referred to as the baseline–based complex gain and has units Jy, and $\mathcal{B}_{jk}$ is a dimensionless quantity that describes the complex frequency–dependence of the baseline response (Perley et al., 1989). These terms can be put into context of the calibration term from Equation 2.15:

$$\mathcal{C}_{jk}(t, \nu) = \mathcal{G}_{jk}(t)\mathcal{B}_{jk}(\nu)e^{-2\pi i\nu(\tau_{jk}(t,\nu) - \tau_\theta - \tau_{\text{str}})} \tag{2.24}$$

where τ_{jk} is the total delay out of the correlator from Equation 2.22, τ_θ and τ_{str} are the source–based delay terms relating to the geometric offset from assumed position and structure respectively.

The complete complex term $\mathcal{G}_{jk}(t)\mathcal{B}_{jk}(\nu)$ can classically be solved for by regularly observing a point-like source that emits equally in the continuum (or in a well–known way) over the bandwidth and has a known flux density. However, for VLBI such sources are nearly non–existent, all candidate quasars have structure at VLBI resolutions and flux density variations (Thompson et al., 2017). Solving for $\mathcal{B}_{jk}(\nu)$ is still possible via this method and is referred to as 'bandpass calibration'.

The complex gain term $\mathcal{G}_{jk}$ results from corruption/inefficiencies occurring at the individual telescopes on the baseline, such that it can be expressed as:

$$\mathcal{G}_{jk}(t) = \sqrt{g_j(t)g_k^*(t)} \tag{2.25}$$

where $g(t)$ is the complex gain of the relevant telescope over time and * indicates a complex conjugation (Perley et al., 1989). In this formalisation, the gains indicate telescope sensitivity in Jy, referred to as system equivalent flux density (SEFD). A smaller SEFD implies a more sensitive telescope.

The SEFD of a telescope (in a particular frequency range) can itself be derived from the geometric diameter of the telescope A, antenna efficiency η and system temperature $T_{\rm sys}$:

$$g(t) = \frac{2k\, T_{\rm sys}(t)}{\eta A} \tag{2.26}$$

where $k = 1.38 \times 10^3$ Jy m^2 K^{-1} is Boltzmann's constant (Rohlfs, 1986). The system temperature $T_{\rm sys}$ intuitively describes the combination of effects including the temperature of the cooled receiver system, amplifiers in the system, interference from the black body spectrum of the ground, sky and atmosphere. The $T_{\rm sys}$ of a telescope can be well–characterised at each observing frequency and as a function of elevation (due to the temperature of the ground and atmospheric path–length Perley et al., 1989). Alternately, the $T_{\rm sys}$ can be directly measured during observations with a noise diode (Wilson, 2013).

2.3.5 Geodetic and Source Position Delay

The largest source of pre-correction delay in a VLBI array is the 'geodetic' delay due to the baseline geometry $\tau_{\rm geo}$. For a baseline $\mathbf{B}$ observing a source at some distance d, if $d \gg |\mathbf{B}|$ then the wavefronts approaching the baseline can be considered plane parallel to a good approximation. The time delay between the signal arriving at one antenna w.r.t the other will be:

$$\tau_{\rm geo} = \frac{\hat{\mathbf{s}} \cdot \mathbf{B}}{c} \tag{2.27}$$

where $\hat{\mathbf{s}}$ is the direction of the radiation, $\mathbf{B}$ is the baseline vector in metres and c is the speed of light (Figure 2.2).

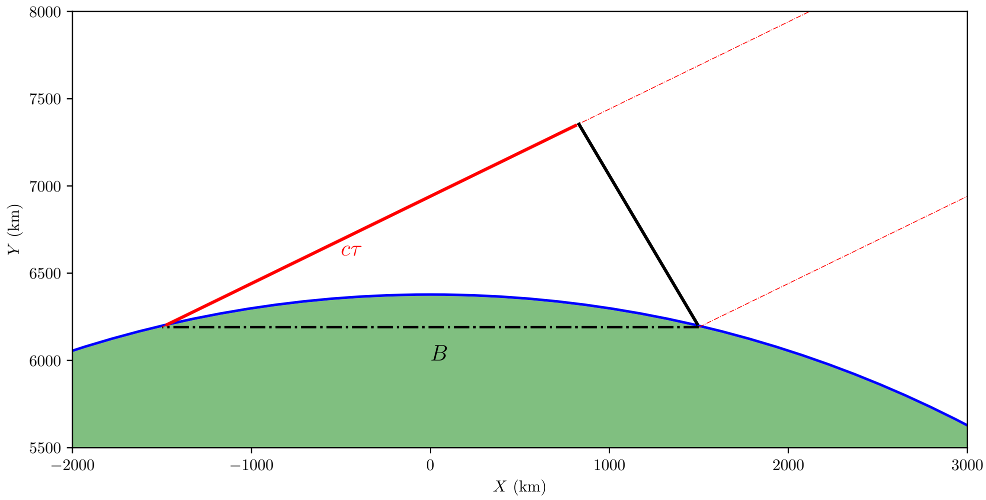

Figure 2.2: To–scale diagram of the geometric delay encountered for 2 telescopes separated by $|\mathbf{B}| =$ 3000 km observing a target source at $\theta = 30°$ to the baseline vector. In this example the measured delay (red) will be $c\tau \approx 2600$ km or $\tau = 8.67$ ms.

Antenna positions are defined on the Geographic coordinate system: a Cartesian grid with the centre of mass of the Earth at $(X, Y, Z) = (0, 0, 0)$, $XY-$plane defined by the equator (latitude 0°) and XZ-plane defined by the prime meridian at Greenwich (longitude 0°). Since this is a fixed reference frame and tectonic plate movement is not accounted for, 'positions' on the Earth are time variable and are also denoted a velocity $\dot{X}$ etc. The baseline between two antennas is the instantaneous difference in their positions.

In the following sections and throughout this thesis I will be using the term 'delay' interchangeably between τ (in seconds) and $c\tau$ (in meters or cm).

The correlation process is able to use *a priori* antenna positions and velocities to model the baseline $\mathbf{B}$ and an assumed source position to generate $\tau_{\text{geo,cmodel}}$ such that the correlator output instead contains:

$$\tau_{\text{geo}} - \tau_{\text{geo,cmodel}} = \tau_{bl} + \tau_{\theta} \tag{2.28}$$

where now τ_{bl} is the error in the baselines due to antenna position offsets from the assumed positions and τ_{θ} is the source position offset from the assumed position. Error in the geometric delay model due to antenna position uncertainty is a function of observed target position (α, δ) and local sidereal time (t_{lst}):

$$c\tau_{bl} = \Delta B_x \cos(t_{lst} - \alpha)\cos\delta - \Delta B_y \sin(t_{lst} - \alpha)\cos\delta + \Delta B_z \sin\delta \tag{2.29}$$

where $\Delta B_x, \Delta B_y, \Delta B_z$ are the baseline offsets from the model in the X, Y, Z directions and $c\tau_{bl}$ is in metres. If the relative magnitudes of the baseline uncertainties are equal then the equation can be reduced to:

$$c\tau_{bl} \approx |\Delta B| \tag{2.30}$$

over the whole sky to a good approximation.

Error in the geometric delay due to source position offset can be described by:

$$\begin{aligned} c\tau_{\theta} &= \sigma_{\alpha}\cos\delta\,(\;B_x \sin(t_{lst} - \alpha) + B_y \cos(t_{lst} - \alpha)\;) \\ &\quad + \sigma_{\delta}(\;-B_x \cos(t_{lst} - \alpha)\sin\delta + B_y \sin(t_{lst} - \alpha)\sin\delta + B_z \cos\delta\;) \\ &\leq \sigma_{\theta}\;|\mathbf{B}| \end{aligned} \tag{2.31}$$

where σ_{α} and σ_{δ} are the associated offsets in the Right Ascension and Declination components of the target source position and $\sigma_{\theta} = \sqrt{\sigma_{\alpha}^2 + \sigma_{\delta}^2}$.

The science of geodesy can solve for source and antenna positions simultaneously using absolute astrometry. Over the past decade the International VLBI Service (IVS) has performed regular observations of quasars and catalogued the International Celestial Reference Frame (ICRF Gontier et al., 1997; Ma et al., 2009; Charlot et al., 2020) and contribute to the International Terrestrial Reference Frame (ITRF Böckmann et al., 2010). The frames provide baseline lengths and quasar positions up to $\Delta B = 1$ cm and $\sigma_{\theta} \geq 0.1 - 0.3$ mas (e.g. Petrov et al., 2009a,b). The International Earth Rotation and Reference Systems Service (IERS) maintain the ICRF and ITRF and provide Earth Orientation Parameters (EOPs)– documentation of various irregularities to the Earth's rotation which are applied directly to VLBI data (Capitaine, 2017).

The high positional accuracy achieved for many quasars is from performing regular IVS observations, then averaging the results. Quasars are so distant that their expected positional change over time due to relative motion is zero and averaging the results should lower the uncertainty. I discuss caveats to this in Section §2.3.7. The positional accuracy as determined by absolute astrometry at a certain epoch will be dependent on the uncertainty in the final residual delay σ_{τ}:

$$\sigma_{\theta} \approx \frac{c\sigma_{\tau}}{|\mathbf{B}|} \geq 0.6 \text{ mas} \tag{2.32}$$

from Equation 2.31 if $|\mathbf{B}| = 3000$ km and $c\sigma_\tau \geq 1$ cm. This positional accuracy is 1–2 orders of magnitude too low for Galactic–scale maser trigonometric parallax estimation, which requires uncertainties on the level of $10 - 100$ μas for fractional parallax uncertainties $f \sim 0.2$. Therefore VLBI astrometry for masers (and pulsars) utilises *relative* astrometry (which I cover in Section §2.3.10).

2.3.6 Electronic and Clock Offset Delays

No radio telescope or consequent signal path is identical and differences in propagation time though cables and devices will cause a bulk electronic delay relative to the other telescopes in the array (τ_e). If the telescope records multiple polarisations and/or sub-bands in the total bandwidth (what I will refer to as intermediate frequencies or IFs), this delay is expected to be slightly different for each one due to small but measurable path differences in the cables and electronic components. This delay is expected to be stable over a whole observational period if there are no equipment changes.

Each radio telescope time stamps recorded data using internal clocks phase-locked to a time and frequency standard (usually a hydrogen maser), making them theoretically accurate to the Allen standard deviation of the masers. For hydrogen masers this is $\sigma_A \sim 3 \times 10^{-15}$ s/s ~ 0.3 ns/day (for an integration time of 100s Nothnagel et al., 2018). However as each maser is independent they gain and lose time at a constant and measurable rate with respect to each other, which I will call the clock delay τ_{cl}. This clock delay will be equivalent to 1 to $10 \times \sigma_A \sim 1$ ns over a day. As 1 ns is equivalent to ~ 30 cm of path length or a positional offset of ~ 20 mas with $\mathbf{B} = 3000$ km, this effect is very important to take into account. All telescopes as part of the ASCI array use Vremya-CH 1005 Hydrogen masers as frequency standards *.

When all telescopes are referenced to one antenna in the array, all the clocks drift linearly w.r.t this antenna (Reid & Honma, 2014). During the correlation, when interference fringes are found at time t_0 the measured delay corresponding to the fringe is added to the correlator model. This process is called 'fringe searching' or 'fringe fitting' and hence the bright quasars used to find fringes are referred to as 'fringe–finders'. Removal of this delay at time t_0 also has the effect of removing the clock delay at that time and the bulk electronic delay that affects all polarisations and IFs. By fringe searching again at another time, a linear model for the clock delay can be constructed and added to the correlator model $\tau_{cl,\mathrm{cmodel}}$. Overall, this leaves residuals in the correlator output per baseline in a particular IF/polarisation i of:

$$\tau_{cl} + \tau_e - \tau_{cl,\mathrm{cmodel}} = \delta\dot{\tau_{cl}}(t - t_0) + \delta\tau_{e,i} \tag{2.33}$$

where now I have the residual clocks $\delta\dot{\tau_{cl}}$ and single band delays $\delta\tau_{e,i}$.

Single-band delays are expected to be $|\delta\tau_{e,i}| \lesssim 100$ ns and the residual clocks can be removed to the level of $|\delta\dot{\tau}_{cl}| < 10^{-15}$ s/s provided that there have been multiple observations of strong fringe–finder sources over the experiment. While there will always be a measurement residual, theoretically clock electronic delays could be removed to the level of pre-reduction levels ($c\delta\tau \sim 1$ cm) at the correlation stage, but in practice this is tedious and time–consuming as it would require a high spectral resolution and additional correlator passes (see Equation 2.20).

During reduction, further single band delay calibration is performed with what is referred to as a *manual phase calibration.* Single-band delays are solved for on a single scan of a fringe finder

*www.vremya-ch.com

target with a well–known position. Application of this solution will greatly minimise electronic delays and the residuals will be time-independent and therefore not correlate with delays due to source position offsets (Equation 2.31). The main benefit of manual phase calibration is that in the presence of only non–dispersive (frequency-independent) and/or small dispersive (frequency-dependent) delays, once the delays are synced up the time–variable single-band delays should also be frequency independent. Therefore the whole bandwidth can be utilised thereafter to solve for multiband delays. The minimum detectable delay depends inversely on bandwidth:

$$\begin{aligned} \tau &= \frac{1}{2\pi}\frac{\Delta\phi}{\Delta\nu} \\ \therefore \tau_{\min} &= \frac{1}{2\pi}\frac{\sigma_\phi}{\Delta\nu} \\ \therefore \tau_{\min} &= \frac{1}{2\pi}\frac{1}{\mathrm{SNR}}\frac{1}{\Delta\nu} \end{aligned} \tag{2.34}$$

where σ_ϕ is the phase–noise in radians and I have made the approximation that phase noise is inversely proportional to the signal–to–noise–ratio (SNR):

$$\sigma_\phi = \frac{1}{\mathrm{SNR}} \tag{2.35}$$

in radians. So a larger bandwidth leads to a more precise delay determination.

2.3.7 Source Structure

Sources, being either spectral-line like masers or continuum like quasars can have structure which is time and/or frequency dependent.

For masers, the frequency-dependent structure is expected and partially resolved by producing visibilities with a very high spectral resolution (e.g. $\delta\nu$ = 1.953 kHz is sufficient for 6.7 GHz methanol masers Green et al., 2010). Final positions and structural information can be determined separately for each frequency–binned visibility (aka channel).

Quasars can also have frequency-dependent source structure (Marcaide et al., 1985). Quasar structure is divided into the ‘core’ and the ‘jet’, where the jet is a parsec–scale structure comprised of relativistic plasma emitting synchrotron radiation (Blandford & Königl, 1979). The core is defined as the apparent origin of the jet, where the optical depth reaches 1. However, pressure and density gradients along the jet leads to a changing saturation point at different frequencies and therefore an apparent shift in the core position (Kovalev et al., 2008). This ‘core–shift’ can lead to a bias in the position of the source, however, if the bandwidth to be averaged over (see Section §2.3.10) is small compared to the observing frequency, then the shift will also be small ($\frac{\Delta\nu}{\nu_{\mathrm{ref}}} \ll 1$; implied from equations presented in Porcas, 2009).

There can be an effective frequency-independent structure within a single maser channel or for quasars observed with $\frac{\Delta\nu}{\nu_{\mathrm{ref}}} \ll 1$. Any source structure apart from the reference component, like quasar jets or spatially/frequency coincident maser regions will cause a bias in the measurable position of the source. The magnitude of this bias is dependent on the relative magnitude and angular separation of the additional features (relative to the beam size θ_b) to the reference feature and is minimised when the flux density of the additional features is small compared to that of the reference feature (Charlot, 1990). Therefore pre-selection of maser targets and quasar calibrators to minimise structure can also minimise this bias (Reid & Honma, 2014).

Structure that is time-independent, imaged with similar *uv*–coverage and the same model (see Section §2.3.12) should lead to consistent astrometry. However, any structural changes that occur over time in either the masers or quasars can be deleterious.

Both 6.7 GHz CH_3OH and 22 GHz H_2O masers are known to undergo flaring and/or bursting events (where I will use the terms synonymously and refer to a rapid increase in flux density) that *can* be associated with structural changes. In addition, both species of maser are known to be variable outside of major flaring events (Caswell et al., 1995a; Brand et al., 2003; Goedhart et al., 2004).

As measurable from single-dish spectra, the burst/flare/variability can occur to a single feature or only part of in the maser spectrum (e.g. MacLeod et al., 2018; Volvach et al., 2019), a complete change in the maser spectrum (e.g. Szymczak et al., 2018b) or an increase of all components during the burst then settling to original spectrum (Sugiyama et al., 2019). The structural/morphological implications of these bursts have only been able to investigate with interferometry in a few instances (e.g. Goedhart et al., 2005a; Burns et al., 2020a, for class II methanol) and (Burns et al., 2020b, for 22.2 GHz water) due to array availability and the often short lifetime of flaring events. In each of these cases, the flaring event has been linked to a different morphological change in the maser structure, not always affecting the whole maser structure. Therefore, in the instance that a flare does occur but does not affect the reference structure (chosen deliberately) then the astrometry can be preserved. Else wise the astrometry would be completely compromised.

Water masers are much more variable than class II methanol masers, with the lifetime of features in the spectrum being often <1 yr (Brand et al., 2003). This means that trigonometric parallax observations spanning ~ 1 yr can be affected by the disappearance or evolution of the reference feature. This too can completely comprise positional accuracy.

Time–variable quasar structure can also negatively impact astrometry. For relative astrometry, maser positions are measured with respect to a nearby quasar, which theoretically should not have any measurable proper motion due. However, time-variable structural changes can lead to a detectable proper motion between quasars (Marcaide et al., 1994; Rioja et al., 1997a; Rioja & Porcas, 2000). These changes are attributed to jet opacity variability and/or jet precession, so quasars with compact jets are expected to be more astrometrically stable (Martí-Vidal et al., 2016). Proper motions of quasars has been measured to be ~ 10 μas/yr (Rioja et al., 1997a), however, is likely to be uncorrelated with the motion expected to measure a trigonometric parallax (Equation 2.72). Therefore the proper motion of quasars *should* only limit the precision that parallax can be determined, rather than cause systematic offsets.

2.3.8 Thermal Noise

Thermal noise τ_{th} is unable to be calibrated. This is not typically considered a limiting factor as it is due to stochastic processes, but takes the form:

$$\tau_{th} = \left(\frac{4}{\pi}\right)^{\frac{1}{4}} \frac{1}{\sqrt{8 \ln 2}} \frac{1}{\mathrm{SNR}} \frac{1}{\nu} \approx 0.64 \frac{1}{\nu\, \mathrm{SNR}} \tag{2.36}$$

where SNR is the signal–to–noise–ratio and ν is the frequency of incident radiation (adopted from Reid et al., 1988). The resultant positional uncertainty from such a delay σ_{th} would be:

$$\sigma_{th} = 0.52 \frac{\theta_b}{\text{SNR}} \tag{2.37}$$

where θ_b is the synthesised beam of an interferometric array (in rads or mas), equivalent to the full–width at half maximum (FWHM) region of the geometric mean antenna beam pattern $\overline{A}(l, m)$ and is defined as:

$$\theta_b = 1.22 \frac{\lambda}{|\mathbf{B}|} \tag{2.38}$$

in rads, where λ is the wavelength of the incident radiation. For the ASCI Array, maximum baseline is $|\mathbf{B}| \sim 3500$ km and observing frequencies 6.7 and 8.4 GHz give synthesised beam size of $\theta_b = 3.1$ and 2.0 mas. For detections in final images SNR ≥ 100, $\sigma_{th} \leq 20$ and 15μas respectively.

2.3.9 Atmospheric Delays

As I have previously mentioned, the nature of VLBI means that atmospheric fluctuations above array elements are largely (if not completely) uncorrelated. The atmosphere can be broadly divided into three components- the wet and dry troposphere and the ionosphere. These three components are split by the time scales that they fluctuate and their dispersive nature.

A dispersive medium is one in which electromagnetic radiation at different frequencies travels at different speeds. This has the effect of changing the apparent path length through the medium as a function of frequency. Therefore light travelling through a dispersive medium has a changing delay at different frequencies, and the same delay at every frequency through a non–dispersive medium.

The ionosphere is a layer of ionised plasma with a characteristic height of 400 km, which is dispersive in nature. As I will discuss in Section 2.3.9.1, the total ionospheric delay at a given frequency depends solely on the path–the length of electrons along the LoS, which is a function of the day-night cycle, solar activity, latitude and season. Typical values for the ionospheric delay at 6.7 and 8.4 GHz are $c\tau_{\text{iono}} = 25$ and 15 cm respectively (Perley et al., 1989).

The troposphere is the atmospheric region closest to the ground, with a max height of 12–17 km (with the discrepancy being polar vs. equatorial regions Gettelman et al., 2002) and contains the majority of atmospheric water vapour within the first 1–2 km (Thompson et al., 2017). The 'dry' component of the troposphere is classically defined as being made up of all constituents that are not water vapour (oxygen, nitrogen and carbon dioxide gas; hence 'dry'), however, in VLBI the term is more commonly used to describe the slow–varying bulk path length of the atmosphere, including that of water vapour (Reid & Honma, 2014). Conversely, the 'wet' tropospheric component describes the rapidly changing path–the length of water vapour along a line–of–sight, well–characterised by clouds.

The total delay due to the troposphere is therefore split into these components to be calibrated separately:

$$\tau_{\text{tropo}} = \tau_{\text{dry}} + \tau_{\text{wet}} \tag{2.39}$$

The dry component of the troposphere contributes $c\tau_{\text{dry}} = 230$ cm or more zenith delay, while the wet component contributes $c\tau_{\text{wet}} = 1 - 20$ cm (Thompson et al., 2017).

The large majority of these delays are removed by the correlator model using seasonally averaged models for temperature, pressure and humidity (Deller et al., 2007). The residual delays ($\delta\tau$) are expected to be of the order of $c|\delta\tau_{\rm dry} + \delta\tau_{\rm wet} + \delta\tau_{\rm iono}| < 30\,{\rm cm}$ (Reid et al., 2014), so further post–correlation calibration is required.

2.3.9.1 Ionospheric Delay Calibration

The dispersive delay due to the ionosphere is:

$$c\,\tau_{\rm iono} = 40.3\,I_e\,\nu^{-2}{\rm cm} \tag{2.40}$$

from Thompson et al. (2017), where ν is frequency in GHz, and I_e is the total electron content (TEC) along the line of sight measured in units of TECU ($1\,{\rm TECU} = 1\times10^{16}\,{\rm electrons\,m^{-2}}$). Typical total zenith values of I_e are expected to be $I_e < 50$ TECU excluding major solar events. Due to the characteristic height of the ionosphere being 400 km, for most elevations, the field of view is very large and small differences in the LOS will lead to very different and likely uncorrelated ionospheres (e.g. shown in Figure 2.3). In turn, this makes it difficult to characterise the ionosphere or link the expected LOS delay to local measurables. The most general method to subtract bulk I_e contributions is to use TEC maps provided by NASA Jet Propulsion Laboratory (JPL) as well as other groups. These maps are calculated from GPS data (which operate at 1.23 and 1.58 GHz) and can be imported to calculate the expected delay through that region of the ionosphere. However Walker & Chatterjee (1999) estimate that the ionospheric residuals in these maps is around $5-10\,{\rm TECU}$, which at is $4.5-9\,{\rm cm}$ at $6.7\,{\rm GHz}$, $2.9-5.7\,{\rm cm}$ at $8.4\,{\rm GHz}$ and $0.4-0.8$ cm at 22 GHz. In addition, the resolution of TEC maps is reduced in the Southern Hemisphere due to the spacing and number of GPS stations compared to the North (4800 vs. 1000 GPS stations).

Dual-frequency observations are considered the ideal method to remove residual line-of-sight delays due to the ionosphere (Thompson et al., 2017), as conducted in geodetic VLBI observations at S (2.3 GHz) and X ($\sim$ 8.2 GHz). Multi-frequency observations are currently the only way to directly 'measure' and therefore accurately remove the ionospheric residuals. Given a total (or total–residual) LOS delay:

$$\tau(t,\nu) = \tau_{\rm dry}(t) + \tau_{\rm wet}(t) + \tau_{\rm iono}(t)\,\nu^{-2} \tag{2.41}$$

the non–dispersive components will affect all frequencies identically and subtracting the total delay at two frequencies leaves only the dispersive delay:

$$\tau(t,\nu_2) - \tau(t,\nu_1) = \tau_{\rm iono}(t)\left(\frac{1}{\nu_2^2} - \frac{1}{\nu_1^2}\right) \tag{2.42}$$

which can then be subtracted along the line–of–sight for the source it was measured on.

2.3.9.2 Dry Tropospheric Delay Calibration

To calibrate the delay better than what models can offer, observational time must be sacrificed on measurements to constrain the delays. ICRF quasars with positions known to be better than 1 mas will have a residual multiband delay dominated by the line–of–sight atmospheric effects. The residual line–of–sight delays on different quasars are related to the residual 'zenith' delay

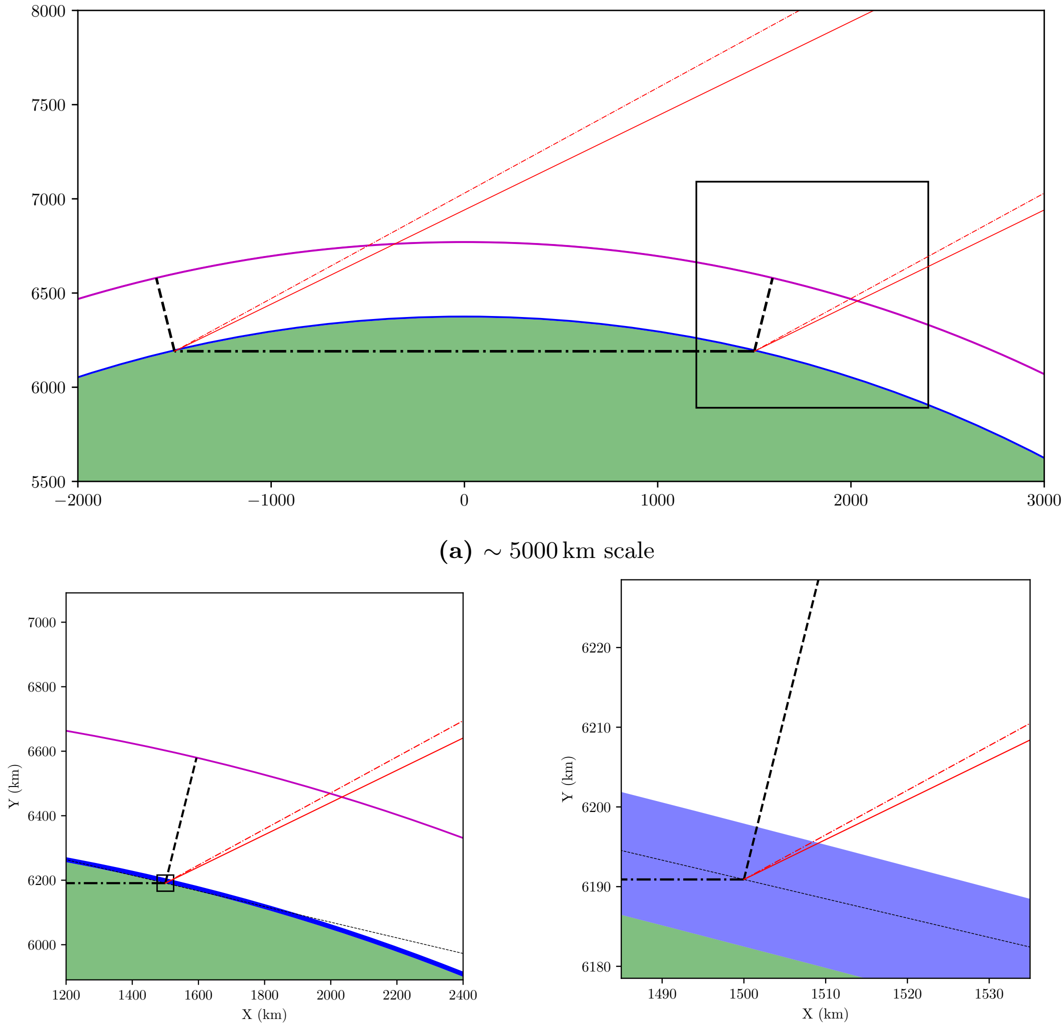

(a) ∼ 5000 km scale

(b) ∼ 1000 km scale

(c) 25 km scale

Figure 2.3: Diagramatic representations of the true VLBI and atmospheric scales present for a VLBI baseline. Baseline length is $B = 3000$ km (black dot–dashed line). Magenta line represents the thin ionosphere (thickness ∼ 10 km approximation) at a height of 400 km above the Earth's surface and red lines are lines–of–sight from each element towards two targets angularly offset by 3° (solid and broken). Blue region is the troposphere with thickness 15 km. Black dashed lines are local zenith for respective baseline elements. Respective rays are parallel due to target distance.

$\delta\tau_z$ by way of an elevation (ε) mapping function $m_i(\varepsilon)$:

$$c\delta\tau = c\delta\tau_z \, m_i(\varepsilon) \tag{2.43}$$

From the geometry and respective heights in Figure 2.3 I derive that relative path–lengths $c\tau_{\rm dry}$

as a function of elevation ε can be described by the following mapping function:

$$m_1(\varepsilon) = \frac{\sin(\varepsilon) - \sqrt{\sin(\varepsilon)^2 + \left(\frac{H}{R_\oplus}\right)^2 + \frac{H}{2\,R_\oplus}}}{1 - \sqrt{1 + \left(\frac{H}{R_\oplus}\right)^2 + \frac{H}{2\,R_\oplus}}} \tag{2.44}$$

where H is the height of the troposphere ($\sim$15 km), $R_\oplus = 6370$ km is the radius of Earth and ε is the antenna elevation measured from local horizon. I take this to be the correct and full mapping function, however, in this thesis I will use two others. Firstly the Niell's mapping function (Niell, 1996):

$$m_2(\varepsilon) = \frac{1}{\sin(\varepsilon) + \frac{a}{\sin(\varepsilon) + \frac{b}{c + \sin(\varepsilon)}}} \tag{2.45}$$

where a, b, c are parameters which depend on station latitude and time of year. This function is used extensively during geoblock and baseline fitting programmes (discussed below). Secondly:

$$m_3(\varepsilon) = \sec\left(\frac{\pi}{2} - \varepsilon\right) = \sec(Z) \tag{2.46}$$

as shown in Honma et al. (2008), where $Z = \frac{\pi}{2} - \varepsilon$ is the zenith angle. Figure 2.4 shows the distribution of these functions and the differences between them.

As is hinted at by the geometry in Figure 2.3 and shown by all the mapping function, the additional path length increases rapidly for decreasing elevations and doubles the zenith delay after $\varepsilon \lesssim 30°$. Equation 2.44 reveals that for elevations $\varepsilon \to 0$, the function approaches a maximum of $m_1(0) \sim \sqrt{\frac{2R_\oplus}{H} \frac{H/R_\oplus + 1}{H/R_\oplus + \frac{1}{2}}} \approx 58$.

The current methodology for removing the residual dry tropospheric delay is called *geoblock fitting* (Reid et al., 2009b). This is performed by scheduling 'geoblocks' during observations spaced roughly every 2–3 hours where each geoblock consists of 10–20 quasars at different elevations and generally takes $\sim$ 30 mins per geoblock.

For each geoblock b, a zenith delay $\tau_{z,b}$ can be determined for antennas j and k on a baseline by fitting the elevations ε_i of each ICRF quasar i and the measured residual delay at time t_i, $\delta\tau(t_i)$ to Equation 2.43. In practice the geoblocks are used to zenith delays at each block **and** the residual clock–delay rates $\delta\dot{\tau}_j$ and $\delta\dot{\tau}_k$ by fitting Equation 2.47:

$$\delta\tau(t_i)_{ij} = \tau_{0,jk} + (\delta\dot{\tau}_i - \delta\dot{\tau}_j)(t_i - t_0) + \tau_{z,bi}\, m_2(\epsilon_{ik}) - \tau_{z,bk}\, m_2(\epsilon_{ji}) \tag{2.47}$$

where $\tau_{0,jk}$ is the constant delay difference between antenna j and k (due to residual electronic effects). If time t_0 is strategically chosen to be the time that manual phase calibration was done, then $\tau_{0,jk} \approx 0$.

It is advantageous to maximise recorded bandwidth to better constrain the delay and each quasar needs to be compact and bright enough to be detected across the whole bandwidth on each baseline to get a reliable multi-band delay detection.

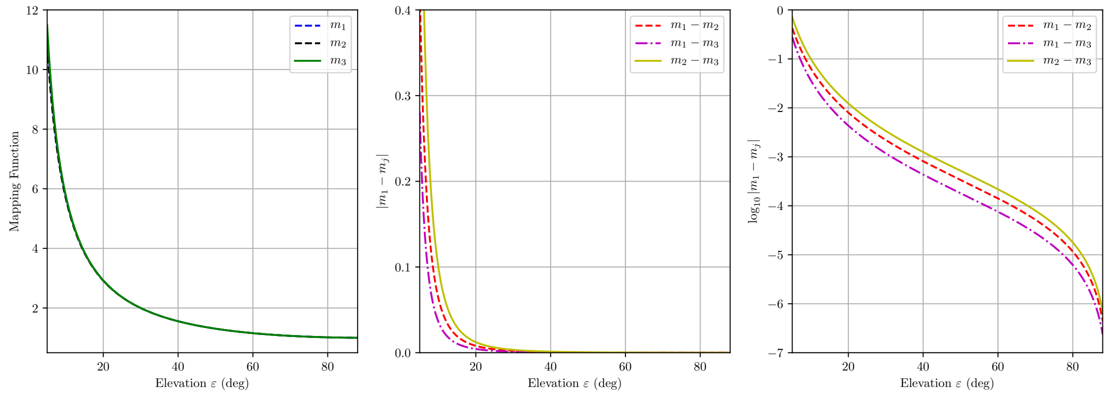

Figure 2.4: Left: magnitudes and **centre/right** differences between mapping functions m_1, m_2 and m_3 given in text against elevation ε. Right plot is in log units to highlight differences difficult to see in centre plot. Parameters for m_2 are $a = 5.6795 \times 10^{-4}$, $b = 1.5139 \times 10^{-3}$ and $c = 4.6730 \times 10^{-2}$ (for latitude 30° Reid et al., 2009b).

2.3.9.3 Wet Tropospheric Delay

The wet atmosphere is characterised by a fast (minute-scale) change in the amount of water vapour present along the LOS. Presently, the only way to remove this effect on the level required for VLBI astrometry is to observe the target and a reference calibrator 'simultaneously'. If the position and structure of the reference calibrator are known and/or accounted for, measured rapid delay and rate variations can be assumed due to the wet troposphere, then solved for and applied to the target. Validity of a delay and rate solution decreases as both time and spatially offset from solution time/position is increased, however, not immediately to zero in either case. The wet–atmosphere retains coherence in a small region and time about the solution position.

To proceed with a discussion of spatial and temporal coherence, I would like to first introduce phase referencing.

2.3.10 Phase Referencing

Hereafter I will refer to VLBI astrometry with the expectation that phase referencing has/will be performed. 'Phase referencing' is the case of measuring the phase instead of the delay of a 'nearby' calibrator and using that to calibrate residual delays.

For weak sources and a finite bandwidth, there is a limitation on the minimum delay that can be detected (Equation 2.34), which would otherwise limit how accurately delays could be calibrated and positions determined. From Equation 2.19 it can be seen that point of phase in the visibility data $\phi_{jk}(m, n)$ carries information about the current delay τ_{jk} and rate $\dot{\tau}_{jk}$. Additionally, phase is $2\pi\nu_{\text{ref}}$ times more sensitive to changes in delay than delay.

Confidently measuring phase (aka with high SNR) from a time– and frequency–binned complex visibility either requires a strong source (such as a maser) or to average in time and/or frequency. In order to coherently average visibility data in time T_{avg}, rate solutions must be sufficiently determined such that:

$$2\pi\nu_{\text{ref}}\dot{\tau}T_{\text{avg}} \ll 1 \tag{2.48}$$

and to coherently average visibilities over total bandwidth $\Delta\nu$, delay has to be sufficiently small such that:

$$2\pi\tau\Delta\nu \ll 1 \tag{2.49}$$

which for $\Delta\nu = 256$ MHz is satisfied for $\tau \ll 0.6$ ns or $c\tau \ll 18$ cm. At the stage when phase referencing is considered, this condition should be met by calibration techniques explained in the previous sections.

In practice, visibilities are averaged in frequency on the continuum sources, giving one visibility amplitude and one phase per time bin m on baseline jk:

$$|V_{jk}(m)|e^{i\phi_{jk}(m)} = \frac{1}{N}\sum_{n=1}^{N}|V_{jk}(m,n)|e^{i\phi_{jk}(m,n)} \tag{2.50}$$

From this point onwards the I will continue to refer to delay τ, however, it is by proxy of a phase $\phi = 2\pi\nu_{\mathrm{ref}}\tau$. Phase also does not have a zero–point and is relative to the 'phase-centre' in the image domain aka $l = m = 0$ from Equation 2.13. This also means that phase referencing can only be used for relative astrometry and absolute astrometry (like that conducted by IVS) must be done using delay.

Phase referencing astrometry is the narrow–field case of measuring relative position/phase differences between a target and calibrator, separated by some angular distance θ_{sep}. The general idea is that as long as θ_{sep} is kept small, atmospheric contributing effects to the delay along a line–of–sight will be identical. If there is a calibrator with a measured delay τ_C at time t_i, this delay can be applied/subtracted from target data/delay τ_T at time t_{i+1} (which may be the same time, see below). The delay in target data is present whether detectable or not (e.g in the case of masers there is a delay in data but as a line source delay is impossible to measure) and the various forms of delay subtract:

$$\begin{aligned}\tau_T(t_{i+1}) - \tau_C(t_i) &= (\tau_{bl,T} - \tau_{bl,C}) + (\tau_{\mathrm{dry},T} - \tau_{\mathrm{dry},C}) + (\tau_{\mathrm{wet},T} - \tau_{\mathrm{wet},C}) + (\tau_{\mathrm{iono},T} - \tau_{\mathrm{iono},C})\\ &\quad + \delta\dot{\tau}_{cl}(t_{i+1} - t_i) + (\delta\tau_e - \delta\tau_e) + (\tau_{\theta,T} - \tau_{\theta,C}) + (\tau_{\sigma,T} - \tau_{\sigma,C}) + \tau_{th}\\ &= \Delta\tau_{bl} + \Delta\tau_{\mathrm{dry}} + \Delta\tau_{\mathrm{wet}} + \Delta\tau_{\mathrm{iono}} + \tau_{\theta,T} - \tau_{\theta,C} + \tau_{\sigma,T} - \tau_{\sigma,C} + \tau_{th}\end{aligned} \tag{2.51}$$

where $\Delta\tau_{bl}, \Delta\tau_{\mathrm{dry}}, \Delta\tau_{\mathrm{wet}}, \Delta\tau_{\mathrm{iono}}$ are the differences in delay due to the baseline offsets, dry and wet troposphere and ionosphere along the lines–of–sight towards the target and calibrator.

The assumption made between lines 1 and 2 of Equation 2.51 is that single-band delays have been bulk removed by manual phase calibration, then residuals multiband delays have been further modelled and subtracted by geoblock fitting. In addition to this, the clocks have been modelled in the correlator, then also fit and subtracted in the geoblock fitting. Not only should this process leave very small residuals in $\delta\tau_e$ and $\delta\dot{\tau}_{cl}$, but in the time $t_{i+1} - t_i$ the residuals in electronic delays and the residual clock delay should be the same along both lines–of–sight.

Therefore all that remains is the structure, positional, tropospheric, ionospheric and baseline–based delay terms. The delay due to the positional offsets of the target and calibrator are the desired observables, where the corresponding structural terms are hopefully identical between epochs and thereby will only bias both positions equally over time (see Section §2.3.7).

Again, due to the above-prescribed calibration which should have been performed by this point, the terms $\Delta\tau_{bl}, \Delta\tau_{\mathrm{dry}}, \Delta\tau_{\mathrm{iono}}$ are the difference in the residual respective delays. In VLBI astrometry we want them (and $\Delta\tau_{\mathrm{wet}}$) to be sufficiently small such that we can still measure a trigonometric parallax of $\varpi \sim 100\ \mu$as with $10-20\%$ fractional uncertainty.

2.3.10.1 Residual Baseline Delay

Taking Equation 2.29 , phase referencing has the effect to reduce the residual baseline uncertainty by $\theta_{\rm sep}$:

$$c\Delta\tau_{bl} = \frac{|\bar{\mathbf{s}}_2 - \bar{\mathbf{s}}_1||\Delta B|}{c} \approx \theta_{\rm sep}|\Delta B| \tag{2.52}$$

which is equivalent to a position error of

$$\sigma_\theta \approx \theta_{sep}\frac{|\Delta B|}{|\mathbf{B}|} \geq 10\,\mu\text{as}$$

if $\theta_{sep} \geq 1\,$deg, $|\Delta B| = 1\,$cm and $|\mathbf{B}| = 3500\,$km.

2.3.10.2 Residual Dry Tropospheric Delay

The target and calibrator are separated by $\theta_{\rm sep}$, which can be arbitrary in Right Ascension and Declination or azimuth and elevation at a given time. The alignment which gives the 'worst-case' scenario is if the target and calibrator are always separated by $\theta_{\rm sep}$ in the zenith direction: $Z_2 = Z_1 + \theta_{\rm sep}$ in radians. I can use this and Equation 2.43 to determine what the expected differential residual dry tropospheric would be if the zenith delay has been incorrectly estimated by $c\delta\tau_z$ in cm:

$$c\Delta\tau_{\rm dry} = c\delta\tau_z(m_3(Z_2) - m_3(Z_1)) \approx \delta\tau_z \sec^2 Z_1 \sin Z_1 \theta_{\rm sep} \tag{2.53}$$

where I have used the m_3 mapping function (Equation 2.46) for mathematical simplicity. This function diverges rapidly for values of $Z_1 \geq 60°$ (aka elevation $\varepsilon_1 \leq 30°$). Therefore, it is generally accepted, that phase referencing observations should be conducted at elevations $\varepsilon > 30°$ so that delay errors are minimised while getting as much $uv-$coverage as possible. For reasonable elevations ε, this reduces the residual dry tropospheric delay error ($\Delta\tau_{\rm dry}$) by a factor of $\theta_{\rm sep}$ in rads.

2.3.11 Residual Ionospheric Delay

The residual ionospheric delay after calibration via TEC maps (and/or dual–frequency observations) then phase referencing will simply be:

$$\Delta\tau_{\rm iono} = \delta\tau_{{\rm iono},T}(t_i) - \delta\tau_{{\rm iono},C}(t_{i+1}) \tag{2.54}$$

where $\delta\tau_{\rm iono}$ in the error in the residual ionospheric delay due along the line–of–sight towards target or calibrator. Dual–frequency observations of the calibrator allow more accurate determination of $\delta\tau_{{\rm iono},C}$ (if the calibrator C emits in continuum).

Connection of $\delta\tau_{{\rm iono},C}$ to $\delta\tau_{{\rm iono},T}$ relies on a spatial and temporal model over $\theta_{\rm sep}$ and $t_{i+1} - t_i$, which is $\delta\tau_{\rm iono}$ is a smooth function would be of the form:

$$\delta\tau_{{\rm iono},T}(t_{i+1}) = \delta\tau_{{\rm iono},C}(t_i) + \frac{\partial(\delta\tau_{\rm iono})}{\partial t}\Big|_{t_i}(t_{i+1} - t_i) + \frac{\partial(\delta\tau_{\rm iono})}{\partial\theta}\theta_{\rm sep} + \ldots \tag{2.55}$$

and is nothing more than an arbitrary Taylor Series in time and angular separation. Therefore combining Equation 2.40 and Equation 2.54:

$$\Delta\tau_{\mathrm{iono}} = \frac{1.34\times10^{9}}{\nu_{\mathrm{ref}}^{2}}\left(\frac{\partial(\delta\mathrm{TEC})}{\partial t}\Delta t + \frac{\partial(\delta\mathrm{TEC})}{\partial\theta}\theta_{\mathrm{sep}}\right) + \ldots \text{ seconds} \tag{2.56}$$

where $\frac{\partial(\delta\mathrm{TEC})}{\partial t}$ and $\frac{\partial(\delta\mathrm{TEC})}{\partial\theta}$ describe the temporal (aka dynamic) and spatial (aka static) variations in the ionospheric TEC and $T_{\mathrm{coh,iono}}$ describes the minimum switching time $t_{i+1} - t_i$ required to remain coherent.

If the coherence time can also be defined such that $\Delta t = T_{\mathrm{coh,iono}}$ and

$$\Delta\phi = 2\pi\sigma_A T_{\mathrm{coh,iono}}\nu_{\mathrm{ref}} = 1 \text{ rad} \tag{2.57}$$

where σ_A is the Allen standard deviation for the system. From this, the Allen standard deviation can be identified in the above equations as:

$$\sigma_A = \frac{1.34\times10^{9}}{\nu_{\mathrm{ref}}^{2}}\frac{\partial(\delta\mathrm{TEC})}{\partial t} \text{ s/s} \tag{2.58}$$

such that Equation 2.56 becomes:

$$\Delta\tau_{\mathrm{iono}} = \sigma_A\Delta t + \frac{1.34\times10^{9}}{\nu_{\mathrm{ref}}^{2}}\frac{\partial(\delta\mathrm{TEC})}{\partial\theta}\theta_{\mathrm{sep}} + \ldots \text{ seconds} \tag{2.59}$$

Asaki et al. (2007) simulate an Allen standard deviation for the ionosphere at 43 GHz of $\sigma_A(43) = 5\times10^{-16}$ s/s, which due to variations in TEC will be $\sigma_A(8.4) = 1.3\times10^{-14}$ s/s and $\sigma_A(6.7) = 2\times10^{-14}$ s/s at frequencies 8.4 GHz and 6.7 GHz respectively. Now the ionospheric coherence time is calculated as $T_{\mathrm{coh,iono}} = 1450$ s and $T_{\mathrm{coh,iono}} = 1200$ s at 8.4 GHz and 6.7 GHz respectively. As I will soon show, this is very large compared to the coherence time imposed by the wet troposphere and in theory, should not be a problem.

For the static term to remain coherent over angular separation θ_{sep}:

$$2\pi\frac{1.34\times10^{9}}{\nu_{\mathrm{ref}}^{2}}\frac{\partial(\delta\mathrm{TEC})}{\partial\theta}\theta_{\mathrm{sep}} \ll 1 \text{ rad} \tag{2.60}$$

then the difference in the line–of–sight TEC must be $\frac{\partial(\delta\mathrm{TEC})}{\partial\theta}\theta_{\mathrm{sep}} \ll 1$ TECU and 0.8 TECU for 8.4 GHz and 6.7 GHz respectively.

2.3.11.1 Wet Tropospheric Delay

In a similar vein as above, I can describe the wet tropospheric delay difference as:

$$\Delta\tau_{\mathrm{wet}} = \tau_{\mathrm{wet},T}(t_{i+1}) - \tau_{\mathrm{wet},C}(t_i) = \frac{\partial\tau_{\mathrm{wet}}}{\partial t}\Big|_{t_i}(t_{i+1} - t_i) + \frac{\partial\tau_{\mathrm{wet}}}{\partial\theta}\theta_{\mathrm{sep}} + \ldots \tag{2.61}$$

where again there is a dynamic term and a static term respectively.

Unlike for the previously mentioned delays, $\Delta\tau_{\mathrm{wet}}$ is not a difference of residual delays and therefore phase referencing is the first and only stage of calibration for the wet troposphere.

The wet tropospheric coherence time ($T_{\mathrm{coh,wet}}$) is defined to be the characteristic time–scale that the wet tropospheric component varies enough to cause a phase ambiguity:

$$2\pi\sigma_A T_{\mathrm{coh,wet}}\nu_{\mathrm{ref}} \sim 1 \tag{2.62}$$

where $\sigma_A = \frac{\partial\tau_{\mathrm{wet}}}{\partial t} = 0.7 \times 10^{-13}$ s/s is the Allan standard deviation for the troposphere (Reid & Honma, 2014). For radiation of frequency 6.7 GHz, this leads to a coherence time of $T_{\mathrm{coh,wet}} \sim$ 5 mins. Thus, to avoid decorrelation and successfully phase reference the wet–tropospheric phase, the source and reference need to be observed within a time-scale of 5 mins or less.

Due to the wet–troposphere being randomly dynamic, there is no known structural form that can reduce the errors by separation between target and calibrator, but to remain spatially coherent the wet troposphere must not vary by more than:

$$c\frac{\partial\tau_{\mathrm{wet}}}{\partial\theta}\theta_{\mathrm{sep}} \ll 60 \text{ mm} \tag{2.63}$$

at 8.4 GHz or 70 mm at 6.7 GHz using the same procedure as above.

2.3.11.2 Phase Referencing Methods

There are two main methods for utilizing phase referencing to reduce delays due to the wet troposphere, residual ionosphere, residual dry troposphere and residual baseline offset.

In–beam calibration involves looking at a source and calibrator simultaneously, with both inside the same primary beam. Therefore, there is no specific time–interpolation required which resolves the issue of temporal coherence. This technique becomes particularly common for low–frequency observations where beam size becomes appreciably large such that there is a high chance of finding in-beam calibrators. However, it is difficult to find a target and calibrator close enough at mid/high frequencies ($\nu \gtrsim 4$ GHz).

Nodding is perhaps the most commonly-used option for mid/high frequency phase-referencing observations. It involves bracketing target source observations with calibrator source observations well within $T_{\mathrm{coh,wet}}$ and $T_{\mathrm{coh,iono}}$. Nodding becomes difficult for high–frequency observations ($\nu \gtrsim 30\,\mathrm{GHz}$) and requires either very sensitive and/or fast-slewing telescopes. Nodding is the primary technique used in Chapter §3 to analyse recent BeSSeL VLBA data.

I will introduce and discuss an alternative technique in Chapter §5.

2.3.12 Imaging

The complex visibility measured by baseline jk at time t (previously by proxy of time–bin m) is only a discrete sample of the total spatial coherence function caused by the source $\mathcal{V}_T(u, v)$:

$$\mathcal{V}_{jk}(t) = \mathcal{V}_T(u, v)S_{jk}(u, v, t) \tag{2.64}$$

where $S_{jk}(u, v, t)$ is the sampling function of baseline jk at time t:

$$S_{jk}(u, v, t) = \delta_D(u - u_{jk}(t), v - v_{jk}(t)) \tag{2.65}$$

where δ_D is the 2D Delta–Dirac function and u_{jk}, v_{jk} are the 'uv' components (Thompson et al., 2017). The uv components of a fixed baseline (on the large scale- ignoring offsets and tectonic movement) are time–variable due to Earth rotation:

$$u_{jk}(t) = \frac{1}{\lambda}\left[B_{x,jk}\sin(t-\alpha) + B_{y,jk}\cos(t-\alpha)\right] \tag{2.66}$$

$$v_{jk}(t) = \frac{1}{\lambda}\left[-B_{x,jk}\cos(t-\alpha)\sin\delta + B_{y,jk}\sin(t-\alpha)\sin\delta + B_{z,jk}\cos\delta\right] \tag{2.67}$$

where $B_{x,jk} = X_j - X_k$ etc are the baseline components in the XYZ directions (see Section §2.3.5) and α, δ is the source position in RA, DEC (Perley et al., 1989). Therefore over time as the baseline rotates it can sample different parts of the '$uv-$plane' and the total spatial coherence function. This is the principle of 'aperture synthesis'.

The Fourier Transform of the true spatial coherence function is the brightness distribution of the source (the 'image'):

$$I(l,m) = \mathcal{F}\left\{\mathcal{V}_T(u,v)\right\} \tag{2.68}$$

while the Fourier Transform of the (summed, time–averaged) sampled visibility is called the 'dirty image':

$$I^D(l,m) = \mathcal{F}\left\{\mathcal{V}_T(u,v)S(u,v)\right\} \tag{2.69}$$

such that the relationship between image and dirty image is a convolution of the image with the Fourier Transform of the sampling function:

$$I^D(l,m) = I(l,m) * B(l,m) \tag{2.70}$$

where $B(l,m) = \mathcal{F}\{S(u,v)\}$ is the 'synthesised beam' with central main lobe FWHM:

$$\theta_B = 1.22\frac{\lambda}{|B|} \tag{2.71}$$

Recovery of the intensity distribution requires deconvolution of the dirty image with the synthesised beam, which I will be doing with the CLEAN algorithm (Högbom, 1974). I direct readers interested in the nuances of imaging via CLEAN or other deconvolution techniques to Thompson et al. (2017).

2.4 Additional Considerations

2.4.1 Annual Parallax Sampling

The first of many pre-data-collection considerations is the time of year when it is best to sample the parallax. A parallax is an angular size and is a constant over all of the observations, however, is modulated by the Earth's orbit around the Sun, where this modulation depends on source position. As the parallax magnitude is (in Galactic maser cases) very small and astrometric data contains comparable uncertainty as it is, further measurement uncertainty should be minimised if possible.

To begin with, a source with equatorial position (RA, DEC) = (α, δ) and distance $d = \frac{1}{\varpi}$ at any given time t (yrs) will have a sampled position:

$$\begin{aligned} x &= \varpi\, T_e\, (Y\, \sin\alpha - X\, \sin\alpha) + \mu_x\, (t - t_{\mathrm{ref}}) \\ y &= \varpi\, T_e\, (Z\, \cos\delta - X\, \cos\alpha\, \sin\delta - Y\, \sin\alpha\, \sin\delta) + \mu_y\, (t - t_{\mathrm{ref}}) \end{aligned} \tag{2.72}$$

where x, y (mas) are the sampled position of the source in the RA, DEC directions, α, δ are the nominal source position in RA and DEC at t_{ref}, t is fractional time of year, ϖ is the parallax (mas) and μ_x, μ_y are the proper motions in x, y (mas/year) directions. The parameters X, Y, Z describe the position of Earth relative to the Sun and T_e describes the eccentricity of Earth's orbit:

$$\begin{aligned} X &= \cos 2\pi(t - t_0) \\ Y &= \sin 2\pi(t - t_0)\, \cos\theta \\ Z &= \sin 2\pi(t - t_0)\, \sin\theta \\ T_e &= 1.0 + 0.0167\, \sin 2\pi\, (t - 0.257) \end{aligned} \tag{2.73}$$

where $\theta = 23.4°$ is obliquity of the Earth and $t_0 = 0.22\,\mathrm{yr}$ is the time of the vernal equinox.

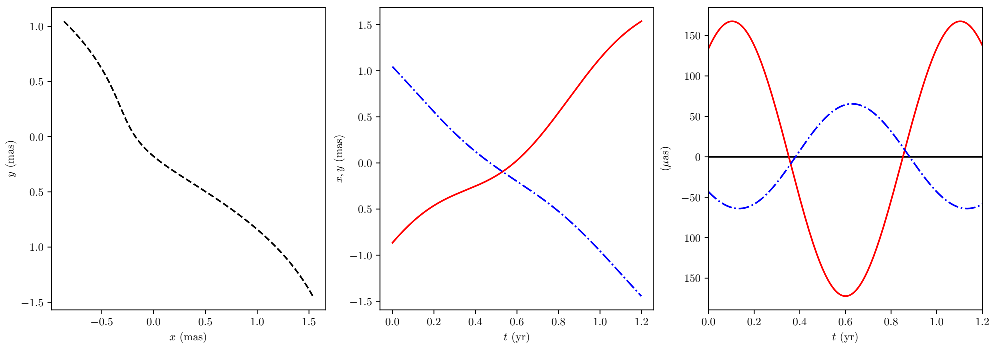

Figure 2.5: Simulated parallax for 6.7 GHz maser G329.339+0.148: $\alpha \sim 16.0\,\mathrm{hr}$, $\delta \sim -52.7°$ and kinematic distance $d \sim 6.0 - 8.5$. I arbitrarily set $\mu_x = 2.0$ and $\mu_y = -2.0\,\mathrm{mas/yr}$, and set $\varpi = 0.143\,\mathrm{mas}$. **Left**: apparent motion of target across sky. **Centre**: respective apparent motions in α (or x, red) and δ (or y, blue). **Right**: projected parallax motion (subtracting proper motion) in x and y.

Since the change in the measured astrometric position for the target source with time depends on the proper motion of the source in RA and DEC and the parallax, a minimum of 3 observations are required. However, this leaves only one degree of freedom remaining to calculate residuals and in practice, many more epochs of observations are generally conducted to reduce the uncertainty in the measured proper motion and parallax. In addition, optimal parallax sampling time has a dependence on target α and δ, weak for high– and very strong for low–declination targets. Figure 2.5 shows a simulated parallax. In this instance the Right Ascension component is 2.5× more sensitive to the parallax amplitude due to the projection of Earth's orbit and therefore observations made at the times when the RA offset due to parallax will be at a maximum magnitude (in this case early July for the minimum and early February for the maxima) is optimal.

2.4.2 Proper motion

A proper motion is defined as the movement of an object tangential to the line of sight (LoS). Spectral line Doppler shift can be used to instantaneously measure relative LoS velocity, a principle kinematic distance determinations utilise. However, proper motions require sufficiently accurate astrometry and/or time to measure.

In VLBI astrometry, cardinal directions are always expressed as RA/DEC (α, δ) and hence the measured proper motions are $\mu_x = \mu_\alpha \cos(\delta), \mu_y = \mu_\delta$. Poleski (2013) provides a succinct conversion from the measured equatorial coordinate system to a more relevant Galactic coordinate system via the introduction of a simple rotation matrix:

$$\begin{bmatrix} \boldsymbol{\mu_{l*}} \\ \boldsymbol{\mu_b} \end{bmatrix} = \frac{1}{\cos b} \begin{bmatrix} C_1 & C_2 \\ -C_2 & C_1 \end{bmatrix} \begin{bmatrix} \boldsymbol{\mu_{\alpha *}} \\ \boldsymbol{\mu_\delta} \end{bmatrix}$$

where

$$\begin{aligned} C_1 &= \sin\delta_G \cos\delta - \cos\delta_G \sin\delta \cos(\alpha - \alpha_G) \\ C_2 &= \cos\delta_G \sin(\alpha - \alpha_G) \\ \cos b &= \sqrt{C_1^2 + C_2^2} \end{aligned}$$

and $\alpha_G = 192.859°$ and $\delta_G = 27.128°$. This method requires no initial conversion into native Galactic coordinates. The '*' on the proper motions indicate reduced proper motions due to the area inequality at high l or δ: $\mu_l* = \mu_l \cos b$ and $\mu_{\alpha*} = \mu_\alpha \cos\delta$. In VLBI astrometry we directly measure $\mu_{\alpha*}$ and μ_δ.

2.5 Summary – Standard Astrometric VLBI Calibration

Throughout this thesis I will refer back to the Standard Astrometric VLBI Calibration scheme outlined in this section. This is a procedure to calibrate VLBI data starting from correlated data product form into a final form - either astrometric images (Chapter §3), *uv*–tracks (Chapter §4) or pre–multiview fitting stage (Chapter §6).

Based heavily on the procedures outlined in Brunthaler et al. (2011); Reid et al. (2009b,c) Standard VLBI Calibration is almost completely performed via $\mathcal{AIPS}$ (Astronomical Image Processing Software; Greisen, 1990) and the python wrapper software *ParselTongue/Obit* (Kettenis et al., 2006). *ParselTongue* enables access to the $\mathcal{AIPS}$ data and tables from within a python environment and facilitated examination and manipulation of the data in ways that are not provided by existing $\mathcal{AIPS}$ tasks. Nevertheless, $\mathcal{AIPS}$ provides the fast calculation and general data visualisation/manipulation via its *tasks, tables* and *catalogue* structure.

Here we concisely summarise the Standard Astrometric VLBI Calibration procedure:

1. The initial calibration step is to flag data that has been collected outside of mutual on-source time (slewing) or influenced by clock–jumps or strong radio frequency interference;
2. Geoblock analysis:
   (a) Taking the geoblock data, delays and phase corrections are applied corresponding to known Earth Orientation Parameter (EOP) corrections and feed rotation effects due

to parallactic angles for circularly polarised feeds. TEC maps are downloaded† and used to estimate ionosphere delays, which are then applied.

(b) A single scan of source within the geoblock dataset is chosen based off mutual on source time by all telescopes and SNR. Manual phase calibration is performed on this scan: single–band delays and phases are calculated (rates are specifically zeroed) for each polarisation/IF and applied to the remaining geoblock data;

(c) All geoblock scans are fringe–fit for a single multi-band delay and rate for each scan. These solutions are then fed into an external tropospheric zenith delay/residual clock delay fitting programme **fit_geoblocks_tropos** which outputs an AIPS–friendly input file containing tropospheric zenith delays vs. time for each antenna;

(d) When wideband observations have also been undertaken, dispersive delay solutions are first taken out of the dispersive geoblock delay inputs before tropospheric zenith delay fitting.

3. The calibrator and maser datasets are calibrated identically and in parallel:

   (a) TEC maps are applied, EOP and feed rotation effects are corrected, then zenith delay solutions are applied;

   (b) Telescope gains and system temperatures are applied to correct the raw voltage amplitudes to Jy;

   (c) If known, target/calibrator positional offsets are applied. This can only be calculated at one epoch and must be applied identically to all epochs thereafter;

   (d) The manual phase calibrator scan is chosen, delays and phases are calculated and applied;

   (e) Telescope motion in the source direction due to Earth orbit and rotation at telescope position not included in correlator model is calculated. This Doppler Shift is applied so that for all telescopes the frequencies observed are those that would be observed at the geocentre.

4. Either a specific channel of the maser or a calibrator is chosen as the phase reference (PR) source. If it is the calibrator is it normal PR and if it is the maser/target it is referred to as reverse–PR;

5. If the quasar is chosen:

   (a) The calibrator is averaged in frequency to increase SNR and a fringe–rates/phases are calculated at the correlated+shifted position. This solution is applied to the maser and itself;

   (b) self–calibration can be performed on the quasar to remove structure phases, solutions are applied to maser and quasar identically;

   (c) if nodding between multiple quasars, maser scans not observed within the coherence time to the relevant quasar are flagged (only if multiple quasars);

   (d) maser channel(s) are imaged via CLEAN algorithm and emission regions are fitted with Gaussian ellipticals. Centroids positions are recorded for parallax fitting.

6. If the maser is chosen:

†ftp://cddis.gsfc.nasa.gov/gps/products/ionex/

(a) A single maser channel is chosen and fringe–rates/phase are calculated at its correlated + shifted position.
   - Side note: in the case of low SNR multiple maser channels can be averaged to increase SNR. However, care must be taken to ensure that emission originates from the same maser spot otherwise astrometric accuracy will be significantly decreased.

(b) fringe solutions can be applied to maser and self–calibration can be performed. Solutions are identically applied to maser and quasar;

(c) quasar is averaged in frequency and the fringe solution is applied;

(d) quasar is imaged via CLEAN algorithm and emission region is fit with Gaussian elliptical. Centroid positions have sign reversed and are recorded for parallax fitting.

All relevant code is publicly available at https://github.com/lucasjord/thesisscripts.

3

Parallax and Proper Motions of First Galactic Quadrant Star Forming Regions

In this chapter, I present measurements of parallaxes and/or proper motions for 4 masers associated with star-forming regions in the First Galactic Quadrant. These masers were observed as part of the Bar and Spiral Structure (BeSSeL) Survey's most recent programme: BR210. I use the measured and previous parallaxes to fit a spiral arm model to the maser distributions in the Perseus arm and use the proper motions to determine local Galactic kinematics. Finally, I discuss the applicability of these techniques to SπRALS.

3.1 Introduction

The BeSSeL Survey has been an ongoing legacy project on the VLBA since 2010 and in that time has collected data on just under 200 masers* cumulating in the reduction and publication of > 90% (Reid et al., 2019, not including parallaxes published as part of the VERA project). These parallaxes, proper motions and resultant distances individually provide important size, luminosity and kinematic information about the specific star-forming region, which can be then used in other studies. When combined in a large collection they are utilized to trace the structure, dynamics and constrain the size and mass of our Galaxy (Reid et al., 2014, 2019).

Despite the large and sweeping success of BeSSeL and VERA (VERA Collaboration et al., 2020), there have been numerous target masers for which a parallax observation has not resulted in a significantly constrained distance. Most of these can be attributed to water maser variability and eventual spot disappearance over the course of a year. Even in cases where the maser spot persists for a majority of a year, disappearance in final epochs can cause the parallax and proper motion to become covariant in the parallax and proper motion fitting process.

Initial BeSSeL observations (made under project codes BR145 and BR198) were limited to targeting 22.2 GHz water and occasional 12.2 GHz class II methanol masers. Upgrades to the VLBA in 2015 allowed observations of 6.7 GHz methanol masers, and in response, BeSSeL conducted the BR149 series exclusively dedicated to targeting these masers. At the sacrifice of generally less compact maser spots, 6.7 GHz methanol masers have greatly reduced average variability compared to their 22 GHz counterparts (Brand et al., 2003; Caswell et al., 1995a; Reid et al., 2017). This means phase reference features persist for periods much longer than a year. In addition at these lower frequencies interferometer, coherence times are much longer and it was believed that phase errors resulting from residual tropospheric delays would allow as stable (if not more stable) phase referencing solutions. Therefore BR149 proceeded with the observations of 6.7 GHz methanol masers as 4 epochs per maser spaced out over 12 months.

Regrettably, parallax measurements for the methanol masers in BR149 were significantly noisier than previous water maser measurements and as a result, sometimes maser distances were very difficult to constrain (Reid et al., 2017). The source of this added uncertainty is attributed to the residual ionosphere, which was not initially expected to be a major influence at intermediate frequencies. In some extreme cases, different quasars would even give systematically different parallax measurements, suggesting a parallax 'gradient' over the sky (Reid et al., 2017; Zhang et al., 2019).

Therefore the next BeSSeL series BR210 was designed to combat the issue of water maser variability and per-epoch systematic positional offsets due to the ionosphere. The primary difference between BR210 and previous BeSSeL series' is that there are 16 epochs observed over a single year and a minimum of 2 reference quasars per target maser.

Figure 3.1 shows modelled locations for the Local, Perseus and Outer arms as derived from pitch angles and rotation curves given in Reid et al. (2019) projected on a l–v diagram with CO emission contours. Included are the locations of many HMSFR as traced by 6.7 GHz methanol masers. Concerning the Perseus arm, there exists a region between $50 < l < 80°$ with little in the way of dense gas regions or HMSFR, which is commonly referred to as the *Perseus gap*, and is inexplicable by either arm projection or sensitivity.

The aim of the parallax observations described in this chapter is to increase our knowledge of

*http://bessel.vlbi-astrometry.org/observations

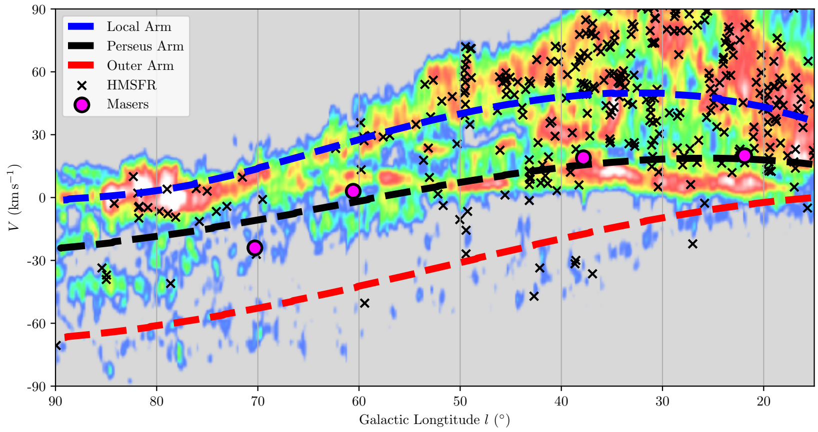

Figure 3.1: $l-v$ diagram of the first Galactic quadrant. **Coloured contours**: Integrated CO emission from Dame et al. (2001); **Blue, black and red dashed lines**: projected arm locations for the Local, Perseus and Outer arms respectively; **Black crosses**: High mass star formation regions as traced by 6.7 GHz methanol masers from Yang et al. (2019); **Pink:** location of masers analysed in this chapter.

the structure of the first Galactic quadrant, particularly concerning the Perseus arm and Perseus gap by analysing BeSSeL VLBA data for three water masers and one methanol maser observed as part of BR210 and discuss the nuances of each parallax and region.

3.2 Observations and Reduction

Observational data were collected on the NRAO VLBA: project codes, epochs of observation and fractional year are shown in Table A.1. BR210 observations were split into six separate groupings, labelled A through to F, each containing 4–5 target masers based on sky distribution. BR210A→E comprises 22.2 GHz water masers while BR210F includes only 6.7 GHz methanol masers.

The individual observing sessions were $\sim 7-9$ hours with approximately identical layouts. Each epoch contains 1 shared track for between 4–5 individual maser targets bracketed by geoblocks. In addition, there are two geoblocks placed bracketing the transit ± 2 hours. Geodetic block data was recorded in left circular polarization with 8×16 MHz bands, and line data was recorded in dual polarisation with 4×16 MHz (8 IFs total and 512 Mbits/s rate in both recording modes). For K–band and C–band the modes were slightly different. The data were correlated with the DiFX software correlator (Deller et al., 2011) in Socorro, New Mexico.

Correlated fits files can be publicly downloaded by using the Advanced Search Tool located here: https://archive.nrao.edu/archive/advquery.jsp, with project codes located in Table A.1.

3.2.1 K–band: BR210A to E

Mode 1, geoblock: These bands were spaced such that the lower edge was

$$\nu_L = 23522 + 14 \times (0, 1, 4, 9, 15, 22, 32, 34) \text{ MHz}$$

for each of the eight 16 MHz bands. This spacing is deliberate as it maximises delay–sensitivity in the synthesised bandwidth by minimising degenerate spacings. Synthesised bandwidth for geoblock data is $\Delta\nu = 492\,\text{MHz}$.

Mode 2, line: Masers, associated calibrators and fringe–finder calibrators were observed $\Delta\nu = 64\,\text{MHz}$ continuous bandwidth centred on $\nu_0 = 22.235$ GHz.

For both modes all sources and IFs were correlated in 32 spectral channels ($\delta\nu_{\text{cont}} = 0.5\,\text{MHz/chan}$). Line data processed in an additional pass: a zoom band for one of the IFs (that contained the maser line), correlated 2000 channels giving fine frequency resolution $\delta\nu_{\text{line}} = 8$ kHz/chan or velocity resolution $\delta v = 0.108\ \text{km}\,\text{s}^{-1}$.

3.2.2 Wide C–band: BR210F

Mode 1: two frequency groupings of 4×16 MHz IFs spaced 2.978 GHz apart. Each grouping was $\Delta\nu = 496$ MHz synthesised bandwidth with lower band edge frequencies as given below:

$$\nu_{L,\text{LO}} = 4112 + 4 \times (1, 20, 80, 120) \text{ MHz}$$
$$\nu_{L,\text{HI}} = 7090 + 4 \times (1, 20, 80, 120) \text{ MHz}$$

again spaced to maximise delay–sensitivity in the individual 4.3 and 7.3 GHz groups. Mode 2: Masers and calibrators were observed in 4 adjacent 16 MHz IFs centred on $\nu_0 = 6.668$ GHz.

All data correlated with 32 channels pass 1. Second pass on mode 2 data: central 8 MHz zoom band (subset total IF bandwidth, usually correlated with much higher spectral resolution to minimise data size and correlation time) of the third IF correlated with 2000 spectral channels $\delta\nu_{\text{line}} = 4$ kHz/chan or velocity resolution $\delta v = 0.18\ \text{km}\,\text{s}^{-1}$.

3.2.3 Sources

The targets consisted of three 22.2 GHz water masers and one 6.7 GHz methanol maser believed to be located in the Perseus Arm of the Milky Way based on kinematic distances and known Galactic structure. Maser and reference quasar information is given in Table 3.1.

3.2.4 Calibration

The VLBA data reduction was conducted via the Standard VLBI Calibration procedure (see Section §2.5) as applicable to the observing frequencies and modes listed above. The only difference to the calibration procedure came in the form of various time range flagging: more often than not there was a clock jump directly after the first geoblock compared to the second. This is a known issue with the VLBA at that time and comes about as a consequence of the first (and only the first) frequency change in an experiment. The resolution to this issue is to flag the time range before the jump at offending stations.

Table 3.1: Information on observed masers and quasars. Columns: **(1)** Name in Galactic coordinates for masers and J2000 for quasars, **(2)** Right Ascention in J2000, **(3)** Declination in J2000, **(4)** median self–calibrated image integrated flux density, **(5)** separation between maser and quasar, **(6)** mean maser emission velocity, **(7)** maser type– either 22.2 GHz H_2O or 6.7 GHz CH_3OH.

Name	$\alpha_{\mathbf{J2000}}$ **(hh:mm:ss)**	$\delta_{\mathbf{J2000}}$ **(dd:mm:ss)**	S **(mJy)**	θ_{sep} **(deg)**	V **(km s^{-1})**	**Type**
G021.87+0.01	18 : 31 : 01.7367	−09 : 49 : 01.116	...	...	+19.6	H_2O
J1825−0737	18 : 25 : 37.6096	−07 : 37 : 30.013	116^{+1}_{-1}	2.566	...	
J1835−1115	18 : 35 : 19.5754	−11 : 15 : 59.326	< 10	1.793	...	
G037.81+0.41	18 : 58 : 53.8794	+04 : 32 : 15.004	...	...	+19.0	H_2O
J1855+0251	18 : 55 : 35.4364	+02 : 51 : 19.563	72^{+16}_{-29}	1.874	...	
J1856+0610	18 : 56 : 31.8388	+06 : 10 : 16.765	151^{+19}_{-29}	1.738	...	
G060.57−0.18	19 : 45 : 52.5019	+24 : 17 : 42.749	...	...	+3.7	CH_3OH
J1946+2418	19 : 46 : 19.9607	+24 : 18 : 56.909	24^{+5}_{-1}	0.116	...	
J1949+2421	19 : 49 : 33.1420	+24 : 21 : 18.245	124^{+12}_{-9}	0.921	...	
G070.29+1.60	20 : 01 : 45.3486	+33 : 32 : 45.711	...	...	−26.7	H_2O
J1957+3338	19 : 57 : 40.5499	+33 : 38 : 27.943	126^{+6}_{-24}	1.024	...	
J2001+3323	20 : 01 : 42.2090	+33 : 23 : 44.765	137^{+13}_{-13}	0.151	...	

3.3 Results and Discussion

3.3.1 Astrometry and Parallax Fitting

The first step after calibration was imaging the calibrated visibility data. I used $\mathcal{AIPS}$ task IMAGR† to Fourier Transform the gridded (u, v) visibility data for the maser spot or quasar of interest. These imaged were iteratively deconvoluted from the beam with the CLEAN algorithm (with options in IMAGR of gain=0.3 and niter=200).

Next I used task **JMFIT** ‡ with options DOPRINT=-4 and NITER=200 to fit elliptical Gaussians to maser or quasar emission in phase referenced images. The region over which the elliptical Gaussians were fit was manually selected with $\mathcal{AIPS}$ verb **TVWIN**. Tables A.2, A.3, A.4 and A.5 show the measured flux densities and astrometric positions of masers or quasars over time resulting from this fitting.

The parallax ϖ and proper motions μ_x, μ_y are solved from the measured position over time (x, y) via least squares on Equation 2.72. This process is undertaken using the FORTRAN programme **fit_parallax_multi_4d** (written and provided by Mark J. Reid and partially described in Reid et al., 2009b)). I have made the programme available at https://github.com/lucasjord/thesisscripts.

The programme accepts independent errors floors in for North-South/East-West data to account for systematic uncertainties that may affect each coordinate separately, then iteratively fits the for the parallax and proper motion. The final fit and uncertainties are those such that the reduced chi-squared $\chi^2_\nu \approx 1$ for each coordinate data.

Measured parallax and proper motions are given in Table 3.2 with the parallax and proper motion curves given in Figures 3.3, 3.5, 3.6, 3.10, 3.11 and 3.15. Images of quasar and maser reference features are given in Section §A.1.1.

3.3.2 G021.87+0.01

G021.87+0.01 is a 22.2 GHz water maser spatially associated with HII regions GAL021.87+00.01 and GAL021.88+00.02 (Rodgers et al., 1960; Wink et al., 1982)(Figure 3.2). There is limited epoch coverage for this source, which persisted for only half a year. Therefore there was not enough data to determine an accurate parallax.

I measured the parallax of $\varpi = 0.172 \pm 0.174$ mas towards G021.87+0.01, which is not statistically significant. Due to the very high fractional uncertainty ($f \sim 1$) no inclusion of priors into the parallax probability can resolve the issue. The measured parallax upper limit is $\varpi_{\max} = \varpi + 3\sigma_\varpi = 0.69$ mas and inversion of this parallax inversion suggests the minimum distance is $D = 1.44$ kpc: even with the uncertainty encountered, a maser at this distance would have a measurable parallax and therefore this is the preliminary lower–bound estimate. Although trigonometric parallax cannot be directly determined from the data, I will attempt to use my measurements to constrain the distance with existing models.

Using the measured recession velocity of the maser $v = 19.6^{+5}_{-2}\,\mathrm{km\,s^{-1}}$, I calculate a kinematic

†http://www.aips.nrao.edu/cgi-bin/ZXHLP2.PL?IMAGR
‡http://www.aips.nrao.edu/cgi-bin/ZXHLP2.PL?JMFIT

Table 3.2: Measured parallax and proper motions of masers. **(1)** Maser name derived from Galactic coordinates, **(2)** quasar name derived from J2000 coordinates, **(3)** measured parallax, **(4)** measured proper motion in East–West direction, **(5)** measured proper motion in North–South direction, **(6)** distance estimates. Sources used as the reference in each case is indicated with *. Errors are given as $\pm 1\sigma$ for parallaxes and proper motions, or 25% and 75% interquartile ranges for distances.

Maser	**Reference**	ϖ **(mas)**	μ_x **(mas yr^{-1})**	μ_y **(mas yr^{-1})**	D **(kpc)**
G021.87+0.01	$J1825-0737^*$	0.172 ± 0.174	-2.79 ± 0.69	-6.10 ± 0.12	$\gtrsim 1.44$
Best estimate					$10.9^{+4.3}_{-4.6}$
G037.82+0.41	$J1855+0251^*$	0.093 ± 0.010	-2.622 ± 0.025	-5.837 ± 0.037	
	$J1856+0610^*$	0.074 ± 0.011	-2.660 ± 0.028	-5.514 ± 0.037	
Variance–Weighted average		0.084 ± 0.008	-2.64 ± 0.02	-5.68 ± 0.03	$11.90^{+0.82}_{-0.72}$
G060.57–0.18*	$J1946+2418$	0.130 ± 0.011	-3.237 ± 0.028	-5.729 ± 0.040	
	$J1949+2421$	0.131 ± 0.014	-3.217 ± 0.036	-5.638 ± 0.033	
Variance–Weighted average		0.130 ± 0.009	-3.23 ± 0.02	-5.67 ± 0.03	$7.69^{+0.38}_{-0.34}$
G070.29+1.60					
Combined fit	$J1957+3338^*$ &				
w/ Jackknife	$J2001+3323^*$	0.109 ± 0.041	-1.52 ± 0.14	-3.75 ± 0.06	$9.2^{+2.6}_{-3.0}$

distance. An analytic rotation curve:

$$\begin{aligned}\Theta(R) &= \Theta_\odot(k_0 + k_1\frac{R}{R_\odot}) \qquad && 3 < R < 8\,\text{kpc} \\ &= \Theta_\odot && R > 8\,\text{kpc}\end{aligned} \tag{3.1}$$

gives an Galactic rotation speed Θ for values of Galactocentric radius R, with $k_0 = 0.889$, $k_1 = 0.171$ (McClure-Griffiths & Dickey, 2016a) and $\Theta_\odot = 235 \pm 5\,\text{km}\,\text{s}^{-1}$, $R_\odot = 8.35 \pm 0.15$ (Reid et al., 2014). Then, Equation 1.2 can be used to infer Galactocentric radius from observed recession velocity. Distance (D) can be calculated from Galactocentric radius via the cosine rule:

$$R^2 = R_\odot^2 + D^2 - 2DR_\odot \cos l \tag{3.2}$$

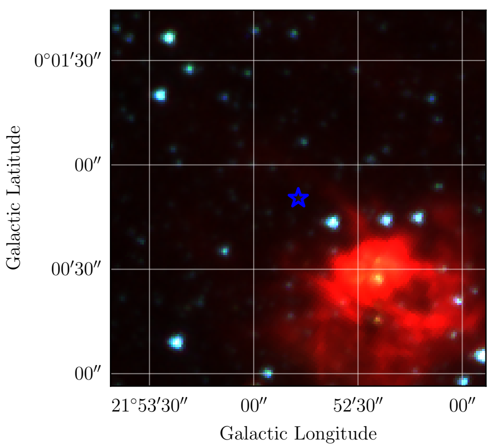

Figure 3.2: Astrometric position of H_2O maser G021.87+0.01 against *Spitzer* GLIMPSE data. **Blue star:** position of G021.87+0.01 $l = 21.87977$, $b = 0.01401$ deg. **RGB image:** 8, 4.5 and 3.6μm emission.

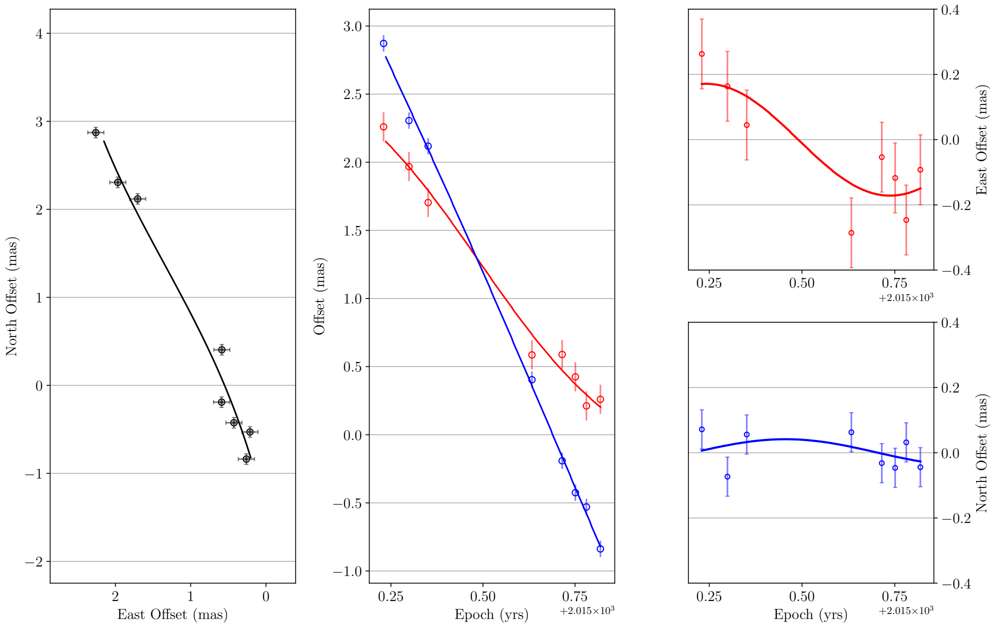

Figure 3.3: Time–varying position of G021.87+0.01 relative to QSO J1825–0737 with solid lines indicating best–fit. **Left panel:** Total sky motion of G021 vs. QSO. **Centre panel:** Time–varying position of G021 relative to QSO in North–South (blue) and East–West (red) vs. time. **Right panels:** Proper motion–subtracted time–varying position of G021 relative to QSO (parallactic motion) in aforementioned directions. Epochs 1, A(10), B(11), C(12), D(13), E(14), F(15), G(16) are excluded from fit due to lack of detectable phase reference feature in either spectrum or map.

As the maser recession velocity is positive in the first quadrant, it implies the maser is inside the solar circle ($R < R_\odot$) and therefore gives near/far kinematic distances $D_n = 1.8^{+0.7}_{-0.9} \pm \sigma_{d,\mathrm{sys}}$ and $D_f = 13.7^{+0.9}_{-0.7} \pm \sigma_{d,\mathrm{sys}}$ kpc. The lower–bound distance estimate from the parallax does not help to resolve the KDA. The uncertainties presented here are: including the velocity spread in the water maser carried in quadrature (e.g. $D^{\mathrm{lower}}_{\mathrm{upper}}$) and some unknown systematic offsets in the model $\sigma_{d,\mathrm{sys}}$ (which could have been determined from a measurable parallax.)

Although the parallax was not statistically significant, the proper motions were. I measured proper motions of $\mu_x = -2.79 \pm 0.69$ and $\mu_y = -6.10 \pm 0.12\,\mathrm{mas/yr}$. In Galactic coordinates this becomes $\mu_{l*} = -7.3 \pm 0.3$, $\mu_b = 0.2 \pm 0.3\,\mathrm{mas/yr}$ and signifies almost complete motion in the negative l–direction (which is towards the Galactic centre). Using the above rotation curve, I calculate the possible velocities tangential to the line of sight (v_t) with:

$$v_{t,\mathrm{model}} = \sqrt{\Theta(R)^2 + \Theta_\odot^2 - 2\Theta(R)\Theta_\odot\,(R_\odot - d\cos l)}$$

The measured Galactic rotation speed of the maser will be

$$v_t = 4.7\,d\,\mu_{l*}\ \mathrm{km\,s^{-1}} \tag{3.3}$$

where 4.7 is the approximate conversion between $\mathrm{km\,s^{-1}}$ and AU/yr if d is in kpc and μ_{l*} is in

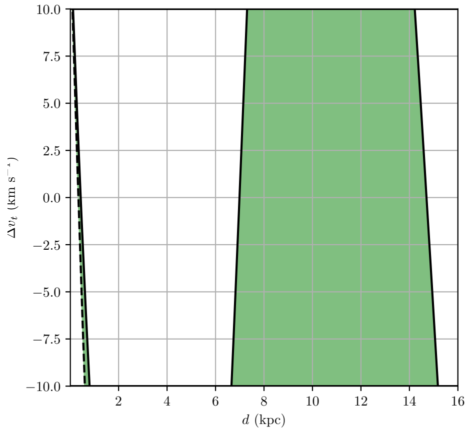

Figure 3.4: Modelled proper motion distance for G021.87+0.01 vs. residual velocity. **Solid line:** Upper 95% CI limit with $\mu_{l*} = -6.4\,\mathrm{mas/yr}$; **Dashed line:** Lower 95% CI with $\mu_{l*} = -8.2\,\mathrm{mas/yr}$. **Green region:** acceptable velocity differences bounded by $\pm 10\,\mathrm{km\,s^{-1}}$.

mas/yr. Figure 3.4 shows the result of the modelling the velocity difference Δv:

$$\Delta v = v_t - v_{t,\mathrm{model}} \tag{3.4}$$

against d. For a maximum velocity difference of $|\Delta v| < 10\ \mathrm{km\,s^{-1}}$, favourable regions include $0.1 < D < 0.8$ and $6.3 < D < 15.2\,\mathrm{kpc}$, the larger of the two being consistent with the lower bound distance **and** the kinematic distance simultaneously.

It should be noted that the line–of–sight does not pass through the Galactic centre region $R \sim 3$ kpc: the closest radius is $R = R_\odot \sin l \approx 3.1$ kpc. Therefore I do not need to include the complex velocity structure present there in Equation 3.1.

Looking at additional information that may be relevant to estimating the distance to this source, it is listed as having an 'Unconstrained' KDA resolution from either HI self-absorption, emission/absorption or 8μm absorption (Ellsworth-Bowers et al., 2015).

Based off the above information, the answer that most consistently agrees with all the data is $D = 10.9^{+4.3}_{-4.6}$ kpc from Figure 3.4. If the maser is at this distance then it would have a parallax of $\varpi = 0.092^{+0.067}_{-0.026}$ mas.

I attribute the poor parallax constraint to maser morphological changes over the course of the observations. The spectrum (Figure A.5) and spot map (Figure A.6) change in the first 3 weeks between epochs 1 and 2, then is relatively stable for the next 44 days between epochs 2 and 4. In the 100 day spacing between epochs 4 and 5, both the spectrum and spot map change drastically: there is only one feature remaining it does not align in velocity with any of the previous features. Regrettably, the spread of the observations does not allow for careful sampling of the flux density variations over time, however, it is clear that the spectrum remained stable for at least 8 weeks after the 5th epoch between epochs 5 and 12. At the 12th epoch the reference spot (Figures A.6, lower left) is very weak. Comparing the calibrator flux density for epoch 12 against previous and future epochs indicates that this dimming is likely intrinsic and not a calibration or on-source time issue; in fact, the noise level in the synthesised images remains similar over the epochs. The maser is not visible in either the spectrum or spot map from epoch 13 onwards.

The spectra for the initial 4 epochs is very likely emanating from a different set of maser spots than the following 7, after which the maser dims below detectable levels. This necessity to 'change' phase reference features whether intended or otherwise introduces large systemic uncertainties that likely mask any detectable parallax signature. The spectral feature from the latter epochs was from the same region and velocity, but likely a different part of the star formation region. Luckily all features shared the same proper motion and this is why it was detectable despite the feature change.

The phase reference feature (post epoch 7) also had structure. Imaging this feature with all 9 antennas proved difficult and began to resolve the internal structure which had varying intensity between the components. Therefore only the inner–five VLBA antennas (FT, KP, LA, OV and PT) with a max baseline of $|\mathbf{B}| = 1508$ km were used and this also placed a lower–bound on the possible astrometric accuracy. If the delay calibration was performed to $c\tau \gtrsim 1$ cm, then the minimum astrometric accuracy of any particular epoch is $\sigma_\theta \gtrsim \theta_{\rm sep}\frac{1\,{\rm cm}}{1508\,{\rm km}} \sim 60\mu$as.

Finally only one of the two calibrators had sufficient intensity to be used as a phase reference calibrator. As the maser was weak and variable, inverse phase referencing was impossible for almost all epochs and normal phase referencing was required. The observations were designed for inverse phase referencing, with half the phase referencing time on the maser and a quarter on each calibrator. Therefore only using a single QSO meant the sensitivity on the maser was reduced by a factor of $\sqrt{2}$ as half the data were outside the coherence time.

3.3.3 G037.81+0.41

G037.81+0.41 is a 22.2 GHz water maser located towards HII regions and submillimeter sources in the inner Galaxy (Figure 3.7). I measured a parallax of $\varpi = 0.084 \pm 0.008$ mas towards this star formation region, which implies a distance of $D = 11.90^{+0.82}_{-0.72}$ kpc. As the parallax has fractional uncertainty $f \simeq 0.1$, no inclusion of priors or additional information is required and this is considered a direct measurement of the distance. The proper motions were measured as $\mu_x = -2.64 \pm 0.02$, $\mu_y - 5.68 \pm 0.03$ mas/yr, which converts to Galactic proper motions of $\mu_{l*} = -6.27 \pm 0.02$, $\mu_b = -0.266 \pm 0.02$ mas/yr. These proper motions may also contain systematic offsets due to the internal motion of the maser. If the internal motions of the maser are of order $v_{\rm int} < 50$ km s^{-1} (e.g like those in Burns et al., 2015), then the maximum systematic offsets in the proper motions would be $\mu_{\rm int} < 0.9$ μas/yr (using the same conversion as Equation 3.3).

Figure 3.8 shows the spectrum and spatial–velocity distribution of maser spots (spot map) for G037.82+0.41. The water maser has a spectrum with ~ 5 peaks but a rich spatial distribution of spots. The spatial distribution of spots is reflective of a bipolar outflow as is commonplace in water maser structures.

The parallax measurement of G037.82+0.41 is a prime example of everything going right: compact maser component, compact and bright quasar sources, non–variable reference feature and no external/weather problems impacting observations. As such the measurement error in the trigonometric parallax can reach the desired value of $\sigma_\varpi < 10$ μas.

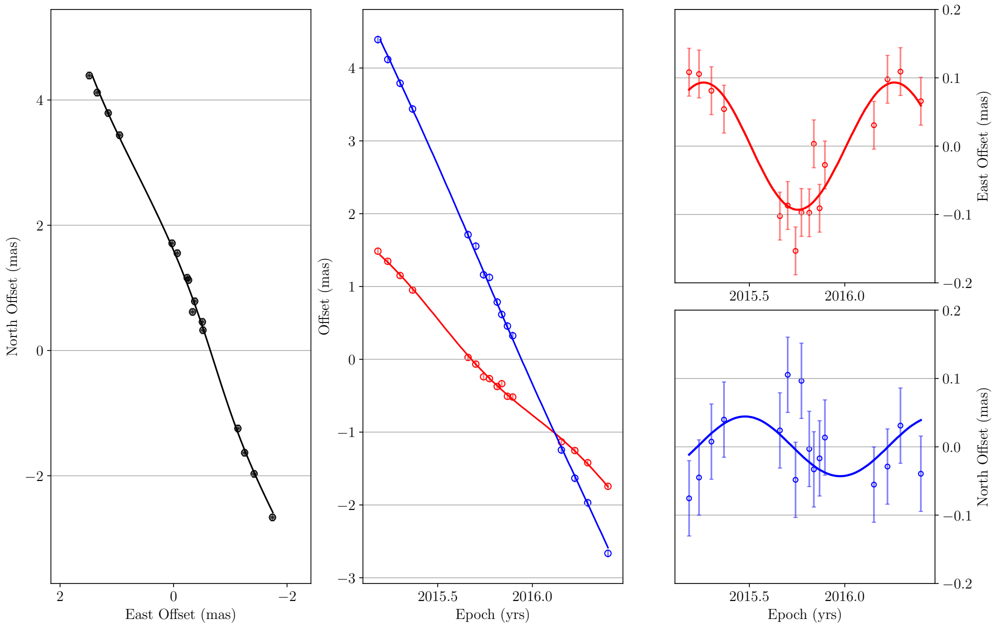

Figure 3.5: Parallaxes and proper motion fit of target G037.82+0.41 with respect to J1855+0251. **Left panel:** Total sky motion **Centre panel:** Time–varying position in North–South (blue) and East–West (red) directions vs. time. **Right panels:** Proper motion–subtracted time–varying position in aforementioned directions.

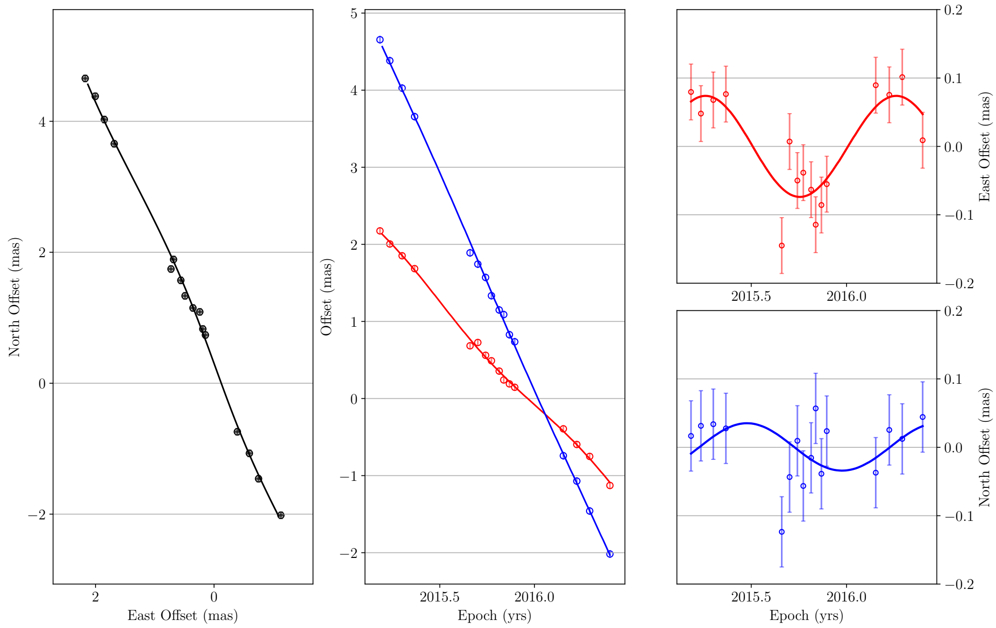

Figure 3.6: Parallaxes and proper motion fit of target G037.82+0.41 with respect to J1856+0610. **Left panel:** Total sky motion **Centre panel:** Time–varying position in North–South (blue) and East–West (red) directions vs. time. **Right panels:** Proper motion–subtracted time–varying position in aforementioned directions.

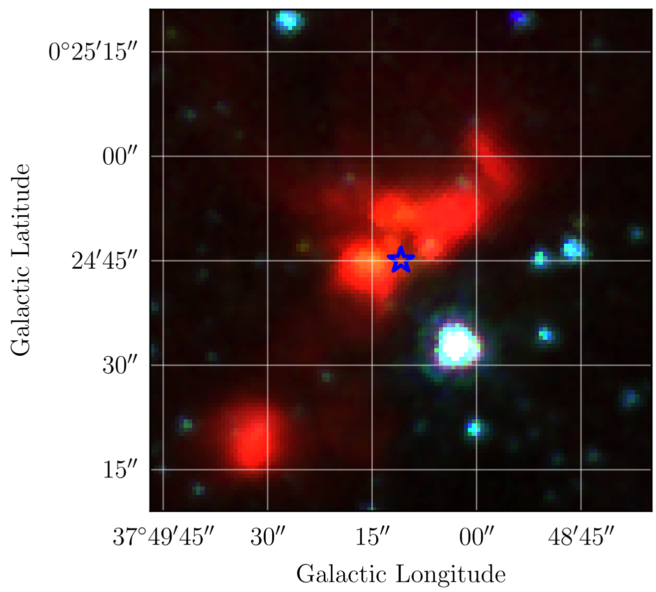

Figure 3.7: Astrometric position of H_2O maser G037.82+0.41 against *Spitzer* GLIMPSE data. **Blue star:** position of G037.82+0.41 l = 37.81968, b = 0.41252 deg. **RGB image:** 8, 4.5 and 3.6μm emission.

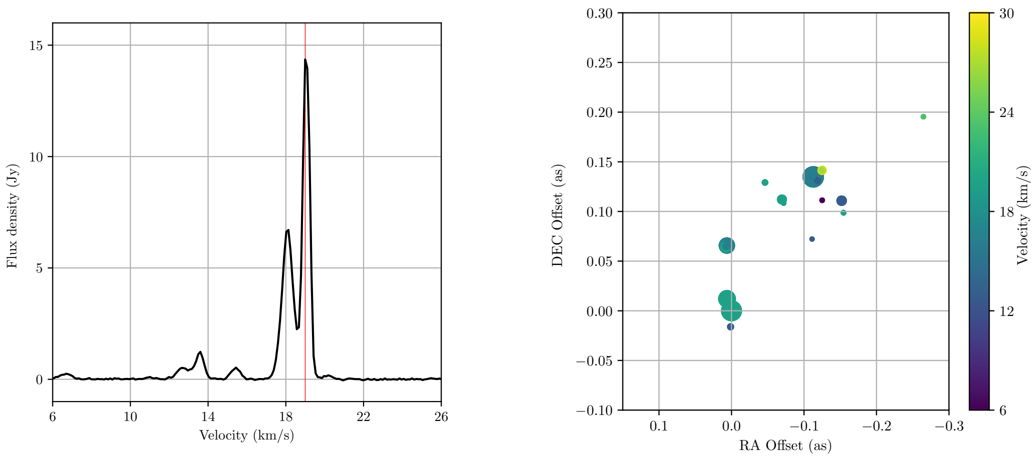

Figure 3.8: Spatial-velocity distribution of emission in G037.82+0.41 on epoch BR210C9. **Left:** Spectrum. Vertical red line indicates phase reference velocity. **Right**: Spotmap. Phase reference feature at (0,0). Phase reference velocity does not line up with peak in spectrum as there are two emission regions overlapping in frequency and spatially proximate (North–East of phase reference feature, similar velocity).

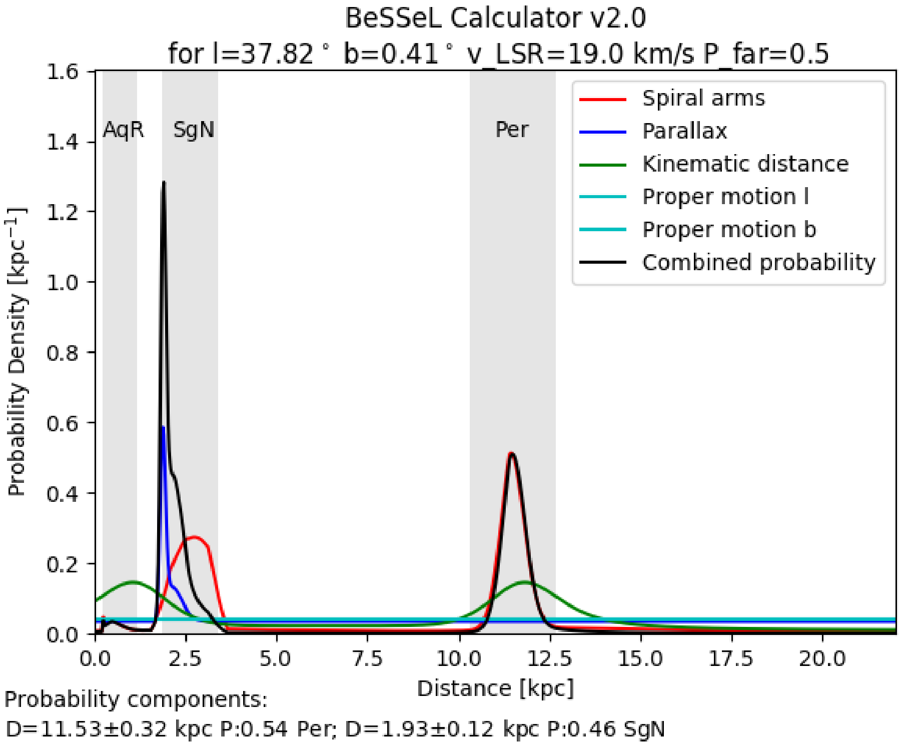

Figure 3.9: Distance prediction from the Bayesian Distance Calculator. The BDC combines the probabilities of each of the predictors (coloured and given in the legend) to estimate the distance. I have excluded my proper motion from this fit to see what would be the prediction with no information from these observations. The calculator favours either $D = 11.53$ or $D = 1.93$, the former being slightly more favoured and also consistent with the distance inferred from the measured parallax.

Finally, I can compare the inferred distance to that predicted by models. The Bayesian distance calculator (BDC; described thoroughly in Reid et al., 2016) predicts the location of an object (usually a maser) using its recession velocity, sky position and (if available) proper motion. Using the sky position and recession velocity the BDC gives a distance to G037.82+0.41 of $D = 11.53$ kpc, which is consistent with the measured distance of $D = 11.90^{+0.82}_{-0.72}$ kpc Figure 3.9.

3.3.4 G060.58–0.18

G060.58–0.18 is 6.7 GHz class II methanol maser located towards a giant molecular cloud and HII region (Figure 3.12). A simple maser with a single emission region present in the auto– and cross-correlation spectrum, only had one maser spot visible in the maps over the 16 epochs. This spot was compact and showed very little sign of variation and no signs of evolution.

I measured a parallax of $\varpi = 0.130 \pm 0.009\,\mathrm{mas}$ for G060.48–0.18 which gives a distance of $D = 7.69^{+0.38}_{-0.34}$ kpc. The low fractional uncertainty $f = 0.07$ makes the distance probability distribution near–Gaussian and therefore unambiguous. I also measured a proper motion of $\mu_x = -3.23 \pm 0.02$ and $\mu_y = -5.67 \pm 0.03\,\mathrm{mas/yr}$ which become $\mu_{l*} = -6.52 \pm 0.05$, $\mu_b = -0.09 \pm 0.01\,\mathrm{mas/yr}$.

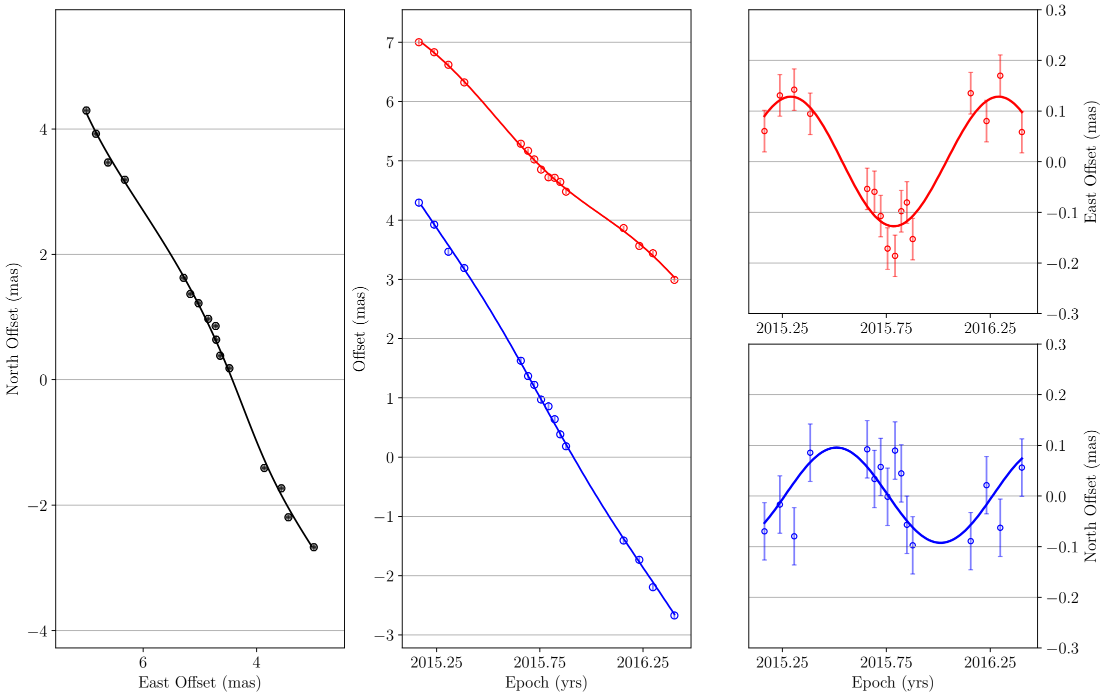

Figure 3.10: Parallaxes and proper motion fit of target G060.57–0.18 with respect to J1946+2418. **Left panel:** Total sky motion **Centre panel:** Time–varying position in North–South (blue) and East–West (red) directions vs. time. **Right panels:** Proper motion–subtracted time–varying position in aforementioned directions.

These values are statistically identical to the published parallax and proper motion of $\varpi = 0.121 \pm 0.015\,\mathrm{mas}$ and $\mu_x = -3.26 \pm 0.15$ and $\mu_y = -5.66 \pm 0.15\,\mathrm{mas/yr}$ (Reid et al., 2019). These older measurements were attained as part of BR149(R) and used a 4–quasar setup of J1946+2418, J1949+2421 (which were used in BR210), J1946+2300 and J1936+2357 observed in 4 epoch total. Even though BR210 had 4× as many epochs there was not an assumed 2× decrease in parallax uncertainty (instead of $\frac{9}{15}$). Either formal errors in the original observations were underestimated, or there are sources of systematic uncertainty, so increasing the number of epochs does not reduce the uncertainty by $\sqrt{N}$. Nevertheless, the systematic errors must be sufficiently small or epoch independent to not skew the result.

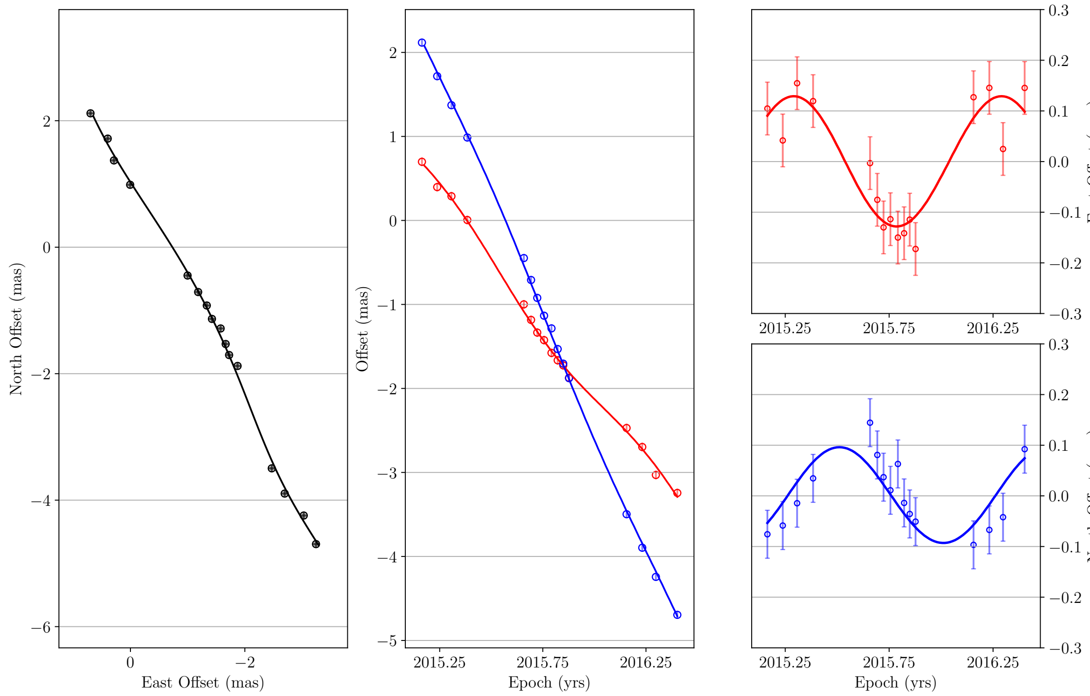

Figure 3.11: Parallaxes and proper motion fit of target G060.57–0.18 with respect to J1949+2421. **Left panel:** Total sky motion **Centre panel:** Time–varying position in North–South (blue) and East–West (red) directions vs. time. **Right panels:** Proper motion–subtracted time–varying position in aforementioned directions.

The maser feature used for astrometry had a constant unresolved flux density of $S_\nu \sim 5\,\mathrm{Jy}$, allowing for inverse PR to both quasars at all epochs with high SNR ≥ 150 (Table A.4). The quasars themselves were of very high quality in terms of flux density, absence of structure (Figure A.3) and perhaps most importantly: angular distance from maser (Figure 3.13).

The two quasars J1946+2421 and J1949+2418 were $\theta_{sep} = 0.116$ and 0.921 deg from the maser respectively. Given the SNR on the detected quasars, the thermal noise is expected to be $\sigma_{th} \sim 4\mu$as and implies that the systematic uncertainty in the per–epoch astrometry is $\sigma_\theta = 2\sigma_\varpi = 22$ and 28μas for each quasar. Since the quasars are offset from the maser in approximately the same direction I consider the case where measurement uncertainty is modelled as being radially dependent on the separation between the calibrator and target:

$$\begin{aligned}\sigma_\theta^2 &= \sigma_{\text{sep}}^2 + \sigma_{\text{const}}^2 \\ &= \left(\frac{c\sigma_\tau}{|B_{\max}|}\theta_{\text{sep}}\right)^2 + \sigma_{\text{const}}^2\end{aligned} \tag{3.5}$$

with a distance independent term σ_{const} and the dependent term σ_{sep},

The fit to the two-point data gives $\sigma_{\text{const}} = 22\mu$as and $\frac{c\sigma_\tau}{|B_{max}}| = 18.8\ \mu$as/deg $= 5.2\times10^{-9}$, with the distant–independent term absorbing most of the uncertainty. Therefore the expected average per–epoch residual delay is $c\sigma_\tau = 4.5$ cm, which, while it is consistent with that expected from

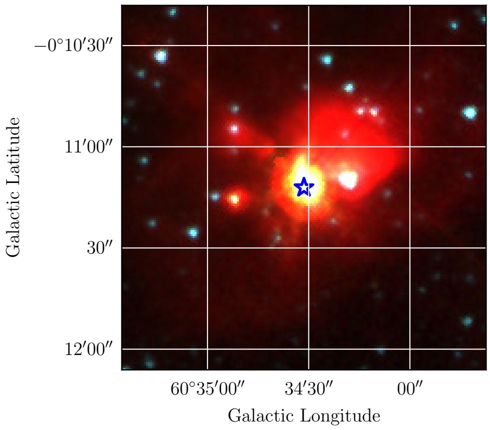

Figure 3.12: Astrometric position of CH_3OH maser G060.58–0.18 against *Spitzer* GLIMPSE data. **Blue star:** position of G060.58–0.18. **RGB:** 5 μm emission; **RGB image:** 8, 4.5 and 3.6μm emission.

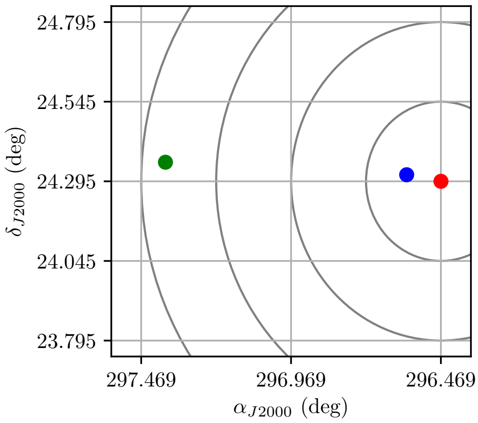

Figure 3.13: Quasar distribution for G060.57–0.18. **Red:** Maser position; **Blue:** J1946+2418 position; **Green:** J1949+2421 position. Quasars are aligned radially in the positive α–direction. Concentric circles eminating from maser postion are spaced 0.25 deg.

ionosphere even after TEC calibration (Walker & Chatterjee, 1999). Extrapolation of Equation 3.5 to theoretical quasars at $\theta_{\rm sep} = 2, 4$ deg away would instead give per–epoch astrometric accuracy of $\sigma_\theta = 44, 80$ μas, which is consistent with the decrease in accuracy of methanol masers as reported in (Reid et al., 2017). In this case, the methanol maser has such close calibrators that, on average, any potential ionospheric residuals could not systematically offset the position of the maser enough to mask the parallax ($\sigma_\theta < 20$ μas).

This maser was repeated in BR210 as the distance estimate must be accurate. G060.57−0.18 is one of the few masers located in the Perseus Gap and the distance to this source has now been independently confirmed.

Figure 3.14 gives the predicted distance for G060.57−0.18 from the BDC of $D = 8.0$ kpc, which is consistent with the inferred distance from the measured parallax of $D = 7.69^{+0.38}_{-0.34}$ kpc. I will discuss this further in the conclusion.

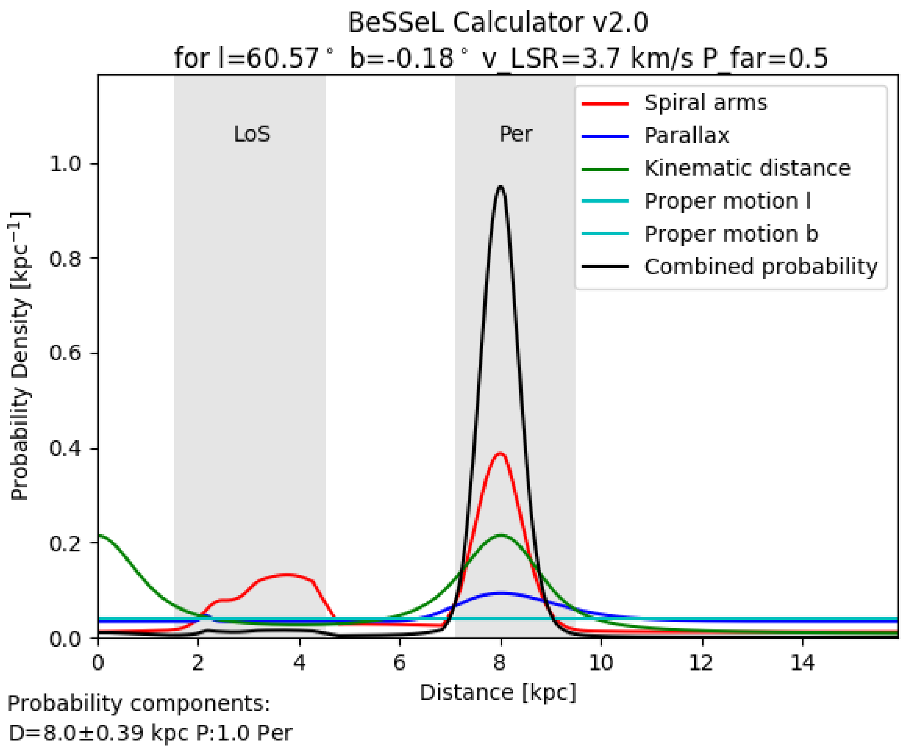

Figure 3.14: Distance prediction from the BDC. I have excluded my proper motion from this fit to see what would be the prediction with no information from these observations. The BDC favours $D = 8.0$ kpc, which is consistent with $D = 7.69^{+0.38}_{-0.34}$ kpc.

3.3.5 G070.29+1.60

G070.29+1.60 is a 22 GHz water maser located in the giant molecular cloud K3-50A/W58a (Kohoutek, 1965; Wynn-Williams, 1969). This maser is located near the centre of strong IR emission revealed by WISE data (Figure 3.16) and has an apparent companion 6.7 GHz methanol maser G070.18+1.74. The velocities of the two masers are not statistically different with $v_{\mathrm{H_2O}} = -26.7 \pm 10$ and $v_{\mathrm{CH_2OH}} = -23 \pm 5\,\mathrm{km\,s^{-1}}$ and appear to be part of the same molecular cloud. G070.18+1.74 is located on an arc offset $\theta = 0.177\,\mathrm{deg}$ away from G070.29+1.60.

I measure a parallax of $\varpi = 0.097 \pm 0.011\,\mathrm{mas}$ towards G070.29+1.60 (Table 3.2). Inverting this parallax suggests the most likely distance is $D = 11.2^{+1.2}_{-1.1}\,\mathrm{kpc}$. Additionally, I measured a proper motion of $\mu_x = -1.45 \pm 0.04$ and $\mu_y = -3.69 \pm 0.05\,\mathrm{mas/yr}$ which convert to $\mu_{l*} = -3.89 \pm 0.06$ and $\mu_b = -0.74 \pm 0.02\,\mathrm{mas/yr}$.

G070.29+1.60 was quite a weak maser with a dynamic and variable spectrum. As far as I could determine there was only a single component that could be reliably located and used for phase referencing between epochs 3 and F, except epochs 4, 5 and D. Strong spectral features were visible in epochs 1, 2 around $v = -37\,\mathrm{km\,s^{-1}}$, heavily diminished in epoch 3, 4 then completely missing from 5 onwards. There was a persistent weak spectral feature (in scalar average cross-correlated spectra) at $v = -23.34\,\mathrm{km\,s^{-1}}$, visible in 14 epochs, however, the spatial position of this feature could not be reliably located after exhaustive searching. This spectral feature is very close to the assumed systemic velocity of the region as traced by the methanol maser.

The parallax fit (Figure 3.15) depends disproportionally on the astrometry attained at epoch 3 compared to other epochs. This is due to the aforementioned spot variability and overall correlation of proper motion and parallax if the peaks are not sampled correctly. With the current fit for the parallax and proper motion of G070.29+1.60, the correlation coefficient between parallax ϖ and proper motions μ are $\rho(\varpi, \mu_x) = -0.48$ and $\rho(\varpi, \mu_y) = -0.06$ for the East–West and North–South respectively. Removal of this point has serious implications for all variables and correlations. The parallax fit without epoch 3 becomes $\varpi = 0.209 \pm 0.029\,\mathrm{mas}$, $\mu_x = -1.84 \pm 0.08\,\mathrm{mas/yr}$ and $\mu_y = -3.90 \pm 0.04\,\mathrm{mas/yr}$ with $\rho(\varpi, \mu_x) = -0.95$ and $\rho(\varpi, \mu_y) = -0.42$! Inverting this alternate parallax would suggests the most likely distance is $D = 3.85^{+0.21}_{-0.19}\,\mathrm{kpc}$ and would imply the maser is in the Local arm and a full 3 kpc away from the distance measured. This suggests formal parallax fitting errors for under–sampled parallax curves are underestimated at best.

To better estimate the parallax, proper motion and respective uncertainties in the presence of a potential outlier, I will use Jackknife resampling to remove one epoch i at a time, refit the data to get ϖ_i, $\mu_{x,i}$ and $\mu_{y,i}$ and repeat for all N epochs. The Jackknife (subscript J) estimates for the parameters and their uncertainties (σ) will be:

$$
\begin{aligned}
\varpi_J &= \frac{1}{N-1} \sum_{i=1}^{N-1} \varpi_i \\
\sigma^2_{\varpi_J} &= \frac{1}{N-2} \sum_{i=1}^{N-1} \left(\varpi_i - \varpi_J\right)^2
\end{aligned}
\tag{3.6}
$$

Since there is only one apparent outlier, the mean of these should be close to that attained by the total fit, however, the uncertainty will be much more conservatively (and likely accurately) estimated. The results of this additional fitting are given in Table 3.3.

Table 3.3: Parallax and proper motions of relevant masers. **Columns (1):** Maser name in Galactic Coordinates; **(2)** Method used to estimate parallax/proper motion; **(3)** Parallax (mas); **(4–5)** Proper motion in East–West and North–South directions (mas/yr); **(6)** Reference. Error bars are given as symmetric 1σ returned by either least–squres (LS) or Jackknife least–squares (J/LS) fitting methods.

Maser	**Method**	$\boldsymbol{\varpi}$ **(mas)**	$\boldsymbol{\mu_x}$ **(mas yr^{-1})**	$\boldsymbol{\mu_y}$ **(mas yr^{-1})**	**Ref**
G070.29+1.60	LS	0.097 ± 0.011	-1.46 ± 0.04	-3.69 ± 0.05	This work
	J/LS	0.109 ± 0.041	-1.52 ± 0.14	-3.75 ± 0.06	This work
G070.18+1.74	LS	0.136 ± 0.014	-2.88 ± 0.15	-5.18 ± 0.18	Zhang et al. (2019)

G070.18+1.74 has a published parallax and proper motion of $\varpi = 0.136 \pm 0.014$ mas and $\mu_x = -2.88 \pm 0.15$ mas/yr, $\mu_y = -5.18 \pm 0.18$ mas/yr (giving $D = 7.3^{+0.8}_{-0.7}$ kpc, $\mu_{l*} = -5.92 \pm 0.15$ and $\mu_b = -0.33 \pm 0.08$ mas/yr; Zhang et al., 2019), from data collected in BR149R. My original parallax is significantly different from this measurement, however, the adjusted parallax agrees within 1σ.

The proper motions of the two masers do not agree within error and I suggest that this is most likely due to internal motions of the water maser. Unfortunately, there is not more than a single phase reference feature visible in enough epochs to determine motions directly. As many water masers are associated with outflows, they do not reliably trace the systemic velocity of the gas. Class II 6.7 GHz methanol are associated with embedded stars and they have been found to trace the gas velocity ± 3km s^{-1} (Green & McClure-Griffiths, 2011). Therefore, I assume the proper motions measured in BR149 more accurately represent the motion of the gas cloud as a whole and calculate the inferred internal motions of G070.29+1.60. This gives $\mu_{x,int} = +1.33 \pm 0.16$ and $\mu_{y,int} = +1.42 \pm 0.19$ mas/yr (or $\mu_{l*,int} = +1.9 \pm 0.3$ and $\mu_{b,int} = -0.36 \pm 0.06$ mas/yr). At the distance of W58a this would be give $v_x = +52 \pm 14$ and $v_y = +55 \pm 15$ km s^{-1} (or $v_{l*} = 75 \pm 20$ and $v_b = -14 \pm 4$ km s^{-1}). The line–of–sight velocity spread of transient spectral features in G070.29+1.60 over the 16 epochs was $v = -40$ to -15 km s^{-1}.

Using the Bayesian distance estimator from Reid et al. (2014, 2019), I can compared the measured parallax distance to that expected from known Galactic structure and dynamics (Figure 3.17). In the left–hand panel I have also used the measured values for the proper motion of the single water maser component. In the right–hand panel I assume that the methanol maser proper motions represent a better estimate for the region. It should be noted that this programme uses known parallaxes around the line of sight; in this case, the solid blue line is the previously determined parallax for the methanol maser G070.18+1.74 and should be ignored. With the raw measurement of the proper motion, the expected distance is ambiguous between $D = 1.35 \pm 0.8$, 6.75 ± 0.92 and 13.36 ± 0.74 kpc. Taken alone, the μ_b proper motion even favours the fourth distance of $D \sim 4$ kpc in the local arm, however, this is unfavoured by the other components. Using the modified proper motion as above, the number of plausible distances is reduced to only $D = 6.77 \pm 0.78$ kpc.

Due to the strength of the phase reference feature ($S \leq 1$ Jy) phases were referenced from the two quasars. Unfortunately, this approach had the effect of reducing the SNR on the maser by an additional factor $\sqrt{2}$. This appears to be the primary reason why it was not possible to reliably image the weak maser feature at multiple epochs along with maser variability. It is likely that the phase reference feature first emerged above the noise at epoch 3.

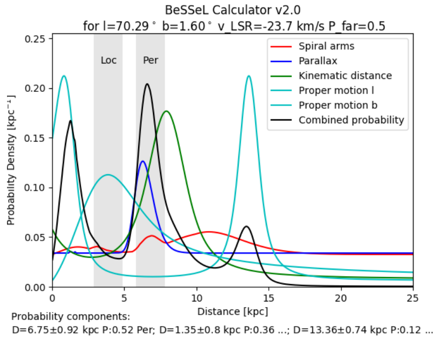

(a) $\mu_x = -1.45 \pm 0.04$ and $\mu_y = -3.69 \pm 0.05\,\mathrm{mas/yr}$

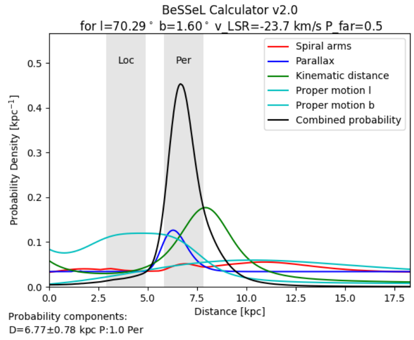

(b) $\mu_x = -2.88 \pm 0.15$ and $\mu_y = -5.18 \pm 0.18\,\mathrm{mas/yr}$

Figure 3.17: Baysian distance estimator output from Reid et al. (2019) for G070.29+1.60 for respective proper motions. Line colours indicate different components of the probability density– **Red:** spiral arm locations; **Blue:** previous parallaxes; **Green:** kinematic distance; **Cyan:** l and b proper motions; **Black:** multiplicably–combined probability density.

As I will show in the next section, the apparent height above the plane for G070.29+1.60 is $z - z_\odot = 247$ pc and has a $Z-$velocity $\dot{Z} = -14$ km s^{-1} (or -29 km s^{-1} using measured values). This is quite an atypical region, far above the plane and with dynamics that are complex and difficult to interpret.

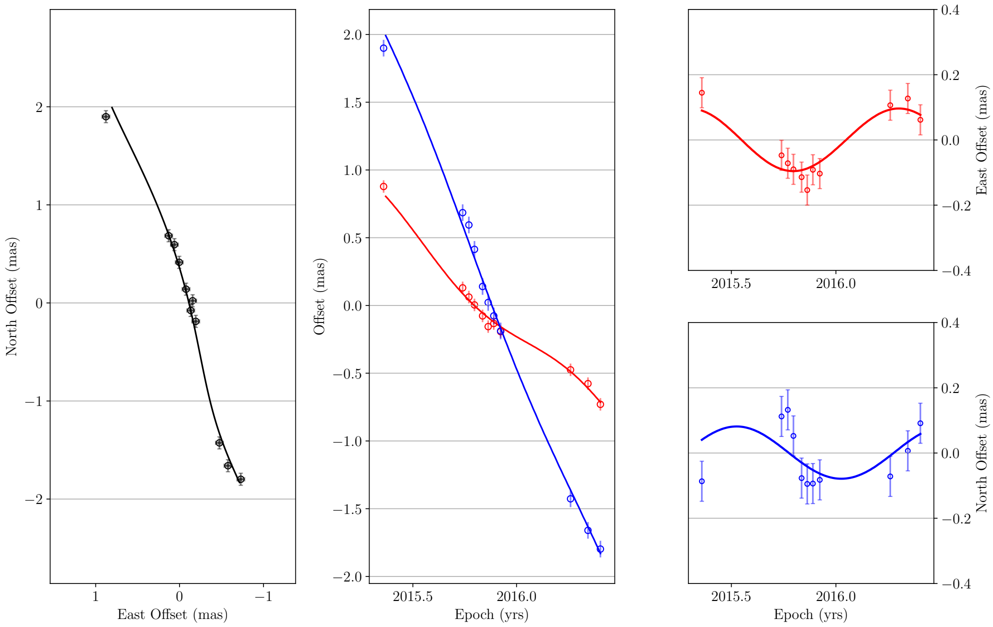

(a) With respect to J1957+3338.

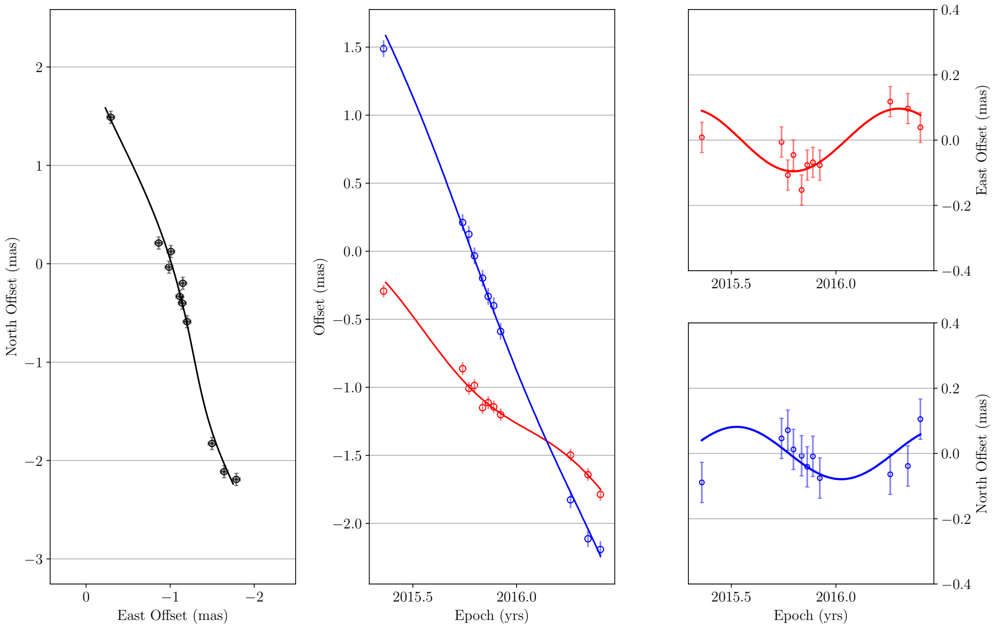

(b) With respect to J2001+3323.

Figure 3.15: Parallax and proper motion fit for target G070.29+1.60 referenced to corresponding calibrators. **Left panel:** Total sky motion **Centre panel:** Time–varying position in North–South (blue) and East–West (red) directions vs. time. **Right panels:** Proper motion–subtracted time–varying position in aforementioned directions. Epochs used are 3, 5, 6, 7, 8, 9, A(10), B(11), C(12), D(13), E(14), F(15) and G(16).

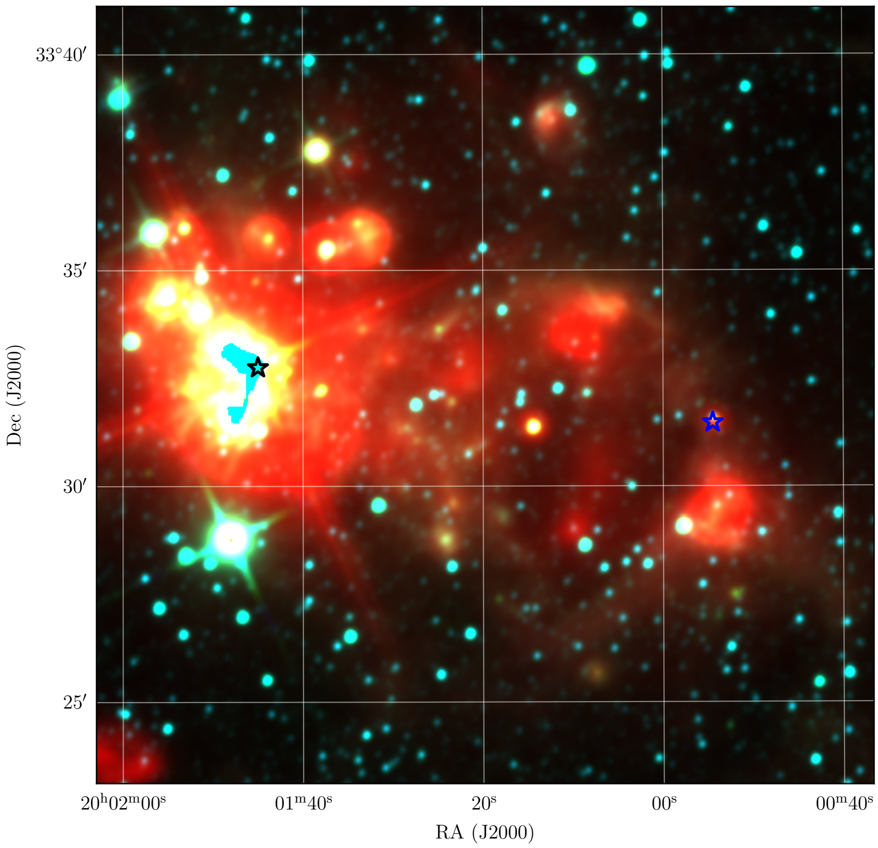

Figure 3.16: K3–50A/W58a giant molecular cloud region. **RGB image:** WISE W4,W2,W1 (22, 4.6, 3.4μm); **Black star:** H_2O maser G070.29+1.60 from this work; **Blue star:** CH_3OH maser G070.18+1.74. Image size is $9' \times 9'$ in J2000 coordinate system.

3.3.6 Kinematics and Spiral Arm Modelling

Following standard definitions, Galactic radius is $R = 0$ kpc at the Galactic centre and Galactic azimuth is $\beta = 0°$ towards the Sun and increasing clockwise following Galactic rotation. Careful

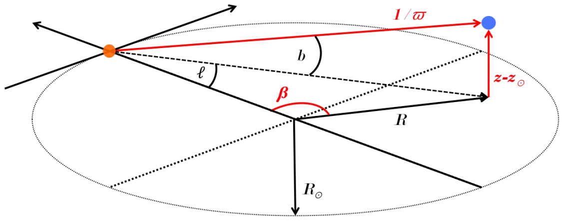

Figure 3.18: Schematic of the relationship between Galactic $(l, b, \frac{1}{\varpi})$ and Galactocentric (R, β, z) coordinate systems.

inspection of Figure 3.18 reveals the conversion from Galactic coordinates $(l, b, \frac{1}{\varpi})$ to cylindrical Galactocentric coordinates (R, β, z) are:

$$R = \sqrt{R_\odot^2 + \frac{\cos^2 b}{\varpi^2} - 2\frac{R_\odot}{\varpi}\cos l \cos b} \tag{3.7}$$

$$\sin\beta = \frac{\cos b \sin l}{\varpi\, R} \tag{3.8}$$

$$z - z_\odot = \frac{1}{\varpi}\sin b \tag{3.9}$$

again using $R_\odot = 8.35 \pm 0.15\,\mathrm{kpc}$ (Reid et al., 2014). Use of a cylindrical coordinate system and general disregard for the height variable z in spiral arm modelling is justified due to apparent solid body rotation and general constraint of maser regions to $|b| < 5°$ (Caswell et al., 2010, 2011; Green et al., 2012). The maser scale height is thought to be 27 ± 1 (Green & McClure-Griffiths, 2011) or $19 \pm 2\,\mathrm{pc}$ (Reid et al., 2019) and this makes the ratio $\frac{z}{D} \ll 1$ for all masers to good approximation.

The reader is left to convert to Galactocentric Cartesian as desired with $X = -R\cos\beta$, $Y = R\sin\beta$ and $Z = z - z_\odot$. Of note however are the instantaneous changes to X, Y, Z called U, V, W in $\mathrm{km\,s^{-1}}$. I can now convert maser Galactic coordinates to Galactocentric cylindrical coordinates. Using the above it can be shown that the conversion from Galactic velocities (v, μ_{l*}, μ_b) to Galactocentric Cartesian velocities (U, V, W) requires the application of another rotation matrix:

$$\begin{bmatrix} \boldsymbol{U} \\ \boldsymbol{V} \\ \boldsymbol{W} \end{bmatrix} = \begin{bmatrix} \cos b \cos l & -\sin l & -\cos l \sin b \\ \cos b \sin l & -\cos l & -\sin l \sin b \\ \sin b & 0 & \cos b \end{bmatrix} \begin{bmatrix} \boldsymbol{v} \\ 4.7\boldsymbol{D\mu_{l*}} \\ 4.7\boldsymbol{D\mu_b} \end{bmatrix}$$

where v is the line–of–sight velocity in $\mathrm{km\,s^{-1}}$ and 4.7 is the approximate conversion from AU/yr to $\mathrm{km\,s^{-1}}$. Galactocentric cylindrical coordinates are particularly useful for the analysis of spiral arm pitch angles. These determinations are given in Table 3.4. Values of U, V and W for masers are likely to contain systematic errors due to maser internal motions on the level of $\pm 20\ \mathrm{km\,s^{-1}}$ (e.g. Burns et al., 2015; Sakai et al., 2017), I have not accounted for here.

I consider spiral arms to take the classic log–spiral form as defined below:

$$\ln\left(\frac{R}{R_0}\right) = -\tan\psi\ (\beta - \beta_0)$$

Table 3.4: Measured position in Galactocentric coordinates for masers based off measured quantities. (1) Maser name in Galactic coordinates, (2) distance between Sun and maser, (3) Galactocentric radii, (4) Galactocentric azimuth, (5) relative Galactic height, (6) X velocity, (7) Y velocity, (8) Z velocity.

Maser	D (kpc)	R (kpc)	β (deg)	$z - z_\odot$ (pc)	U (km s^{-1})	V (km s^{-1})	W (km s^{-1})
G021.88+0.02	10.9	7.1	131	4.2	173.7	398.7	−17.9
G037.82+0.41	11.9	7.4	97.5	86.4	266.1	324.8	+13.8
G060.57−0.18	7.7	8.1	55.3	−24.3	207.8	120.4	−3.3
G070.29+1.60	8.4	9.9	56.5	247	222.2	69.0	−14.7

where ψ is the spiral arm pitch angle and R_0 and β_0 are the values of the spiral arm distribution at some arbitrary reference position. When plotted as $\ln R$ vs. β, maser distribution should form a straight line with slope $= -\tan\psi$. I also wish to only consider a spiral change in a 'small' Galactic azimuthal section such that $0 \leq \beta - \beta_0 < 360°$.

In addition to the distances calculated/measured in this chapter, I include known parallaxes thought to be associated with the Perseus arm (Reid et al., 2019, and references therein). I aim to simultaneously confirm that the masers measured here indeed are Perseus–associated and also determine a Perseus arm pitch angle including them.

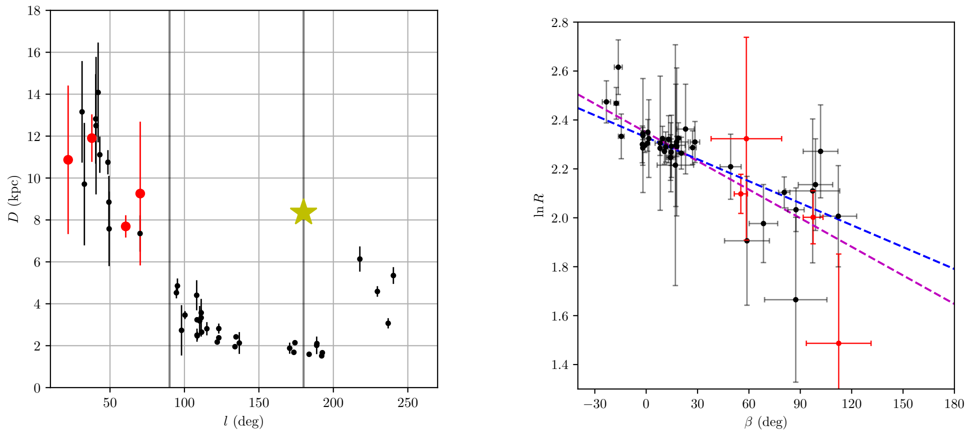

Figure 3.19: Spiral arm fitting. **Left panel:** Distribution of relevent masers in Galactic Longitude l vs. distance D. **Right panel:** Distance and l converted to $\ln R$ and β with distance errors propagated and shown as 1σ. **Black markers:** Perseus arm associated masers; **red markers:** masers analysed in this work; **magenta line:** fit from unweighted least–squares including this work; **blue line:** from unweighted least squares excluding this work. **Yellow star:** Position of Galactic centre.

Fitting $(\ln R, \beta)$ with weighted least squares gives pitch angle for the Perseus arm of $\psi_{p,w} = 10.25 \pm 0.03$ deg. Un–weighted least squares gives a more conservative estimate of with $\psi_{p,uw} = 12.7 \pm 2.7$ deg. The pitch angle curve resulting from $\psi_{p,uw}$ is shown in blue in Figure 3.19. Both these values agree statistically with previous estimates $\psi = 9.1 \pm 1.4$ deg from Reid et al. (2014) or $\psi_< = 10.3 \pm 1.4$, $\psi_> = 8.7 \pm 2.7$ from Reid et al. (2019). As a note on notation, $\psi_<$ and $\psi_>$ indicate values for the pitch angle before and after the so–called 'kink' in the spiral arms (see Reid et al., 2019, for details). Fitting the previously known parallaxes without the additional

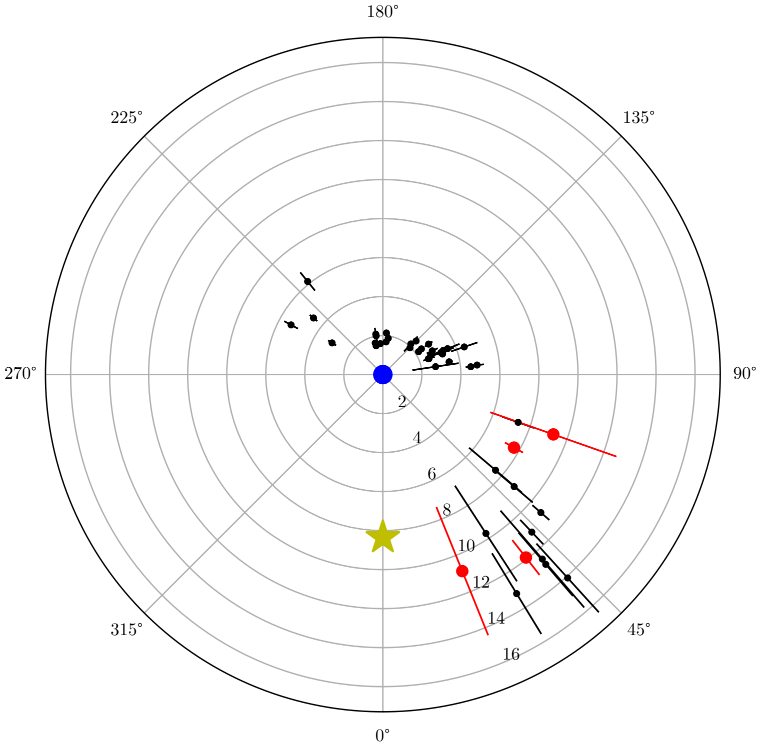

Figure 3.20: The likely and measured locations of the four masers analysised in this chapter. Coordinates and Galactic latitude l and distance D. **Black dots:** Locations previous water and methanol masers in the Perseus spiral arm; **Red dots:** Locations of masers from this work. **Yellow star:** Location of Galactic centre. **Blue dot:** Location of Solar system.

values presented here give $\psi_w = 9.72 \pm 0.04$ deg for weighted and $\psi_{uw} = 10.91 \pm 3.47$ deg for unweighted least–squares fitting methods. The pitch angle curve resulting from the unweighted estimate ψ_{uw} is shown as the blue in Figure 3.19.

3.4 Concluding Remarks

I have determined the distances to and calculated the Galactic dynamics of 4 HMSFR in the First Galactic Quadrant. I have also identified them with the Perseus spiral arm and calculated an updated pitch angle. Figure 3.20.

The analysis performed here has contributed to the knowledge pool concerning Galactic structure visible from the Northern Hemisphere, but it is representative of the priorities necessary for accurate parallax measurements. Although interpolation of spiral structure is possible, SπRALS will not be able to directly benefit from previously measured parallaxes or accurately known Galactic dynamics. SπRALS aims to provide the measurements for future modelling and therefore it is important to learn lessons from BeSSeL.

Astrometry of G021.87+0.01 and G070.29+1.60 demonstrate the degrading influence of water maser variability and evolution. Both distance determinations would not have been possible without additional constraints otherwise unavailable for SπRALS and these are due to maser evolution. Evolutionary and variability effects are only apparent once the data are observed and reduced and cannot be mitigated through calibration or other techniques.

Particular to these two masers is their low flux density, so astrometric observations would benefit greatly from more on-source time. Due to a large number of baselines available on the VLBA (36 or 45) shared tracks generally still provide sufficient on-source time and $uv-$coverage. It is also recognised that time has to be optimised for observations made using an application-based, time-competitive facility. SπRALS will largely *not* be weighted down due to facility availability. The ASCI array is owned and operated by the University of Tasmania and therefore there will be ample time available for well-sampled parallax measurements. This is extremely important due to the much smaller number of baselines (6 or 10) with generally lower sensitivity suggesting that it is more important to focus on sampling few targets well.

G021.87+0.01 individually demonstrates the importance of high-quality quasars. When inverse phase referencing was not possible, normal PR techniques were required. Unfortunately, both reference quasars were too weak to get reliable fringe solutions and entire epochs had to be discarded. If at least one quasar had been bright enough with an uncertain position or structure; calibration techniques exist to mitigate or model those effects. So intrinsically weak quasars limit the calibration approaches that can be used and are probably not worth using them at all because of this. G037.81+0.41 demonstrates that two 'far' quasars ($\theta_{sep} \sim 1.8\,\mathrm{deg}$) at $K-$band still can give good parallaxes.

The parallax and proper analysis of G060.58–0.18 reveals that there is not necessarily a benefit to huge numbers of epochs spread out over a year. While it is true that a Jackknife or bootstrapping method (e.g. that employed in Deller et al., 2019) to estimate uncertainty in the original 4 epoch parallax (Reid et al., 2019) would make if much higher, the parallaxes statistically agree. This reveals that the original 4 epoch experiment was sufficient and not plagued by systematic uncertainty (as might be expected from the ionosphere Reid et al., 2017), likely due to the proximity of the calibrators. However, in the presence of systematic uncertainties and more distant calibrators, 4 epochs may not be enough, but 16 is difficult to justify. At least 8 epochs should be a decent middle ground, spaced 2-4-2 over the peak times.

Finally from G070.29+0.01 it is demonstrated that correct sparse sampling is more important than intense sampling. In theory, intense sampling of parallax curvature about the peak can break the fit degeneracy in the case of a missing first or last peak. However, in practice, this should not be relied upon, especially for potentially distant targets. The correlation of proper motion and parallax in these cases makes the parallax unreliable at best and misleading at worst.

The BR210 series aimed to use a denser sampling of epochs to measure more accurate parallaxes to both 6.7 GHz methanol and 22.2 GHz water masers. For the water masers, the denser sampling would make it more likely for a single feature to persist over multiple epochs. For methanol masers, the extra epochs would push down the errors due to ionospheric 'wedges' systematically shifting the astrometric positions independently at each epoch (Reid et al., 2017). While the astrometric accuracy of water maser G037.81+0.41 was extremely good at $\varpi = 0.084 \pm 0.008$ mas, it was not as good as that reported for G007.47+0.05 ($\varpi = 0.049 \pm 0.006$ mas in 6 epochs Sanna et al., 2017), G045.07+0.13 ($\varpi = 0.129 \pm 0.007$ mas in 14 epochs Wu et al., 2014), G048.61+0.02 ($\varpi = 0.093 \pm 0.005$ mas in 10 epochs Zhang et al., 2013) or G075.30+1.32 ($\varpi = 0.108 \pm 0.005$ mas in 4 epochs Sanna et al., 2012). However, apart from the first and last, these very high accuracy maser parallaxes have a large number of epochs comparable to the number for G037.81+0.41, all of which were usable for the parallax. This point is further exaggerated by the relative failure of the parallax estimates for G021.87+0.01 or G070.29+0.01, where spot variability ruined the potential high accuracy parallax despite the 16 epochs. Conversely, the parallax accuracy attained for methanol maser G060.58–0.18 is the best yet reported for a 6.7 GHz methanol maser (Reid et al., 2019), however as I have already commented on, this is partially due to a very close calibrator rather than solely due to a large number of epochs.

Critical analysis of the parallax measurements undertaken for this thesis suggests that the formal parallax and proper motion uncertainties resulting from normal/weighted least-squares fitting are underestimated. The simple Jackknife method used in the analysis of G021 reveals this. Future work in trigonometric parallaxes will include an alternative fitting approach, most likely Markov–Chain Monte Carlo Bayesian orientated to accurately estimate parallax and proper motion curves and uncertainties from astrometric data in SπRALS.

It is apparent that although the work here has contributed to the knowledge of the Galaxy as visible from the Northern Hemisphere, it has not been able to add much new information. The parallaxes to masers (G037 and G060) agree with the predictions from the existing Bayesian distance model (Reid et al., 2016), and in some cases, the model itself is used to constrain the distance from the proper motions (G070 and G021). Lastly, even with the addition of two high precision and model-independent parallaxes, the fit to the Perseus arm was not significantly different from the previous estimates, nor was particularly more precise. For me, these points cement the idea that: a further sampling of the Northern Hemisphere will not help the purposes of studying the large–scale structure of the Milky Way. Further time and resources should be spent focusing on upgrading/constructing Southern Hemisphere facilities capable such that this goal can be met.

4

Southern Hemisphere 6.7 GHz methanol maser compactness catalogue

Many of the problems encountered during the BeSSeL VLBI maser astrometry analysis completed in the previous chapter are immediately resolved by using class II methanol masers instead of 22 GHz water masers. Class II 6.7 GHz methanol masers are almost as intrinsically bright as 22 GHz water masers and are known to be stable for periods much longer than a year.

There are over 1000 known individual 6.7 GHz class II methanol masers visible from the Southern Hemisphere, approximately half exclusively so. However, compared to water masers, methanol masers spots are typically larger– in many cases being resolved. If SπRALS is to use 6.7 GHz masers as astrometric targets these diffuse, weak and/or structured masers need to be identified so that they can be avoided. The desirability of a maser target for astrometry is often summarised with a quantity called 'compactness'.

In this chapter, I determine a first target list for SπRALS by modelling angular sizes of 6.7 GHz methanol maser spots and relating them with metrics that characterise compactness. In this way, I construct a VLBI compactness catalogue for all relevant Southern Hemisphere 6.7 GHz methanol masers.

4.1 Introduction

Class II 6.7 GHz methanol masers are the second brightest masing transition observed in astronomy after 22 GHz water masers. However, it can be the case that a large fraction of the flux density emanates from large diffuse structures ($> 0.1 - 1.5$ arcseconds at a distance of 4 kpc; Caswell, 1997) or many small velocity/spatially overlapping regions of low flux density. The surveys that discover these masers (e.g. Caswell et al., 2010, etc) will use single–dish observation and the intrinsic size of methanol maser emitting regions are much smaller than a single dish beam. Therefore the exact angular size, extent and compactness of many masing species are unknown until high resolution imaging with interferometry (e.g. Phillips et al., 1998) or VLBI (e.g. Minier et al., 2002; Goedhart et al., 2005a; Bartkiewicz et al., 2009).

SπRALS is scheduled to spend hundreds of hours observing class II 6.7 GHz methanol masers for high–accuracy, high–precision astrometry. Therefore there is an initiative to find 6.7 GHz methanol masers that are the most compact and can give the best astrometry.

The Methanol Multibeam catalogue (MMB; Caswell et al., 2010; Green et al., 2010; Caswell et al., 2011; Green et al., 2012; Breen et al., 2015) is the most complete survey of Southern Hemisphere ($l = 186° \rightarrow 0° \rightarrow 60°$) 6.7 GHz class II methanol masers with a depth of $3\sigma = 0.51$ Jy (Green et al., 2009, 2017). In order to determine which ones are the best for astrometry in SπRALS, it was decided to observe all appropriate (see below) masers from this list with VLBI.

4.2 Source Selection and Observations

As discussed in Section §1.4.3, the AuScope–Ceduna Interferometer (ASCI) array will be the instrument used for SπRALS. The ASCI array is not specifically designed for maser astrometry and is comprised of sensitive but heterogeneous large telescopes and homogeneous geodetic 12 m telescopes. The new 6.7 GHz capable receivers being installed on the 12 m telescopes have a focus on broad frequency coverage and low maintenance, rather than maximising performance at 6.7 GHz (SEFD estimations around 3500 Jy).

Considering these factors, I can estimate a detection limit for masers. The baseline sensitivity between Ceduna 30m (SEFD $\approx 650\,$Jy) to a geodetic 12 m antenna is expected to be

$$\sigma = \sqrt{\frac{S_1\,S_2}{2\,\tau_{\rm int}\Delta\nu}} = \sqrt{\frac{3500 \times 650}{2 \times 60 \times 2 \times 10^3}} = 3.0\,\mathrm{Jy} \tag{4.1}$$

for $\tau_{\rm int} = 60\,$s integration and $\Delta\nu = 2$ kHz spectral resolution ($\Delta v = 0.09\,\mathrm{km\,s^{-1}}$). Therefore, for a 5σ detection ASCI needs to observe masers on baselines $|\mathbf{B}|/\lambda = B_\lambda = 35$ Mλ with a correlated flux density of at least $S_{B_\lambda} \geq 15$ Jy.

As such, I take all masers with autocorrelated ($B_\lambda = 0$) peak flux density catalogued $S_0 \geq 10$ Jy for completeness and accounting for possible flux density variability. Although it is unlikely the peak flux density will remain constant for all baselines, this sub-catalogue of targets then also provides sampling for weaker sources appropriate for the more sensitive Australian Long Baseline Array (LBA), Square–Kilometer Array (SKA) or potential future iterations of ASCI.

This subset of masers was observed using the LBA on 4th March 2016 and 22 March 2016 (project code V534). The participating telescope parameters are listed in Table 4.1 and the baselines and

Table 4.1: V534 LBA telescopes. **Columns:** **(1)** Telescope colloquial name; **(2)** two letter station code; **(3)** latitude; **(4)** longitude; **(5)** height above sea–level; **(6)** dish diameter; **(7)** 6.7 GHz primary beam size; **(8)** 6.7 GHz nominal SEFD; **(9)** owner/operating institute. All telescopes participated in both epochs of V534.

Station	**Code**	**Latitude (deg)**	**Longtitude (deg)**	z **(m)**	**D (m)**	$\theta_{6.7}$ **(as)**	**SEFD (Jy)**	**Institute**
ATCA (tied)	At	30.31288 S	149.56476 E	252	5×22	413	50	CSIRO
Ceduna	Cd	31.86769 S	133.80983 E	165	30	303	650	UTAS
Hobart	Ho	42.80358 S	147.44052 E	65	26	350	850	UTAS
Mopra	Mp	31.26781 S	149.09964 E	867	22	413	850	CSIRO
Parkes	Pa	32.99840 S	148.26352 E	415	64	142	110	CSIRO
Warkworth	Wa	36.43316 S	174.66295 E	123	30	303	650	WRAO

Table 4.2: **Left:** VLBI baselines for the Australian LBA participating telescopes. **Upper Left:** Linear distances (km) between the antennas as calculated by NRAO VLBI scheduling program SCHED. **Lower Left:** Approximate mean uv–distance (Mλ) for 6.7 GHz observations. **Right:** Approximate ($\pm$10%) baseline sensitivites (Jy) for a 1 min integration and 2 kHz spectral resolution.

	|**B**|						σ_S **(Jy)**					
	At	**Cd**	**Ho**	**Mp**	**Pa**	**Wa**	**At**	**Cd**	**Ho**	**Mp**	**Pa**	**Wa**
At		1508	1396	114	322	2409						
Cd	34		1702	1448	1361	3718	0.4					
Ho	31	38		1286	1089	2415	0.5	1.8				
Mp	2	32	29		207	2411	0.5	1.8	2.1			
Pa	7	30	24	5		2425	0.2	0.7	0.8	0.8		
Wa	54	83	54	54	54		0.4	1.6	1.8	1.8	0.7	

sensitivities are listed in Table 4.2. The LBA utilised a Data Acquisition System (DAS) which recorded two IF bands, each 16 MHz dual circular polarisation centred on 6308 and 6668 MHz at a total data rate of 256 Mbits/s. The lower IF at 6308 MHz was only used to measure multiband delays on the continuum sources.

Observational structure was 150 s scans on each of 187 separate 6.7 GHz maser targets distributed between $l = 188 \rightarrow 360^\circ$ and $|b| \leq 2^\circ$ over two epochs (Figures 4.1 and 4.2). Scans on fringe–finder quasars were also scheduled every ~ 3 hours, with an average onsource time of ~ 5 min. While the LBA can see up to at least Declination $\delta \approx 20^\circ$ ($l \approx 55^\circ$ for $b = 0$) and other methanol masers exist in the range outside the cut, this area has been extensively done by the VLBA in BeSSeL. Therefore it was decided to focus on the potential sources largely or completely inaccessible to the VLBA.

Telescope baseband data was correlated with DiFX (Deller et al., 2007, 2011) at the Pawsley supercomputer facilities in association with Curtin University, WA. The data for each experiment were correlated in one pass with an integration time of $\tau_{\rm int} = 2$ s and 8192 spectral channels. This gave a frequency resolution of $\delta\nu = 1.95$ kHz or a velocity resolution of $\delta v = 0.09\,{\rm km\,s^{-1}}$ at 6.7 GHz in each IF.

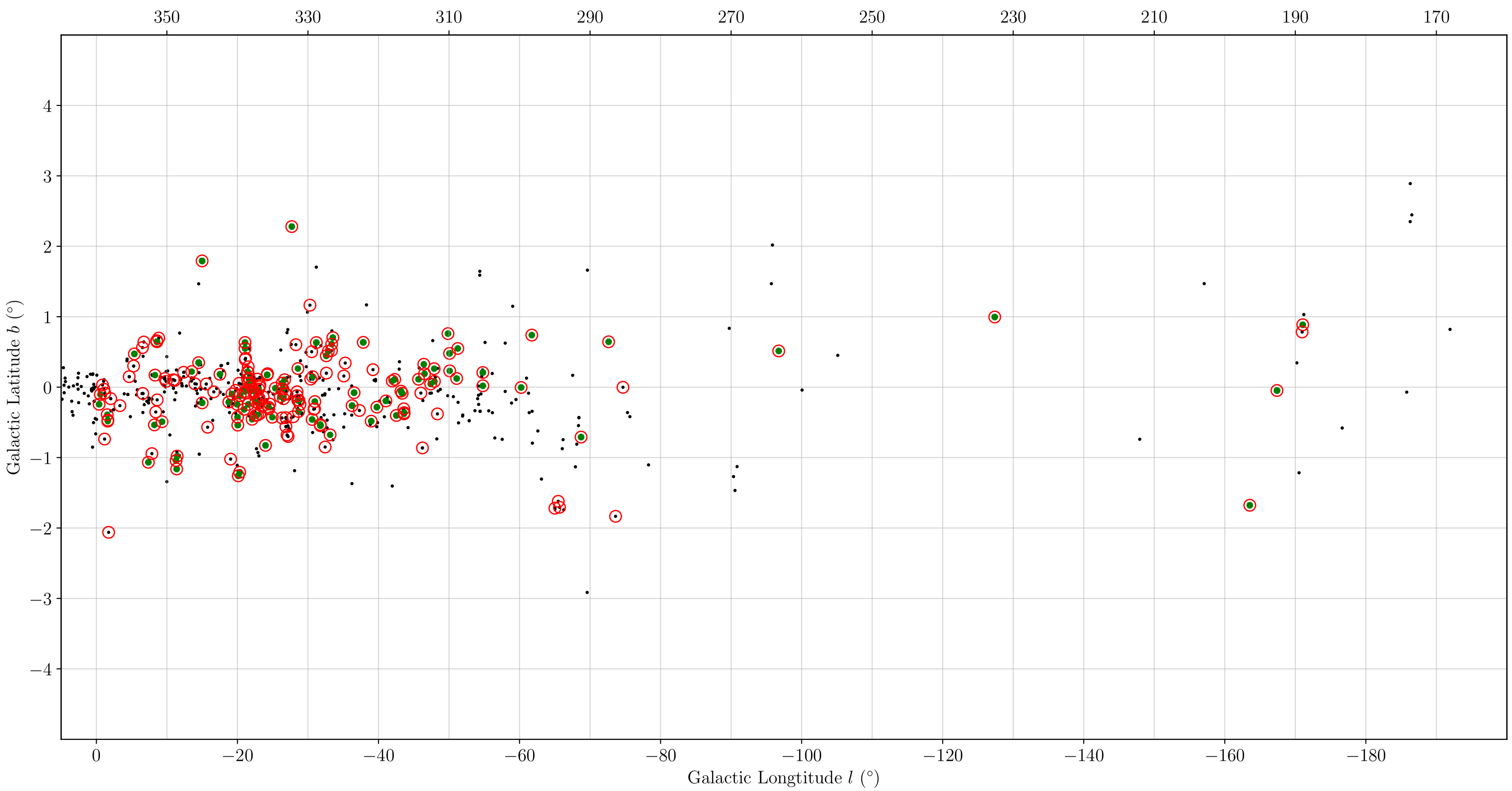

Figure 4.1: Black: The positions of all known Galactic 6.7 GHz methanol masers collected in Yang et al. (2019), primarily from Caswell et al. (2010); Green et al. (2010); Caswell et al. (2011); Green et al. (2012); Breen et al. (2015) (and additional referenced therein) between $-200 < l < 20°$, $|b| < 5°$. Only 4 methanol masers (G206.542 − 16.355, G208.996 − 19.386, G209.016 − 19.398, G213.705 − 12.597) are catalogued $-200 < l < 20°$, $|b| > 6°$ and were not included in this survey. **Red circles:** The positions of all 6.7 GHz methanol masers included in this survey. **Green:** Positions of modelled masers.

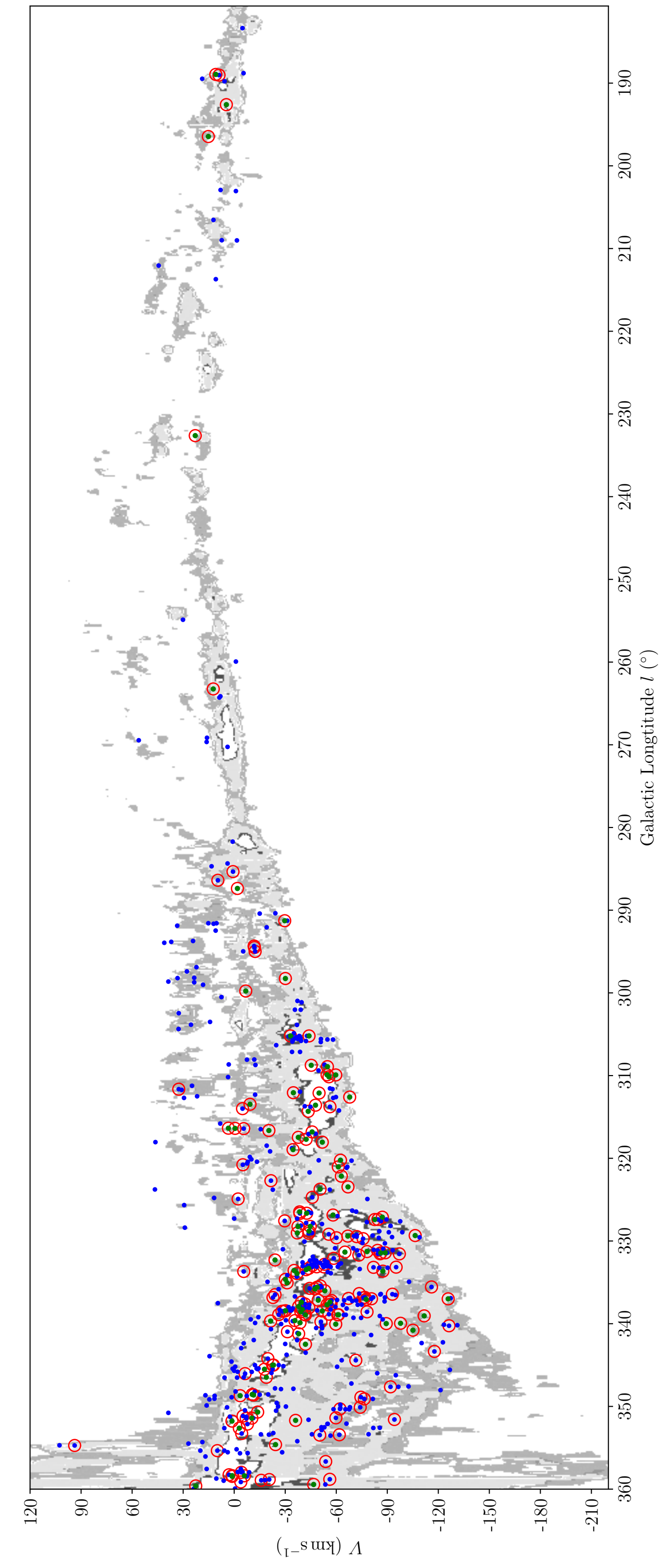

Figure 4.2: Longtitude–velocity (l–v) diagram of the 3rd and 4th quadrants of the Milky Way. **Grey:** Greyscale CO integrated emission (K/arcdeg) from the $b \leq 4°$ central strip of the Milky Way, adapted from Dame et al. (2001) (Figure 3 therein). **Blue:** Positions of all known 6.7 GHz methanol masers between $180 < l \leq 360°$. **Red circles:** Positions of targeted masers. **Green:** Modelled masers.

4.3 Data Reduction

4.3.1 $\mathcal{AIPS}$ reduction

Correlated FITS files are available for public download from https://data.pawsey.org.au/public/?path=/VLBI/Archive/LBA/v534. ParselTongue scripts used for data reduction available from https://github.com /lucasjord/thesisscripts.

Data were reduced in $\mathcal{AIPS}$ using the procedure shown schematically in Figure 4.3. As a note on the nomenclature, some $\mathcal{AIPS}$ 'tasks' calculate and produce a solution table (*SN*) which can then be applied to multi-source data by being merged with a calibration (*CL*) table. New *CL* tables can be applied directly to the multi-source data upon inspection or further calibration/analysis. Descriptions of the various steps are given below.

1. Using the task 'FITLD', the data were loaded into AIPS from the correlated FITS files as $uv-$data sets and basic header tables.
2. The analog signal measured by a telescope is first digitised (in this case 2–bit) before being recorded. The task 'ACCOR' is used to calculate potential errors resulting from sampler thresholds by determining how much the autocorrelation spectra deviate from unity. This creates *SN1* which is merged with *CL1* using the task 'CLCAL' to create *CL2*.
3. Where available, the antenna temperatures over the experiment are extracted from the antenna .log files. *TY1* and *GC1* are created from the antenna temperatures and gain–curves (at $\sim 6.7\,$GHz) respectively by $\mathcal{AIPS}$ task 'ANTAB'. *TY1* and *GC1* are then merged into an amplitude gain calibration table *SN2* which is merged with *CL2* via 'CLCAL' to make *CL3*. Where tsys information was not available, nominal SEFD values (Table 4.2) were added to *CL3* with task 'CLCOR'. This approximate amplitude calibration procedure made *step 8* necessary.
4. Antenna .log files are used to determine off-source slewing times, wind-stows and downtime. Offending times are flagged with 'UVFLG' to produce flag table *FG1*.
5. Autocorrelation data on a strong fringe finder was used to determine time–variable bandpass shape for each antenna IF/polarisation via task 'BPASS', creating a bandpass table *BP1*.
6. Bulk–electronic and instrumental delays for each antenna/polarisation/IF are solved by task 'FRING'. The scan chosen for this solution is a bright continuum source for which all antennas had on-source time. Rate solutions are zeroed. This created *SN3* which is merged into *CL3* by 'CLCAL' to create *CL4*.
7. Task 'FRING' is used to measure the multiband delays (over the two IFs) of fringe finder sources (excluding the one used for the manual phase calibration) observed over the experiments. These give the time–variable multiband delay, where the slope will approximate the antenna clock drift rate. This clock rate is externally calculated with a piecewise linear fit ($\dot{\tau} \approx \frac{\Delta\tau}{\Delta t}$), then applied via task 'CLCOR' into *CL5*.
8. The first IF at 6308MHz is flagged from the methanol maser sources with task 'UVFLG'.

9. Externally, the ParselTongue script *maser_amplitude_calibrate.py*[*] is run. The amplitudes of the cross–correlation data are corrected using the autocorrelation flux density of the masers, which in effect scales the antenna gains to that of the reference. This process generates *CL6*. See Section §4.3.2 for more information on this external processing.

10. Now that antenna gains, clock–rates and delays are approximately accounted for, the internal integration time for the $uv-$data is increased from $\tau_{\text{int}} = 2$ to 60 s with task 'UVAVG'. This has the effect of averaging the data. This process applies all pre-existing calibration, bandpass and flag tables, and generates a new $uv-$data set. The integration time of 60 s was chosen as it proved to be sufficiently long that the data size was reduced (to save on computational time) without significant loss of coherence due to any residual delay rates due to the atmosphere, maser position offsets, etc.

11. Task 'SETJY' is used to set the reference frequency of the data to the rest–frequency of CH_3OH $5_1 \rightarrow 6_0\,A^+$, at 6.6685192(8) GHz (Müller et al., 2004). This re-calculates Doppler velocities and results in spectra. 'CVEL' can then be used to shift the spectral line data to account for the rotation of the Earth and Solar System movement. This creates a final $uv-$data set.

[*] Code is publicly available at https://github.com/lucasjord/thesisscripts

Figure 4.3: Data reduction process for V534 data involving AIPS (green), ParselTongue (red) and Python (white) steps.

4.3.2 Notes on external ParselTongue scripts

Both scripts mentioned below have been made publicly available at https://github.com/lucasjord/thesisscripts.

ParselTonuge script *maser_amplitude_calibration.py* is a custom alternative to the $\mathcal{AIPS}$ task 'ACFIT'. 'ACFIT' uses well-calibrated template autocorrelation spectra from one antenna and a short time range to determine amplitude gain errors in the remaining spectra. This generates an *SN* table of time-variable gains to be reapplied to the data. Regrettably, 'ACFIT' is suited for a single/limited number of individual maser sources observed in one epoch. The alternative but approximate technique as introduced in Section §B.1 uses a similar approach to 'ACFIT' but tailored for observations of hundreds of masers in a single observing session. At each scan, for each antenna/polarisations the $S_\nu > 10\sigma$ peaks are located in the baseline–subtracted autocorrelated spectra. A reference antenna is chosen (either Ho or Cd due to largest experiment participation time and stable gains) and matching–velocity peaks in the various spectra are divided by the reference. This gives a correction factor (Γ) for that antenna/polarisation/time (equal to 1 for the reference). Similarly determining Γ for each scan gives a time–variable scaling factor for each antenna/polarisation. If no peaks can be found above the threshold for an antenna/polarisation at time $t_{\mathrm{ant,pol}_i}$, the final $\Gamma_{\mathrm{ant,pol}}$ is interpolated to that time. Finally $\sqrt{\Gamma_{\mathrm{ant,pol}}}$ are internally applied via task 'CLCOR' to generate a new *CL* table. The reason $\sqrt{\Gamma_{\mathrm{ant,pol}}}$ is applied to the visibility data ($\overline{s_i}$) to correct is because $\Gamma_{\mathrm{ant,pol}}$ is determined from autocorrelation products ($\overline{s_i} \cdot \overline{s_i}$).

As with 'ACFIT', this method re–weights the visibility data to a reference antenna without the consolation of maser amplitude catalogues (e.g. MMB). As I discuss later, this advantageously can identify extreme cases of maser variability or flare rather than blindly assuming static flux density. Figure 4.4 demonstrates that combined data collected over two epochs with independent amplitude calibration agree at the < 3 Jy level.

ParselTongue script *find_peak_uv.py* is used to find potential maser spots of interest and extracts the relevant calibrated $uv-$data. Basically, this ParselTongue script runs $\mathcal{AIPS}$ tasks POSSM to generate spectra, finds peaks in the spectra, goes back into $\mathcal{AIPS}$ and runs task UVPRT on the relevant channel(s) to generate visibility amplitude (Jy) vs. uv-distance data for later fitting.

Without appropriately precise gain and accurate polarisation calibration, true polarisation analysis as part of this survey is not feasible. In addition, Class II methanol masers are considered to be only weakly circularly polarised ($< 1\%$; Stack & Ellingsen, 2011) and so in the interest of improving mean amplitude calibration, the polarisations are averaged together to form stokes–I in all further analysis.

Using the final visibility data set after the application of the $\mathcal{AIPS}$ task CVEL, I used $\mathcal{AIPS}$ task POSSM is used to generate scalar/baseline averaged stokes–I spectra for each maser. I also included a lower bound $uv-$distance of $20\,\mathrm{M}\lambda$ to simulate an array without 'short' baselines (like that which will be present in ASCI $B_\lambda \gtrsim 30$ Mλ). Large and diffuse physical structures are assumed to have a kinematic 'continuum' of emission centred at the mean LSR velocity and by excluding the short baselines, I remove the contribution in the spectrum from these components. This biases the spectra towards tracing the compact regions only. Figure 4.5 shows the effect of removing baselines from the scalar averaged spectrum of G192.600–0.048. As seen in Table 4.1, a

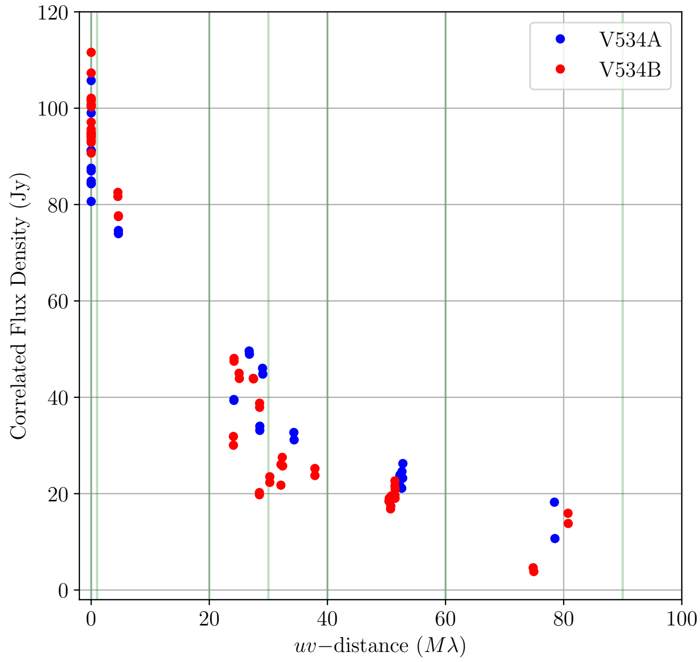

Figure 4.4: Example maser visibility data for G345.010+1.792 velocity feature $v = -17.46$ km s^{-1} for the two epochs. Epochs have had seperate amplitude calibration. The average difference in flux density between the two epochs of data binned in the ranges $0-1$, $1-20$, $20-30$, $30-40$, $40-60$ and $60-90$ Mλ (vertical green lines) is $\overline{S_A - S_B} = 2.6$ Jy.

$uv = 20\,\mathrm{M}\lambda$ cutoff removes At–Mp, At–Pa and Mp–Pa baselines. Therefore masers detected only on these baselines are automatically filtered out by this process and are automatically considered poor candidates.

I output these spectra to .txt files with POSSM option outprint=*filename*, which are then reloaded back into python. Peaks are identified with tools provided by python package peakutils†. Peaks identification is based on an SNR cut-off. The cut-off I used was $S_\nu > 20\sigma_m$ where σ_m is the noise in the spectrum and is expected to be:

$$\sigma_m = \frac{1}{\sqrt{5}} \frac{\sum_{i=1}^{12} \sigma_{S,i}}{12} \approx 0.5\,\mathrm{Jy} \tag{4.2}$$

for the 2×2.5 min scans for each maser, where $\sigma_{S,i}$ are the approximate baseline sensitivities (Jy min$^{1/2}$) and there are 12 baselines with $B_\lambda > 20$ Mλ Table 4.2). Therefore a $20\sigma_m$ detection in this spectrum implies an average spectral amplitude of ≈ 10 Jy.

The identified velocities/channels for the maser peaks are then stored and used in $\mathcal{AIPS}$ task UVPRT. For each maser, UVPRT is run on each identified maser peak channel (on all baselines

†https://pypi.org/project/PeakUtils/

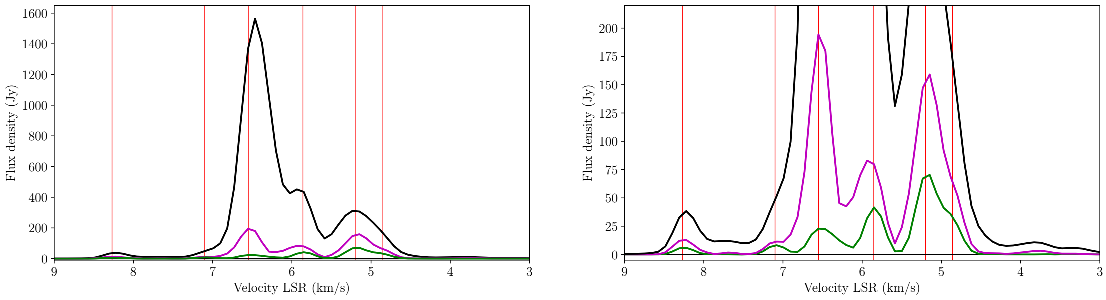

Figure 4.5: Comparison of various baseline/scalar–averaged spectra of G192.600–0.048. **Black:** Baselined, combined autocorrelated spectrum. **Magenta:** Scalar averaged cross–correlated spectrum from all 15 baselines. **Green:** Scalar averaged cross–correlated spectrum from 12 baselines, excluding baselines with $B_\lambda \leq 20\,\mathrm{M}\lambda$. **Red:** Vertical lines indicated the derived position for potential compact structures by fitting the peak of the green spectrum. The reader is encouraged to note that the peaks of the green spectrum do not necessarily line up with peaks in the magenta or black spectra.

this time, including autocorrelations) to print out visibility amplitude S_{B_λ} and total projected baseline $uv = \sqrt{u^2 + v^2}$. These values are all stored for fitting.

4.3.3 Maser Visibility Fitting

To avoid a degenerate naming scheme, I will refer to the whole region as the *maser*; emission from each extracted velocity channel an assumed separate *maser spot*; and different apparent emission structures at the same velocity channel as *maser components*.

The *find_peak_uv.py* script, specifically the peakutils package, fits line profiles to the maser spectra and only returns one channel from each peak/velocity feature. This ensures that there is only one visibility dataset out per peak and hence likely maser spot. The vertical red lines in Figure 4.5 show identified peaks by the *find_peak_uv.py* script contrasted against whole spectrum. Discrepancies to these assumptions are discussed in Section §4.5.4.

So I aim to determine which masers have appropriate spots to use for inverse phase–referencing by analysing the spatial and energetic properties of their components. To determine meaningful component properties, I require a model with realistic attributes. The model considered for a maser spot is a simple two-component Core/Halo model, where each component is estimated by a Gaussian brightness distribution:

$$I(r) = \frac{2\,I_0}{\sqrt{\pi \ln 2\theta^2}} \exp\left(-\frac{8 \ln 2\, r^2}{2\theta^2}\right) \tag{4.3}$$

The Gaussian component has an unresolved flux density of $\int_0^\infty I(r) = I_0$; where r is the radius from the centre of the distribution; and an angular diameter characterised by the FWHM of the Gaussian θ. If I assume there are 2 components centrally co–located, then the corresponding visibility amplitude vs. baseline length ($S_\nu(B_\lambda)$; which is the Fourier Transform of this model) is also a Gaussian and is given by:

$$S_\nu(B_\lambda) = S_C \exp\left(-\frac{2\pi^2}{8 \ln 2}(\theta_C\, B_\lambda)^2\right) + S_H \exp\left(-\frac{2\pi^2}{8 \ln 2}(\theta_H\, B_\lambda)^2\right) \tag{4.4}$$

where θ_C, θ_H are the Core/Halo angular sizes (in mas), S_C, S_H are the Core/Halo peak flux densities (in Jy) and B_λ is the baseline length expressed in units of the observing wavelength λ (aka *uv*–distance). The Core/Halo components are defined such that $\theta_C < \theta_H$. This is quite possibly the simplest model geometrically, computationally and for many sources on milliarcsecond scales will be a reasonable assumption (Minier et al., 2002).

Script *lst_fit_maser_uv.py*[‡] was used to determine maser parameters from visibility data in each channel. This script uses non–linear least-squares fitting and estimates the amplitude uncertainties (σ_{S_ν}) from noise in the spectrum away from the maser location along the velocity axis. Constraints that were imposed on the modelling process were $\theta_H > \theta_C$, $\theta_j \in [0.1, 500]$ mas, $S_j \geq 0.3$ Jy for $j = C$ or H.

Initial χ^2 values were produced from the fit, then the uncertainties were re–weighted such that they produced $\chi^2 \approx 1$. These more representative uncertainties (presumably accounting for systematic model offsets) are shown as errors bars in visibility plots (Appendix B.4). Model parameters and modified uncertainties are included in Table B.2 .

All maser spot fits are shown in Appendix B.4.

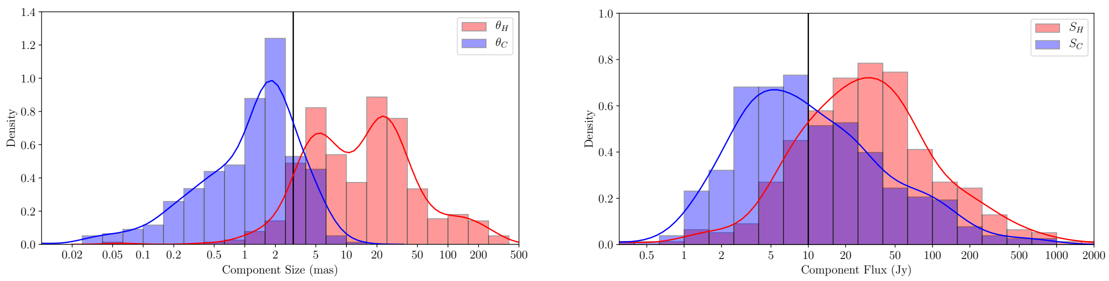

(a) Distribution of modelled component size (mas) for all detected maser components. x–axis has $\log_{10}$ scale and histogram bins are equally spaced in $\log_{10}$ at 0.05 units.

(b) Distribution of modelled component flux density (Jy) for all detected maser components. x–axis has $\log_{10}$ scale and histogram bins are equally spaced in $\log_{10}$ at 0.1 units.

Figure 4.6: Global distributions for fitted parameters S_C, θ_C, S_H and θ_H. Blue components are attributed to a core and red to a halo, where the definition for each was assigned during modelling when $\theta_H > \theta_C$.

Figure 4.6 shows the global distribution of parameters for the 393 modelled maser spots in 104 masers. I find the median $\theta_H = 13.6^{+25.8}_{-9.8}$ mas and $\theta_C = 1.3^{+1.9}_{-1.3}$ mas (error bars expressing 75% CI) which agrees with the expectation imposed by model constrains and definition of core vs. halo components ($\theta_H > \theta_C$).

I find the component flux density of the halo structure is globally greater at $S_H = 27.8^{+98.8}_{-20.4}$ Jy compared to $S_C = 7.3^{+50.0}_{-5.2}$ Jy at 75% CI. Now that the model parameters have been determined, I aim to compose them into a thorough categorisation that hints at the quality for parallax measurements, and which naturally relates to compactness.

‡Code is publicly available at https://github.com/lucasjord/thesisscripts

4.4 Categorisation

Given the model parameters, I wish to categorise the maser spots and therefore their host masers on an intuitive grading scheme that quantifies compactness. Immer et al. (2011) conducted a VLBA survey to find quasar calibrators appropriate for BeSSeL maser astrometry and graded detections on a decreasing scale from A to D, and then F for non–detections. Compactness was solely associated with this grade and the grade determined by the baseline length at which the normalised visibility amplitude (NVA; S_{B_λ}/S_0) fell below a threshold value of 20%. Following this, I will also grade the methanol masers on a scale from A to D, however, since masers have a more complex structure than quasars, I will use additional metrics in an attempt to quantify this. In the next few sections, I will define these additional metrics and establish cut-offs in those metrics that encompass what characteristics I expect $A-$, $B-$, $C-$ and D–grade masers to have.

To that end, I expect $A-$grade will represent as close to a perfect astrometric candidate as I can determine, B will be a good candidate, C will represent a possible but not recommended candidate, and D will be reserved for masers for which high accuracy astrometry is unlikely. Unmodelled masers are classed as such, having failed the basic detection constraints in *find_peak_uv.py*. Depending on the reason, they are classed as failed (F) or undetected/unknown (U). These masers are discussed in Section §4.5.1.

4.4.1 Fitting Results

To categorise the maser spots, I needed metrics that represented the physical properties attributed to compactness. Figure 4.7 shows the global distributions of model parameters against one another. A weak correlation between halo and core component flux density, but almost no correlation between core and halo sizes is implied. The lack of an apparent global (and quite possibly inherent) correlation between core and halo parameters implies the ratios S_C/S_H, θ_C/θ_H vary independently and possibly randomly for each spot. This unknown variability limits the independent inference power of NVA for compactness and supports that I must rely on multiple metrics to describe it fully.

4.4.2 Visibility Amplitude vs. $uv-$distance

Possibly the most intuitive metric to characterise compactness are visibility amplitudes thresholds at fixed $uv-$distance cuts (S_{B_λ}). To represent average Cd–AuScope12m, AuScope12m–AuScope12m and/or future Cd–Warkworth 30m (Petrov et al., 2015) uv–distances, baseline cuts are set at $B_\lambda = 35$ and $80\,\mathrm{M}\lambda$. Global estimates for the median visibility amplitudes from fits are $S_{35\mathrm{M}\lambda} = 5.6^{+61.6}_{-3.9}$ Jy and $S_{80\mathrm{M}\lambda} = 2.2^{+21.5}_{-2.2}$ Jy respectively (90% CI; Figure 4.8a).

Despite potentially weak individual inference power, I still will consider NVA ($R_{B_\lambda} = \frac{S_{B_\lambda}}{S_0}$) evaluated at fixed baseline cuts of $B_\lambda = 35$ and $80\,\mathrm{M}\lambda$. Global median estimates for the NVA are $R_{35\mathrm{M}\lambda} = 0.20^{+0.45}_{-0.17}$ and $R_{80\mathrm{M}\lambda} = 0.07^{+0.36}_{-0.07}$ (90% CI; Figure 4.8b).

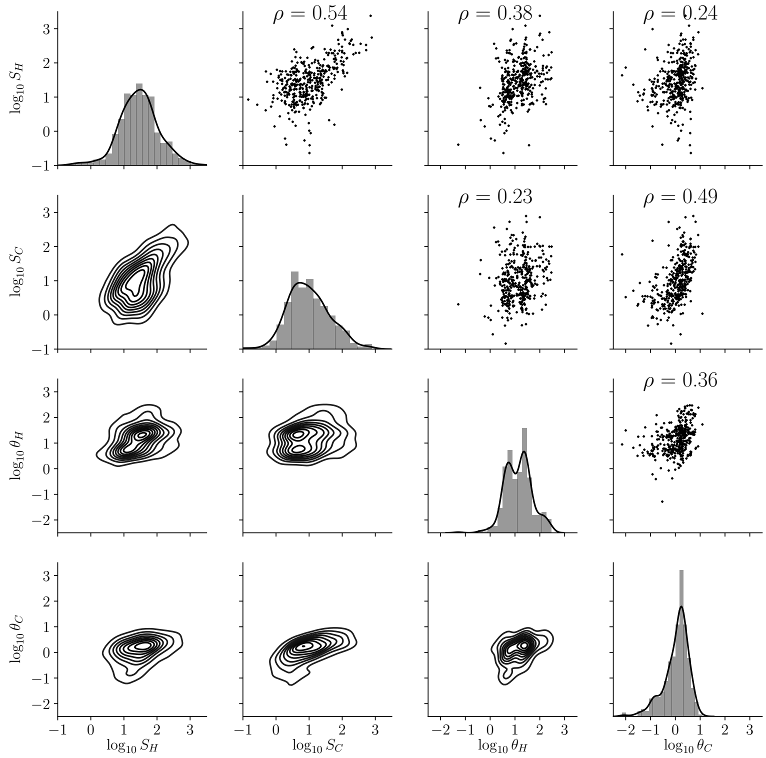

Figure 4.7: Correlation distributions between the 4 model parameters in the 2 component fit for all fitted masers. All axis are in $\log_{10}$ space to allow the visualisation of the full dynamic ranges and acts as more sensitive visual correlation probe. **Upper:** Scatter plot for parameters and associated correlation coefficients for the exponentiated populations (x not $\log_{10}$x). **Diagonal:** Self–correlated histograms of parameter distribution density and single–variable KDE distribution. **Lower:** KDE distribution for two parameter comparison. Fit parameters are each randomly modulated with 'weak' Gaussian distribution to represent the respective uncertainty at the lower bound cut-off. This smooths the visual transition at the bound edges (otherwise 'unresolved' cores stack at the $\theta_C = 0.1$ mas level) and leaves the remaining distribution unchanged. Modulations are sampled from distribution $P_m = \frac{1}{\sqrt{2\pi}} \exp\left(-\frac{1}{2}(x-\sigma)^2/(3\sigma)^2\right)$ for $\sigma_\theta = 0.1$ mas, $\sigma_S = 0.3$ Jy respectively.

4.4.3 Emission density/compactness index ξ

The next metric I use for maser spot classification is (pseudo) emission density, ξ:

$$\xi_{comp} = \frac{S_{comp}}{(\theta_{comp}^2 + \theta_B^2)^4} \tag{4.5}$$

where θ is the particular component size in mas, S is the flux density of the component in Jy and θ_B is the synthesized beam size of the array in mas and ξ has units $\mathrm{Jy\,mas^{-8}}$. Descriptor 'comp' can be substituted by either core or halo. This metric describes a size weighted surface flux density for each of the modelled components where the denominator $\left((\theta^2 + \theta_B^2)^4\right)$ was constructed in such a way that ξ does not diverge at small modelled sizes and is most sensitive to changes in component size $\theta = \frac{\theta_B}{3}$ $\left(\frac{\partial^2 \xi}{\partial\,\theta^2}|_{\theta_B/3} = 0\right)$.

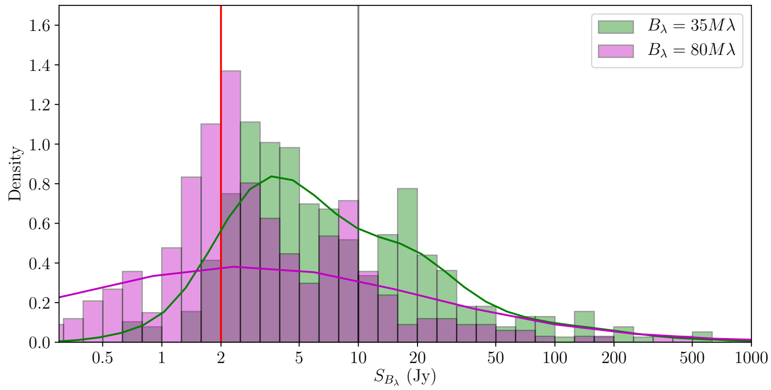

(a) Distribution of total spot flux (Jy) derived from model and model parameters at baseline lengths $35\,\mathrm{M}\lambda$ (green) and $80\,\mathrm{M}\lambda$ (magenta) respectively. x–axis has $\log_{10}$ scale and histogram bins are equally spaced in $\log_{10}$ at 0.1 units.

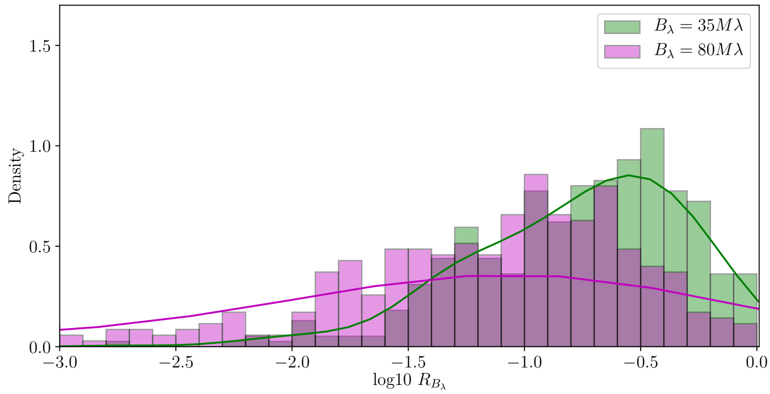

(b) Distribution of total spot flux to autocorrelated flux ratio ($R_{B_\lambda} = S_{B_\lambda}/S_0$). Histogram has lower cut–off at $R_{B_\lambda} = -3$ or 0.1%.

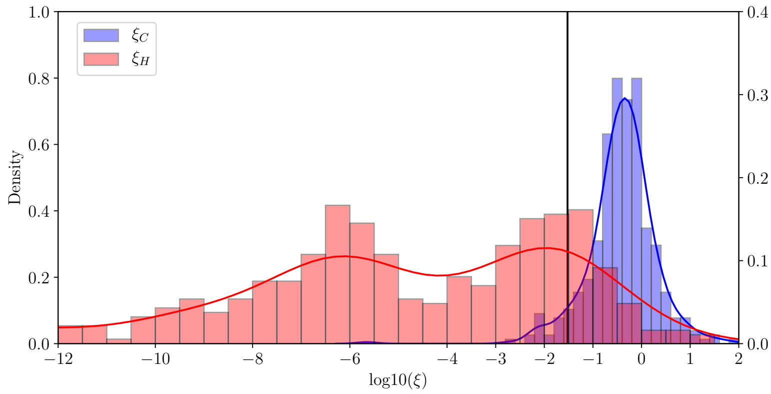

(c) Distribution of pseudo emission density ξ. x–axis has $\log_{10}$ scale and histogram bins are equally spaced in $\log_{10}$ space at 0.1 units. Vertical black line indicates $\xi_{\min} = 0.3\,\mathrm{Jy\,mas}^{-8}$.

Figure 4.8: Distributions of various calculated metrics for the purposes of quantifying and therefore classifying compactness.

Global median estimates for the emission density are $\xi_H = 0.11^{+1.22}_{-0.10}\,\mathrm{Jy\,mas^{-8}}$ for the diffuse halo component and $\xi_C = 0.38^{+4.61}_{-0.27}\,\mathrm{Jy\,mas^{-8}}$ for the core component (90% CI; Figure 4.8c), which expectedly implies core components typically have a higher concentration of emission compared to halo components.

4.4.4 Constraints and grades

As I wish to not only categorise masers but to do so in a way that graduates them on a scale from most to least appropriate for my purposes, I will again consider the observational constraints. As calculated in Section §4.2, the baseline sensitivity from Ceduna 30m to an AuScope12m antenna would theoretically be 3 Jy (each $\sqrt{\text{minute}}$ integration) at a $uv-$distance of 35 Mλ. AuScope12m–AuScope12m baseline sensitivities can be calculated to be $\sim$ 5 Jy min$^{\frac{1}{2}}$ and a possible Ceduna 30m–Warkworth 30m baseline would be $\sim$ 1 Jy min$^{\frac{1}{2}}$, both approximately at 80 Mλ. Therefore, I define an A–grade maser spot as one that has a minimum 3σ detection on every baseline (or $S_{80} \geq 15$ Jy). B–grade maser spots have a 5σ detection detected on every Ceduna baseline, but not AuScope–AuScope baselines. Ceduna–AuScope baselines are $B_\lambda \sim 35$ Mλ, meaning the correlated flux density of the maser has to be $S_{35} \geq 10$ Jy. Both $A-$ and B–grade masers would be acceptable for SπRALS in the current era.

Figure 4.9 are representative examples of maser spots which demonstrate a compactness grade from A to D. These masers serve as a general guide to the proportions and magnitudes of parameters that result in said grades. The aforementioned specific visibility amplitude cuts are shown for every maser compactness plot in Appendix B.4.

C–grade masers would fail both the previous constraints and therefore not be ideal first targets for SπRALS . However, foreseeing possible future sensitivity upgrades, I further separate C–grade and D–grade maser spots. C–grade masers are classically weak, but compared to D–grade masers they are compact. $D-$grade masers are weak and almost immediately resolve out to fall below detection thresholds. The emission measure metric ξ serves to separate these two classifications.

Figure 4.10 shows the distributions and correlations of the metrics explained above from the global sample of maser spots overlayed with the metrics derived from the ideal maser spots. I only include metrics S_{35}, S_{80} and ξ_C and for all these cases the compactness grades are arranged left to right. A value of $\xi_C \geq 0.3\,\mathrm{mJy/mas^8}$ implies if $S_C = 5\,\mathrm{Jy}$, $\theta_C/\theta_B \leq 0.5$ or if $\theta_C/\theta_B \geq 1$, $S_C \geq 30\,\mathrm{Jy}$. Since bright compact objects ($\xi \gg 0.3$) have been most likely identified by either S_{80} or S_{35}, ξ serves as a method to segregate fits to marginally weak cores from fits to noise/baseline non–detections. This is because ξ simultaneously takes into account and weights the core component modelled flux density and size under a certain threshold.

4.4.5 Summary

Finally, I categorise all modelled maser spots from these cuts. Figures B.2 and B.1 show correlations with the determined categorisations against the original modelled parameters and full range of metrics. It can be seen here that NVA (R_{35} and R_{80}) do not separate into the populations as determined by this method. This can likely be attributed to the inclusion of the diffuse flux density from the halo which is uncorrelated with the core size and flux density and therefore compactness. Maser regions are then categorised via the highest grade maser spot (Table B.2). Masers with multiple 'equal' grade spots (apart from D–grade) are all included.

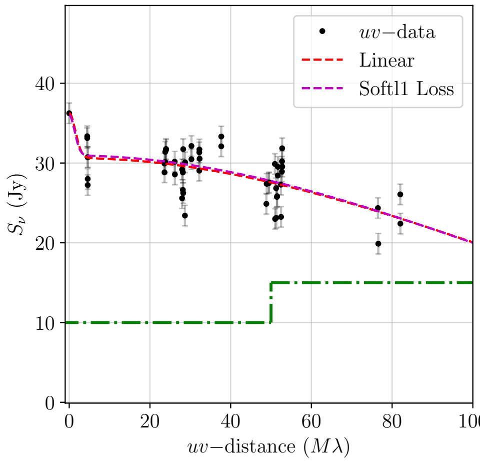

(a) G339.622–0.121, $v = -33.16\,\mathrm{km\,s^{-1}}$ is a very good example of an A–grade maser feature. Although not intrinsically luminous with an autocorrelated flux density of only $\sim$ 35 Jy, the modelled core is unresolved and bright with model parameters $(S_C, \theta_C, S_H, \theta_H) = (30.6\,\mathrm{Jy}, 0.7\,\mathrm{mas}, 5.6\,\mathrm{Jy}, 50\,\mathrm{mas})$. Due to the relative scaling of the components it is possible the halo fit is superfluous.

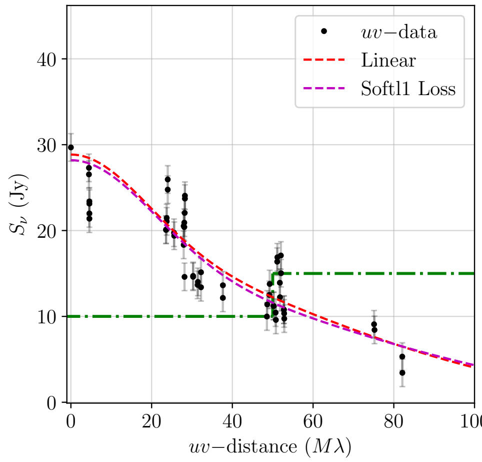

(b) G338.925+0.634, $v = +58.99\,\mathrm{km\,s^{-1}}$ is an example of a B–grade maser feature. The model parameters $(S_C, \theta_C, S_H, \theta_H) = (17.2\,\mathrm{Jy}, 1.3\,\mathrm{mas}, 11.7\,\mathrm{Jy}, 4.3\,\mathrm{mas})$ imply a slightly resolved core structure responsible for the majority of the flux density, surrounded by a weaker marginally resolved halo structure.

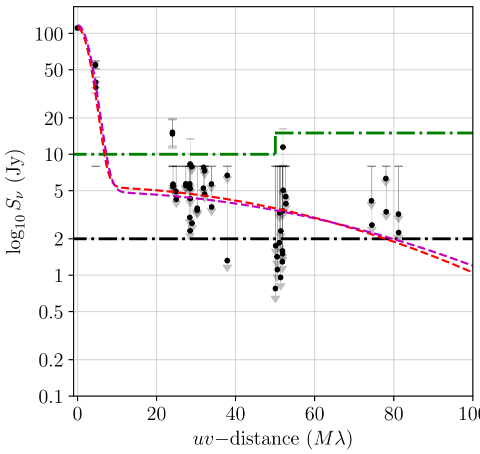

(c) G345.003–0.223, $v = -26.84\,\mathrm{km\,s^{-1}}$ is an example of a C–grade maser feature with model parameters $(S_C, \theta_C, S_H, \theta_H) = (5.4\,\mathrm{Jy}, 1.4\,\mathrm{mas}, 105.4\,\mathrm{Jy}, 28.4\,\mathrm{mas})$. The model parameters clearly reflect that this maser spot has a diffuse halo surrounding slightly resolved weak core. Given appropriate calibrator sources in the neighbourhood of this maser, phase–referencing astrometry could be conducted as the maser spot is marginally detected on the long baselines. To note: The y−axis for this plot has a log 10 scale, and the black line indicates the detection threshold.

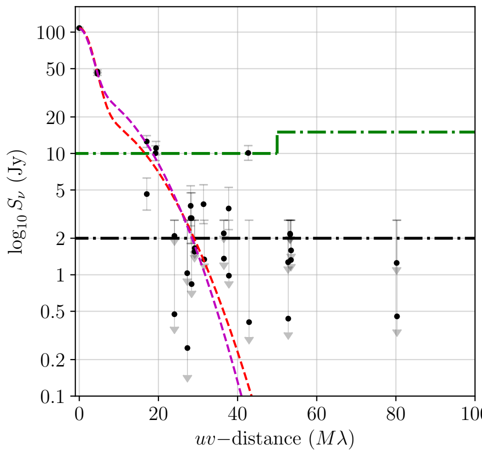

(d) G359.436–0.104, $v = -46.66\,\mathrm{km\,s^{-1}}$ is a good example of a D–grade maser feature. As the model parameters imply $(S_C, \theta_C, S_H, \theta_H) = (21.9\,\mathrm{Jy}, 5.8\,\mathrm{mas}, 86.2\,\mathrm{Jy}, 26.3\,\mathrm{mas})$, the bright autocorrelation emission (133 ± 4 Jy) can be explained by a very diffuse halo and a very resolved core. Due to the limited correlated flux density remaining at intermediate to longer baselines, it is not recommended that phase–referencing observations be conducted towards this maser.

Figure 4.9: Examples of the 4 categories of detected masers in the survey. ***x*−axis:** Projected wavelength–scaled baseline distance (Mλ). **Top *y*−axis:** Correlated flux density (Jy) of specified maser channel velocity. **Bottom *y*−axis:** $\log_{10} S_\nu$ scaled axis. **Black dots:** 60 s–averaged uv−data with scaled errors bars to attain $\chi^2 = 1$. **Red:** Gaussian Core/Gaussian Halo model for maser structure with linear residual scaling. **Magenta:** GCGH model with robust residual loss. **Green:** Categorisation thresholds at 10 Jy and 15 Jy for 35 and 80 M λ respectively. **Black line:** Noise detection threshold – values below are included in model it but not considered detected.

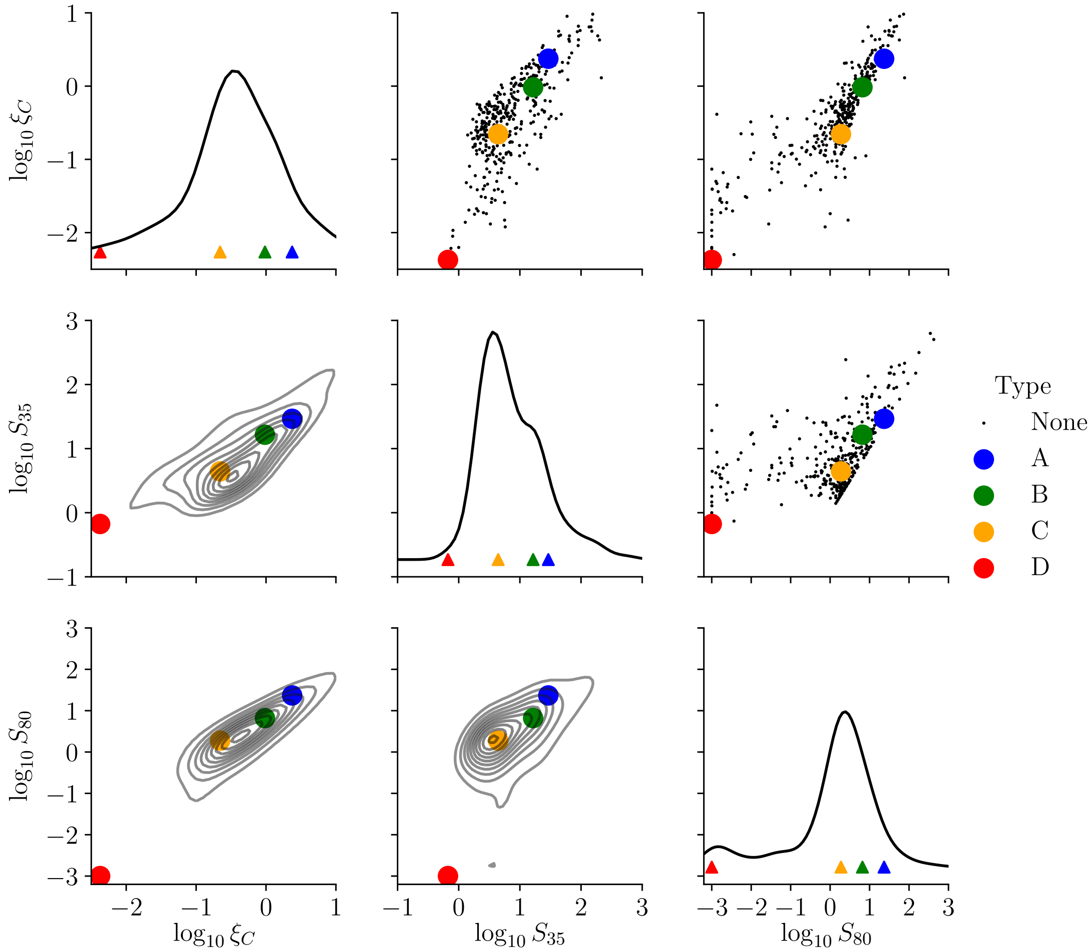

Figure 4.10: Correlation distributions between 3 compactness metrics for – **black:** All modelled maser spots; **blue:** A–grade maser spot G339.622–0.121 $v = -33.16\,\mathrm{km\,s^{-1}}$; **green:** B–grade maser spot G338.925+0.634 $v = +58.99\,\mathrm{km\,s^{-1}}$; **orange:** C–grade maser spot G345.003–0.223 $v = -26.84\,\mathrm{km\,s^{-1}}$; **red:** and D–grade maser spot G359.436–0.104 $v = -46.66\,\mathrm{km\,s^{-1}}$. **Upper:** Scatter plot for parameters. **Diagonal:** Self–correlated single–variable KDE distribution and markers indicating classic maser spot positions. **Lower:** KDE distribution for two parameter comparison.

Table 4.3: Compact maser catagorisation descriptions. **Rows:** Condition that core–compactness index is greater than the threshold value $\xi_C \geq 0.3\,\mathrm{mJy\,mas^{-8}}$, condition that correlated flux density at $35\,\mathrm{M}\lambda$ is greater than five times the detection limit $5\sigma_S = 15\,\mathrm{Jy}$, condition that the correlated flux density at $80\,\mathrm{M}\lambda$ is greater than 10 Jy.

Grade	$\boldsymbol{S_{35} \geq 10}$ (Jy)	$\boldsymbol{S_{80} \geq 15}$ (Jy)	$\boldsymbol{\xi_C \geq 0.3}$ ($\mathrm{mJy\,mas^{-8}}$)	**Description**
A	Y	Y	Y	Compact and strong on all baselines.
B	Y	N	Y	Compact, flux density tapers off on long baselines but still good for reverse–phase reference
C	N	N	Y	Compact but weak. Okay for normal phase referencing subject to quasars availability
D	N	N	N	Diffuse and weak.
F	N	N	-	Only detected on $uv < 20\,\mathrm{M}\lambda$ baselines. Target maser was too weak to initially find peaks to fit $uv-$data from
U	-	-	-	Unknown grade. Maser had insufficient valid $uv-$data due to issues.

4.5 Discussion

4.5.1 Non–detections

I consider masers that were unable to have a single maser spot modelled successfully (degrees of freedom> 1) as non–detections. Out of the 187 masers surveyed, 85 are considered as non–detections, and are given the grade of either F(ailed) or U(nknown) (Table 4.3). If maser is designated F–grade, it had no significant detection on non– At–Mp, At–Pa or Mp–Pa baselines ($B_\lambda \geq 25$ Mλ). This implies that the angular size of any present components were much larger that the synthesized beam at that $uv-$distance $\theta_C \gg \theta_B = 10\,\mathrm{mas}$ or that any small angular components present were much weaker than the detection thresholds (Table 4.2). If given a U-grade, maser had no autocorrelated or cross correlated detection due to scheduling, correlation or observational issues. All non-detected masers are given in Table B.3.

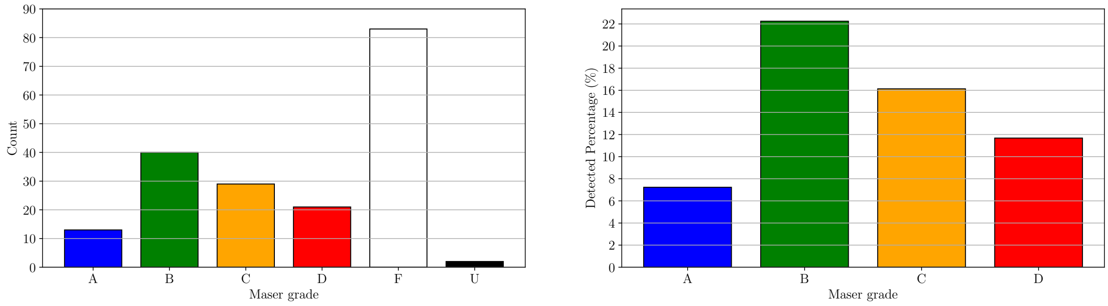

Figure 4.11: Histograms showing number/percentages of masers categorised into each grade. **Left:** Number of masers graded $A \rightarrow D$ compared against non–detections F and unknown U. **Right:** Percentage of detected masers categorised into each grade.

4.5.2 Interstellar scattering

It is well known that multipath diffraction through the Interstellar Medium (ISM) causes scintillation and angular broadening (e.g. Cordes et al., 1991; Fey et al., 1991; Pushkarev & Kovalev, 2015). From Cordes (2001) the Galactic angular broadening (Θ; mas) at 6.7 GHz as a function of the scattering measure (SM) and frequency (ν; GHz) is given by:

$$\Theta = 71\,\frac{SM^{3/5}}{\nu^{11/5}}\,\text{mas}$$

Minier et al. (2002) investigated whether the presence of extended emission (halos) around maser spots can be explained by scattering broadening. They argue that while some degree of scattering is expected ($\Theta \sim 0.3$ and 1 mas at 12.2 and 6.7 GHz respectively), it is not large enough in magnitude to give rise to the 5–50 mas halos–like structures seen in their sample of 12.2 GHz masers. In addition, they found that the ratio of halo size at the two frequencies did not behave as λ^2 as would be expected if the halo size originates primarily from scatter broadening. Therefore they concluded that apparent distinct core/halo structures are the result of either saturation in some uniform spherical cloud, physically different environments (dense gas vs. weak diffuse gas), or turbulence in a homogeneous medium. A similar argument was put forward by Menten et al. (1992), comparing the spot sizes of 6.7 GHz CH_3OH against 12.2 GHz CH_3OH and 1.665 GHz OH at the same velocities in W3(OH). The conclusion was that since a λ^2 variation was not seen, the observed spot size was intrinsic.

Masers are confined to the plane of the Milky Way, however, not all to the same extent (Figure 4.1). Since HMSF–associated masers have a scale height from the Galactic Plane of 19 ± 2 pc (Reid et al., 2019), masers at higher Galactic b are more biased towards being closer to us. In addition, regardless of whether the masers are closer, a higher Galactic Latitude line–of–sight passes through less of the Galactic Plane. Either way, it is not unreasonable to suggest that higher Galactic b masers might be affected less by scattering.

Pushkarev & Kovalev (2015) surveyed VLBI quasar size as a function of Galactic b and frequency. They found that there was a significant difference in the modelled angular size of AGN inside $|b| < 10°$ and outside the Galactic plane $|b| > 10°$. While data at 5 GHz suffered from completeness issues, 2/8 GHz data were collected simultaneously allowing for the frequency dependence to be explored about 5 GHz. For sources within the plane, 33% had a frequency–dependant core size ratio with index ~ 2, suggesting scatter broadening. The exact graduation of this effect was not explored, most likely due to diminishing sample size as $|b| \rightarrow 0$. However the maximum observed size of quasars at 2 GHz and 8 GHz at $|b| = 2, 1, < 1$ were approximately $10, 10, 20$ mas and $4, 6, 4,$ mas. From this I derive approximate max values of $SM = 0.5, 0.5, 1.5$ for $|b| = 2, 1, < 1$ (removing extreme values by consulting expected values for the scattering measure from Cordes et al., 1991). This gives $\Theta = 0.7, 0.7, 1.4$ mas.

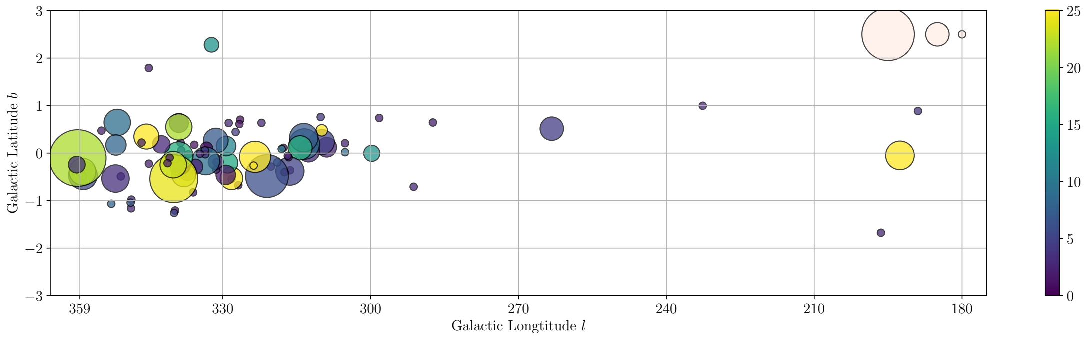

Figure 4.12: Distribution of maser minimum modelled size vs. Galactic coordinates. **Point size:** Radius scales with modelled size– Key top left: $5.0, 1.0, 0.1$ mas left to right. **Colourmap:** Component flux density in Jy.

Next, I compared modelled values against values in Cordes et al. (1991) Fig 3, where the expected angular broadening at 1 GHz is modelled against l and b towards the Galactic Centre. Values closer to $\Theta = 0.5, 1.9, 3.8$ mas are implied, most likely due to Galactic Centre and/or Galactic Plane proximity ($|b| < 10$). I take the geometric average and see that my graduated scale is approximated as $\Theta = 0.6, 1.2, 2.3$ mas for $|b| = 2, 1, < 1$.

If there is a minimum size due to interstellar scattering, I expect to see a tendency for targets at low Galactic latitudes to have a larger minimum size than those at higher latitudes. Also, if that effect is larger than the intrinsic maser size and variations to it, I would expect to see a maser minimum size ‘cap’ at the values derived above. Taking the smallest ‘significant’ maser spot core size for each maser (no D–grade spots), I examine the distribution in both l and $|b|$ (Figure 4.12). I have 8 masers outside of $|b| > 1$, 18 masers inside the range $0.5 < |b| < 1$ and 56 masers inside $|b| < 0.5$. I find the average spot minimum spot size within those ranges as $\theta_{|b|>1.0} = 0.22 \pm 0.17$ mas, $\theta_{0.5<|b|<1.0} = 0.55 \pm 0.66$ mas and $\theta_{|b|<1.0} = 0.58 \pm 0.59$ mas respectively.

I cannot detect any significant difference between minimum maser spot sizes as a function of $|b|$. In addition, is it clear that derived minimum spot sizes do not cap at the above values of $\Theta = 0.6, 1.2, 2.3$ mas for $|b| = 2, 1, < 1$.

Therefore, it is safe to infer that the values and variation between my modelled Core/Halo spot sizes are unlikely the product of interstellar scattering at the level that can be both detected by the LBA ($\Theta \gg \theta_B$) or able to limit the possible astrometric accuracy. Therefore, maser spot size appears to be purely intrinsic at 6.7 GHz on the level of $\theta_B \sim 2.5$ mas.

4.5.3 Class II Methanol Variability and Flaring

Class II methanol masers are known to be variable on time scales of more than months to years (Caswell et al., 1995a; Szymczak et al., 2018a). While this variability is normally by a factor of less than 2 and rarely by a factor of less than 10, there have been some extreme examples in recent years. These rapid increases in flux density are called flares. G192.600 − 0.048 as observed in this survey serendipitously was undergoing flaring (Szymczak et al., 2018a).

In this survey the maser region G192.600–0.048 (also known as S255) is considered an $A-$grade candidate due to the $v_1 = 5.20\,\mathrm{km\,s^{-1}}$ and $v_2 = 5.90\,\mathrm{km\,s^{-1}}$ components, with the v_1 component being the most compact and preferable for astrometry.

In June 2015, S255 began to rapidly increase in luminosity. Szymczak et al. (2018b) presents a detailed overview of burst and Figure 4.13 is Fig. 3, page 3 from that article. Figure 4.13 shows that at the time of these observations (MJD 57451 and 57469) S255 was very close to the peak of the burst, especially the 5.2 and 5.9 $\mathrm{km\,s^{-1}}$ velocity components. This coincidental occurrence explains the extremely enhanced flux density encountered for this source compared to that catalogued by the MMB, and the different spectral features and spectra. Although the previous methanol parallax was for a $v = 4.6\,\mathrm{km\,s^{-1}}$ component, that feature is no longer present in auto- or cross-correlation spectra. The accretion event led to the appearance of some very compact emission regions at $v_1 = 5.20\,\mathrm{km\,s^{-1}}$ and $v_2 = 5.90\,\mathrm{km\,s^{-1}}$. Therefore, I acknowledge that in this relatively blind survey with a very short time baseline there is a non–zero chance that the derived compactness for some targets may appear significantly different at a later date due to unmonitored episodic accretion resulting in morphological, spectroscopic and luminous variations.

4.5.4 Variation from Model

Maser regions are complex dynamic structures, and multiple emission regions in the field of view can coincide within a single line–of–sight velocity channel. The relatively high-velocity resolution aims to combat this ambiguity without sacrificing thermal sensitivity. Nevertheless < 500 s worth of integration time spread over 2 to 4 scans per maser provides very little $uv-$coverage, especially continuous coverage required for accurate and precise imaging. As a consequence, it is very difficult to ascertain whether the measured flux density is due to more than one spatially separate emission region and to what fraction. Furthermore, the determination of individual structure for each region becomes highly degenerate when one considers potential flux density variation due to component separation and position angle.

This point is illustrated by Figures 2 and 3 from Goedhart et al. (2005b), where the authors image the strong methanol maser G9.62+0.2E with the VLBA. This maser has a complex morphology– the diffuse components are quite elongated and it is easy to see that one or two cuts at different hour angles on structures like this are going to give quite different visibility amplitudes on similar baseline lengths. Therefore, there can be the case that there are multiple spatially distinct maser spots that overlap in velocity and/or there can be complex morphologies in a single maser spot. Both of these can produce results that may be confusing or inconsistent when there are only one or two small cuts.

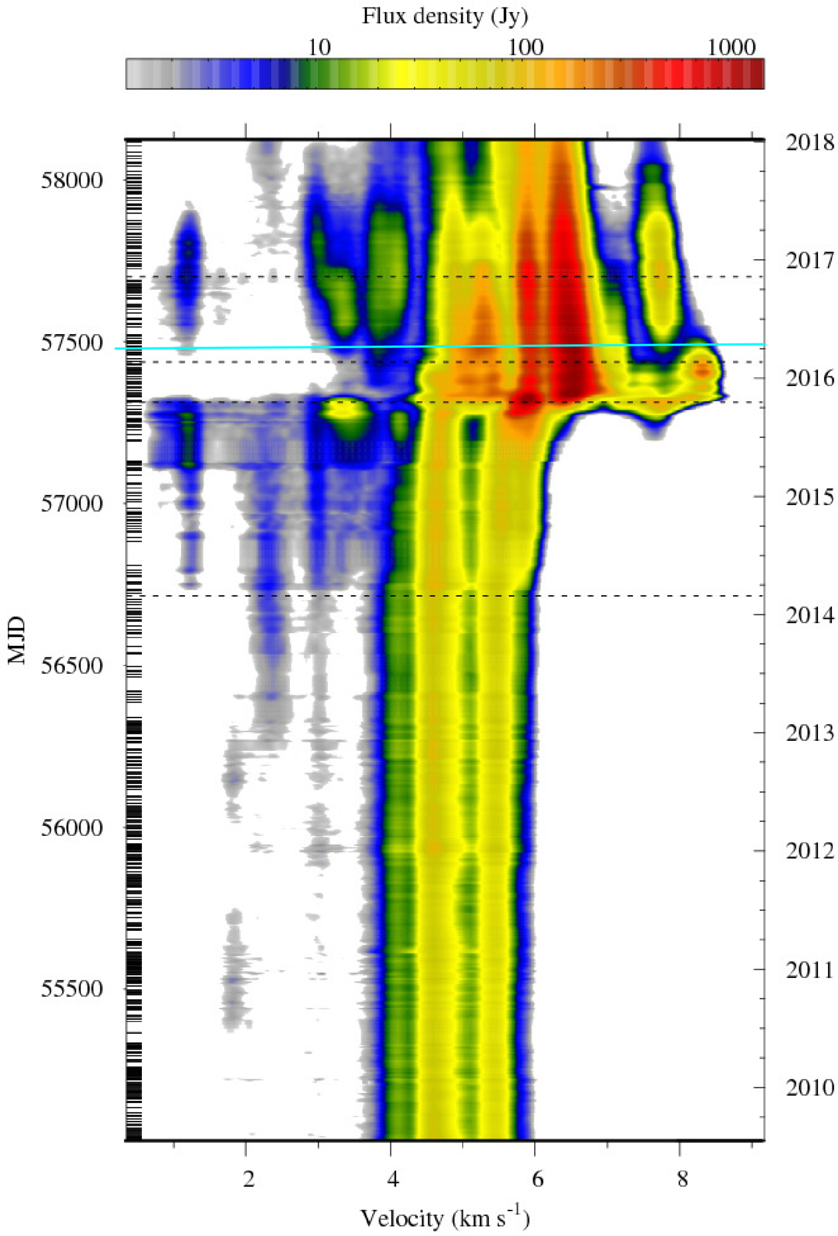

Figure 4.13: Original Caption: *Fig. 3. Dynamic spectrum of the 6.7 GHz methanol maser emission for S255IR-NIRS3. The colour scale maps to the flux density as shown in the wedge on the top. The flux densities are linearly interpolated between consecutive 32 m telescope spectra. The velocity scale is relative to the local standard of rest. Individual observation dates are indicated by black tick marks near the left ordinates. The horizontal dashed lines from bottom to top mark the approximate times of the start first peak, dip, and second peak of the burst.* **Cyan line:** Approximate dates for V534A and B epochs.

4.5.5 Comparison with the BeSSeL survey

The BR149 series of the BeSSeL project was dedicated to determining the proper motion and parallax of 6.7 GHz methanol masers after the upgrade of the VLBA allowed them to observe that frequency range (Brunthaler et al., 2011). The first five epochs of this series, BR149A1 to BR149A5, were a targeted survey of known methanol masers to determine visibility amplitude vs. baseline length in the same vein as this survey§. Unfortunately, the results from these surveys remain unpublished. However, I can infer the 'strike rate' of compact and/or suitable 6.7 GHz methanol masers by comparing which masers from these targets surveys were followed up with parallax observations in the BR149B1 to BR149U4 epochs.

There were 234 6.7 GHz methanol masers observed in the BR149A target survey between the Galactic longitudes of $358 \lesssim l < 360$, $0 < l \lesssim 213$ deg, with ~ 65 6.7 GHz methanol masers listed as being in the parallax observations for the further BR149 epochs¶ or in the corresponding experiment key files‖. Therefore of the targets masers in BR149A, 26% were deemed appropriate for further VLBA parallax observations.

The VLBA is a much more sensitive instrument than the ASCI array and so the flux density thresholds need to be accounted for slightly before a direct comparison of the two surveys can be made. Figure 4.14 shows the peak flux density distribution of all known 6.7 GHz methanol masers and those observed in the surveys and follow-ups in the relevant Galactic longitude ranges. Maser flux densities from Yang et al. (2019) and references therein. The VLBA SEFD

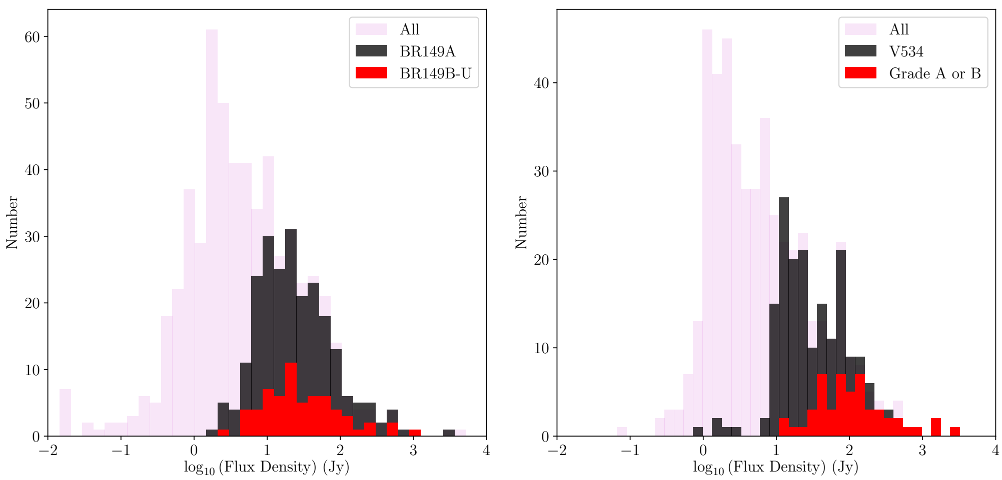

Figure 4.14: Comparison between peak flux density distribution of 6.7 GHz methanol masers observed in BR149A vs. V534. **Left:** Flux density distribution of all known 6.7 GHz masers between $358 \lesssim l < 360$, $0 < l \lesssim 213$ deg (pink), those observed in BR149A series (grey) and those used for further BeSSeL parallax observations that were also observed in BR149A (red). **Right:** Flux density distribution of all known 6.7 GHz masers between $188 < l < 360$ deg (pink), those observed in V534 (grey) and those from V534 that I have graded A or B (red). In both plots the $y-$axis is number of masers and the $x-$axis is flux density in Jy with $\log_{10}$ scale and binning.

at $\nu = 6.7$ GHz is SEFD ~ 300 Jy, therefore the baseline sensitivity for a $t = 60$ s scan in a

§http://www.vlba.nrao.edu/astro/VOBS/astronomy/jun12/br149a1/br149a1.key
¶http://bessel.vlbi-astrometry.org/observations
‖Available here http://www.vlba.nrao.edu/astro/VOBS/astronomy/

$\Delta\nu = 2$ kHz channel is $\sigma = 0.6$ Jy (using Equation 4.1). A 5σ detection in this channel requires a peak flux density of 3 Jy, which is consistent with the apparent flux density cut-off of the masers observed in BR149A (Figure 4.14). If we raise this minimum flux density to 10 Jy, then we decrease the number of masers that would have been observed in BR149A from 234 to 174. The number of masers that were then observed in BR149B-U from this subset was 49, however, this does not take into account whether these masers would have been selected as A or B grade by my selection criteria above. As such, 49 is an upper bound and the percentage of masers above 10 Jy observed between $358 \lesssim l < 360$, $0 < l \lesssim 213$ deg suitable for parallax observations was $\lesssim 28\%$.

Out of the 187 masers targeted in this work, 53 were deemed appropriate for SπRALS observations on the ASCI array. There were some observational issues which meant that two of the masers did not have any valid data and a further 10 that do not have catalogues flux densities about the cut-off and were possibly erroneously targeted. Therefore the total number of valid targets was 175, where 53 of these remain as A or B (Figure 4.14). This implies that $\geq 30\%$ of masers with a peak flux density above 10 Jy are suitable for parallax observations between $188 < l < 360$ deg, comparable with the result from BeSSeL's BR149A and the northern sky.

4.6 Conclusion - First Targets

I have surveyed 187 individual 6.7 GHz methanol masers from the Methanol Multibeam Catalogue and have determined which ones are currently most appropriate for future SπRALS observations that will culminate in a parallax measurement. I report successful detections of over 90% of the surveyed sources and have modelled structural parameters for over 50% of them. Table B.1 contains a list of the 53 (A and B) recommended first targets for VLBI parallax measurements set to begin mid–2020, while Figure 4.15 shows the distribution of first targets in l–v space. I

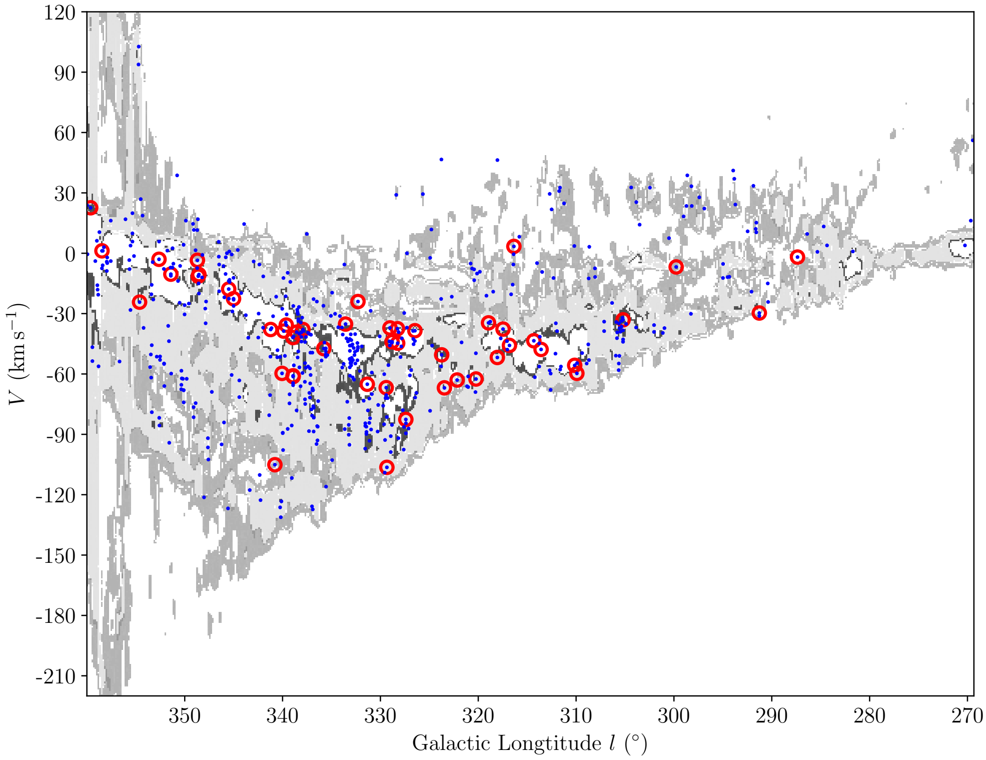

Figure 4.15: $l-$v distribution of 6.7 GHz visible from the Southern Hemisphere. **Blue:** Positions of all known masers between $270 < l < 2°$. **Red:** Positions of best maser targets determined by this survey. The best masers appear to have a fairly good sampling of the 4th Galactic quadrant with the exception of $l < 285°$.

find that out of the sample of 187 masers, 13 are categorised as $A-$grade, 40 as $B-$grade, 29 as $C-$grade and 21 as $D-$grade. A further 82 can be classed as unsuitable for milliarcsecond astrometry in the current era (if at all) due to extremely heavy resolution on small to intermediate baselines (10–20 Mλ), and a further 2 as unknown due to observational issues (Figure 4.11).

5 MultiView

The ASCI array is a much sparser, less sensitive array containing fewer telescopes than the VLBA, European VLBI Network (EVN) or LBA. ASCI also cannot rely on sophisticated dual-beam receivers like those that assist VERA in atmospheric calibration. To achieve the same level of astrometric accuracy as BeSSeL or VERA, SπRALS must rely on observational methods and calibration techniques to overcome the current limitations of ASCI.

In this chapter I will introduce the background, theory and observational methodology of the calibration technique to be tested in Chapter §6 : MultiView. The core idea of the MultiView astrometric calibration technique is that if it were possible to simultaneously observe multiple calibrators positioned around the target, then all residual delays could be determined and perfectly removed.

Certain technology may allow direct use of Multiview in its purest conceptual form: phased array feeds or multi-beam receivers can simultaneously observe target and calibrator(s) providing direct calibration. However, as ASCI does not have access to any of these systems, I need to develop an observational-based version of MultiView.

Following a brief background, I step through the delay budget after calibration, each component, in turn, to explain how inverse MultiView can calibrate that effect. I finish off with an explanation of how I will structure the inverse MultiView part of observations and consequently solve for target positions.

5.1 Background

MultiView is a relatively new approach to astrometric calibration. The first iteration of MultiView was called 'cluster–cluster' phase referencing (Rioja et al., 1997b, 2002). This involved simultaneous observations of a target and multiple calibrators at low frequencies by utilising multi-element single stations. Unfortunately, the availability of such observing sites (let alone multiple sites for VLBI) is extremely limited, and therefore, the modification was required. Despite this, cluster–cluster showed promise in removing residual ionospheric and tropospheric delays that plagued low–frequency astrometry.

The next iteration was the phase referencing stage demonstrated by Rioja et al. (2017). Observations were structured such that the calibrators and an OH maser were looped through as C1–C3–(M+C4)–C3–C1..., where the total duty cycle was ~ 5 mins (Figure 5.1). The OH maser had an in-beam calibrator that was used as an astrometric comparison. This is what I will refer to as traditional MultiView – an important caveat is that all sources have to be observed within the tropospheric and ionospheric coherence times (hence the 5 mins; Orosz et al., 2017) and this was considered the definition of simultaneity.

The method involved extracting phases from the 4 calibrators and 2D linear interpolating them to the position of the maser and in–beam calibrator. Phase ambiguities that were multiples of 2π were iteratively removed from calibrator phases to minimise residuals and optimise image RMS noise. Although effective at lower frequencies ($\sim$ 1.5 GHz) this technique has limited

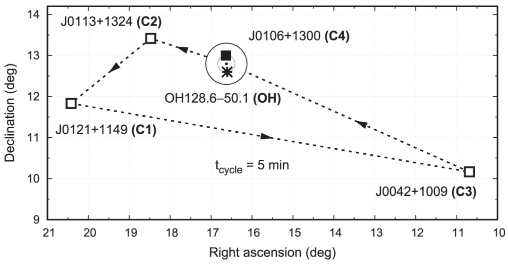

Figure 5.1: Rioja et al. (2017) Figure 1. Original caption: *Sky distribution of the sources observed with the VLBA at 1.6 GHz ... Dashed lines and arrows mark the source switching order during the observations with 5 min duty cycles. Star and solid symbols mark the simultaneously observed OHC4 pair, with the VLBA antennas, pointed halfway between the two. The two concentric circles represent the half-power beamwidth and full beam width of the antennas. Both OH and C4 are targets in the astrometric analyses ... C1 was used as the fringe finder.*

direct applicability at intermediate frequencies ($\sim$ 7 GHz) where tropospheric coherence times are shorter and in–beam calibrators are rare.

Inverse phase referencing (iPR) is commonplace in maser astrometry as it uses the strong maser as the fringe fit location rather than the often weak quasar calibrators. As the masers are strong, less on-source integration time is required to get sufficient SNR, and therefore observations of maser/calibrator can be kept within the increasingly shorter coherence times as the frequency increases. Doing so transfers the (opposite of the) positional information from the maser to calibrator and therefore, the offsets, proper motion and parallax. This technique is important as you can nod between a maser and calibrator in many different ways and also maximise the time on, and $uv-$ coverage on the maser (for imaging and structure analysis).

Therefore, instead of MultiView, I will do *inverse MultiView* (iMV) using the maser as the reference. Again, time on and $uv-$coverage of the maser can be maximised and because the maser is strong, the individual scan on-source time can be minimised while still measuring fringe solutions. Calibration is achieved by iteratively nodding to various calibrators at different position angles and angular separations, and then measuring phases referenced to the maser. Individual calibrators can be chosen less rigorously than normal PR/iPR: compactness and calibrators with more flux density are a higher priority than target–calibrator separation to achieve stable phase solutions with high SNR. Clear benefits to this are: retention of the 50% on-source time for the target as with normal nodding and more reference calibrators. The obvious downsides are that each added calibrator decreases the individual calibrator on-source time.

In the final steps, a phase plane solution or wedge can be fit over the FoV above each telescope based on the measured phases and their change over time. As I will show, the application of this solution to the target will return the positional information while minimising the effect of residual delays. I also will investigate how accurately the positions of target and calibrators need to be determined to avoid phase ambiguities in the phase plane solution.

5.2 Inverse MultiView Theory

I want to establish how MultiView is expected to reduce phase referencing errors using a theoretical approach. To this end, I am going to start by assuming there is a target (T) separated θ_{sep} radians away from a calibrator (C) on a single baseline. I will use σ to signify an error/uncertainty and Δ to signify a difference.

Recall the total delay budget after phase referencing (Equation 2.51):

$$\begin{aligned}\tau_C(t_{i+1}) - \tau_T(t_i) &= \Delta\tau_{bl} + \Delta\tau_{\text{dry}} + \Delta\tau_{\text{wet}} + \Delta\tau_{\text{iono}} + \tau_{\theta,T} - \tau_{\theta,C} + \tau_{\sigma,T} - \tau_{\sigma,C} + \tau_{th} \\ &= \tau_{\theta,C} - \tau_{\theta,T} + \sigma_{\tau_{pr}}\end{aligned} \tag{5.1}$$

where $\Delta\tau_{bl}, \Delta\tau_{\text{dry}}, \Delta\tau_{\text{wet}}, \Delta\tau_{\text{iono}}$ refer to difference in the respective LoS delays due to baseline, dry/wet troposphere and ionosphere residual delays and τ_{th} is the thermal uncertainty. Therefore the difference in delay between the target and calibrator gives the relative positional offset corrupted by a factor $\sigma_{\tau_{pr}}$.

The parallax and proper motion of the target will shift its position between epochs as predicted by Equation 2.72, which lead to delays as given by Equation 2.31. If the position of the calibrator were to remain constant over all the epochs, this would then allow the parallax and proper motion to be identified by the changes in $\tau_{\theta,C} - \tau_{\theta,T}$.

As discussed in Section §2.3.7, quasars can have apparent positional shifts due to jet evolution. Therefore, in reality, changes in the difference $\tau_{\theta,C} - \tau_{\theta,T}$ between epochs can be due to either the target or calibrator. However, the positional shifts caused by the quasar proper motions have no physical reason to be correlated with the parallax motion and instead introduce positional scatter or proper motion uncertainty at the level of $10 - 20$ μas/yr (Rioja et al., 1997b; Reid & Honma, 2014).

Accepted wisdom (e.g. Reid & Honma, 2014) is that delay errors are effectively reduced by phase referencing such that the final error becomes:

$$\sigma_{\tau_{pr}} \leq \theta_{\text{sep}}\sigma_{\tau} + \tau_{th} \tag{5.2}$$

where σ_τ is the quadrature sum of all individual sources of delay uncertainty (calibration uncertainty). This function increases linearly with the target-calibrator separation, and therefore, for a fixed upper limit on calibration delay uncertainty σ_τ, smaller separations are expected to give increasingly better astrometry up to the thermal limit τ_{th}.

The uncertainty $\sigma_{\tau_{pr}}$ can be interpreted as 'the maximum value residual delay could be over angular distance θ_{sep}'. Rather than accept this upper limit, MultiView is a technique to indirectly measure σ_τ and subtract the effect it has on the data.

Following Rioja et al. (2017) I will be using 2D phase–planes in equatorial coordinates RA, DEC (α, δ) as the MultiView model. However, I would like to take a moment to justify why. In the following few sections, I will show that the residual LoS delay terms $\Delta\tau_{bl}$ and $\Delta\tau_{tr}$ can be modelled by 2D delay (or phase) planes out to reasonable target–calibrator separations.

5.2.1 Residual Baseline Delay

The baseline component $\Delta\tau_{bl}$ from Equation 5.1 is the difference in residual baseline error for each line of sight. The residual baseline delay for any LoS depends on the individual baseline uncertainties, hour angle and declination, and is given in Equation 2.29. Target and calibrator are separated by $\mathbf{a}$ radians in RA and $\mathbf{b}$ radians in DEC: $\alpha_C - \alpha_T = \mathbf{a}$, $\delta_C - \delta_T = \mathbf{b}$ and $\theta^2_{\text{sep}} = (\mathbf{a}\cos\delta)^2 + \mathbf{b}^2$. Subtracting the measured target delay from the calibrator data would give:

$$\begin{aligned} c(\tau_{bl,C} - \tau_{bl,T}) = c\Delta\tau_{bl} =& \Delta B_x \cos(t_{lst} - \alpha_1)\cos\delta_1 - \Delta B_y \sin(t_{lst} - \alpha_1)\cos\delta_1 + \Delta B_z \sin\delta_1 \\ & - \Delta B_x \cos(t_{lst} - \alpha_2)\cos\delta_2 + \Delta B_y \sin(t_{lst} - \alpha_2)\cos\delta_2 - \Delta B_z \sin\delta_2 \end{aligned} \tag{5.3}$$

where ΔB_i are the baseline errors in the geocentric coordinate system x, y, z and t_{lst} is the local sidereal time. Substitution of $\alpha_C = \mathbf{a} + \alpha_T$ and $\delta_C = \mathbf{b} + \delta_T$ gives:

$$\begin{aligned} c\Delta\tau_{bl} &= \mathbf{a}\cos\delta_T\left[\Delta B_x \sin(t_{lst} - \alpha_T) - \Delta B_y \cos(t_{lst} - \alpha_T)\right] \\ &\quad + \mathbf{b}\left[\Delta B_x \cos(t_{lst} - \alpha_T)\sin\delta_T - \Delta B_y \sin(t_{lst} - \alpha_T)\sin\delta_T + \Delta B_z \cos\delta_T\right] + \sigma_{O^2} \\ &= \mathbf{a}\mathcal{A}_{bl}(t_{lst}) + \mathbf{b}\mathcal{B}_{bl}(t_{lst}) + c\sigma_{O^2} \end{aligned} \tag{5.4}$$

Where I have put the full derivation in Appendix C.1.3. This is an equation for a plane in Right Ascension offset and Declination offset from target position with respective time–variable slopes $\mathcal{A}(t_{lst})$ and $\mathcal{B}(t_{lst})$. The σ_{O^2} is the error in this model due to ignoring O^2 terms.

In traditional phase referencing, the slope $c\Delta\tau_{bl}$ over angular separation cannot be determined. The maximum value the slope can take will be determined by the magnitude of baseline component errors ΔB_i and the distances $\mathbf{a}$, $\mathbf{b}$. The error in ignoring the slope (which is the O^1 term) is:

$$\begin{aligned} c|\sigma_{O^1}| &\leq |\mathbf{a}\cos\delta_T\,(\Delta B_x + \Delta B_y) + \mathbf{b}\,(\Delta B_x + \Delta B_y + \Delta B_z)\,| \\ &\leq \sqrt{(\mathbf{a}\cos\delta_T)^2 + \mathbf{b}^2}\sqrt{\Delta B_x^2 + \Delta B_y^2 + \Delta B_z^2} \\ &= \theta_{\text{sep}}\sigma_{bl} \end{aligned} \tag{5.5}$$

where σ_{bl} is the quadrature sum of individual sources of uncertainty (in this case only baseline) and θ_{sep} is in radians. This form is consistent with Equation 5.2.

If the error in phase referencing (effectively the O^0/DC solution) is the maximum value the O^1 term can take, then it follows the (baseline) error in MultiView is the maximum value O^2

term can take. σ_{O^2} is the error in the plane due to not accounting for higher-order terms (aka. curvature) and is given by:

$$c\sigma_{O^2} = \mathbf{a}\,\mathbf{b}\,\mathcal{C}_{bl} + \frac{1}{2}\mathbf{a}^2\mathcal{D}_{bl} + \frac{1}{2}\mathbf{b}^2\mathcal{E}_{bl} \tag{5.6}$$

where functions for the O^2 coefficients $\mathcal{C}_{bl}$, $\mathcal{D}_{bl}$ and $\mathcal{E}_{bl}$ are given in derivation (Appendix C.1.3). All high order coefficients depend linearly on ΔB_i and have the same sinusoidal dependence on hour angle and declination. Therefore, they all have maximum values which only depend on baseline uncertainty ΔB_i:

$$\begin{aligned}
c|\sigma_{O^2}| &= |\mathbf{a}\,\mathbf{b}\,\mathcal{C}_{bl} + \frac{1}{2}\mathbf{a}^2\mathcal{D}_{bl} + \frac{1}{2}\mathbf{b}^2\mathcal{E}_{bl}| \\
&\leq |\frac{1}{2}\mathbf{a}^2\left(\Delta B_x + \Delta B_y\right) + \mathbf{ab}\left(\Delta B_x + \Delta B_y\right) + \frac{1}{2}\mathbf{b}^2\left(\Delta B_x + \Delta B_y + \Delta B_z\right)| \\
&\leq |\frac{1}{2}\mathbf{a}^2 + \mathbf{ab} + \frac{1}{2}\mathbf{b}^2||\Delta B_x + \Delta B_y + \Delta B_z| \\
&\leq \frac{1}{2}\left(\mathbf{a}+\mathbf{b}\right)^2\sqrt{\Delta B_x^2 + \Delta B_y^2 + \Delta B_z^2} \\
&\leq \theta_{\rm sep}^2\ \sigma_{bl}
\end{aligned} \tag{5.7}$$

This implies that even in the presence of baseline errors $\Delta B = 3$ cm, MultiView plane fitting uncertainty is at the level of $c\sigma_{O^2} = 0.0002$ cm at $\theta_{\rm sep} = 5$ deg, equivalent to an astrometric uncertainty of $\sigma_\theta = 13\mu$as with a baseline of $B = 3500$ km. This is opposed to the case of not fitting the plane in traditional phase referencing and getting values $\sigma_{O^1} = 0.002$ cm and $\sigma_\theta = 150\ \mu$as. This theoretical result is similar to the order of magnitude improvement gained by using empirical 'traditional' multiview (Rioja et al., 2017).

Equation 5.7 describes the minimum value for baseline delay uncertainty. In practice, the total delay uncertainty will be larger as it depends on how accurately the delay slopes can be measured, and this depends on other delay slopes such as the one due to the residual dry tropospheric path delay.

5.2.2 Residual Dry Tropospheric Delay

The total difference in delay between a target and calibrator due to the troposphere will have two components, dry and wet. For the moment I will only consider the difference between residual dry tropospheric delay $\Delta\tau_{\rm dry}$. For a single source at some zenith angle Z, the residual dry tropospheric zenith delay will be:

$$c\tau_{\rm dry} = c\sigma_{\tau_z}(t)\sec Z \tag{5.8}$$

where $\sigma_{\tau_z}(t)$ is the zenith delay error arising from either uncertainty in geoblock fitting or systematic effects like ionosphere (see Section §2.3.9.2 for more information of geoblock fitting). I have used the dry tropospheric mapping function $m_3 = \sec Z$ (Equation 2.46) as it is quantitatively easy to deal with (and I have previously shown various mapping functions m_1, m_2 and m_3 equivalent; see Figure 2.4).

After phase referencing from the target at some zenith angle Z_T to the calibrator at another zenith angle Z_C, the hypothetical delay difference for the two positions for a *single antenna* is:

$$\begin{aligned} c\Delta\tau_{\text{dry}} &= c\sigma_{\tau_z}\left(\frac{1}{\cos Z_C} - \frac{1}{\cos Z_T}\right) \\ &= \frac{\sigma_{\tau_z}}{\sin\delta_C \sin\varphi + \cos\delta_C \cos\varphi \cos(t_{lst} - \alpha_C)} \\ &\quad - \frac{\sigma_{\tau_z}}{\sin\delta_T \sin\varphi + \cos\delta_T \cos\varphi \cos(t_{lst} - \alpha_T)} \end{aligned} \tag{5.9}$$

where I have used $\cos Z = \sin\delta \sin\varphi + \cos\delta \cos\varphi \cos(t_{lst} - \alpha)$ and φ is the antenna latitude. I make this substitution because I want to determine a plane in equitorial coordinates. As in the previous example, the calibrator is arbitrarily offset from the target $\alpha_C = \alpha_T + \mathbf{a}$ and $\delta_C = \delta_T + \mathbf{b}$. In Appendix C.1.3 I detail the expansion leading to:

$$\begin{aligned} c\Delta\tau_{\text{dry}} &= \frac{\sigma_{\tau_z}}{\cos^2 Z_T}\big(\,\mathbf{a}\left[-\cos\delta_T \cos\varphi \sin\left(t_{lst} - \alpha_T\right)\right] \\ &\quad + \mathbf{b}\left[\cos\varphi \cos\left(t_{lst} - \alpha_T\right)\sin\delta_T - \sin\varphi\cos\delta_T\right]\,\big) + \sigma_{O^2} \\ &= \mathbf{a}\mathcal{A}_{\text{dry}}(t_{lst}) + \mathbf{b}\mathcal{B}_{\text{dry}}(t_{lst}) + c\sigma_{O^2} \end{aligned} \tag{5.10}$$

As before, the σ_{O^2} term is the error in the plane fit due to the omission of higher-order terms that describe curvature. Unlike in the plane due to a baseline residual, σ_{O^2} is difficult to interpret in the equatorial coordinate system. Instead, I will interpret this in a local telescope local coordinate system.

The worst-case scenario leading to the largest value for σ_{O^2} is that as the target moves towards $Z_T \to 90$ deg at a particular antenna location (aka. sets), the target and calibrator are coincidentally aligned in the direction of maximum elevation change. This depends on the antenna location, for example, at the equator this will always be in the RA direction. So to retain generality, I assume that in this scenario only the difference in zenith angles between the two sources is needed to parametrize the difference in residual delay.

In this case the difference in residual delay between the two sources can be described by:

$$\begin{aligned} c\Delta\tau_{\text{dry}} &= \sigma_{\tau_z}\left(\frac{1}{\cos\left(Z_T + \theta_{\text{sep}}\right)} - \frac{1}{\cos Z_T}\right) \\ &= c\sigma_{\tau_z}\sec^2 Z_T \sin Z_T \theta_{\text{sep}} + c\sigma_{\tau_z}\left(\sin^2 Z_T + 1\right)\sec^3 Z_T \frac{\theta_{\text{sep}}^2}{2} + c\sigma_{O^3} \end{aligned} \tag{5.11}$$

where again, θ_{sep} in in radians. The O^1 term is the same as that previously identified in Section 2.3.9.2, Equation 2.53 and would be the error if no plane fitting was performed (aka. the error in phase referencing). Therefore, it stands to reason that the maximum error in plane fitting from ignoring curvature is:

$$c|\sigma_{O^2}| \leq c\sigma_{\tau_z}\left(\sin^2 Z_T + 1\right)\sec^3 Z_T \left(\frac{\theta_{\text{sep}}^2}{2}\right) \tag{5.12}$$

Figure 5.2 shows a comparison between theoretical uncertainties in phase referencing and inverse MultiView. At $Z_T = 60$ deg, with residual zenith troposphere $c\sigma_{\tau_z} = 3$ cm and a target–calibrator separation $\theta_{\text{sep}} = 3$ deg, normal phase referencing at this elevation would yield:

$$c\sigma_{O^1} = c\sigma_{\tau_z}\sec^2 Z_T \sin Z_T \theta_{\text{sep}} = 0.55 \text{ cm} \tag{5.13}$$

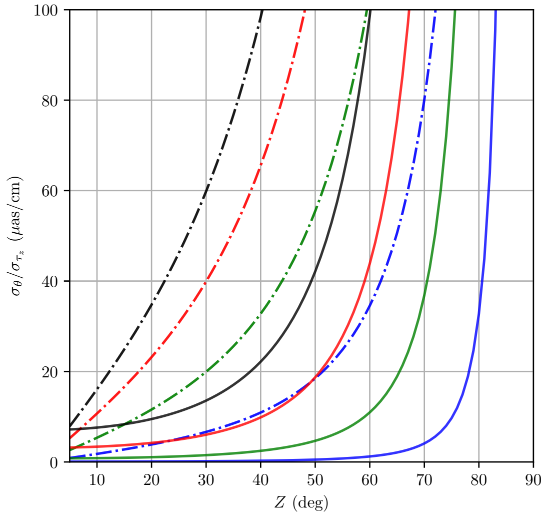

Figure 5.2: Comparison of theoretical maximum residual dry troposphere effect in inverse MultiView and phase referencing for different target–calibrator separations. **y-axis:** Positional uncertainty σ_θ per unit residual zenith delay σ_{τ_z}; **x-axis:** Observing zenith angle. **Dotted lines:** phase referencing uncertainties (σ_{O^1}); **Solid lines:** inverse MultiView uncertainties (σ_{O^2}). **Blue, green, red and black lines** indicated target–calibrator separations $\theta_{sep} = 1,\ 3,\ 6,\ 9$ deg respectively. All values are calculated with maximum ASCI baseline of $|\mathbf{B}| \sim 3500$ km.

equivalent to an astrometric accuracy of $\sigma_\theta = 312\mu$as with a maximum baseline $|\mathbf{B}| = 3500$ km. Alternatively, with MultiView plane fitting and the same parameters, this becomes

$$c\sigma_{O^2} = c\sigma_{\tau_z}\left(\sin^2 Z_T + 1\right)\sec^3 Z_T\left(\frac{\theta^2_{\text{sep}}}{2}\right) = 0.06\text{ cm} \tag{5.14}$$

equivalent to an astrometric accuracy of $\sigma_\theta = 33\mu$as, an order of magnitude improvement!

Based on the above, inverse MultiView is expected to perform better than phase referencing for dry tropospheric calibration, especially in the presence of large residual tropospheric delay uncertainties ($c\sigma_{\tau_z} \geq 1 - 2$ cm), low–elevations and/or large target–calibrator separations. Theoretically, inverse MultiView should be able to give astrometric accuracy better than 10μas at ~ 15 deg elevation in the presence of well-calibrated zenith delays (~ 1 cm) and given proximal calibrators (~ 1 deg) on a baseline $|\mathbf{B}| = 3500$ km.

5.2.3 Calibrator Positional Delay

So far I have shown that $\Delta\tau_{bl}$ and $\Delta\tau_{\text{dry}}$ terms can be expressed by planes with uncertainties which depend on $\sigma_{O^2} \propto \theta^2_{sep}$ and are in general smaller than equivalent uncertainties for normal phase referencing. Now I want to discuss how positional errors in target and calibrator affect the inverse MultiView method.

Equation 2.31 gives the delay uncertainty expected due to a source position error:

$$\begin{aligned} c\tau_\theta &= \sigma_\alpha \cos\delta_C (B_x \sin(t-\alpha) + B_y \cos(t-\alpha)) \\ &\quad + \sigma_\delta(-B_x \cos(t-\alpha)\sin\delta + B_y \sin(t-\alpha)\sin\delta_C + B_z\cos\delta) \end{aligned}$$

where σ_α and σ_δ are the positional uncertainties in Right Ascension and Declination in radians and B_i are the baseline components in geocentric coordinates x, y, z.

Inverse phase referencing subtracts delay of the target from the calibrator, which serves to subtract the above respective expressions for the target and calibrator:

$$\begin{aligned} c\,(\tau_{\theta,C} - \tau_{\theta,T}) &= \sigma_{\alpha,C} \cos\delta_C (B_x \sin(t-\alpha_C) + B_y \cos(t-\alpha_C)) \\ &\quad + \sigma_{\delta,C}(-B_x \cos(t-\alpha_C)\sin\delta_C + B_y \sin(t-\alpha_C)\sin\delta_C + B_z\cos\delta_C) \\ &\quad -\sigma_{\alpha,T}\cos\delta_T\,(B_x\sin(t-\alpha_T) + B_y\cos(t-\alpha_T)) \\ &\quad -\sigma_{\delta,T}\,(-B_x\cos(t-\alpha_T)\sin\delta_T + B_y\sin(t-\alpha_T)\sin\delta_T + B_z\cos\delta_T) \end{aligned} \tag{5.15}$$

The target and calibrator will always be separated by some $\theta_{sep}^2 = \mathbf{a}^2 + \mathbf{b}^2$ s.t $\alpha_C = \alpha_T + \mathbf{a}$ and $\delta_C = \delta_T + \mathbf{b}$. I can substitute these expansions, and as shown in Appendix C.1.3, it then simplifies to:

$$\begin{aligned} c\Delta\tau_\theta =& \big[\big(\sigma_{\alpha,C} - \sigma_{\alpha,T}\big)\cos\delta_T\big(B_x\sin(t-\alpha_T) + B_y\cos(t-\alpha_T)\big) \\ &\quad + \big(\sigma_{\delta,C} - \sigma_{\delta,T}\big)\big(B_x\sin\delta_T\cos(t-\alpha_T) - B_y\sin\delta_T\sin(t-\alpha_T) - B_z\cos\delta_T\big)\big] \\ &+\mathbf{a}\,\big[\sigma_{\alpha,C}\cos\delta_T\,(B_x\cos(t-\alpha_T) - B_y\sin(t-\alpha_T)) \\ &\quad - \sigma_{\delta,C}\sin\delta_T\,(B_x\sin(t-\alpha_T) + B_y\cos(t-\alpha_T))\big] \\ &+\mathbf{b}\,\big[\sigma_{\alpha,C}\sin\delta_T\,(B_x\sin(t-\alpha_T) - B_y\cos(t-\alpha_T)) \\ &\quad + \sigma_{\delta,C}(B_x\cos\delta_T\cos(t-\alpha_T) - B_y\cos\delta_T\sin(t-\alpha_T) - B_z\sin\delta_T)\big] \end{aligned} \tag{5.16}$$

This expression describes a plane, however, there is more nuance in this case than encountered in planes arising from dry tropospheric or baseline uncertainties. Firstly, there is an additional time–variable 'constant' offset term $\tau_0(t_{lst})$ that depends on the difference in positional offsets of the two sources:

$$\begin{aligned} c\tau_0(t_{lst}) =& \big(\sigma_{\alpha,C} - \sigma_{\alpha,T}\big)\cos\delta_T\big(B_x\sin(t-\alpha_T) + B_y\cos(t-\alpha_T)\big) \\ &+ \big(\sigma_{\delta,C} - \sigma_{\delta,T}\big)\big(B_x\sin\delta_T\cos(t-\alpha_T) - B_y\sin\delta_T\sin(t-\alpha_T) - B_z\cos\delta_T\big) \end{aligned} \tag{5.17}$$

This is the astrometric result. Synthesising an image (say of the target) with only this delay applied (subtracted) would give the astrometric offset $\Delta\alpha_T = \sigma_{\alpha,T} - \sigma_{\alpha,C}$ and $\Delta\delta_T = \sigma_{\delta,T} - \sigma_{\delta,C}$. If the target was a maser and the calibrator a quasar, and $\sigma_{\alpha,C}$ and $\sigma_{\delta,C}$ were constant over consecutive epochs (see below for a discussion of this), $\sigma_{\alpha,T}$ and $\sigma_{\delta,T}$ over time give the parallax and proper motion (see Equations 2.72).

The second nuance is that there is not a 'shared plane' for multiple calibrators. In planes arising from residual dry troposphere or baseline offsets, RA or DEC slopes $\mathcal{A}$ and $\mathcal{B}$ can be solved for by using multiple calibrators and sampling the effect at different positions ($\mathbf{a}$, $\mathbf{b}$). In the case of planes arising from positional uncertainties between the target and a calibrator i:

$$c\Delta\tau_\theta = c\tau_0(t_{lst}) + a_i\mathcal{A}_{\theta,i}(t_{lst}) + b_i\mathcal{B}_{\theta,i}(t_{lst}) \tag{5.18}$$

there will be slopes $\mathcal{A}_{\theta,i}$ and $\mathcal{B}_{\theta,i}$, where:

$$\begin{aligned} \mathcal{A}_{\theta,i} &= \sigma_{\alpha,i} \cos\delta_T \,(B_x \cos h_T - B_y \sin h_T\,) - \sigma_{\delta,i} \sin\delta_T \,(B_x \sin h_T + B_y \cos h_T) \\ \mathcal{B}_{\theta,i} &= \sigma_{\alpha,i} \sin\delta_T \,(B_x \sin h_T - B_y \cos h_T\,) + \sigma_{\delta,i}(B_x \cos\delta_T \cos h_T - B_y \cos\delta_T \sin h_T) \\ &\quad - \sigma_{\delta,i} B_z \sin\delta_T\,) \end{aligned} \tag{5.19}$$

in m/rad for each calibrator i, where $h_T = t_{\rm lst} - \alpha_T$ is the hour angle of the target. If the positional uncertainty of all calibrators could be zero, then there are 'no slopes' to measure at the calibrator position, only the negative of target positional offset. This is the desired result in normal phase referencing, however, is very unlikely to be the case.

The uncertainty in inverse MultiView fitting of the delay due to target–calibrator offset from assumed positions $\Delta\tau_\theta$ will be the first order term σ_{O^1} as in the case of normal phase referencing:

$$c\Delta\tau_\theta = c\tau_0(t_{lst}) + c\sigma_{O^1} \tag{5.20}$$

where the uncertainty is the average quadrature sum of source planes:

$$c|\sigma_{O^1}| \leq \frac{1}{N}\sum_{i=1}^{N} |\,(a_i\mathcal{A}_{\theta,i} + b_i\mathcal{B}_{\theta,i})\,| \text{ metres} \tag{5.21}$$

The planes i for $a_i\mathcal{A}_{\theta,i} + b_i\mathcal{B}_{\theta,i}$ depend linearly on calibrator uncertainty, which nominally are $\sigma_{\alpha,i} = \sigma_{\delta,i} = 0.1 - 0.3$ mas if taken from astrometric catalogues, and distance offset from the target in each direction a_i, b_i in rads. In general, the term σ_{O^1} is quite small even for large distances:

$$\begin{aligned} \frac{1}{N}\sum_{i=1}^{N} (a_i\mathcal{A}_{\theta,i} + b_i\mathcal{B}_{\theta,i}) &\leq \frac{1}{N}\sum_{i=1}^{N} \sqrt{a_i^2 + b_i^2}\sqrt{\mathcal{A}_{\theta,i}^2 + \mathcal{B}_{\theta,i}^2} \\ &\leq \frac{1}{N}\sum_{i=1}^{N} \theta_{\text{sep},i}\sqrt{\sigma_{\alpha,i}^2 + \sigma_{\delta,i}^2}\sqrt{B_x^2 + B_y^2 + B_z^2} \\ &\leq \frac{1}{N}\theta_{\text{sep,max}}|\mathbf{B}|\sum_{i=1}^{N}\sigma_{\text{pos},i} \\ &\leq \theta_{\text{sep,max}}|\mathbf{B}|\sigma_{\text{pos,max}} \end{aligned} \tag{5.22}$$

where I have substituted: individual target-calibrator separations $\theta_{\text{sep},i}$, that the plane slopes have maximum values that depend on the max baseline $|\mathbf{B}| = \sqrt{B_x^2 + B_y^2 + B_z^2}$ and the total per–calibrator uncertainty $\sigma_{\text{pos},i} = \sqrt{\sigma_{\alpha,i}^2 + \sigma_{\delta,i}^2}$, and the maximum values $\sigma_{\text{pos,max}}$, $\theta_{\text{sep,max}}$. For $\theta_{\text{sep,max}} = 8$ deg and $\sigma_{\text{pos,max}} = 0.3$ mas, the resultant positional uncertainty using Equation 2.32 would be $\sigma_\theta \leq 42$ μas. This is a potentially overly conservative estimate, as the position offsets of the calibrators are not only unlikely to be uncorrelated, but also unlikely to all be the maximum value.

The sum of N random processes (in this case a Gaussian distribution, with mean 0 and standard deviation σ_{pos}) is:

$$\sum_{i=1}^{N}\sigma_{\text{pos},i} \sim \sqrt{N}\sigma_{\text{pos}} \tag{5.23}$$

Therefore Equation 5.21 more likely equates to:

$$c|\sigma_{O^1}| \lesssim \frac{1}{\sqrt{N}}\theta_{\text{sep,max}}|\mathbf{B}|\sigma_{\text{pos}} \tag{5.24}$$

Now the astrometric positional uncertainty introduced in the target will be:

$$|\sigma_\theta| \lesssim \frac{1}{\sqrt{N}}\sigma_{\text{pos}}\theta_{\text{sep,max}} \tag{5.25}$$

Using the above example values of $\sigma_{\text{pos}} = 0.3$ mas, $\theta_{\text{sep,max}} = 8$ deg $= 0.14$ rads and $N = 4$ calibrators, the positional uncertainty introduced into the target would be $\sigma_\theta \sim 20$ μas. Comparatively, for a 'typical' phase referencing experiment, the calibrators as closer $\theta_{\text{sep,max}} < 2$ deg $=$ 0.035 rads and only one is referenced to at a time s.t the equivalent error would be $\sigma_\theta \sim 10$ μas. So while the positional uncertainty of calibrators cannot be removed via the MultiView plane, the necessity of multiple calibrators to perform that operation serves to reduce the uncertainty by $\sqrt{N}$.

The last point of discussion is target or calibrator evolution as discussed in Section §2.3.7. The measurement of $c\tau_0$ from the plane over the epoch, applied to the target then imaged gives the difference in target source position offset and the mean offset of the calibrators from the phase centre:

$$x_T - \frac{1}{N}\sum_{i=1}^{N} x_i, \qquad y_T - \frac{1}{N}\sum_{i=1}^{N} y_i \tag{5.26}$$

where $x_T,\ y_T$ can be used to measure the proper motion and parallax in Equations 2.72, which I simplify here with:

$$\begin{aligned} x_T &= \varpi_T f(t) + \mu_x t + x_0 \\ y_T &= \varpi_T g(t) + \mu_y t + y_0 \end{aligned} \tag{5.27}$$

where $f(t)$ and $g(t)$ are the relevant functions from Equations 2.72 and $x_0,\ y_0$ are the positions are $t = 0$ and t is in years. I can do the same for the quasars:

$$\begin{aligned} x_i &= \mu_{x,i} t + x_{0,i} \\ y_i &= \mu_{y,i} t + y_{0,i} \end{aligned} \tag{5.28}$$

so Equation 5.26 becomes at epoch t for $x(t)$:

$$x(t) = \left(\varpi_T f(t) + t\left(\mu_x - \frac{1}{N}\sum_{i=1}^{N}\mu_{x,i}\right) + x_0 - \frac{1}{N}\sum_{i=1}^{N} x_{0,i}\right) \pm \sigma_{th} \pm \sigma_\theta \tag{5.29}$$

and the same for $y(t)$ where σ_θ is the positional uncertainty due to post–inverse MultiView fitting (inc. calibrator position uncertainty, baseline uncertainty, wet/dry troposphere and ionosphere) and σ_{th} is the thermal uncertainty.

There is no reason that time-varying quasar source structure leading to an apparent proper motion should be correlated between quasars. Additionally, quasars should not necessarily exhibit proper motion or random movement in the same direction at the same. Therefore I expect a large number of quasars necessary for inverse MultiView to have the effect of 'smoothing out' time-varying quasar structure and position shifts.

5.2.4 Wet Tropospheric and Ionospheric Delays

The only delays from Equation 5.1 that I have not yet discussed are those associated with the wet–tropospheric delay and the ionosphere.

As previously discussed in Section §2.3.9.3, the wet–troposphere is close to a stochastic system and depends on clumpy structures moving across the line–of–sight. This makes it difficult to analytically predict what amount of residual water vapour will be along a line–of–sight ($\mathbf{a}$, $\mathbf{b}$) degrees away from the phase reference position.

From Equations 2.55 and 2.61 I can get the following expressions:

$$\Delta\tau_{\text{iono}} = \sigma_{A,\text{iono}}\Delta t + \frac{\partial\tau_{\text{iono}}}{\partial\theta}\theta_{\text{sep}} + \frac{1}{2}\frac{\partial^2\tau_{\text{iono}}}{\partial\theta^2}\theta_{\text{sep}} + \frac{\partial^2\tau_{\text{iono}}}{\partial\theta\partial t}\theta_{\text{sep}}\Delta t + \frac{1}{2}\frac{\partial^2\tau_{\text{iono}}}{\partial t^2}\Delta t \tag{5.30}$$

$$\Delta\tau_{\text{wet}} = \sigma_{A,\text{wet}}\Delta t + \frac{\partial\tau_{\text{wet}}}{\partial\theta}\theta_{\text{sep}} + \frac{1}{2}\frac{\partial^2\tau_{\text{wet}}}{\partial\theta^2}\theta_{\text{sep}} + \frac{\partial^2\tau_{\text{wet}}}{\partial\theta\partial t}\theta_{\text{sep}}\Delta t + \frac{1}{2}\frac{\partial^2\tau_{\text{wet}}}{\partial t^2}\Delta t \tag{5.31}$$

where I have added the extra second–order spatial (w.r.t $\partial\theta^2$), second–order temporal (w.r.t ∂t^2) and second–order spatial–temporal (w.r.t $\partial\theta\partial t$) terms to the original equations.

The angular separation dependence of the delay can be further split into an East–West/Right Ascension (α) and North–South/Declination (δ) directions via $\theta^2 = \Delta(\alpha\cos\delta)^2 + \Delta\delta^2$:

$$\begin{aligned} \frac{\partial\tau_{\text{wet}}}{\partial\theta}\theta_{\text{sep}} &= \mathbf{a}\mathcal{A}_{\text{wet}} + \mathbf{b}\mathcal{B}_{\text{wet}} \\ \frac{\partial\tau_{\text{iono}}}{\partial\theta}\theta_{\text{sep}} &= \mathbf{a}\mathcal{A}_{\text{iono}} + \mathbf{b}\mathcal{B}_{\text{iono}} \end{aligned} \tag{5.32}$$

where $\mathbf{a} = \Delta(\alpha\cos\delta)$ and $\mathbf{b} = \Delta\delta$.

The magnitude of spatial and temporal variations of the wet–troposphere away from the phase referencing position is difficult to determine. It has already been shown that the non-dynamic ionospheric structure is very described by planar structure (Rioja et al., 2018, Figure 5), therefore is it a grounded assumption that much of the residual ionosphere (after TEC GPS correction; see Section §2.3.9.1) is also well–described by a 2D plane in RA and DEC. However, the magnitude of temporal and spatial-temporal variations (aka the additional terms in the expansion) are instantaneously unknown with the inverse MultiView method and will serve to introduce a phase error. I will discuss this topic further in Section 6.5.3.2.

5.2.5 Total delay/phase solution

I have derived delay–plane solutions for the known potential causes for an angular delay difference. Each of these (apart from source position error) was derived for a particular antenna at a fixed location and is expected to change based on the hour angle $h = t_{lst} - \alpha$. However, in reality, a delay can only be measured relative to another telescope and is a baseline quantity. Each antenna will have an individual set of time-variable slopes $\mathcal{A}, \mathcal{B}$ which depend on $\alpha, \delta, t_{lst}, \varphi$ and the various potentially time-dependent/variable (e.g. $\delta\tau_z, \delta\tau_I, \dots$), or time-independent/stable (e.g. $\Delta B_x, \Delta\alpha, \dots$) sources of delay. The measured delay difference between the target (observed at time t_{j+1}) and calibrator (observed at time t_j), will be the delay difference above antenna i

minus the delay difference above the reference antenna r:

$$\begin{aligned}(\tau_T(t_{i+1})_j - \tau_T(t_{i+1})_k) - (\tau_C(t_i)_j - \tau_C(t_i)_k) &= \tau_0(t_{gst}) + \tau_{th} \\ &+ \mathbf{a}\,[\,\mathcal{A}_{bl,j} - \mathcal{A}_{bl,k} + \mathcal{A}_{dt,j} - \mathcal{A}_{dt,k}\ldots)]\,(t_{gst}) \\ &+ \mathbf{b}\,[\,\mathcal{B}_{bl,j} - \mathcal{B}_{bl,k} + \ldots]\,(t_{gst}) \\ &= \tau_0(t_{gst}) + \mathbf{a}\,\mathcal{A}_{\text{total}}\,(t_{gst}) + \mathbf{b}\,\mathcal{B}_{\text{total}}\,(t_{gst})\end{aligned} \tag{5.33}$$

where $t_{gst} = t_{lst} - \psi_j$ is Greenwich sidereal time and ψ_j is the antenna East–Longitude in hours for antenna j.

Thus far I have limited discussion to the idea of slopes in delay. However, if maximum the delay difference between target and calibrator are kept within a observing wavelength ($c\tau \ll \lambda$), then phase is an effective tool to sample the changes more precisely. Recall:

$$\begin{aligned}\phi &= 2\pi\nu\tau \\ \therefore \frac{\partial\phi}{\partial\tau} &= 2\pi\nu\end{aligned} \tag{5.34}$$

which shows that phase is $2\pi\nu$ times more sensitive to changes in delay than the delay itself, with the caveat that phase is subject to 2π measurement ambiguities. As phase referencing is the standard procedure, a phase–plane will be the assumed model and phases are expected to be $-\pi < \phi < \pi$.

Combining Equation 5.33 and $\phi = 2\pi\tau\nu$ gives the slopes in phase:

$$\Delta\phi = \phi_T(t_{i+1})_{jk} - \phi_C(t_i)_{jk} = \phi_0(t_{gst}) + 2\pi\nu\ \mathbf{a}\,\mathcal{A}_{\text{total}}\,(t_{gst}) + 2\pi\nu\ \mathbf{b}\,\mathcal{B}_{\text{total}}\,(t_{gst}) \tag{5.35}$$

where the left–hand side is the measured phase on the target after phase referencing from the calibrator on baseline jk, and the right–hand side describes the total phase–plane, with the ϕ_0 term containing the information about target–calibrator differential offset from the phase centre.

5.2.6 Phase Wrap Ambiguities

While the phase plane can be described mathematically outwards from the phase reference location, the only relevant locations are where quasars exist and the phase plane can be sampled. If at any point in time, the difference between two sampled points on the plane exceeds 2π radians, a phase wrap ambiguity (PWA) is said to occur. In a PWA, a phase of $\phi = 10$ deg is equivocal and could 'really' be a phase of -350 deg or 360 deg (assuming only one wrap).

While it is possible to correct for PWA in the fitting process (by searching and iteratively fitting 2π offsets Rioja et al., 2017), the simplest method to resolve possible PWAs is to sufficiently calibrate the data such that they are unlikely to arise. Either way, it is beneficial to know the conditions when they could arise such that they can be identified and/or avoided.

Taking Equation 5.35 to avoid a PWA the residual phase (after phase referencing) at two calibrator positions must not exceed 2π:

$$2\pi\nu\,(\mathbf{a}_1\,\mathcal{A}_{\text{total},1} + \mathbf{b}_1\,\mathcal{B}_{\text{total},1} - \mathbf{a}_2\,\mathcal{A}_{\text{total},2} - \mathbf{b}_2\,\mathcal{B}_{\text{total},2}) < 2\pi \tag{5.36}$$

where $\mathbf{a}_1$, $\mathbf{b}_2$, $\ldots$ indicate the positions of the two calibrators offset from the phase reference position in rads and $A_{\text{total},1}$, $B_{\text{total},2}$, ... indicate the slopes 'experienced' by each calibrator in s/rad at some arbitrary time.

First, I assume the calibrators are equidistant from the phase reference position and 'opposite' each other s.t they will be shifted in phase w.r.t each other the largest amount for a given slope $\mathbf{a}_2 = -\mathbf{a}_1$, $\mathbf{b}_2 = -\mathbf{b}_1$. Additionally, the total slopes at each calibrator for a given time will only be differentiated by the unique 'positional offset slopes' (Equation 5.19):

$$\begin{aligned} A_{\text{shared}} &= A_{\text{total},2} - A_{\theta,2} = A_{\text{total},1} - A_{\theta,1} \\ B_{\text{shared}} &= B_{\text{total},2} - B_{\theta,2} = B_{\text{total},1} - B_{\theta,1} \end{aligned} \tag{5.37}$$

This gives:

$$2\pi\nu \left(2\mathbf{a}_1\ A_{\text{shared}} + 2\mathbf{b}_1\ B_{\text{shared}} - \mathbf{a}_1(\mathcal{A}_{\theta,1} + \mathcal{A}_{\theta,2}) - \mathbf{b}_1(\mathcal{B}_{\theta,1} + \mathcal{B}_{\theta,2})\right) < 2\pi \tag{5.38}$$

In many cases below I will be substituting $\mathbf{a}$ and $\mathbf{b}$ with θ_{sep} as a characteristic distance in the distribution of calibrators in the inverse MultiView setup.

5.2.6.1 Calibrator Position Error

The slopes $A_{\theta,1}$ etc. will be independent and the conditions required for just one of them to contribute to a PWA can be described by (from Equation 5.22):

$$2\pi\nu|\mathbf{a}\ A_\theta| \sim 2\pi\nu\sigma_{\text{pos}}\frac{|\mathbf{B}|}{c}\theta_{\text{sep}} = \pi \tag{5.39}$$

which would require the positional uncertainty of the calibrator to be $\sigma_{\text{pos}} = 7$ mas if $|\mathbf{B}| = 3000$ km, $\nu = 8.2$ GHz and $\theta_{\text{sep}} = 10$ deg (converted to rad). Therefore it is unlikely that calibrator positional uncertainties, even after phase referencing from a faraway target would significantly contribute to PWAs.

The shared planes A_{shared} and B_{shared} are the sum of residual dry/wet tropospheric, residual ionospheric, baseline offset planes derived in the previous sections. They will individually have maximum values that depend on the corresponding residual delays and/or spatial distribution, and I will now look at the conditions required for them to individually cause a PWA.

5.2.6.2 Baseline Error

From Equation 5.5, the phase difference between two oppositely positioned calibrators resulting from a baseline offset plane will be:

$$2\pi\nu\frac{\sigma_{bl}}{c}2\theta_{\text{sep}} < 2\pi \tag{5.40}$$

which requires $\sigma_{bl} = 10$ cm at $\nu = 8.2$ GHz and $\theta_{\text{sep}} = 10$ deg. Again, this is very unlikely to be the case as VLBI array baselines are known to $\sigma_{bl} < 3$ cm except in the cases for new antennas (Petrov et al., 2009b). The additional factor of 2 is from the calibrators being oppositely positioned around the target.

5.2.6.3 Zenith Dry Tropospheric Path Length

Equation 5.13 describes the maximum delay encountered due to the residual dry troposphere after phase referencing as a function of angular offset from phase referencing position and zenith angle. The resulting maximum phase difference on the plane resulting from this residual delay on baseline jk will be:

$$\phi_{jk} = 2\pi\nu \left(\sigma_{\tau_z,j} \sec^2 Z_{T,j} \sin Z_{T,j} - \sigma_{\tau_z,k} \sec^2 Z_{T,k} \sin Z_{T,k}\right) 2\theta_{\rm sep} \tag{5.41}$$

where σ_{τ_z} and Z_T are the respective residual zenith delay errors and target zenith angles for either antenna j or k. Again, the factor of $2\theta_{\rm sep}$ results from the plane being sampled at opposite but equal offsets from the target.

The limiting case will be whichever antenna has the larger zenith angle (for example antenna j)

$$2\pi\nu\sigma_{\tau_z,j} \sec^2 Z_{T,j} \sin Z_{T,j} 2\theta_{\rm sep} < 2\pi \tag{5.42}$$

which with $\nu = 8.2$ GHz and $\theta_{\rm sep} = 10$ deg requires $c\sigma_{\tau_z,j} = 3, 7, 15$ cm for zenith angles $Z_{T,j} = 60, 45, 30$ deg respectively. Geoblock calibration should be leave residual zenith tropospheric delays on of 1 cm (Reid & Honma, 2014), however, corruption from residual ionosphere after TEC map application could lead to systematic errors of ~ 4 cm (see Sectio §2.3.9.1).

A separation of $\theta_{\rm sep} = 8$ deg gives $c\sigma_{\tau_z,j} = 3.5, 9, 20$ cm and a separation of $\theta_{\rm sep} = 4$ deg gives $c\sigma_{\tau_z,j} = 7.5, 18, 40$ cm for zenith angles $Z_{T,j} = 60, 45, 30$ deg respectively. This indicates that PWAs should only occur at $Z_T \gtrsim 60$ deg in general considering that Equation 5.42 is an extreme case of an upper bound. Therefore it is possible that residual tropospheric delay errors on the level of $\sigma_{\tau_z} = 4$ cm may lead to PWA only at low elevations and in the presence of poorly constrained zenith tropospheric delays.

5.2.6.4 Wet Troposphere

I have not been able to determine expressions that analytically describe the residual ionosphere or wet troposphere. The wet troposphere has fluctuations of $c\tau_{\rm wet} = 1$ cm (Thompson et al., 2017), and therefore in the worst-case scenario two oppositely placed calibrators about might have a total path length difference due to the wet troposphere of $\Delta\tau_{\rm wet} = 2$ cm. At $\nu = 8.2$ GHz this would not be enough to cause a PWA ($\Delta\phi = 2\pi\Delta\tau_{\rm wet}\nu \sim 0.55 \times 2\pi$), however at 22 GHz it would be enough ($\Delta\phi = 1.5 \times 2\pi$). Such a large phase difference would also likely indicate that the wet troposphere is uncorrelated/out of phase in time between two calibrators. Therefore at $\nu = 8.2$ GHz, I do not expect PWA due to the wet troposphere given coherent phase solutions.

5.2.6.5 Ionosphere

Figure 5.3 shows the JPL TEC map 2018–09–24 at 04:00:00 UTC over Australia. the maximum North–South slope in the JPL TEC maps $|\frac{\partial I_e}{\partial\theta_{\rm lat}}| = 2$ TECU/deg (over whole map). At $\nu = 8.2$ GHz, this equates to a delay slope of $c\frac{\partial\tau_{\rm iono}}{\partial\theta} = 1.2$ cm/deg.

Taking the first order term from Equation 2.59, multiplying the separation $\theta_{\rm sep}$ by 2 and converting to phase gives the condition that:

$$2\pi \frac{1.34 \times 10^9}{\nu} \frac{\partial I_e}{\partial \theta} 2\theta_{\text{sep}} < 2\pi \tag{5.43}$$

which would limit the separation at $\nu = 8.2$ GHz to only $\theta_{\text{sep}} = 1.5$ deg before a PWA would occur. However, for most of the Earth and most of the day $|\frac{\partial I_e}{\partial \theta}| \leq 0.5$ TECU/deg, giving $\theta_{\text{sep}} \geq 6$ deg at $\nu = 8.2$ GHz.

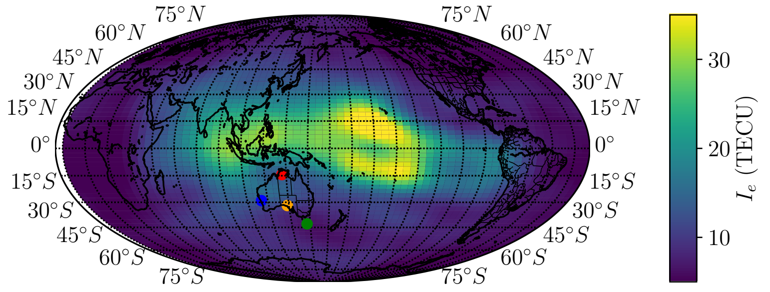

(a) Total TEC map over Australia. Colourmap has units TECU.

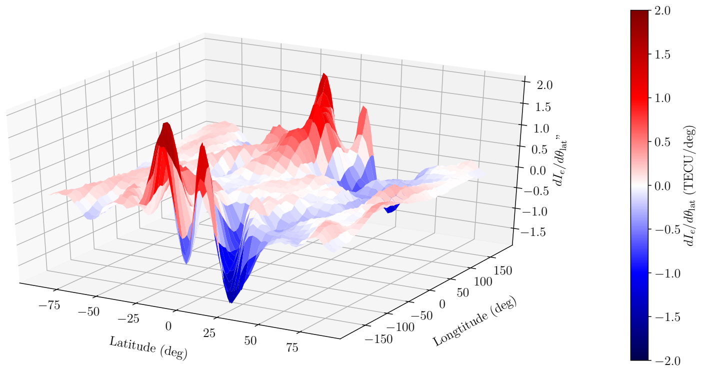

(b) TEC map slope in latitude direction over whole Earth. Colourmap is slope in latitude direction with units TECU/deg.

Figure 5.3: JPL Total Electron Content (TEC) map 2018-09-24 04:00:00 UTC over Australia. Coloured points are ASCI array telescope positions: Ceduna (orange), Hobart (green), Katherine (red) and Yarragadee (blue). Map available from ftp://gdc.cddis.eosdis.nasa.gov/gnss/products/ionex/2018/267/jplg2670.18i.Z.

The above estimates are calculated *before* application of the TEC maps, which have been shown to improve phase results (Walker & Chatterjee, 1999). Therefore the residual TEC in the data will be smaller than the maps and slopes in the residual TEC *should* also be smaller, however, the residual slopes remain difficult to quantify.

5.2.6.6 Recognising Phase Wraps and Summary

Assuming that a phase slope has been measured via fitting the phases (see Section §5.3), the magnitude of the measured slope can be used to determine whether a PWA has occurred. The fitting process will measure ϕ_0, $A_{\rm total}$, $B_{\rm total}$ at each time–step and if for any calibrator i:

$$\begin{aligned} A_{\rm total}\ a_i &> 180 \text{ deg} \\ B_{\rm total}\ b_i &> 180 \text{ deg} \end{aligned} \tag{5.44}$$

it is possible a PWA has occurred, where a_i and b_i are East–West and North–South offsets from the target position in deg and the slopes are in deg/deg. This requires $A_{\rm total}, B_{\rm total} > 45, 30, 22.5$ deg/deg for $a_i, b_i = 4, 6, 8$ deg respectively. Therefore consistent slope results of this magnitude should be considered suspect.

In summary, phase wrap ambiguities should not occur due to baseline offsets, calibrator position offsets, wet troposphere at $\nu = 8.2$ GHz, or if the measured slopes are less than 20 deg/deg. However, phase wrap ambiguities *may* occur due to the error in the dry tropospheric zenith delay at low elevations and/or for large separations. I am not able to confidently say whether PWAs will occur due to the residual ionosphere after TEC map calibration, however, I hypothesise that they will not in the majority of situations as they are only rarely able to occur due to the *uncalibrated* ionosphere for separations $\theta_{\rm sep} > 6$ deg.

5.3 Observing Method and Phase–Fitting

In the previous sections I showed that after phase referencing, any and all residual delay can be treated as a 2D phase plane in RA and DEC offset from the phase reference position. Taking Equation 5.35, I recognise that $\mathbf{a} = \alpha\cos\delta - \alpha_T\cos\delta_T$ and $\mathbf{b} = \delta - \delta_T$ and simply combine $2\pi\nu\mathcal{A}_{\rm total}(t_{lst}) = \mathbf{A}(t)$ etc., so that I get the simple equation (per baseline):

$$\phi\left(\alpha,\delta,t\right) = \boldsymbol{\phi}_0\left(t\right) + \mathbf{A}\left(t\right)\left(\alpha\cos\delta - \alpha_T\cos\delta_T\right) + \mathbf{B}\left(t\right)\left(\delta - \delta_T\right) \tag{5.45}$$

where $\mathbf{A}$ and $\mathbf{B}$ are the (somewhat arbitrary) phase–gradients in α and δ directions respectively in rad/rad or deg/deg, ϕ_0 is the residual phase on the target and ϕ is the phase at some point in space away from the target (presumable at the location of a calibrator). The units for this plane depend on the units of phase and angular separation that are used, but I will be mostly using phase in degrees and angular offset in degrees s.t that gradients have units deg/deg. The assumption is that $\mathbf{A}$ and $\mathbf{B}$ are time variable based off the analytic derivations in the previous sections and the unknown but likely spatially–dynamic residual wet–troposphere/ionosphere.

The method to immediately get a solution would be to be able to simultaneously observe the target and multiple calibrators (similar to the VERA telescope dual–beam system; Honma et al., 2007)), however, simultaneous observations of target and calibrators are unavailable. Therefore we will have to tactically approximate simultaneity. In maser astrometry, we are lucky to have an obvious solution that I have previously hinted at: I will use the maser (the target) as the reference and observe all the calibrators in the (wet–tropospheric) coherence time of the maser about ~ 5 mins. Therefore observational structure will be T–C1–T–C2–T–C3–T where T is the target and Ci are the calibrators.

As the calibrator sources are not observed simultaneously, there cannot be an exact solution for the entire plane for each time-stamp as the plane may very well tilt in that time it takes to slew to the next calibrator. To get a solution of the plane using all the calibrators, I will consider a moving solution for each cluster of sources. Say if there are n calibrators in the ring (henceforth orbit sources) then the measured phase for each loop (and each baseline) will be:

$$\mathbf{\Phi}\left(\overline{t_i}\right) = \begin{bmatrix} \phi_1(t_{i,1}) \\ \phi_2(t_{i,2}) \\ \phi_3(t_{i,3}) \\ \vdots \\ \phi_{n-1}(t_{i,n-1}) \\ \phi_n(t_{i,n}) \end{bmatrix}$$

Where $t_{ij} = t_{i,j-1}{+}2\left(t_{\text{dwell}} + t_{\text{slew}}\right)$. Practically, this implies that the time-stamp for the solution is $\overline{t} = t_{i,\frac{n}{2}}$. Despite the fact that each loop around the ring will take $t = 2n\left(t_{\text{dwell}} + t_{\text{slew}}\right)$ and I practically want to use all n points to solve for the plane at a given time, I can sample the time more regularly than every loop. If I take the next phase solution from the same quasar in the following loop, I can set finer time sampling of $\delta t \approx 2\left(t_{\text{dwell}} + t_{\text{slew}}\right)$. Then the next phase vector is:

$$\mathbf{\Phi}\left(\overline{t}_{i+1}\right) = \begin{bmatrix} \phi_2(t_{i+1,2}) \\ \phi_3(t_{i+1,3}) \\ \phi_4(t_{i+1,4}) \\ \vdots \\ \phi_n(t_{i+1,n}) \\ \phi_1(t_{i+1,1}) \end{bmatrix}$$

At each time step i, the problem and solutions are:

$$\mathbf{\Phi}\left(\overline{t_i}\right) = \left[\phi_{i,j}\right] = \begin{bmatrix} 1 & \alpha_1 \cos\delta_1 - \alpha_T \cos\delta_T & \delta_1 - \delta_T \\ 1 & \alpha_2 \cos\delta_2 - \alpha_T \cos\delta_T & \delta_2 - \delta_T \\ & \vdots & \\ 1 & \alpha_j \cos\delta_j - \alpha_T \cos\delta_T & \delta_j - \delta_T \end{bmatrix} \begin{bmatrix} \boldsymbol{\phi_0}_i \\ \mathbf{A}_i \\ \mathbf{B}_i \end{bmatrix} = \mathbb{M}\boldsymbol{\lambda}_i$$

$$\therefore \boldsymbol{\lambda}_i = (\mathbb{M}^T\mathbb{M})^{-1}\mathbb{M}^T\,\mathbf{\Phi}_i \tag{5.46}$$

This solution weights all points equally, which makes sense if all data is equally certain. However ‘weaker’ calibrators will have a less certain phase solution and that measurement error has to be taken into account. If a calibrator is measured to have a phase of ϕ with a signal–to–noise of SNR; then I consider the uncertainty in that measurement to be:

$$\sigma_\phi = \frac{1}{\text{SNR}} \tag{5.47}$$

in radians. Finally I assume that the weights will take the form

$$\begin{aligned} w_i &= \frac{1}{\sigma^2} \\ \sigma^2 &= \sigma_s^2 + \left(\frac{180}{\pi\,\text{SNR}}\right)^2 \end{aligned} \tag{5.48}$$

where I have assumed a static error floor of $\sigma_s \sim 10\,\text{deg}$. This ensures that extremely luminous quasars do not dominate the solution while sufficiently weak quasars are rightfully down–weighted. Therefore, I have the diagonal weight matrix:

$$\mathbb{W} = \begin{bmatrix} w_1 & 0 & 0 & \dots & 0 \\ 0 & w_2 & 0 & \dots & 0 \\ 0 & 0 & w_3 & \dots & 0 \\ \vdots & \vdots & & \ddots & \vdots \\ 0 & 0 & \dots & \dots & w_n \end{bmatrix}$$

which is incorporated into the equation at each time step as:

$$\begin{aligned} \mathbb{W}\boldsymbol{\Phi}_i &= \mathbb{W}\mathbb{M}\boldsymbol{\lambda}_i \\ \therefore \boldsymbol{\lambda}_i &= (\mathbb{M}^T\mathbb{W}\mathbb{M})^{-1}\mathbb{M}^T\mathbb{M}\boldsymbol{\Phi}_i \end{aligned} \tag{5.49}$$

Hence, I can calculate a solution $\boldsymbol{\lambda}\left(\bar{\boldsymbol{t}}\right)$ for each baseline, which I can use to return positional information to the target source while correcting for the presence of phase slopes between the orbit sources and target due to residual phase errors.

5.4 Summary

In this chapter I derived analytical expressions that describe the time dependence and maximum values of delay slopes due to baseline offsets, unconstrained dry tropospheric zenith delays and calibrator source positional uncertainties. These slopes are expected to be present in calibrator data after phase referencing from the target. Unfortunately, exact analytical expressions were not able to be determined for the wet troposphere and residual ionosphere due to their stochastic nature.

Irrespective of the exact form those delay slopes take at a given time, simultaneous observations of multiple calibrators would be able to measure the shift in delay over angular distance and therefore be able to infer the total delay slopes. However, the true advantage for astrometry would be being able to measure the calibrator phase, which is $2\pi\nu$ times more sensitive to positional offsets. This would allow microarcsecond astrometry to be undertaken at a far larger distance than conventionally available.

The primary caveat to using phases to fit the 2D planes is the presence of phase wrap ambiguities that do not exist in delay data. I calculate that it is unlikely to encounter phase wrap ambiguities at 8.2 GHz except in the most extreme cases of large separations or poor calibration/models. Additionally, I show a simple method to determine whether a PWA has occurred in the fitted data by using the magnitude of the directional phase slopes.

To this end, have outlined a possible way to perform inverse phase referencing and MultiView at the same time (inverse MultiView) for equipment that does not have simultaneous target–calibrator observing capabilities. The main deterrent for using this procedure is that the angular separation between the target and calibrators where the phases remain coherent due to the spatially dynamic wet–troposphere and ionosphere are largely unknown. This is what I aim to determine in the next chapter.

6

MultiView–Ring Calibration

The lack of well–characterised VLBI calibrators in the Southern Hemisphere limits the number of targets available within a given radius of a target. This is especially detrimental when conducting astrometry within the Galactic Plane where there is additional obscuration and many radio continuum surveys stop as they approach the plane (usually $|b| \leq 5$ deg). For traditional phase referencing, this means observations have to rely on 'distant' and/or poor quality quasars, or luck. The only alternative to these three is not to conduct observations at all. This is extremely unfortunate as the vast majority of the central Galaxy is visible from the Southern Hemisphere.

The standard approach for phase referencing observations is to seek calibrators as close as possible to the target to minimise the differential effects of uncompensated delays. However, as I have shown in the previous chapter, phase referencing using more distant quasars should be possible if the differential delay effects can be measured and hence corrected.

In this chapter, I present results of the first demonstration of inverse MultiView, the first phase referencing observations utilising the ASCI Array and the first microarcsecond astrometric result in the Southern Hemisphere. I provide an overview of the processes I undertook to achieve this, including scheduling, observing, correlating, reduction and analysis. I then discuss results, uncertainty limitations of the technique and recommendations for future observations.

6.1 Introduction

The primary cause of residual delay at mid–frequencies ($\sim 4-8$ GHz) is generally attributed to a combination of the uncalibrated static ionospheric and dynamic wet–troposphere (Thompson et al., 2017; Reid & Honma, 2014) in normal phase referencing (see Sections §2.3.9). In inverse MultiView calibration, the same two sources of delay have somewhat unknown static and dynamic properties at angular separations away from the phase reference location, which may limit the inverse MultiView technique. From the previous chapter, the primary theoretical benefit to inverse MultiView over inverse phase referencing is that the residual delays can be calibrated more accurately, however, an important secondary benefit is that the target–calibrator separation can be increased without significant detriment to said accuracy. This second point is especially important in situations where calibrators are sparsely distributed around targets.

SπRALS aims to achieve high accuracy astrometry for 6.7 GHz masers on the ASCI array (Section 1.4.3), however, it will likely encounter the same large residual delays as Krishnan et al. (2015, 2017) on the LBA. Authors of those papers suspect the main cause of residual delay was the ionosphere and uncalibrated dry troposphere. As I have shown in Chapter 5 inverse MultiView should be able to calibrate spatially coherent residual delays. Therefore I want to collect and analyse real data to test these predictions.

In this chapter I develop the methodology and reduction processes for inverse MultiView, allowing for high accuracy astrometry at intermediate frequencies in the presence of suspected residual delays. The questions that I address are:

1. What is the astrometric accuracy of MultiView vs. what would be expected from inverse phase referencing at a similar target–calibrator separation. Does it perform better? As I will show, inverse MultiView increases calibration overheads and is non-trivial to observe or reduce. Does it return a proportionally better result? I address this question in Section §6.5.1;

2. What is the maximum separation between target and calibrators for which inverse MultiView can measure coherent solutions and what is the cause of this decoherence? There are generally fewer suitable (compact, high flux density) calibrators in the immediate neighbourhood of Galactic masers so the larger separation for which high accuracy astrometry can be undertaken, the better. Rioja et al. (2017) use a maximum separation between calibrators of $\theta \sim 10$ deg at low frequencies for non–inverse MultiView, where the ionosphere is expected to be the largest source of error. At higher frequencies ($> 6-8$ GHz) the troposphere is expected to be dominant, however, the residual effects of both can be equivalent in magnitude. So after including dry tropospheric calibration techniques (geoblocks) and GPS TEC maps, is MultiView at intermediate frequencies limited by ionosphere, dry/wet troposphere or some other factor? I address this question in Section §6.5.1.

3. Is it possible to use measured phase slopes to determine residual delays? The derived equations in the previous chapter provide clear relationships between instantaneous sources of residual delay, LST and/or UTC, longitude, latitude, RA and DEC. It is possible to decouple the relationships and approximate residual path delay and therefore estimate the calibration fidelity. The phase–slopes derived in the previous chapter are sensitive to residual delay and therefore could be used as a probe for delay calibration fidelity. I discuss the nature of phase slopes and feasibility of delay determination in Section §6.5.2.

4. How should MultiView be conducted in the future? Is there an optimal number of calibrators, what calibrator parameters should be optimised and what spacing/positioning might give the best results? I address this question in Section §6.5.3.

These experiments provide the opportunity to not only develop and test these techniques but to do so on the VLBI array that will be used for SπRALS . Therefore these observations additionally serve as a pilot in terms of array capabilities and technique.

6.2 Source Selection

The ultimate aim of this chapter is to test the ability of inverse MultiView to measure and remove the residual delay for maser astrometry in SπRALS , so the observing structure is nearly identical to that of a maser phase–referencing observation (see Section §6.3.2). The ASCI array does not currently have mutual frequency coverage over the rest frequencies of any known and/or appropriately bright maser species, so I have used quasars as both the calibrators and targets for these MultiView tests. Although this does not allow me to test MultiView under identical conditions as a parallax observation, it does present other advantages. In the next few sections, I will discuss these advantages and quasar selection criteria.

6.2.1 Quasar benefits and Quality Q

The primary benefit of using quasars as targets is that their positions are expected to be constant with time at the level of 10-20μas/yr (Reid & Honma, 2014). In addition, they can have, or be specifically chosen such that they have little to no structure and due to frequent observations by global VLBI arrays, often have known positional and flux density values. The lack of detectable proper motion and parallax implies any measured offsets that change over time are due to residual delay or phase–noise, which can be directly used for an estimate of calibration quality. This fact will be used to compare traditional phase referencing methods to inverse MultiView and determine the overall capability of the array.

Although many quasars can appear point-like, others can have jets that may offset the astrometric results. Care is taken to avoid resolved quasars or those with jets as they can make phase referencing solutions confusing or add positional uncertainty. Frequent VLBI observations of a subset of quasars place good constraints on their absolute positions. Henceforth I will refer to the positional uncertainty of a quasar as its quality Q in mas. Generally speaking, the smaller Q is, the more desirable that quasar is for astrometry

Another advantageous characteristic of quasars is that they are very common compared to masers (referring to individual maser regions per species). The 2019a Radio Fundamental Catalogue contains 15740 objects*, which gives an average sky density of $\sim 0.38\,\text{deg}^{-2}$ or roughly 1.2 quasars per circle of radius 1 deg. In contrast, the catalogue of all known 6.7 GHz methanol masers (Yang et al., 2019, and referenced therin) contains 1085 masers largely confined to the Galactic Plane $|b| < 5°$ and only observable between $7 - 17$ LST for the Southern Hemisphere. This difference not only allows for a larger pool to select from and a greater time window to observe but allows one to have strict selection criteria.

*http://astrogeo.org/rfc/

While the total quasar sky–density remains 0.38 $\deg^{-2}$ at intermediate–to–high Declinations, at low Declinations ($\delta < -30°$) the total density drops to $\sim 0.19 \deg^{-2}$ (Figure 6.1). This discrepancy is unlikely due to a lack of quasars, which are isotropically distributed but represents a relatively lower amount of regular and high–sensitive quasar surveys in the Southern Hemisphere. In addition, due to the relative lack of frequent observations, the number of quasars known in the Southern Hemisphere is proportionally biased towards 'low–quality' quasars (Figure 6.1). In

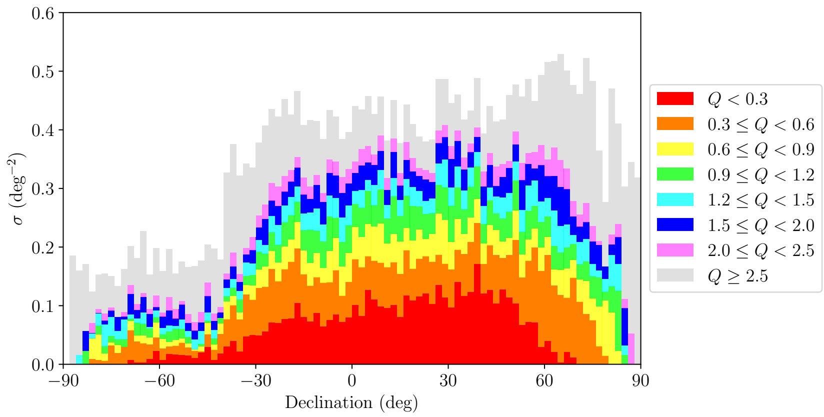

Figure 6.1: Stacked Declination–binned quasar density distribution. Colour represents relative contribution of each quasar-Q (legend) to the Declination–binned quasar density. Units of Q are mas. Data from rfc2019a.

catalogues, quasars are presented with estimated positional accuracies. As I want to focus on the atmospheric aspects of MultiView calibration, I chose only quasars with $Q < 0.3$ mas. Finally, to limit the effects of target elevation, sources are only selected from the South celestial region $\delta < 0$. Next, I need to consider quasars from the perspective of array sensitivity.

6.2.2 Sensitivity Limitations

I want to use the nominal SEFDs of the telescopes to determine the detection limit. Taking the Cd–Ke baseline and nominal SEFD = 800 Jy and SEFD = 3500 Jy for Ceduna and Katherine respectively, a $\tau = 40$ s integration with a spanned-bandwidth of $\Delta\nu = 256$ MHz will yield a noise level σ_S of:

$$\begin{aligned} \sigma_S &= 1.2\sqrt{\frac{\text{SEFD}_i\ \text{SEFD}_j}{2\tau\Delta\nu}} = 1.2\sqrt{\frac{800 \times 3500}{2 \times 40 \times 256 \times 10^6}} \\ &= 11\,\text{mJy} \end{aligned} \tag{6.1}$$

Therefore, for a strong, per-scan detection of SNR $= \frac{S_c}{\sigma_N} > 10$, I require quasars with a correlated flux density $S_c > 110$ mJy. Constraining S_c, $\delta < 0.0$ deg and $Q < 0.3$ mas I find there are a total of 824 available quasars. From this list of good quasars, I desire the ones which have a sky distribution favourable for testing inverse MultiView.

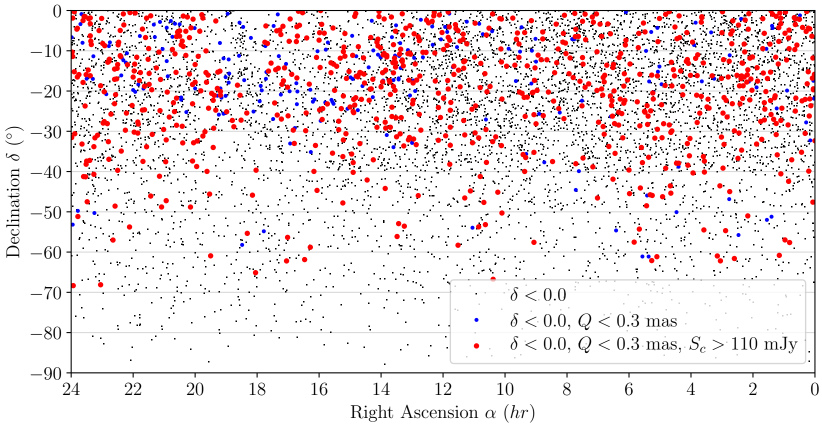

Figure 6.2: Sky positions of all $\delta < 0.0^\circ$ quasars. **Black:** Non–suitable quasars due to positional uncertainty $Q > 0.3$ mas. **Blue:** Non–suitable quasars on the basis of catalogued correlated flux $S_c < 110$ mJy. **Red:** All suitable quasars.

6.2.3 Quasar Arrangement

The final determination is to choose which clusters of quasars I want to select as the targets and calibrators from this list of 824 quasars. The expectation is that for a clumpy and non–uniform residual ionosphere, there should be a maximum distance beyond which phase decoherence occurs. To test this theory, I use the idea of a calibration ring with an approximate radius around a target quasar to compare the astrometric accuracy for each ring radii.

A search was conducted for quasars that had $N \geq 6$ surrounding quasars within the sample, confined to ring radii or range 2–4, 4–5, 5–6, 6–7 and 7–8 degrees. The number of quasars in the ring was chosen for redundancy and to minimise the contribution from directionality. Quasar clusters were selected from the sample that had a good position angle ($\theta_i = \arctan(\Delta\delta, \Delta\alpha)$) sampling about the target such that the root sum of squares (RSS) of the angle was:

$$\mathrm{RSS} = \frac{\sqrt{\sum \theta_i^2}}{2\pi} \leq 1.2 \tag{6.2}$$

As a side note, there is no practical need for a lower bound as it would be extremely unusual for multiple ($N > 3$) quasars to be stacked together at the same distance and small positional angle.

In total this gave a list of 29 potential rings. Visual inspection of the rings was performed to cut down the list of candidates to 9. Three at around $\alpha = 7$ hrs, $\alpha = 14$ hrs and $\alpha = 20$ hrs. The three rings would share a 7 hour track over a ~ 24 hour experiment, sampling the different radii and effects due to Local Time.

Largely for historical and internal reasons, sources names are indicated via the following rules: Source names starting with G indicates a target at the centre of a ring, J indicates a calibrator (orbit source) within the ring and F a fringe finder. In all cases, the name of the sources is based on the J2000 right ascension and declination.

Pathfinder observations MV022 and MV025 revealed that some of these rings contained poorly constrained calibrator and target positions and/or lower flux density sources than expected from the catalogued values. Therefore the final list of rings was cut down to the best 3 at differing LST and radii in experiments MV026, 27 and 28. These rings were centred at the quasar positions of: G0634–2335 with a mean radius of $\overline{R} = 3$ deg; G1901–0809 with $\overline{R} = 6.5$ deg and; G1336–0829 with $\overline{R} = 7.5$ deg (see Figures 6.3, 6.4 and 6.5, respectively). Considering the isoplatonic radius for the wet–troposphere is considered to be smaller than $R = 7-9$ deg, this was expected to give a good idea of the limitations of inverse MultiView calibration before and after this transitional point.

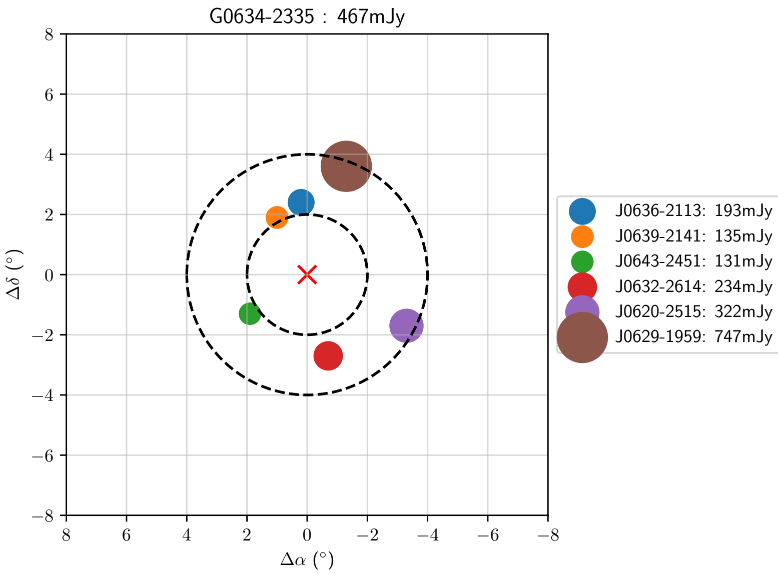

Figure 6.3: Ring plot for target quasar G0634–2335. This ring is between 2° and 4° as smaller rings with sufficient quasars that fit the criteria did not exist. The catalogued correlated flux density for G0634–2335 is 467 mJy.

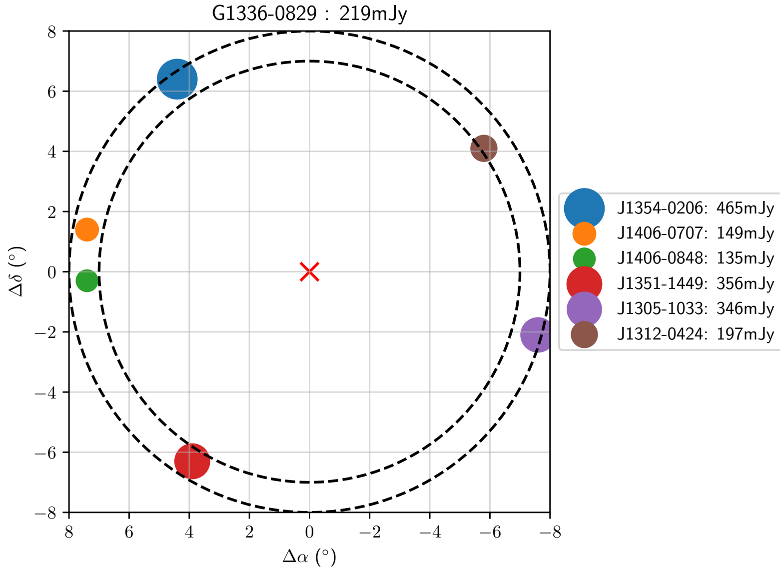

Figure 6.4: Ring plot for target quasar G1336–0829. This ring is between 7° and 8° and the central quasar has flux density 219 mJy.

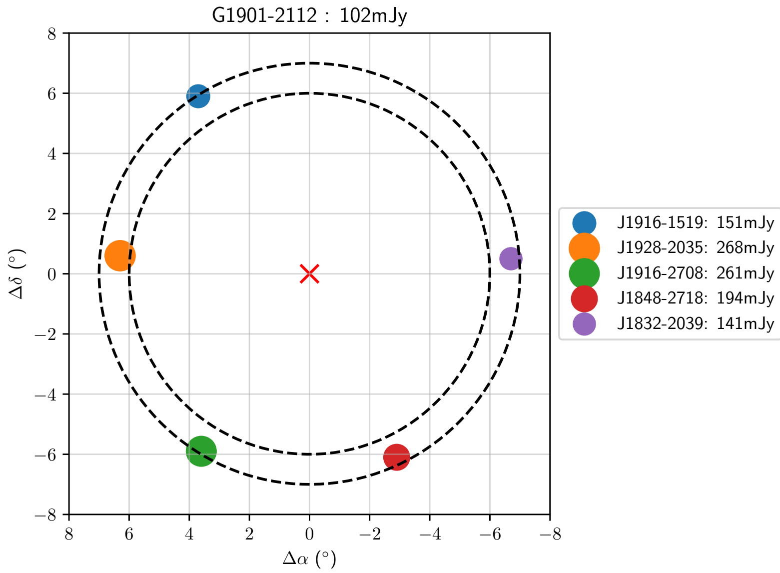

Figure 6.5: Ring plot for target quasar G1901–2112. This ring is between 6° and 7° and the central quasar has flux density 120 mJy.

6.3 Method and Observations

6.3.1 Array and Frequency

Observations were conducted using the ASCI Array (Section §1.4.3). The AuScope portion of this array is comprised of Katherine (Ke), Yarragadee (Yg) and Hobart26m (Ho). Ke/Yg are identical 12 m Patriot geodetic dishes equipped with S/X receivers, DBBC2 digitisers and Mark5B recording units (Lovell et al., 2013). Ho is a 26m X/Y mount equipped with cryogenic cooled L, X, 4.8 GHz, 6.7 GHz, 12 GHz, S/X, K–band and uncooled S-band receivers, DBBC2 and Fila10G/Flexbuf recorder. Ho/Ke and Yg all regularly participate in IVS geodetic observations. The final telescope, Ceduna (Cd; McCulloch et al., 2005) only participates in LBA VLBI observations. It is a 30 m ex-telecommunications dish, equipped with uncooled L, S, X, 4.8 GHz, 6.7 GHz, 12 GHz and K–band receivers, a DBBC2 and Fila10G/Mark5C recorder.

Baselines and approximate sensitivities are given in Table 6.1. The ASCI Array is quite sparse, lacking baselines $uv < 45$ Mλ. For compact targets and calibrators such as those determined in Chapter §4 or chosen in the previous section, this sparse uv–sampling should prove less of an issue, except for potentially higher sidelobe levels than an array with more elements.

Table 6.1: Left: VLBI baselines for the ASCI Array. **Upper Left:** Linear distances (km) between the antennas as calculated by NRAO VLBI scheduling program SCHED. **Lower Left:** Approximate mean uv-distance (Mλ) for 8.34 GHz observations. **Right:** Baseline sensitivites ($\pm$10%, mJy) for a 40 s integration and $\Delta\nu = 256$ MHz.

	$\|\mathbf{B}\|$				σ_S (mJy)			
	Cd	**Ho**	**Ke**	**Yg**	**Cd**	**Ho**	**Ke**	**Yg**
Cd	-	1703	1937	1792	-			
Ho	47.3	-	3432	3211	5	-		
Ke	53.9	95.4	-	2360	11	9	-	
Yg	49.8	89.3	65.6	-	11	9	21	-

The optimal frequency range to observe the quasars was deemed to be X–band due to mutual frequency coverage, ionospheric/tropospheric stability and most importantly, frequency–proximity to the planned observing frequency of 6.7 GHz methanol masers. S-band was also an available option for mutual frequency coverage but lacked other factors. If the aims had been to test ionospheric residual delay and compensation by MultiView, perhaps future observations could involve this. However, to test inverse MultiView as applicable to maser phase referencing, X-band was the best option.

All observations were recorded with 16×16 MHz packed bands, single polarisation RCP, giving 256 MHz sky frequency and the following setup:

$$\nu_L = 8196.99 + 16 \times (0, 1, 2, 3, 4, 5, 6, 7, 8, 9, 10, 11, 12, 13, 14, 15) \text{ MHz} \tag{6.3}$$

where ν_L is the lower edge frequency for each band. Single polarisation 256 MHz was chosen over the optional 128 MHz dual polarisation as the former prioritises delay sensitivity and the latter discrete frequency sensitivity. As quasars emit in the continuum, wide-band single polarisation was prioritised.

6.3.2 Observing Structure

The general observing structure is modelled on that used for the VLBA BeSSeL BR210 epochs (see Section §2.5 and Chapter 3) and consists of three full tracks spanning $\sim$ 23 hours. Each 7 hour track is defined as the time in which the target source is at an elevation above 30° at all stations, bracketed by 45 mins for calibration (see Figure 6.6).

Observations begin with a 30 minute geoblock, followed by a ~15 min block with electronic delay calibrators (EDC). For redundancy, 3–4 bright fringe finder quasars sources were scheduled in each EDC to ensure that one or more is sufficiently bright and has enough onsource time. Slewing accounts for the remaining time. Potentially overzealous redundancy was due to uncertain quasar brightness and array performance. The fringe finders were used to calculate clock drift–rate, bulk clock–offsets and confirm fringes during correlation, calibrate individual telescope electronic delays (manual phase calibration) as well as check delay residuals after application of global atmospheric delay solution. Although the pre–calibration (geoblock + fringe finder) overhead is about 30%, good *a priori* solutions for the delays and fringe–rates are required to avoid the possibility of phase–wrap ambiguities (see Section §5.2.6). As seen in the previous chapter, the magnitude of the delay/phase planes depends on residual delay and might cause general loss of coherence in the phase domain if left uncalibrated.

At beginning of the track after the first geoblock and EDC block, the target source was at an elevation $\varepsilon \gtrsim 30°$ at all sites and the MultiView nodding began. The observing mode here was Target, Calibrator 1, Target, Calibrator 2, ... and so on. For eventual fringe–fitting on the target (inverse phase referencing), target source scans observations bracket the calibrator scans to ensure long–term phase coherence. I decided it was best to observe orbit sources in a 'star' pattern rather than progressing azimuthally around the ring. This was to minimise the effect of a possible directional sampling bias and ensuring that the slope measured at any time was representative. There may be more an optimal time-spatial sampling for a given quasar distribution that accounts for likely slope differential changes over the loop interval, however, that investigation is a refinement on the basic method and is a potential topic for future study.

The above process was repeated once, with a second geoblock in the centre of the track to avoid losing time due to tracking the target source through the zenith at the larger, more slowly slewing antennas. The third geoblock and electronic delay calibrator blocks are directly after the target was below 30° at least two stations. Geoblocks must also bracket ring blocks for interpolation of the clock and dry tropospheric delay solutions, with a minimum of 3 geoblocks necessary for a reasonable estimate for the clock–rate and residuals at each station. Tracks can be tiled together, sharing the middle and fringe–finder blocks such that observations can contain at least 3 tracks per day for a total of approximately 23 hrs.

Table 6.2 summaries the results of epochs MV020 through to MV028. Only epochs MV025 through to MV028 are used in further analysis for the reasons outlined in the bottom section of Table 6.2.

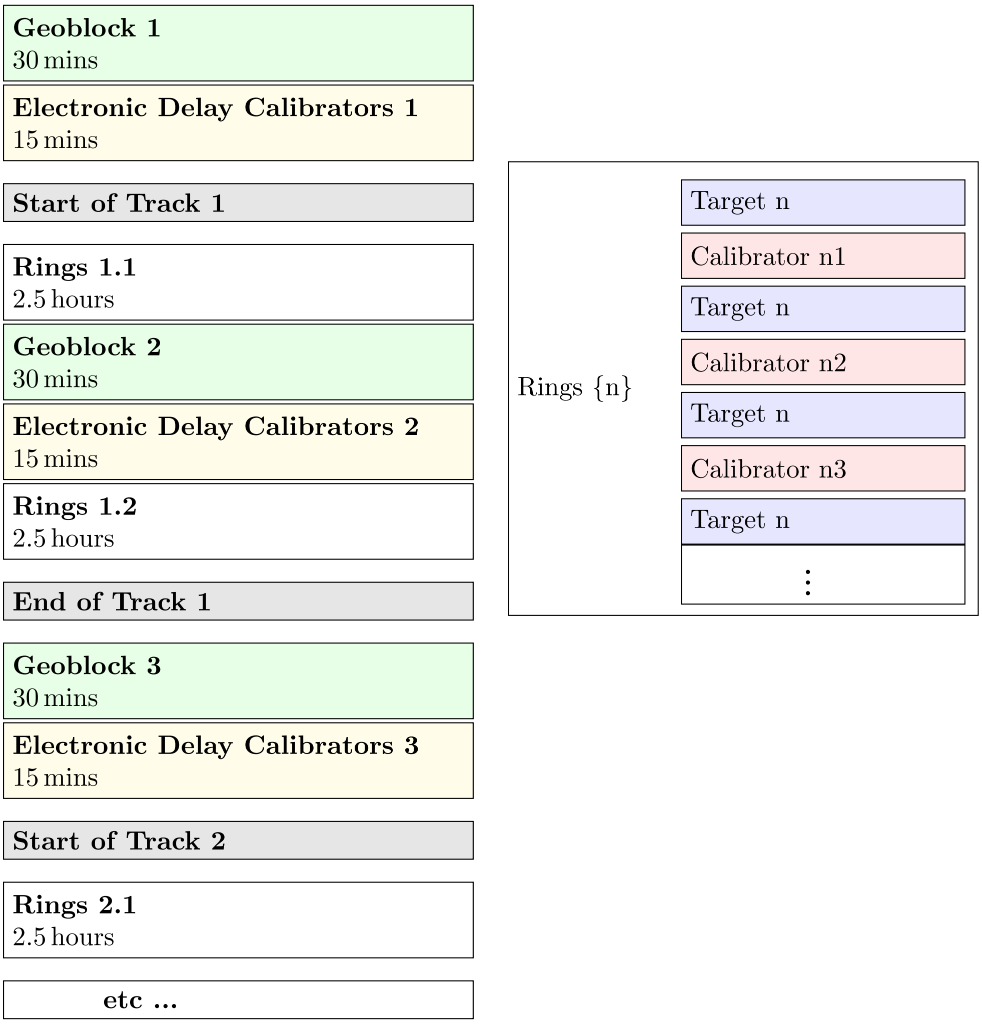

Figure 6.6: Block Diagram for the MV02* observing structure.

Table 6.2: MV02* epochs. **Top:** Successful epochs, characterised by minimal or acceptable issues and or loss of data. **Bottom:** Unsuccessful MV02X epochs where one or more major telescope, backend or data problems caused the loss of almost all the data at one or more antennas.

Epoch	Date	N_r	Notes
Used:			
MV025	17-Feb-2019	9	9 ring experiment, otherwise no issues
MV026	17-Mar-2019	3	Ceduna 30m power failure in last 3 hours and subsequent clock jump
MV027	13-Apr-2019	3	No issues to note
MV028	4-May-2019	3	No issues to note
Unused:			
MV022	9-Feb-2019	9	Unexplained $> 2\,ns$ clock oscillation at Ceduna 30m
Unsuccessful:			
MV020	20-Jul-2018	9	6 hour pilot observation. No Hobart 26m fringes
MV021	23-Sep-2018	9	Incorrect Hobart26m mode and bitmask
MV023	9-Feb-2019	9	Incorrect receiver configuration at Ceduna 30m
MV024	10-Feb-2019	9	Incorrect Mark5B frame size at Ceduna 30m, data recorded incorrectly; Katherine taken offline after 6 hours for maser maintenance

6.4 Reduction Processes

The data were all reduced in an identical manner over the four epochs (MV025, 26, 27 and 28) with the Standard VLBI calibration method (Section 2.5) with minor variation:

1. Some antenna positions needed to be corrected and updated. This was performed by fitting the residual multiband delays for a diurnal sinusoidal offset in addition to geodetic delays;
2. The amplitudes were initially calibrated with antenna system temperature measurements from the telescope sites, and then again using an iterative method (see Section §C.1.2). This was achieved by using script *quasar_amplitude_autocorrect.py*[†];
3. After manual phase calibration, data is fit with inverse phase referencing (iPR) and can proceed to be split out and imaged. Then, post-iPR data is fit with inverse MultiView methods and this data is also split out and imaged.

6.4.1 Correlation

I correlated the baseband data from the telescopes with DiFX-2.6.1 (Deller et al., 2011) running on a local cluster. As per Section 2.3.3 this process involved fringe verification and manual clock–searching. For fringe–finding, a strong source from the EDC blocks (optimally near the centre of the observation; EDC block 2 or 3) with all telescopes on-source is correlated at a high spectral resolution (often $\delta\nu < 0.0625$MHz/channel or 256 channels in a 16 MHz band). The detection of fringes on this source indicates that telescopes had a correct frequency setup and indeed was on source for this time (potentially eliminating extreme pointing issues). In addition, high spectral resolution correlation allows the detection of higher single-band delays that might otherwise wrap over a channel. The maximum detectable delay goes as $\tau = 2\pi/\delta\nu < 100\ \mu$s, so failure to find fringes might indicate a too low correlation resolution such that the phases are decorrelating over the channels. Once fringes are found, the antenna delays for that scan can be used to zero the delays (within the measurement uncertainty of the delay determination). Once clocks were zeroed about the middle of the experiment, all fringe–finder scans were correlated and clocks rates were fit with least–squares regression (Figure 6.7). Fitted clock–rates were applied and final correlation was performed in one pass - all sources correlated over the full bandwidth (16 MHz) with 32 spectral channels per IF, giving a spectral resolution of 0.5 MHz.

6.4.2 Antenna Position Corrections

For correlation I used antenna positions and velocities determined from the information on the AstroGeo website[‡] given in Table 6.3. These positions come from past IVS and geodesy-style experiments nominally involving the 4 stations of interest as part of the LBA. Hobart 26m, Katherine 12m and Yarragadee 12m partake in IVS experiments at least once per week, and therefore their positions are known to the level of $|\Delta B| \sim 1$ cm. Ceduna 30m does not regularly partake in IVS–style experiments and therefore has a more uncertain position.

Single-frequency geoblock fitting nominally takes measured LoS delay (after manual phase calibration, EOP and TEC corrections; see Section §2.5) and fits for a likely clock rate and zenith

[†]Publicaly available at https://github.com/lucasjord/thesisscripts
[‡]http://astrogeo.org/vlbi/solutions/

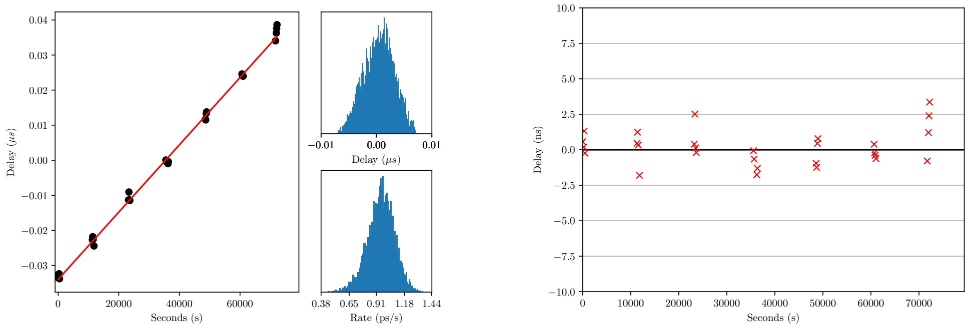

Figure 6.7: Delays measured on fringe–finder quasars for experiment MV028, baseline Ho–Cd. **Left:** fitting and removing clock drift rate between stations. Measured and removed clock rate is $\frac{d\tau}{dt} = 97 \pm 13$ ps/s in this case. The fit for residual electronic delay $\tau_e = 1 \pm 30$ ns. **Right:** Residual delay after clock removal is $|\delta\tau| < 3$ ns which can be explained by individual IF electronic delays or atmospheric effects. This will be removed in $\mathcal{AIPS}$ calibration. The low residual delay allows for a much coarser correlation resolution in FITS output at 0.5 MHz/chan as this will still allow this small delay to be easily detected and corrected during processing.

Table 6.3: Correlated antenna positions and velocities at epoch 2000.0 from AstroGeo RFC_2018. Ceduna velocity taken from RFC_2009. **Columns (1)** Antenna name; **(2-3)** X position and velocity; **(4-5)** Y position and velocity; **(6-7)** Z position and velocity.

Antenna	$\boldsymbol{X}$ (m)	$\boldsymbol{\dot{X}}$ (m/yr)	$\boldsymbol{Y}$ (m)	$\boldsymbol{\dot{Y}}$ (m/yr)	$\boldsymbol{Z}$ (m)	$\boldsymbol{\dot{Z}}$ (m/yr)
Ceduna 30m	−3753442.7457	−0.04173	3912709.7530	0.00267	−3348067.6095	0.04990
Hobart 26m	−3950237.5960	−0.03834	2522347.7530	0.00849	−4311561.6600	0.03942
Katherine 12m	−4147354.8680	−0.03477	4581542.3320	−0.01545	−1573302.9130	0.05427
Yarragadee 12m	−2388896.4240	−0.04673	5043350.0760	0.00824	−3078590.5910	0.04838

non–dispersive delay. If other delays are present, they will be included in this fitting process and skew the zenith delay estimate (see Section §2.3.9.2). In the presence of suspected baseline errors, I used an alternate programme[§] (written by Mark J. Reid) to simultaneously fit for tropospheric non-dispersive delay, clock rate and positional offsets in the Ceduna 30m correlated position ΔX, ΔY, ΔZ. Results of this fitting are shown in Table 6.4. The expected effect of uncorrected ionosphere on the LoS delays is $c\tau_{\text{iono}} < 6$ cm (Section §2.3.9.1), however, the repeatability of the positional result appears to indicate that it must have not correlated with the baseline delay and therefore did not systematically skew the answer over four epochs.

I measured the Ceduna 30m position offset to be $(\Delta X, \Delta Y, \Delta Z) = (7, -9, 22)$ cm. The reason behind this difference is attributed to offsets in the used AstroGeo catalogues for the position of Ceduna 30m. Figure 6.8 shows Ceduna 30m X,Y, Z position vs. time for my two primary sources of telescope position measurements: AstroGeo and ATNF (Australia Telescope National Facility) scheduling programme SCHED. It is clear the catalogued positions in SCHED are much closer to those measured, however are given without uncertainty measurements. AstroGeo is far more generous in terms of errors estimation, quoting large errors $\sigma = 25$ cm and therefore are always going to be consistent with most measurements. However, assuming a conservative estimate of 3 cm in the SCHED positions easily leaves them consistent with the measurements

[§]Code is publicly available from https://github.com/lucasjord/thesisscripts

Table 6.4: Measured position offsets and formal uncertainty for Ceduna 30m over the 4 epochs. *The Y component offset was fit as +9 cm, however, when applied this made things twice as bad. When the sign was reversed this fixed the issue. Positional accuracy in epoch MV026 is understandably lower due to positional determination from 6 geoblocks rather than 7 (data flagged following a clock jump).

Epoch	**ΔX (cm)**	**$\sigma_{\Delta X}$ (cm)**	**ΔY (cm)**	**$\sigma_{\Delta Y}$ (cm)**	**ΔZ (cm)**	**$\sigma_{\Delta Z}$ (cm)**
MV025	5.31	2.67	9.24	2.66	24.23	2.31
MV026	8.69	2.88	10.97	2.99	21.43	2.94
MV027	6.09	2.64	6.87	2.68	20.55	2.60
MV028	6.83	2.67	9.13	2.72	22.87	2.62
AVG	6.7	1.4	−9.1*	1.4	22.3	1.3

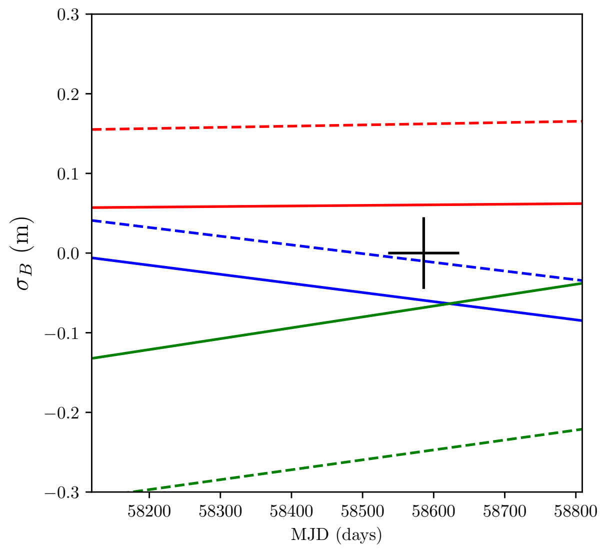

Figure 6.8: Ceduna X (red), Y (blue) and Z (green) position vs. time for SCHED (solid) and AstroGeo (dotted) catalogued positions as compared to the mean position determined at all MV02* epchs (black + error bars).

here. Therefore for all future SπRALS correlation, ATNF SCHED positions will be used. Further position measurement–dedicated sessions should nevertheless be undertaken to confirm this.

Individual coordinate offset errors in the delay measurements are approximately ~ 3 cm, however, I confidently report that the consistent measurements over the 4 epochs allow the accurate estimation at around ~ 1 cm considering the maximum position change due to station velocity is < 1 cm over the 70 day period. Figure 6.9 shows images with identical calibration processes with the exception of the baseline offsets being applied or not. There is an extremely clear increase in image fidelity for the case where the improved position for Ceduna is used.

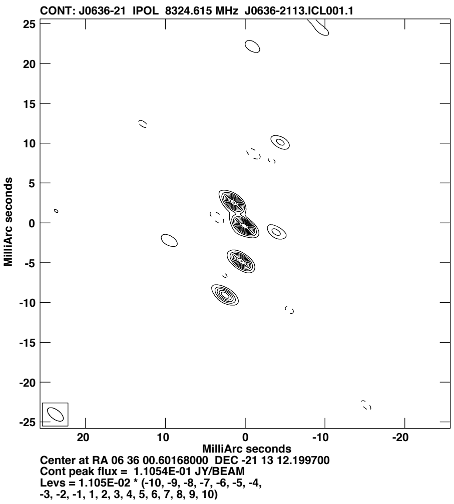

(a) J0636–2115 before

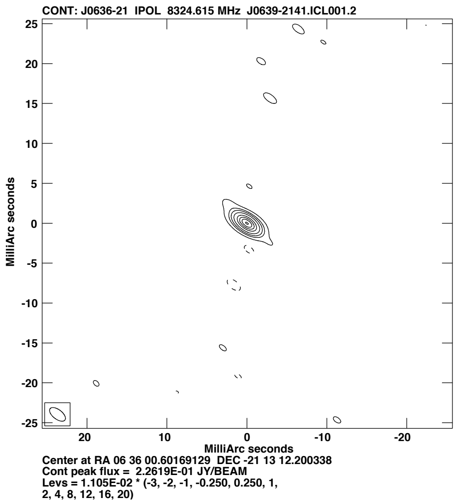

(b) J0636–2115 after

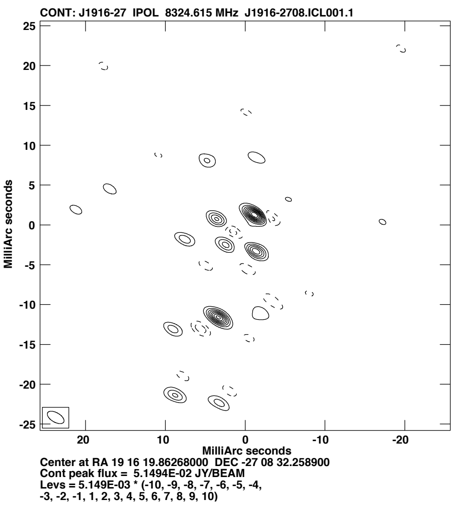

(c) J1916–2708 before

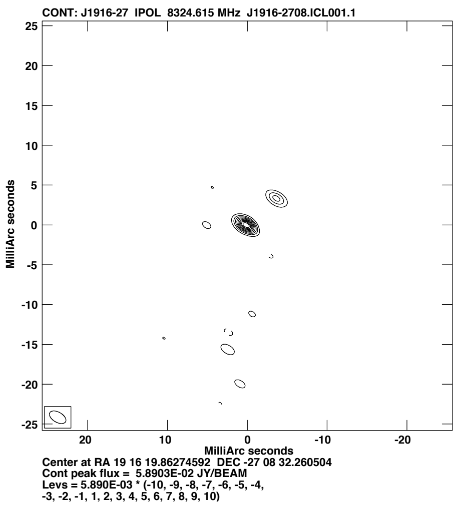

(d) J1916–2708 after

Figure 6.9: Phase referenced images of J0636–2113 and J1916–2708 from epoch MV027 with and without the estimated Ceduna position solutions applied. Apart from differing Ceduna position and resultant tropospheric delay solutions, analysis process is identical for all images. J0636–2113 is at distance $R = 2.4$ deg from centre while J1916–2708 is $R = 6.9$. No self-calibration has been applied.

6.4.3 Antenna Amplitude Calibration

Where available, system temperatures were extracted from telescope logs and applied in conjunction with gain curves. Where system temperature information was not available, nominal SEFD values were applied. This provided a rough conversion between raw voltages to flux density values. To improve the amplitude calibration where no system temperature information was available, additional steps were required.

Certain IFs at Ceduna 30m presented a practical difficulty. There was an unexplained drop ('notch') in apparent sensitivity of some of the IFs in the frequency range observed. This is thought to be due to a power–slope input into the DBBC unit. Nevertheless, since it was very unlikely originating from the target quasars, the method described in Section §C.1.2 was used to calibrate the spectral data pre-imaging. Source F1256–0547 (aka. 3C279) was used to correct amplitude over frequency as it is exceptionally luminous $S_c \sim 10$ Jy. I wrote a custom ParselTongue script (*quasar_amplitude_autocorrect.py*)[¶] to do this (Figure 6.10).

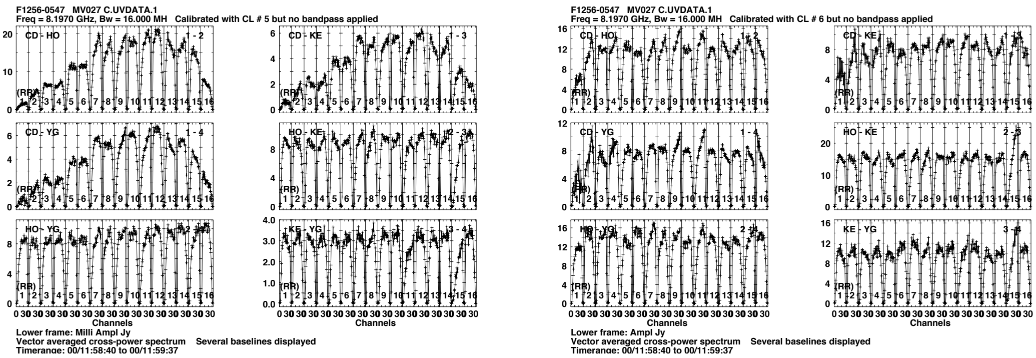

Figure 6.10: IF calibration for Ceduna 30m. **Left:** Amplitude of F1256–0547 after system temperature calibration but before IF calibration; **Right:** After IF calibration.

Although F1256–0547 (3C279) is a very strong, compact source, it is also quite variable and hosts a large luminous jet. So while it is useful for estimating the relative amplitude of the IFs on a particular baseline, it is not suitable for amplitude calibration of baseline relative to the others. The quasar G0634–2335 is less variable, more compact and was used as the centre target source in the $R = 2 - 4$ degree ring. The catalogued flux density for this source was tabulated as $S_c = 620$ mJy in December 2012, however, in MV02* epochs, it was observed to have a total flux density of approximately 1 Jy on most baselines after nominal SEFD's and/or T_{sys} were applied. It is unlikely that the ASCI array sensitivity is almost twice as high as the expected or nominal values, therefore either G0634–2335 has brightened, or catalogued flux densities are systematically lower. Nevertheless, the quasar is known to be quite bright, have a 0.1 mas positional uncertainty and be very compact for the array. Figure 6.11 shows a core-halo model fit for G0634–2335 used in the amplitude vs. baseline calibration:

$$S(B_\lambda) = S_c \exp\left(\frac{-2\pi^2}{8\ln 2}\theta_C^2 B_\lambda^2\right) + S_H \exp\left(\frac{-2\pi^2}{8\ln 2}\theta_H^2 B_\lambda^2\right) \tag{6.4}$$

One can derive that the likely core size is $\theta_c = 0.145\,\text{mas}$ with a flux density $S_c = 400\,\text{mJy}$, which represents about 70% of the flux density.

[¶]Code is publicly available from https://github.com/lucasjord/thesisscripts

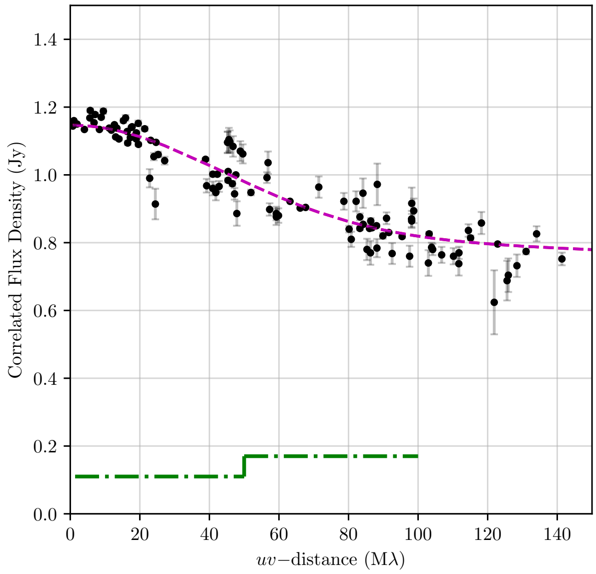

Figure 6.11: Radplot of G0634–2335 extracted from AstroGeo and my fit to visibility data. Derived parameters are $S_c = 810$ mJy, $S_H = 340$ mJy, $\theta_c = 0.145$ mas and $\theta_H = 1.75$ mas for a core/halo model for the source. The least–squares fits are plotted on top of the $uv-$flux data (magenta). Green lines indicate 10σ sensitivity threshold for baselines Cd–Ke/Yg (lower) and Ke–Yg (higher) in a single $\tau = 40$ s scan.

With the core/halo size parameters considered reliable and flux density parameters set to $S_c =$ 0.81 Jy and $S_H = 0.34$ Jy, G0634–2335 was used as an amplitude calibrator for all four epochs using the custom ParselTongue script and method described in Section §C.1.2.

6.4.4 Initial Phase Referencing and Orbit Source Position Corrections

After I had completed and checked amplitude and pre-delay calibration, I used F1256–0547 (3C279) as the manual phase calibrator for all epochs. After the application of these solutions, I averaged the data in frequency and split the rings into separate $\mathcal{AIPS}$ catalogues. For each ring, I fringe fit the target source for a phase ϕ and rate $\frac{d\phi}{dt}$ over the entire observational period (e.g. Figure 6.12). Positional offsets present in orbit calibrators cannot be removed by MultiView as they cause uncorrelated source–specific plane structures in the measured phases.

If an orbit source has a small positional offset, the resultant slope in the phase domain is dominated by the position offset of the target source and all orbit source position slopes become correlated (see Section 5.2.3). Therefore, the positions of the orbit sources need to be checked and corrected using iPR before an astrometric campaign using MultiView. While the initial positional uncertainty in some MultiView calibrators may be quite large, provided there are some calibrators with accurate positions nearby, these should be sufficient to correct for large offsets before later refinement with inverse MultiView (iMV).

To this end I used epoch MV027 to determine the position of any ring sources without good *a priori* position determination. I applied the fringe fit solution from the target to each of the orbit sources, imaged them and fitted elliptical Gaussians to the peak emission. For the

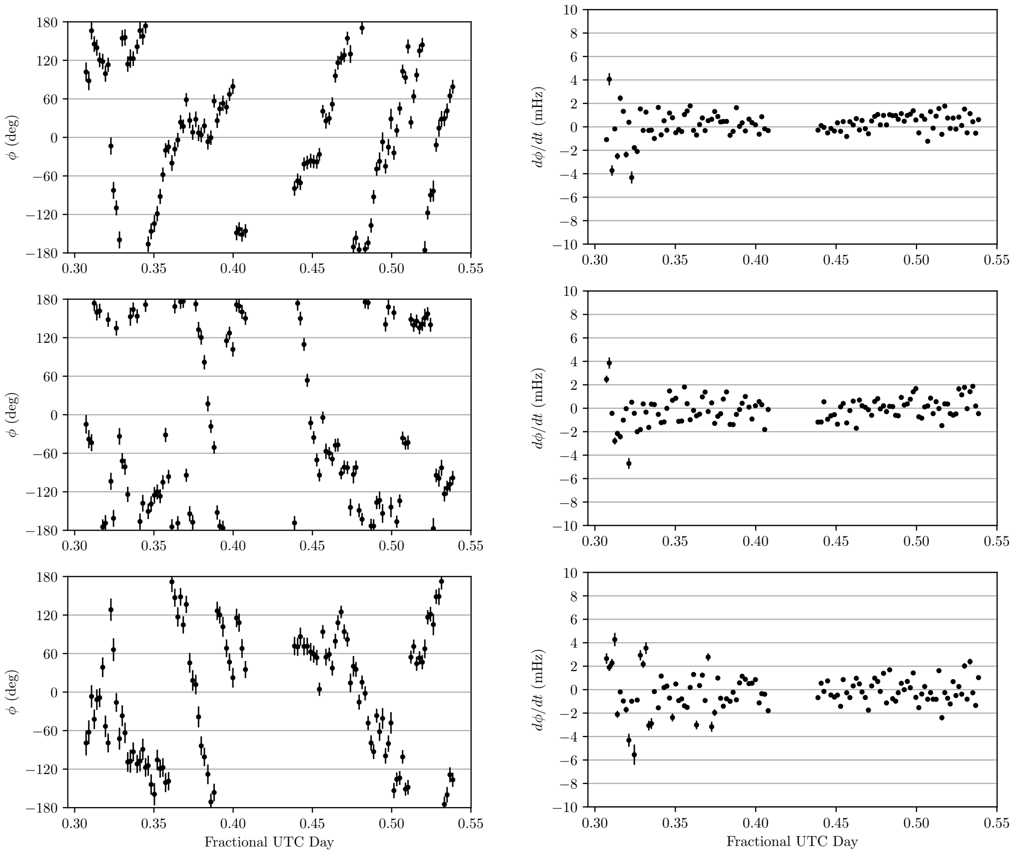

Figure 6.12: Example phase and rate solutions before MultiView fitting. **Left:** Phase and **right:** rate solutions for centre source G0634–2335 for the experiment MV026. **Top to bottom:** baselines Cd–Ho, Ke–Ho and Yg–Ho.

largest ring, it was difficult to determine which peak corresponded to the 'real' quasar as phase referencing imaging was very unreliable. This indicated that phase variations to the distant quasars were > 1 radian and that I needed multiple epochs to check which positional shift was 'correct'. Therefore in the initial positioning stage, trial and error are required in multiple epochs to determine ~ 0.1 mas positions for the calibrators.

Final determined offsets are given in Table 6.5. These positional offsets were applied for all epochs. As discussed, the quasars observed were taken from the RFC_2018 with $S > 110\,$mJy and with nominal positional quality $Q < 0.3$ mas. However, despite this positional offsets were on average much larger than expected (median shift 0.73 mas, minimum 0.2 mas, maximum of 1.48 mas).

6.4.5 MultiView Fitting

I fringe fit orbit sources for phase, one solution per scan and output phase vs. time data. All principle data used for fitting is shown in Appendix C.2. These phases are fed into a custom

Table 6.5: Correlated and shifted positions of orbit quasars. All shifts are applied in AIPS task CLCOR. **Columns (1)**: Quasar name in J2000 format; **(2)**: correlated Right Ascension J2000; **(3)**: correlated Declination J2000; **(4)**: updated Right Ascension J2000; **(5)**: updated Declination J2000; **(6)**: Right Ascension shift; **(7)**: Declination shift; **(8)**: total shift.

Source	α_B (hh:mm:ss)	δ_B (dd:mm:ss)	α_A (hh:mm:ss)	δ_A (dd:mm:ss)	$\Delta\alpha$ (mas)	$\Delta\delta$ (mas)	$\Delta\theta$ (mas)
J0636–2113	06:36:00.60168	-21:13:12.1997	06:36:00.601601	-21:13:12.200019	0.079	−0.319	0.329
J0643–2451	06:43:07.46892	-24:51:21.3120	06:43:07.469343	-24:51:21.313112	−0.423	−1.112	1.190
J0620–2515	06:20:32.11700	-25:15:17.4851	06:20:32.117785	-25:15:17.486352	−0.785	−1.252	1.478
J0639–2141	06:39:28.72567	-21:41:57.8045	06:39:28.725476	-21:41:57.805075	0.194	−0.575	0.607
J0632–2614	06:32:06.50180	-26:14:14.0353	06:32:06.501723	-26:14:14.034143	0.077	1.157	1.160
J0629–1959	06:29:23.76186	-19:59:19.7236	06:29:23.761793	-19:59:19.723399	0.067	0.201	0.212
J1354–0206	13:54:06.89532	-02:06:03.1906	13:54:06.895183	-02:06:03.190118	0.137	0.482	0.501
J1351–1449	13:51:52.64960	-14:49:14.5569	13:51:52.649078	-14:49:14.557691	0.522	−0.791	0.948
J1312–0424	13:12:50.90123	-04:24:49.8923	13:12:50.901495	-04:24:49.891692	−0.265	0.608	0.663
J1406–0848	14:06:00.70186	-08:48:06.8806	14:06:00.700617	-08:48:06.881194	1.243	−0.594	1.378
J1305–1033	13:05:33.01504	-10:33:19.4281	13:05:33.014697	-10:33:19.427271	0.343	0.829	0.897
J1406–0707	14:06:00.70186	-08:48:06.8806	14:06:00.702585	-07:07:06.880665	−0.725	−0.065	0.728
J1916–1519	19:16:52.51100	-15:19:00.0716	19:16:52.510923	-15:19:00.071417	0.077	0.183	0.199
J1848–2718	18:48:47.50417	-27:18:18.0722	18:48:47.504007	-27:18:18.072451	0.163	−0.251	0.299
J1928–2035	19:28:09.18336	-20:35:43.7843	19:28:09.183320	-20:35:43.784797	0.040	−0.497	0.499
J1832–2039	18:32:11.04649	-20:39:48.2033	18:32:11.045556	-20:39:48.202587	0.934	0.713	1.175
J1916–2708	19:16:52.51100	-15:19:00.0716	19:16:52.510560	-27:08:00.072402	0.440	−0.802	0.915

ParselTongue fitting script (called *fit_phase_plane_v6.py*)[‖] that performs a weighted least–squares fit at each time step for a the phase plane on each baseline referenced to the reference antenna. This is the same as the procedure described in Section 5.3. Figure 6.13 shows a 3D representation of the phase plane fit for a few time steps over the observation.

The MultiView fitting script outputs an $\mathcal{AIPS}$–compatible input file (SN table) containing phase corrections for the target source and orbit quasars. I applied these solutions directly to the target and orbit sources in $\mathcal{AIPS}$. Finally, target and orbit sources are imaged in $\mathcal{AIPS}$ and the peak emission in CLEANed images fit with elliptical Gaussians. The measured positions of targets and orbit sources are given in Appendix C.3.2.

6.4.6 Inverse Phase Referencing and Self–Calibrating

To compare inverse MultiView with inverse phase referencing, I imaged the central targets and orbit sources directly after the initial fringe fit to the central target. I fitted the emission within the central 25% of CLEANed images with elliptical Gaussians. This was to have a reasonable comparison between iMV and iPR because while there was still emission at the centre of such images, the peak emission was sometimes $\theta \geq 5$ mas away. This effect can be seen in the fractional flux density recovery (FFR), which I defined as the fraction of integrated flux density in a phase referenced image region compared to the same region in a self–calibrated image. To get the FFR metric, single–cycle self-calibration was applied to all quasar sources. Again, the peak emission in the central 25% was fit with elliptical Gaussians. The results of the iPR and self–calibration astrometry are presented in Appendices C.3.1 and C.3.3.

[‖]Code is publicly available from https://github.com/lucasjord/thesisscripts

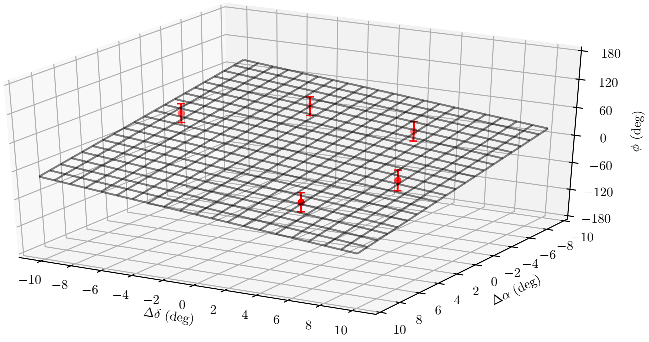

(a) $t = 19.260$ hrs

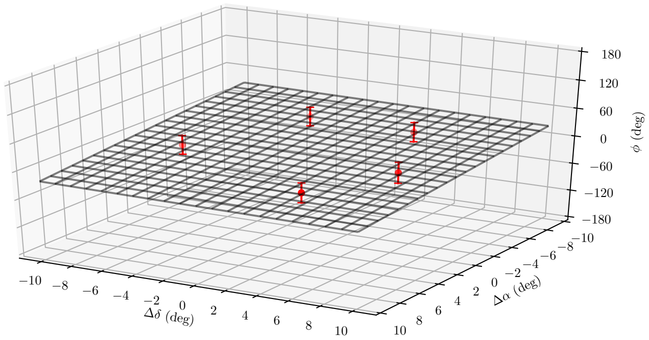

(b) $t = 21.247$ hrs

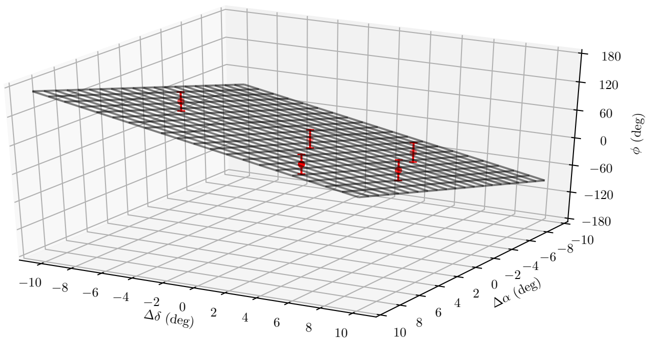

(c) $t = 23.988$ hrs

Figure 6.13: Phase plane for baseline Cd–Ho for ring G1901–2112 for epoch MV027 at given time steps. Time steps are given in UTC.

6.5 Results and Discussion

6.5.1 Astrometry

Overall, it is not possible to do a fair comparison between iPR and iMV with the data attained in these observations as that was not the aim. For a much fairer comparison, the 3–4 new epochs would have to be scheduled where the focus was to get the best possible iPR solutions, nodding only to 1–2 of the calibrators such that the visibility coverage etc. was optimised for them. Alas, my intention with these observations was to successfully apply iMV and test the astrometric accuracy vs. target–calibrator separation.

I define the astrometric accuracy in these observations to be the standard deviation of the position of the sources over the 4 epochs. This is done independently for the East-West σ_α and North-South σ_δ directions.

The *fairest* comparison to make is between iPR and iMV is to compare the astrometry of the orbit sources in iPR vs. the target source in iMV (Figure 6.14). This is because the position of the target quasar is always at the centre of the image in iPR after the application of the phase and rate solution to itself. Similarly, the fitting of the phase planes to the orbit source in iMV is very close to self–calibration.

Although quasar positions were updated to be centred for the MV027 epoch, the astrometric accuracy of iPR decreased as calibrator–target distance increased. The quality of the results obtained from iPR look quite reasonable if Figure 6.14 is considered in isolation, however, Figure 6.15 which shows the fraction flux density recovery (FFR) better demonstrates the significant degradation in the image quality produced on average by iPR. The FFR was $\sim 70\%$ for iPR at radii $R < 7$ deg, dropping off rapidly for $R > 7$ deg. This seemingly demonstrates how the dynamic delays (whichever the cause) increase radially outwards from the target position.

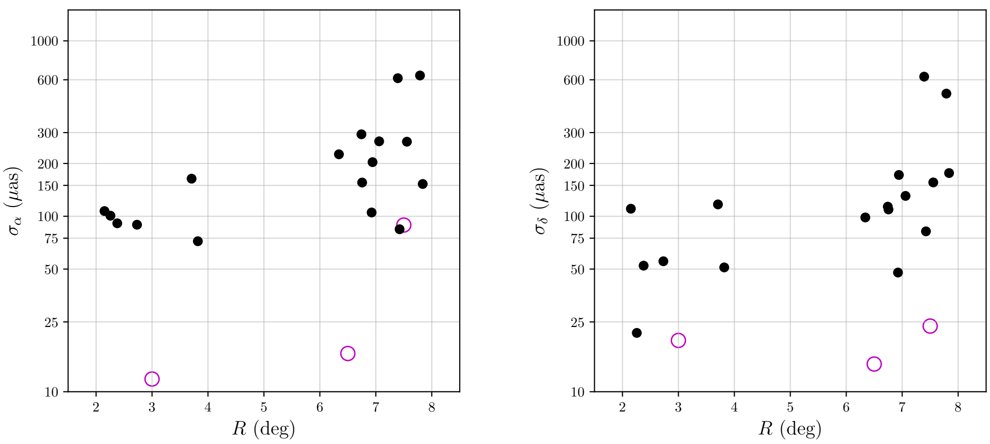

Figure 6.14: Scatter in postion σ vs. ring radius for inverse MultiView (magenta) and inverse PR (black). **Left:** Results from East–West and; **Right:** North–South directions. Both plots have a $\log_{10}$–scaled y–axis to fit all data.

Conversely, all images of target sources after inverse MultiView had been applied had high FFR ~ 0.95 and repeatable positions. Orbit sources after iMV had been applied had FFR ~ 0.85, suggesting that the fitting process evenly spreads the noise over all calibrators at the level of 15%. This suggests a very rough approximation to the typical residual phases is $180/\pi * 0.15 \approx 9$ deg, in rough agreement with the assumed 10 deg phase noise floor for fitting. Taking the worst case FFR of 0.6, the upper limit on systematic deviations from the planar approximation are 20 deg at a target–calibrator separation of 8 deg (which does not take into account the likely influence of phase noise). The thermal noise in the synthesised images is $\sigma_{th} = \frac{\theta_B}{2\ \mathrm{SNR}} \gtrsim \frac{2.0}{2\times 100} = 10\mu$as

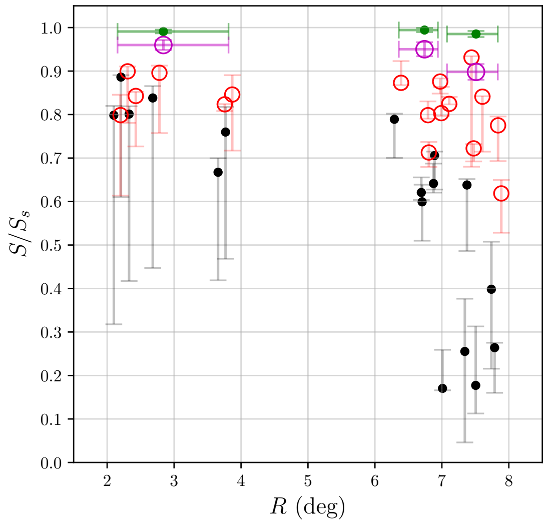

Figure 6.15: Fractional flux density recovery against radial target–calibrator separation. Orbit sources **black:** for inverse phase–referencing **red:** for iMV. Target **green:** for iPR **magenta:** for iMV. Points are the median FFR and error bars indicate the upper and lower quartile range for all three epochs.

suggesting that thermal uncertainty is not a predominant source of astrometric error.

To investigate whether inverse MultiView is robust to small positional offsets (such as those due to maser proper motions), I perturbed target sources positions by $\Delta\alpha = 0.2$ and $\Delta\delta = 0.4$ mas for all rings and epochs excluding MV025. In the case of inverse phase referencing this will move all orbit sources by the negative of both offsets. In the case of MultiView, I expect that this offset is returned to the centre source after the application of the inverse MultiView solution. The application of this position shift is performed in $\mathcal{AIPS}$ with task CLCOR then reduction is continued onwards from EOP/PANG corrections (see Section §2.5).

Figure 6.16 shows the results of this perturbation for the MV026, 27 and 28 epochs. The position shift has clearly been translated into the orbit sources for iPR and returned to the target source in iMV. While there are cases where iPR returns the position shift more precisely, iMV more consistently provides an answer closer to the applied offset.

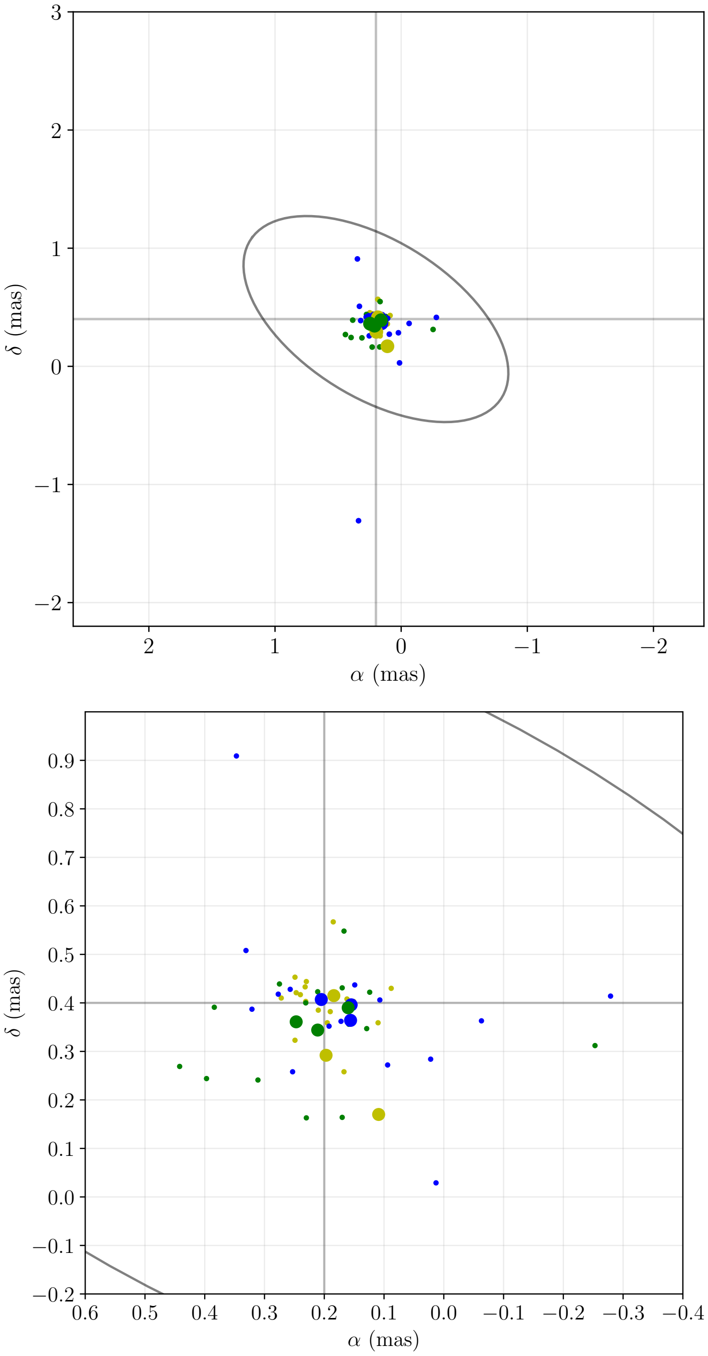

Figure 6.16: Measured position shifts for iPR (small dots) and iMV (big dots); **Colours:** Rings G0634–2335 $\overline{R} = 3$ deg (blue); G1336–0809 $\overline{R} = 7.5$ deg (yellow) and; G1901–2112 $\overline{R} = 6.5$ deg (green). Applied position shifts were $\Delta\alpha = 0.2$, $\Delta\delta = 0.4$ mas and this is indicated on the plot as vertical and horizonal black lines. The measured position shifts for iPR have had a sign reversal. Also included is the mean synthesised beam (2.4×1.4 mas position angle $60°$).

6.5.2 Phase Slopes

As derived in Chapter 5, the phase/delay slopes at any given time depend on the instantaneous residual delay modulated by the effects of various locational parameters such as latitude, longitude, RA, DEC, hour angle and local time. In this section, I discuss the measured slopes over the four epochs, what they mean and where they might be useful.

Figure 6.17 shows measured phase slopes and phase on the Katherine 12m–Hobart 26m baseline for all four epochs. All measured slopes and phases for Hobart 26m baselines for epochs MV025, 26, 27 and 28 are given in Appendix C.2.2. In many cases, the measured phase slopes have a clear trend with time and one that is different for the slope in RA and DEC. I am going to compare the trends and shapes with those expected from the residual ionosphere, dry troposphere and baseline offsets.

While it is well known that the total ionospheric delay is at a maximum around local midday and a minimum at midnight local time, it is not unreasonable to assume that there must also be a maximum and minimum to the residual ionosphere. I suggest two cases:

- a maximum at midday and minimum at midnight
- a maxima at sunrise/sunset, and minimum at midday/midnight

The former would suggest that the residual ionosphere is proportional to the total ionosphere.

The latter may be due to changes in the ionosphere being most rapid around those times, while the temporal GPS sampling of the ionosphere is consistently averaged over a day. Combined with this is the realisation that sunrise and sunset are not necessarily shared for pair of telescopes. Therefore a baseline may have a sunrise/sunset affected period approximately stretching ≤ 3 hrs (for the ASCI Array). Mutual nighttime periods are hypothesised to have a minimum total- and residual ionospheric delay. Therefore any delay slope that is observed these times are not *expected* to be significantly affected by the residual ionosphere and must be explained by other sources.

The local nighttime at the telescope sites changes over the course of the year at the sidereal rate (0.00273 s/s or 3m56s/day). The total time–baseline for the four experiments observations is 76 days or 0.208 yrs. This amounts to a Local Sidereal/UTC shift of 4 hrs 59 min. Over this time sunrise/sunset shifted a maximum of +1.5/-2 hrs at Hobart and a minimum at Katherine of +0.2/-0.8 hrs (days receding and nights increasing). This caused the 'sunrise affected' period to change from the middle of the G1336–0809 ($\overline{R}$ = 7.5 deg ring) track into the G1901–2112 ($\overline{R}$ = 6.5 deg ring) track (see Figure 6.17). The 'sunset affected' period was only every time–coincident with the G0634–2335 ($\overline{R}$ = 3 deg ring) track, however, it moved from affecting the beginning to the end of the track.

The smallest ring $R = 2 \rightarrow 4$ (blue) has the highest scatter in measured slope however, this is mostly bounded by the larger error bars. The error bars themselves are weighted least–squares formal errors:

$$\sigma_A = \sqrt{\frac{\sum_{i=1}^{N}\left(\phi_i - \overline{\phi}\right)^2}{N-2}} \Bigg/ \sqrt{\sum_{i=1}^{N}\left(a_i - \overline{a}\right)^2} \tag{6.5}$$

where a_i is an example RA coordinate offset and σ_A is the uncertainty in the measured RA slope. While I will explore this in more detail soon, for a larger sampled distance the slope measurement is expected to be more accurate and therefore the slope measurement uncertainty is largest for the smallest ring.

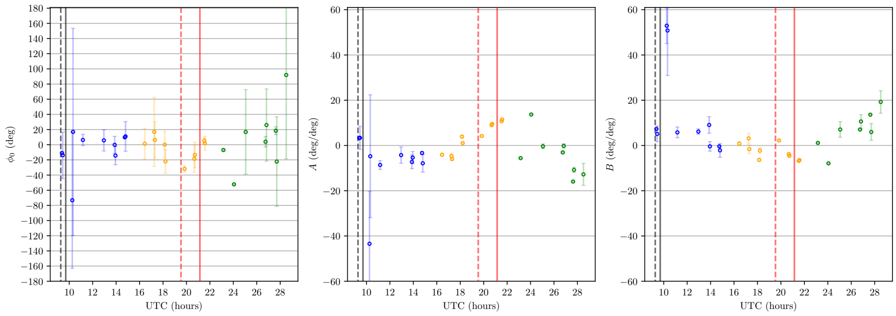

(a) MV025

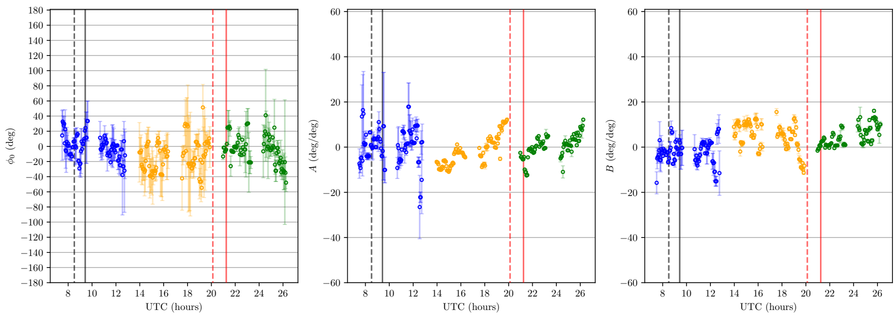

(b) MV026

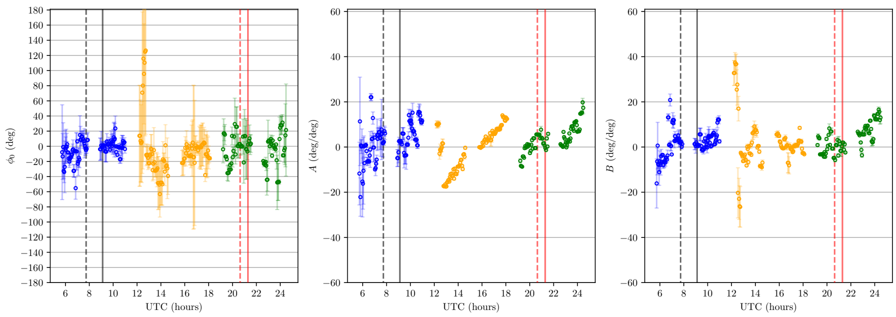

(c) MV027

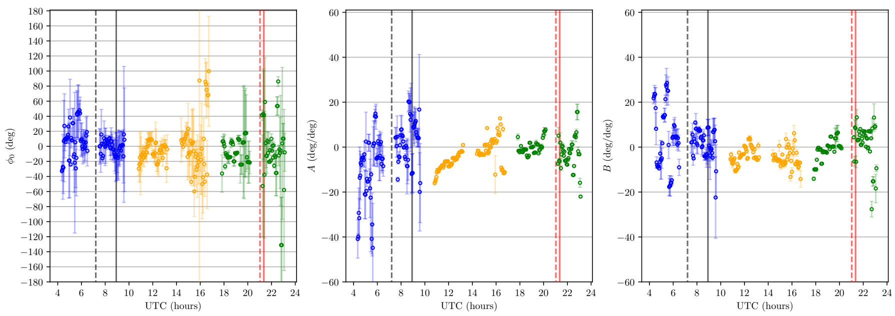

(d) MV028

Figure 6.17: Measured target source phases and slopes for baseline Ke–Ho. **Columns**: (1) Phases; (2) Slopes in East–West (RA) and; (3) North–South (DEC). **Rows:** Epochs MV025; MV026; MV027; MV028. **Colours:** Rings (blue) G0634–2335 $\overline{R} = 3$ deg; (yellow) G1336–0809 $\overline{R} = 7.5$ deg and; (green) G1901–2112 $\overline{R} = 6.5$ deg. **Vertical lines:** Local sunrise (red) and sunset (black) for antenna (solid; e.g. Katherine) and reference antenna (dotted; e.g. Hobart). Error bars are given by weighted–least squared fitting.

There does not seem to be any clear correlation between local sunrise/sunset time and phase slope magnitude and/or stability or derived phase stability (see all plots Appendix C.2.2). While there appears to be enhanced slope scatter about the sunset period for some epochs/baselines, it is not repeatable nor necessarily outside the slope measurement error. The larger inherent uncertainty in slope measurement for the smallest ring appears to explain almost all scatter rather than coincident observational period with local sunset. Therefore, based on the prediction that residual ionosphere will have a local sunrise/sunset dependant enhancement, I find it difficult to ascertain whether this prediction is false or the effect of the enhancement on phase slope magnitude is smaller than that due to other effects (residual dry troposphere or baseline offset).

All experiments coincide with solar cycle 24, which began in December 2008, peaked in April 2014 and ended in December 2019. This solar cycle was one of the least active in recent history, with a maximum of 81 sunspots compared to 180 in the previous cycle (solar cycle 23). In addition, the 2018–2019 period where observation takes place are at the very tail end of the cycle, with a maximum monthly sunspot number of less than 7 (https://www.swpc.noaa.gov/products/solar-cycle-progression).

Katherine–Hobart and Yarragadee–Hobart baselines are nearly identical in terms of sensitivity and total length. However, Katherine–Hobart baselines appear to have generally greater phase and phase–slope stability for all rings and epochs. The main differences between the baselines are orientation and latitude. Baseline orientation is unlikely to be the contributing factor as many targets all over the sky should not necessarily have the same structure/compactness. Therefore it is not unreasonable to conclude that the Katherine antenna latitude and resultant elevation over the track is the separating factor. All targets and resultant rings have declinations $\delta \pm 5 \approx \varphi_{\mathrm{Ke}} = -14.3$ deg implying that they track relatively high at Katherine compared to Yarragadee. However, if elevation alone was the culminating factor, I would expect to see increased phase scatter and increased magnitude and/or scatter of phase slopes increasing at both ends of the track which is not evident. Therefore, I cannot find a reason for this disparity and it should be investigated further as more data is collected in future SπRALS observations.

Even though the residual ionospheric delay is expected to be at a minimum at 'mutual' midnight, clear phase slopes are measured at all epochs at this time. In addition, the phase slopes have obvious time–dependant trends. I want to determine whether a phase slope such as these can be explained purely by either a baseline offset or residual dry tropospheric error. Since I have already derived equations for the delay slopes caused by either of these two effects (see Chapter 5) I will compare these models to the measured phase slopes to ascertain the feasibility that these effects could be a major contributor.

The first phase plane I will model and compare to data is that arising from a baseline offset. Taking Equation 5.4, for a four–telescope array there are 12 antenna position offsets $\Delta X_i, \Delta Y_i, \Delta Z_i$ for $i = \mathrm{Cd}, \mathrm{Ho}, \mathrm{Ke}$ and Yg. Figure 6.18 shows baseline offset phase slope model against measured data for epoch MV027, target ring G1336–0809 on baselines referenced to Hobart.

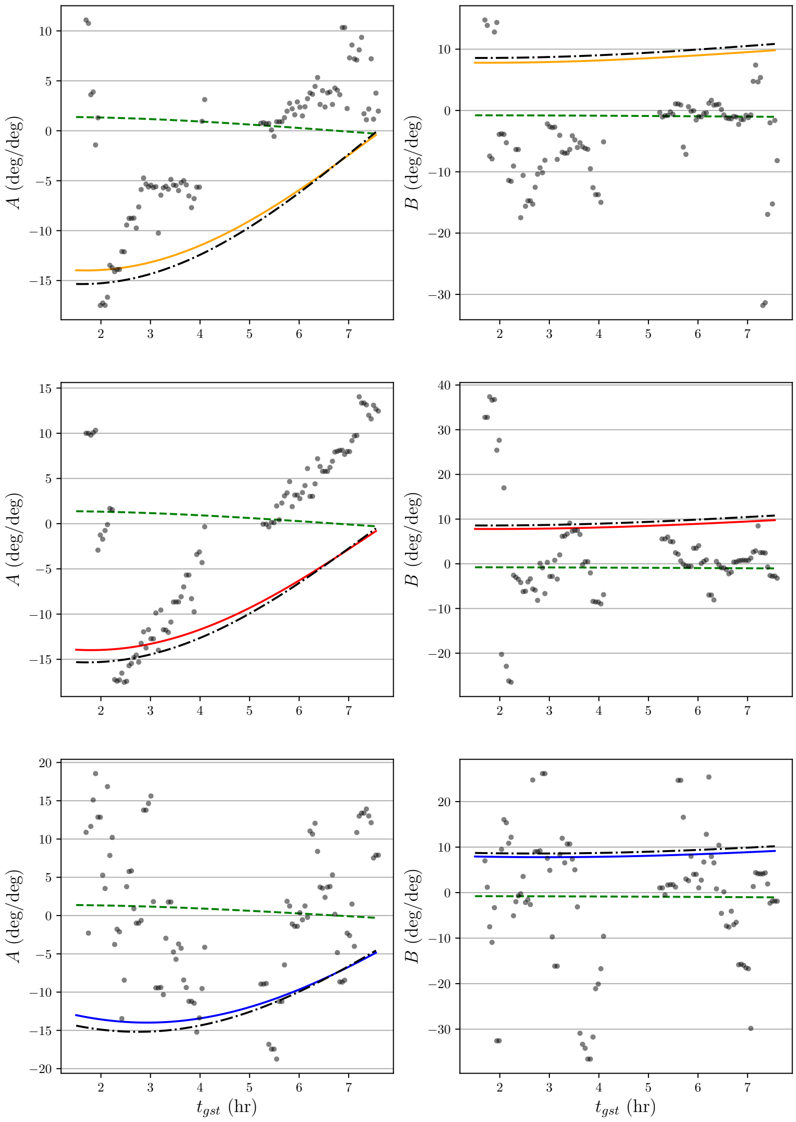

Figure 6.18: Measured slopes vs. baseline slope model. **Left column:** Phase slopes in RA; **right column:** in DEC. **Green line (all plots):** modelled phase slope above reference antenna Hobart. **Yellow, red and blue solid lines:** modelled phase slopes above Ceduna, Katherine and Yarragadee. **Dashed black line:** resultant modelled phase slope above baseline (coloured antenna slope minus green reference slope). **Black points:** Measured phase slopes on G1336–0809 at epoch MV027.

Model parameters were unable to replicate the measured phase slope trends or magnitudes. The example shown uses parameters $(\Delta X_i, \Delta Y_i, \Delta Z_i) = (10, 10, 10)$ cm for Cd, Ke and Yg and $(-1, -1, -1)$ cm for Ho, however, this is because this combination gives results which show some similarity to the measured RA trend, unlike many others. To match the magnitude more closely ΔX and ΔY have to be increased over 20 cm which is far outside the realm of possibility given IVS observations at Ke, Yg and Ho and the reduction process here for Cd. In addition, ΔX and ΔY are the coordinates geodetic observations are most sensitive to. Therefore I find it safe to conclude that baseline errors (even if present on the 5 cm level) do not significantly contribute to the phase slopes.

The next comparison I want to make is for a phase slope purely arising from a residual (zenith) dry tropospheric delay. Taking the equation for a likely residual dry tropospheric phase slope (Equation 5.10), the model parameters will be residual zenith delay errors $\sigma_{\tau_z,i}$ above each telescope $i = \mathrm{Cd}, \mathrm{Ho}, \mathrm{Ke}$ and Yg. I will be using a constant value for $\sigma_{\tau_z,i}$ over the track, however, this is unlikely to be the case. Each geoblock solves for a $\tau_{z,i}$, so for a track, there will be a measured value at the beginning, middle and end. Instantaneous values are interpolated between these three.

While in theory there can be a different and changing value for $\sigma_{\tau_z,i}$ for each half of the track resulting from interpolating the derived value in each geoblock fit, I will only consider some average value for each telescope over the whole time range.

Figure 6.19 shows an example of this modelling with parameters $\sigma_{\tau_z,i} = -2, 3, 8, -5$ cm against measured data for epoch MV027, target ring G1336–0809 on baselines referenced to Hobart. These model parameters (± 1 cm) give a consistent match to the trend and magnitudes of the phase slopes, especially when compared against the phase slopes arising from baseline offsets.

The tropospheric plane models are relatively degenerate even just considering this single source of delay error, as the slopes are the difference between the planes above the antennas (Cd, Ke or Yg) and the plane above the reference (Ho). Model parameters were adjusted using realistic values ($-15 < \sigma_{\tau_z} \leq 15$ cm) to best match data. While it seems apparent that the tropospheric model presented can explain the trends it does not fully encapsulate the magnitudes over time with a single value of delay. Adding further complexity (such as a time–variable version of the residual tropospheric delay σ_{τ_z}) will of course match the measured slopes more closely, however, there is no guarantee that this is representative of the true delay.

In summary: seems possible to use the measured slopes to deduce what residual delays were present in the phase data, however, as it was not the primary focus of this testing, it should be investigated more closely in future studies. The most feasible method would be a Bayesian Markov–Chain Monte Carlo to solve for the parameters baseline errors, residual zenith troposphere (per geoblock per antenna) and potentially some additional terms to include ionosphere. Therefore at this time, measured slopes serve two purposes; to roughly estimate the degree that residuals delays from any source had been pre-calibrated and; calculate phase solutions for orbit sources and re-apply thereby determining an estimate for residual phases.

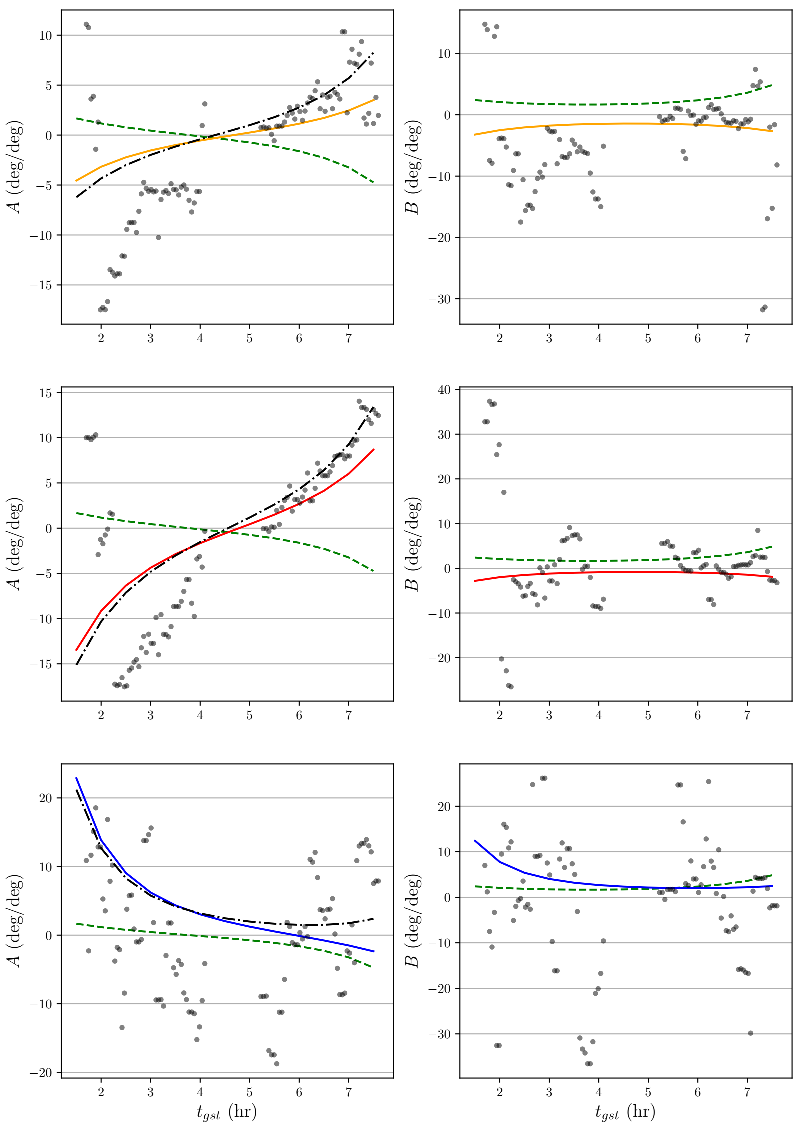

Figure 6.19: Measured slopes vs. tropospheric slope model. **Left column:** Phase slopes in RA; **right column:** in DEC. **Green dotted line (all plots):** modelled phase slope above reference antenna Hobart. **Yellow, red and blue solid lines:** modelled phase slopes above Ceduna, Katherine and Yarragadee. **Dashed black line:** resultant modelled phase slope above baseline (antenna slope minus reference slope). **Black points:** Measured phase slopes on G1336–0809 at epoch MV027.

6.5.3 Astrometric Uncertainty

I would like to understand how the details of inverse MultiView calibrations such as the number of calibrators, target–calibrator separation and SNR affects the astrometric accuracy of the results from a theoretical standpoint and compare it to the observational results. The uncertainty in derived phase measurement on the target $\sigma^2_{\phi,T}$ at a given time step will be the quadrature combination of the measurement uncertainty and the systematic errors:

$$\sigma^2_{\phi,T} = \sigma^2_{\phi,\mathrm{meas}} + \sigma^2_{\phi,\mathrm{sys}} \tag{6.6}$$

where $\sigma_{\phi,\mathrm{meas}}$ is the measurement uncertainty and $\sigma_{\phi,\mathrm{sys}}$ is the systematic uncertainty (both in units of degrees)

6.5.3.1 Plane Measurement Uncertainty

At each time–step, the measurement phase uncertainty on the target $\sigma_{\phi,T}$ source should be:

$$\sigma^2_{\phi,\mathrm{meas}} = \overline{R}^2 \, (\sigma^2_A + \sigma^2_B) \tag{6.7}$$

where there is the measurement uncertainty in the slope fits σ_A and σ_B (deg/deg).

The measurement uncertainty in the slope from a least squares fit is:

$$\sigma^2_A = \frac{\sum_{i=1}^{N}(\phi_i - \overline{\phi}_i)^2}{\sum_{i=1}^{N}(\mathbf{a}_i - \overline{\mathbf{a}})^2} \tag{6.8}$$

where ϕ_i is the phase measurement on each of the calibrators and $\overline{\phi}$ is the average phase on the calibrators (with the same expression for σ_B and $\mathbf{b}_i$).

Firstly, it is not unreasonable to assume that the numerator (which is the residual sum of squares; RSS) is equal to the average phase uncertainty squared in the calibrators $\sigma^2_{\phi,i}$. I further define the phase measurement uncertainty on the calibrators to be inversely proportional to the signal–to–noise ratio SNR of the scan:

$$\sigma_{\phi,C} = \frac{180/\pi}{\mathrm{SNR}} \tag{6.9}$$

in deg. For each quasar (with an unique flux density), SNR only depends on integration time τ: SNR $\propto \sqrt{\tau}$.

Since I have approximately identical radii and uniformly distributed position angles ($\sqrt{\sum_{i=1}^{N}\theta_i}^2 \approx 2\pi$), all $\mathbf{a}_i$ (or $\mathbf{b}_i$) coordinates can be expressed as the combination of radius and position angle relative to the target at the centre: $\mathbf{a}_i = R_i \cos(\theta_i + \psi)$ and $\overline{\mathbf{a}} \approx 0$. The angle ψ is an arbitrary constant rotational offset from the designated coordinate system to retain generality. Therefore I am left with:

$$\sum_{i}^{N}(\mathbf{a}_i - \overline{\mathbf{a}})^2 = \sum_{i=1}^{N}(R_i \cos(\theta_i + \psi))^2 = \left(\frac{\overline{R}^2 + \sigma^2_R}{2}\right) N \tag{6.10}$$

where and σ^2_R is the variance in R (indicating the spread in R) and I go through the simplification in Appendix C.1.4.

Therefore the slope measurement error will look something like

$$\sigma_A = \frac{360/\pi}{\overline{\mathrm{SNR}}\sqrt{\left(\overline{R}^2 + \sigma_R^2\right) N}} \tag{6.11}$$

where the phase slope uncertainty has units degree of phase per degree of separation and where I consider the average SNR of sampled quasars. So the slope measurement uncertainty decreases with a higher average radius $\overline{R}$, radial scatter σ_R, average SNR and $\sqrt{N}$ number of orbit sources. The analytic form of Equation 6.10 (and consequentially derived slope measurement uncertainty) assumes 'perfect' azimuthal sampling and increases in a complex manner depending on N and the magnitude of azimuthal under-sampling. For such cases, the non simplified form of Equation 6.10 may be considered.

Qualitatively, the best quasar configuration would optimise azimuthal sampling, time/spatial–coherence and on-source time for both target and orbit sources weighted by their flux density. To first order, a near-perfect linear configuration target and two orbit sources would be a very interesting case. Instead of a plane, a simple linear slope could be fit. While previous authors suggest such a strategy (e.g. Reid et al., 2017), such configurations of reference quasars with respect to target sources of interest will be relatively uncommon.

For 2D slope fitting as prescribed here, the practical minimum is 4 quasars, where the best combination of those is in a perfect cross pattern with the target source at the centre. Such a configuration would give the highest sampling rate of the phase slope and determination of the 3 parameter fit with a free parameter to constrain residuals. Again, I expect this configuration to be quite rare and in almost all cases the number of calibrators is expected to be $N \geq 4$.

The other consideration is that there is a trade-off between on-source time (which improves SNR) and the number of calibrators N. The total time to observe a single loop comprises of all dwell and slew times. For every N calibrator scans, there are $N + 1$ target scans and $2N + 1$ slews. Atmospheric terms will have temporal variability, so there must be an upper limit to the time over which a solution to the phase plane can be determined. If this time is the 'spatial coherence time' T_{coh}, then it must be the case that:

$$\begin{aligned} T_{\mathrm{coh}} \geq & N\left(t_T + t_s + t_C + t_s\right) + \tau_t \\ \geq & \left(N+1\right) t_T + 2N t_s + N t_C \end{aligned} \tag{6.12}$$

where t_T, t_C are dwell times for the calibrators and target respectively, t_s is the slew time and T_{coh} is the total plane approximate coherence time. All times are in seconds. I consider the slowest slewing telescope to be the limiting factor in the slew times such that the slew time is the angular distance between target and calibrator (aka. R) divided by that telescopes slew time plus settle time:

$$t_s = \frac{R}{v_s} + t_{\mathrm{set}} \tag{6.13}$$

I note that in the case of short slews, the slew times can be dominated by the antenna acceleration and settling time so also added the t_{set} term. However, these cases also are unlikely to be coherence limited due to the small separations.

For MV02* epochs, the target and calibrator had the same integration time of $\tau_t = \tau_c = 40$ s and I find coherent plane solutions for $\overline{R} = 7.5$ deg and $N = 6$ which gives a lower–limit coherence time of $T_{coh} = 10.9$ min at 8.2 GHz. Considering this limit, I investigate if there exists a theoretically ideal number of quasars and respective angular distances.

The average $\overline{\text{SNR}}$ is given by the radiometry equation and target quasar strength:

$$\overline{\text{SNR}} = \frac{\overline{S_c}}{\sigma_S} = \overline{S_c}\frac{\sqrt{2\tau\Delta\nu}}{\overline{\text{SEFD}}} \tag{6.14}$$

where σ_S is the noise, $\overline{S_c}$ is the average quasar strength, $\Delta\nu$ is the integrated bandwidth and $\overline{\text{SEFD}}$ is the average baseline SEFD. Solving Equation 6.12 for quasar onsource integration time t and assuming that $t_C = t_T = t$:

$$\begin{aligned} T_{\text{coh}} &= (N+1)\,t + 2N\left(\frac{R}{v_s} + t_{\text{set}}\right) + Nt \\ \therefore t &= \frac{T_{\text{coh}} - 2N\left(\frac{R}{v_s} + t_{\text{set}}\right)}{2N+1} \end{aligned} \tag{6.15}$$

Substituting Equation 6.14 and 6.15 into Equation 6.11 the final form for the slope measurement uncertainty is:

$$\sigma_A = \frac{360}{\pi}\frac{\overline{\text{SEFD}}}{\overline{S_c}}\frac{1}{\sqrt{2\Delta\nu}}\frac{1}{\sqrt{\overline{R}^2 + \sigma_R^2}}\sqrt{\frac{2N+1}{N\left(T_{\text{coh}} - 2N\left(\frac{R}{v_s} + t_{\text{set}}\right)\right)}} \tag{6.16}$$

in degrees of phase per degree of separation.

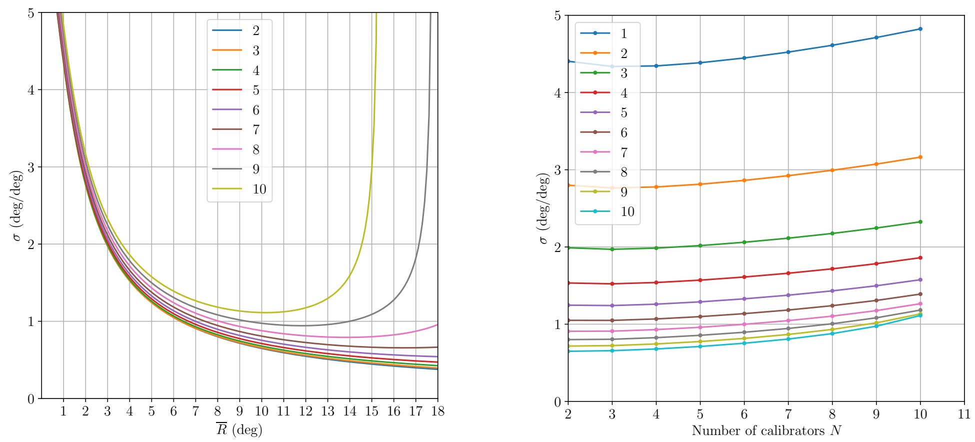

Figure 6.20: Slope uncertainty σ as a function of- **Left:** $\overline{R}$, with different lines correspond to different values of N given in legend; and **Right:** N, with lines corresponding to different values of $\overline{R}$ given in legend. For all lines $\overline{\text{SEFD}} = 2000$ Jy, $\sigma_R = 1$ deg, $T_{\text{coh}} = 11$ min, $v_s = 40$ deg/min, $\overline{S_c} = 100$ mJy and $\Delta\nu = 256$ MHz.

Figure 6.20 shows the theoretical measurement uncertainty in the slopes introduced by increasing mean radius $\overline{R}$ or number of quasars N for the ASCI array sensitivities. The slope measurement uncertainty is a strong function of radius and a weak function of quasar number provided loops are kept within coherence time. In addition, the slope measurement uncertainty is as strong a function of mean quasar correlated flux density $\overline{S_c}$ as it is of radius. The reason for the turn up that occurs at extreme values of $\overline{R}$ and N is as the total loop time approaches the spatial coherence time, scans have to be increasingly shorter and SNR rapidly decreases.

The slope measurement uncertainty having this form is unsurprising- a larger sampled distance with more points and a higher precision to which they are known increases the certainty that the slope can be determined. A more useful relationship is the uncertainty in the phase measured on the target. Substituting Equation 6.16 into Equation 6.7 and letting $\sigma_A = \sigma_B$ gives:

$$\sigma_{\phi,\mathrm{meas}} = \sqrt{2}\,\overline{R}\sigma_A \tag{6.17}$$

and converting this into a positional uncertainty gives:

$$\begin{aligned}
\sigma_{\theta,\mathrm{meas}} &= \frac{c\sigma_\tau}{|\mathbf{B}|} \\
&= \frac{\pi}{180}\frac{c}{|\mathbf{B}|}\frac{1}{2\pi\nu}\sigma_{\phi,\mathrm{meas}} \\
&= \frac{1}{180}\frac{\lambda}{|\mathbf{B}|}\frac{1}{\sqrt{2}}\overline{R}\sigma_A \\
&= \frac{\theta_B}{\pi}\frac{\overline{\mathrm{SEFD}}}{S_c}\frac{1}{\sqrt{\Delta\nu}}\frac{\overline{R}}{\sqrt{\overline{R}^2+\sigma_R^2}}\sqrt{\frac{2N+1}{N\left(T_{\mathrm{coh}}-2N\left(\frac{R}{v_s}+t_{\mathrm{set}}\right)\right)}}
\end{aligned} \tag{6.18}$$

where I have identified the synthesised beam size $\theta_B = \frac{\lambda}{|\mathbf{B}|}$ in mas. Therefore the units of $\sigma_{\theta,\mathrm{meas}}$ are also mas.

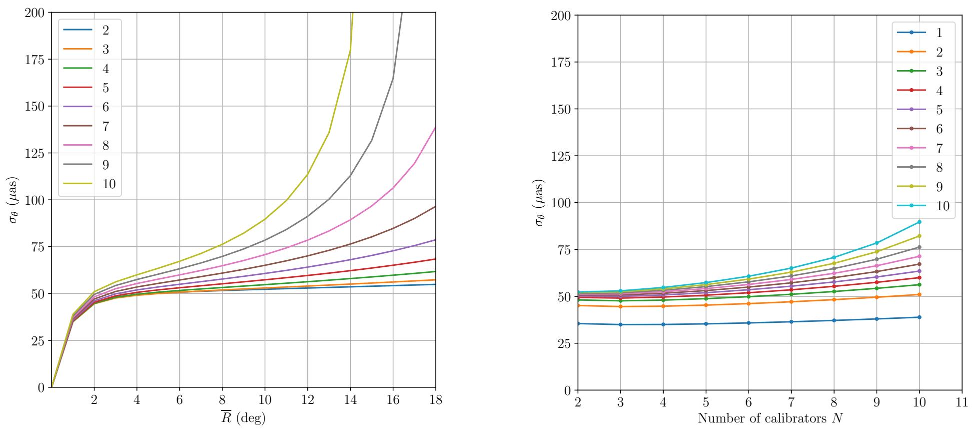

Figure 6.21: Target position uncertainty σ_θ due to slope measurement uncertainty as a function of- **Left:** $\overline{R}$, with different lines correspond to different values of N given in legend; and **Right:** N, with lines corresponding to different values of $\overline{R}$ given in legend. For all lines $\overline{\mathrm{SEFD}} = 2000$ Jy, $\sigma_R = 1$ deg, $T_{\mathrm{coh}} = 11$ min, $t_{\mathrm{set}} = 10$ s, $v_s = 40$ deg/min, $\overline{S_c} = 100$ mJy, $\Delta\nu = 256$ MHz and $\theta_B = 2$ mas.

Figure 6.21 shows the derived target position uncertainty due to measurement uncertainty in the slope fitting as a function of average target–calibrator separation $\overline{R}$ and number of calibrators N. For reasonable distances $\overline{R} < 8$ deg and $N \leq 8$, the target position uncertainty is roughly less than $\sigma_{\theta,\mathrm{meas}} \lesssim 50\mu$as. As before, the turn up at large values of $\overline{R}$ is due to the total time to complete the loop approaching the coherence time.

A useful simplification to Equation 6.18 for values of $\overline{R} > 2$ deg is:

$$\sigma_{\theta,\mathrm{meas}} \approx 0.022\theta_B \frac{\overline{\mathrm{SEFD}}}{S_c} \frac{1}{\sqrt{\Delta\nu}} \text{ mas} \tag{6.19}$$

which makes it clear that the main limitation on the error floor is not number of calibrators or the distance to them, but sensitivity.

There is only a very little detriment as viewed purely from a measurement uncertainty perspective to increasing the angular offset of the orbit sources and adding more calibrators as long as the total cycle time is less than the coherence time. However, this model does not yet include systematic phase offsets. In practice, it is understood that increasing target–calibrator distance will run the risk of a breakdown in the planar assumption and introduce other systematics.

6.5.3.2 Plane Systematic Error

From the equations derived in Chapter 5, it was shown that the systematic underestimation of the *delay* plane (aka. $c\sigma_{\tau,\mathrm{sys}}$ in metres) should take the form:

$$\begin{aligned}(c\sigma_{\tau,\mathrm{sys}})^2 &\leq \overline{R}^4 \left(c^2\sigma_{bl}^2 + c^2\sigma_{\mathrm{iono}}^2 + c^2\sigma_{\mathrm{wet}}^2 + c^2\sigma_{\tau_z}^2 \sec^6 Z_T \left(\sin^2 Z_T + 1\right)^2\right) + \overline{R}^2 \left(\frac{1}{\sqrt{N}}|\mathbf{B}|\sigma_{\mathrm{pos},C}\right)^2 \\ &\leq \overline{R}^4 \left(c^2\sigma_{\mathrm{biw}}^2 + c^2\sigma_{\tau_z}^2 \sec^6 Z_T \left(\sin^2 Z_T + 1\right)^2\right) + \overline{R}^2 \left(\frac{1}{\sqrt{N}}|\mathbf{B}|\sigma_{\mathrm{pos},C}\right)^2\end{aligned} \tag{6.20}$$

where there are the residual delays due to a baseline offset $c\sigma_{bl}$ and error in the measured value of the residual dry tropospheric zenith delay $c\sigma_{\tau_z}$ (both in meters), the target zenith angle Z_T in radians, maximum baseline $|\mathbf{B}|$ in metres, number of calibrators N, 'characteristic' positional uncertainty of the calibrators $\sigma_{\mathrm{pos},C}$ in radians, average target–calibrator separation $\overline{R}$ in radians, delay due to the wet troposphere $c\sigma_{\mathrm{wet}}$ and due to the residual ionosphere $c\sigma_{\mathrm{iono}}$ in meters. The term $c\sigma_{\mathrm{biw}}$ is the quadrature sum of the baseline, wet tropospheric and residual ionospheric delays in metres.

To form this equation I have taken the relationships shown in Equations 5.7, 5.12 and 5.25, relabelled $\theta_{\mathrm{sep}} = \overline{R}$, assumed that both the wet troposphere and residual ionosphere terms have a similar form to Equations 5.7 then added them in quadrature.

6.5.4 Total Uncertainty

The total astrometric accuracy expected from inverse MultiView should therefore be:

$$\begin{aligned}\sigma_\theta^2 = &\left(\frac{\theta_B}{\pi}\right)^2 \left(\frac{\overline{\mathrm{SEFD}}}{S_c}\right)^2 \frac{1}{\Delta\nu} \frac{\overline{R}^2}{\overline{R}^2 + \sigma_R^2} \frac{2N+1}{N\left(T_{\mathrm{coh}} - 2N\left(\frac{\overline{R}}{v_s} + t_{\mathrm{set}}\right)\right)} \\ &+ \overline{R}^4 \frac{1}{|\mathbf{B}|}\left(c^2\sigma_{\mathrm{biw}}^2 + c^2\sigma_{\tau_z}^2 \sec^6 Z_T \left(\sin^2 Z_T + 1\right)^2\right) + \overline{R}^2 \frac{1}{N}\sigma_{\mathrm{pos},C}^2 + \frac{\sigma_{\mathrm{struct}}^2}{N}\end{aligned} \tag{6.21}$$

in where σ_θ is in rads (with θ_B, $\sigma_{\mathrm{pos},C}$ and σ_{struct} in rads). I have introduced a final term to account for random structural evolutionary changes in the quasars σ_{struct}. Since this effect will not correlate between quasars, it is reduced by $\frac{1}{\sqrt{N}}$.

Figure 6.22 shows Equation 6.21 against both $\overline{R}$ and N with the same parameters as the previous examples. These parameters approximately resemble expectations from the ASCI array at 8.2 GHz ($\overline{\mathrm{SEFD}}$ = 2000 Jy, $\theta_B = 2$ mas, etc) and Southern Hemisphere calibration capabilities ($\sigma_{\mathrm{biw}} = 5$ cm, $\sigma_{\tau_z} = 3$ cm with geoblocks). At small radii the dominating term is due to the plane measurement uncertainty with a value of $\sigma_\theta \sim 60$ μas (as comparable to 55μas from Equation 6.19). This uncertainty limit is a linear function of array SEFD and/or inverse function of average source flux density.

The next fundamental limit (for small radii and very low/good array SEFD) is the calibrator positional uncertainty. For the values of $\sigma_{\mathrm{pos},C} = 0.3$ μas, $\sigma_{\mathrm{struct}} = 10$ μas, $N = 6$ and $R \leq 1$, this would be $\sigma_\theta \leq 5$ μas. This uncertainty scales almost linearly with the target-calibrator separation and inverse–squared with the number of calibrators. As I have said previously, inverse MultiView is less affected by calibrator positional uncertainty than phase referencing only because of the larger number of calibrators. However, it is more likely to remove the atmospheric/baseline systematics to allow calibrator positional uncertainty to have any measurable effect. Tied in with the calibrator positional uncertainty is the possibility of source structural changes that may result in apparent quasar proper motions. Firstly, for parallax observations, this motion should not be correlated with the annual sinusoid and should rather systematically offset the proper motion. Secondly, for multi–calibrator experiments this motion should not correlate between quasars and this should serve to reduce systematics in the proper motion by $1/\sqrt{N}$. Therefore Multiview with $N > 2$ should have maximum offsets due to this effect of $5 - 10$ μas/yr (see Section §2.3.7 for more details on source structure).

Figure 6.23 is the case where I have used parameters which more closely match the VLBA at 8.2 GHz, namely $\overline{\mathrm{SEFD}}$ = 300 Jy** and $\theta_B = 0.9$ mas††, $v_s = 55$ deg/min (the average of the azimuth rate of 80 deg/min and the elevation rate of 30 deg/min from SCHED catalogues), $\sigma_{\tau_z} = 1$ cm (with dual frequency SX geoblocks) and $\sigma_{\mathrm{biw}} = 3$ cm (conservative estimate of Northern Hemisphere ionosphere systematics and baseline errors).

As I discussed in Sections §2.3.11, §2.3.11.1 and §5.2.4, it is not unreasonable to assume that at a given time interval, there are both spatial and dynamic terms to the wet troposphere and ionosphere despite their stochastic nature. The initial phase reference from the target to calibrators should remove a large part of the dynamic term for both, while inverse Multiview should remove a large part of the spatial term. What remains is the spatially–dynamic term (aka $\frac{\partial^2\tau}{\partial R \partial t}$, dynamic variations a distance away from the target), which cannot be solved for in a single loop. However, solving the plane equation at every loop or in my case at every scan should serve to also minimise this.

The first order and second order purely dynamic terms are linked to the target–calibrator switching time, which is set to be much lower than the coherence time. At 8.2 GHz the minimum coherence time (out of those due to the wet–troposphere and ionosphere) is $T_{\mathrm{coh,wet}} = 4.5$ min and the switching time I used was $t_{sw} \sim 2$ min (target to calibrator to target). Inverse phase referencing solves for phase and rate on the target at the two bracketing scans then interpolates to the calibrator. This effectively solves for the first-order dynamic term, leaving the second-order term as the error.

The first-order term can vary by $\Delta\phi = 2\pi\sigma_{\mathrm{A,wet}}\nu_{\mathrm{ref}}\frac{t_{sw}}{2} = 12°$ in the time between the target and

**http://www.vlba.nrao.edu/astro/system_plots/SEFD/
††https://public.nrao.edu/telescopes/vlba/

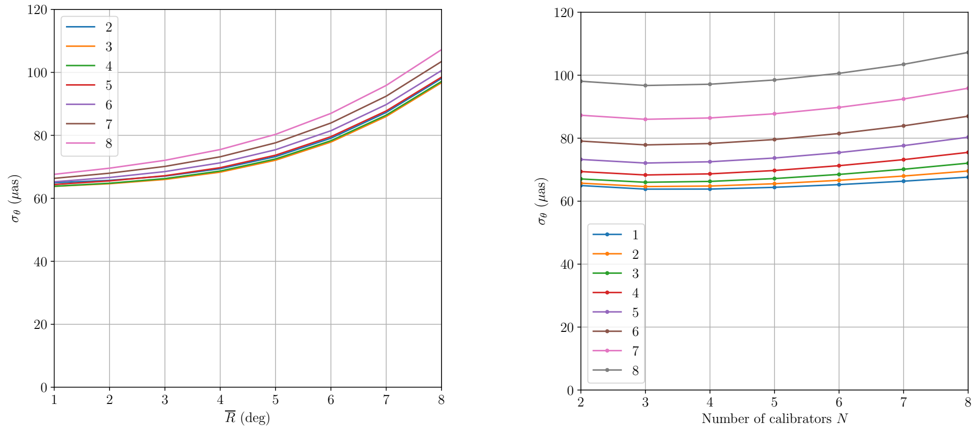

Figure 6.22: Total target position uncertainty σ_θ as a function of- **Left:** $\overline{R}$, with different lines correspond to different values of N given in legend; and **Right:** N, with lines corresponding to different values of $\overline{R}$ given in legend. For all lines $\overline{\text{SEFD}} = 2000$ Jy, $\sigma_R = 1$ deg, $T_{\text{coh}} = 11$ min, $t_{\text{set}} = 10$ s, $v_s = 40$ deg/min, $\overline{S_c} = 100$ mJy, $\Delta\nu = 256$ MHz, $\theta_B = 2$ mas, $\sigma_{\text{biw}} = 5$ cm, $\sigma_{\tau_z} = 3$ cm, $\sigma_{\text{pos},C} = 0.3$ mas and $Z_T = 45$ deg.

calibrator scans (1 min) and the second-order term will be (on average) smaller than the first-order term, otherwise phase referencing would regularly fail. So the phase error should be much smaller than 12° at 8.2 GHz. Finally, this phase error is not constant and will not introduce a systematic shift, but rather serve to randomly perturb the position at each measurement. Final imaging serves to average these phase errors out and they should only serve to increase image noise and hence thermal positional uncertainty rather than cause a systematic positional offset.

Therefore inverse Multiview should remove the first-order spatial, first-order dynamic and partially remove the second-order spatial–dynamic terms, where the uncertainty (known) should approximately be the second-order spatial term and error (unknown) the second-order spatial–dynamic term.

There will be a distance at which inverse MultiView should break down due to this spatially–dynamic term. For early BeSSeL pilot observations and testing periods, target–calibrator separations of $\theta_{sep} \geq 2.5$ deg were found to regularly fail (Mark J. Reid, private communication) due to phase decoherence. If I assume this spatial decoherence at 22.2 GHz is solely due to uncorrelated fluctuations ($\phi_C - \phi_T > 1$ rad) in the wet tropospheric component and the target–calibrator separation at which this happens ($\theta_{\text{wet,max},\nu}$) scales linearly with wavelength:

$$\frac{\theta_{\text{wet,max},\nu}}{\theta_{\text{wet,max},22}} = \frac{22 \text{ GHz}}{\nu} \tag{6.22}$$

then I can establish values for other wavelengths; $\theta_{\text{wet,max},8.2} = 6.6$ deg and $\theta_{\text{wet,max},6.7} = 8.3$ deg. While this does not help establish a similar term for the ionosphere $\theta_{\text{iono,max},8.2}$, it is a reasonable starting point. The smallest value of $\theta_{\text{iono,max},8.2}$ or $\theta_{\text{wet,max},8.2}$ will set the maximum value that coherent solutions should be able to be attained. I will discuss this more in the next section.

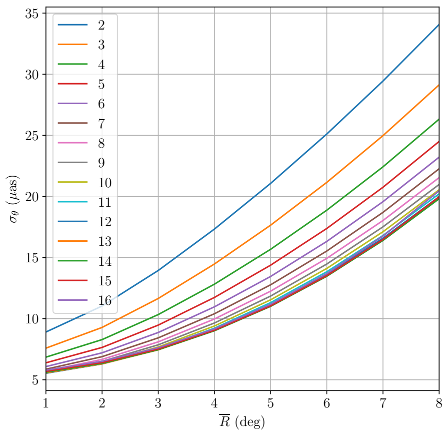

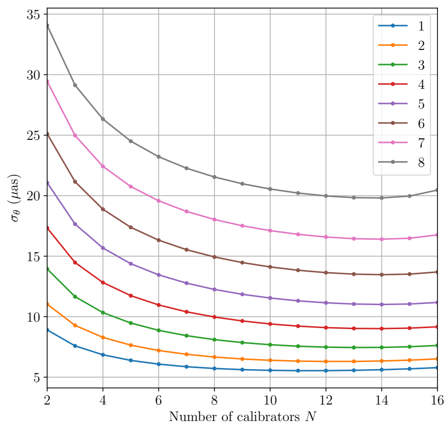

Figure 6.23: Total target position uncertainty σ_θ as a function of- **Left:** $\overline{R}$, with different lines correspond to different values of N given in legend; and **Right:** N, with lines corresponding to different values of $\overline{R}$ given in legend. For all lines $\overline{\text{SEFD}} = 300$ Jy, $\sigma_R = 1$ deg, $T_{\text{coh}} = 11$ min, $t_{\text{set}} = 6$ s, $v_s = 55$ deg/min, $\overline{S_c} = 100$ mJy, $\Delta\nu = 256$ MHz, $\theta_B = 0.9$ mas, $\sigma_{\text{biw}} = 3$ cm, $\sigma_{\tau_z} = 1$ cm, $\sigma_{\text{pos},C} = 0.3$ mas, $\sigma_{\text{struct}} = 10$ μas and $Z_T = 30$ deg.

6.5.5 Comparison with Observations

Figure 6.24 shows Equation 6.21 plotted against the positional scatter in the 4 epochs of experimental data, MV025 to MV028, while Table 6.6 summarised the parameters used.

There is a stark difference between positional uncertainty in East-West and North-South directions. In all cases, calibration applied to the East-West direction results in a *poorer* positional accuracy than the North-South direction. This is in direct contrast to conventional wisdom where synthesised beams are generally elongated in the North-South direction and delay terms are expected to be larger due to dry tropospheric residuals, where changes in declination translate more directly to changes in zenith angle.

I suggest that is due to the phase/delay planes having a time–dependence that is primarily dependent on the hour angle and hence Right Ascension. The slope in the East-West direction changes more rapidly than North-South directions, so phase errors arise quicker in that direction. This can be seen in the measured slopes vs. time plots in Appendix C.2.2). This also implies that sampling the plane primarily in Declination may lead to better overall astrometric solutions.

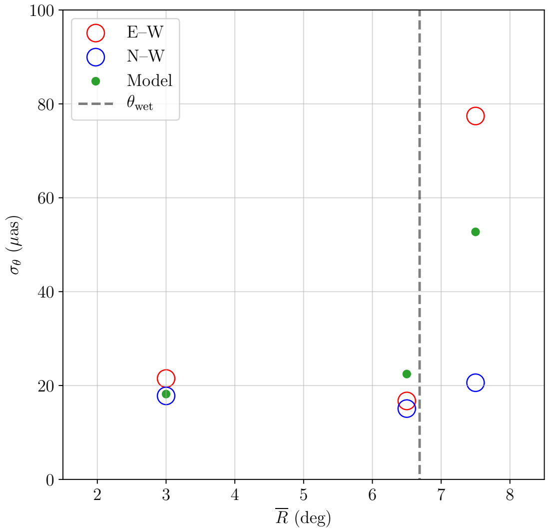

Figure 6.24: Positional scatter over epochs vs. theoretical model for uncertainty at 8.2 GHz. **Coloured circles:** Positional uncertainty from MV025 to MV028 epochs in East–West/Right Ascention (red) and North–South/Declination (blue) directions respectively. **Green points:** Model with known and estimated parameters for each ring as given in Table 6.6. **Black dashed line:** Expected radius that wet–tropospheric decoherence occurs $\theta_{\rm wet,max,8.2} = 6.6$ deg. For all green points: $\overline{\rm SEFD} = 2000$ Jy, $T_{\rm coh} = 11$ min, $t_{\rm set} = 10$ s, $v_s = 40$ deg/min, $\Delta\nu = 256$ MHz, $\theta_B = 2$ mas, $\sigma_{{\rm pos},C} = 0.3$ mas, $\sigma_{\rm struct} = 10$ μas and $Z_T = 30$ deg.

There seems to be a moderate agreement between model and astrometric trends, and numerical agreement for certain parameter combinations. This modelling agrees with of residual delay present in calibrated data was of order $c\sqrt{\sigma^2_{\rm biw} + \sigma^2_{\tau_z}} \sim 6 \pm 1$ cm, where the majority is in the combination of baseline, ionospheric and wet–tropospheric delays. Since the baselines were updated to ~ 3 cm and the wet–troposphere is ~ 1 cm, it is reasonable to assume the possible LOS residual ionosphere was ~ 5 cm as expected from Walker & Chatterjee (1999).

Table 6.6: Ring–dependent model parameters used in Equation 6.21 compare model to observations. **Column (1:)** Target source in ring aka ring name; **(2:)** Average target–calibrator separation/ring radius in degrees; **(3:)** radial scatter in degrees; **(4:)** Number of calibrators in ring; **(5:)** Average calibrator flux density in ring over all four epochs; **(6:)** Quadrature sum of baseline, residual ionosphere and wet–tropospheric uncertainties in cm; **(7:)** Residual dry tropospheric zenith delay error in cm.

Ring	$\overline{R}$ (deg)	σ_R (deg)	N	$\overline{S}_c$ (mJy)	$c\sigma_{\rm biw}$ (cm)	$c\sigma_{\tau_z}$ (cm)
G0634–2335	3.0	1	6	280	7	3
G1901–2112	7.5	0.5	5	290	3	1
G1336–0809	6.5	0.5	6	180	4	3

The astrometric uncertainty in the Right Ascension direction increases after $R > \theta_{\rm wet,max,8.2}$. Whether this is due to the spatial-temporal decoherence of the wet–troposphere (in only that direction), larger delays than those estimated in Table 6.6 or systematic plane fitting error at the large radius, is unknown. However, the data presented here implied that spatial-temporal decoherence due to either the residual ionosphere or wet–troposphere at 8.2 GHz should occur after $R > 6.5$ deg.

6.6 Final comments

The VLBA can achieve parallax accuracy that can be better than 10μas, representative of a per–epoch target positional uncertainty around $\sim 20 - 40$ μas (depending on the number of epochs). Key to this accuracy is that they can use a wideband system to get accurate estimates of the zenith tropospheric delay and that there is also a good a priori ionospheric delay model available from GPS measurements. They also benefit from comprehensive quasar catalogues which allow multiple quasars to be found within 1–2 degrees of the target source.

We have an array where some of the antennas do not have dual-band or wideband receiver systems which reduces the accuracy of the tropospheric zenith delay determination significantly (further exacerbated by slow slewing of some antennas reducing the sampling of the sky in geoblocks). The ionospheric models and the quasar catalogues are poorer. So to achieve the same sort of accuracy that they have with the VLBA we either need a VLBA in the south and the time to expand the quasar catalogue or a different method.

I have shown the methodology and reduction processes to achieve microsecond astrometry in the Southern Hemisphere. Inverse MultiView appears promising as a method to achieve high astrometric accuracy even in the suspected presence of large residual delays, almost regardless of the cause. Using the empirical model (Equation 6.21) as applicable to SπRALS observing frequency of 6.7 GHz with target quasars $\overline{S} = 250$ mJy in the presence of $|c\tau| = 5$ cm residual delays, I predict a per–epoch astrometric uncertainty $\sigma_\theta \leq 40\mu$as. With 8 parallax epochs spread over a year this would give a parallax error $\sigma_\varpi \approx \frac{\sigma_\theta}{\sqrt{8}} = 14\mu$as.

Therefore inverse MultiView will be the astrometric calibration scheme for SπRALS . The selected masers (Chapter 4) are compact and luminous, allowing for easy phase-detection within a scan. Immediate future work is quasar classification within ~ 8 deg of target masers. While quasar classifications exist, additional surveys to measure quasars as detectable by the ASCI array would be very beneficial.

As astrometric uncertainty and minimum possible astrometric accuracy depends on slope measurement certainty and therefore SNR, I recommend strong SNR $= 10 - 15$ detections. This additionally limits the total number of calibrators.

The ideal number of orbit sources is the minimum that optimally samples azimuthally while staying under a total loop time of $10 - 11$ min. While 4 is the practical minimum (for non–linear arrangements), not only is it unlikely to have 4 orbit sources in optimal spacing, it only leaves one free parameter for estimating residuals and for redundancy. A good rule of thumb is 5 orbit sources if optimally spaced or 6 to achieve it. If calibrator positional errors are expected to dominate, then the more calibrators that can be observed within the spatial coherence time and coherent radius the better.

While these experiments suggest that inverse MultiView can calibrate residual delay up to the measurement and/or calibrator positional uncertainty, it remains beneficial to include additional calibration overheads such as tropospheric zenith delay determining 'geoblocks'. Good *a priori* delay calibration is key to solving for position offsets in the phase domain- theoretically, too much residual delay will cause phase planes to be too steep and phases to wrap.

I have applied MultiView 12 times (4 epochs x 3 sources) and it has worked on each occasion, even out to target–calibrator separations of 7–8 degrees. Therefore the technique seems robust. The observations to date only span a limited range of times and a single frequency, but there is no reason to expect that comparable observations at other frequencies and other arrays cannot be similarly successful. MultiView should increase the centimetre wavelength accuracy achievable with heterogeneous arrays such as the LBA, EVN and East-Asian VLBI Network (EAVN) - which at the moment perform much less well than the VLBA astrometrically.

The obvious application of inverse MultiView is to test the current limit of astrometric accuracy on the VLBA, however, I will discuss that more in the final chapter.

7

Conclusion

Since the inception of BeSSeL and resultant accurate determination of Galactic structure as visible from the Northern Hemisphere, the astrometric community has strived to do the same in the Southern Hemisphere. Early attempts on the LBA were affected by suspected ionospheric effects, limited mutual bandwidth on the heterogeneous array and time unavailability. With the material contained within this thesis, it should now be possible to determine the structure and kinematics of the Galaxy as visible from Southern Hemisphere. This is a significant breakthrough.

7.1 Summary of Results

I reduce BeSSeL data and measure the proper motion and parallax for three 22 GHz water masers and a 6.7 GHz methanol maser. With these measurements, I determine distances for the host star-forming regions and use these distances to place all four masers in the Perseus arm of the Galaxy. Finally, I combine my results with previously known Perseus arm maser parallaxes to calculate a Perseus spiral arm pitch angle.

I conduct a targeted VLBI survey of all known Southern Hemisphere 6.7 GHz methanol masers with flux density > 10 Jy. I model spatial and energetic properties for each maser velocity feature and determine overall maser compactness. I catalogue the individual maser properties and compactness for future studies and select out the best targets for astrometry.

I introduce and discuss inverse MultiView calibration. I derive relationships to predict how inverse MultiView will be able to remove residual delays. I find that inverse MultiView is robust to target source positional uncertainties, baseline, ionosphere and troposphere delay uncertainties given prior calibration. I expect uncertainty in inverse MultiView calibration to increase as separation (in radians) squared θ^2 rather than θ for traditional phase referencing.

Finally, I conduct pilot SπRALS observations using quasars to test inverse MultiView and the BeSSeL observation/calibration approaches as applicable to the new ASCI array. This process involves scheduling, observing, correlating, data reduction, inverse MultiView application and astrometric analysis. I find that inverse MultiView allows the ASCI array to achieve micro-arcsecond astrometry out to average target–calibrator separations ~ 7.5 deg.

7.2 Current and Future work

SπRALS began pilot observations of 6.7 GHz methanol masers in September 2019 and fully began taking observations in May 2020. At the time of writing, over 400 hours of data have been collected. All SπRALS targets have been $A-$grade sources as catalogued. Early astrometric estimates show that inverse MultiView is working at the level of $40 - 60\mu$as per epoch, in–line with expectations.

Before pilot observations began, Warkworth Radio Astronomical Observatory, New Zealand joined the SπRALS collaboration. They brought access to the Warkworth 30m radio telescope into ASCI. This extends the maximum baseline from Hobart–Katherine at $|\mathbf{B}| = 3500$ km to Yarragadee–Warkworth at $|\mathbf{B}| = 5500$ km and increases the array sensitivity.

Ceduna 30m, Yarragadee 12m and Warkworth 30m have a planned receiver upgrade. While all three upgrades are at various stages, all three are very likely to be completed in the next year. All receivers will have a mutual spanned bandwidth of at least 3–7 or 8 GHz. This spanned bandwidth will allow dispersive delay removal during geoblock fitting and consequential accurate zenith tropospheric delay determination. I presented evidence to suggest a large amount of residual zenith delay (5 cm) in inverse MultiView test observations from the phase slopes, so accurate determination would most likely leave only ionosphere residuals above 1 cm. As residual dry tropospheric delay tends to diverge at an elevation dependant target–calibrator radius compared to the delay slopes expected from the much thinner ionosphere, this may allow either an extension to how low in elevation tracks can be or an observing scheme comprised of only one low–elevation track.

The parallax measured for the 22 GHz water maser G021.87+0.01 was not sufficiently constrained by the astrometry to directly determine a distance. This was largely due to observed source evolution and/or flux density variability common in water masers. It would be beneficial to independently confirm the distance of $D = 13.7$ kpc as I determined from kinematic models of recession velocity and proper motion. The region in question appears to have a nearby 6.7 GHz methanol maser G021.880+0.014 (Caswell et al., 1995b; Breen et al., 2015). The methanol maser G021.880+0.014 is offset 0.6 amin from water maser G021.87+0.01 with identical velocity range $v = 17$ to $22\,\mathrm{km\,s^{-1}}$. However, the methanol maser has a catalogued flux density between $S = 15$ and 5 Jy with unknown compactness. Therefore, it is not immediately obvious whether it is suitable for inverse phase referencing or inverse MultiView.

As I saw from the reduction of G021.87+0.01, only the nearby calibrator J1825–0737 at $\Delta\theta =$ 2.566 deg was suitable for phase referencing (at ~ 200 mJy). The other calibrator J1835–1115 at $\Delta\theta = 1.793$ deg was too–weak (~ 20 mJy). In the neighbourhood of $\Delta\theta < 6$ deg there are 9 quasars suitable for phase referencing; all appear compact and have flux densities $S > 80$ mJy. Depending on the compactness of the quasar, this could prove to be a very good chance to test non–inverse MultiView (by phase referencing on a quasar and interpolating phase slopes to maser) or inverse MultiView on the VLBA. Ideally, I would do initial observations of the maser and calibrators within $\theta_{\mathrm{sep}} > 8$ deg separation, perform similar analysis as Chapter §4 and/or Immer et al. (2011), then plan accordingly.

I chose to conduct the MultiView tests at X-band, however, there is little preventing a repeat of observations at S-band (~ 2 GHz). All ASCI array telescopes (and the possible inclusion of Warkworth 12m) have access to S-band receivers, so there is the possibility to test whether MultiView holds up as residual delays increase on the target solely due to the ionosphere. I attributed the majority of the measured phase slopes at X–band to the residual dry troposphere, however, at S-band the ionosphere and variations to it should be dominant. I intend to pursue this in a future study.

If dry tropospheric residuals, baseline offsets and ionospheric residuals were brought down to VLBA levels of $c\sigma_\tau < 3$ cm, with dual-frequency geodetic blocks, for a target–calibrator separation of 3 deg, for $N \geq 5$ with good azimuthal sampling, I calculate the inverse MultiView should be able to achieve an astrometric accuracy of $\sigma_\theta = 5$ μas per epoch for these effects. However, this does not include systematic core–shift or quasar proper motion effects. Multi-frequency observations utilising the fast–frequency systems at the VLBA may be able to resolve the core–shift phenomena (e.g. Dodson et al., 2017) as it combines with the ionospheric delay model (Porcas, 2009), however, I do not see how apparent quasar proper motions can be calibrated. Nevertheless, if quasar apparent motion is the limiting factor at (conservatively) 10 μas *per epoch*, then as always, multiple epochs and the sinusoidal parallax signature may allow parallax to be determined accurately (rather than formally) down past the 3μas point in 8 epochs.

The application of the high astrometric accuracy provided by MultiView carrying the most impact may be the ability to measure parallaxes to masers in the Large Magellanic Cloud (Green et al., 2008, 2009; Imai et al., 2013). While this is not currently possible from a logistical perspective, it is no longer impossible. The ability to directly measure distances to star formation regions at ~ 50 kpc would affect the whole cosmic distance ladder by almost an order of magnitude; allowing the whole Universe to be brought into sharper focus.

Another very promising avenues are low–frequency astrometry, which struggles to surpass the limits of the ionosphere. Pulsar astrometry (Deller et al., 2019) rely heavily on in-beam calibrators to achieve microsecond astrometry due to the overwhelming influence of the ionosphere at low frequencies (1.66 GHz). Even for target–calibrator separations 0.5 deg, which would be an in–beam calibrator on the VLBA, a residual TEC of the only 1 TECU at 1.66 GHz would mean a delay difference of almost 15 cm! At 0.5 deg separation this constitutes an astrometric accuracy of 35μas, however, this requires the existence of an in-beam calibrator. The ionosphere is largely planar at even lower frequencies (≤ 150 MHz; Rioja et al., 2018, and given good weather) so MultiView should be able to achieve the θ^2 dependence of plane fitting. With a similar setup at 1 deg separation, MultiView should achieve 20μas per epoch.

I am confident in saying that the most significant result of this thesis is the demonstration of inverse MultiView calibration. Trigonometric parallax is the gold standard for distance estimates in astronomy and any ability to increase the accuracy that parallaxes can be determined affects all aspects of astronomy and cosmology. Inverse MultiView has the potential to be the next big leap in astrometric calibration, one that may allow accurate distance determination order of magnitude larger.

BIBLIOGRAPHY

Abellán, F. J., Martí-Vidal, I., Marcaide, J. M., & Guirado, J. C. 2018, A&A, 614, A74

Amaral, L. H., & Lepine, J. R. D. 1997, MNRAS, 286, 885

Antoja, T., Figueras, F., Romero-Gómez, M., et al. 2011, MNRAS, 418, 1423

Asaki, Y., Imai, H., Sobolev, A. M., & Parfenov, S. Y. 2014, ApJ, 787, 54

Asaki, Y., Sudou, H., Kono, Y., et al. 2007, PASJ, 59, 397

Asiain, R., Figueras, F., & Torra, J. 1999, A&A, 350, 434

Bailer-Jones, C. A. L. 2015, PASP, 127, 994

Barnard, E. E. 1916, AJ, 29, 181

Bartkiewicz, A., Szymczak, M., van Langevelde, H. J., Richards, A. M. S., & Pihlström, Y. M. 2009, A&A, 502, 155

Batrla, W., Matthews, H. E., Menten, K. M., & Walmsley, C. M. 1987, Nature, 326, 49

Benjamin, R. A. 2008, in Astronomical Society of the Pacific Conference Series, Vol. 387, Massive Star Formation: Observations Confront Theory, ed. H. Beuther, H. Linz, & T. Henning, 375

Bhat, N. D. R., Cordes, J. M., Camilo, F., Nice, D. J., & Lorimer, D. R. 2004, ApJ, 605, 759

Blandford, R. D., & Königl, A. 1979, ApJ, 232, 34

Blitz, L. 1979, ApJ, 231, L115

Böckmann, S., Artz, T., & Nothnagel, A. 2010, Journal of Geodesy, 84, 201

Brand, J., Cesaroni, R., Comoretto, G., et al. 2003, A&A, 407, 573

Breen, S. L., Ellingsen, S. P., Caswell, J. L., et al. 2016, MNRAS, 459, 4066

Breen, S. L., Ellingsen, S. P., Contreras, Y., et al. 2013, MNRAS, 435, 524

Breen, S. L., Fuller, G. A., Caswell, J. L., et al. 2015, MNRAS, 450, 4109

Bronfman, L., Nyman, L. A., & May, J. 1996, A&AS, 115, 81

Brunthaler, A., Reid, M. J., Menten, K. M., et al. 2011, Astronomische Nachrichten, 332, 461

Burns, R. A., Handa, T., Nagayama, T., Sunada, K., & Omodaka, T. 2016, MNRAS, 460, 283

Burns, R. A., Imai, H., Handa, T., et al. 2015, MNRAS, 453, 3163

Burns, R. A., Handa, T., Imai, H., et al. 2017, MNRAS, 467, 2367

Burns, R. A., Sugiyama, K., Hirota, T., et al. 2020a, Nature Astronomy, 10

Burns, R. A., Orosz, G., Bayandina, O., et al. 2020b, MNRAS, 491, 4069

Capitaine, N. 2017, in The Science of Time 2016, ed. E. F. Arias, L. Combrinck, P. Gabor, C. Hohenkerk, & P. K. Seidelmann, Vol. 50, 167–196

Capitaine, N., Klioner, S., & McCarthy, D. 2012, in IAU Joint Discussion, Vol. 7, IAU Joint Discussion, 40

Carroll, B. W., & Ostlie, D. A. 2017, An Introduction to Modern Astrophysics, 2nd edn. (Cambridge University Press), doi:10.1017/9781108380980

Caswell, J. L. 1997, MNRAS, 289, 203

Caswell, J. L., & Haynes, R. F. 1987, A&A, 171, 261

Caswell, J. L., Vaile, R. A., & Ellingsen, S. P. 1995a, PASA, 12, 37

Caswell, J. L., Vaile, R. A., Ellingsen, S. P., Whiteoak, J. B., & Norris, R. P. 1995b, MNRAS, 272, 96

Caswell, J. L., Fuller, G. A., Green, J. A., et al. 2010, MNRAS, 404, 1029

—. 2011, MNRAS, 417, 1964

Charlot, P. 1990, AJ, 99, 1309

Charlot, P., Jacobs, C. S., Gordon, D., et al. 2020, A&A, 644, A159

Cheung, A. C., Rank, D. M., Townes, C. H., Thornton, D. D., & Welch, W. J. 1969, Nature, 221, 626

Choi, Y. K., Hachisuka, K., Reid, M. J., et al. 2014, ApJ, 790, 99

Cordes, J. 2001, Ap&SS, 278, 11

Cordes, J. M. 2004, in Astronomical Society of the Pacific Conference Series, Vol. 317, Milky Way Surveys: The Structure and Evolution of our Galaxy, ed. D. Clemens, R. Shah, & T. Brainerd, 211

Cordes, J. M., & Lazio, T. J. 1991, ApJ, 376, 123

Cordes, J. M., Weisberg, J. M., Frail, D. A., Spangler, S. R., & Ryan, M. 1991, Nature, 354, 121

Cornwell, T. J. 1989, Science, 245, 263

Dame, T. M., Hartmann, D., & Thaddeus, P. 2001, ApJ, 547, 792

de Bruijne, J. H. J., Allen, M., Azaz, S., et al. 2015, A&A, 576, A74

de Vaucouleurs, G. 1959, Handbuch der Physik, 53, 275 de Vaucouleurs, G., de Vaucouleurs, A., Corwin, Jr., H. G., et al. 1991, Third Reference Catalogue of Bright Galaxies. Volume I: Explanations and references. Volume II: Data for galaxies between 0^h and 12^h. Volume III: Data for galaxies between 12^h and 24^h.

de Vaucouleurs, G., & Pence, W. D. 1978, AJ, 83, 1163

Deller, A. T., Tingay, S. J., Bailes, M., & West, C. 2007, PASP, 119, 318

Deller, A. T., Brisken, W. F., Phillips, C. J., et al. 2011, PASP, 123, 275

Deller, A. T., Goss, W. M., Brisken, W. F., et al. 2019, ApJ, 875, 100

Dickey, J. M., & Lockman, F. J. 1990, ARA&A, 28, 215

Dodson, R., Rioja, M., Asaki, Y., et al. 2013, AJ, 145, 147

Dodson, R., Rioja, M. J., Molina, S. N., & Gómez, J. L. 2017, ApJ, 834, 177

Dos Santos, P. M., & Lepine, J. R. D. 1979, Nature, 278, 34

Dougherty, S. M., & Perley, R. 2011, Bulletin de la Societe Royale des Sciences de Liege, 80, 491

Draine, B. T. 2010, Physics of the Interstellar and Intergalactic Medium (Princeton University Press)

Drimmel, R. 2000, A&A, 358, L13

Drimmel, R., & Spergel, D. N. 2001, ApJ, 556, 181

Elitzur, M. 1992, ARA&A, 30, 75

Ellingsen, S. P. 1996, PhD thesis, Physics Department, University of Tasmania, GPO Box 252C, Hobart 7001, Australia

—. 2006, ApJ, 638, 241

Ellingsen, S. P., Voronkov, M. A., Cragg, D. M., et al. 2007, in IAU Symposium, Vol. 242, IAU Symposium, ed. J. M. Chapman & W. A. Baan, 213–217

Ellsworth-Bowers, T. P., Rosolowsky, E., Glenn, J., et al. 2015, ApJ, 799, 29

Englmaier, P. 2000, in Reviews in Modern Astronomy, Vol. 13, Reviews in Modern Astronomy, ed. R. E. Schielicke, 97

Englmaier, P., & Gerhard, O. 1999, in Astronomical Society of the Pacific Conference Series, Vol. 182, Galaxy Dynamics - A Rutgers Symposium, ed. D. R. Merritt, M. Valluri, & J. A. Sellwood

Englmaier, P., Pohl, M., & Bissantz, N. 2011, Memorie della Societa Astronomica Italiana Supplementi, 18, 199

Fernández, D., Figueras, F., & Torra, J. 2001, A&A, 372, 833

Fernie, J. D. 1969, PASP, 81, 707

Fey, A. L., Spangler, S. R., & Cordes, J. M. 1991, ApJ, 372, 132

Fich, M., Blitz, L., & Stark, A. A. 1989, ApJ, 342, 272

Foster, T., & Cooper, B. 2010, in Astronomical Society of the Pacific Conference Series, Vol. 438, The Dynamic Interstellar Medium: A Celebration of the Canadian Galactic Plane Survey, ed. R. Kothes, T. L. Landecker, & A. G. Willis, 16

Francis, C., & Anderson, E. 2009, Proceedings of the Royal Society of London Series A, 465, 3425

Gaia Collaboration, Brown, A. G. A., Vallenari, A., et al. 2018, A&A, 616, A1

Georgelin, Y. M., & Georgelin, Y. P. 1976, A&A, 49, 57

Gettelman, A., Salby, M. L., & Sassi, F. 2002, Journal of Geophysical Research (Atmospheres), 107, 4080

Goedhart, S., Gaylard, M. J., & van der Walt, D. J. 2004, MNRAS, 355, 553

Goedhart, S., Minier, V., Gaylard, M. J., & van der Walt, D. J. 2005a, MNRAS, 356, 839

—. 2005b, MNRAS, 356, 839

Gómez, G. C. 2006, AJ, 132, 2376

Gontier, A. M., Feissel, M., & Ma, C. 1997, IERS Technical Note, 23, I

Gordon, J. P., Zeiger, H. J., & Townes, C. H. 1955, Physical Review, 99, 1264

Gray, M. 2012, Maser Sources in Astrophysics

Green, J., Van Langevelde, H. J., Brunthaler, A., et al. 2015, Advancing Astrophysics with the Square Kilometre Array (AASKA14), 119

Green, J. A., & McClure-Griffiths, N. M. 2011, MNRAS, 417, 2500

Green, J. A., Caswell, J. L., Fuller, G. A., et al. 2008, MNRAS, 385, 948

Green, J. A., Caswell, J. L., Fuller, G. A., et al. 2009, in The Magellanic System: Stars, Gas, and Galaxies, ed. J. T. Van Loon & J. M. Oliveira, Vol. 256, 227–232

—. 2010, MNRAS, 409, 913

Green, J. A., Caswell, J. L., McClure-Griffiths, N. M., et al. 2011, ApJ, 733, 27

Green, J. A., Caswell, J. L., Fuller, G. A., et al. 2012, MNRAS, 420, 3108

Green, J. A., Breen, S. L., Fuller, G. A., et al. 2017, MNRAS, 469, 1383

Greisen, E. W. 1990, in Acquisition, Processing and Archiving of Astronomical Images, 125–142

Hachisuka, K., Brunthaler, A., Menten, K. M., et al. 2009, ApJ, 696, 1981

Hachisuka, K., Choi, Y. K., Reid, M. J., et al. 2015, ApJ, 800, 2

Hawarey, M., Hobiger, T., & Schuh, H. 2005, Geophys. Res. Lett., 32, L11304

Henderson, A. P. 1977, A&A, 58, 189

Högbom, J. A. 1974, A&AS, 15, 417

Honma, M. 2013, in Astronomical Society of the Pacific Conference Series, Vol. 476, New Trends in Radio Astronomy in the ALMA Era: The 30th Anniversary of Nobeyama Radio Observatory, ed. R. Kawabe, N. Kuno, & S. Yamamoto, 81

Honma, M., Nagayama, T., & Sakai, N. 2015, PASJ, 67, 70

Honma, M., Tamura, Y., & Reid, M. J. 2008, PASJ, 60, 951

Honma, M., Fujii, T., Hirota, T., et al. 2003, PASJ, 55, L57

Honma, M., Bushimata, T., Choi, Y. K., et al. 2007, PASJ, 59, 889

Hou, L. G., & Han, J. L. 2014, A&A, 569, A125

Hou, L. G., Han, J. L., & Shi, W. B. 2009, A&A, 499, 473

Hubble, E. 1926, Contributions from the Mount Wilson Observatory / Carnegie Institution of Washington, 324, 1

Hubble, E. P. 1936, Realm of the Nebulae

Hyland, L. J. 2015, Master's thesis, Physical Sciences

Hyland, L. J., Ellingsen, S. P., & Reid, M. J. 2018, in IAU Symposium, Vol. 336, Astrophysical Masers: Unlocking the Mysteries of the Universe, ed. A. Tarchi, M. J. Reid, & P. Castangia, 154–157

Igoshev, A., Verbunt, F., & Cator, E. 2016, A&A, 591, A123

Imai, H., Burns, R. A., Yamada, Y., et al. 2016, ArXiv e-prints, arXiv:1603.02042

Imai, H., Katayama, Y., Ellingsen, S. P., & Hagiwara, Y. 2013, MNRAS, 432, L16

Immer, K., Reid, M. J., Menten, K. M., Brunthaler, A., & Dame, T. M. 2013, A&A, 553, A117

Immer, K., Brunthaler, A., Reid, M. J., et al. 2011, ApJS, 194, 25

Jansen, P., Kleiner, I., Xu, L.-H., Ubachs, W., & Bethlem, H. 2011, Physical Review A - PHYS REV A, 84, doi:10.1103/PhysRevA.84.06250

Junqueira, T. C., Chiappini, C., Lépine, J. R. D., Minchev, I., & Santiago, B. X. 2015, MNRAS, 449, 2336

Kellermann, K. I., Pauliny-Toth, I. I. K., & Williams, P. J. S. 1969, ApJ, 157, 1

Kettenis, M., van Langevelde, H. J., Reynolds, C., & Cotton, B. 2006, Astronomical Society of the Pacific Conference Series, Vol. 351, ParselTongue: AIPS Talking Python, ed. C. Gabriel, C. Arviset, D. Ponz, & S. Enrique, 497

Kohoutek, L. 1965, Bulletin of the Astronomical Institutes of Czechoslovakia, 16, 221

Kounkel, M., Hartmann, L., Loinard, L., et al. 2017, ApJ, 834, 142

Kovalev, Y. Y., Lobanov, A. P., Pushkarev, A. B., & Zensus, J. A. 2008, A&A, 483, 759

Krishnan, V., Ellingsen, S. P., Reid, M. J., et al. 2017, MNRAS, 465, 1095

—. 2015, ApJ, 805, 129

Lépine, J. R. D., Mishurov, Y. N., & Dedikov, S. Y. 2001, ApJ, 546, 234

Lépine, J. R. D., Roman-Lopes, A., Abraham, Z., Junqueira, T. C., & Mishurov, Y. N. 2011, MNRAS, 414, 1607

Levine, E. S., Blitz, L., & Heiles, C. 2006, Science, 312, 1773

Lin, C. C., & Shu, F. H. 1964, ApJ, 140, 646

Lockman, F. J. 1979, ApJ, 232, 761

Lockman, F. J. 2002, in Astronomical Society of the Pacific Conference Series, Vol. 276, Seeing Through the Dust: The Detection of HI and the Exploration of the ISM in Galaxies, ed. A. R. Taylor, T. L. Landecker, & A. G. Willis, 107

Lovell, J. E. J., McCallum, J. N., Reid, P. B., et al. 2013, Journal of Geodesy, 87, 527

Lutz, T. E., & Kelker, D. H. 1973, PASP, 85, 573

Ma, C., Arias, E. F., Bianco, G., et al. 2009, IERS Technical Note, 35, 1

MacLeod, G. C., Smits, D. P., Green, J. A., & van den Heever, S. P. 2021, MNRAS, 502, 5658

MacLeod, G. C., Smits, D. P., Goedhart, S., et al. 2018, MNRAS, 478, 1077

Malkin, Z., Jacobs, C., Arias, F., et al. 2015, in Journées 2014 "Systèmes de référence spatio-temporels", ed. Z. Malkin & N. Capitaine, 3–8

Marcaide, J. M., Elosegui, P., & Shapiro, I. I. 1994, AJ, 108, 368

Marcaide, J. M., Shapiro, I. I., Corey, B. E., et al. 1985, A&A, 142, 71

Marochnik, L. S., Mishurov, Y. N., & Suchkov, A. A. 1972, Ap&SS, 19, 285

Martí-Vidal, I., Abellán, F. J., Marcaide, J. M., et al. 2016, A&A, 596, A27

Martin-Pintado, J., Bachiller, R., & Fuente, A. 1992, A&A, 254, 315

Martos, M., Hernandez, X., Yáñez, M., Moreno, E., & Pichardo, B. 2004, MNRAS, 350, L47

McClure-Griffiths, N. M., & Dickey, J. M. 2007, ApJ, 671, 427

—. 2016a, ApJ, 831, 124

—. 2016b, ArXiv e-prints, arXiv:1608.03683

McCulloch, P. M., Ellingsen, S. P., Jauncey, D. L., et al. 2005, AJ, 129, 2034

Melis, C., Reid, M. J., Mioduszewski, A. J., Stauffer, J. R., & Bower, G. C. 2013, in IAU Symposium, Vol. 289, Advancing the Physics of Cosmic Distances, ed. R. de Grijs, 60–65

Melis, C., Reid, M. J., Mioduszewski, A. J., Stauffer, J. R., & Bower, G. C. 2014, Science, 345, 1029

Menten, K. M. 1991a, in Astronomical Society of the Pacific Conference Series, Vol. 16, Atoms, Ions and Molecules: New Results in Spectral Line Astrophysics, ed. A. D. Haschick & P. T. P. Ho, 119–136

Menten, K. M. 1991b, ApJ, 380, L75

Menten, K. M., Reid, M. J., Pratap, P., Moran, J. M., & Wilson, T. L. 1992, ApJ, 401, L39

Merritt, D. 1999, PASP, 111, 129

Minier, V., Booth, R. S., & Conway, J. E. 2002, A&A, 383, 614

Moran, J. M., & Rosen, B. R. 1981, Radio Science, 16, 235

Moscadelli, L., Reid, M. J., Menten, K. M., et al. 2009, ApJ, 693, 406

Müller, H. S. P., Menten, K. M., & Mäder, H. 2004, A&A, 428, 1019

Nakanishi, H. 2005, Astronomical Herald, 98, 670

Nakanishi, H., & Sofue, Y. 2003, PASJ, 55, 191

—. 2006, PASJ, 58, 847

—. 2016, PASJ, 68, 5

Naudet, C. J. 1996, Telecommunications and Data Acquisition Progress Report, 126, 1

Neufeld, D. A., Melnick, G. J., Kaufman, M. J., et al. 2017, ApJ, 843, 94

Niell, A. E. 1996, J. Geophys. Res., 101, 3227

Nothnagel, A., Nilsson, T., & Schuh, H. 2018, Space Sci. Rev., 214, 66

Oh, C. S., Kobayashi, H., Honma, M., et al. 2010, PASJ, 62, 101

Oort, J. H., Kerr, F. J., & Westerhout, G. 1958, MNRAS, 118, 379

Orosz, G., Dodson, R., Imai, H., et al. 2014, Testing methods for accurate OH maser astrometry, ATNF Proposal

Orosz, G., Imai, H., Dodson, R., et al. 2017, AJ, 153, 119

Orosz, G., Gómez, J. F., Imai, H., et al. 2019, MNRAS, 482, L40

Osterbrock, D. E. 2005, Astrophysics Of Gas Nebulae and Active Galactic Nuclei (University Science Books)

Oudmaijer, R. D., Groenewegen, M. A. T., & Schrijver, H. 1998, MNRAS, 294, L41

Perley, R. A., Schwab, F. R., & Bridle, A. H., eds. 1989, Astronomical Society of the Pacific Conference Series, Vol. 6, Synthesis imaging in radio astronomy: a collection of lectures from the third NRAO synthesis imaging summer school

Perryman, M. 2012, European Physical Journal H, 37, 745

Perryman, M. A. C. 2002, Ap&SS, 280, 1

Perryman, M. A. C., Lindegren, L., Kovalevsky, J., et al. 1997, A&A, 500, 501

Perryman, M. A. C., de Boer, K. S., Gilmore, G., et al. 2001, A&A, 369, 339

Petrov, L., Gordon, D., Gipson, J., et al. 2009a, Journal of Geodesy, 83, 859

Petrov, L., Natusch, T., Weston, S., et al. 2015, PASP, 127, 516

Petrov, L., Phillips, C., Bertarini, A., et al. 2009b, PASA, 26, 75

Phillips, C. J., Norris, R. P., Ellingsen, S. P., & McCulloch, P. M. 1998, MNRAS, 300, 1131

Poleski, R. 2013, arXiv e-prints, arXiv:1306.2945

Porcas, R. W. 2009, A&A, 505, L1

Pradel, N., Charlot, P., & Lestrade, J. F. 2006, A&A, 452, 1099

Pushkarev, A. B., & Kovalev, Y. Y. 2015, MNRAS, 452, 4274

Quiroga, R. J. 1977, Ap&SS, 50, 281

Quiroga-Nuñez, L. H., Immer, K., van Langevelde, H. J., Reid, M. J., & Burns, R. A. 2019, A&A, 625, A70

Radcliffe, J. F., Garrett, M. A., Beswick, R. J., et al. 2016, A&A, 587, A85

Reid, M. J. 1993, ARA&A, 31, 345

Reid, M. J. 2008, in Revista Mexicana de Astronomia y Astrofisica Conference Series, Vol. 34, Revista Mexicana de Astronomia y Astrofisica Conference Series, 53–59

Reid, M. J., Dame, T. M., Menten, K. M., & Brunthaler, A. 2016, ApJ, 823, 77

Reid, M. J., & Honma, M. 2014, ARA&A, 52, 339

Reid, M. J., Menten, K. M., Brunthaler, A., & Moellenbrock, G. A. 2009a, in ArXiv Astrophysics e-prints, Vol. 2010, astro2010: The Astronomy and Astrophysics Decadal Survey

Reid, M. J., Menten, K. M., Brunthaler, A., et al. 2009b, ApJ, 693, 397

Reid, M. J., Schneps, M. H., Moran, J. M., et al. 1988, ApJ, 330, 809

Reid, M. J., Menten, K. M., Zheng, X. W., et al. 2009c, ApJ, 700, 137

Reid, M. J., Menten, K. M., Brunthaler, A., et al. 2014, ApJ, 783, 130

Reid, M. J., Brunthaler, A., Menten, K. M., et al. 2017, AJ, 154, 63

Reid, M. J., Menten, K. M., Brunthaler, A., et al. 2019, ApJ, 885, 131

Rioja, M., Dodson, R., Porcas, R. W., et al. 2009, in 8th International e-VLBI Workshop, 14

Rioja, M. J., Dodson, R., & Franzen, T. M. O. 2018, MNRAS, 478, 2337

Rioja, M. J., Dodson, R., Orosz, G., Imai, H., & Frey, S. 2017, AJ, 153, 105

Rioja, M. J., Marcaide, J. M., Elosegui, P., & Shapiro, I. I. 1997a, A&A, 325, 383

Rioja, M. J., & Porcas, R. W. 2000, A&A, 355, 552

Rioja, M. J., Porcas, R. W., Desmurs, J. F., et al. 2002, in Proceedings of the 6th EVN Symposium, 57

Rioja, M. J., Stevens, E., Gurvits, L., et al. 1997b, Vistas in Astronomy, 41, 213

Rix, H.-W., & Bovy, J. 2013, A&A Rev., 21, 61

Rodgers, A. W., Campbell, C. T., & Whiteoak, J. B. 1960, MNRAS, 121, 103

Rohlfs, K. 1986, Tools of Radio Astronomy (Berlin : Springer-Verlag)

Russeil, D. 2003a, in IAU Symposium, Vol. 212, A Massive Star Odyssey: From Main Sequence to Supernova, ed. K. van der Hucht, A. Herrero, & C. Esteban, 431

Russeil, D. 2003b, A&A, 397, 133

Rygl, K. L. J., Brunthaler, A., Reid, M. J., et al. 2010, A&A, 511, A2

Rygl, K. L. J., Brunthaler, A., Sanna, A., et al. 2012, A&A, 539, A79

Sakai, D., Oyama, T., Nagayama, T., Honma, M., & Kobayashi, H. 2017, in The Multi-Messenger Astrophysics of the Galactic Centre, ed. R. M. Crocker, S. N. Longmore, & G. V. Bicknell, Vol. 322, 166–167

Sakai, N. 2015, in Revista Mexicana de Astronomia y Astrofisica Conference Series, Vol. 46, Revista Mexicana de Astronomia y Astrofisica Conference Series, 56–60

Sakai, N., Honma, M., Nakanishi, H., Sakanoue, H., & Kurayama, T. 2013, in IAU Symposium, Vol. 289, Advancing the Physics of Cosmic Distances, ed. R. de Grijs, 95–98

Sakai, N., Honma, M., Nakanishi, H., et al. 2012, PASJ, 64, 108

Sakai, N., Reid, M. J., Menten, K. M., Brunthaler, A., & Dame, T. M. 2019, ApJ, 876, 30

Sakai, N., Sato, M., Motogi, K., et al. 2014, PASJ, 66, 3

Sakai, N., Nakanishi, H., Matsuo, M., et al. 2015, PASJ, 67, 69

Sanna, A., Reid, M. J., Dame, T. M., Menten, K. M., & Brunthaler, A. 2017, Science, 358, 227

Sanna, A., Reid, M. J., Dame, T. M., et al. 2012, ApJ, 745, 82

Sanna, A., Menten, K. M., Carrasco-González, C., et al. 2015, ApJ, 804, L2

Sevenster, M. N. 1999, MNRAS, 310, 629

Shaviv, N. J. 2003, New A, 8, 39

Sobolev, A. M., Cragg, D. M., Ellingsen, S. P., et al. 2007, in IAU Symposium, Vol. 242, IAU Symposium, ed. J. M. Chapman & W. A. Baan, 81–88

Sofue, Y., & Fujimoto, M. 1983, ApJ, 265, 722

Stack, P. D., & Ellingsen, S. P. 2011, PASA, 28, 338

Stotskii, A., Elgered, K. G., & Stotskaya, I. M. 1998, Astronomical and Astrophysical Transactions, 17, 59

Stotskii, A. A., & Stotskaya, I. M. 1992, Astronomical and Astrophysical Transactions, 2, 327

Sugiyama, K., Saito, Y., Yonekura, Y., & Momose, M. 2019, The Astronomer's Telegram, 12446, 1

Szymczak, M., Hrynek, G., & Kus, A. J. 2000, A&AS, 143, 269

Szymczak, M., & Kus, A. J. 2000, A&A, 360, 311

Szymczak, M., Kus, A. J., Hrynek, G., Kěpa, A., & Pazderski, E. 2002, A&A, 392, 277

Szymczak, M., Olech, M., Sarniak, R., Wolak, P., & Bartkiewicz, A. 2018a, MNRAS, 474, 219

Szymczak, M., Olech, M., Wolak, P., Gérard, E., & Bartkiewicz, A. 2018b, A&A, 617, A80

Taylor, J. H., & Cordes, J. M. 1993, ApJ, 411, 674

Thompson, A. R., Moran, J. M., & Swenson, George W., J. 2017, Interferometry and Synthesis in Radio Astronomy, 3rd Edition, doi:10.1007/978-3-319-44431-4

Titmarsh, A. M., Ellingsen, S. P., Breen, S. L., Caswell, J. L., & Voronkov, M. A. 2013, ApJ, 775, L12

Townes, C. H., & Schawlow, A. L. 1955, Microwave Spectroscopy

Tralli, D. M., & Lichten, S. M. 1990, Bulletin Geodesique, 64, 127

Urquhart, J. S., Hoare, M. G., Purcell, C. R., et al. 2010, PASA, 27, 321

Vallee, J. P. 1995, ApJ, 454, 119

Vallée, J. P. 2002, ApJ, 566, 261

van de Hulst, H. C., Muller, C. A., & Oort, J. H. 1954, Bull. Astron. Inst. Netherlands, 12, 117

VERA Collaboration, Hirota, T., Nagayama, T., et al. 2020, PASJ, arXiv:2002.03089

Verbiest, J. P. W., Weisberg, J. M., Chael, A. A., Lee, K. J., & Lorimer, D. R. 2012, ApJ, 755, 39

Volvach, L. N., Volvach, A. E., Larionov, M. G., et al. 2019, A&A, 628, A89

Walker, C., & Chatterjee, S. 1999, in VLBA Scientific Memo 23

Weaver, C. P., & Ramanathan, V. 1995, Journal of Geophysical Research: Atmospheres, 100, 11585

Weaver, H., Williams, D. R. W., Dieter, N. H., & Lum, W. T. 1965, Nature, 208, 29

Wilson, T. L. 2013, Techniques of Radio Astronomy, ed. T. D. Oswalt & H. E. Bond, 283

Wilson, T. L., Rohlfs, K., & Hüttemeister, S. 2009, Tools of Radio Astronomy (Springer-Verlag), doi:10.1007/978-3-540-85122-6

—. 2013, Tools of Radio Astronomy, doi:10.1007/978-3-642-39950-3

Wilson, W. E., Ferris, R. H., Axtens, P., et al. 2011, MNRAS, 416, 832

Wink, J. E., Altenhoff, W. J., & Mezger, P. G. 1982, A&A, 108, 227

Wright, E. L., Eisenhardt, P. R. M., Mainzer, A. K., et al. 2010, AJ, 140, 1868

Wu, Y. W., Sato, M., Reid, M. J., et al. 2014, A&A, 566, A17

Wu, Y. W., Reid, M. J., Sakai, N., et al. 2019, ApJ, 874, 94

Wynn-Williams, C. G. 1969, Astrophys. Lett., 3, 195

Xu, Y., Reid, M. J., Zheng, X. W., & Menten, K. M. 2006, Science, 311, 54

Xu, Y., Reid, M. J., Moscadelli, L., et al. 2012, in IAU Symposium, Vol. 287, Cosmic Masers - from OH to H0, ed. R. S. Booth, W. H. T. Vlemmings, & E. M. L. Humphreys, 368–376

Xu, Y., Li, J. J., Reid, M. J., et al. 2013, ApJ, 769, 15

Yang, K., Chen, X., Shen, Z.-Q., et al. 2019, ApJS, 241, 18

Yao, J. M., Manchester, R. N., & Wang, N. 2017, ApJ, 835, 29

Yao, X., & Liu, Q.-h. 2018, Chinese Astron. Astrophys., 42, 155

Zhang, B., Reid, M. J., Menten, K. M., et al. 2013, ApJ, 775, 79

Zhang, B., Reid, M. J., Zhang, L., et al. 2019, AJ, 157, 200

Zinnecker, H., & Yorke, H. W. 2007, ARA&A, 45, 481

$\mathcal{A}$

First Quadrant Parallaxes

A.1 Additional Figures

A.1.1 Maser and Calibrator Synthesised Maps

This appendix contains additional information, tables and figures from the BeSSeL VLBA data analysed that was would otherwise clutter Chapter §3 while still being useful and relevant.

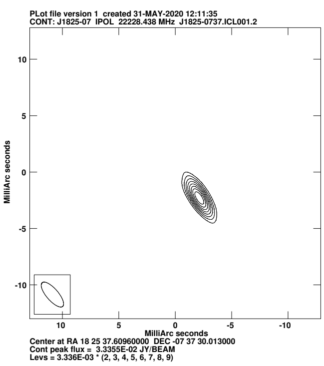

(a) J1825–0737

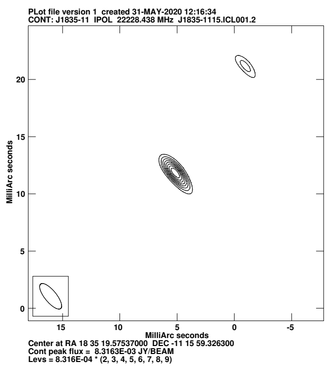

(b) J1835–1115

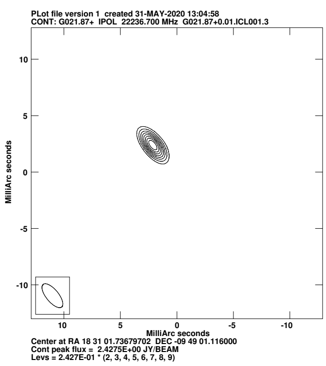

(c) G021.88+0.02 velocity feature $v = 19.3\mathrm{km\,s^{-1}}$

Figure A.1: Phase referenced images at epoch BR210B3. J1825–0737 and J1835–1115 are phase referenced against G021.87+0.01 $v = 19.3\,\mathrm{km\,s^{-1}}$ feature. G021.87+0.01 $v = 19.3\mathrm{km\,s^{-1}}$ map is phase referenced from J1825–0737.

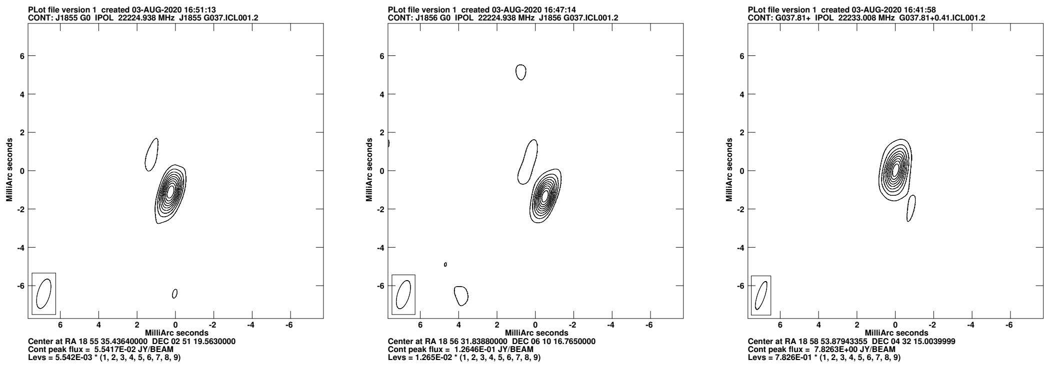

(a) J1855+0251

(b) J1856+0610

(c) G037.82+0.41 velocity feature $v = 19.0\ \mathrm{km\,s^{-1}}$

Figure A.2: Phase referenced images at epoch BR210C8. Both quasars J1855+0251 and J1856+0610 are phase referenced from G037.82+0.41 $v = 19.0\ \mathrm{km\,s^{-1}}$ feature.

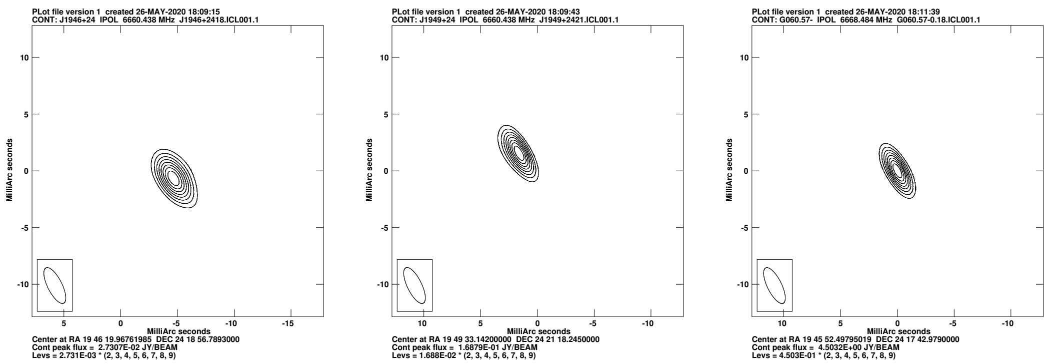

(a) J1946+2418

(b) J1949+2421

(c) G060.58+0.18 velocity feature $v = +3\,\mathrm{km\,s^{-1}}$.

Figure A.3: Calibrators J1946+2418 and J1949+2421 phase referenced to G060.58+0.18 on epoch BR210FA. The channel used for fringe fit is also shown.

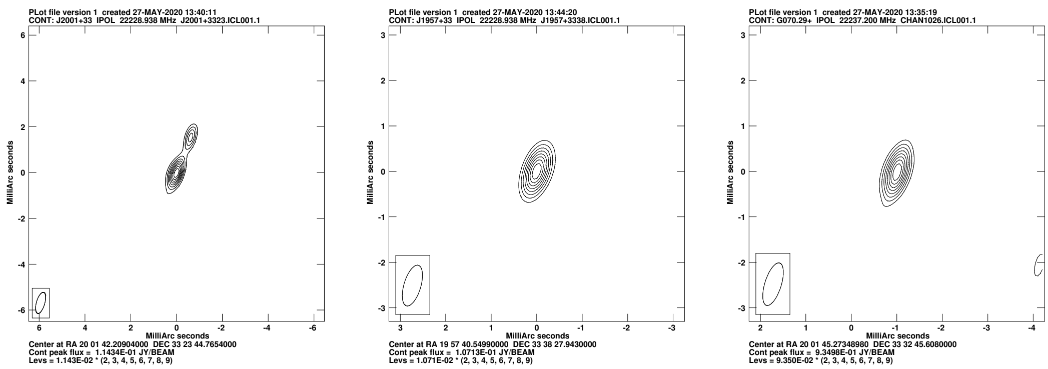

(a) J2001–3323

(b) J1957–3338

(c) G070.29+1.60 velocity feature at $v - 26.7\,\mathrm{km\,s^{-1}}$

Figure A.4: Synthesised maps of G070.29+1.60 and calibrators.

A.1.2 G021.87+0.01 Time–Series Spectra and Maps

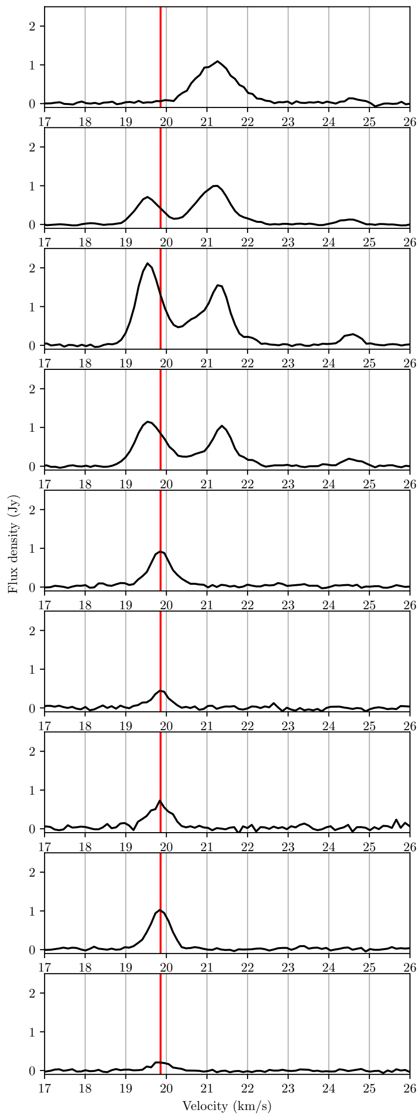

Figure A.5: Spectra of G021.87+0.01 on epochs 1, 2, 3, 4, 5, 6, 7, 8 and 12 (C) respectively; **y-axis:** scalar–averaged cross–power flux density (Jy) for antennas BR, FD, KP, LA, NL, OV and PT; **x-axis:** LSR recession velocity (km/s). Spectra undergoes almost no changes between epochs 8 and 12 apart from slight flux density variation. Time spacings from epoch 1 are $t \simeq 0, 19, 44, 63, 166, 185, 196, 209, 256$ days respectively.

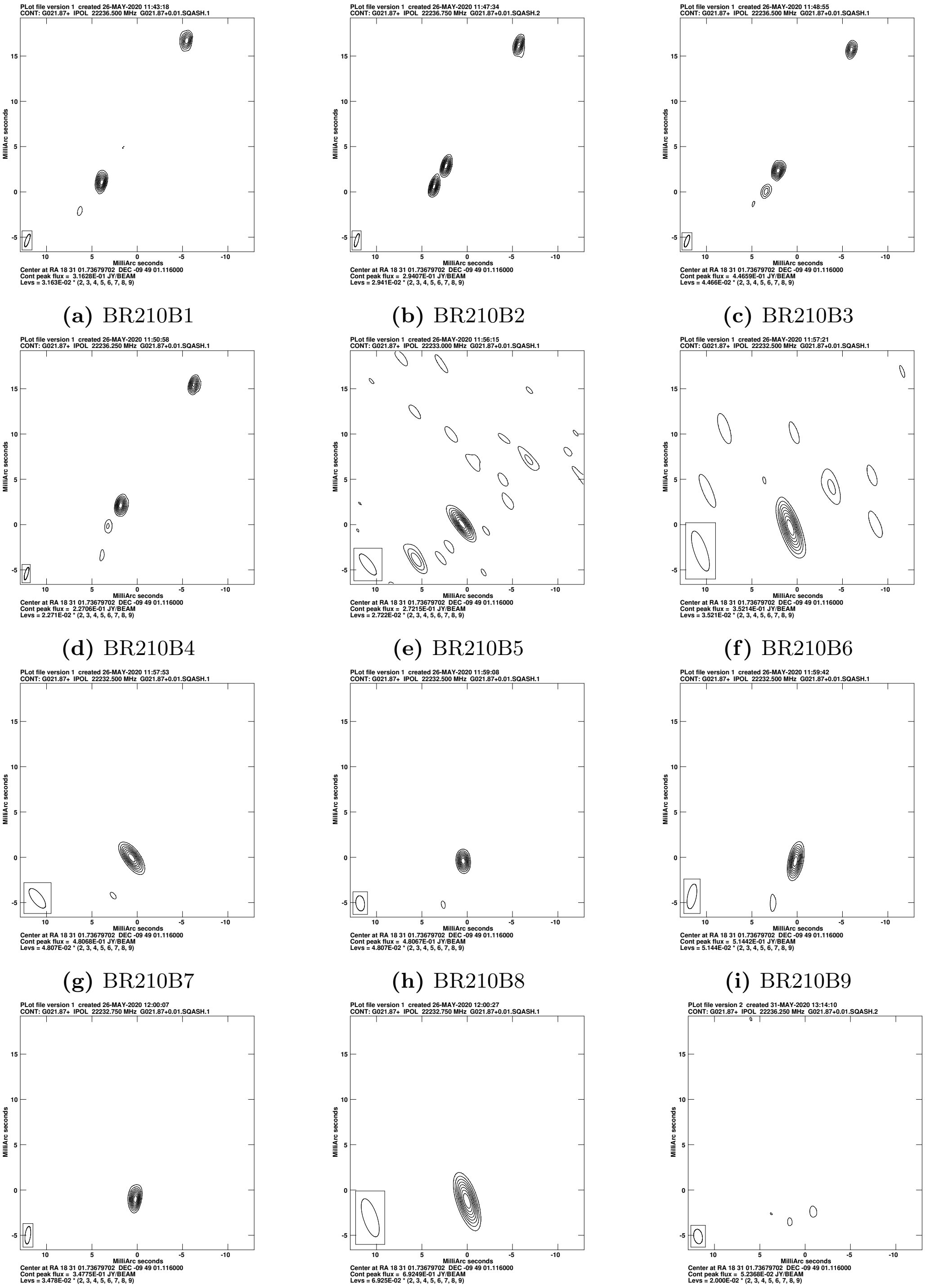

(a) BR210B1 (b) BR210B2 (c) BR210B3

(d) BR210B4 (e) BR210B5 (f) BR210B6

(g) BR210B7 (h) BR210B8 (i) BR210B9

(j) BR210BA (k) BR210BB (l) BR210BD

Figure A.6: G021.87+0.01 spotmaps over the coarse of the first 12 epochs. Maser region apparently undergoes relatively major morphological changes between the 4th and 5th epoch which are spaced ~ 103 days apart. Despite the fact that the maser was detected in spectrum in epoch C (12), the fringe-fit failed on both calibrators and so no positions could be measured. Finally BR210BD is shown in the bottom-most right panel to illustrate the maser reference spot disappeared below the detectable level

A.2 Additional Tables

A.2.1 BR210 Epochs

Table A.1: Observational epochs for relevant BR210 experiments. **Horizontal:** Project code pertaining to a specific group of maser targets; **Vertical:** Epochs 1 to 16 (G). All values given in fractional year.

Epoch	BR210B (yr)	BR210C (yr)	BR210D (yr)	BR210F (yr)
1	2015.178	2015.183	2015.189	2015.164
2	2015.230	2015.235	2015.277	2015.238
3	2015.298	2015.301	2015.359	2015.307
4	2015.350	2015.367	2015.408	2015.383
5	2015.632	2015.660	2015.698	2015.657
6	2015.684	2015.701	2015.739	2015.693
7	2015.715	2015.742	2015.769	2015.723
8	2015.750	2015.772	2015.797	2015.756
9	2015.780	2015.813	2015.835	2015.791
A	2015.819	2015.838	2015.862	2015.821
B	2015.846	2015.868	2015.890	2015.849
C	2015.879	2015.895	2015.923	2015.876
D	2016.134	2016.153	2016.197	2016.156
E	2016.205	2016.225	2016.260	2016.233
F	2016.279	2016.293	2016.345	2016.298
G	2016.350	2016.400	2016.405	2016.402

A.2.2 Astrometric Products

Table A.2: Final position vs. time values for G021.87+0.02 relative to quasar J1825 − 0737. Maser position was found and corrected initially at epoch 9 to be in the centre of the field relative to the quasar.

QSO	**Epoch (yr)**	**X offset (mas)**	$\boldsymbol{\sigma_x}$ **(mas)**	**Y offset (mas)**	$\boldsymbol{\sigma_y}$ **(mas)**	**Flux (Jy)**	**Experiment** BR210
J1825 − 0737	2015.230	2.260	0.010	2.872	0.022	0.55	B2
	2015.299	1.968	0.017	2.306	0.017	0.67	B3
	2015.351	1.704	0.015	2.118	0.026	0.57	B4
	2015.633	0.586	0.019	0.404	0.042	0.77	B5
	2015.715	0.589	0.027	−0.191	0.051	0.50	B7
	2015.751	0.425	0.015	−0.425	0.026	0.99	B8
	2015.781	0.212	0.012	−0.530	0.030	1.03	B9
	2015.819	0.260	0.022	−0.838	0.040	0.86	BA

Table A.3: Final position vs. time values for quasars J1855+0251 and J1856+0610 relative to reference feature of G037.81+0.41. The maser was found and approximately zeroed relative to the quasars at epoch 9.

QSO	**Epoch** (yr)	**X offset** (mas)	σ_x (mas)	**Y offset** (mas)	σ_y (mas)	**Flux** (mJy)	**Experiment** BR210
J1855 + 0251	2015.184	1.485	0.004	4.391	0.006	86.5	C1
	2015.236	1.346	0.005	4.118	0.009	110.2	C2
	2015.301	1.151	0.006	3.791	0.008	107.8	C3
	2015.367	0.951	0.008	3.438	0.013	64.2	C4
	2015.660	0.026	0.015	1.712	0.023	38.0	C5
	2015.701	−0.066	0.007	1.554	0.009	56.0	C6
	2015.742	−0.240	0.007	1.161	0.008	65.2	C7
	2015.773	−0.265	0.006	1.125	0.010	57.7	C8
	2015.814	−0.373	0.005	0.786	0.007	70.2	C9
	2015.838	−0.335	0.005	0.616	0.008	67.3	CA
	2015.868	−0.508	0.007	0.457	0.012	64.4	CB
	2015.896	−0.518	0.007	0.324	0.011	52.3	CC
	2016.153	−1.134	0.004	−1.245	0.005	85.0	CD
	2016.224	−1.253	0.005	−1.633	0.009	70.0	CE
	2016.292	−1.420	0.009	−1.970	0.016	41.5	CF
	2016.399	−1.744	0.007	−2.665	0.009	75.7	CG
J1856 + 0610	2015.184	2.175	0.004	4.655	0.006	109.5	C1
	2015.236	2.005	0.006	4.383	0.010	119.7	C2
	2015.301	1.852	0.007	4.027	0.009	122.4	C3
	2015.367	1.685	0.008	3.657	0.012	97.5	C4
	2015.660	0.684	0.010	1.890	0.013	98.0	C5
	2015.701	0.727	0.008	1.744	0.011	118.3	C6
	2015.742	0.561	0.006	1.571	0.007	155.1	C7
	2015.773	0.490	0.007	1.334	0.011	132.2	C8
	2015.814	0.356	0.005	1.149	0.007	164.6	C9
	2015.838	0.241	0.005	1.089	0.007	157.0	CA
	2015.868	0.190	0.005	0.828	0.009	175.6	CB
	2015.896	0.146	0.005	0.736	0.008	137.2	CC
	2016.153	−0.393	0.004	−0.742	0.005	189.4	CD
	2016.224	−0.596	0.004	−1.071	0.007	148.2	CE
	2016.292	−0.751	0.009	−1.459	0.013	89.1	CF
	2016.399	−1.128	0.007	−2.017	0.008	132.8	CG

Table A.4: Final position vs. time values for quasars J1946+2418 and J1949+2421 relative to reference feature of maser G060.57–0.18. The maser was found and approximately zeroed relative to the quasars at epoch 8.

QSO	**Epoch (yr)**	**X offset (mas)**	σ_x **(mas)**	**Y offset (mas)**	σ_y **(mas)**	**Flux (mJy)**	**Experiment** BR210
J1946 + 2418	2015.164	7.001	0.005	4.295	0.007	23.9	F1
	2015.238	6.832	0.007	3.924	0.011	30.0	F2
	2015.307	6.620	0.005	3.466	0.008	23.0	F3
	2015.384	6.323	0.007	3.190	0.010	21.5	F4
	2015.658	5.288	0.007	1.627	0.011	28.4	F5
	2015.693	5.169	0.007	1.368	0.010	23.3	F6
	2015.723	5.024	0.004	1.220	0.005	21.7	F7
	2015.756	4.853	0.004	0.972	0.005	28.8	F8
	2015.792	4.722	0.005	0.857	0.007	22.7	F9
	2015.822	4.713	0.008	0.640	0.010	32.5	FA
	2015.849	4.643	0.006	0.384	0.010	29.3	FB
	2015.877	4.480	0.010	0.183	0.013	25.4	FC
	2016.156	3.865	0.006	−1.407	0.010	22.2	FD
	2016.232	3.564	0.007	−1.732	0.012	23.4	FE
	2016.298	3.440	0.005	−2.194	0.007	31.2	FF
	2016.402	2.992	0.004	−2.671	0.006	21.8	FG
J1949 + 2421	2015.164	0.698	0.006	2.117	0.009	103.1	F1
	2015.238	0.397	0.005	1.717	0.008	161.7	F2
	2015.307	0.288	0.005	1.372	0.008	131.4	F3
	2015.384	0.005	0.007	0.987	0.010	116.7	F4
	2015.658	−0.999	0.006	−0.448	0.010	136.8	F5
	2015.693	−1.184	0.006	−0.709	0.010	114.9	F6
	2015.723	−1.335	0.002	−0.922	0.004	105.5	F7
	2015.756	−1.425	0.003	−1.134	0.004	140.5	F8
	2015.792	−1.577	0.006	−1.285	0.010	107.7	F9
	2015.822	−1.665	0.006	−1.531	0.008	181.3	FA
	2015.849	−1.725	0.006	−1.705	0.010	136.8	FB
	2015.877	−1.873	0.008	−1.878	0.011	115.2	FC
	2016.156	−2.471	0.004	−3.497	0.008	125.9	FD
	2016.232	−2.697	0.006	−3.896	0.011	122.7	FE
	2016.298	−3.030	0.005	−4.243	0.008	141.0	FF
	2016.402	−3.244	0.006	−4.695	0.010	124.4	FG

Table A.5: Final position vs. time values for reference feature of G070.29+1.60 relative to quasars $J1957+3338$ and $J2001+3323$.

QSO	**Epoch** (yr)	**X offset** (mas)	σ_x (mas)	**Y offset** (mas)	σ_y (mas)	**Flux** (Jy)	**Experiment** BR210
$J1957+3338$	2015.359	0.878	0.023	1.899	0.035	0.207	D3
	2015.740	0.130	0.003	0.685	0.004	1.593	D6
	2015.770	0.062	0.002	0.594	0.006	1.085	D7
	2015.797	0.004	0.002	0.414	0.004	1.566	D8
	2015.836	−0.077	0.004	0.140	0.004	2.142	D9
	2015.863	−0.156	0.003	0.022	0.003	2.355	DA
	2015.890	−0.133	0.003	−0.077	0.003	2.378	DB
	2015.923	−0.193	0.002	−0.188	0.004	2.156	DC
	2016.260	−0.475	0.003	−1.427	0.004	1.710	DE
	2016.344	−0.577	0.010	−1.660	0.027	0.555	DF
	2016.404	−0.730	0.006	−1.798	0.009	0.874	DG
$J2001+3323$	2015.359	−0.293	0.016	1.489	0.024	0.211	D3
	2015.740	−0.863	0.004	0.211	0.006	1.331	D6
	2015.770	−1.008	0.004	0.125	0.009	0.945	D7
	2015.797	−0.986	0.010	−0.034	0.013	0.745	D8
	2015.836	−1.150	0.004	−0.198	0.005	1.819	D9
	2015.863	−1.113	0.005	−0.332	0.006	2.112	DA
	2015.890	−1.144	0.003	−0.400	0.003	1.921	DB
	2015.923	−1.201	0.002	−0.589	0.004	1.862	DC
	2016.260	−1.498	0.003	−1.827	0.006	1.297	DE
	2016.344	−1.642	0.012	−2.113	0.017	0.891	DF
	2016.404	−1.787	0.011	−2.192	0.011	0.745	DG

$\mathcal{B}$

Maser Compactness

In this appendix I have additional derivations, tables and figures that were too expansive or tangentially related to be contained in the main text of Chapter §4. This appendix primarily contains the table of all first targets for SπRALS (Table B.1), the table of all derived parameters for all detected maser spots (Table B.2) and plots of the visibility amplitudes vs. uv-distance for all surveyed masers (Figure B.3).

B.1 Alternative maser amplitude calibration

In the event that amplitude calibration methods such as applying system temperature measurements are unavailable, masers can be used as a method of relative amplitude calibration. At any one time, if the angular size of the maser is smaller than the primary beam of all telescopes in an array, then the velocity–corrected autocorrelation spectrum of the maser on all telescopes should be the same. If at least one telescope in the array has stable and accurate pre–calibration applied (ie. with system temperature measurements), or if the maser has a known spectral flux density this can be used as a reference for the remaining spectra. This technique sacrifices absolute amplitude calibration for relative amplitude calibration under the condition that the above criteria are met.

As we want to correct the baseline–based power s_{jk}, we need to solve for antenna–based voltages corrections (Equation 2.8). So if a baseline measures flux density s_{jk}, when it should measure S_{jk}, then the corrections are:

$$S_{jk} = \Gamma_j \Gamma_k s_{jk} \tag{B.1}$$

where Γ_j is the voltage correction factor for antenna j.

If a maser has some reference spectral flux density S_{ν_r} (in Jy) and a telescope measures an autocorrelated flux density s_{jj}, then the correction factor for antenna j will be:

$$\Gamma_j = \sqrt{\frac{S_{\nu_r}}{s_{jj}}} \tag{B.2}$$

This is also how the ParselTongue script *maser_amplitude_autocorrect.py*[*], which is used in Chapter §4 works.

[*]Available from https://github.com/lucasjord/thesisscripts

B.2 Maser Compactness Tables

Table B.1: First target masers as determined by the V534 survey in Chapter §4. **Column (1)**: Unique maser number; **(2):** Source name in galactic coordinates; **(3):** Right Ascention; **(4):** Declination; **(5):** Maser spot local standard of rest recession velocity ($\mathrm{km\,s^{-1}}$); **(6):** Spot autocorrelated flux density (Jy); **(7):** Maser Grade A/B; **(8-10): Near/Far/Outer kinematic distance (kpc).**

N	**Name**	**RA (J2000)** hh:mm:ss	**DEC (J2000)** dd:mm:ss	V ($\mathrm{km\,s^{-1}}$)	S_0 (Jy)	**Grade**	D_{near} (kpc)	D_{far} (kpc)	D_{outer} (kpc)
1	192.600 − 0.048	06 : 12 : 53.99	+17 : 59 : 23.7	+5.90	291.7	A			0.76
				+5.20	144.4	A			
2	232.620 + 0.996	07 : 32 : 09.79	−16 : 58 : 12.4	+22.89	157.7	A			1.72
3	287.371 + 0.644	10 : 48 : 04.44	−58 : 27 : 01.0	−1.89	83.4	A			5.18
4	291.274 − 0.709	11 : 11 : 53.35	−61 : 18 : 23.7	−30.69	42.0	A	2.62	3.85	
5	299.772 − 0.005	12 : 23 : 48.97	−62 : 42 : 25.3	−6.68	22.6	A			8.14
6	309.921 + 0.479	13 : 50 : 41.78	−61 : 35 : 10.2	−57.85	102.5	A	4.22	6.85	
				−58.46	244.5	A			
				−58.81	161.1	A			
				−59.69	447.3	A			
7	318.050 + 0.087	14 : 53 : 42.67	−59 : 08 : 52.4	−51.47	12.1	A	2.97	9.77	
8	323.740 − 0.263	15 : 31 : 45.45	−56 : 30 : 50.1	−47.93	118.3	A	2.91	10.84	
				−48.46	552.2	A			
				−48.98	743.8	A			
				−50.39	2412.8	A			
				−51.18	1123.0	A			
				−52.41	69.4	A			
				−49.34	815.0	A			
9	326.475 + 0.703	15 : 43 : 16.64	−54 : 07 : 14.6	−38.43	64.1	A	2.25	11.94	
10	327.402 + 0.445	15 : 49 : 19.50	−53 : 45 : 13.9	−81.76	18.8	A	4.72	9.61	
				−82.02	33.3	A			
				−82.90	72.3	A			
				−83.25	37.6	A			
11	328.237 − 0.547	15 : 57 : 58.28	−53 : 59 : 22.7	−44.48	778.3	A	2.68	11.77	
				−44.74	676.6	A			
12	328.254 − 0.532	15 : 57 : 59.75	−53 : 58 : 00.4	−36.83	90.1	A	2.25	12.21	
13	329.029 − 0.205	16 : 00 : 31.80	−53 : 12 : 49.6	−36.12	50.0	A	2.25	12.32	
14	332.295 + 2.280	16 : 05 : 41.72	−49 : 11 : 30.3	−23.67	79.0	A	1.51	13.50	
				−24.02	117.7	A			
15	337.920 − 0.456	16 : 41 : 06.05	−47 : 07 : 02.5	−38.62	34.5	A	2.84	12.82	
16	339.622 − 0.121	16 : 46 : 05.99	−45 : 36 : 43.3	−33.16	31.0	A	2.85	12.98	
16	339.884 − 1.259	16 : 52 : 04.67	−46 : 08 : 34.2	−34.84	306.6	A	3.07	12.78	
				−35.63	858.9	A			
				−36.51	309.1	A			
				−37.39	523.5	A			
17	345.010 + 1.792	16 : 56 : 47.58	−40 : 14 : 25.8	−17.02	132.1	A	2.47	13.79	
				−17.46	82.8	A			
				−20.18	121.4	A			
				−21.76	277.4	A			
				−22.03	299.1	A			
18	345.505 + 0.348	17 : 04 : 22.91	−40 : 44 : 21.7	−14.06	242.3	A	2.06	14.24	
				−19.06	190.8	A			
19	348.550 − 0.979	17 : 19 : 20.41	−39 : 03 : 51.6	−10.41	29.3	A	1.58	14.88	
20	351.417 + 0.645	17 : 20 : 53.37	−35 : 47 : 01.2	−9.71	621.2	A	2.18	14.41	
				−10.32	1597.3	A			
21	352.630 − 1.067	17 : 31 : 13.91	−35 : 44 : 08.7	−2.91	134.8	A	0.59	16.03	
				−3.27	127.8	A			
22	263.250 + 0.514	08 : 48 : 47.84	−42 : 54 : 28.3	+12.35	46.9	B			2.11

Continued on Next Page...

Table B.1 – Continued...

N	Name	RA (J2000) hh:mm:ss	DEC (J2000) dd:mm:ss	V ($\mathrm{km\,s^{-1}}$)	S_0 (Jy)	Grade	D_{near} (kpc)	D_{far} (kpc)	D_{outer} (kpc)
23	188.946 + 0.886	06 : 08 : 53.32	+21 : 38 : 29.1	+10.85	602.9	B			2.98
24	305.200 + 0.019	13 : 11 : 16.93	−62 : 45 : 55.1	−32.04	39.7	B	1.77	8.23	
				−33.09	37.3	B			
25	310.144 + 0.760	13 : 51 : 58.43	−61 : 15 : 41.3	−55.89	36.9	B	3.67	7.45	
26	313.577 + 0.325	14 : 20 : 08.58	−60 : 42 : 00.8	−47.80	67.9	B	2.77	9.08	
27	314.320 + 0.112	14 : 26 : 26.20	−60 : 38 : 31.3	−43.42	34.9	B	2.43	9.57	
				−43.69	19.2	B			
28	316.359 − 0.362	14 : 43 : 11.20	−60 : 17 : 13.3	+3.38	65.3	B			12.65
29	316.811 − 0.057	14 : 45 : 26.43	−59 : 49 : 16.3	−45.61	46.6	B	2.57	9.93	
30	318.948 − 0.196	15 : 00 : 55.40	−58 : 58 : 52.1	−34.63	435.3	B	1.83	11.08	
				−36.30	63.1	B			
31	320.231 − 0.284	15 : 09 : 51.94	−58 : 25 : 38.5	−62.28	49.7	B	3.65	9.49	
32	322.158 + 0.636	15 : 18 : 34.64	−56 : 38 : 25.3	−54.51	58.6	B	3.65	9.83	
				−62.94	166.0	B			
				−63.29	115.5	B			
				−64.08	125.0	B			
33	323.459 − 0.079	15 : 29 : 19.33	−56 : 31 : 22.8	−67.15	112.1	B	3.87	9.83	
				−68.29	189.0	B			
				−68.99	204.5	B			
				−69.26	326.5	B			
				−70.48	59.1	B			
				−66.98	121.6	B			
34	328.808 + 0.633	15 : 55 : 48.45	−52 : 43 : 06.6	−44.40	251.8	B	2.66	11.87	
				−45.10	63.3	B			
				−46.24	154.0	B			
				−46.59	78.3	B			
35	329.339 + 0.148	16 : 00 : 33.13	−52 : 44 : 39.8	−106.28	19.9	B	6.05	8.56	
36	329.407 − 0.459	16 : 03 : 32.65	−53 : 09 : 26.9	−66.64	76.2	B	3.92	10.70	
37	331.342 − 0.346	16 : 12 : 26.45	−51 : 46 : 16.4	−67.08	19.9	B	3.90	10.99	
38	333.562 − 0.025	16 : 21 : 08.80	−49 : 59 : 48.0	−35.30	32.9	B	2.36	12.81	
39	335.789 + 0.174	16 : 29 : 47.33	−48 : 15 : 51.7	−47.39	303.6	B	3.23	12.20	
				−48.53	199.2	B			
40	338.561 + 0.218	16 : 40 : 37.96	−46 : 11 : 25.8	−39.05	31.3	B	2.98	12.75	
41	338.925 + 0.634	16 : 40 : 13.56	−45 : 38 : 33.2	−58.99	25.5	B	4.16	11.60	
				−60.75	51.8	B			
42	338.920 + 0.550	16 : 40 : 34.01	−45 : 42 : 07.1	−61.29	50.8	B	4.18	11.58	
43	338.935 − 0.062	16 : 43 : 16.01	−46 : 05 : 40.2	−41.87	32.9	B	3.17	12.59	
44	340.054 − 0.244	16 : 48 : 13.89	−45 : 21 : 43.5	−59.36	38.7	B	4.21	11.66	
				−60.86	23.3	B			
45	340.785 − 0.096	16 : 50 : 14.84	−44 : 42 : 26.3	−108.02	764.9	B	5.94	9.99	
46	341.218 − 0.212	16 : 52 : 17.86	−44 : 26 : 52.3	−44.42	539.1	B	3.16	12.81	
47	348.617 − 1.162	17 : 20 : 18.65	−39 : 06 : 50.8	−11.47	38.9	B	1.72	14.75	
48	348.703 − 1.043	17 : 20 : 04.06	−38 : 58 : 30.9	−3.40	42.0	B	0.24	16.23	
				−7.36	84.6	B			
				−9.90	47.6	B			
50	354.615 + 0.472	17 : 30 : 17.13	−33 : 13 : 55.1	−24.21	164.4	B			
51	358.460 − 0.391	17 : 43 : 26.76	−30 : 27 : 11.3	+1.26	48.0	B	4.07	12.63	
52	359.615 − 0.243	17 : 45 : 39.09	−29 : 23 : 30.0	+24.50	26.4	B			
				+19.58	59.3	B			

Table B.2: Determined parameters for detected maser spots in Chapter §4. **Columns:** **(1)** Source name in Galactic coordinates; **(2)** maser right ascention (J2000); **(3)** maser declination (J2000); **(4)**; maser spot LSR (km/s); **(5)** flux density of halo component (Jy); **(6)** angular size of halo component (mas); **(7)** flux density of core component (Jy); **(8)** angular size of core component (mas); **(9)** RMS error in fit (Jy); **(10)** degrees of freedom for fit; **(11)** maser spot grade.

Name	α_{J2000} hh:mm:ss	δ_{J2000} dd:mm:ss	V (km s^{-1})	S_H (Jy)	θ_H (mas)	S_C (Jy)	θ_C (mas)	Error (Jy)	DF (N−4)	Grade
192.600 − 0.048	06 : 12 : 53.99	+17 : 59 : 23.7	5.90	246	40.0	46	1.5	5	38	A
192.600 − 0.048	06 : 12 : 53.99	+17 : 59 : 23.7	5.20	70	7.3	74	1.6	12	38	A
196.454 − 1.677	06 : 14 : 37.03	+13 : 49 : 36.6	14.73	14	48.2	7	1.2	3	56	C
232.620 + 0.996	07 : 32 : 09.79	−16 : 58 : 12.4	22.89	50	21.3	108	2.0	7	32	A
263.250 + 0.514	08 : 48 : 47.84	−42 : 54 : 28.3	12.35	21	143.6	26	2.4	6	23	C
188.946 + 0.886	06 : 08 : 53.32	+21 : 38 : 29.1	10.85	482	7.0	121	2.7	31	15	B
287.371 + 0.644	10 : 48 : 04.44	−58 : 27 : 01.0	−1.89	59	13.4	25	0.5	14	47	A
291.274 − 0.709	11 : 11 : 53.35	−61 : 18 : 23.7	−30.69	31	20.4	11	0.0	6	28	B
298.262 + 0.739	12 : 11 : 47.65	−61 : 46 : 20.9	−30.13	8	18.8	2	0.0	2	38	D
298.262 + 0.739	12 : 11 : 47.65	−61 : 46 : 20.9	−29.86	5	22.9	3	0.9	1	16	D
299.772 − 0.005	12 : 23 : 48.97	−62 : 42 : 25.3	−6.68	9	2.3	13	0.5	3	48	A
305.199 + 0.005	13 : 11 : 17.20	−62 : 46 : 46.0	−32.04	31	3.6	9	0.0	5	20	B
305.199 + 0.005	13 : 11 : 17.20	−62 : 46 : 46.0	−33.09	12	31.1	25	1.8	3	20	B
305.208 + 0.206	13 : 11 : 13.71	−62 : 34 : 41.4	−44.04	43	7.5	10	1.2	7	26	C
308.754 + 0.549	13 : 40 : 57.60	−61 : 45 : 43.4	−39.21	3	3.6	0	3.6	2	4	D
308.754 + 0.549	13 : 40 : 57.60	−61 : 45 : 43.4	−45.27	6	6.6	2	0.0	3	16	D
308.918 + 0.123	13 : 43 : 01.85	−62 : 08 : 52.2	−54.25	28	49.9	4	1.9	2	32	D
308.918 + 0.123	13 : 43 : 01.85	−62 : 08 : 52.2	−54.60	19	9.9	3	0.9	2	32	D
308.918 + 0.123	13 : 43 : 01.85	−62 : 08 : 52.2	−54.78	20	8.9	3	0.7	1	32	D
309.901 + 0.231	13 : 51 : 01.05	−61 : 49 : 56.0	−54.29	3	7.1	5	1.1	2	4	D
309.921 + 0.479	13 : 50 : 41.78	−61 : 35 : 10.2	−57.85	43	8.7	59	0.2	13	32	A
309.921 + 0.479	13 : 50 : 41.78	−61 : 35 : 10.2	−58.46	120	78.8	125	1.8	48	32	A
309.921 + 0.479	13 : 50 : 41.78	−61 : 35 : 10.2	−58.81	55	13.3	106	0.5	17	32	A
309.921 + 0.479	13 : 50 : 41.78	−61 : 35 : 10.2	−59.69	391	3.0	56	0.0	113	32	A
310.144 + 0.760	13 : 51 : 58.43	−61 : 15 : 41.3	−55.89	19	33.9	18	1.7	5	32	C
312.071 + 0.082	14 : 08 : 58.20	−61 : 24 : 23.8	−34.18	25	6.3	1	0.0	1	8	D
312.071 + 0.082	14 : 08 : 58.20	−61 : 24 : 23.8	−34.80	2	6.0	33	6.0	2	8	D
312.108 + 0.262	14 : 08 : 49.31	−61 : 13 : 25.1	−49.94	11	4.9	5	1.6	2	20	D
312.598 + 0.045	14 : 13 : 15.03	−61 : 16 : 53.6	−67.78	9	7.3	3	0.9	1	20	D
313.469 + 0.190	14 : 19 : 40.94	−60 : 51 : 47.3	−9.44	28	7.2	9	1.7	6	20	C
313.469 + 0.190	14 : 19 : 40.94	−60 : 51 : 47.3	−11.81	12	29.7	10	1.9	3	20	C
313.577 + 0.325	14 : 20 : 08.58	−60 : 42 : 00.8	−47.80	32	7.3	36	1.8	4	32	B
314.320 + 0.112	14 : 26 : 26.20	−60 : 38 : 31.3	−43.42	19	5.2	16	1.1	4	20	B
316.412 − 0.308	14 : 43 : 23.34	−60 : 13 : 00.9	3.38	42	3.0	23	1.4	12	32	B
316.640 − 0.087	14 : 44 : 18.45	−59 : 55 : 11.5	−20.36	109	57.1	3	0.0	3	32	D
316.640 − 0.087	14 : 44 : 18.45	−59 : 55 : 11.5	−19.77	67	40.5	3	0.0	1	8	D
316.640 − 0.087	14 : 44 : 18.45	−59 : 55 : 11.5	−19.95	62	16.3	3	1.2	1	8	D
316.640 − 0.087	14 : 44 : 18.45	−59 : 55 : 11.5	−22.23	49	73.1	3	1.3	1	8	D
316.811 − 0.057	14 : 45 : 26.43	−59 : 49 : 16.3	−45.61	39	3.1	7	0.0	9	32	B
317.466 − 0.402	14 : 51 : 19.69	−59 : 50 : 50.7	−38.87	10	6.9	8	0.0	8	20	C
317.466 − 0.402	14 : 51 : 19.69	−59 : 50 : 50.7	−39.57	14	5.9	9	0.0	11	20	C
317.701 + 0.110	14 : 51 : 11.69	−59 : 17 : 02.1	−42.15	9	4.2	5	0.0	6	12	C
318.050 + 0.087	14 : 53 : 42.67	−59 : 08 : 52.4	−51.47	2	4.1	10	0.0	3	22	B
318.948 − 0.196	15 : 00 : 55.40	−58 : 58 : 52.1	−34.63	356	9.0	79	2.2	40	32	B
318.948 − 0.196	15 : 00 : 55.40	−58 : 58 : 52.1	−36.30	31	34.8	32	1.9	12	32	B
320.231 − 0.284	15 : 09 : 51.94	−58 : 25 : 38.5	−62.28	29	9.9	21	1.3	7	32	B
321.033 − 0.483	15 : 15 : 52.63	−58 : 11 : 07.7	−57.27	10	3.3	0	2.7	5	8	D
321.033 − 0.483	15 : 15 : 52.63	−58 : 11 : 07.7	−60.88	12	3.4	0	3.4	5	8	D
321.033 − 0.483	15 : 15 : 52.63	−58 : 11 : 07.7	−61.23	10	4.0	0	3.2	4	8	D
321.033 − 0.483	15 : 15 : 52.63	−58 : 11 : 07.7	−61.40	10	3.9	0	3.9	4	8	D
322.158 + 0.636	15 : 18 : 34.64	−56 : 38 : 25.3	−62.94	107	11.7	59	2.5	16	29	B
322.158 + 0.636	15 : 18 : 34.64	−56 : 38 : 25.3	−63.29	79	50.4	37	2.8	10	29	B
322.158 + 0.636	15 : 18 : 34.64	−56 : 38 : 25.3	−64.08	74	54.7	51	2.8	13	29	B
323.459 − 0.079	15 : 29 : 19.33	−56 : 31 : 22.8	−67.15	70	67.2	42	2.2	9	20	B
323.459 − 0.079	15 : 29 : 19.33	−56 : 31 : 22.8	−68.29	124	8.3	65	1.9	25	32	B
323.459 − 0.079	15 : 29 : 19.33	−56 : 31 : 22.8	−68.99	112	9.7	92	3.3	12	32	B
323.459 − 0.079	15 : 29 : 19.33	−56 : 31 : 22.8	−69.26	227	81.6	100	3.8	15	32	B
323.459 − 0.079	15 : 29 : 19.33	−56 : 31 : 22.8	−70.48	33	8.3	26	1.8	10	32	B
323.459 − 0.079	15 : 29 : 19.33	−56 : 31 : 22.8	−66.98	83	9.5	39	2.1	12	8	B
323.740 − 0.263	15 : 31 : 45.45	−56 : 30 : 50.1	−47.93	83	11.0	35	1.5	16	26	A
323.740 − 0.263	15 : 31 : 45.45	−56 : 30 : 50.1	−48.46	337	8.7	215	1.9	74	26	A
323.740 − 0.263	15 : 31 : 45.45	−56 : 30 : 50.1	−48.98	640	93.4	104	1.3	30	26	A
323.740 − 0.263	15 : 31 : 45.45	−56 : 30 : 50.1	−50.39	1420	3.7	993	1.7	237	26	A
323.740 − 0.263	15 : 31 : 45.45	−56 : 30 : 50.1	−51.18	975	7.8	148	0.0	106	26	A
323.740 − 0.263	15 : 31 : 45.45	−56 : 30 : 50.1	−52.41	47	10.2	22	1.1	8	14	A
323.740 − 0.263	15 : 31 : 45.45	−56 : 30 : 50.1	−49.34	717	149.5	98	2.0	32	8	A
326.475 + 0.703	15 : 43 : 16.64	−54 : 07 : 14.6	−38.43	38	52.8	26	1.1	5	14	A
326.641 + 0.611	15 : 44 : 33.33	−54 : 05 : 31.5	−42.64	6	43.4	11	3.1	2	14	D
326.641 + 0.611	15 : 44 : 33.33	−54 : 05 : 31.5	−42.99	14	3.9	1	0.0	3	14	D
326.859 − 0.677	15 : 51 : 14.19	−54 : 58 : 04.8	−58.03	18	8.9	2	0.0	2	20	D
327.120 + 0.511	15 : 47 : 32.73	−53 : 52 : 38.4	−83.60	7	6.0	2	0.0	1	20	D
327.120 + 0.511	15 : 47 : 32.73	−53 : 52 : 38.4	−87.03	15	5.2	2	0.0	4	20	D
327.402 + 0.445	15 : 49 : 19.50	−53 : 45 : 13.9	−81.76	8	0.8	11	0.8	4	10	A
327.402 + 0.445	15 : 49 : 19.50	−53 : 45 : 13.9	−82.90	31	54.3	42	0.0	9	22	A
327.402 + 0.445	15 : 49 : 19.50	−53 : 45 : 13.9	−83.25	13	16.6	24	0.7	6	22	A
328.237 − 0.547	15 : 57 : 58.28	−53 : 59 : 22.7	−44.48	475	37.4	304	2.1	36	22	A
328.237 − 0.547	15 : 57 : 58.28	−53 : 59 : 22.7	−44.74	482	25.6	194	1.7	37	22	A
328.254 − 0.532	15 : 57 : 59.75	−53 : 58 : 00.4	−36.83	57	9.0	33	0.9	13	23	A
328.809 + 0.633	15 : 55 : 48.70	−52 : 43 : 05.5	−44.40	151	9.4	101	2.3	27	34	B
328.809 + 0.633	15 : 55 : 48.70	−52 : 43 : 05.5	−45.10	30	28.9	33	2.5	6	34	B
328.809 + 0.633	15 : 55 : 48.70	−52 : 43 : 05.5	−46.24	126	29.1	28	1.7	12	34	B
329.031 − 0.198	16 : 00 : 30.32	−53 : 12 : 27.3	−35.06	15	5.3	18	1.2	9	28	B

Continued on Next Page...

Table B.2 – Continued...

Name	α_{J2000} hh:mm:ss	δ_{J2000} dd:mm:ss	V (km s^{-1})	S_H (Jy)	θ_H (mas)	S_C (Jy)	θ_C (mas)	Error (Jy)	DF (N−4)	Grade
329.031 − 0.198	16 : 00 : 30.32	−53 : 12 : 27.3	−36.12	35	18.6	15	0.8	12	16	B
329.031 − 0.198	16 : 00 : 30.32	−53 : 12 : 27.3	−37.17	25	5.0	16	1.0	12	28	B
329.339 + 0.148	16 : 00 : 33.13	−52 : 44 : 39.8	−106.28	9	5.9	11	0.7	3	22	C
329.407 − 0.459	16 : 03 : 32.65	−53 : 09 : 26.9	−66.64	47	21.7	29	1.6	8	34	B
331.278 − 0.188	16 : 11 : 26.59	−51 : 41 : 56.7	−77.63	30	10.8	15	2.8	2	22	D
331.278 − 0.188	16 : 11 : 26.59	−51 : 41 : 56.7	−77.98	55	6.2	5	2.2	2	34	D
331.278 − 0.188	16 : 11 : 26.59	−51 : 41 : 56.7	−78.16	35	12.5	19	3.4	2	22	D
331.278 − 0.188	16 : 11 : 26.59	−51 : 41 : 56.7	−78.77	37	13.2	18	3.3	2	22	D
331.278 − 0.188	16 : 11 : 26.59	−51 : 41 : 56.7	−83.25	25	3.7	1	0.0	2	22	D
331.278 − 0.188	16 : 11 : 26.59	−51 : 41 : 56.7	−84.31	15	3.3	1	0.0	2	22	D
331.278 − 0.188	16 : 11 : 26.59	−51 : 41 : 56.7	−85.09	17	14.1	14	3.4	2	22	D
331.342 − 0.346	16 : 12 : 26.45	−51 : 46 : 16.4	−67.08	13	2.2	7	0.0	11	26	C
331.442 − 0.187	16 : 12 : 12.49	−51 : 35 : 10.1	−88.72	11	19.3	7	1.1	5	20	C
332.295 + 2.280	16 : 05 : 41.72	−49 : 11 : 30.3	−23.67	56	28.0	23	1.2	7	40	A
333.315 + 0.105	16 : 19 : 29.01	−50 : 04 : 41.3	−43.86	5	0.7	1	0.7	3	36	D
333.466 − 0.164	16 : 21 : 20.18	−50 : 09 : 48.6	−41.96	8	1.4	2	1.4	2	36	D
333.562 − 0.025	16 : 21 : 08.80	−49 : 59 : 48.0	−35.30	15	4.8	18	1.1	7	48	B
333.646 + 0.058	16 : 21 : 09.14	−49 : 52 : 45.9	−87.39	4	6.9	4	0.0	6	18	D
333.900 − 0.099	16 : 22 : 57.39	−49 : 48 : 35.1	−36.94	9	4.3	2	1.0	2	36	D
334.635 − 0.015	16 : 25 : 45.73	−49 : 13 : 37.4	−29.13	15	4.4	2	0.0	2	36	D
334.635 − 0.015	16 : 25 : 45.73	−49 : 13 : 37.4	−30.18	14	4.3	2	0.0	2	36	D
335.060 − 0.427	16 : 29 : 23.13	−49 : 12 : 27.1	−46.93	28	15.3	18	4.2	4	42	D
335.585 − 0.285	16 : 30 : 57.28	−48 : 43 : 39.7	−43.88	21	3.6	2	0.4	3	36	D
335.585 − 0.285	16 : 30 : 57.28	−48 : 43 : 39.7	−48.19	10	5.2	2	0.0	2	36	D
335.585 − 0.285	16 : 30 : 57.28	−48 : 43 : 39.7	−48.62	7	5.8	3	1.2	1	36	D
335.585 − 0.285	16 : 30 : 57.28	−48 : 43 : 39.7	−51.43	63	24.9	5	1.9	6	36	D
335.789 + 0.174	16 : 29 : 47.33	−48 : 15 : 51.7	−47.39	209	48.1	95	4.1	25	42	B
336.018 − 0.827	16 : 35 : 09.26	−48 : 46 : 47.4	−41.34	101	20.6	6	2.7	6	36	D
336.018 − 0.827	16 : 35 : 09.26	−48 : 46 : 47.4	−45.11	27	17.8	2	0.0	2	36	D
336.018 − 0.827	16 : 35 : 09.26	−48 : 46 : 47.4	−47.83	44	15.2	4	1.7	2	36	D
336.018 − 0.827	16 : 35 : 09.26	−48 : 46 : 47.4	−53.28	55	11.7	3	1.2	2	36	D
336.994 − 0.027	16 : 35 : 33.98	−47 : 31 : 12.0	−120.47	13	18.0	3	0.0	3	8	D
336.994 − 0.027	16 : 35 : 33.98	−47 : 31 : 12.0	−125.74	25	16.6	3	0.0	2	24	D
337.052 − 0.226	16 : 36 : 40.17	−47 : 36 : 38.4	−77.19	7	19.4	4	1.8	1	8	D
337.052 − 0.226	16 : 36 : 40.17	−47 : 36 : 38.4	−77.54	8	30.0	3	1.7	1	8	D
337.153 − 0.395	16 : 37 : 48.86	−47 : 38 : 56.5	−49.32	12	5.0	4	0.6	3	48	D
337.404 − 0.402	16 : 38 : 50.52	−47 : 28 : 00.2	−39.70	50	30.2	7	2.2	2	48	D
337.388 − 0.210	16 : 37 : 56.01	−47 : 21 : 01.2	−55.92	23	25.4	6	2.3	2	48	D
337.705 − 0.053	16 : 38 : 29.63	−47 : 00 : 35.5	−50.19	80	21.4	6	2.5	2	48	D
337.705 − 0.053	16 : 38 : 29.63	−47 : 00 : 35.5	−51.07	29	27.8	2	0.0	1	8	D
337.705 − 0.053	16 : 38 : 29.63	−47 : 00 : 35.5	−52.74	46	128.9	18	5.5	2	48	D
337.705 − 0.053	16 : 38 : 29.63	−47 : 00 : 35.5	−53.26	25	24.9	3	1.7	1	8	D
337.705 − 0.053	16 : 38 : 29.63	−47 : 00 : 35.5	−53.62	18	18.7	2	0.0	1	8	D
337.705 − 0.053	16 : 38 : 29.63	−47 : 00 : 35.5	−54.58	66	21.6	67	6.1	4	48	D
337.920 − 0.456	16 : 41 : 06.05	−47 : 07 : 02.5	−38.62	12	6.2	23	1.0	6	48	A
338.287 + 0.120	16 : 40 : 00.13	−46 : 27 : 37.1	−40.01	5	4.2	7	1.9	2	38	D
338.396 − 0.007	16 : 40 : 58.41	−46 : 27 : 47.8	−30.10	27	5.6	2	0.0	2	48	D
338.497 + 0.207	16 : 40 : 25.89	−46 : 14 : 43.5	−49.35	17	6.2	2	0.7	2	48	D
338.497 + 0.207	16 : 40 : 25.89	−46 : 14 : 43.5	−49.79	27	12.3	21	4.0	3	48	D
338.497 + 0.207	16 : 40 : 25.89	−46 : 14 : 43.5	−51.81	30	5.0	2	0.0	10	48	D
338.497 + 0.207	16 : 40 : 25.89	−46 : 14 : 43.5	−52.43	45	5.7	1	0.0	7	48	D
338.497 + 0.207	16 : 40 : 25.89	−46 : 14 : 43.5	−52.95	30	20.6	3	2.0	1	8	D
338.497 + 0.207	16 : 40 : 25.89	−46 : 14 : 43.5	−54.62	13	16.9	4	2.3	1	8	D
338.497 + 0.207	16 : 40 : 25.89	−46 : 14 : 43.5	−62.79	5	8.0	3	0.7	2	8	D
338.561 + 0.218	16 : 40 : 37.96	−46 : 11 : 25.8	−39.05	16	4.1	15	1.9	3	56	C
338.925 + 0.634	16 : 40 : 13.56	−45 : 38 : 33.2	−58.99	9	3.5	17	1.3	3	48	B
338.920 + 0.550	16 : 40 : 34.01	−45 : 42 : 07.1	−61.29	29	18.3	22	1.3	5	40	B
338.935 − 0.062	16 : 43 : 16.01	−46 : 05 : 40.2	−41.87	17	3.3	16	1.5	4	48	B
339.053 − 0.315	16 : 44 : 48.99	−46 : 10 : 13.0	−111.63	143	14.0	5	0.5	4	56	D
339.053 − 0.315	16 : 44 : 48.99	−46 : 10 : 13.0	−111.81	148	13.9	4	0.5	3	56	D
339.053 − 0.315	16 : 44 : 48.99	−46 : 10 : 13.0	−111.05	33	16.5	5	0.5	6	36	D
339.622 − 0.121	16 : 46 : 05.99	−45 : 36 : 43.3	−33.16	18	1.0	14	0.0	3	48	A
339.681 − 1.208	16 : 51 : 06.21	−46 : 16 : 02.9	−21.42	40	14.8	9	1.8	6	48	D
339.681 − 1.208	16 : 51 : 06.21	−46 : 16 : 02.9	−22.21	34	16.4	5	1.9	2	48	D
339.681 − 1.208	16 : 51 : 06.21	−46 : 16 : 02.9	−34.33	24	5.7	2	0.0	3	48	D
339.681 − 1.208	16 : 51 : 06.21	−46 : 16 : 02.9	−37.52	5	3.9	7	1.6	2	28	D
339.884 − 1.259	16 : 52 : 04.67	−46 : 08 : 34.2	−34.84	190	5.8	117	1.6	47	56	A
339.884 − 1.259	16 : 52 : 04.67	−46 : 08 : 34.2	−35.63	334	29.3	525	0.6	40	56	A
339.884 − 1.259	16 : 52 : 04.67	−46 : 08 : 34.2	−36.51	228	5.0	81	1.0	28	56	A
339.884 − 1.259	16 : 52 : 04.67	−46 : 08 : 34.2	−37.39	197	4.5	326	1.1	58	56	A
339.949 − 0.539	16 : 49 : 07.97	−45 : 37 : 58.8	−91.07	38	4.7	3	4.7	4	46	D
339.949 − 0.539	16 : 49 : 07.97	−45 : 37 : 58.8	−91.51	38	4.2	3	4.2	2	46	D
339.949 − 0.539	16 : 49 : 07.97	−45 : 37 : 58.8	−96.51	9	22.0	25	4.4	2	46	D
339.949 − 0.539	16 : 49 : 07.97	−45 : 37 : 58.8	−97.39	31	20.1	3	2.7	1	14	D
339.949 − 0.539	16 : 49 : 07.97	−45 : 37 : 58.8	−97.83	41	34.2	12	3.6	3	46	D
339.949 − 0.539	16 : 49 : 07.97	−45 : 37 : 58.8	−100.46	22	15.2	17	3.4	2	46	D
339.949 − 0.539	16 : 49 : 07.97	−45 : 37 : 58.8	−103.88	12	3.1	3	3.1	2	46	D
339.949 − 0.539	16 : 49 : 07.97	−45 : 37 : 58.8	−91.98	9	3.7	3	3.7	2	28	D
339.949 − 0.539	16 : 49 : 07.97	−45 : 37 : 58.8	−97.25	26	25.9	8	4.0	1	28	D
339.986 − 0.425	16 : 48 : 46.31	−45 : 31 : 51.3	−87.70	31	20.0	2	0.0	1	56	D
339.986 − 0.425	16 : 48 : 46.31	−45 : 31 : 51.3	−88.49	27	113.3	46	6.3	3	56	D
339.986 − 0.425	16 : 48 : 46.31	−45 : 31 : 51.3	−89.19	59	30.9	4	1.8	2	56	D
340.054 − 0.244	16 : 48 : 13.89	−45 : 21 : 43.5	−59.36	8	6.0	30	1.8	4	56	B
340.054 − 0.244	16 : 48 : 13.89	−45 : 21 : 43.5	−60.86	7	1.3	17	1.3	3	56	B
340.785 − 0.096	16 : 50 : 14.84	−44 : 42 : 26.3	−108.02	133	6.0	632	6.0	18	56	B
341.218 − 0.212	16 : 52 : 17.86	−44 : 26 : 52.3	−44.42	373	11.0	166	4.0	13	56	B
342.446 − 0.072	16 : 55 : 59.94	−43 : 24 : 22.5	−41.24	22	13.7	4	1.6	1	56	D
342.446 − 0.072	16 : 55 : 59.94	−43 : 24 : 22.5	−42.03	44	27.6	3	0.6	2	56	D
342.446 − 0.072	16 : 55 : 59.94	−43 : 24 : 22.5	−42.30	42	20.6	3	0.9	2	56	D
345.012 + 1.797	16 : 56 : 46.82	−40 : 14 : 08.9	−17.02	113	5.0	19	0.8	9	56	A
345.012 + 1.797	16 : 56 : 46.82	−40 : 14 : 08.9	−17.46	54	5.1	29	1.3	7	56	A
345.012 + 1.797	16 : 56 : 46.82	−40 : 14 : 08.9	−20.18	67	3.5	55	1.4	13	56	A

Continued on Next Page...

Table B.2 – Continued...

Name	$\alpha_{\rm J2000}$ hh:mm:ss	$\delta_{\rm J2000}$ dd:mm:ss	V (km s^{-1})	S_H (Jy)	θ_H (mas)	S_C (Jy)	θ_C (mas)	Error (Jy)	DF (N−4)	Grade
$345.012 + 1.797$	16 : 56 : 46.82	−40 : 14 : 08.9	−21.76	265	1.6	12	0.0	37	56	A
$345.012 + 1.797$	16 : 56 : 46.82	−40 : 14 : 08.9	−22.03	280	2.6	19	0.0	50	56	A
$345.003 - 0.223$	17 : 05 : 10.89	−41 : 29 : 06.2	−22.37	57	34.7	4	1.1	4	56	D
$345.003 - 0.223$	17 : 05 : 10.89	−41 : 29 : 06.2	−22.89	98	30.5	19	3.1	10	56	D
$345.003 - 0.223$	17 : 05 : 10.89	−41 : 29 : 06.2	−23.68	60	34.0	3	1.0	5	56	D
$345.003 - 0.223$	17 : 05 : 10.89	−41 : 29 : 06.2	−26.05	72	26.0	4	1.2	7	56	D
$345.003 - 0.223$	17 : 05 : 10.89	−41 : 29 : 06.2	−26.41	72	31.3	2	0.0	4	56	D
$345.003 - 0.223$	17 : 05 : 10.89	−41 : 29 : 06.2	−26.84	106	28.5	5	1.4	8	56	D
$345.003 - 0.223$	17 : 05 : 10.89	−41 : 29 : 06.2	−27.64	56	22.3	3	0.9	6	56	D
$345.487 + 0.314$	17 : 04 : 28.24	−40 : 46 : 28.7	−14.06	193	27.9	49	1.1	27	56	A
$345.487 + 0.314$	17 : 04 : 28.24	−40 : 46 : 28.7	−19.06	49	23.7	142	2.1	16	56	A
$346.480 + 0.221$	17 : 08 : 00.11	−40 : 02 : 15.9	−19.04	20	4.5	2	0.0	3	28	D
$348.579 - 0.920$	17 : 19 : 10.61	−39 : 00 : 24.2	−10.41	19	3.1	10	0.0	3	16	A
$348.617 - 1.162$	17 : 20 : 18.65	−39 : 06 : 50.8	−11.47	13	6.8	26	1.5	3	36	B
$348.727 - 1.037$	17 : 20 : 06.54	−38 : 57 : 09.1	−7.36	60	18.3	25	1.4	10	11	B
$350.686 - 0.491$	17 : 23 : 28.63	−37 : 01 : 48.8	−13.76	24	5.9	5	0.0	6	28	C
$351.417 + 0.645$	17 : 20 : 53.37	−35 : 47 : 01.2	−9.71	441	6.9	181	1.3	93	28	A
$351.417 + 0.645$	17 : 20 : 53.37	−35 : 47 : 01.2	−10.32	1232	7.7	365	2.0	399	28	A
$351.688 + 0.171$	17 : 23 : 34.52	−35 : 49 : 46.3	−36.07	11	5.2	8	0.8	5	28	C
$351.775 - 0.536$	17 : 26 : 42.57	−36 : 09 : 17.6	1.80	77	6.6	16	6.6	13	28	D
$351.775 - 0.536$	17 : 26 : 42.57	−36 : 09 : 17.6	1.27	43	23.8	3	1.4	2	28	D
$352.630 - 1.067$	17 : 31 : 13.91	−35 : 44 : 08.7	−2.91	121	4.1	14	0.0	12	28	A
$352.630 - 1.067$	17 : 31 : 13.91	−35 : 44 : 08.7	−3.27	53	4.4	75	1.6	19	28	A
$354.615 + 0.472$	17 : 30 : 17.13	−33 : 13 : 55.1	−24.21	60	165.3	105	4.2	6	22	B
$358.371 - 0.468$	17 : 43 : 31.95	−30 : 34 : 10.7	−5.98	6	53.9	7	0.0	3	14	C
$358.460 - 0.393$	17 : 43 : 27.24	−30 : 27 : 14.6	1.26	26	15.4	22	1.3	4	22	B
$359.436 - 0.102$	17 : 44 : 40.21	−29 : 28 : 12.5	−46.66	86	26.3	22	5.8	3	28	D
$359.615 - 0.243$	17 : 45 : 39.09	−29 : 23 : 30.0	24.50	5	34.6	21	1.8	3	28	B
$359.615 - 0.243$	17 : 45 : 39.09	−29 : 23 : 30.0	19.58	0	2.5	59	2.5	4	28	B

Table B.3: Non–detections and 'unknown'-grade sources surveyed from Chapter §4. **Columns: (1)** Maser name in Galactic coordinates, **(2)** right ascention (J2000), **(3)** declination (J2000), **(4)** peak velocity (km/s) from MMB - confirmed same peak in this survey, **(5)** MMB autocorrelated peak flux density (Jy). Notes: Both U–grade masers 332.963–0.679 and 353.410–0.360 were observed at the incorrect coordinates, $\Delta\delta = 1$ amin and $\Delta\alpha = 10$ amin offset respectively.

Name	α_{J2000} (hh:mm:ss)	δ_{J2000} (dd:mm:ss)	Vp (km s^{-1})	Sp (Jy)	Grade
285.337 − 0.002	10 : 32 : 09.62	−58 : 02 : 04.6	+0.7	17.9	F
286.383 − 1.834	10 : 31 : 55.12	−60 : 08 : 38.6	+9.6	17.6	F
294.337 − 1.706	11 : 33 : 49.91	−63 : 16 : 32.5	-11.7	14.5	F
294.511 − 1.621	11 : 35 : 32.25	−63 : 14 : 43.2	-11.9	9.0	F
311.643 − 0.380	14 : 06 : 38.77	−61 : 58 : 23.1	32.6	11.13	F
313.767 − 0.863	14 : 25 : 01.73	−61 : 44 : 58.1	-56.3	9.0	F
313.994 − 0.084	14 : 24 : 30.78	−60 : 56 : 28.3	-4.9	15.2	F
320.780 + 0.248	15 : 11 : 23.48	−57 : 41 : 25.1	-5.1	40.0	F
322.705 − 0.331	15 : 25 : 47.52	−57 : 09 : 15.5	-21.6	2.0	F
324.716 + 0.342	15 : 34 : 57.47	−55 : 27 : 23.6	-45.9	10.8	F
324.915 + 0.158	15 : 36 : 51.17	−55 : 29 : 22.9	-2.3	12.1	F
326.662 + 0.520	15 : 45 : 02.95	−54 : 09 : 03.1	-38.6	29.1	F
327.392 + 0.199	15 : 50 : 18.48	−53 : 57 : 06.3	-84.5	11.4	F
327.566 − 0.850	15 : 55 : 47.61	−54 : 39 : 11.4	-29.7	15.0	F
329.066 − 0.308	16 : 01 : 09.93	−53 : 16 : 02.6	-43.8	21.9	F
329.183 − 0.314	16 : 01 : 47.01	−53 : 11 : 43.3	-55.6	10.7	F
329.469 + 0.503	15 : 59 : 40.71	−52 : 23 : 27.3	-72.0	21.6	F
329.610 + 0.114	16 : 02 : 03.14	−52 : 35 : 33.5	-60.1	49.9	F
329.719 + 1.164	15 : 58 : 07.09	−51 : 43 : 32.6	-75.8	24.4	F
331.132 − 0.244	16 : 10 : 59.76	−51 : 50 : 22.6	-84.3	37.4	F
331.542 − 0.066	16 : 12 : 09.02	−51 : 25 : 47.6	-85.8	7.0	F
331.556 − 0.121	16 : 12 : 27.21	−51 : 27 : 38.2	-97.1	69.3	F
331.710 + 0.603	16 : 10 : 01.77	−50 : 49 : 32.3	-73.3	13.0	F
332.094 − 0.421	16 : 16 : 16.45	−51 : 18 : 25.7	-58.5	21.8	F
332.813 − 0.701	16 : 20 : 48.12	−51 : 00 : 15.6	-53.1	12.9	F
332.963 − 0.679	16 : 21 : 22.92	−50 : 52 : 58.5	-45.9	63.3	U
333.128 − 0.560	16 : 21 : 35.38	−50 : 40 : 56.5	-52.7	18.0	F
333.121 − 0.434	16 : 20 : 59.66	−50 : 35 : 51.9	-48.5	54.59	F
333.163 − 0.101	16 : 19 : 42.67	−50 : 19 : 53.2	-95.2	11.8	F
333.184 − 0.091	16 : 19 : 45.62	−50 : 18 : 35.0	-81.9	12.5	F
333.683 − 0.437	16 : 23 : 29.78	−50 : 12 : 08.6	-5.6	40.6	F
335.426 − 0.240	16 : 30 : 05.58	−48 : 48 : 44.8	-50.6	91.2	F
335.556 − 0.307	16 : 30 : 55.98	−48 : 45 : 50.2	-116.0	25.0	F
335.726 + 0.191	16 : 29 : 27.37	−48 : 17 : 53.2	-44.4	75.4	F
336.358 − 0.137	16 : 33 : 29.17	−48 : 03 : 43.9	-73.5	13.2	F
336.433 − 0.262	16 : 34 : 20.22	−48 : 05 : 32.2	-93.0	32.0	F
336.526 − 0.156	16 : 34 : 15.00	−47 : 57 : 07.4	-94.8	0.7	F
336.864 + 0.005	16 : 34 : 54.44	−47 : 35 : 37.3	-76.0	66.2	F
336.830 − 0.375	16 : 36 : 26.19	−47 : 52 : 31.1	-22.8	33.9	F
336.864 + 0.005	16 : 34 : 54.44	−47 : 35 : 37.3	-76.0	66.2	F
336.941 − 0.156	16 : 35 : 55.19	−47 : 38 : 45.4	-67.2	22.0	F
336.983 − 0.183	16 : 36 : 12.41	−47 : 37 : 58.2	-80.7	14.9	F
337.202 − 0.094	16 : 36 : 41.22	−47 : 24 : 40.2	-71.7	1.7	F
337.613 − 0.060	16 : 38 : 09.54	−47 : 04 : 59.9	-41.6	19.5	F
337.632 − 0.079	16 : 38 : 19.12	−47 : 04 : 53.3	-56.9	13.6	F
338.069 + 0.011	16 : 39 : 37.95	−46 : 41 : 45.3	-39.3	4.0	F
338.566 + 0.110	16 : 41 : 07.03	−46 : 15 : 28.3	-78.1	10.0	F
338.875 − 0.084	16 : 43 : 08.25	−46 : 09 : 12.8	-41.4	21.2	F
338.850 + 0.409	16 : 40 : 54.29	−45 : 50 : 52.0	-55.7	1.4	F
338.902 + 0.394	16 : 41 : 10.06	−45 : 49 : 05.4	-26.2	1.7	F
339.762 + 0.054	16 : 45 : 51.56	−45 : 23 : 32.6	-51.0	11.7	F
340.249 − 0.046	16 : 48 : 05.18	−45 : 05 : 08.4	-126.3	10.1	F
340.970 − 1.022	16 : 54 : 57.32	−45 : 09 : 05.2	-31.3	10.1	F
343.354 − 0.067	16 : 59 : 04.23	−42 : 41 : 35.0	-117.7	20.3	F
344.419 + 0.044	17 : 02 : 08.62	−41 : 47 : 10.3	-63.2	2.3	F
346.036 + 0.048	17 : 07 : 20.02	−40 : 29 : 49.0	-6.4	10.4	F
347.628 + 0.149	17 : 11 : 50.92	−39 : 09 : 29.2	-96.5	19.0	F
348.884 + 0.096	17 : 15 : 50.13	−38 : 10 : 12.4	-74.5	12.9	F
349.092 + 0.105	17 : 16 : 24.74	−37 : 59 : 47.2	-76.5	23.1	F
350.104 + 0.084	17 : 19 : 26.68	−37 : 10 : 53.1	-68.1	14.6	F
350.299 + 0.122	17 : 19 : 50.87	−36 : 59 : 59.9	-62.2	31.2	F
351.161 + 0.697	17 : 19 : 57.50	−35 : 57 : 52.8	-5.2	12.0	F
351.382 − 0.181	17 : 24 : 09.58	−36 : 16 : 49.3	-59.8	16.9	F
351.581 − 0.353	17 : 25 : 25.12	−36 : 12 : 46.1	-94.2	47.5	F
352.133 − 0.944	17 : 29 : 22.32	−36 : 05 : 00.2	-7.8	15.7	F
353.273 + 0.641	17 : 26 : 01.58	−34 : 15 : 15.4	-4.4	12.7	F
353.410 − 0.360	17 : 30 : 26.18	−34 : 41 : 45.6	-20.4	109.0	F
353.429 − 0.090	17 : 29 : 23.48	−34 : 31 : 50.3	-61.8	13.0	N
353.464 + 0.562	17 : 26 : 51.53	−34 : 08 : 25.7	-50.3	12.8	F
354.724 + 0.300	17 : 31 : 15.55	−33 : 14 : 05.7	+93.8	12.2	F
355.346 + 0.149	17 : 33 : 28.91	−32 : 47 : 49.5	+9.9	9.2	F
356.662 − 0.263	17 : 38 : 29.16	−31 : 54 : 38.8	-53.8	10.1	F
357.967 − 0.163	17 : 41 : 20.26	−30 : 45 : 06.9	-4.2	55.1	F
358.263 − 2.061	17 : 49 : 37.63	−31 : 29 : 18.0	+3.0	0.0	F
358.809 − 0.085	17 : 43 : 05.40	−29 : 59 : 45.8	-56.2	12.0	F
358.841 − 0.737	17 : 45 : 44.29	−30 : 18 : 33.6	-20.6	13.1	F
358.931 − 0.030	17 : 43 : 10.02	−29 : 51 : 45.8	-15.9	10.1	F
359.138 + 0.031	17 : 43 : 25.67	−29 : 39 : 17.3	-3.9	19.6	F

B.3 Maser Compactness Statistics

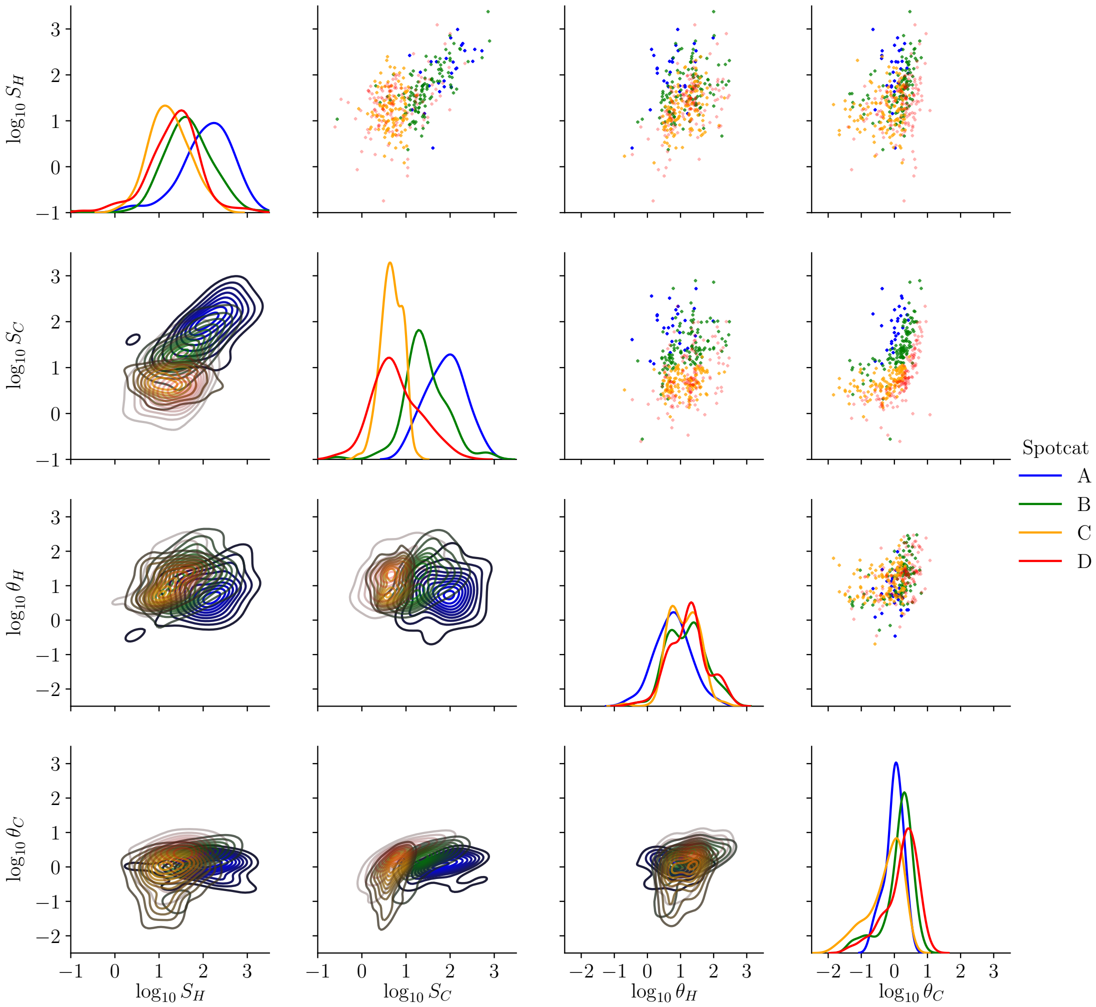

Figure B.1: Distributions of fitted parameters categorised by the compactness of the host maser spot (unique velocity feature). The fitted parameters are flux density of halo S_H (Jy), flux density of core S_C (Jy), size of halo θ_H (mas) and size of core θ_C (mas). All metrics are $\log_{10}$ in this figure. A is the best compactness where D is not measureably compact at all.

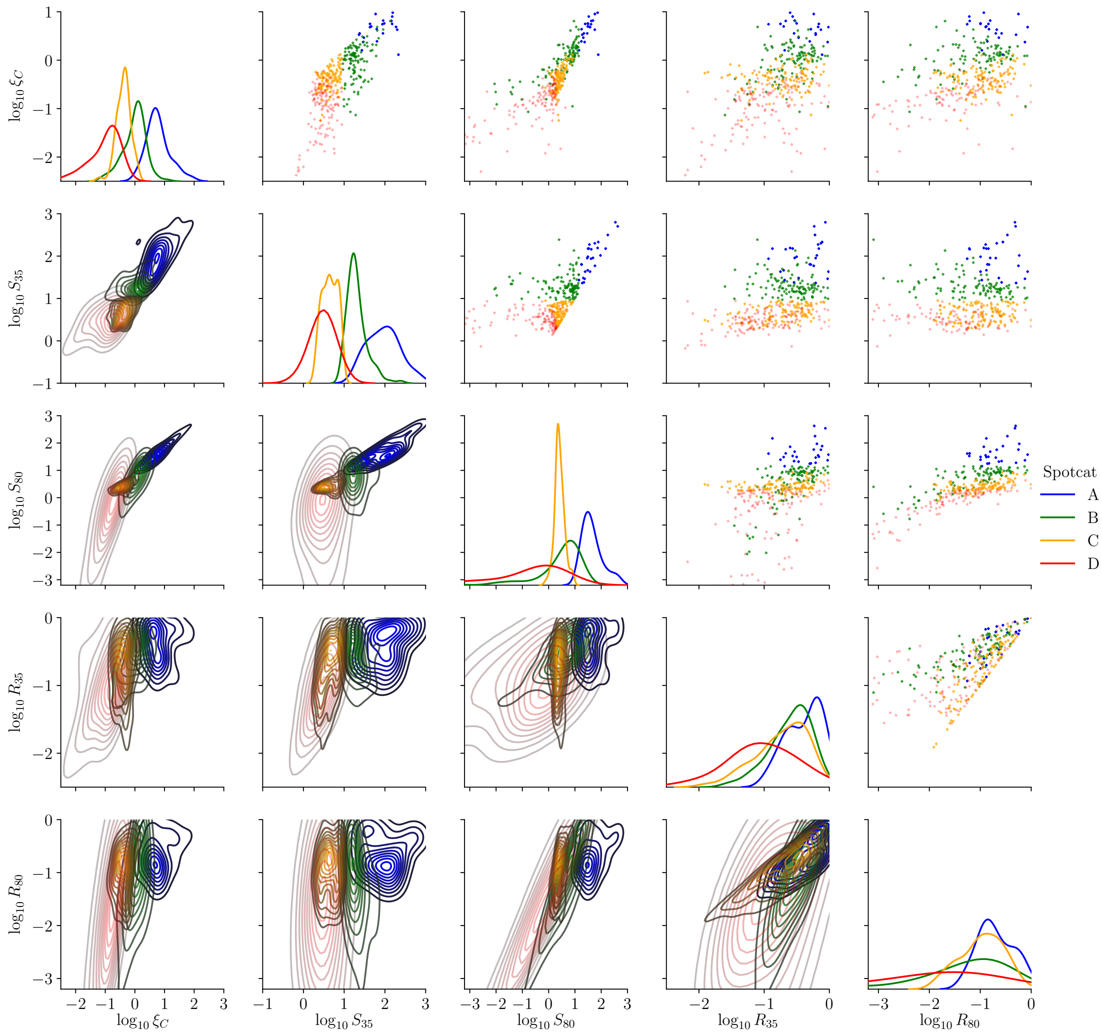

Figure B.2: Final distributions of metrics as categorised by the host maser spot (unique velocity feature). **Top to bottom:** Emission measure of core ξ_C, flux density at 35Mλ S_{35}, flux density at 80Mλ S_{80}, radio of flux density at 35Mλ to flux density of autocorrelation R_{35}, radio of flux density at 80Mλ to flux density of autocorrelation R_{80}. All metrics are $\log_{10}$ in this figure. A is the best compactness where D is not measureably compact at all.

B.4 All Maser Spot Compactness

The following large figure shows the amplitude of the visibility data (Jy) vs. $uv-$distance (Mλ) for each peak velocity channel of each maser spot surveyed in Chapter §4. There are often multiple spots per maser, so the caption contains the maser name (in Galactic coordinates) and velocity (km s^{-1}). In addition, the each figure shows the relevant core–halo least–squares fit to the visibility data (Chapter 4).

Figure B.3: Calibrated visibility amplitude (Jy) vs. uv-distance (Mλ) plots for all maser spots identified. Subcaptions contain maser name in Galactic coordinates and maser spot recession velocity ($\pm$0.09 km s^{-1}). **Black points:** Extracted visiblity data with error bars identified from the standard deviation of the autocorrelated flux densities, then re-weighted s.t. the reduced chi–squared $\chi^2_\nu \approx 1$ for the linear least–squares fit. **Red line:** Least–squares fit to the visibility data for the core–halo model; **Green lines:** Sensitivity threasholds for the Ceduna–Auscope baseline ($3\sigma = 10$ Jy) and AuScope-AuScope baseline ($3\sigma = 15$ Jy) in a 40s scan.

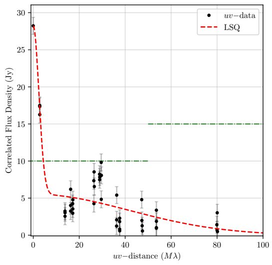

(1) G192.600-0.048
$v = 8.27\,\mathrm{km\,s^{-1}}$

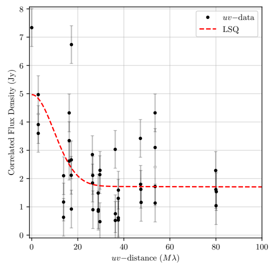

(2) G192.600-0.048
$v = 7.75\,\mathrm{km\,s^{-1}}$

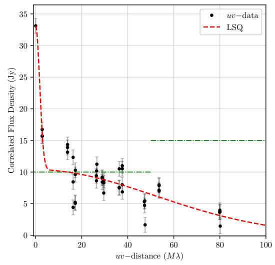

(3) G192.600-0.048
$v = 7.13\,\mathrm{km\,s^{-1}}$

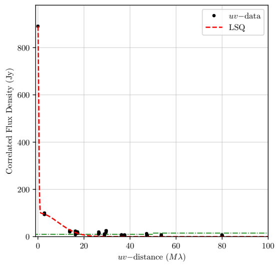

(4) G192.600-0.048
$v = 6.60\,\mathrm{km\,s^{-1}}$

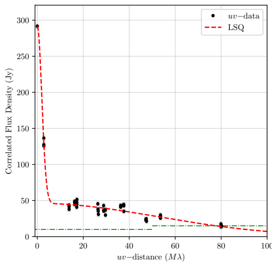

(5) G192.600-0.048
$v = 5.90\,\mathrm{km\,s^{-1}}$

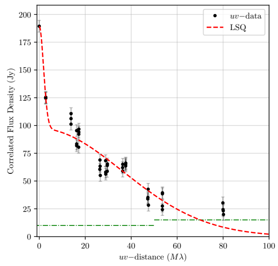

(6) G192.600-0.048
$v = 5.20\,\mathrm{km\,s^{-1}}$

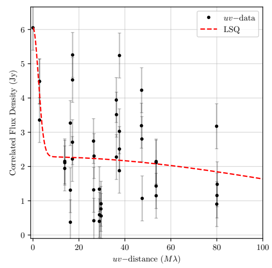

(7) G192.600-0.048
$v = 3.79\,\mathrm{km\,s^{-1}}$

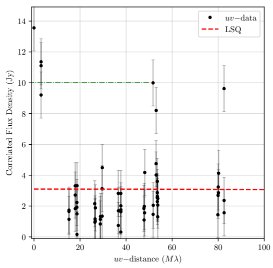

(8) G196.454-1.677
$v = 15.88\,\mathrm{km\,s^{-1}}$

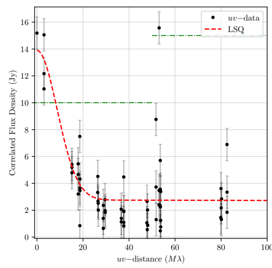

(9) G196.454-1.677
$v = 15.44\,\mathrm{km\,s^{-1}}$

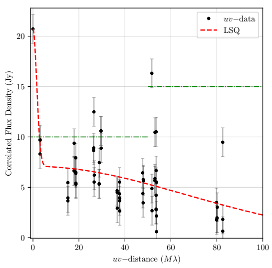

(10) G196.454-1.677
$v = 14.73\,\mathrm{km\,s^{-1}}$

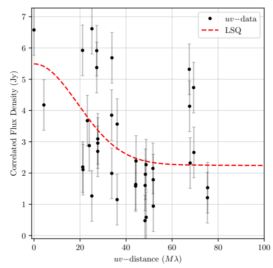

(11) G232.620+0.996
$v = 23.68\,\mathrm{km\,s^{-1}}$

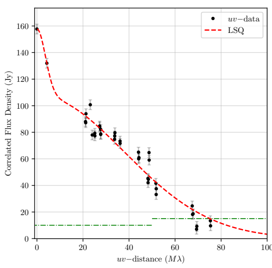

(12) G232.620+0.996
$v = 22.89\,\mathrm{km\,s^{-1}}$

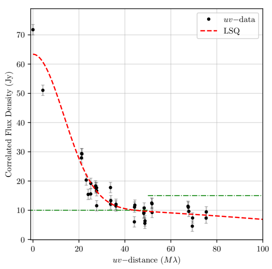

(13) G232.620+0.996
$v = 22.36\,\mathrm{km\,s^{-1}}$

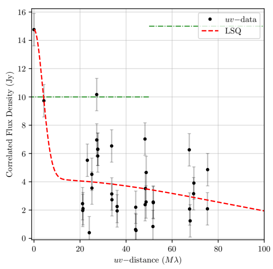

(14) G232.620+0.996
$v = 21.66\,\mathrm{km\,s^{-1}}$

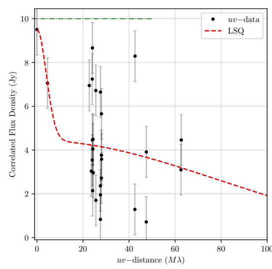

(15) G263.250+0.514
$v = 13.14\,\mathrm{km\,s^{-1}}$

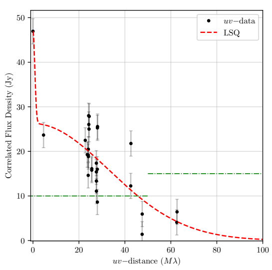

(16) G263.250+0.514
$v = 12.35\,\mathrm{km\,s^{-1}}$

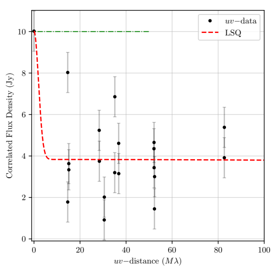

(17) G188.946+0.886
$v = 11.82\,\mathrm{km\,s^{-1}}$

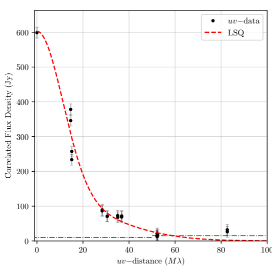

(18) G188.946+0.886
$v = 10.85\,\mathrm{km\,s^{-1}}$

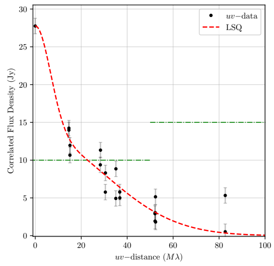

(19) G188.946+0.886
$v = 9.71\,\mathrm{km\,s^{-1}}$

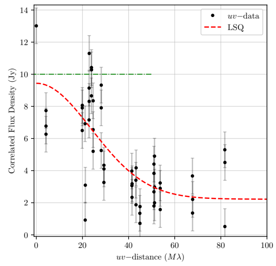

(20) G287.371+0.644
$v = -0.92\,\mathrm{km\,s^{-1}}$

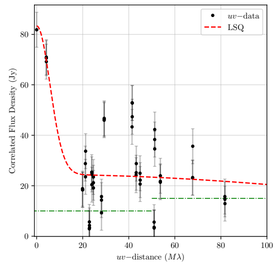

(21) G287.371+0.644
$v = -1.89\,\mathrm{km\,s^{-1}}$

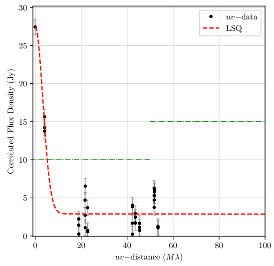

(22) G291.274-0.709
$v = -28.85\,\mathrm{km\,s^{-1}}$

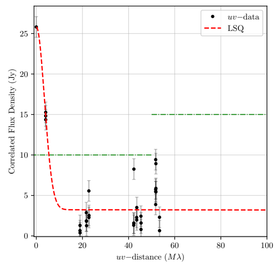

(23) G291.274-0.709
$v = -29.20\,\mathrm{km\,s^{-1}}$

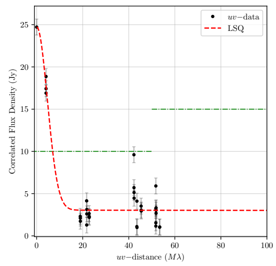

(24) G291.274-0.709
$v = -29.64\,\mathrm{km\,s^{-1}}$

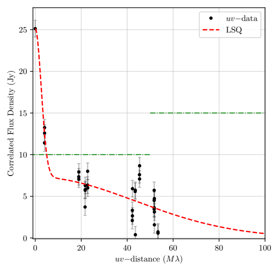

(25) G291.274-0.709
$v = -30.08\,\mathrm{km\,s^{-1}}$

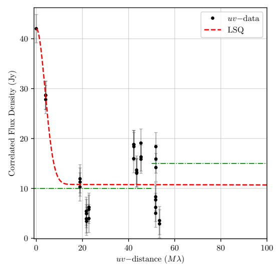

(26) G291.274-0.709
$v = -30.69\,\mathrm{km\,s^{-1}}$

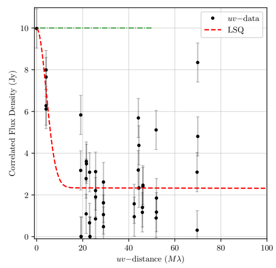

(27) G298.262+0.739
$v = -30.13\,\mathrm{km\,s^{-1}}$

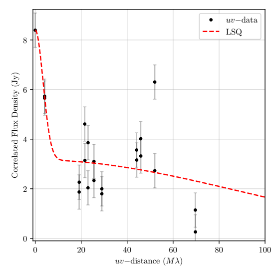

(28) G298.262+0.739
$v = -29.86\,\mathrm{km\,s^{-1}}$

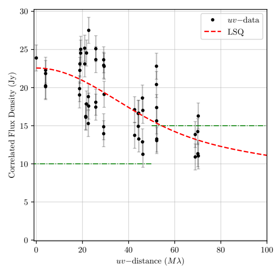

(29) G299.772-0.005
$v = -6.68\,\mathrm{km\,s^{-1}}$

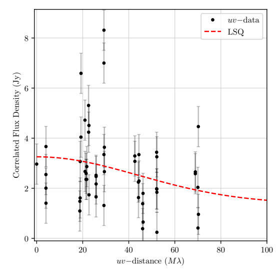

(30) G299.772-0.005
$v = -7.56\,\mathrm{km\,s^{-1}}$

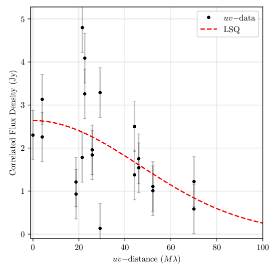

(31) G299.772-0.005
$v = -7.37\,\mathrm{km\,s^{-1}}$

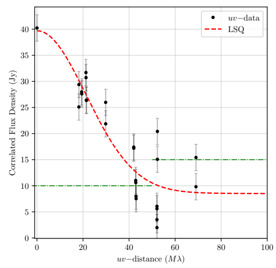

(32) G305.200+0.019
$v = -32.04\,\mathrm{km\,s^{-1}}$

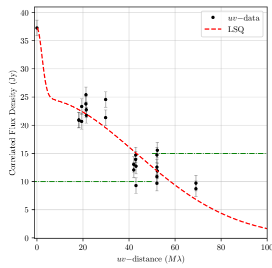

(33) G305.200+0.019
$v = -33.09\,\mathrm{km\,s^{-1}}$

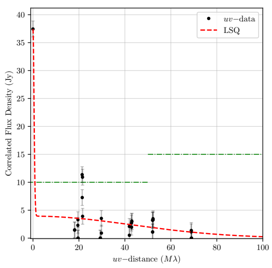

(34) G305.202+0.208
$v = -36.05\,\mathrm{km\,s^{-1}}$

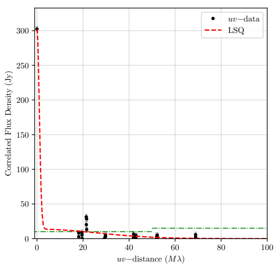

(35) G305.202+0.208
$v = -38.34\,\mathrm{km\,s^{-1}}$

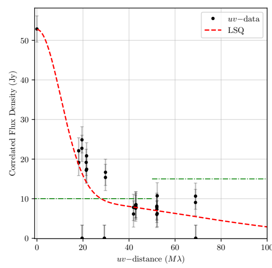

(36) G305.202+0.208
$v = -44.04\,\mathrm{km\,s^{-1}}$

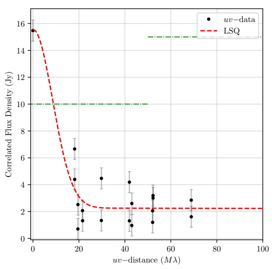

(37) G305.202+0.208
$v = -44.57\,\mathrm{km\,s^{-1}}$

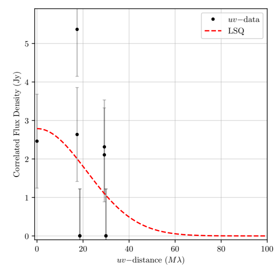

(38) G308.754+0.549
$v = -39.21\,\mathrm{km\,s^{-1}}$

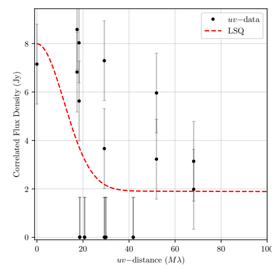

(39) G308.754+0.549
$v = -45.27\,\mathrm{km\,s^{-1}}$

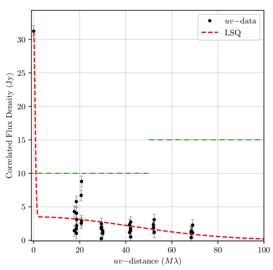

(40) G308.918+0.123
$v = -54.25\,\mathrm{km\,s^{-1}}$

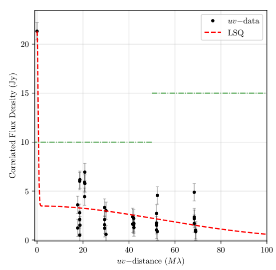

(41) G308.918+0.123
$v = -54.60\,\mathrm{km\,s^{-1}}$

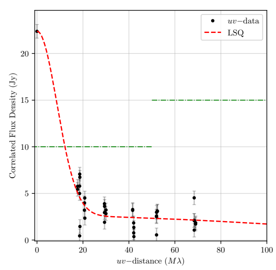

(42) G308.918+0.123
$v = -54.78\,\mathrm{km\,s^{-1}}$

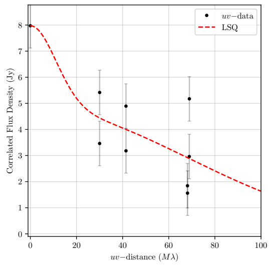

(43) G309.901+0.231
$v = -54.29\,\mathrm{km\,s^{-1}}$

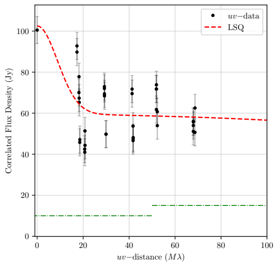

(44) G309.921+0.479
$v = -57.85\,\mathrm{km\,s^{-1}}$

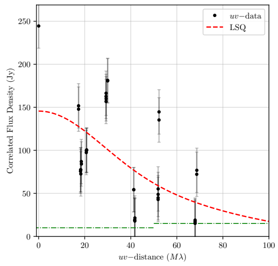

(45) G309.921+0.479
$v = -58.46\,\mathrm{km\,s^{-1}}$

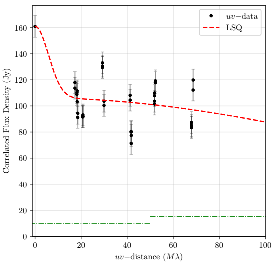

(46) G309.921+0.479
$v = -58.81\,\mathrm{km\,s^{-1}}$

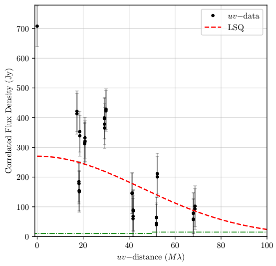

(47) G309.921+0.479
$v = -59.69\,\mathrm{km\,s^{-1}}$

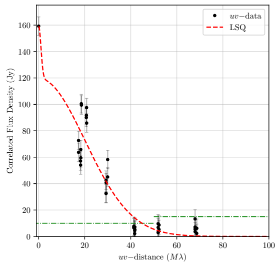

(48) G309.921+0.479
$v = -60.66\,\mathrm{km\,s^{-1}}$

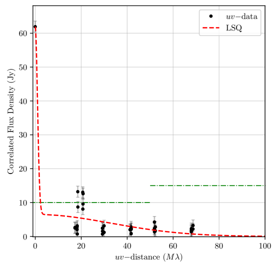

(49) G309.921+0.479
$v = -61.27\,\mathrm{km\,s^{-1}}$

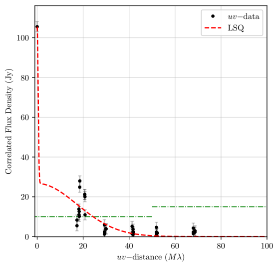

(50) G309.921+0.479
$v = -61.62\,\mathrm{km\,s^{-1}}$

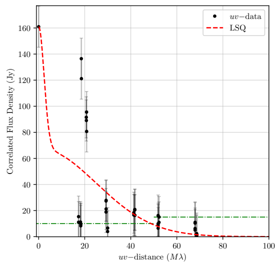

(51) G309.921+0.479
$v = -62.32\,\mathrm{km\,s^{-1}}$

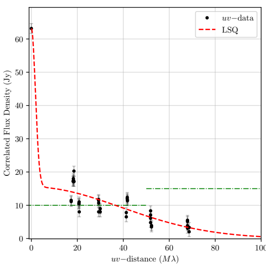

(52) G309.921+0.479
$v = -62.94\,\mathrm{km\,s^{-1}}$

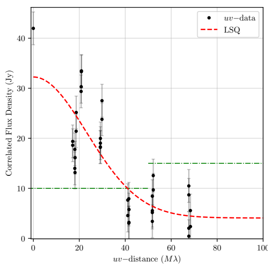

(53) G310.144+0.760
$v = -55.45\,\mathrm{km\,s^{-1}}$

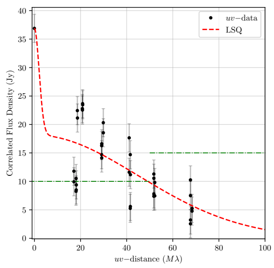

(54) G310.144+0.760
$v = -55.89\,\mathrm{km\,s^{-1}}$

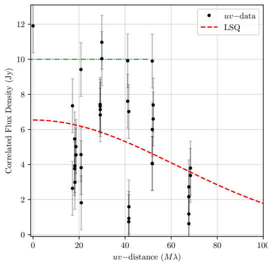

(55) G310.144+0.760
$v = -57.55\,\mathrm{km\,s^{-1}}$

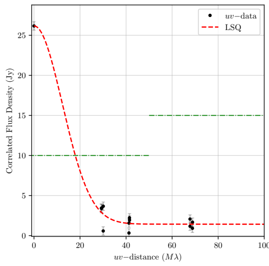

(56) G312.071+0.082
$v = -34.18\,\mathrm{km\,s^{-1}}$

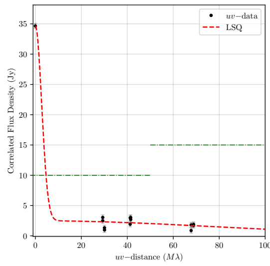

(57) G312.071+0.082
$v = -34.80\,\mathrm{km\,s^{-1}}$

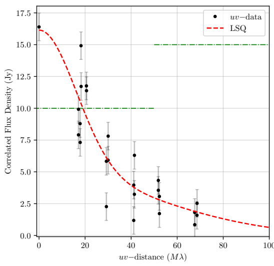

(58) G312.108+0.262
$v = -49.94\,\mathrm{km\,s^{-1}}$

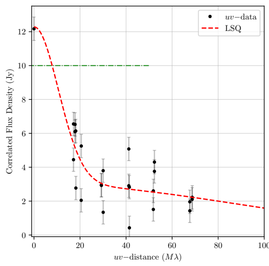

(59) G312.598+0.045
$v = -67.78\,\mathrm{km\,s^{-1}}$

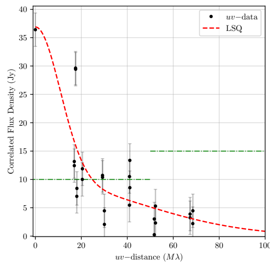

(60) G313.469+0.190
$v = -9.44\,\mathrm{km\,s^{-1}}$

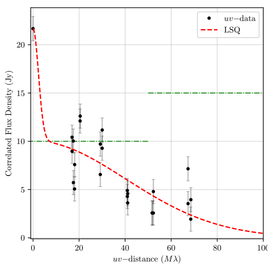

(61) G313.469+0.190
$v = -11.81\,\mathrm{km\,s^{-1}}$

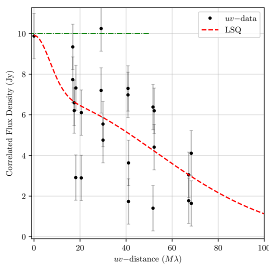

(62) G313.577+0.325
$v = -47.10\,\mathrm{km\,s^{-1}}$

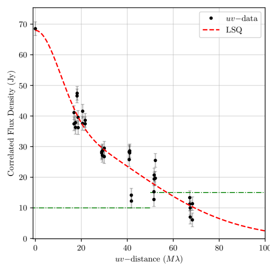

(63) G313.577+0.325
$v = -47.80\,\mathrm{km\,s^{-1}}$

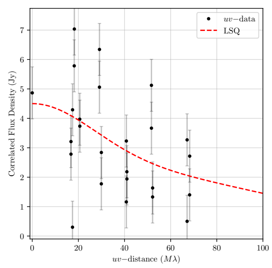

(64) G314.320+0.112
$v = -42.98\,\mathrm{km\,s^{-1}}$

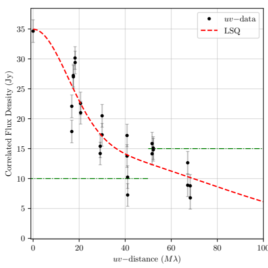

(65) G314.320+0.112
$v = -43.42\,\mathrm{km\,s^{-1}}$

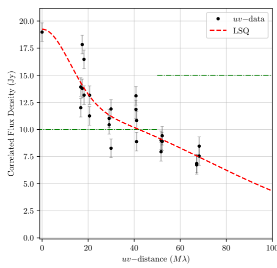

(66) G314.320+0.112
$v = -43.69\,\mathrm{km\,s^{-1}}$

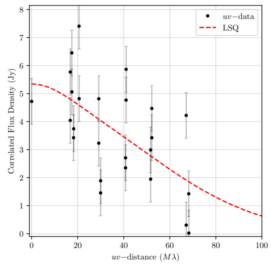

(67) G314.320+0.112
$v = -44.21\,\mathrm{km\,s^{-1}}$

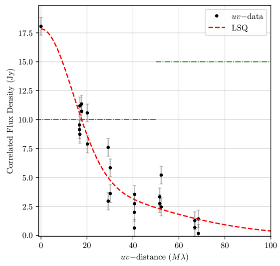

(68) G316.359-0.362
$v = 6.98\,\mathrm{km\,s^{-1}}$

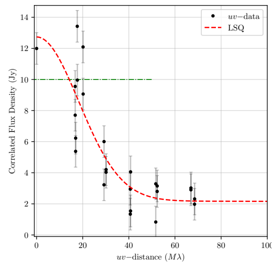

(69) G316.359-0.362
$v = 6.01\,\mathrm{km\,s^{-1}}$

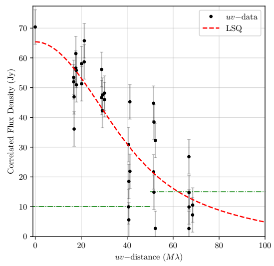

(70) G316.359-0.362
$v = 3.38\,\mathrm{km\,s^{-1}}$

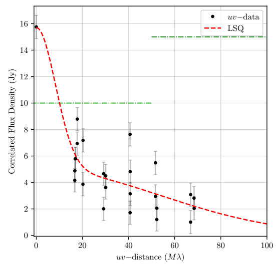

(71) G316.381-0.379
$v = -0.47\,\mathrm{km\,s^{-1}}$

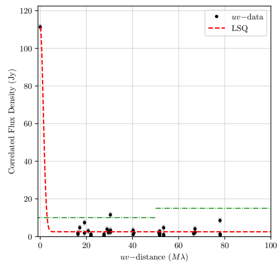

(72) G316.640-0.087
$v = -20.36\,\mathrm{km\,s^{-1}}$

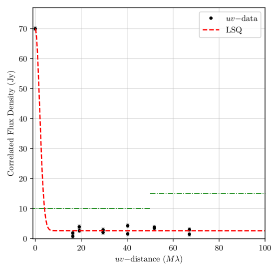

(73) G316.640-0.087
$v = -19.77\,\mathrm{km\,s^{-1}}$

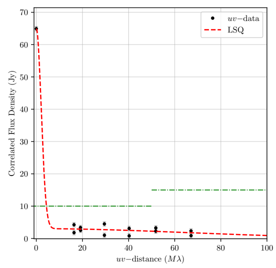

(74) G316.640-0.087
$v = -19.95\,\mathrm{km\,s^{-1}}$

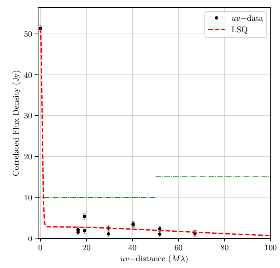

(75) G316.640-0.087
$v = -22.23\,\mathrm{km\,s^{-1}}$

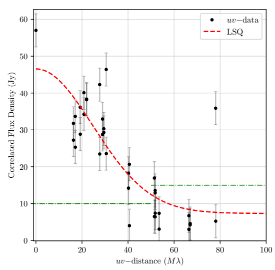

(76) G316.811-0.057
$v = -45.61\,\mathrm{km\,s^{-1}}$

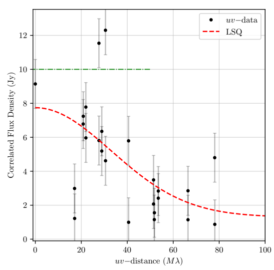

(77) G316.811-0.057
$v = -46.75\,\mathrm{km\,s^{-1}}$

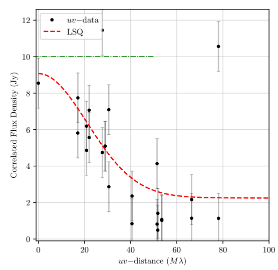

(78) G316.811-0.057
$v = -47.28\,\mathrm{km\,s^{-1}}$

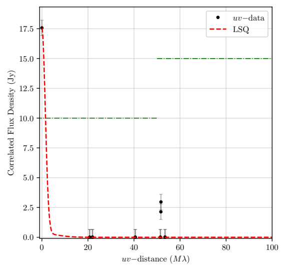

(79) G317.466-0.402
$v = -37.47\,\mathrm{km\,s^{-1}}$

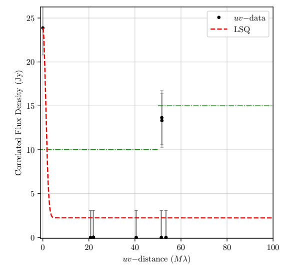

(80) G317.466-0.402
$v = -37.73\,\mathrm{km\,s^{-1}}$

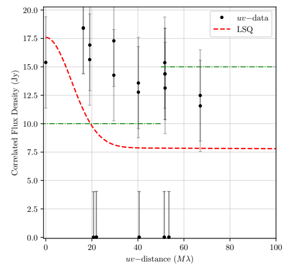

(81) G317.466-0.402
$v = -38.87\,\mathrm{km\,s^{-1}}$

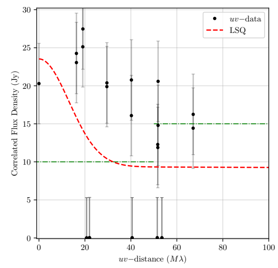

(82) G317.466-0.402
$v = -39.57\,\mathrm{km\,s^{-1}}$

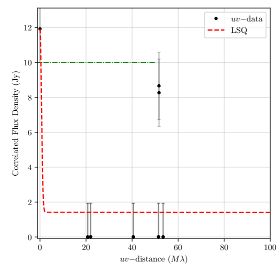

(83) G317.466-0.402
$v = -40.98\,\mathrm{km\,s^{-1}}$

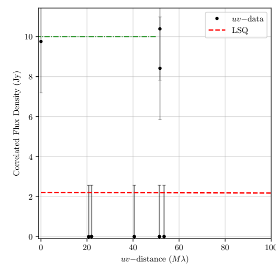

(84) G317.466-0.402
$v = -41.86\,\mathrm{km\,s^{-1}}$

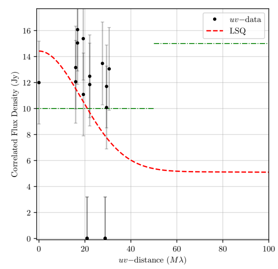

(85) G317.701+0.110
$v = -42.15\,\mathrm{km\,s^{-1}}$

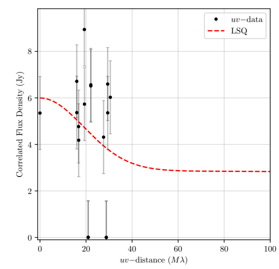

(86) G317.701+0.110
$v = -43.55\,\mathrm{km\,s^{-1}}$

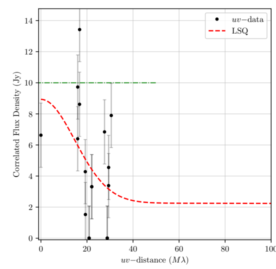

(87) G317.701+0.110
$v = -46.01\,\mathrm{km\,s^{-1}}$

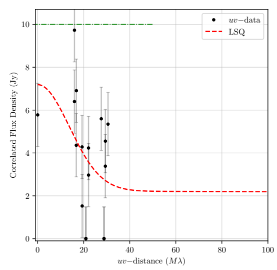

(88) G317.701+0.110
$v = -46.19\,\mathrm{km\,s^{-1}}$

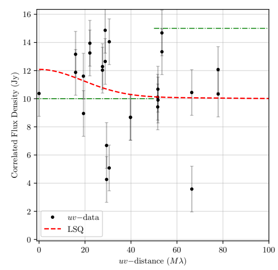

(89) G318.050+0.087
$v = -51.47\,\mathrm{km\,s^{-1}}$

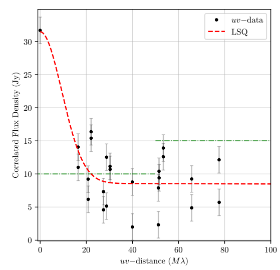

(90) G318.948-0.196
$v = -32.09\,\mathrm{km\,s^{-1}}$

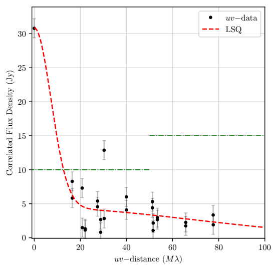

(91) G318.948-0.196
$v = -32.88\,\mathrm{km\,s^{-1}}$

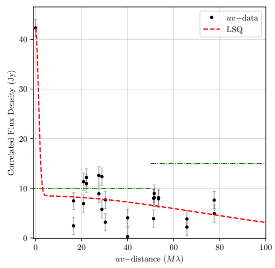

(92) G318.948-0.196
$v = -33.58\,\mathrm{km\,s^{-1}}$

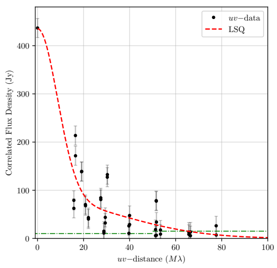

(93) G318.948-0.196
$v = -34.63\,\mathrm{km\,s^{-1}}$

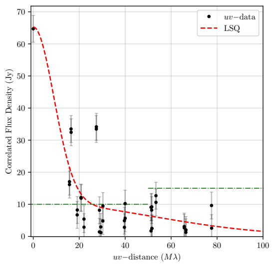

(94) G318.948-0.196
$v = -35.34\,\mathrm{km\,s^{-1}}$

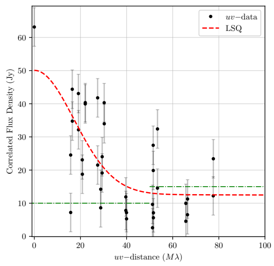

(95) G318.948-0.196
$v = -36.30\,\mathrm{km\,s^{-1}}$

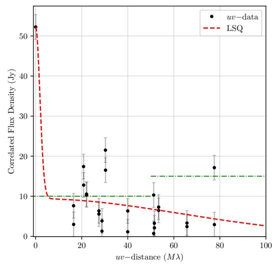

(96) G318.948-0.196
$v = -36.83\,\mathrm{km\,s^{-1}}$

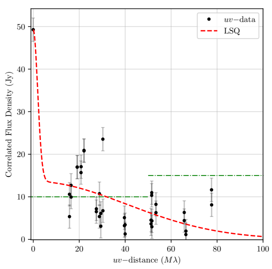

(97) G318.948-0.196
$v = -37.18\,\mathrm{km\,s^{-1}}$

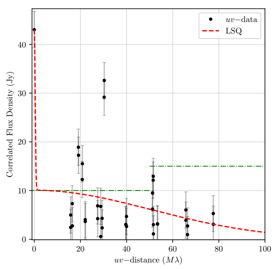

(98) G318.948-0.196
$v = -38.23\,\mathrm{km\,s^{-1}}$

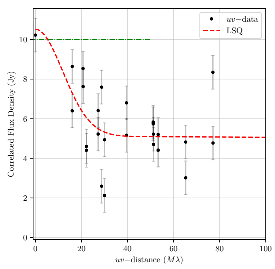

(99) G320.231-0.284
$v = -61.14\,\mathrm{km\,s^{-1}}$

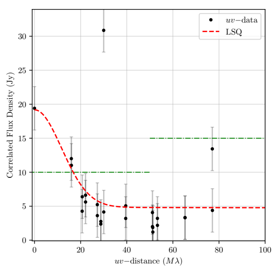

(100) G320.231-0.284
$v = -61.49\,\mathrm{km\,s^{-1}}$

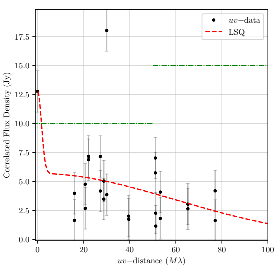

(101) G320.231-0.284
$v = -61.67\,\mathrm{km\,s^{-1}}$

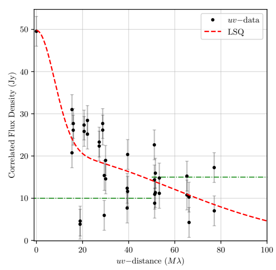

(102) G320.231-0.284
$v = -62.28\,\mathrm{km\,s^{-1}}$

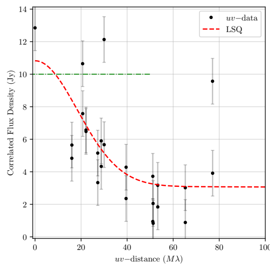

(103) G320.231-0.284
$v = -62.90\,\mathrm{km\,s^{-1}}$

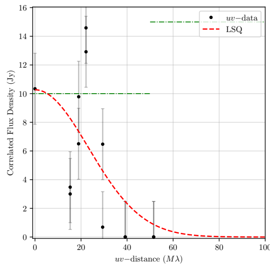

(104) G321.033-0.483
$v = -57.27\,\mathrm{km\,s^{-1}}$

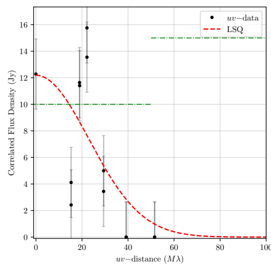

(105) G321.033-0.483
$v = -60.88\,\mathrm{km\,s^{-1}}$

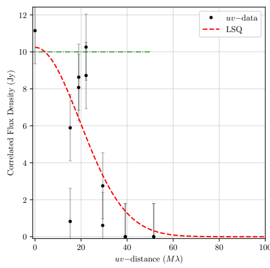

(106) G321.033-0.483
$v = -61.23\,\mathrm{km\,s^{-1}}$

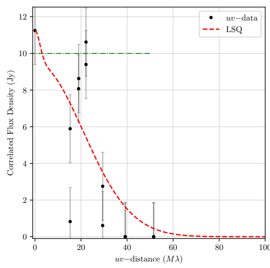

(107) G321.033-0.483
$v = -61.40\,\mathrm{km\,s^{-1}}$

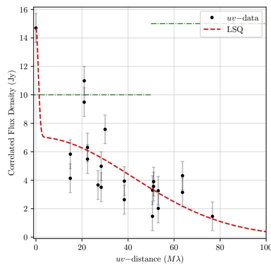

(108) G322.158+0.636
$v = -53.54\,\mathrm{km\,s^{-1}}$

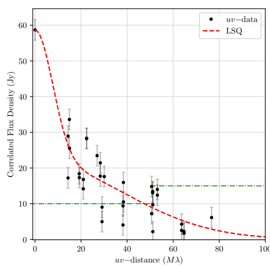

(109) G322.158+0.636
$v = -54.51\,\mathrm{km\,s^{-1}}$

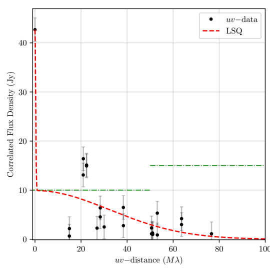

(110) G322.158+0.636
$v = -55.03\,\mathrm{km\,s^{-1}}$

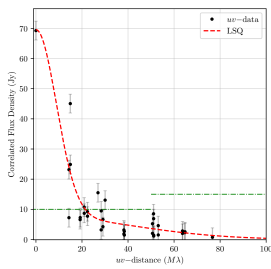

(111) G322.158+0.636
$v = -56.09\,\mathrm{km\,s^{-1}}$

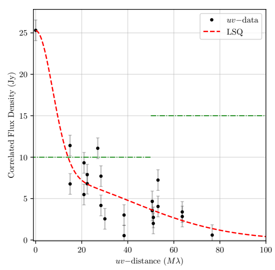

(112) G322.158+0.636
$v = -56.88\,\mathrm{km\,s^{-1}}$

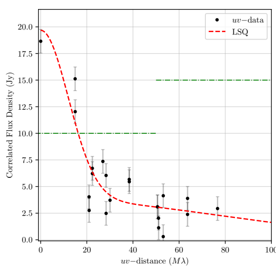

(113) G322.158+0.636
$v = -60.04\,\mathrm{km\,s^{-1}}$

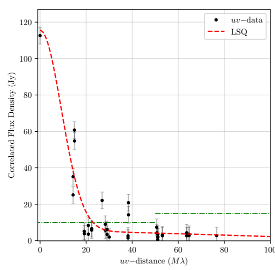

(114) G322.158+0.636
$v = -62.06\,\mathrm{km\,s^{-1}}$

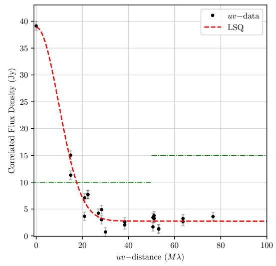

(115) G322.158+0.636
$v = -62.50\,\mathrm{km\,s^{-1}}$

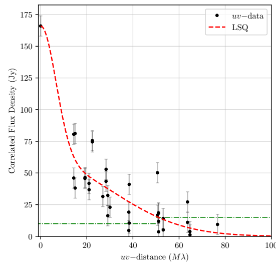

(116) G322.158+0.636
$v = -62.94\,\mathrm{km\,s^{-1}}$

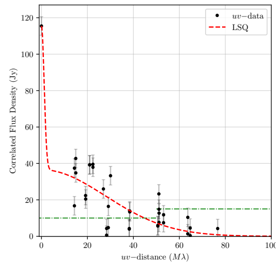

(117) G322.158+0.636
$v = -63.29\,\mathrm{km\,s^{-1}}$

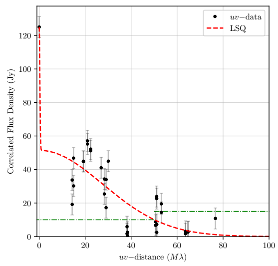

(118) G322.158+0.636
$v = -64.08\,\mathrm{km\,s^{-1}}$

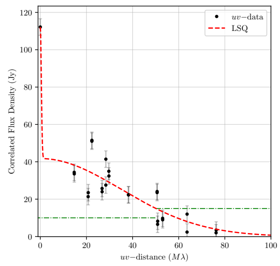

(119) G323.459-0.079
$v = -67.15\,\mathrm{km\,s^{-1}}$

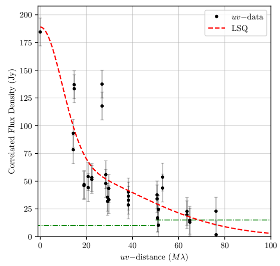

(120) G323.459-0.079
$v = -68.29\,\mathrm{km\,s^{-1}}$

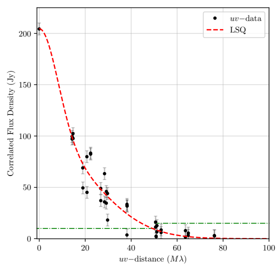

(121) G323.459-0.079
$v = -68.99\,\mathrm{km\,s^{-1}}$

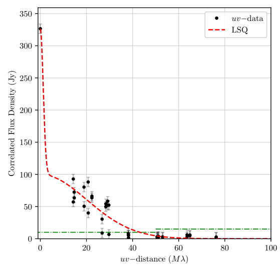

(122) G323.459-0.079
$v = -69.26\,\mathrm{km\,s^{-1}}$

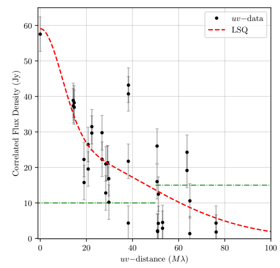

(123) G323.459-0.079
$v = -70.48\,\mathrm{km\,s^{-1}}$

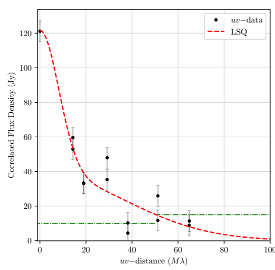

(124) G323.459-0.079
$v = -66.98\,\mathrm{km\,s^{-1}}$

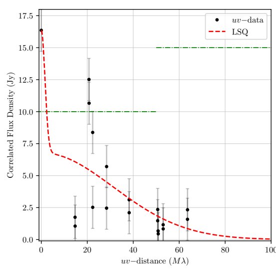

(125) G323.740-0.263
$v = -46.88\,\mathrm{km\,s^{-1}}$

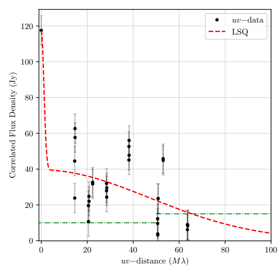

(126) G323.740-0.263
$v = -47.93\,\mathrm{km\,s^{-1}}$

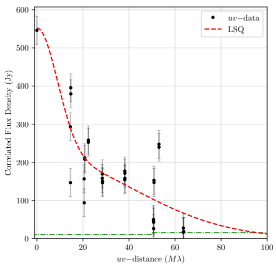

(127) G323.740-0.263
$v = -48.46\,\mathrm{km\,s^{-1}}$

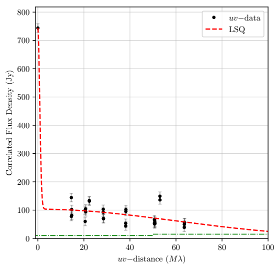

(128) G323.740-0.263
$v = -48.98\,\mathrm{km\,s^{-1}}$

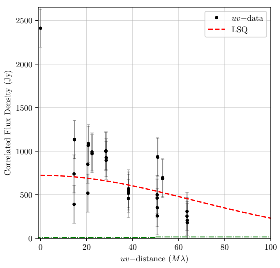

(129) G323.740-0.263
$v = -50.39\,\mathrm{km\,s^{-1}}$

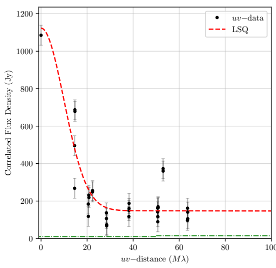

(130) G323.740-0.263
$v = -51.18\,\mathrm{km\,s^{-1}}$

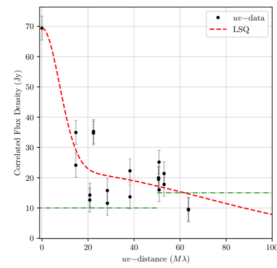

(131) G323.740-0.263
$v = -52.41\,\mathrm{km\,s^{-1}}$

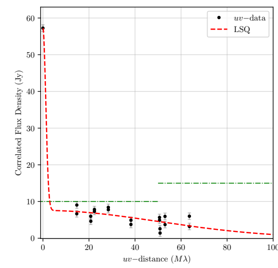

(132) G323.740-0.263
$v = -52.85\,\mathrm{km\,s^{-1}}$

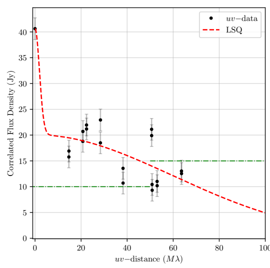

(133) G323.740-0.263
$v = -53.29\,\mathrm{km\,s^{-1}}$

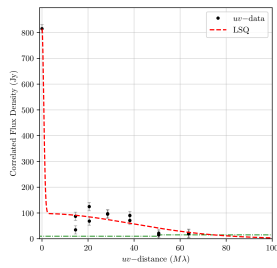

(134) G323.740-0.263
$v = -49.34\,\mathrm{km\,s^{-1}}$

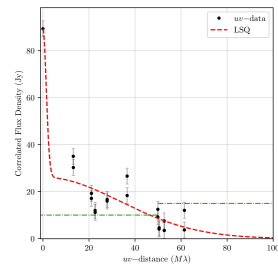

(135) G326.475+0.703
$v = -37.99\,\mathrm{km\,s^{-1}}$

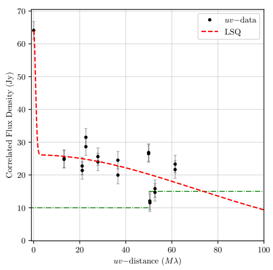

(136) G326.475+0.703
$v = -38.43\,\mathrm{km\,s^{-1}}$

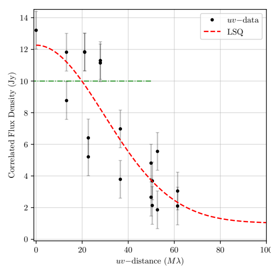

(137) G326.475+0.703
$v = -49.14\,\mathrm{km\,s^{-1}}$

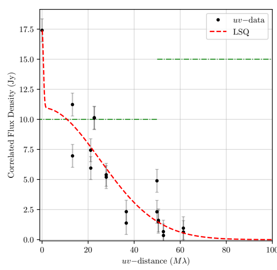

(138) G326.641+0.611
$v = -42.64\,\mathrm{km\,s^{-1}}$

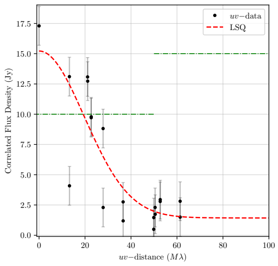

(139) G326.641+0.611
$v = -42.99\,\mathrm{km\,s^{-1}}$

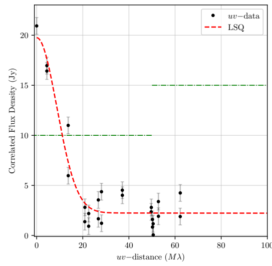

(140) G326.859-0.677
$v = -58.03\,\mathrm{km\,s^{-1}}$

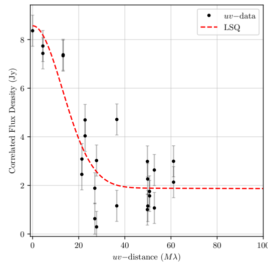

(141) G327.120+0.511
$v = -83.60\,\mathrm{km\,s^{-1}}$

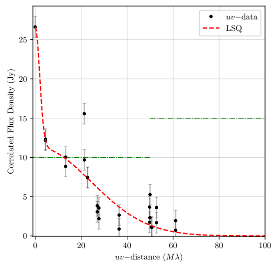

(142) G327.120+0.511
$v = -87.03\,\mathrm{km\,s^{-1}}$

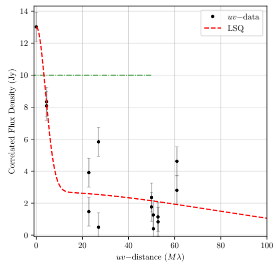

(143) G327.402+0.445
$v = -77.90\,\mathrm{km\,s^{-1}}$

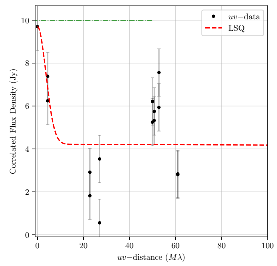

(144) G327.402+0.445
$v = -81.06\,\mathrm{km\,s^{-1}}$

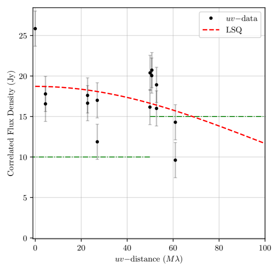

(145) G327.402+0.445
$v = -81.76\,\mathrm{km\,s^{-1}}$

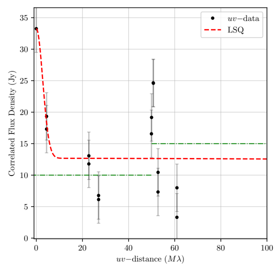

(146) G327.402+0.445
$v = -82.02\,\mathrm{km\,s^{-1}}$

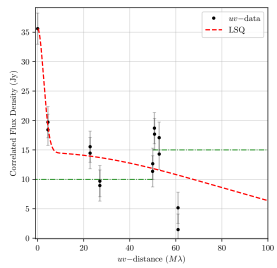

(147) G327.402+0.445
$v = -82.37\,\mathrm{km\,s^{-1}}$

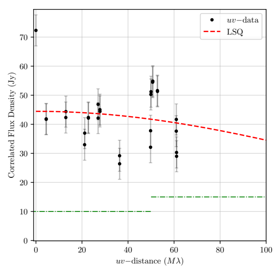

(148) G327.402+0.445
$v = -82.90\,\mathrm{km\,s^{-1}}$

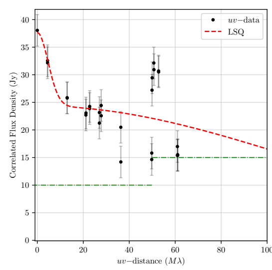

(149) G327.402+0.445
$v = -83.25\,\mathrm{km\,s^{-1}}$

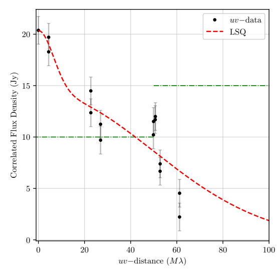

(150) G328.237-0.547
$v = -34.73\,\mathrm{km\,s^{-1}}$

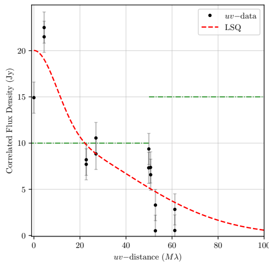

(151) G328.237-0.547
$v = -36.40\,\mathrm{km\,s^{-1}}$

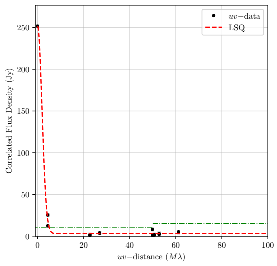

(152) G328.237-0.547
$v = -37.45\,\mathrm{km\,s^{-1}}$

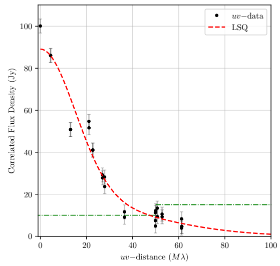

(153) G328.237-0.547
$v = -43.25\,\mathrm{km\,s^{-1}}$

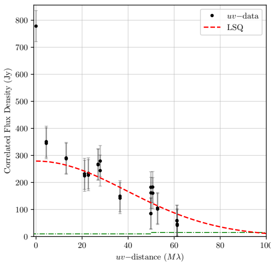

(154) G328.237-0.547
$v = -44.48\,\mathrm{km\,s^{-1}}$

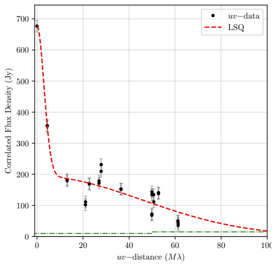

(155) G328.237-0.547
$v = -44.74\,\mathrm{km\,s^{-1}}$

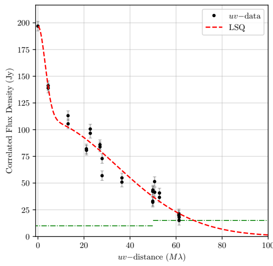

(156) G328.237-0.547
$v = -45.36\,\mathrm{km\,s^{-1}}$

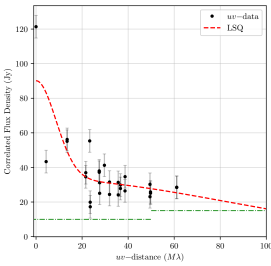

(157) G328.254-0.532
$v = -36.83\,\mathrm{km\,s^{-1}}$

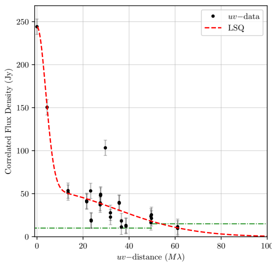

(158) G328.254-0.532
$v = -37.36\,\mathrm{km\,s^{-1}}$

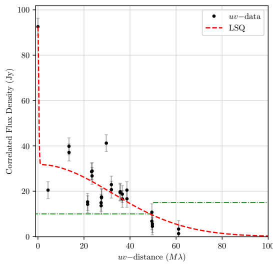

(159) G328.254-0.532
$v = -37.89\,\mathrm{km\,s^{-1}}$

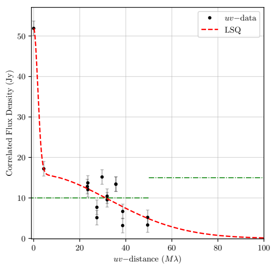

(160) G328.254-0.532
$v = -38.50\,\mathrm{km\,s^{-1}}$

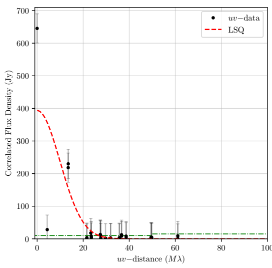

(161) G328.254-0.532
$v = -44.47\,\mathrm{km\,s^{-1}}$

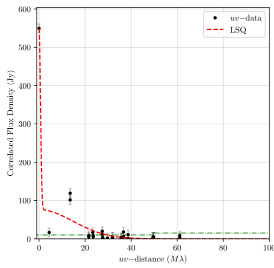

(162) G328.254-0.532
$v = -44.73\,\mathrm{km\,s^{-1}}$

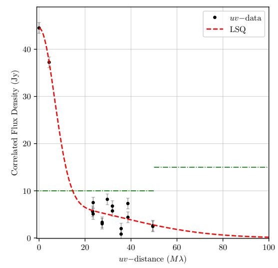

(163) G328.254-0.532
$v = -49.39\,\mathrm{km\,s^{-1}}$

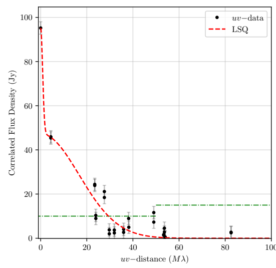

(164) G328.808+0.633
$v = -43.43\,\mathrm{km\,s^{-1}}$

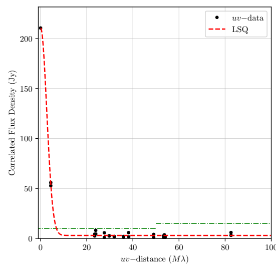

(165) G328.808+0.633
$v = -43.87\,\mathrm{km\,s^{-1}}$

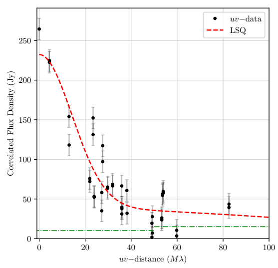

(166) G328.808+0.633
$v = -44.40\,\mathrm{km\,s^{-1}}$

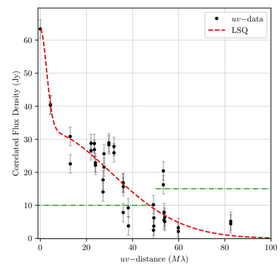

(167) G328.808+0.633
$v = -45.10\,\mathrm{km\,s^{-1}}$

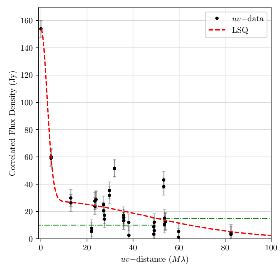

(168) G328.808+0.633
$v = -46.24\,\mathrm{km\,s^{-1}}$

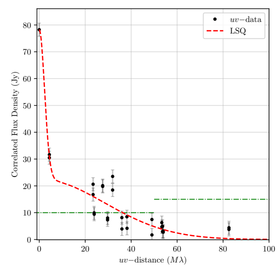

(169) G328.808+0.633
$v = -46.59\,\mathrm{km\,s^{-1}}$

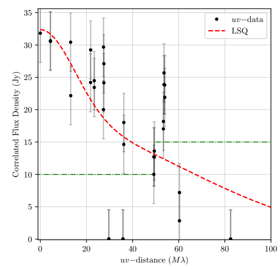

(170) G329.029-0.205
$v = -35.06\,\mathrm{km\,s^{-1}}$

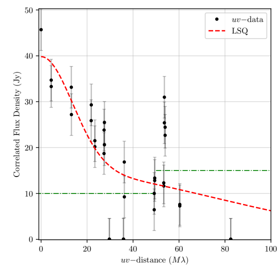

(171) G329.029-0.205
$v = -35.59\,\mathrm{km\,s^{-1}}$

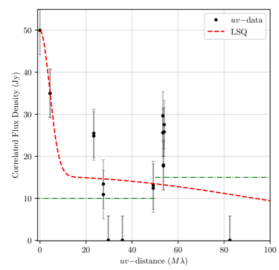

(172) G329.029-0.205
$v = -36.12\,\mathrm{km\,s^{-1}}$

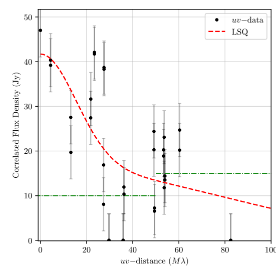

(173) G329.029-0.205
$v = -37.17\,\mathrm{km\,s^{-1}}$

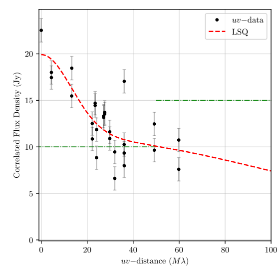

(174) G329.339+0.148
$v = -106.28\,\mathrm{km\,s^{-1}}$

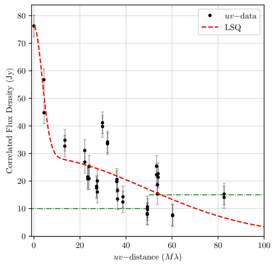

(175) G329.407-0.459
$v = -66.64\,\mathrm{km\,s^{-1}}$

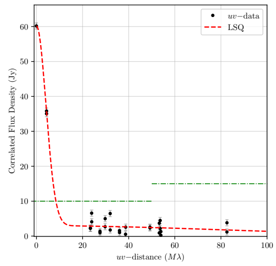

(176) G329.407-0.459
$v = -67.08\,\mathrm{km\,s^{-1}}$

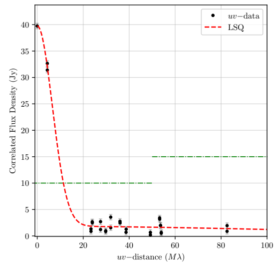

(177) G329.407-0.459
$v = -70.42\,\mathrm{km\,s^{-1}}$

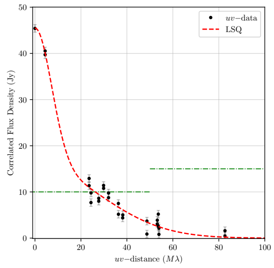

(178) G331.278-0.188
$v = -77.63\,\mathrm{km\,s^{-1}}$

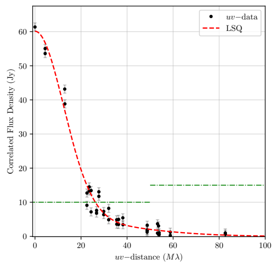

(179) G331.278-0.188
$v = -77.98\,\mathrm{km\,s^{-1}}$

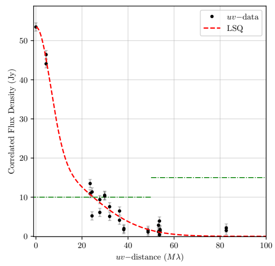

(180) G331.278-0.188
$v = -78.16\,\mathrm{km\,s^{-1}}$

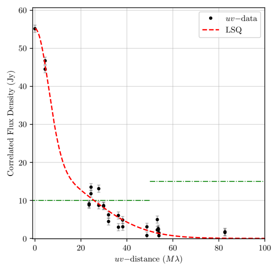

(181) G331.278-0.188
$v = -78.77\,\mathrm{km\,s^{-1}}$

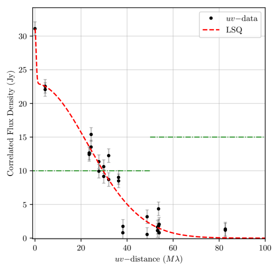

(182) G331.278-0.188
$v = -83.25\,\mathrm{km\,s^{-1}}$

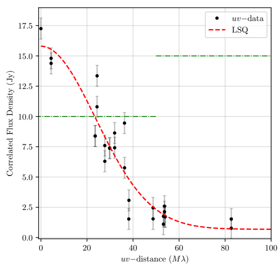

(183) G331.278-0.188
$v = -84.31\,\mathrm{km\,s^{-1}}$

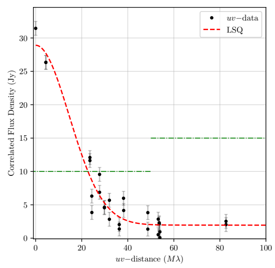

(184) G331.278-0.188
$v = -85.09\,\mathrm{km\,s^{-1}}$

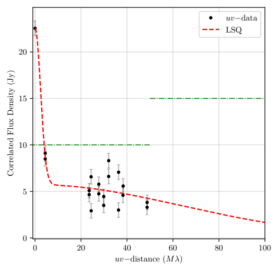

(185) G331.342-0.346
$v = -65.41\,\mathrm{km\,s^{-1}}$

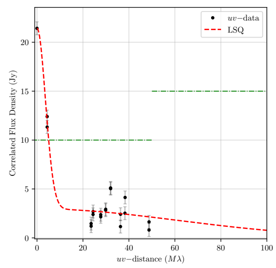

(186) G331.342-0.346
$v = -65.67\,\mathrm{km\,s^{-1}}$

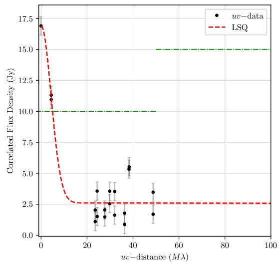

(187) G331.342-0.346
$v = -65.94\,\mathrm{km\,s^{-1}}$

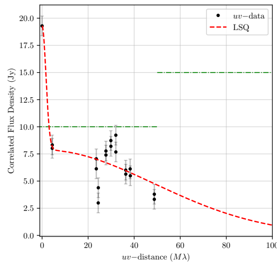

(188) G331.342-0.346
$v = -66.38\,\mathrm{km\,s^{-1}}$

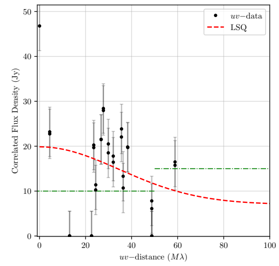

(189) G331.342-0.346
$v = -67.08\,\mathrm{km\,s^{-1}}$

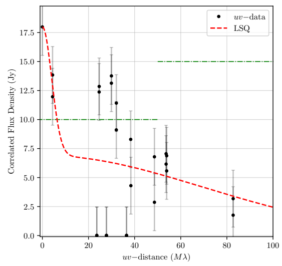

(190) G331.425+0.264
$v = -88.72\,\mathrm{km\,s^{-1}}$

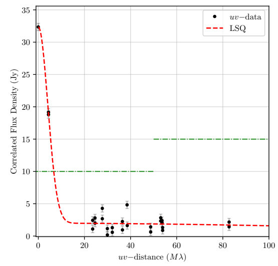

(191) G331.442-0.187
$v = -87.28\,\mathrm{km\,s^{-1}}$

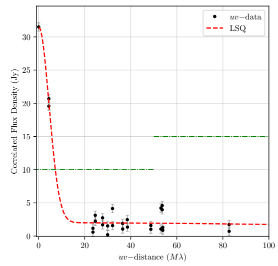

(192) G331.442-0.187
$v = -87.63\,\mathrm{km\,s^{-1}}$

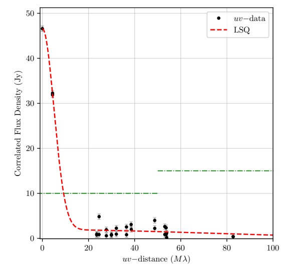

(193) G331.442-0.187
$v = -88.51\,\mathrm{km\,s^{-1}}$

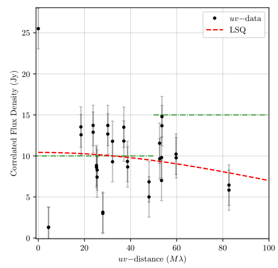

(194) G332.295+2.280
$v = -23.05\,\mathrm{km\,s^{-1}}$

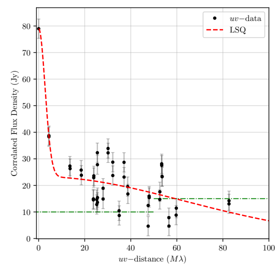

(195) G332.295+2.280
$v = -23.67\,\mathrm{km\,s^{-1}}$

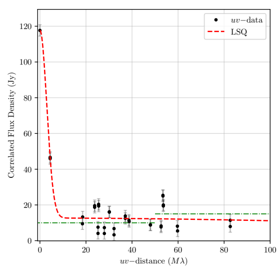

(196) G332.295+2.280
$v = -24.02\,\mathrm{km\,s^{-1}}$

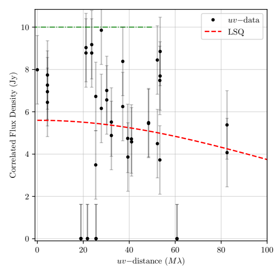

(197) G333.315+0.105
$v = -43.86\,\mathrm{km\,s^{-1}}$

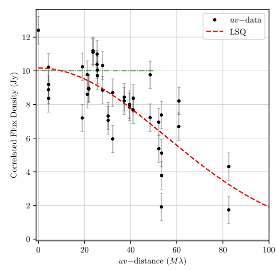

(198) G333.466-0.164
$v = -41.96\,\mathrm{km\,s^{-1}}$

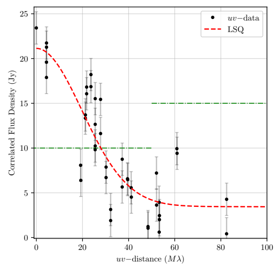

(199) G333.562-0.025
$v = -34.86\,\mathrm{km\,s^{-1}}$

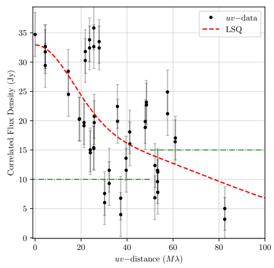

(200) G333.562-0.025
$v = -35.30\,\mathrm{km\,s^{-1}}$

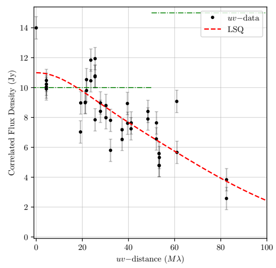

(201) G333.562-0.025
$v = -36.09\,\mathrm{km\,s^{-1}}$

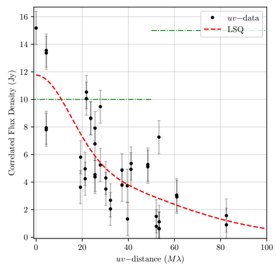

(202) G333.562-0.025
$v = -36.44\,\mathrm{km\,s^{-1}}$

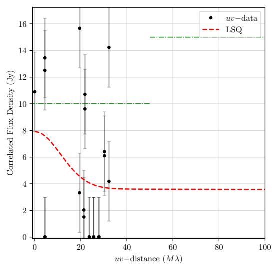

(203) G333.646+0.058
$v = -87.39\,\mathrm{km\,s^{-1}}$

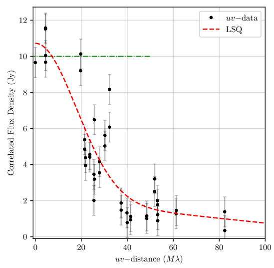

(204) G333.931-0.135
$v = -36.94\,\mathrm{km\,s^{-1}}$

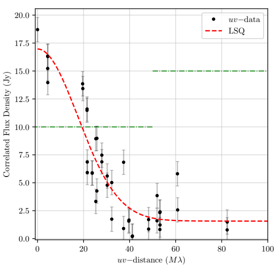

(205) G334.635-0.015
$v = -29.13\,\mathrm{km\,s^{-1}}$

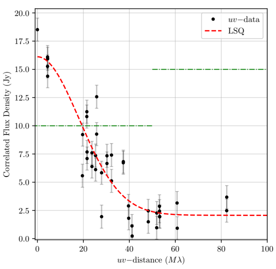

(206) G334.635-0.015
$v = -30.18\,\mathrm{km\,s^{-1}}$

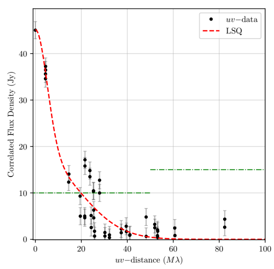

(207) G335.060-0.427
$v = -46.93\,\mathrm{km\,s^{-1}}$

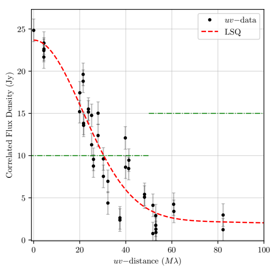

(208) G335.585-0.285
$v = -43.88\,\mathrm{km\,s^{-1}}$

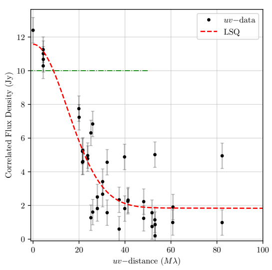

(209) G335.585-0.285
$v = -48.19\,\mathrm{km\,s^{-1}}$

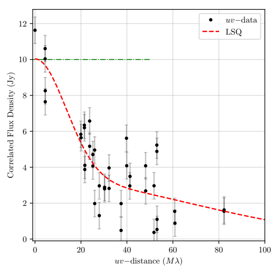

(210) G335.585-0.285
$v = -48.62\,\mathrm{km\,s^{-1}}$

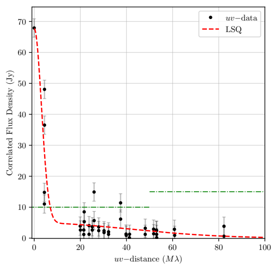

(211) G335.585-0.285
$v = -51.43\,\mathrm{km\,s^{-1}}$

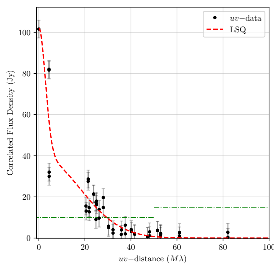

(212) G335.789+0.174
$v = -46.16\,\mathrm{km\,s^{-1}}$

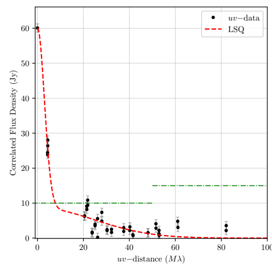

(213) G335.789+0.174
$v = -46.60\,\mathrm{km\,s^{-1}}$

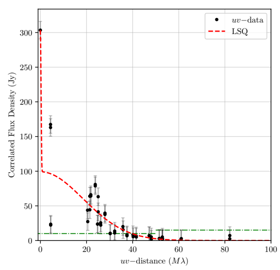

(214) G335.789+0.174
$v = -47.39\,\mathrm{km\,s^{-1}}$

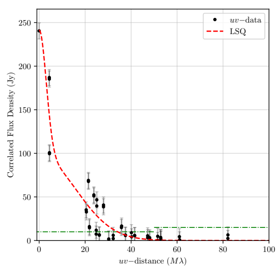

(215) G335.789+0.174
$v = -47.74\,\mathrm{km\,s^{-1}}$

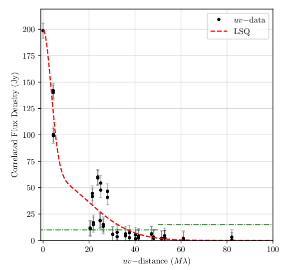

(216) G335.789+0.174
$v = -48.53\,\mathrm{km\,s^{-1}}$

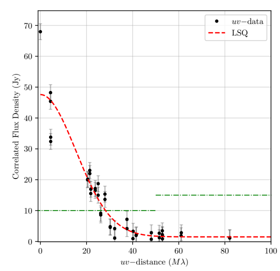

(217) G335.789+0.174
$v = -49.23\,\mathrm{km\,s^{-1}}$

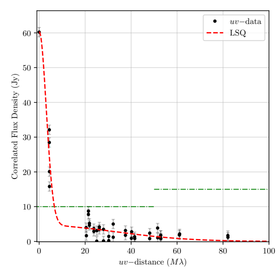

(218) G335.789+0.174
$v = -50.02\,\mathrm{km\,s^{-1}}$

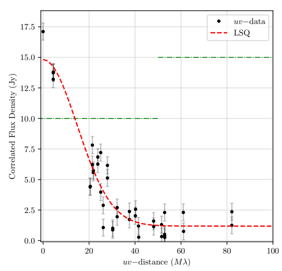

(219) G335.789+0.174
$v = -51.69\,\mathrm{km\,s^{-1}}$

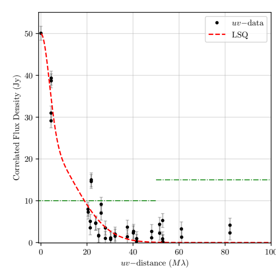

(220) G335.789+0.174
$v = -54.33\,\mathrm{km\,s^{-1}}$

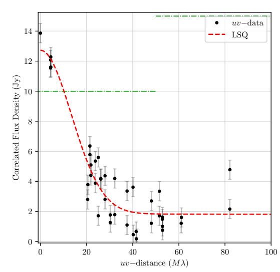

(221) G335.789+0.174
$v = -55.29\,\mathrm{km\,s^{-1}}$

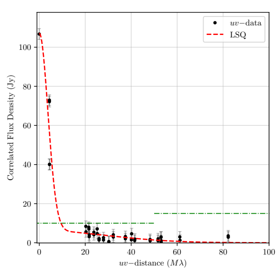

(222) G336.018-0.827
$v = -41.34\,\mathrm{km\,s^{-1}}$

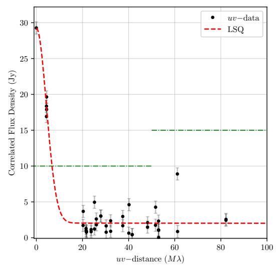

(223) G336.018-0.827
$v = -45.11\,\mathrm{km\,s^{-1}}$

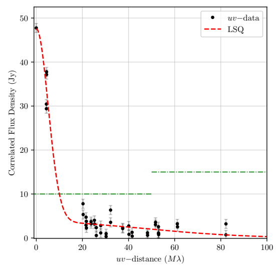

(224) G336.018-0.827
$v = -47.83\,\mathrm{km\,s^{-1}}$

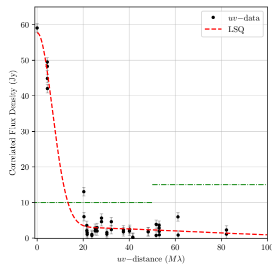

(225) G336.018-0.827
$v = -53.28\,\mathrm{km\,s^{-1}}$

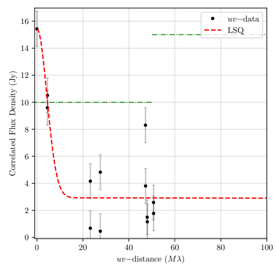

(226) G336.994-0.027
$v = -120.47\,\mathrm{km\,s^{-1}}$

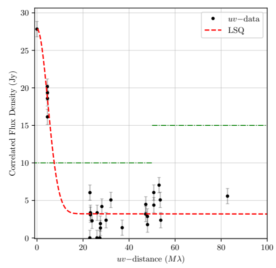

(227) G336.994-0.027
$v = -125.74\,\mathrm{km\,s^{-1}}$

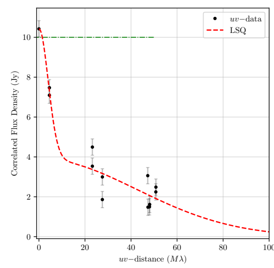

(228) G337.052-0.226
$v = -77.19\,\mathrm{km\,s^{-1}}$

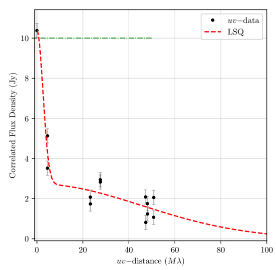

(229) G337.052-0.226
$v = -77.54\,\mathrm{km\,s^{-1}}$

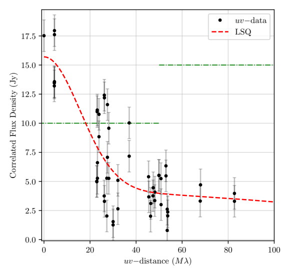

(230) G337.153-0.395
$v = -49.32\,\mathrm{km\,s^{-1}}$

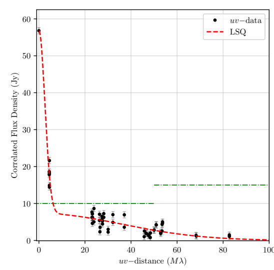

(231) G337.404-0.402
$v = -39.70\,\mathrm{km\,s^{-1}}$

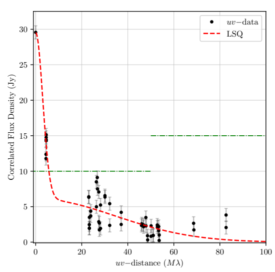

(232) G337.388-0.210
$v = -55.92\,\mathrm{km\,s^{-1}}$

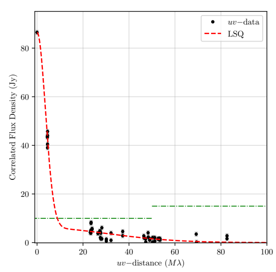

(233) G337.705-0.053
$v = -50.19\,\mathrm{km\,s^{-1}}$

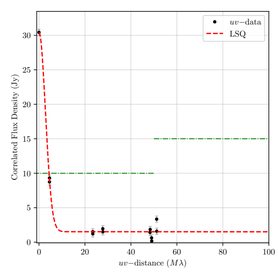

(234) G337.705-0.053
$v = -51.07\,\mathrm{km\,s^{-1}}$

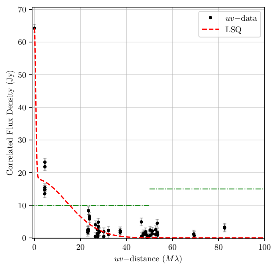

(235) G337.705-0.053
$v = -52.74\,\mathrm{km\,s^{-1}}$

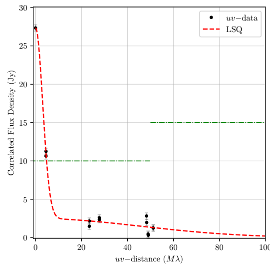

(236) G337.705-0.053
$v = -53.26\,\mathrm{km\,s^{-1}}$

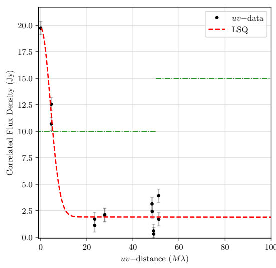

(237) G337.705-0.053
$v = -53.62\,\mathrm{km\,s^{-1}}$

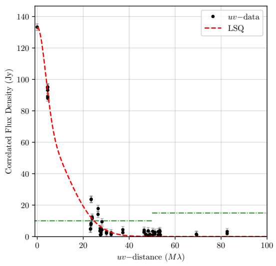

(238) G337.705-0.053
$v = -54.58\,\mathrm{km\,s^{-1}}$

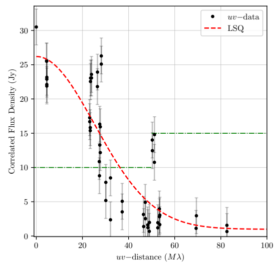

(239) G337.920-0.456
$v = -37.83\,\mathrm{km\,s^{-1}}$

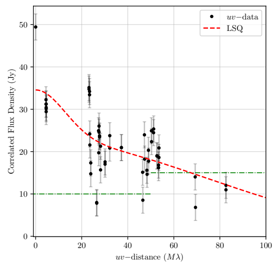

(240) G337.920-0.456
$v = -38.62\,\mathrm{km\,s^{-1}}$

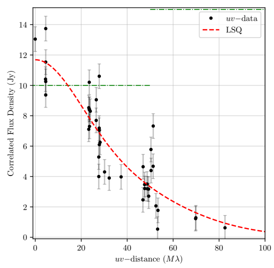

(241) G338.287+0.120
$v = -40.01\,\mathrm{km\,s^{-1}}$

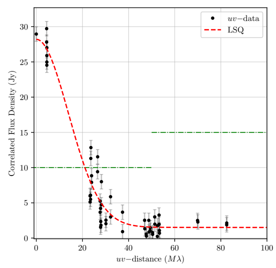

(242) G338.432+0.058
$v = -30.10\,\mathrm{km\,s^{-1}}$

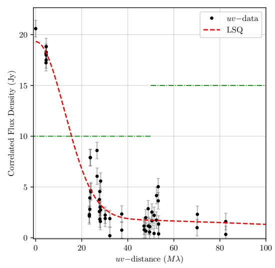

(243) G338.461-0.245
$v = -49.35\,\mathrm{km\,s^{-1}}$

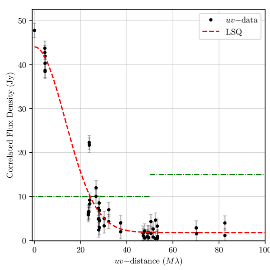

(244) G338.461-0.245
$v = -49.79\,\mathrm{km\,s^{-1}}$

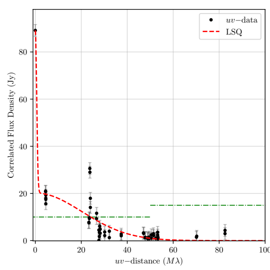

(245) G338.461-0.245
$v = -51.81\,\mathrm{km\,s^{-1}}$

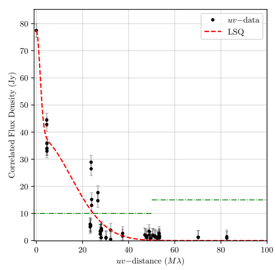

(246) G338.461-0.245
$v = -52.43\,\mathrm{km\,s^{-1}}$

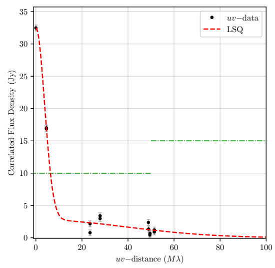

(247) G338.461-0.245
$v = -52.95\,\mathrm{km\,s^{-1}}$

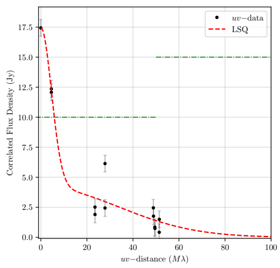

(248) G338.461-0.245
$v = -54.62\,\mathrm{km\,s^{-1}}$

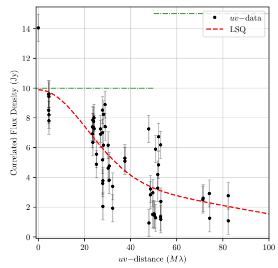

(249) G338.561+0.218
$v = -37.56\,\mathrm{km\,s^{-1}}$

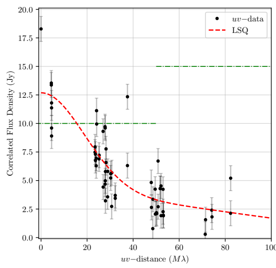

(250) G338.561+0.218
$v = -38.00\,\mathrm{km\,s^{-1}}$

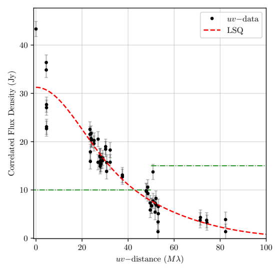

(251) G338.561+0.218
$v = -39.05\,\mathrm{km\,s^{-1}}$

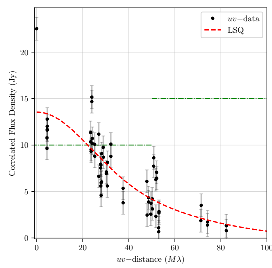

(252) G338.561+0.218
$v = -39.67\,\mathrm{km\,s^{-1}}$

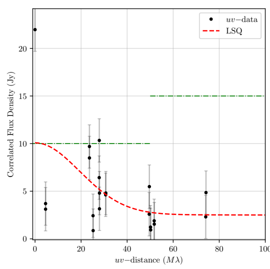

(253) G338.561+0.218
$v = -40.19\,\mathrm{km\,s^{-1}}$

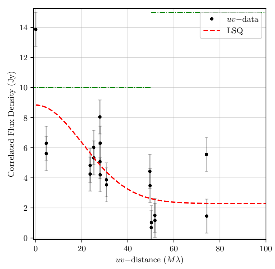

(254) G338.561+0.218
$v = -40.46\,\mathrm{km\,s^{-1}}$

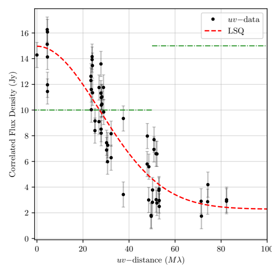

(255) G338.561+0.218
$v = -42.21\,\mathrm{km\,s^{-1}}$

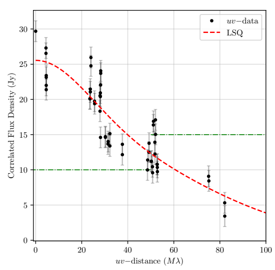

(256) G338.925+0.634
$v = -58.99\,\mathrm{km\,s^{-1}}$

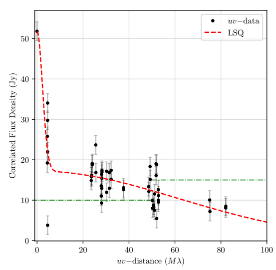

(257) G338.925+0.634
$v = -60.75\,\mathrm{km\,s^{-1}}$

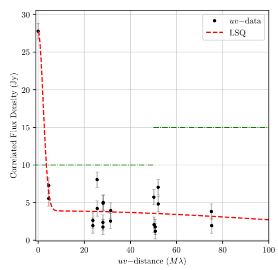

(258) G338.925+0.634
$v = -61.36\,\mathrm{km\,s^{-1}}$

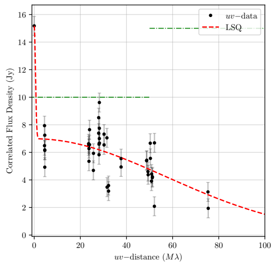

(259) G338.920+0.550
$v = -60.41\,\mathrm{km\,s^{-1}}$

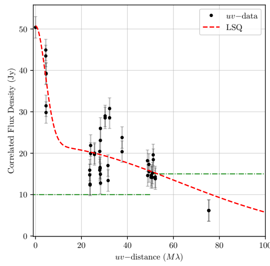

(260) G338.920+0.550
$v = -61.29\,\mathrm{km\,s^{-1}}$

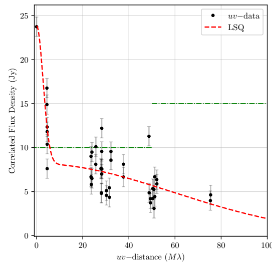

(261) G338.920+0.550
$v = -63.13\,\mathrm{km\,s^{-1}}$

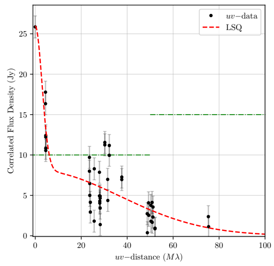

(262) G338.920+0.550
$v = -63.39\,\mathrm{km\,s^{-1}}$

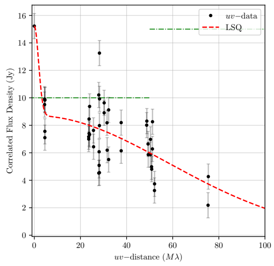

(263) G338.920+0.550
$v = -65.59\,\mathrm{km\,s^{-1}}$

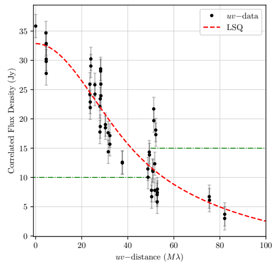

(264) G338.935-0.062
$v = -41.87\,\mathrm{km\,s^{-1}}$

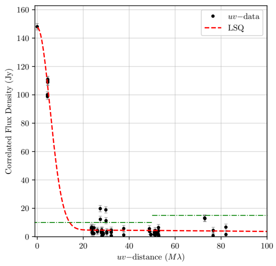

(265) G339.053-0.315
$v = -111.63\,\mathrm{km\,s^{-1}}$

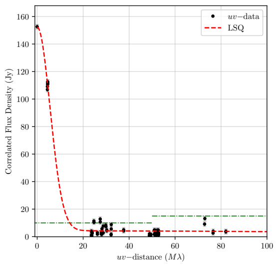

(266) G339.053-0.315
$v = -111.81\,\mathrm{km\,s^{-1}}$

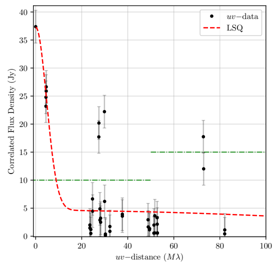

(267) G339.053-0.315
$v = -111.05\,\mathrm{km\,s^{-1}}$

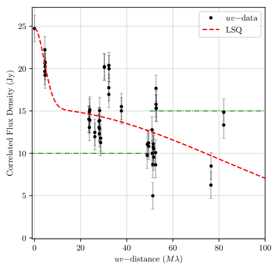

(268) G339.622-0.121
$v = -31.93\,\mathrm{km\,s^{-1}}$

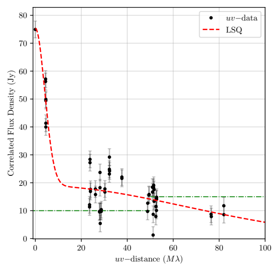

(269) G339.622-0.121
$v = -32.72\,\mathrm{km\,s^{-1}}$

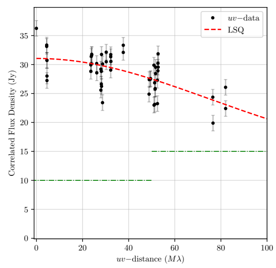

(270) G339.622-0.121
$v = -33.16\,\mathrm{km\,s^{-1}}$

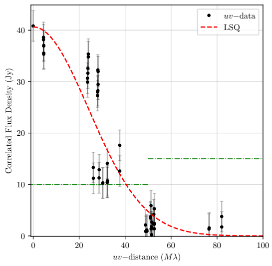

(271) G339.622-0.121
$v = -35.53\,\mathrm{km\,s^{-1}}$

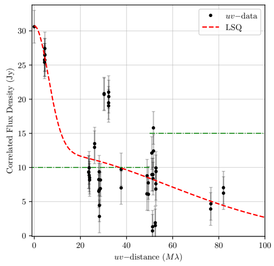

(272) G339.622-0.121
$v = -37.81\,\mathrm{km\,s^{-1}}$

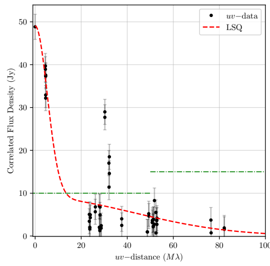

(273) G339.681-1.208
$v = -21.42\,\mathrm{km\,s^{-1}}$

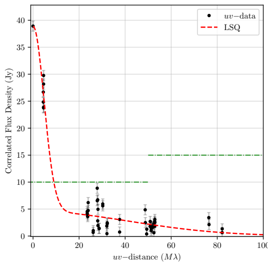

(274) G339.681-1.208
$v = -22.21\,\mathrm{km\,s^{-1}}$

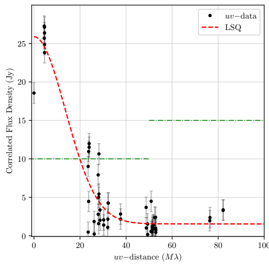

(275) G339.681-1.208
$v = -34.33\,\mathrm{km\,s^{-1}}$

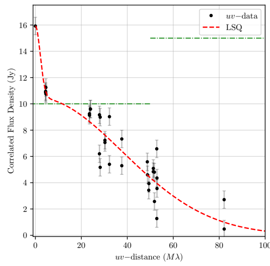

(276) G339.681-1.208
$v = -37.52\,\mathrm{km\,s^{-1}}$

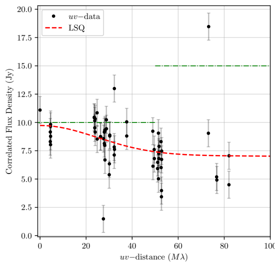

(277) G339.884-1.259
$v = -32.29\,\mathrm{km\,s^{-1}}$

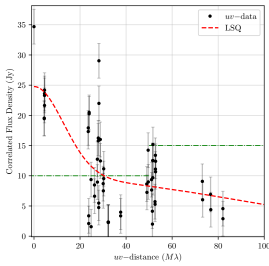

(278) G339.884-1.259
$v = -33.00\,\mathrm{km\,s^{-1}}$

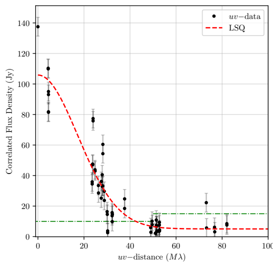

(279) G339.884-1.259
$v = -33.52\,\mathrm{km\,s^{-1}}$

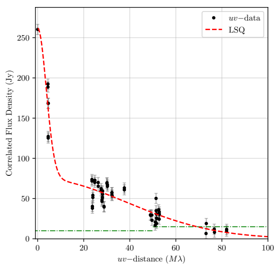

(280) G339.884-1.259
$v = -33.96\,\mathrm{km\,s^{-1}}$

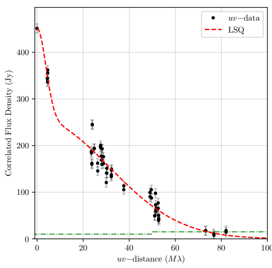

(281) G339.884-1.259
$v = -34.40\,\mathrm{km\,s^{-1}}$

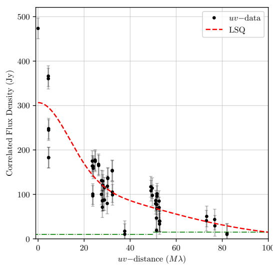

(282) G339.884-1.259
$v = -34.84\,\mathrm{km\,s^{-1}}$

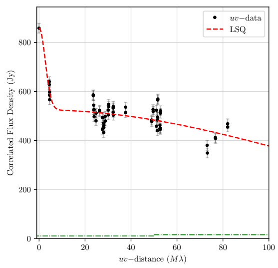

(283) G339.884-1.259
$v = -35.63\,\mathrm{km\,s^{-1}}$

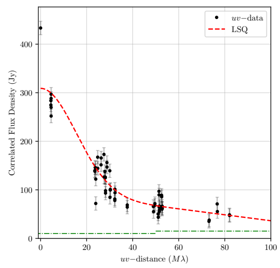

(284) G339.884-1.259
$v = -36.51\,\mathrm{km\,s^{-1}}$

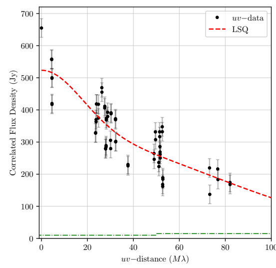

(285) G339.884-1.259
$v = -37.39\,\mathrm{km\,s^{-1}}$

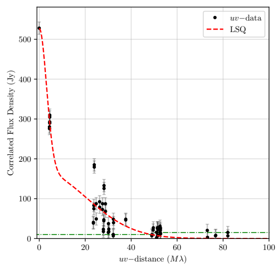

(286) G339.884-1.259
$v = -38.00\,\mathrm{km\,s^{-1}}$

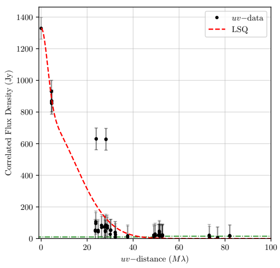

(287) G339.884-1.259
$v = -38.70\,\mathrm{km\,s^{-1}}$

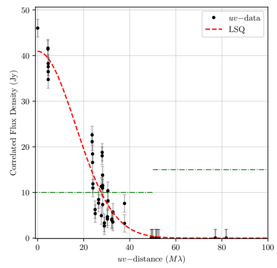

(288) G339.949-0.539
$v = -91.07\,\mathrm{km\,s^{-1}}$

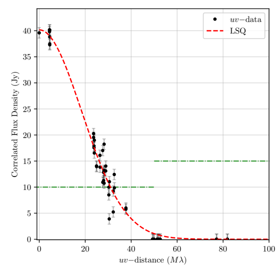

(289) G339.949-0.539
$v = -91.51\,\mathrm{km\,s^{-1}}$

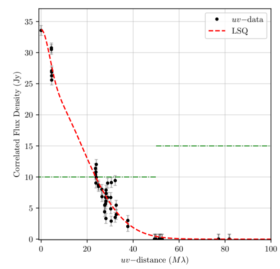

(290) G339.949-0.539
$v = -96.51\,\mathrm{km\,s^{-1}}$

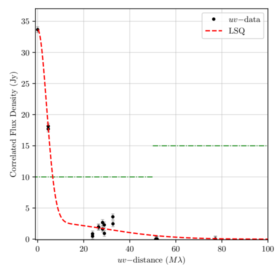

(291) G339.949-0.539
$v = -97.39\,\mathrm{km\,s^{-1}}$

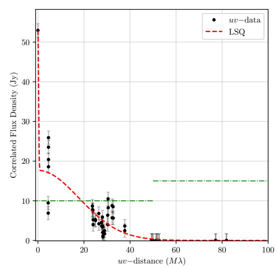

(292) G339.949-0.539
$v = -97.83\,\mathrm{km\,s^{-1}}$

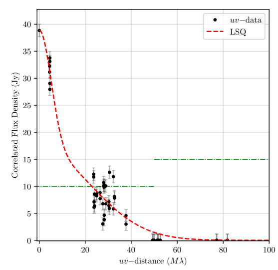

(293) G339.949-0.539
$v = -100.46\,\mathrm{km\,s^{-1}}$

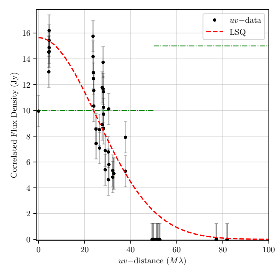

(294) G339.949-0.539
$v = -103.88\,\mathrm{km\,s^{-1}}$

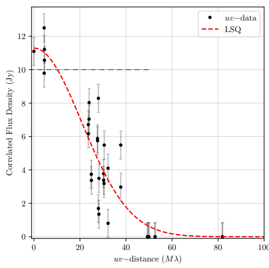

(295) G339.949-0.539
$v = -91.98\,\mathrm{km\,s^{-1}}$

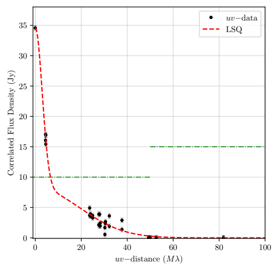

(296) G339.949-0.539
$v = -97.25\,\mathrm{km\,s^{-1}}$

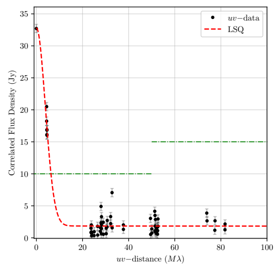

(297) G339.986-0.425
$v = -87.70\,\mathrm{km\,s^{-1}}$

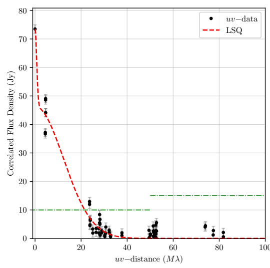

(298) G339.986-0.425
$v = -88.49\,\mathrm{km\,s^{-1}}$

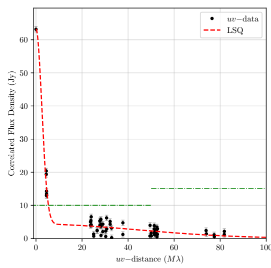

(299) G339.986-0.425
$v = -89.19\,\mathrm{km\,s^{-1}}$

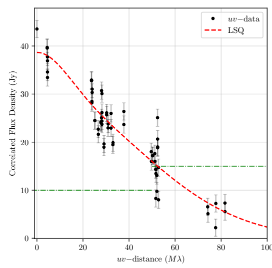

(300) G340.054-0.244
$v = -59.36\,\mathrm{km\,s^{-1}}$

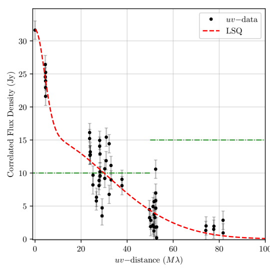

(301) G340.054-0.244
$v = -59.72\,\mathrm{km\,s^{-1}}$

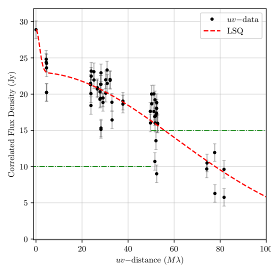

(302) G340.054-0.244
$v = -60.86\,\mathrm{km\,s^{-1}}$

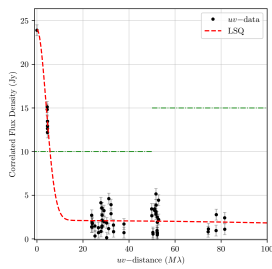

(303) G340.785-0.096
$v = -99.07\,\mathrm{km\,s^{-1}}$

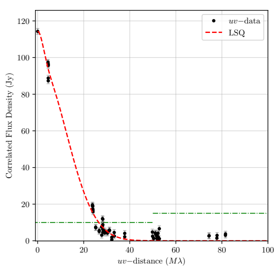

(304) G340.785-0.096
$v = -103.72\,\mathrm{km\,s^{-1}}$

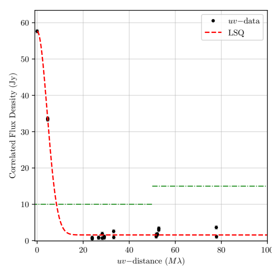

(305) G340.785-0.096
$v = -104.69\,\mathrm{km\,s^{-1}}$

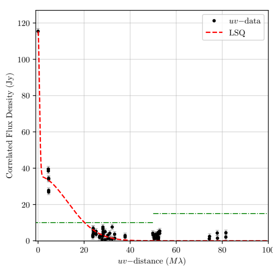

(306) G340.785-0.096
$v = -105.13\,\mathrm{km\,s^{-1}}$

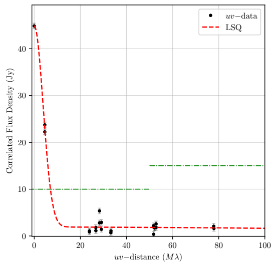

(307) G340.785-0.096
$v = -105.48\,\mathrm{km\,s^{-1}}$

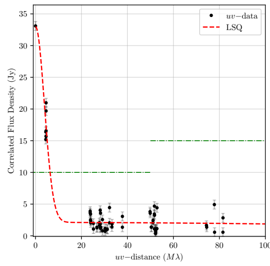

(308) G340.785-0.096
$v = -106.00\,\mathrm{km\,s^{-1}}$

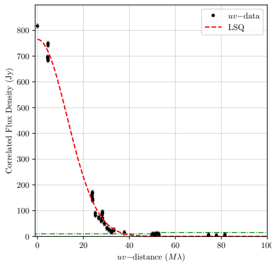

(309) G340.785-0.096
$v = -108.02\,\mathrm{km\,s^{-1}}$

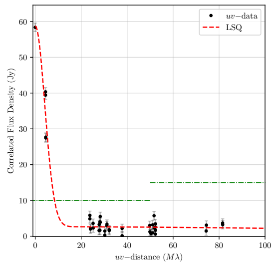

(310) G340.785-0.096
$v = -104.54\,\mathrm{km\,s^{-1}}$

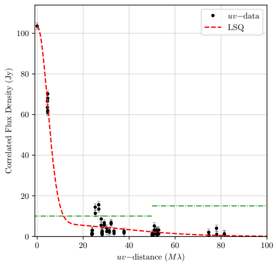

(311) G341.218-0.212
$v = -37.84\,\mathrm{km\,s^{-1}}$

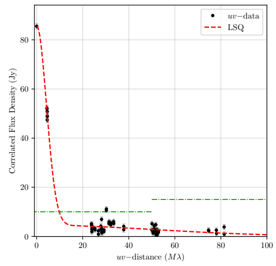

(312) G341.218-0.212
$v = -38.63\,\mathrm{km\,s^{-1}}$

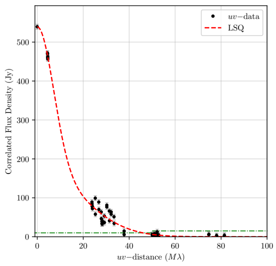

(313) G341.218-0.212
$v = -44.42\,\mathrm{km\,s^{-1}}$

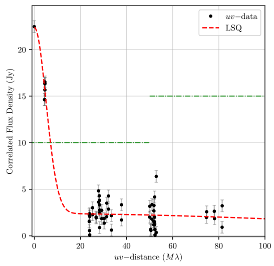

(314) G341.218-0.212
$v = -47.14\,\mathrm{km\,s^{-1}}$

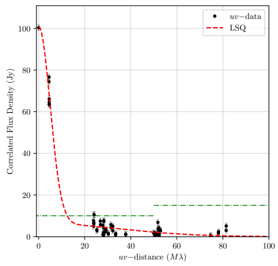

(315) G341.218-0.212
$v = -47.67\,\mathrm{km\,s^{-1}}$

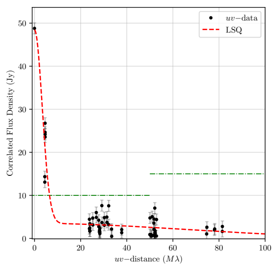

(316) G341.218-0.212
$v = -48.28\,\mathrm{km\,s^{-1}}$

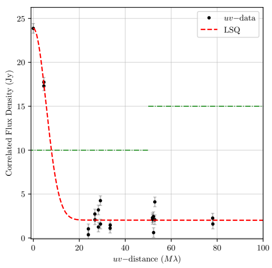

(317) G341.218-0.212
$v = -49.16\,\mathrm{km\,s^{-1}}$

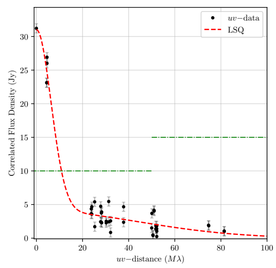

(318) G341.218-0.212
$v = -45.07\,\mathrm{km\,s^{-1}}$

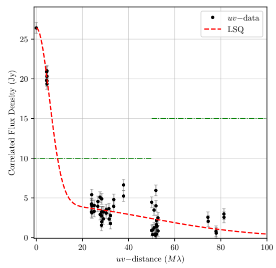

(319) G342.484+0.183
$v = -41.24\,\mathrm{km\,s^{-1}}$

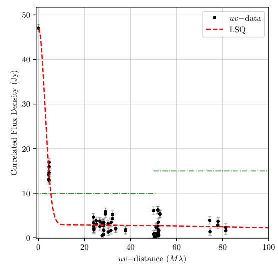

(320) G342.484+0.183
$v = -42.03\,\mathrm{km\,s^{-1}}$

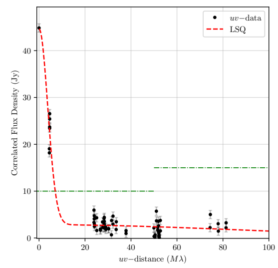

(321) G342.484+0.183
$v = -42.30\,\mathrm{km\,s^{-1}}$

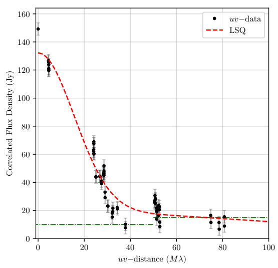

(322) G345.010+1.792
$v = -17.02\,\mathrm{km\,s^{-1}}$

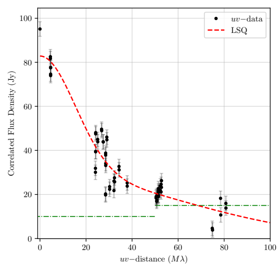

(323) G345.010+1.792
$v = -17.46\,\mathrm{km\,s^{-1}}$

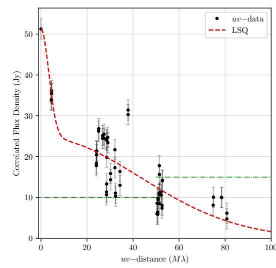

(324) G345.010+1.792
$v = -17.90\,\mathrm{km\,s^{-1}}$

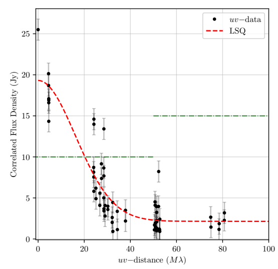

(325) G345.010+1.792
$v = -19.30\,\mathrm{km\,s^{-1}}$

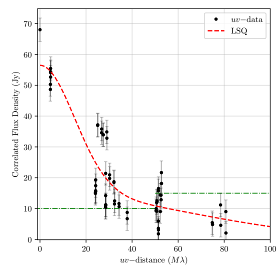

(326) G345.010+1.792
$v = -19.83\,\mathrm{km\,s^{-1}}$

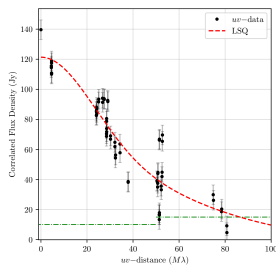

(327) G345.010+1.792
$v = -20.18\,\mathrm{km\,s^{-1}}$

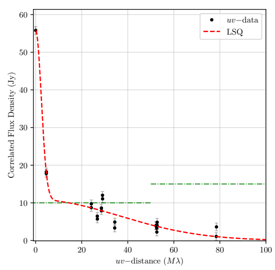

(328) G345.010+1.792
$v = -20.62\,\mathrm{km\,s^{-1}}$

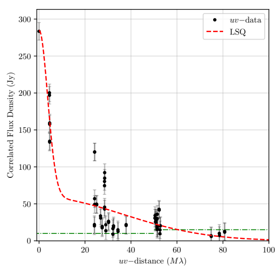

(329) G345.010+1.792
$v = -20.97\,\mathrm{km\,s^{-1}}$

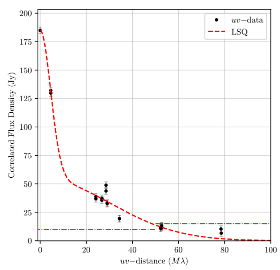

(330) G345.010+1.792
$v = -21.24\,\mathrm{km\,s^{-1}}$

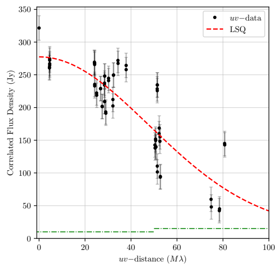

(331) G345.010+1.792
$v = -21.76\,\mathrm{km\,s^{-1}}$

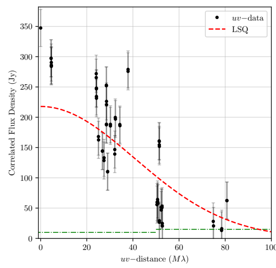

(332) G345.010+1.792
$v = -22.03\,\mathrm{km\,s^{-1}}$

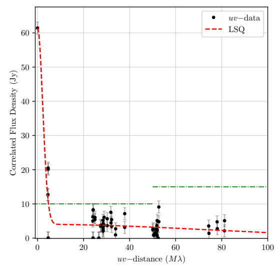

(333) G345.003-0.223
$v = -22.37\,\mathrm{km\,s^{-1}}$

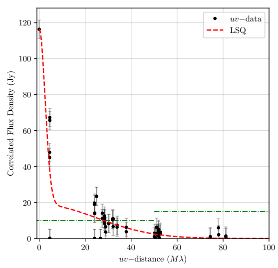

(334) G345.003-0.223
$v = -22.89\,\mathrm{km\,s^{-1}}$

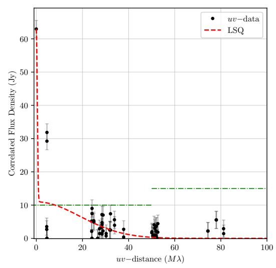

(335) G345.003-0.223
$v = -23.68\,\mathrm{km\,s^{-1}}$

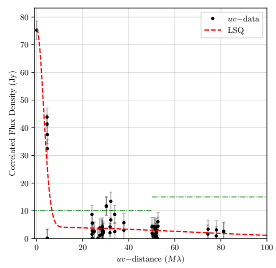

(336) G345.003-0.223
$v = -26.05\,\mathrm{km\,s^{-1}}$

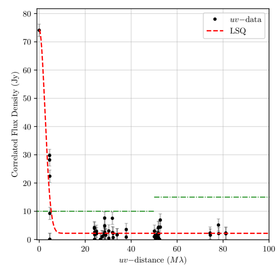

(337) G345.003-0.223
$v = -26.41\,\mathrm{km\,s^{-1}}$

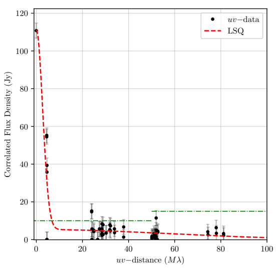

(338) G345.003-0.223
$v = -26.84\,\mathrm{km\,s^{-1}}$

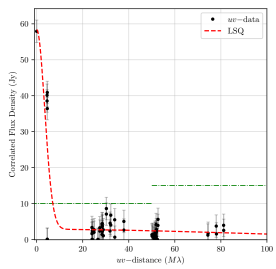

(339) G345.003-0.223
$v = -27.64\,\mathrm{km\,s^{-1}}$

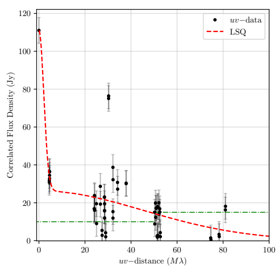

(340) G345.505+0.348
$v = -13.70\,\mathrm{km\,s^{-1}}$

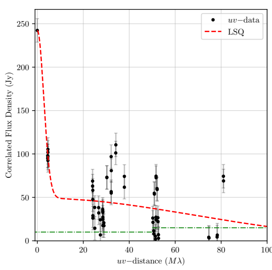

(341) G345.505+0.348
$v = -14.06\,\mathrm{km\,s^{-1}}$

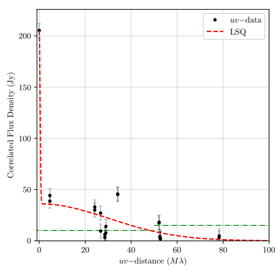

(342) G345.505+0.348
$v = -14.41\,\mathrm{km\,s^{-1}}$

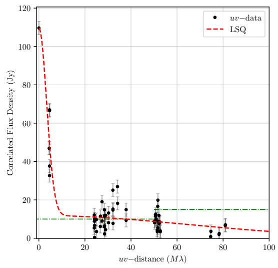

(343) G345.505+0.348
$v = -15.46\,\mathrm{km\,s^{-1}}$

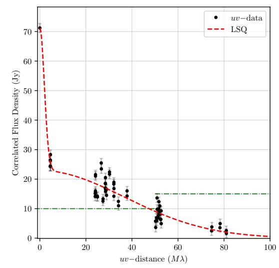

(344) G345.505+0.348
$v = -16.34\,\mathrm{km\,s^{-1}}$

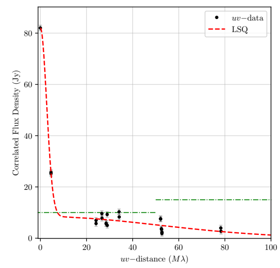

(345) G345.505+0.348
$v = -16.69\,\mathrm{km\,s^{-1}}$

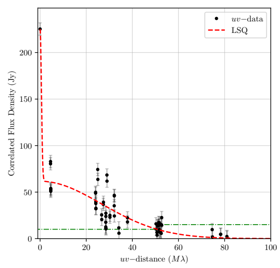

(346) G345.505+0.348
$v = -17.83\,\mathrm{km\,s^{-1}}$

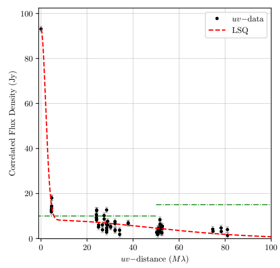

(347) G345.505+0.348
$v = -18.36\,\mathrm{km\,s^{-1}}$

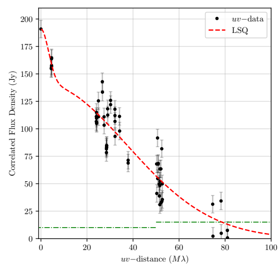

(348) G345.505+0.348
$v = -19.06\,\mathrm{km\,s^{-1}}$

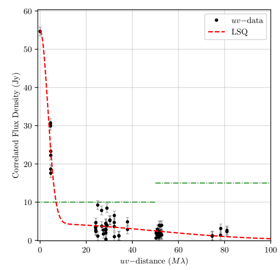

(349) G345.505+0.348
$v = -19.76\,\mathrm{km\,s^{-1}}$

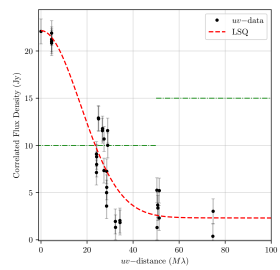

(350) G346.480+0.221
$v = -19.04\,\mathrm{km\,s^{-1}}$

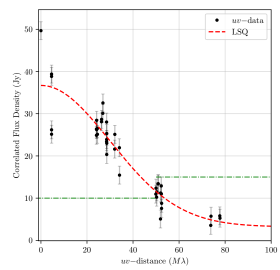

(351) G348.550-0.979
$v = -10.59\,\mathrm{km\,s^{-1}}$

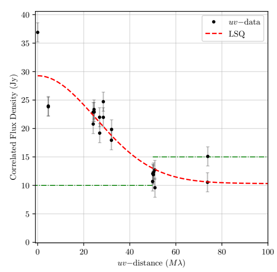

(352) G348.550-0.979
$v = -10.41\,\mathrm{km\,s^{-1}}$

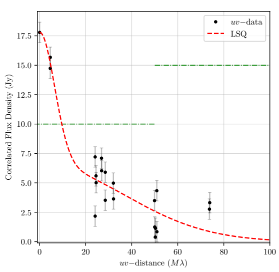

(353) G348.550-0.979
$v = -20.07\,\mathrm{km\,s^{-1}}$

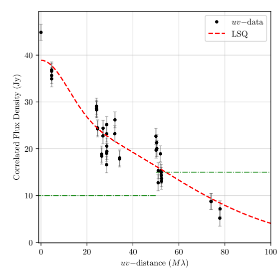

(354) G348.617-1.162
$v = -11.47\,\mathrm{km\,s^{-1}}$

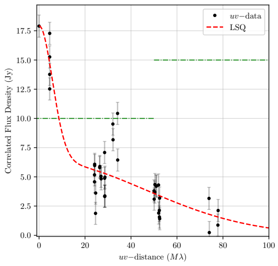

(355) G348.617-1.162
$v = -19.19\,\mathrm{km\,s^{-1}}$

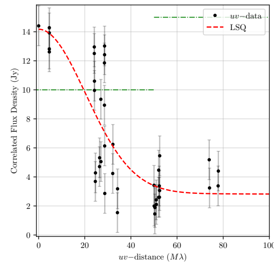

(356) G348.617-1.162
$v = -19.81\,\mathrm{km\,s^{-1}}$

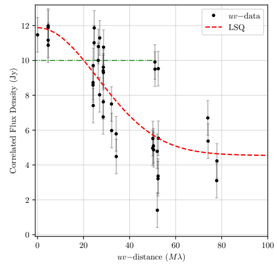

(357) G348.617-1.162
$v = -20.60\,\mathrm{km\,s^{-1}}$

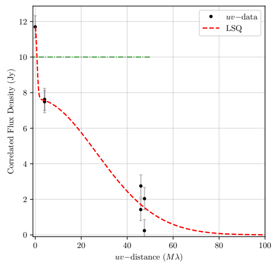

(358) G294.990-1.719
$v = -12.24\,\mathrm{km\,s^{-1}}$

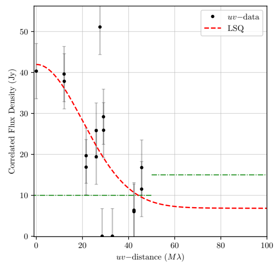

(359) G348.703-1.043
$v = -3.40\,\mathrm{km\,s^{-1}}$

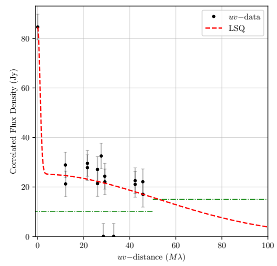

(360) G348.703-1.043
$v = -7.36\,\mathrm{km\,s^{-1}}$

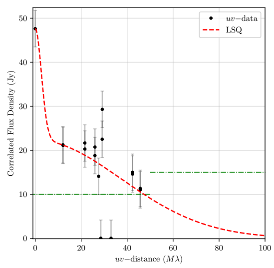

(361) G348.703-1.043
$v = -9.90\,\mathrm{km\,s^{-1}}$

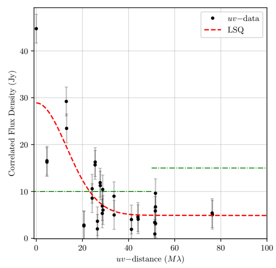

(362) G350.686-0.491
$v = -13.76\,\mathrm{km\,s^{-1}}$

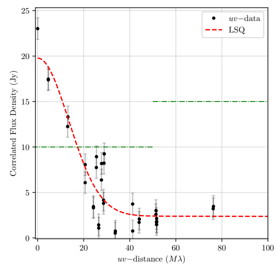

(363) G350.686-0.491
$v = -14.20\,\mathrm{km\,s^{-1}}$

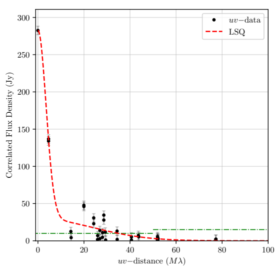

(364) G351.417+0.645
$v = -6.37\,\mathrm{km\,s^{-1}}$

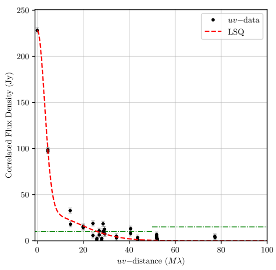

(365) G351.417+0.645
$v = -6.90\,\mathrm{km\,s^{-1}}$

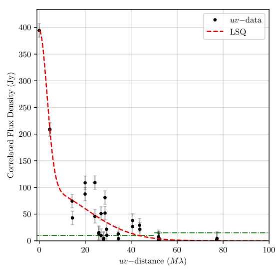

(366) G351.417+0.645
$v = -7.34\,\mathrm{km\,s^{-1}}$

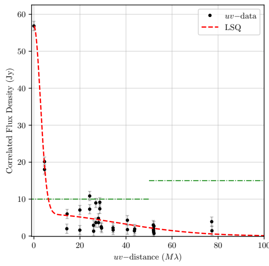

(367) G351.417+0.645
$v = -8.13\,\mathrm{km\,s^{-1}}$

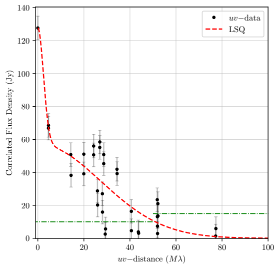

(368) G351.417+0.645
$v = -8.48\,\mathrm{km\,s^{-1}}$

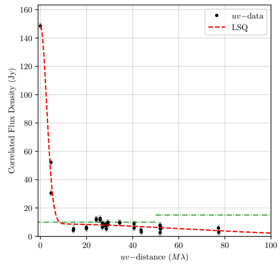

(369) G351.417+0.645
$v = -8.92\,\mathrm{km\,s^{-1}}$

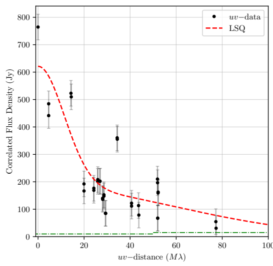

(370) G351.417+0.645
$v = -9.71\,\mathrm{km\,s^{-1}}$

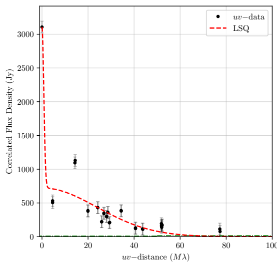

(371) G351.417+0.645
$v = -10.32\,\mathrm{km\,s^{-1}}$

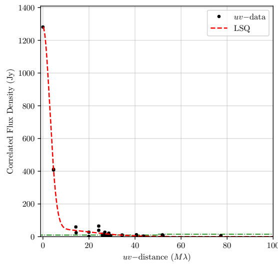

(372) G351.417+0.645
$v = -11.11\,\mathrm{km\,s^{-1}}$

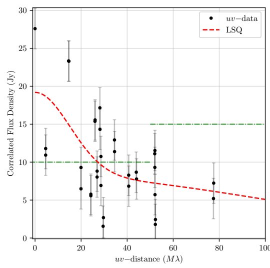

(373) G351.688+0.171
$v = -36.07\,\mathrm{km\,s^{-1}}$

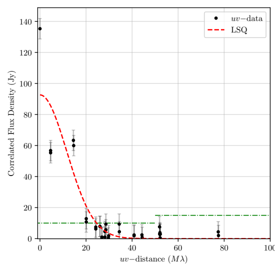

(374) G351.775-0.536
$v = 1.80\,\mathrm{km\,s^{-1}}$

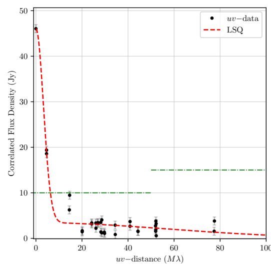

(375) G351.775-0.536
$v = 1.27\,\mathrm{km\,s^{-1}}$

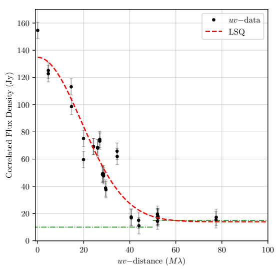

(376) G352.630-1.067
$v = -2.91\,\mathrm{km\,s^{-1}}$

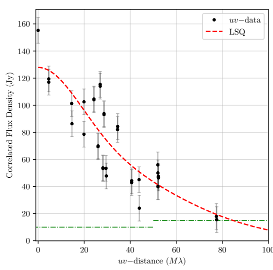

(377) G352.630-1.067
$v = -3.27\,\mathrm{km\,s^{-1}}$

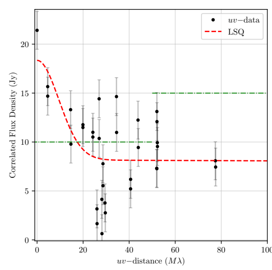

(378) G352.630-1.067
$v = -5.28\,\mathrm{km\,s^{-1}}$

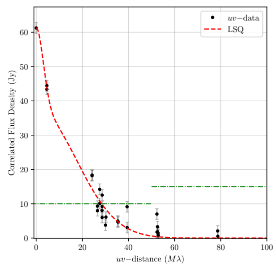

(379) G354.615+0.472
$v = -16.48\,\mathrm{km\,s^{-1}}$

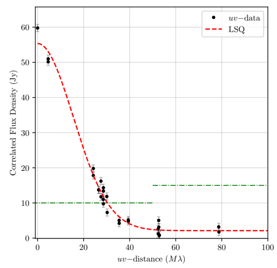

(380) G354.615+0.472
$v = -23.16\,\mathrm{km\,s^{-1}}$

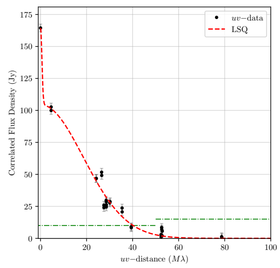

(381) G354.615+0.472
$v = -24.21\,\mathrm{km\,s^{-1}}$

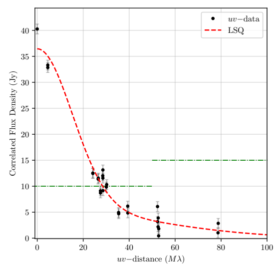

(382) G354.615+0.472
$v = -24.91\,\mathrm{km\,s^{-1}}$

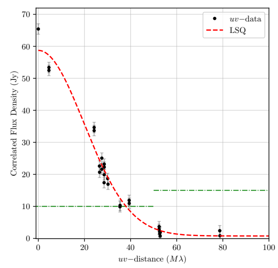

(383) G354.615+0.472
$v = -25.53\,\mathrm{km\,s^{-1}}$

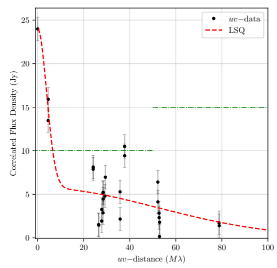

(384) G358.371-0.468
$v = 1.30\,\mathrm{km\,s^{-1}}$

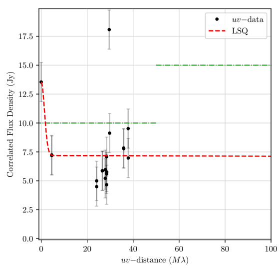

(385) G358.386-0.483
$v = -5.98\,\mathrm{km\,s^{-1}}$

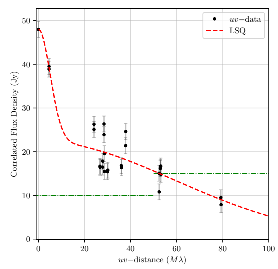

(386) G358.460-0.391
$v = 1.26\,\mathrm{km\,s^{-1}}$

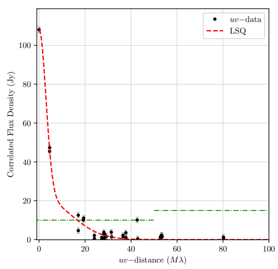

(387) G359.436-0.104
$v = -46.66\,\mathrm{km\,s^{-1}}$

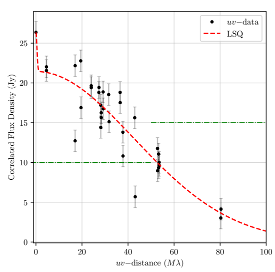

(388) G359.615-0.243
$v = 24.50\,\mathrm{km\,s^{-1}}$

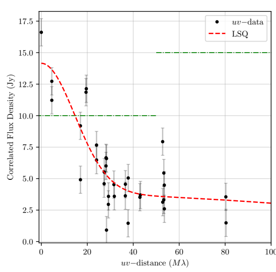

(389) G359.615-0.243
$v = 23.00\,\mathrm{km\,s^{-1}}$

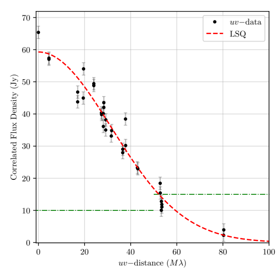

(390) G359.615-0.243
$v = 19.58\,\mathrm{km\,s^{-1}}$

C
MultiView Ring Calibration

In this appendix I have additional derivations, figures and tables relevant to Chapter 5 and Chapter 6.

- Section §C.1 goes through various derivations of equations and expressions presented in text, primarily amplitude calibration of quasars utilised in Chapter 6 and expressions for delay vs. angular separation shown in Chapter 5.
- Section §C.2 contains plots showing the raw phase vs. time data that was used for MultiView fitting in Chapter 6 and the resulting solution phase and phase-slopes.
- Section §C.3 contains tables of the position vs. time of the target and references quasars before and after the application of inverse MultiView from Chapter 6.

C.1 Additional Equations

C.1.1 Calibrating quasar amplitude over frequency

Due to synchrotron emission contributing the majority of flux density to the quasars, they are well modelled by a power law spectrum:

$$S_\nu = S_0\,\nu^\alpha \tag{C.1}$$

where S_ν is the flux density at frequency ν in Jy and α is the spectral index. Taylor expanding the above equation about some reference frequency ν_0 (assuming that $\alpha \neq 0$) will allow me to determine the flux density change over a spanned-bandwidth from ν_0 to $\nu_0 + \Delta\nu$:

$$S_\nu(\nu_0 + \Delta\nu) = S_0\,\nu_0^\alpha \sum_{n=0}^{\infty} \frac{\alpha(\alpha-1)...(\alpha-n)}{n!}\left(\frac{\Delta\nu}{\nu_0}\right)^n \tag{C.2}$$

For typical frequencies and spanned-bandwidths explored in this thesis (e.g. $\nu_0 = 6300\,\mathrm{MHz}$, $\Delta\nu = 374\,\mathrm{MHz}$ and $\nu_0 = 8213\,\mathrm{MHz}$, $\Delta\nu = 256\,\mathrm{MHz}$) it is reasonable to assume that $(\Delta\nu/\nu_0)^n \ll 1, n > 1$. Now equation Equation C.2 reduces to:

$$S_\nu(\nu_0 + \Delta\nu) = S_0\,\nu_0^\alpha \left(1 + \alpha\frac{\Delta\nu}{\nu_0}\right) \tag{C.3}$$

Using Kellermann et al. (1969), I take the median spectral index of quasars to be $\alpha \approx -1.0$ in the neighbourhood of our frequencies of interest. Now I can see the fractional change of the flux density over the bandwidth is:

$$\begin{aligned}\frac{S_\nu(\nu_0+\Delta\nu)-S_\nu(\nu_0)}{S_\nu(\nu_0)} &\approx -1.0\frac{\Delta\nu}{\nu_0}\\ &= 6\% \text{ at } 6.3\,\text{GHz}\\ &= 3\% \text{ at } 8.2\,\text{GHz}\end{aligned}$$

Therefore a constant amplitude over a small bandwidth is a reasonable assumption. This allows one to assume a fixed flux density of a quasar over the whole bandwidth, and calibrate the bandwidth compared to this number. In addition I can average a quasar over the spanned bandwidth and ensure the imaged flux density is accurate for each baseline.

C.1.2 Calibrating amplitude over baseline

Assuming a quasar of known zero–spacing flux density S_0 in Jy that has emission resembling a 2D Gaussian with angular size (full width at half maximum) θ in rads, then the visibility amplitude of the quasar can be represented as:

$$S_{uv} = S_0 \exp\left(-\frac{2\pi^2}{8\ln 2}(\theta B_\lambda)^2\right) \tag{C.4}$$

where $B_\lambda = uv/\lambda$ is the projected baseline length uv expressed in terms of wavelength λ and S_{uv} is the corresponding flux density in Jy. If the peak flux density of such a source were constant over time and the quasar never underwent evolutionary/structural changes we could use the source as a VLBI flux density calibrator.

If the detected flux density on baseline B_{ij} between antenna i and antenna j is

$$s_{ij} = |\sqrt{\bar{\mathbf{s}}_\mathbf{i}\bar{\mathbf{s}}_\mathbf{j}}|, i \neq j$$

then the ratio of s_{ij} to $S_{uv}(B_{ij})$ serves as a diagnostic for the 'goodness of calibration' as a function of baseline pairs. Consider

$$s_{ij} = x_i x_j$$

being the 'true' flux density and

$$S_{uv}(B_{ij}) = \delta x_i \delta x_j x_i x_j$$

being the detected flux density, with $0 < \delta x \leq 1$. If the model and source flux are identical for all baseline pairs, then $\delta x_i = 1\ \forall i$ and the data is perfectly calibrated. Elsewise we can simply solve for the antenna–dependent offset between baselines and correct it.

To isolate the parameters we consider that for N antennas there are $\frac{N(N-1)}{2}$ independent baselines. While the immediate problem is non-linear:

$$\delta x_i \delta x_j = \frac{S_{uv}(b_{ij})}{s_{ij}}, i \neq j \tag{C.5}$$

we can assume that the required corrections are small $\delta x_i = 1 + \epsilon_i$ so that we can get:

$$(1+\epsilon_i)(1+\epsilon_j) = (1+\epsilon_i+\epsilon_j+\epsilon_i\epsilon_j) = \frac{S_{uv}(b_{ij})}{s_{ij}} \tag{C.6}$$

and it is likely that $\epsilon_i\epsilon_j \ll 1$. We now can convert this to a matrix formula to solve for the offsets.

$$\epsilon_i + \epsilon_j = \frac{S_{uv}(b_{ij})}{s_{ij}} - 1 = d_{ij} \tag{C.7}$$

$$\begin{bmatrix} 1 & 1 & 0 & 0 & \dots & 0 & 0 & 0 \\ 1 & 0 & 1 & 0 & \dots & 0 & 0 & 0 \\ \vdots & \vdots & \vdots & & \ddots & \vdots & \vdots & \vdots \\ 0 & 0 & 0 & \dots & \dots & 0 & 1 & 1 \end{bmatrix} \begin{bmatrix} \epsilon_1 \\ \epsilon_2 \\ \vdots \\ \epsilon_N \end{bmatrix} = \begin{bmatrix} 0 & d_{12} & d_{13} & \dots & d_{1N} \\ d_{21} & 0 & d_{23} & \dots & d_{2N} \\ d_{31} & d_{32} & 0 & \dots & d_{3N} \\ \vdots & \vdots & \vdots & \ddots & \vdots \\ d_{N1} & d_{N2} & d_{N3} & \dots & 0 \end{bmatrix}$$

Where we set $d_{ii} = 0$ to mask the solution. The above is the matrix equation

$$\mathbb{P}\mathbf{x} = \mathbb{D}$$

where $\mathbb{P}$ is a $N \times N(N-1)/2$ matrix, $\mathbf{x}$ is a $1 \times N$ vector containing the solutions and $\mathbb{D}$ is a $N \times N$ matrix of the observables. $\mathbb{P}$ is non-singular if $N \geq 3$ and therefore has in inverse such that we can solve the above for $\mathbf{x}$:

$$\mathbf{x} = (\mathbb{P}^T\mathbb{P})^{-1}\mathbb{P}^T\mathbb{D} \tag{C.8}$$

The array $1 + \mathbf{x}$ contains the correction that needs to be applied to each telescope in the array to match the model and therefore calibrate the telescope SEFDs.

C.1.3 Delay Plane Derivations

In this part of the appendix I want to provide mathematical justification for the planar approximations for baseline, dry tropospheric and source position offset in Section §5.2.

Baseline Error: starting from the difference of two LoS geodetic delays caused by a baseline error, I substitute that $\alpha_1 = \alpha_2 + a$ and $\delta_1 = \delta_2 + b$:

$$\begin{aligned} c(\tau_1 - \tau_2) =& \Delta B_x \cos(t-\alpha_1)\cos\delta_1 - \Delta B_y \sin(t-\alpha_1)\cos\delta_1 + \Delta B_z \sin\delta_1 \\ & - \Delta B_x \cos(t-\alpha_2)\cos\delta_2 + \Delta B_y \sin(t-\alpha_2)\cos\delta_2 - \Delta B_z \sin\delta_2 \\ =& \Delta B_x \cos(t-\alpha_2-a)\cos(\delta_2+b) - \Delta B_y \sin(t-\alpha_2-a)\cos(\delta_2+b) + \Delta B_z \sin(\delta_2+b) \\ & - \Delta B_x \cos(t-\alpha_2)\cos\delta_2 + \Delta B_y \sin(t-\alpha_2)\cos\delta_2 - \Delta B_z \sin\delta_2 \end{aligned}$$

I can use the double angle formulae to reduce to expression down:

$$\begin{aligned} \cos(t-\alpha_2-a)\cos(\delta_2+b) &= (\cos(t-\alpha_2)\cos a + \sin(t-\alpha_2)\sin a)(\cos\delta_2\cos b - \sin\delta_2 \sin b) \\ &= \left(\cos(t-\alpha_2)\left(1-\frac{a^2}{2}\right) + a\sin(t-\alpha_2)\right)\left(\cos\delta_2\left(1-\frac{b^2}{2}\right) - b\sin\delta_2\right) \\ &= \cos(t-\alpha_2)\cos\delta_2\left(1-\frac{a^2}{2}-\frac{b^2}{2}\right) - b\cos(t-\alpha_2)\sin\delta_2 - a\sin(t-\alpha_2)\cos\delta_2 \\ &\quad + a\,b\,\sin(t-\alpha_2)\sin\delta_2 \end{aligned}$$

$$\begin{aligned} \sin(t-\alpha_2-a)\cos(\delta_2+b) &= (\sin(t-\alpha_2)\cos a - \cos(t-\alpha_2)\sin a)(\cos\delta_2\cos b - \sin\delta_2 \cos b) \\ &= \sin(t-\alpha_2)\cos\delta_2\left(1-\frac{a^2}{2}-\frac{b^2}{2}\right) + b\sin(t-\alpha_2)\sin\delta_2 + a\cos(t-\alpha_2)\cos\delta_2 \\ &\quad - a\,b\,\cos(t-\alpha_2)\sin\delta_2 \end{aligned}$$

$$\begin{aligned} \sin(\delta_2+b) &= \sin\delta_2\cos b + \cos\delta_2 \sin b \\ &= \sin\delta_2\left(1-\frac{b^2}{2}\right) + b\cos\delta_2 \end{aligned}$$

where I have omitted terms with O^3 or greater. All O^0 terms cancel with the second half of the original expression. If I group terms by $\mathbf{a}$, $\mathbf{b}$, $\mathbf{a}^2$, ..., $\mathbf{a}\times\mathbf{b}$ I arrive at:

$$\begin{aligned}
c(\tau_1-\tau_2) &= \mathbf{a}\left(-\Delta B_x \sin(t-\alpha_2)\cos\delta_2 + \Delta B_y \cos(t-\alpha_2)\cos\delta_2\right)\\
&\quad + \mathbf{b}\left(-\Delta B_x \cos(t-\alpha_2)\sin\delta_2 + \Delta B_y \sin(t-\alpha_2)\sin\delta_2 + \Delta B_z\cos\delta_2\right)\\
&\quad + \mathbf{a}\,\mathbf{b}\left(\Delta B_x \sin(t-\alpha_2)\sin\delta_2 - \Delta B_y \cos(t-\alpha_2)\sin\delta_2\right)\\
&\quad + \frac{\mathbf{a}^2}{2}\left(-\Delta B_x \cos(t-\alpha_2)\cos\delta_2 + \Delta B_y \sin(t-\alpha_2)\cos\delta_2\right)\\
&\quad + \frac{\mathbf{b}^2}{2}\left(-\Delta B_x \cos(t-\alpha_2)\cos\delta_2 + \Delta B_y \sin(t-\alpha_2)\cos\delta_2 - \Delta B_z \sin\delta_2\right)\\
&= \mathbf{a}\mathcal{A}_{bl} + \mathbf{b}\mathcal{B}_{bl} + \mathbf{a}\,\mathbf{b}\,\mathcal{C}_{bl} + \frac{1}{2}\mathbf{a}^2\mathcal{D}_{bl} + \frac{1}{2}\mathbf{b}^2\mathcal{E}_{bl}
\end{aligned} \tag{C.9}$$

If $\mathbf{a}$, $\mathbf{b}$ are 'small' then the O^2 terms are comparatively reduced.

Dry Tropospheric Error I have a target (T) and calibrator (C) at respective equatorial coordinates (α, δ) for a sample telescope at Earth latitude φ and Z is the respective zenith angles. The target and calibrator are (as in the previous derivation) offset from one another $\mathbf{a}$ radians in RA and $\mathbf{b}$ radians in DEC.

$$\begin{aligned}
\Delta\tau_{\text{dry}} &= \sigma_{\tau_z}\left(\frac{1}{\cos Z_C} - \frac{1}{\cos Z_T}\right)\\
&= \sigma_{\tau_z} F\\
\therefore F &= \left(\sin\delta_C \sin\varphi + \cos\delta_C\cos\varphi\cos(t_{lst}-\alpha_C)\right)^{-1}\\
&\quad - \left(\sin\delta_T \sin\varphi + \cos\delta_T\cos\varphi\cos(t_{lst}-\alpha_T)\right)^{-1}\\
F(\mathbf{a},\mathbf{b}) &= \left(\sin(\delta_T+\mathbf{b})\sin\varphi + \cos(\delta_T+\mathbf{b})\cos\varphi\cos(t_{lst}-\alpha_T-\mathbf{a})\right)^{-1}\\
&\quad - \left(\sin\delta_T \sin\varphi + \cos\delta_T\cos\varphi\cos(t_{lst}-\alpha_T)\right)^{-1}
\end{aligned} \tag{C.10}$$

where σ_{τ_z} is the error in the zenith delay determination. This function F is obviously more complex than in the previous example. While it is possible to Taylor expand the sin and cos terms, it is easier to perform a 2D Maclaurin expansion and determine magnitudes after:

$$F(\mathbf{a},\mathbf{b}) = F(0,0) + F_a(0,0)\ \mathbf{a} + F_b(0,0)\ \mathbf{b} + F_{aa}(0,0)\ \frac{1}{2}\mathbf{a}^2 + F_{ab}(0,0)\ \frac{1}{2}\mathbf{ab} + F_{bb}(0,0)\ \frac{1}{2}\mathbf{b}^2 + \sigma_{O^3}$$

where $F_a = \frac{\partial F}{\partial a}$, $F_{ab} = \frac{\partial^2 F}{\partial a \partial b}$ etc.

I am going to let $h_T = t_{lst} - \alpha_T$ as the hour angle for the target and define

$$\kappa = \sin(\delta_T+\mathbf{b})\sin\varphi + \cos(\delta_T+\mathbf{b})\cos\varphi\cos(h_T-\mathbf{a})$$

as it appears frequently. Performing the partial derivatives gives:

$$\begin{aligned}
F_a(\mathbf{a},\mathbf{b}) &= \frac{1}{\kappa^2}\left(-\cos(\delta_T+\mathbf{b})\cos\varphi\sin(h_T-\mathbf{a})\right)\\
F_b(\mathbf{a},\mathbf{b}) &= \frac{1}{\kappa^2}\left(\cos\varphi\cos(h_T-\mathbf{a})\sin(\delta_T+\mathbf{b}) - \sin\varphi\cos(\delta_T+\mathbf{b})\right)\\
F_{aa}(\mathbf{a},\mathbf{b}) &= \frac{1}{\kappa^3}\left(\cos\varphi\cos(\delta_T+\mathbf{b})\left(\cos\varphi\cos(\delta_T+\mathbf{b})\left(1+\sin^2(h_T+\mathbf{a})\right) + \sin\varphi\cos(h_T+\mathbf{a})\sin(\delta_T+\mathbf{b})\right)\right)\\
F_{ab}(\mathbf{a},\mathbf{b}) &= \frac{1}{\kappa^3}\left(-\cos\varphi\sin(h_T-\mathbf{a})\left(\cos\varphi\cos(h_T+\mathbf{a})\sin(\delta_T+\mathbf{b})\cos(\delta_T+\mathbf{b}) - \sin\varphi\left(\cos^2(\delta_T+\mathbf{b})\right)\right)\right)\\
F_{bb}(\mathbf{a},\mathbf{b}) &= \frac{1}{\kappa} + \frac{2}{\kappa^3}\left(\cos\varphi\cos(h_T-\mathbf{a})\sin(\delta_T+\mathbf{b}) - \sin\varphi\cos(\delta_T+\mathbf{b})\right)^2
\end{aligned}$$

And evaluating them at $(\mathbf{a}, \mathbf{b}) = (0, 0)$ gives:

$$
\begin{aligned}
F(0,0) &= 0 \\
F_a(0,0) &= \frac{-1}{\cos^2 Z_T} \cos\delta_T \cos\varphi \sin h_T \\
F_b(0,0) &= \frac{1}{\cos^2 Z_T} \left(\cos\varphi \cos h_T \sin\delta_T - \sin\varphi \cos\delta_T\right) \\
F_{aa}(0,0) &= \frac{1}{\cos^3 Z_T} \left(\cos\varphi \cos\delta_T \left(\cos\varphi \cos\delta_T \left(1 + \sin^2 h_T\right) + \sin\varphi \cos h_T\right) \sin\delta_T\right)\right) \\
F_{ab}(0,0) &= \frac{-1}{\cos^3 Z_T} \cos\varphi \sin h_T \left(\cos\varphi \cos h_T \sin\delta_T \cos\delta_T - \sin\varphi \left(\cos^2 \delta_T + 1\right)\right) \\
F_{bb}(0,0) &= \frac{1}{\cos Z_T} + \frac{2}{\cos^3 Z_T} \left(\cos\varphi \cos h_T \sin\delta_T - \sin\varphi \cos\delta_T\right)^2
\end{aligned}
$$

And therefore total delay slope is:

$$
\begin{aligned}
\Delta\tau_{\mathrm{dry}} &= \sigma_{\tau_z} \left(F(0,0) + F_a(0,0)\ \mathbf{a} + F_b(0,0)\ \mathbf{b} + F_{aa}(0,0)\ \frac{1}{2}\mathbf{a}^2 + F_{ab}(0,0)\ \frac{1}{2}\mathbf{ab} + F_{bb}(0,0)\ \frac{1}{2}\mathbf{b}^2\right) + \sigma_{O^3} \\
&= \mathbf{a}\mathcal{A}\mathrm{dry} + \mathbf{b}\mathcal{B}\mathrm{dry} + \mathbf{a}\,\mathbf{b}\,\mathcal{C}\mathrm{dry} + \frac{1}{2}\mathbf{a}^2\mathcal{D}\mathrm{dry} + \frac{1}{2}\mathbf{b}^2\mathcal{E}\mathrm{dry} + \sigma_{O^3}
\end{aligned}
$$

Source Position Error starting from the difference of two delays caused by a position errors in the target σ_T and calibrator error σ_C, I substitute that $\alpha_C = \alpha_T + a$ and $\delta_C = \delta_T + b$:

$$
\begin{aligned}
c\left(\tau_{\theta,C} - \tau_{\theta,T}\right) = c\Delta\tau_\theta &= \sigma_{\alpha,C} \cos\delta_C (B_x \sin(t - \alpha_C) + B_y \cos(t - \alpha_C)) \\
&\quad + \sigma_{\delta,C}(-B_x \cos(t - \alpha_C) \sin\delta_C + B_y \sin(t - \alpha_C) \sin\delta_C + B_z \cos\delta_C) \\
&\quad - \sigma_{\alpha,T} \cos\delta_T \left(B_x \sin(t - \alpha_T) + B_y \cos(t - \alpha_T)\right) \\
&\quad - \sigma_{\delta,T} \left(-B_x \cos(t - \alpha_T) \sin\delta_T + B_y \sin(t - \alpha_T) \sin\delta_T + B_z \cos\delta_T\right) \\
&= \sigma_{\alpha,C} \cos\left(\delta_T + b\right) \left(B_x \sin(t - \alpha_T - a) + B_y \cos(t - \alpha_T - a)\right) \\
&\quad + \sigma_{\delta,C}(-B_x \cos(t - \alpha_T - a) \sin\left(\delta_T + b\right) + B_y \sin(t - \alpha_T - a) \sin\left(\delta_T + b\right) + B_z \cos\left(\delta_T + b\right)) \\
&\quad - \sigma_{\alpha,T} \cos\delta_T \left(B_x \sin(t - \alpha_T) + B_y \cos(t - \alpha_T)\right) \\
&\quad - \sigma_{\delta,T} \left(-B_x \cos(t - \alpha_T) \sin\delta_T + B_y \sin(t - \alpha_T) \sin\delta_T + B_z \cos\delta_T\right)
\end{aligned}
$$

where σ_α and σ_δ are the positional uncertainties in Right Ascension and Declination respectively.

I can use the expansions for $\cos(t - \alpha_T - a) \cos\left(\delta_T + b\right)$, $\sin(t - \alpha_T - a) \cos\left(\delta_T + b\right)$ and $\sin\left(\delta_T + b\right)$

shown in Section §C.1.3 as well as the expansions below:

$$\begin{aligned}
\cos(t-\alpha_T-a)\sin(\delta_T+b) &= (\cos(t-\alpha_T)\cos a+\sin(t-\alpha_T)\sin a)\,(\sin\delta_T\cos b+\cos\delta_T\sin b)\\
&= \left(\cos(t-\alpha_T)\left(1-\frac{a^2}{2}\right)+a\sin(t-\alpha_T)\right)\left(\sin\delta_T\left(1-\frac{b^2}{2}\right)+b\cos\delta_T\right)\\
&= \cos(t-\alpha_T)\sin\delta_T\left(1-\frac{a^2}{2}-\frac{b^2}{2}\right)+a\sin(t-\alpha_T)\sin\delta_2+b\cos(t-\alpha_T)\cos\delta_T\\
&\quad + a\,b\,\sin(t-\alpha_T)\cos\delta_T
\end{aligned}$$

$$\begin{aligned}
\sin(t-\alpha_T-a)\sin(\delta_T+b) &= (\sin(t-\alpha_T)\cos a-\cos(t-\alpha_T)\sin a)\,(\sin\delta_T\cos b+\cos\delta_T\sin b)\\
&= \sin(t-\alpha_T)\sin\delta_T\left(1-\frac{a^2}{2}-\frac{b^2}{2}\right)-a\cos(t-\alpha_T)\sin\delta_T+b\sin(t-\alpha_T)\cos\delta_T\\
&\quad - a\,b\,\cos(t-\alpha_2)\cos\delta_2
\end{aligned}$$

$$\begin{aligned}
\cos(\delta_T+b) &= \cos\delta_T\cos b-\sin\delta_T\sin b\\
&= \cos\delta_T\left(1-\frac{b^2}{2}\right)-b\sin\delta_T
\end{aligned}$$

If I substitute the expansions then collect terms in $\mathbf{a}$, $\mathbf{b}$, $\mathbf{ab}$, $\mathbf{a}^2$ and $\mathbf{b}^2$ I am left with:

$$\begin{aligned}
c\Delta\tau_\theta =& \big[\big(\sigma_{\alpha,C}-\sigma_{\alpha,T}\big)\cos\delta_T\big(B_x\sin(t-\alpha_T)+B_y\cos(t-\alpha_T)\big)\\
&\quad+\big(\sigma_{\delta,C}-\sigma_{\delta,T}\big)\big(B_x\sin\delta_T\cos(t-\alpha_T)-B_y\sin\delta_T\sin(t-\alpha_T)-B_z\cos\delta_T\big)\big]\\
&+\mathbf{a}\,\big[-\sigma_{\alpha,C}\cos\delta_T\,(B_x\cos(t-\alpha_T)+B_y\sin(t-\alpha_T))\\
&\qquad-\sigma_{\delta,C}\sin\delta_T\,(B_x\sin(t-\alpha_T)+B_y\cos(t-\alpha_T))\big]\\
&+\mathbf{b}\,\big[\sigma_{\alpha,C}\sin\delta_T\,(B_x\sin(t-\alpha_T)+B_y\cos(t-\alpha_T))\\
&\qquad+\sigma_{\delta,C}(B_x\cos\delta_T\cos(t-\alpha_T)-B_y\cos\delta_T\sin(t-\alpha_T)+B_z\sin\delta_T)\big]\\
&-\left(\frac{\mathbf{a}^2}{2}+\frac{\mathbf{b}^2}{2}\right)\big[\sigma_{\alpha,C}\cos\delta_T\big(B_x\sin(t-\alpha_T)+B_y\cos(t-\alpha_T)\big)\\
&\quad+\sigma_{\delta,C}\big(B_x\sin\delta_T\cos(t-\alpha_T)-B_y\sin\delta_T\sin(t-\alpha_T)\big)\big]\\
&-\frac{\mathbf{b}^2}{2}B_z\cos\delta_T\\
&+\mathbf{ab}\big[-\sigma_{\alpha,C}B_x\cos(t-\alpha_T)\sin\delta_T+\sigma_{\alpha,C}B_y\sin(t-\alpha_T)\sin\delta_T\\
&\qquad-\sigma_{\delta,C}B_x\sin(t-\alpha_T)\cos\delta_T-\sigma_{\delta,C}B_y\cos(t-\alpha_T)\cos\delta_T\big]
\end{aligned}$$

C.1.4 Finite Sum of Angles

Here I show justification for an expression given in text. I have the sum S:

$$S=\sum_{i=1}^{N}R_i^2\,\cos^2(\theta_i+\psi) \tag{C.11}$$

where R_i is the target–calibrator separation and θ_i is the orientation ($\theta = 0$ being due North) for calibrator i, N is the total number of calibrators and ψ is an arbitrary angular offset (in rads).

$$\begin{aligned} S =& \sum_{i=1}^{N} \frac{R_i^2}{2} \left(1 + \cos\left(2\theta_i + 2\psi\right)\right) \\ =& N\frac{\overline{R^2}}{2} + \sum_{i=1}^{N} \frac{R_i^2}{2} \left(\cos 2\psi \cos 2\theta_i - \sin 2\psi \sin 2\theta_i\right) \end{aligned}$$

In the rings we have $R_i \approx \overline{R}$ and $\theta_i = \frac{2\pi(i-1)}{N}$ aka. azimuthally well sampled. Continuing:

$$\begin{aligned} S =& N\frac{\overline{R^2}}{2} + \frac{\overline{R}^2}{2}\left(\cos 2\psi \sum_{i=1}^{N} \left(\cos\frac{4\pi\,(i-1)}{N}\right) - \sin 2\psi \sum_{i=1}^{N}\left(\sin\frac{4\pi\,(i-1)}{N}\right)\right) \\ =& N\frac{\overline{R^2}}{2} + \frac{\overline{R}^2}{2}\cos 2\psi \left(\cos\left(\frac{4\pi}{N}\right)\sum_{i=1}^{N}\cos\left(\frac{4\pi}{N}i\right) + \sin\left(\frac{4\pi}{N}\right)\sum_{i=1}^{N}\sin\left(\frac{4\pi}{N}i\right)\right) \\ & - \frac{\overline{R}^2}{2}\sin 2\psi\left(\cos\left(\frac{4\pi}{N}\right)\sum_{i=1}^{N}\sin\left(\frac{4\pi}{N}i\right) - \sin\left(\frac{4\pi}{N}\right)\sum_{i=1}^{N}\cos\left(\frac{4\pi}{N}i\right)\right) \end{aligned}$$

The trigonometric identities

$$\begin{aligned} \sum_{n=1}^{N}\cos(n\theta) &= -\frac{1}{2} + \frac{\sin\theta(N+\frac{1}{2})}{2\sin\frac{\theta}{2}} \\ \sum_{n=1}^{N}\sin(n\theta) &= \frac{1}{2}\cot\frac{\theta}{2} - \frac{\cos\theta(N+\frac{1}{2})}{2\sin\frac{\theta}{2}} \end{aligned}$$

can be used to simplify the expression. Since $\theta = \frac{4\pi}{N}$ it should first be noted that:

$$\begin{aligned} \cos\frac{4\pi}{N}(N+\frac{1}{2}) &= \cos(\frac{2\pi}{N}) \\ \sin\frac{4\pi}{N}(N+\frac{1}{2}) &= \sin(\frac{2\pi}{N}) \end{aligned}$$

Therefore:

$$\begin{aligned} \sum_{i=1}^{N}\cos\left(\frac{4\pi}{N}i\right) &= -\frac{1}{2} + \frac{\sin(\frac{2\pi}{N})}{2\sin(\frac{2\pi}{N})} = 0 \\ \sum_{i=1}^{N}\sin\left(\frac{4\pi}{N}i\right) &= \frac{1}{2}\cot\frac{2\pi}{N} - \frac{\cos(\frac{2\pi}{N})}{2\sin(\frac{2\pi}{N})} = 0 \end{aligned}$$

$$\therefore \sum_{i=1}^{N}\left(R_i\cos\left(\theta_i+\psi\right)\right)^2 = \frac{\overline{R^2}}{2}N = \frac{\overline{R}^2 + \sigma_R^2}{2}N$$

where $\overline{R^2}$ is the mean of the square of R, $\overline{R}^2$ is the mean squared and σ_R^2 is the variance of R.

C.2 Additional Figures

C.2.1 Raw Phases

The following plots show the raw phases that are used to fit the MultiView planes. Each figure contains 3 panels where top to bottom they are the baselines Ceduna–Hobart, Katherine–Hobart and Yarragadee–Hobart. Error bars as presented in the plots are $\sigma_\phi = \frac{57}{SNR}$ in degrees and where SNR is the signal–to–noise of the $t \sim 40$ s solution. Epoch MV025 has far fewer data points as it shared the track with 9 rings rather than the later agreed upon 3. As indicated by the legend on each figure, orbit sources are colour–coded per ring. Phase ϕ units are in degrees and time units are in fractional day where 00:00:00 UTC = 0 days.

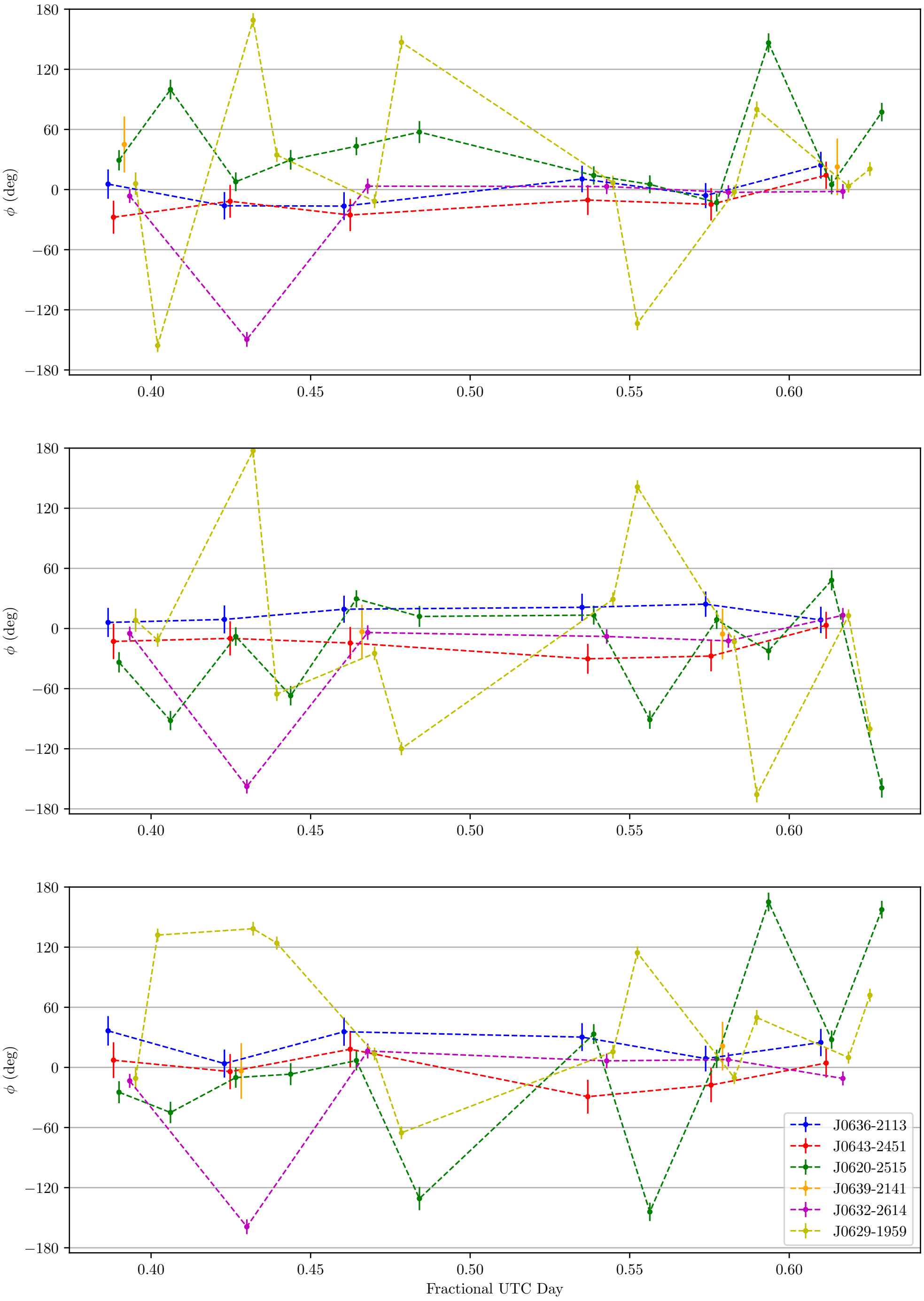

Figure C.1: G0634–2335 $\overline{R} = 3$ deg Ring, MV025

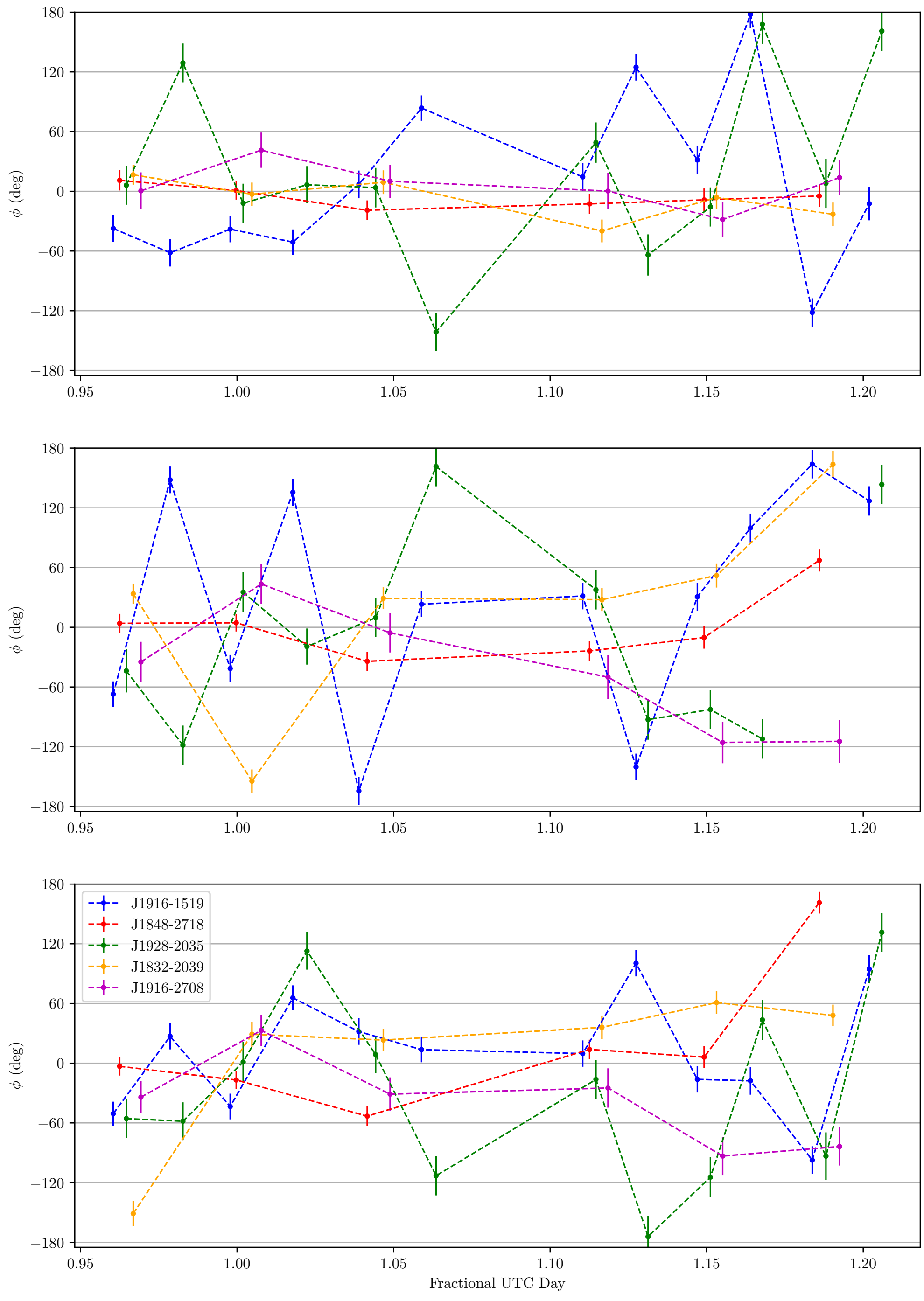

Figure C.2: G1901–2112 $\overline{R} = 6.5$ deg Ring, MV025

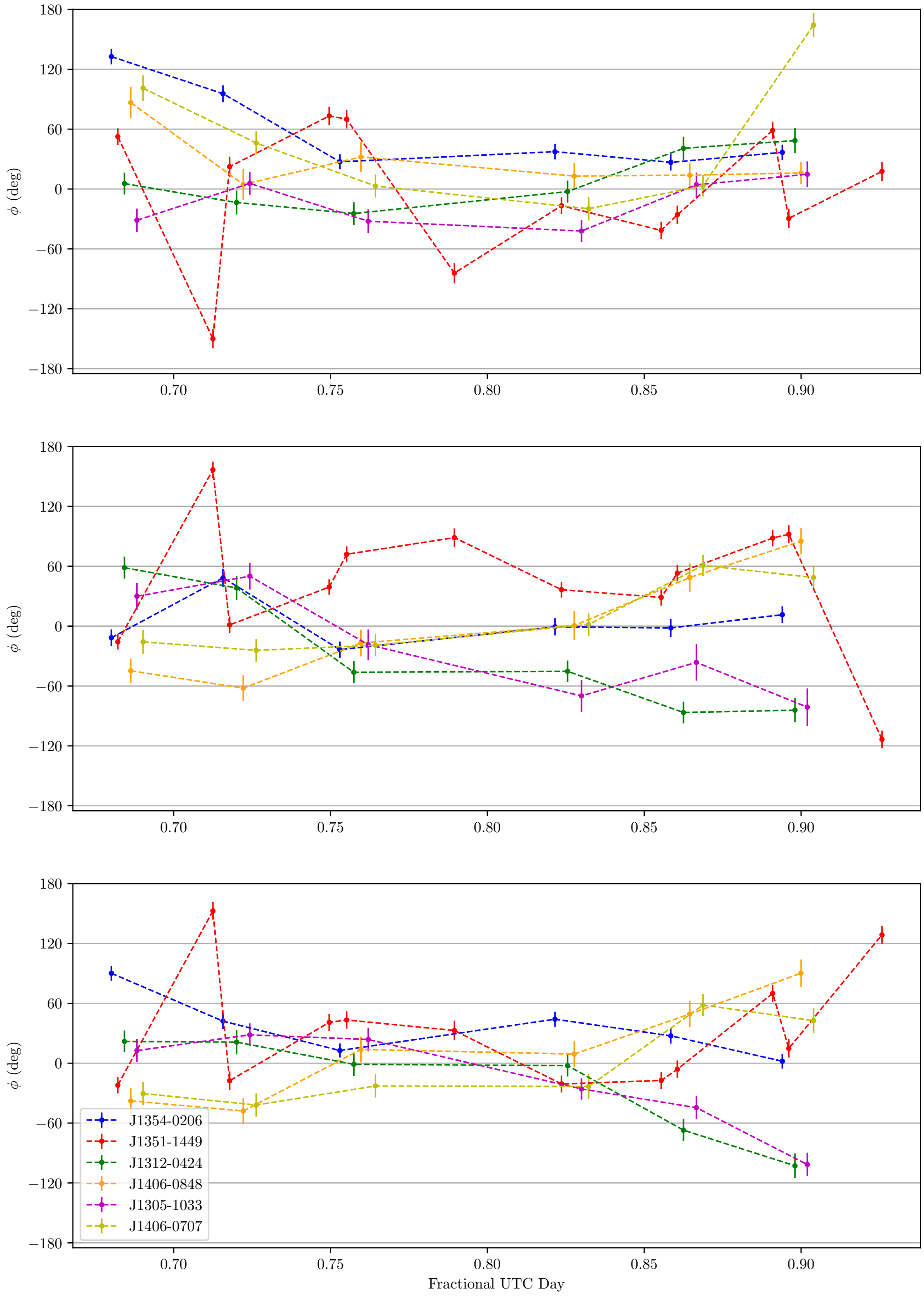

Figure C.3: G1336–0829 $\overline{R} = 7.5$ deg Ring, MV025

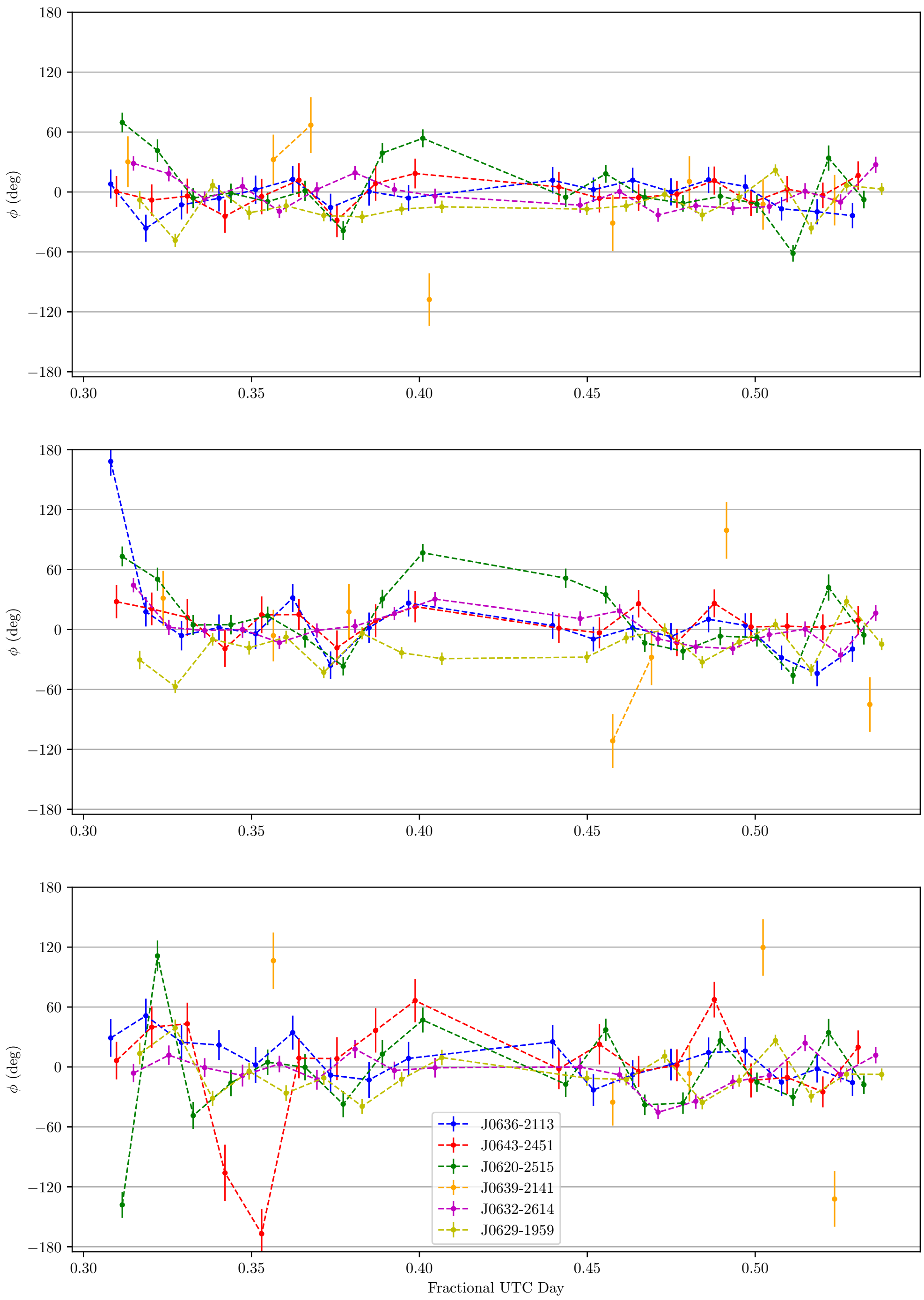

Figure C.4: G0634–2335 $\overline{R} = 3$ deg Ring, MV026

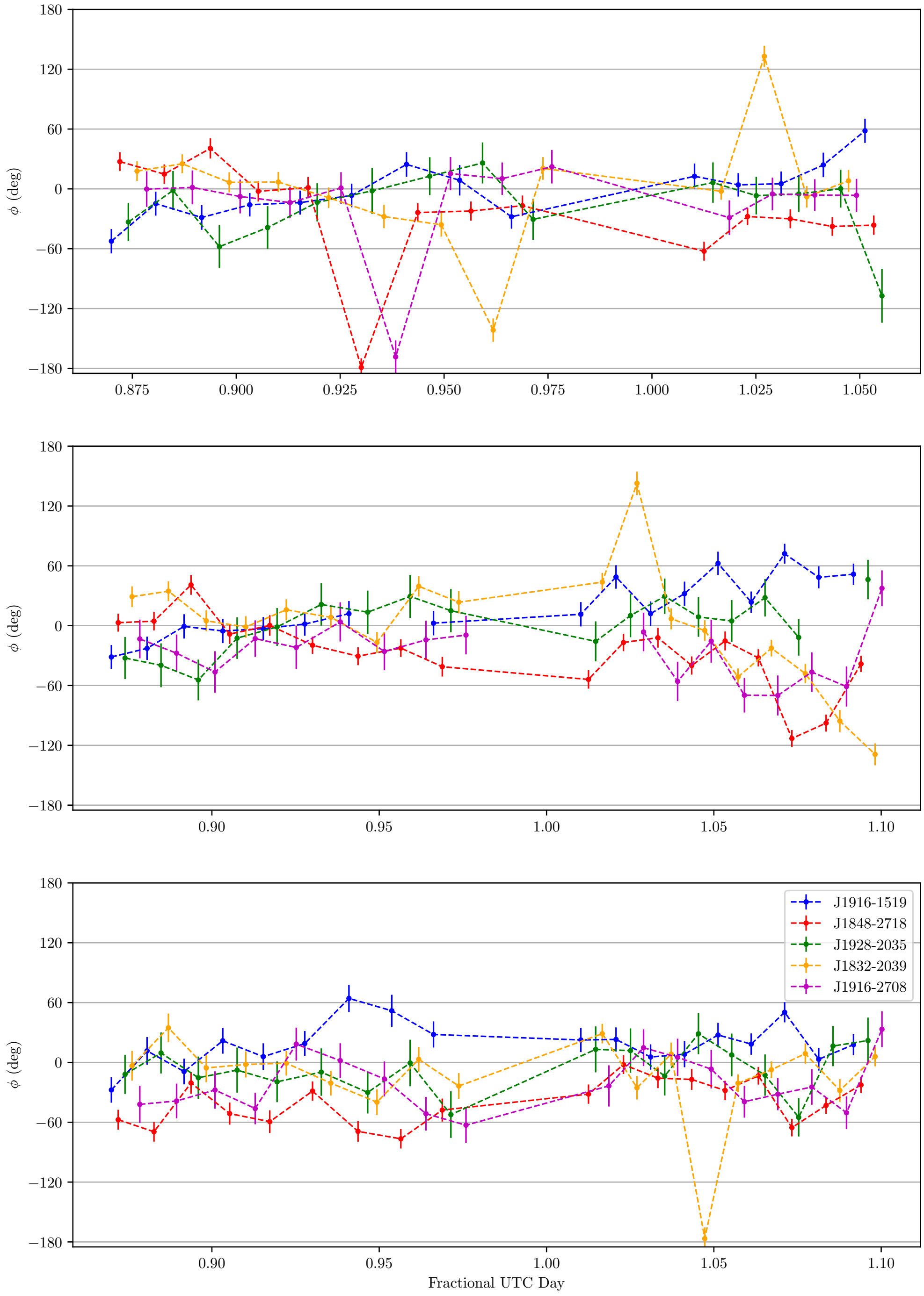

Figure C.5: G1901–2112 $\overline{R} = 6.5$ deg Ring, MV026

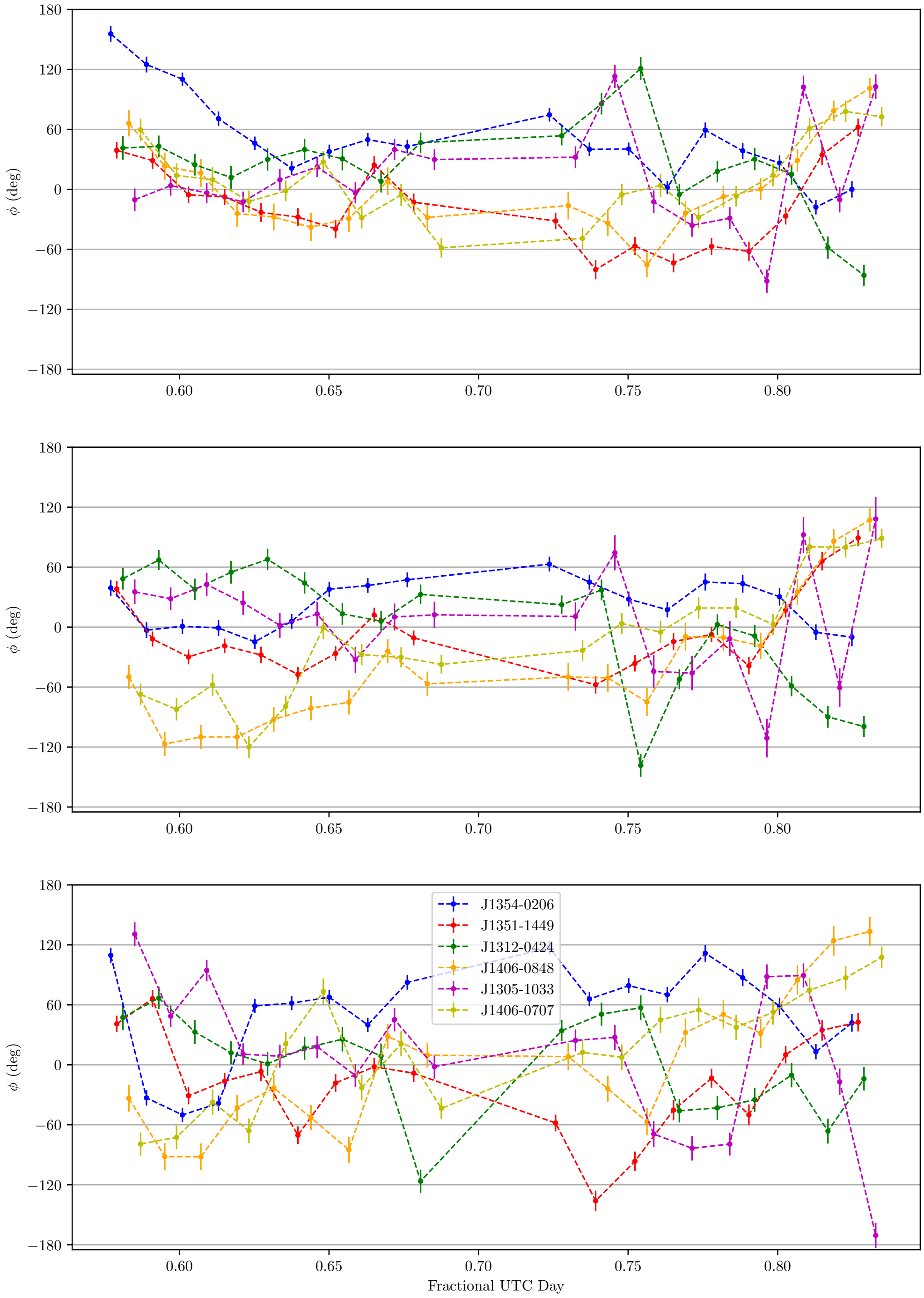

Figure C.6: G1336–0829 $\overline{R} = 7.5$ deg Ring, MV026

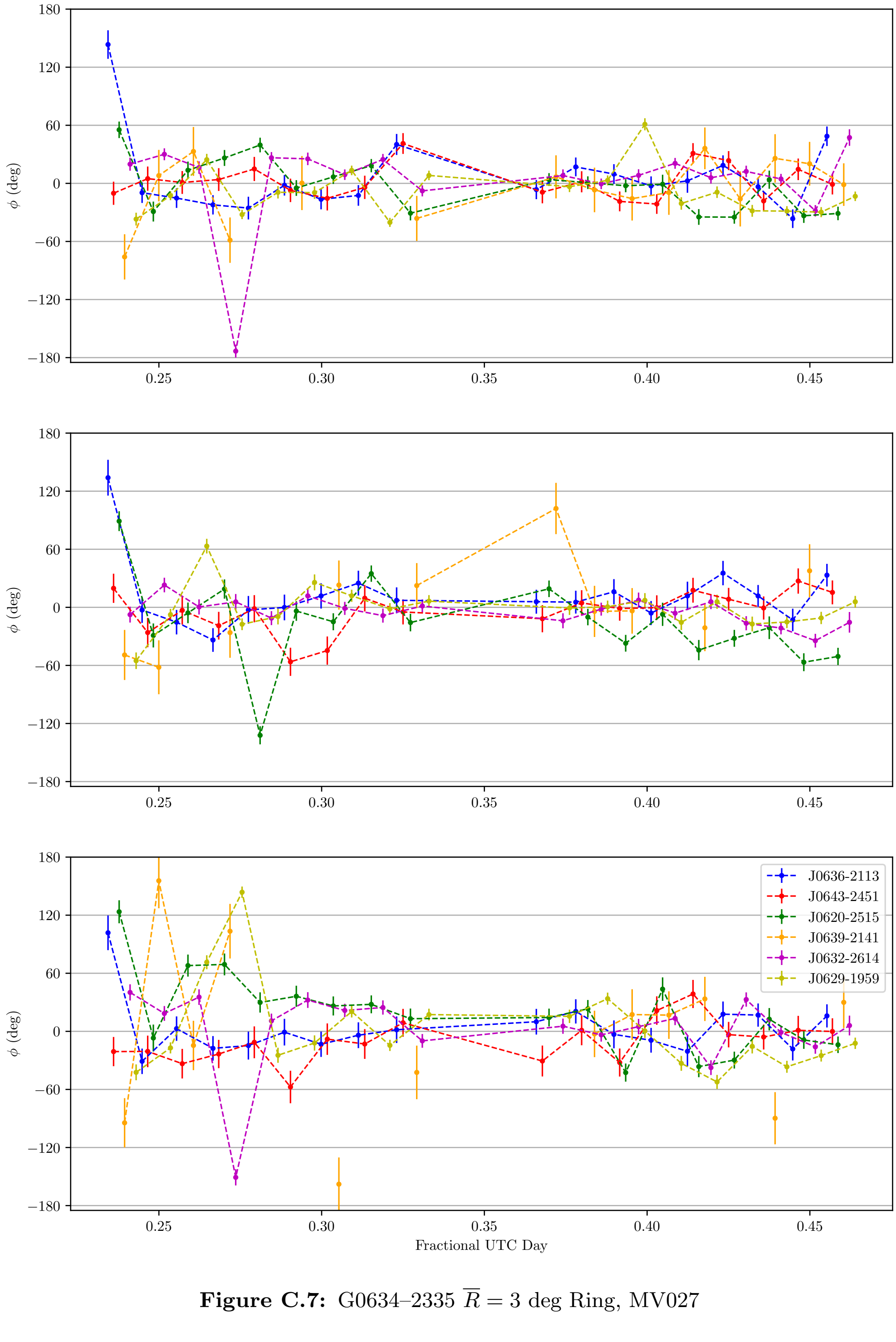

Figure C.7: G0634–2335 $\overline{R} = 3$ deg Ring, MV027

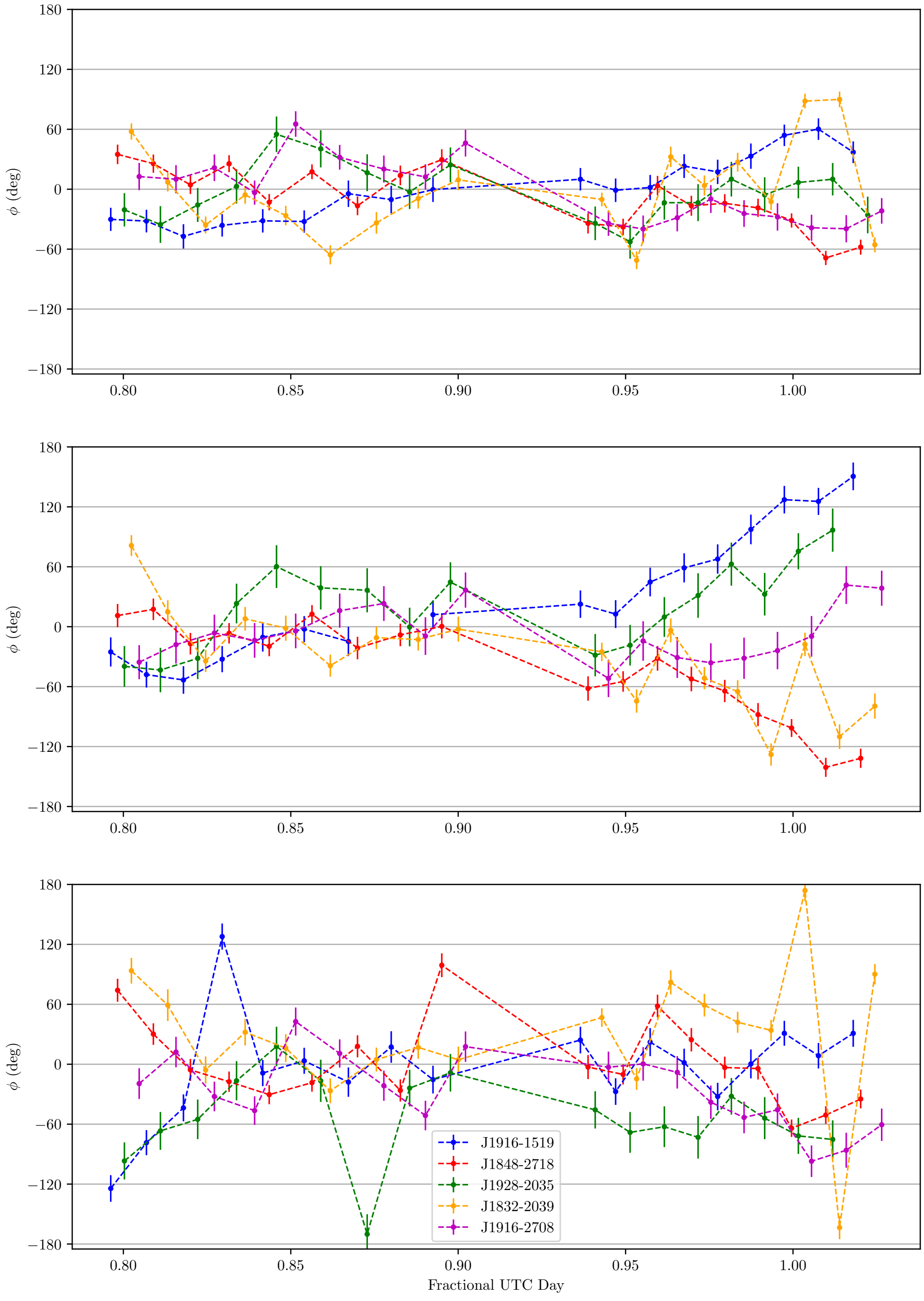

Figure C.8: G1901–2112 $\overline{R} = 6.5$ deg Ring, MV027

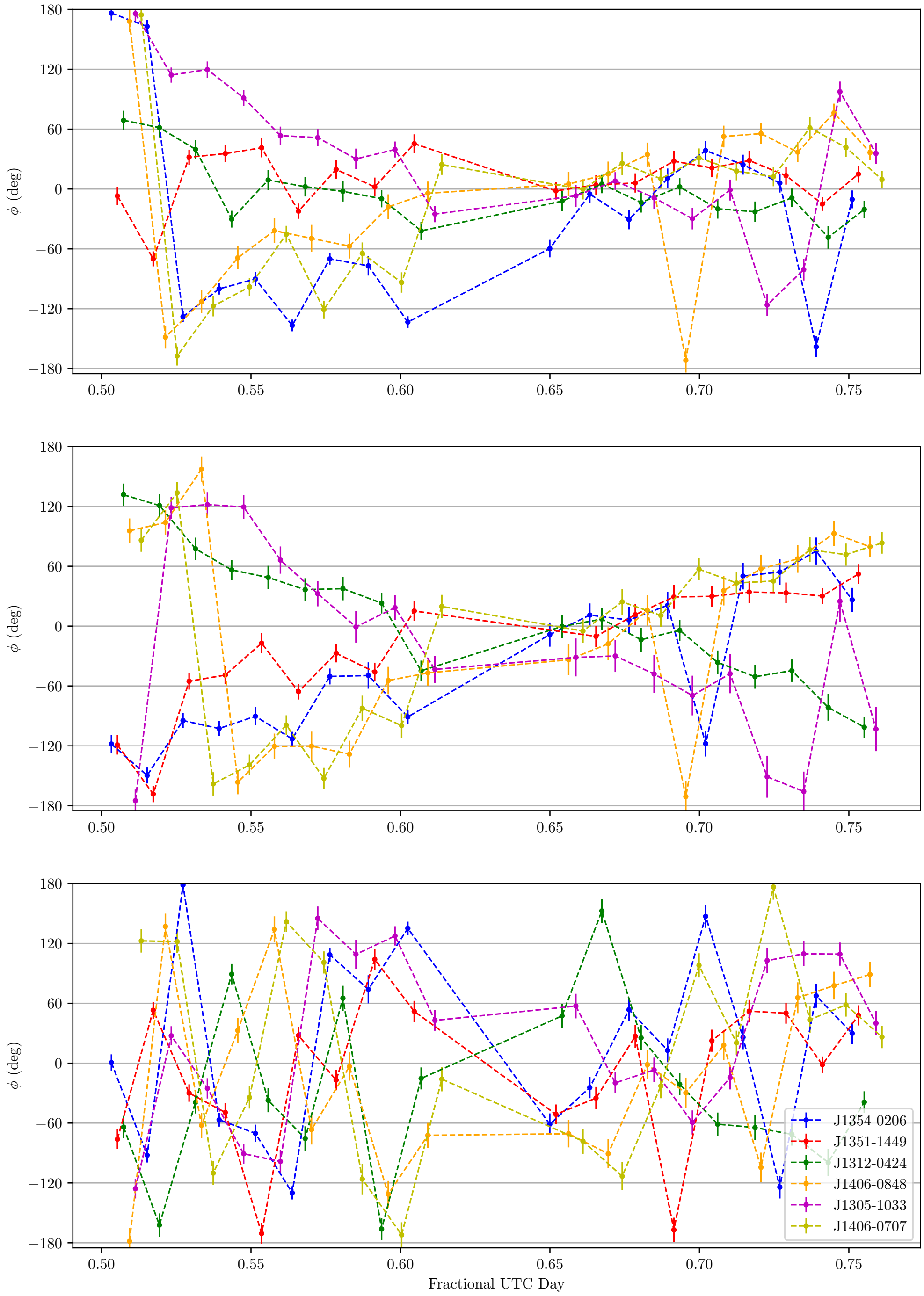

Figure C.9: G1336–0829 $\overline{R} = 7.5$ deg Ring, MV027

Figure C.10: G0634–2335 $\overline{R} = 3$ deg Ring, MV028

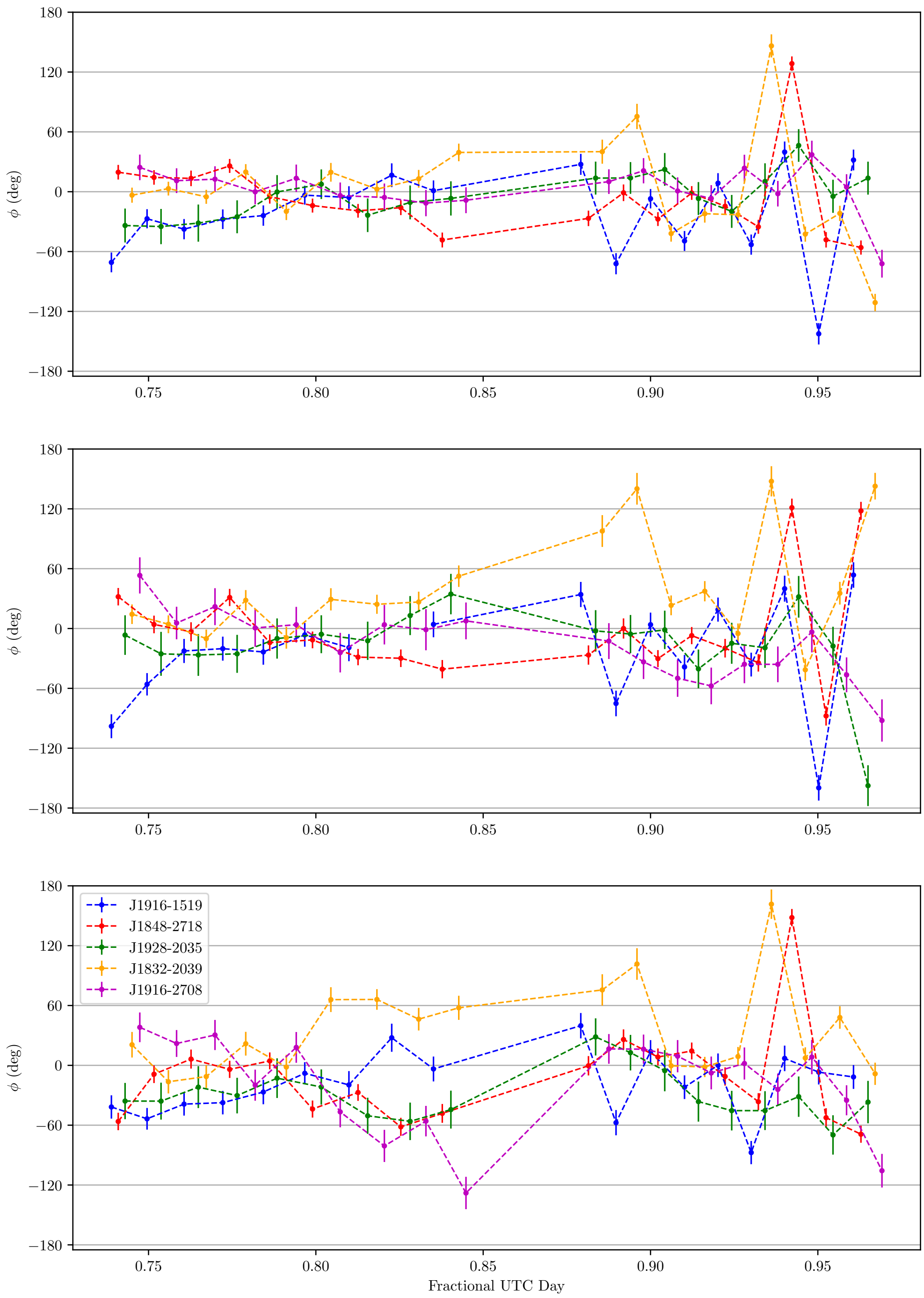

Figure C.11: G1901–2112 $\overline{R} = 6.5$ deg Ring, MV028

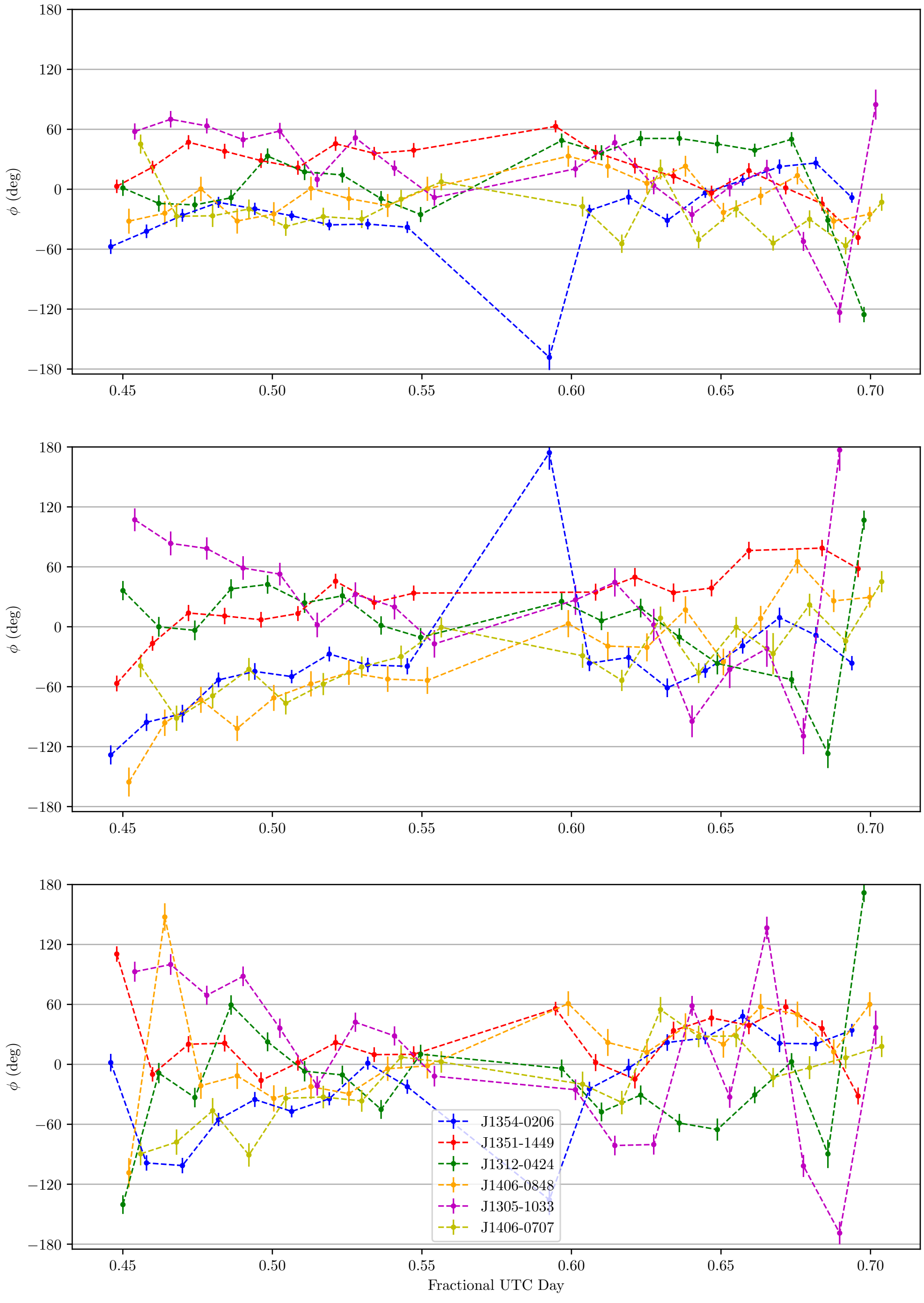

Figure C.12: G1336–0829 $\overline{R} = 7.5$ deg Ring, MV028

C.2.2 Phase and Phase Slopes measured by Inverse MultiView

The following four figures show the results from inverse MultiView fitting at each of the four epochs. The three parameters are the phase at the position $\alpha\cos\delta - \alpha_T\cos\delta_T = 0,\ \delta - \delta_T = 0$ ϕ_0 (deg), the phase slope in the East–West direction A (deg/deg) and the phase slope in the North–South direction B (deg/deg) in the equation:

$$\phi\left(\alpha,\delta,t\right) = \boldsymbol{\phi}_0\left(t\right) + \mathbf{A}\left(t\right)\left(\alpha\cos\delta - \alpha_T\cos\delta_T\right) + \mathbf{B}\left(t\right)\left(\delta - \delta_T\right)$$

The raw phases from the previous $\phi_i(\alpha_i,\delta_i,t)$ section are measurements of this plane at the positions of the calibration i.

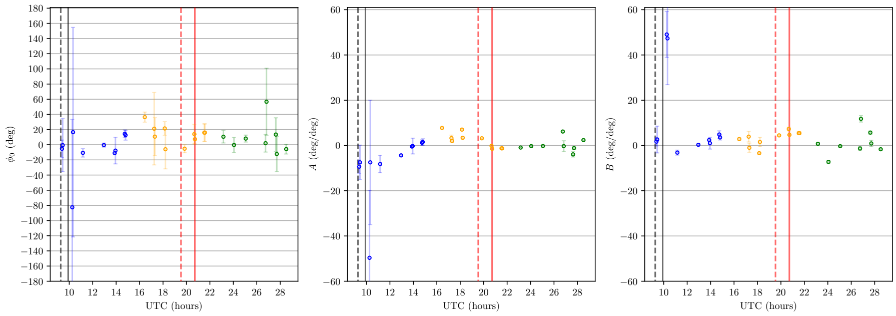

(1) Cd–Ho

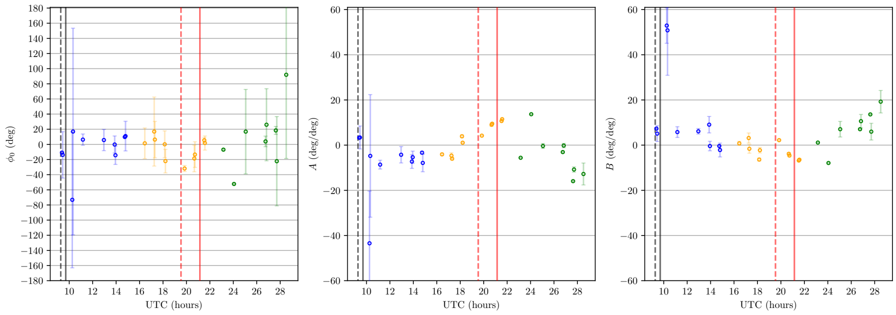

(2) Ke–Ho

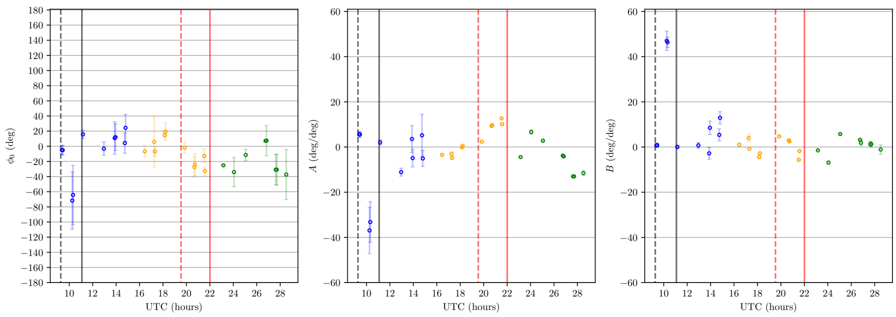

(3) Yg–Ho

Figure C.13: Three parameter 2D plane fit over time (in UTC hours) in inverse MultiView for epoch MV025. **Panels left to right:** Phase on target ϕ_0 (deg), slope in East–West direction A (deg/deg), slope in North–South direction B (deg/deg). **Panels top to bottom:** Baselines Ceduna–Hobart, Katherine–Hobart and Yaragadee–Hobart. **Colours:** Rings G0634–2335 $\overline{R} = 3$ deg (blue); G1336–0809 $\overline{R} = 7.5$ deg (yellow) and; G1901–2112 $\overline{R} = 6.5$ deg (green).

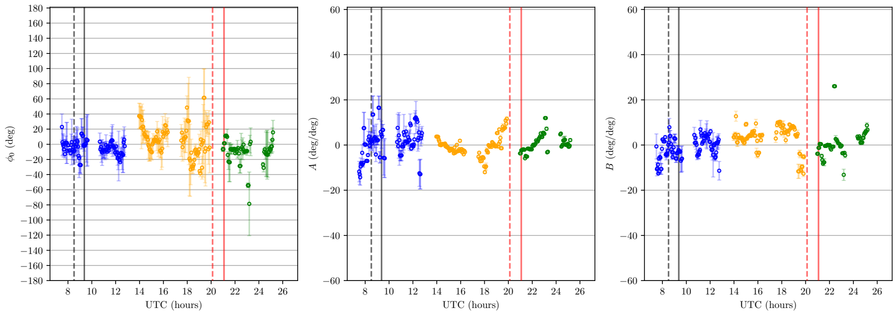

(1) Cd–Ho

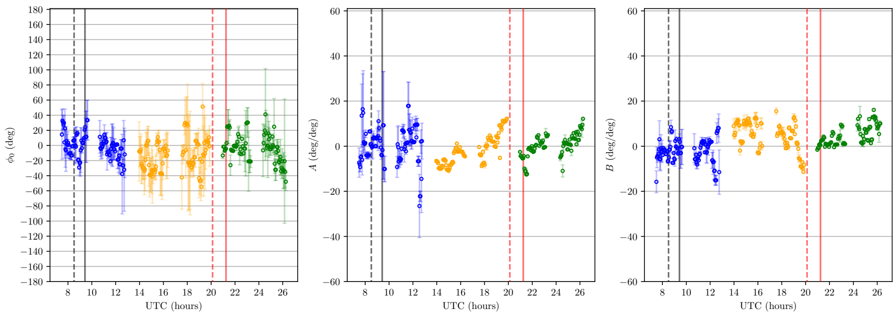

(2) Ke–Ho

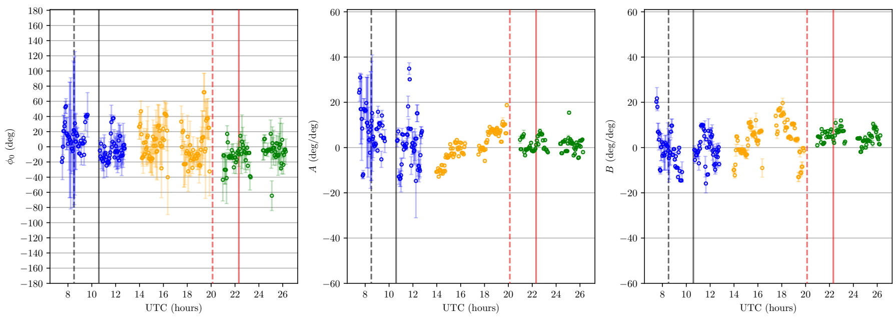

(3) Yg–Ho

Figure C.14: Three parameter 2D plane fit over time (in UTC hours) in inverse MultiView for epoch MV026. **Panels left to right:** Phase on target ϕ_0 (deg), slope in East–West direction A (deg/deg), slope in North–South direction B (deg/deg). **Panels top to bottom:** Baselines Ceduna–Hobart, Katherine–Hobart and Yaragadee–Hobart. **Colours:** Rings G0634–2335 $\overline{R} = 3$ deg (blue); G1336–0809 $\overline{R} = 7.5$ deg (yellow) and; G1901–2112 $\overline{R} = 6.5$ deg (green).

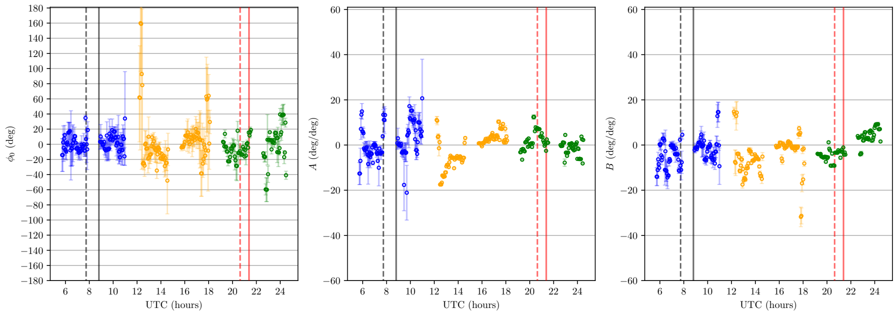

(1) Cd–Ho

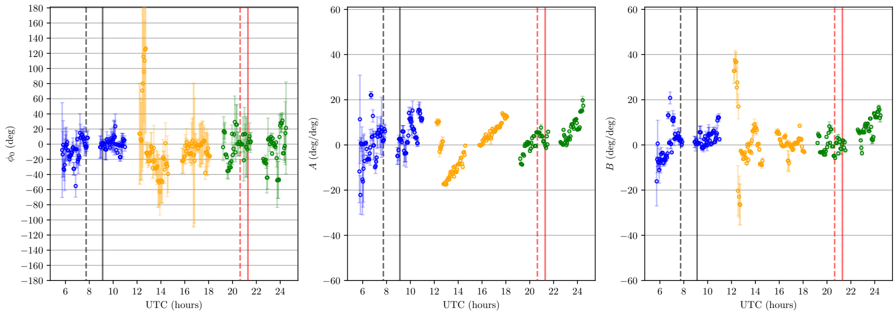

(2) Ke–Ho

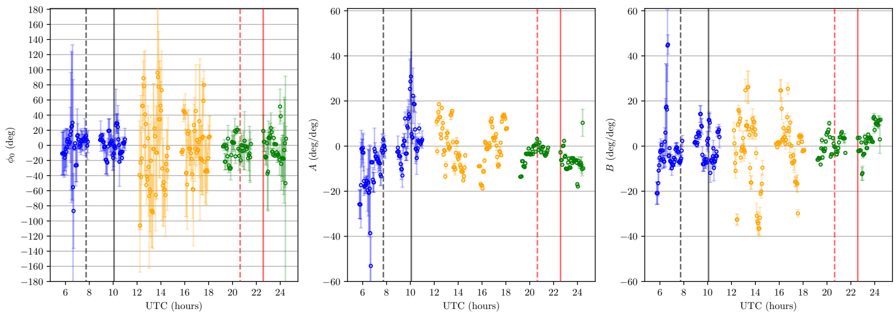

(3) Yg–Ho

Figure C.15: Three parameter 2D plane fit over time (in UTC hours) in inverse MultiView for epoch MV027. **Panels left to right:** Phase on target ϕ_0 (deg), slope in East–West direction A (deg/deg), slope in North–South direction B (deg/deg). **Panels top to bottom:** Baselines Ceduna–Hobart, Katherine–Hobart and Yaragadee–Hobart. **Colours:** Rings G0634–2335 $\overline{R} = 3$ deg (blue); G1336–0809 $\overline{R} = 7.5$ deg (yellow) and; G1901–2112 $\overline{R} = 6.5$ deg (green).

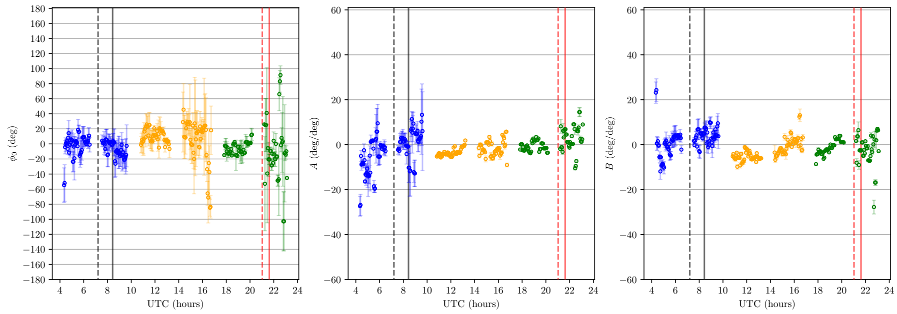

(1) Cd–Ho

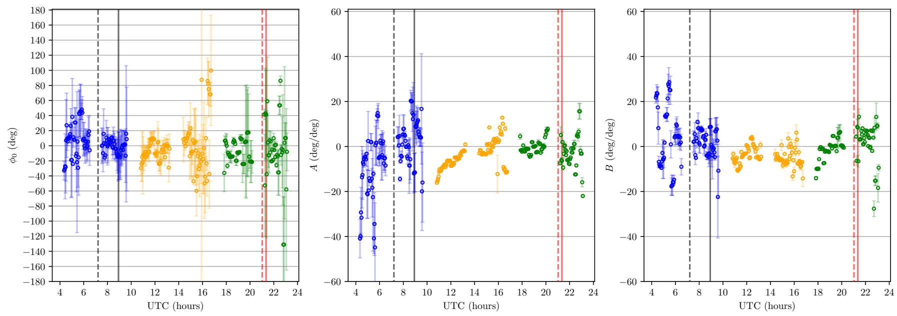

(2) Ke–Ho

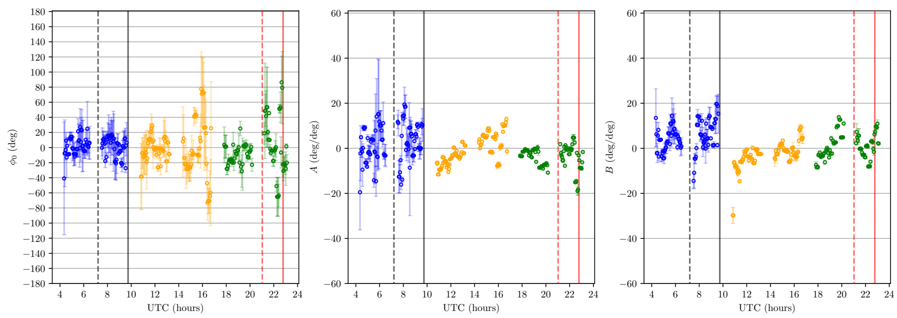

(3) Yg–Ho

Figure C.16: Three parameter 2D plane fit over time (in UTC hours) in inverse MultiView for epoch MV028. **Panels left to right:** Phase on target ϕ_0 (deg), slope in East–West direction A (deg/deg), slope in North–South direction B (deg/deg). **Panels top to bottom:** Baselines Ceduna–Hobart, Katherine–Hobart and Yaragadee–Hobart. **Colours:** Rings G0634–2335 $\overline{R} = 3$ deg (blue); G1336–0809 $\overline{R} = 7.5$ deg (yellow) and; G1901–2112 $\overline{R} = 6.5$ deg (green).

C.3 Additional Tables

C.3.1 Inverse Phase Referencing Astrometry

Table C.1: Positional fits to target G0634-2335 and orbit calibrators from JMFIT after inverse Phase Referencing. **Columns (1):** Epoch name; **(2):** Source name; **(3):** Quasar flux density (mJy); **(4):** Synthesised image RMS noise (mJy); **(5):** Centroid offset from phase centre in East–West direction (mas); **(6):** Formal fitting error in centroid East–West position (mas); **(7):** Centroid offset from phase centre in North–South direction (mas); **(8):** Formal fitting error in centroid North–South position (mas).

Epoch	**Source**	**S (mJy)**	**σ_S (mJy)**	**$\Delta\alpha$ (mas)**	**$\sigma_{\Delta\alpha}$ (mas)**	**$\Delta\delta$ (mas)**	**$\sigma_{\Delta\delta}$ (mas)**
MV025	G0634–2335	1407.0	4.00	-0.002	0.002	0.001	0.002
	J0636–2113	230.75	1.02	-0.163	0.004	0.018	0.003
	J0643–2451	176.24	0.98	-0.062	0.005	-0.102	0.004
	J0620–2515	99.67	6.03	0.219	0.049	0.113	0.035
	J0639–2141	37.52	1.15	0.032	0.024	0.076	0.022
	J0632–2614	497.08	3.24	0.013	0.005	-0.038	0.005
	J0629–1959	219.00	19.60	-0.296	0.073	-0.038	0.058
MV026	G0634–2335	910.99	0.74	0.001	0.001	0.001	0.001
	J0636–2113	134.82	1.22	-0.106	0.008	-0.048	0.006
	J0643–2451	114.56	0.67	-0.119	0.006	0.027	0.004
	J0620–2515	211.28	2.61	0.033	0.011	0.059	0.008
	J0639–2141	27.11	0.41	0.041	0.014	0.022	0.010
	J0632–2614	462.77	2.51	0.048	0.005	0.027	0.004
	J0629–1959	658.78	3.04	0.024	0.004	-0.096	0.003
MV027	G0634–2335	1136.0	1.00	-0.002	0.001	-0.001	0.001
	J0636–2113	190.00	1.77	0.079	0.008	0.073	0.007
	J0643–2451	170.11	0.87	0.124	0.005	0.053	0.004
	J0620–2515	315.82	3.59	-0.314	0.010	-0.203	0.008
	J0639–2141	33.82	0.40	0.201	0.010	0.143	0.008
	J0632–2614	568.78	3.99	-0.134	0.006	-0.100	0.005
	J0629–1959	811.42	6.37	0.052	0.007	-0.019	0.005
MV028	G0634–2335	947.04	1.06	-0.004	0.001	0.000	0.001
	J0636–2113	146.42	1.56	-0.122	0.009	0.049	0.008
	J0643–2451	130.05	0.74	0.040	0.006	0.000	0.004
	J0620–2515	211.60	3.15	0.034	0.013	0.028	0.010
	J0639–2141	29.40	0.34	-0.059	0.010	-0.127	0.008
	J0632–2614	442.38	4.12	0.063	0.008	0.005	0.006
	J0629–1959	606.29	7.91	-0.113	0.012	0.028	0.009

Table C.2: Positional fits to target G1336–0829 and orbit calibrators from JMFIT after inverse Phase Referencing. **Columns (1):** Epoch name; **(2):** Source name; **(3):** Quasar flux density (mJy); **(4):** Synthesised image RMS noise (mJy); **(5):** Centroid offset from phase centre in East–West direction (mas); **(6):** Formal fitting error in centroid East–West position (mas); **(7):** Centroid offset from phase centre in North–South direction (mas); **(8):** Formal fitting error in centroid North–South position (mas).

Epoch	**Source**	S (mJy)	σ_S (mJy)	$\Delta\alpha$ (mas)	$\sigma_{\Delta\alpha}$ (mas)	$\Delta\delta$ (mas)	$\sigma_{\Delta\delta}$ (mas)
MV025	G1336–0829	743.35	0.94	-0.023	0.001	-0.076	0.001
	J1354–0206	292.82	6.32	-0.229	0.020	-0.110	0.018
	J1351–1449	322.14	8.45	0.111	0.022	0.363	0.018
	J1312–0424	46.39	2.38	0.031	0.055	-0.054	0.046
	J1406–0848	74.33	3.25	-0.216	0.046	0.198	0.030
	J1305–1033	139.79	2.87	0.114	0.018	-0.068	0.014
	J1406–0707	132.32	3.37	0.199	0.022	0.105	0.019
MV026	G1336–0829	415.98	0.77	-0.036	0.002	-0.067	0.002
	J1354–0206	282.82	4.80	-0.462	0.016	-0.012	0.013
	J1351–1449	242.44	3.41	0.153	0.012	0.008	0.011
	J1312–0424	74.49	1.72	-0.351	0.021	-0.120	0.016
	J1406–0848	43.62	2.27	-0.175	0.042	-0.350	0.037
	J1305–1033	47.61	2.12	-0.202	0.041	-0.073	0.031
	J1406–0707	9.86	2.06	-0.019	0.167	-0.003	0.163
MV027	G1336–0829	571.82	1.14	-0.025	0.002	-0.019	0.002
	J1354–0206	21.86	8.21	-1.577	0.513	-1.182	0.425
	J1351–1449	175.39	5.10	0.155	0.025	0.107	0.024
	J1312–0424	48.62	3.30	-0.460	0.071	-0.275	0.049
	J1406–0848	-39.05	3.81	1.089	0.100	-1.581	0.088
	J1305–1033	14.80	3.60	-0.490	0.243	-0.288	0.238
	J1406–0707	44.40	2.45	-0.461	0.048	0.267	0.040
MV028	G1336–0829	476.14	0.77	-0.023	0.002	-0.028	0.001
	J1354–0206	201.55	4.17	-0.081	0.020	-0.281	0.017
	J1351–1449	287.88	5.78	-0.025	0.017	0.209	0.015
	J1312–0424	43.01	2.55	0.154	0.055	0.045	0.039
	J1406–0848	95.91	1.96	-0.243	0.020	-0.177	0.017
	J1305–1033	59.97	2.91	-0.139	0.046	0.144	0.039
	J1406–0707	88.94	1.54	0.175	0.016	-0.102	0.014

Table C.3: Positional fits to target G1901–2112 and orbit calibrators from JMFIT after inverse Phase Referencing. **Columns (1):** Epoch name; **(2):** Source name; **(3):** Quasar flux density (mJy); **(4):** Synthesised image RMS noise (mJy); **(5):** Centroid offset from phase centre in East–West direction (mas); **(6):** Formal fitting error in centroid East–West position (mas); **(7):** Centroid offset from phase centre in North–South direction (mas); **(8):** Formal fitting error in centroid North–South position (mas).

Epoch	**Source**	S **(mJy)**	σ_S **(mJy)**	$\Delta\alpha$ **(mas)**	$\sigma_{\Delta\alpha}$ **(mas)**	$\Delta\delta$ **(mas)**	$\sigma_{\Delta\delta}$ **(mas)**
MV025	G1901–2112	191.052	0.820	-0.031	0.004	-0.006	0.003
	J1916–1519	61.031	3.805	0.247	0.052	0.333	0.043
	J1848–2718	274.016	1.606	0.106	0.005	-0.009	0.004
	J1928–2035	15.209	1.641	-1.743	0.055	-2.446	0.206
	J1832–2039	125.929	4.012	-0.223	0.033	0.342	0.019
	J1916–2708	81.726	1.116	0.060	0.012	-0.278	0.008
MV026	G1901–2112	119.279	0.233	-0.005	0.002	-0.005	0.001
	J1916–1519	122.695	1.164	-0.014	0.008	0.132	0.006
	J1848–2718	171.466	1.901	0.161	0.010	-0.162	0.006
	J1928–2035	46.523	0.417	0.092	0.008	0.024	0.005
	J1832–2039	132.461	2.469	-0.080	0.018	0.028	0.011
	J1916–2708	59.731	0.670	0.111	0.010	-0.147	0.007
MV027	G1901–2112	140.980	0.208	-0.004	0.001	-0.002	0.001
	J1916–1519	89.282	1.358	0.477	0.014	0.371	0.011
	J1848–2718	228.981	2.463	-0.502	0.011	-0.367	0.007
	J1928–2035	40.462	0.718	0.631	0.016	0.225	0.012
	J1832–2039	108.851	3.585	-0.454	0.033	-0.105	0.021
	J1916–2708	61.593	1.076	0.226	0.014	-0.041	0.011
MV028	G1901–2112	137.140	0.246	-0.001	0.002	-0.001	0.001
	J1916–1519	113.679	1.646	0.157	0.014	-0.049	0.010
	J1848–2718	176.485	2.970	0.069	0.017	-0.102	0.010
	J1928–2035	46.149	0.524	0.256	0.010	0.009	0.008
	J1832–2039	161.779	2.108	-0.202	0.013	0.163	0.008
	J1916–2708	58.530	0.826	-0.031	0.013	-0.137	0.010

C.3.2 Inverse MultiView Astrometry

Table C.4: Positional fits to target G0634-2335 and orbit calibrators from JMFIT. **Columns (1):** Epoch name; **(2):** Source name; **(3):** Quasar flux density (mJy); **(4):** Synthesised image RMS noise (mJy); **(5):** Centroid offset from phase centre in East–West direction (mas); **(6):** Formal fitting error in centroid East–West position (mas); **(7):** Centroid offset from phase centre in North–South direction (mas); **(8):** Formal fitting error in centroid North–South position (mas).

Epoch	**Source**	S (mJy)	σ_S (mJy)	$\Delta\alpha$ (mas)	$\sigma_{\Delta\alpha}$ (mas)	$\Delta\delta$ (mas)	$\sigma_{\Delta\delta}$ (mas)
MV025	G0634–2335	1256.0	7.0	0.069	0.005	0.026	0.004
	J0636–2113	244.2	0.9	-0.112	0.003	-0.035	0.003
	J0643–2451	152.8	1.8	-0.079	0.011	-0.065	0.008
	J0620–2515	211.5	6.4	0.172	0.027	0.037	0.020
	J0639–2141	39.9	0.7	0.087	0.016	0.033	0.014
	J0632–2614	503.1	6.1	0.075	0.010	0.020	0.008
	J0629–1959	380.3	6.7	-0.082	0.039	-0.164	0.030
MV026	G0634–2335	869.9	1.7	0.042	0.002	0.029	0.001
	J0636–2113	145.0	1.0	-0.024	0.006	0.026	0.005
	J0643–2451	116.2	0.5	0.014	0.004	0.044	0.003
	J0620–2515	250.9	2.1	-0.081	0.008	0.035	0.005
	J0639–2141	27.1	0.4	0.192	0.016	0.067	0.012
	J0632–2614	481.6	1.7	0.050	0.003	0.024	0.002
	J0629–1959	636.9	3.3	0.007	0.005	-0.037	0.004
MV027	G0634–2335	1114.0	2.0	0.016	0.002	0.026	0.001
	J0636–2113	191.3	1.7	0.059	0.008	0.048	0.007
	J0643–2451	175.2	0.9	0.061	0.005	-0.004	0.004
	J0620–2515	355.5	2.8	-0.028	0.007	0.000	0.005
	J0639–2141	35.8	0.3	0.091	0.009	0.062	0.006
	J0632–2614	608.0	3.7	0.011	0.005	0.016	0.004
	J0629–1959	998.6	5.3	-0.075	0.005	-0.031	0.004
MV028	G0634–2335	919.0	1.4	0.018	0.001	-0.014	0.001
	J0636–2113	151.1	1.3	-0.040	0.008	0.032	0.006
	J0643–2451	139.1	0.7	0.064	0.005	0.020	0.004
	J0620–2515	282.1	3.0	-0.088	0.010	-0.069	0.007
	J0639–2141	29.8	0.3	0.084	0.010	-0.120	0.008
	J0632–2614	515.9	2.2	0.001	0.004	0.032	0.003
	J0629–1959	697.5	6.4	-0.008	0.008	-0.061	0.006

Table C.5: Positional fits to target G1336–0829 and orbit calibrators from JMFIT. **Columns (1):** Epoch name; **(2):** Source name; **(3):** Quasar flux density (mJy); **(4):** Synthesised image RMS noise (mJy); **(5):** Centroid offset from phase centre in East–West direction (mas); **(6):** Formal fitting error in centroid East–West position (mas); **(7):** Centroid offset from phase centre in North–South direction (mas); **(8):** Formal fitting error in centroid North–South position (mas).

Epoch	**Source**	S (mJy)	σ_S (mJy)	$\Delta\alpha$ (mas)	$\sigma_{\Delta\alpha}$ (mas)	$\Delta\delta$ (mas)	$\sigma_{\Delta\delta}$ (mas)
MV025	G1336–0829	675.0	3.0	-0.100	0.004	-0.048	0.003
	J1354–0206	408.2	6.0	-0.134	0.013	-0.041	0.012
	J1351–1449	474.3	5.8	-0.020	0.010	0.104	0.008
	J1312–0424	347.1	0.8	0.048	0.002	0.018	0.002
	J1406–0848	314.3	1.9	-0.275	0.006	0.007	0.005
	J1305–1033	298.8	1.1	-0.022	0.004	-0.043	0.003
	J1406–0707	198.9	2.7	0.127	0.012	0.067	0.011
MV026	G1336–0829	386.9	1.5	-0.015	0.004	-0.052	0.003
	J1354–0206	355.2	4.9	-0.152	0.013	-0.058	0.011
	J1351–1449	281.9	2.6	-0.024	0.008	0.029	0.007
	J1312–0424	176.0	1.1	0.046	0.006	-0.046	0.005
	J1406–0848	159.1	1.6	-0.247	0.010	0.040	0.009
	J1305–1033	122.7	1.2	-0.076	0.010	-0.017	0.008
	J1406–0707	173.0	0.9	0.016	0.005	0.026	0.004
MV027	G1336–0829	516.2	1.8	-0.212	0.003	-0.011	0.003
	J1354–0206	404.5	7.5	-0.121	0.018	-0.114	0.015
	J1351–1449	347.7	3.7	0.051	0.010	0.015	0.008
	J1312–0424	235.3	2.4	-0.074	0.010	0.005	0.008
	J1406–0848	102.6	2.8	-0.221	0.030	-0.094	0.021
	J1305–1033	162.3	2.0	0.071	0.012	-0.095	0.011
	J1406–0707	147.4	1.8	0.120	0.012	-0.010	0.010
MV028	G1336–0829	429.1	2.3	-0.032	0.005	-0.067	0.005
	J1354–0206	413.0	3.9	-0.077	0.009	-0.036	0.008
	J1351–1449	312.5	5.0	0.044	0.014	0.069	0.012
	J1312–0424	228.0	1.5	-0.005	0.007	-0.029	0.005
	J1406–0848	180.4	1.7	-0.255	0.010	-0.045	0.009
	J1305–1033	91.6	2.6	-0.250	0.029	-0.330	0.027
	J1406–0707	167.2	1.6	0.144	0.009	0.089	0.008

Table C.6: Positional fits to target G1901–2112 and orbit calibrators from JMFIT. **Columns (1):** Epoch name; **(2):** Source name; **(3):** Quasar flux density (mJy); **(4):** Synthesised image RMS noise (mJy); **(5):** Centroid offset from phase centre in East–West direction (mas); **(6):** Formal fitting error in centroid East–West position (mas); **(7):** Centroid offset from phase centre in North–South direction (mas); **(8):** Formal fitting error in centroid North–South position (mas).

Epoch	**Source**	S (mJy)	σ_S (mJy)	$\Delta\alpha$ (mas)	$\sigma_{\Delta\alpha}$ (mas)	$\Delta\delta$ (mas)	$\sigma_{\Delta\delta}$ (mas)
MV025	G1901–2112	167.9	1.1	-0.014	0.006	0.012	0.004
	J1916–1519	59.0	5.0	0.169	0.080	0.255	0.059
	J1848–2718	398.9	2.3	0.130	0.005	0.040	0.003
	J1928–2035	46.1	1.2	0.072	0.022	0.033	0.016
	J1832–2039	245.6	2.0	-0.022	0.008	0.051	0.005
	J1916–2708	118.0	1.0	-0.156	0.008	-0.153	0.006
MV026	G1901–2112	114.4	0.3	-0.057	0.003	0.013	0.002
	J1916–1519	156.5	1.0	0.081	0.006	0.036	0.004
	J1848–2718	238.0	2.0	0.060	0.008	0.013	0.005
	J1928–2035	49.2	0.3	0.045	0.007	0.004	0.005
	J1832–2039	142.8	1.9	-0.052	0.013	0.074	0.008
	J1916–2708	66.8	0.6	-0.117	0.008	-0.077	0.006
MV027	G1901–2112	136.4	0.4	-0.026	0.003	0.034	0.002
	J1916–1519	130.5	1.2	-0.012	0.009	0.039	0.007
	J1848–2718	264.9	2.2	-0.202	0.008	-0.084	0.005
	J1928–2035	57.7	0.5	0.052	0.009	0.044	0.007
	J1832–2039	184.4	3.4	-0.077	0.018	0.010	0.012
	J1916–2708	91.4	0.7	-0.087	0.007	0.022	0.006
MV028	G1901–2112	128.8	0.4	-0.019	0.004	0.048	0.003
	J1916–1519	127.2	1.6	0.044	0.012	-0.097	0.009
	J1848–2718	235.4	2.2	0.095	0.009	-0.006	0.006
	J1928–2035	56.8	0.2	0.041	0.005	0.028	0.004
	J1832–2039	181.5	2.6	-0.045	0.014	0.133	0.009
	J1916–2708	79.9	0.8	-0.096	0.010	-0.059	0.008

C.3.3 Self–Calibration Astrometry

Table C.7: Fitted centroid positions and flux densities after a single self–calibration cycle each of the quasar G0634–2335 and orbit calibrators from JMFIT. **Columns (1):** Epoch name; **(2):** Source name; **(3):** Quasar flux density (mJy); **(4):** Synthesised image RMS noise (mJy); **(5):** Centroid offset from phase centre in East–West direction (mas); **(6):** Formal fitting error in centroid East–West position (mas); **(7):** Centroid offset from phase centre in North–South direction (mas); **(8):** Formal fitting error in centroid North–South position (mas).

Epoch	**Source**	S **(mJy)**	σ_S **(mJy)**	$\Delta\alpha$ **(mas)**	$\sigma_{\Delta\alpha}$ **(mas)**	$\Delta\delta$ **(mas)**	$\sigma_{\Delta\delta}$ **(mas)**
MV025	G0634–2335	1419.0	3.0	-0.003	0.002	0.001	0.001
	J0636–2113	256.1	0.8	-0.002	0.003	-0.009	0.002
	J0643–2451	201.0	0.7	-0.005	0.003	-0.011	0.002
	J0620–2515	495.7	1.1	0.000	0.002	0.003	0.001
	J0639–2141	54.0	0.6	0.035	0.010	-0.026	0.008
	J0632–2614	762.9	1.0	-0.013	0.001	-0.004	0.001
	J0629–1959	1146.0	2.0	-0.008	0.001	0.021	0.001
MV026	G0634–2335	917.3	0.5	0.002	0.001	0.001	0.000
	J0636–2113	168.3	0.4	0.022	0.002	0.013	0.002
	J0643–2451	129.2	0.4	0.005	0.004	0.019	0.002
	J0620–2515	316.6	0.4	-0.026	0.001	-0.008	0.001
	J0639–2141	33.9	0.3	0.057	0.009	0.008	0.008
	J0632–2614	518.3	0.5	0.003	0.001	0.000	0.001
	J0629–1959	752.8	0.6	0.010	0.001	0.022	0.001
MV027	G0634–2335	1142.0	1.0	-0.001	0.001	0.000	0.001
	J0636–2113	227.0	0.6	-0.001	0.002	0.004	0.002
	J0643–2451	190.0	0.4	-0.009	0.002	0.001	0.002
	J0620–2515	431.7	0.6	-0.004	0.001	-0.004	0.001
	J0639–2141	40.2	0.3	0.074	0.007	0.049	0.006
	J0632–2614	678.6	0.8	0.000	0.001	-0.001	0.001
	J0629–1959	1068.0	1.0	0.001	0.001	0.008	0.001
MV028	G0634–2335	961.4	0.8	-0.003	0.001	-0.002	0.001
	J0636–2113	185.2	0.4	0.009	0.002	0.006	0.002
	J0643–2451	152.1	0.3	0.006	0.002	0.008	0.002
	J0620–2515	343.3	0.4	-0.008	0.001	-0.003	0.001
	J0639–2141	35.7	0.3	0.028	0.007	0.006	0.006
	J0632–2614	555.8	0.5	-0.003	0.001	0.000	0.001
	J0629–1959	913.4	0.6	0.009	0.001	0.011	0.001

Table C.8: Fitted centroid positions and flux densities after a single self–calibration cycle each of the quasar G1336-0829 and orbit calibrators from JMFIT. **Columns (1):** Epoch name; **(2):** Source name; **(3):** Quasar flux density (mJy); **(4):** Synthesised image RMS noise (mJy); **(5):** Centroid offset from phase centre in East–West direction (mas); **(6):** Formal fitting error in centroid East–West position (mas); **(7):** Centroid offset from phase centre in North–South direction (mas); **(8):** Formal fitting error in centroid North–South position (mas).

Epoch	**Source**	S (mJy)	σ_S (mJy)	$\Delta\alpha$ (mas)	$\sigma_{\Delta\alpha}$ (mas)	$\Delta\delta$ (mas)	$\sigma_{\Delta\delta}$ (mas)
MV025	G1336-0829	745.7	1.0	-0.024	0.001	-0.072	0.001
	J1354-0206	833.3	0.9	-0.005	0.001	-0.017	0.001
	J1351-1449	682.6	1.9	-0.030	0.002	-0.031	0.002
	J1312-0424	360.2	0.6	0.011	0.002	0.015	0.001
	J1406-0848	293.8	1.4	-0.168	0.005	0.085	0.004
	J1305-1033	304.3	0.6	0.007	0.002	0.000	0.002
	J1406-0707	376.8	0.7	-0.008	0.002	-0.009	0.002
MV026	G1336-0829	419.1	0.7	-0.036	0.002	-0.067	0.001
	J1354-0206	458.2	0.7	-0.009	0.002	-0.022	0.001
	J1351-1449	379.9	1.2	-0.019	0.003	-0.016	0.002
	J1312-0424	214.1	0.3	-0.009	0.002	0.002	0.001
	J1406-0848	170.8	0.5	-0.169	0.003	0.076	0.002
	J1305-1033	180.3	0.3	0.001	0.002	-0.006	0.002
	J1406-0707	205.7	0.3	-0.019	0.002	-0.009	0.001
MV027	G1336-0829	586.0	0.8	-0.021	0.001	-0.015	0.001
	J1354-0206	662.4	1.0	-0.002	0.001	-0.004	0.001
	J1351-1449	525.0	1.3	-0.008	0.002	-0.010	0.002
	J1312-0424	285.4	0.5	0.010	0.002	0.003	0.001
	J1406-0848	239.3	0.8	-0.030	0.004	-0.019	0.003
	J1305-1033	262.4	0.6	0.004	0.002	0.000	0.002
	J1406-0707	250.6	0.6	-0.001	0.002	-0.013	0.002
MV028	G1336-0829	482.2	0.7	-0.022	0.001	-0.034	0.001
	J1354-0206	506.0	0.7	0.000	0.001	-0.011	0.001
	J1351-1449	432.8	0.7	-0.002	0.002	-0.004	0.001
	J1312-0424	266.2	0.5	-0.004	0.002	-0.005	0.001
	J1406-0848	192.6	0.5	-0.109	0.003	0.015	0.002
	J1305-1033	209.2	0.5	0.022	0.003	0.021	0.003
	J1406-0707	198.3	0.4	0.003	0.002	-0.005	0.002

Table C.9: Fitted centroid positions and flux densities after a single self–calibration cycle each of the quasar G1901-2112 and orbit calibrators from JMFIT. **Columns (1):** Epoch name; **(2):** Source name; **(3):** Quasar flux density (mJy); **(4):** Synthesised image RMS noise (mJy); **(5):** Centroid offset from phase centre in East–West direction (mas); **(6):** Formal fitting error in centroid East–West position (mas); **(7):** Centroid offset from phase centre in North–South direction (mas); **(8):** Formal fitting error in centroid North–South position (mas).

Epoch	Source	S (mJy)	σ_S (mJy)	$\Delta\alpha$ (mas)	$\sigma_{\Delta\alpha}$ (mas)	$\Delta\delta$ (mas)	$\sigma_{\Delta\delta}$ (mas)
MV025	G1901-2112	194.849	0.7	0.005	0.003	0.005	0.002
	J1916-1519	262.732	0.9	-0.004	0.003	-0.004	0.002
	J1848-2718	489.364	0.8	-0.031	0.002	-0.018	0.001
	J1928-2035	119.137	0.7	0.011	0.005	-0.006	0.004
	J1832-2039	355.095	1.0	0.006	0.003	0.009	0.002
	J1916-2708	141.664	0.6	-0.006	0.004	-0.023	0.003
MV026	G1901-2112	119.500	0.2	-0.008	0.002	-0.007	0.001
	J1916-1519	169.457	0.6	0.001	0.003	-0.001	0.002
	J1848-2718	276.205	0.4	0.002	0.001	0.002	0.001
	J1928-2035	57.081	0.2	-0.027	0.004	-0.016	0.003
	J1832-2039	221.002	0.6	0.015	0.003	0.010	0.002
	J1916-2708	81.466	0.4	-0.022	0.005	-0.059	0.004
MV027	G1901-2112	141.389	0.2	-0.005	0.001	-0.002	0.001
	J1916-1519	162.480	0.4	0.002	0.003	0.003	0.002
	J1848-2718	331.769	0.4	0.000	0.001	0.005	0.001
	J1928-2035	66.154	0.3	0.006	0.004	0.014	0.003
	J1832-2039	258.812	0.8	-0.002	0.003	0.003	0.002
	J1916-2708	102.706	0.3	-0.024	0.003	-0.019	0.003
MV028	G1901-2112	138.847	0.2	0.015	0.001	0.006	0.001
	J1916-1519	161.067	0.4	-0.003	0.003	0.001	0.002
	J1848-2718	300.784	0.4	-0.002	0.001	0.003	0.001
	J1928-2035	58.481	0.2	-0.018	0.004	-0.015	0.003
	J1832-2039	238.530	0.7	-0.006	0.003	0.003	0.002
	J1916-2708	91.239	0.3	-0.022	0.003	-0.033	0.003